LBNL-40112
CONF-9608146--
UC-404

Proceedings of the Workshop on High Resolution Computed Microtomography (CMT)

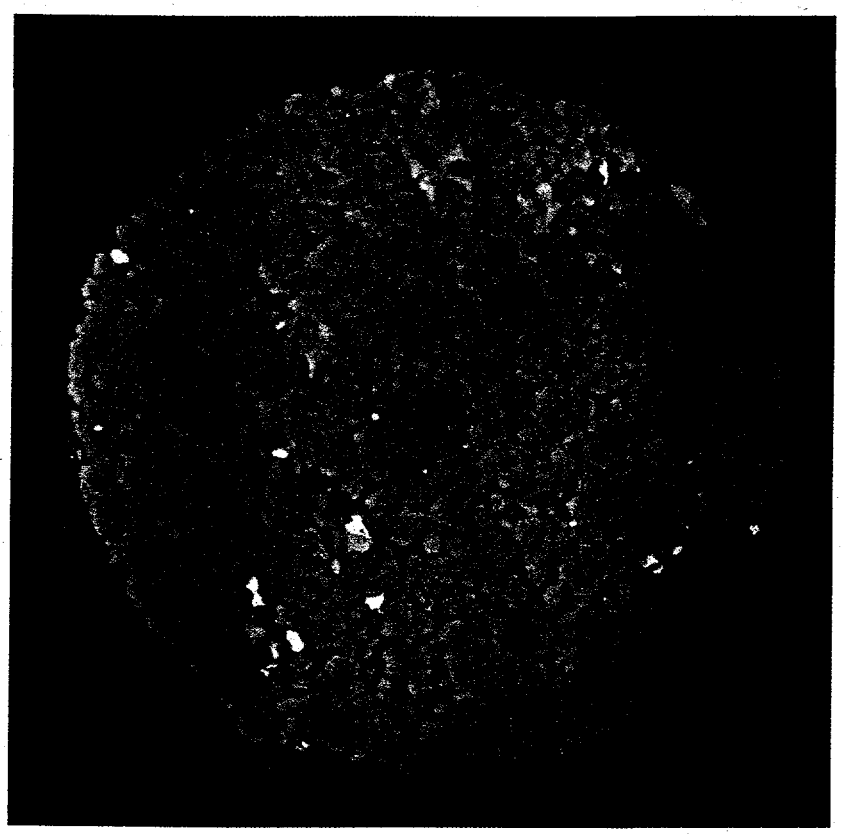

August 12-13, 1996

Ernest Orlando Lawrence Berkeley National Laboratory
University of California

CMT Workshop Coordinators
Erika Schlueter, *Earth Sciences Division*
Fred Schlachter, *ALS, Accelerator & Fusion Research Division*

Prepared for the U.S. Department of Energy under Contract No. DE-AC03-76SF00098

Proceedings of the Workshop *on* High Resolution Computed Microtomography (CMT)

August 12-13, 1996

Ernest Orlando Lawrence Berkeley National Laboratory
University of California, Berkeley, California

CMT Workshop Coordinators

Erika Schlueter
Earth Sciences Division

Fred Schlachter
Advanced Light Source
Accelerator and Fusion Research Division

February 1997

This work was supported by the Director, Office of Energy Research, Office of Basic Energy Sciences, Materials Sciences Division, of the U.S. Department of Energy under Contract No. DE-AC03-76SF00098.

TABLE OF CONTENTS

PREFACE

These proceedings of the High Resolution X-ray Computed Microtomography (CMT) Workshop, held at the Ernest Orlando Lawrence Berkeley National Laboratory (LBNL) on August 12 and 13, 1996, serve as permanent record of important worldwide research and development activities in computed tomography. The purpose of the workshop was to determine the status of the field, to define instrumental and computational requirements, and to establish minimum specifications required by possible users. The workshop audience included Advanced Light Source (ALS)/LBNL scientists and a number of invited guests, bringing together users and implementers from around the world.

The most important message sent by implementers was the reminder that CMT is a tool. It solves a wide spectrum of scientific problems and is complementary to other microscopy techniques, with certain important advantages that the other methods do not have. Therefore, because experiments have differing characteristic radiation specs, CMT should not be concentrated only at the National Synchrotron Light Source (NSLS), the Advanced Photon Source (APS), or ALS. Rather, it should be pursued at light sources around the world. From the users' point of view, materials scientists, for example, need to be able to further investigate the applications of three-dimensional imaging. Current training in electron microscopy and two-dimensional analysis of data misses the fact that there is a third dimension, which in some cases may significantly alter scientific findings.

Third-generation synchrotron x-ray radiation sources such as the ALS offer the advantage of high fluence, brightness, and energy tunability to the nearly collimated photons from the synchrotron source, along with the possibility of monochromatic measurements. This is particularly important in medical and biological applications. For medical applications, for example, use of monochromatic energy allows higher signal-to-noise and contrast ratios compared to conventional tomography — with the same adsorbed dose per subject. High-resolution CMT can be used non-invasively and non-destructively to study a variety of hierarchical three-dimensional microstructures (including bone, lung, liver and pancreas), which in turn control body function.

X-ray computed microtomography can also be used at the frontiers of physics, in the study of granular systems, for example. With high-resolution CMT, for example, three-dimensional pore geometries and topologies of soils and rocks can be obtained readily and implemented directly in transport models. In turn, these geometries can be used to calculate fundamental physical properties, such as permeability and electrical conductivity, from first principles. Clearly, use of the high-resolution CMT technique will contribute tremendously to the advancement of current R&D technologies in the production, transport, storage, and utilization of oil and natural gas. It can also be applied to problems related to environmental pollution, particularly to spilling and seepage of hazardous chemicals into the Earth's subsurface. Applications to energy and environmental problems will be far-ranging and may soon extend to disciplines such as materials science — where the method can be used in the manufacture of porous ceramics, filament-resin composites, and microelectronics components — and to biomedicine, where it could be used to design biocompatible materials such as artificial bones, contact lenses, or medication-releasing implants.

The proceedings include: summaries of the talks, copies of the viewgraphs, and transcriptions of the Monday and Tuesday discussion sessions. These discussion sessions ("User-Driven Microtomography Applications and Radiation Requirements" and "Technical Challenges and Strategies Towards Achieving High Resolution ($\sim$1 μm) Tomography") were especially timely and aided in the CMT user/CMT implementer interaction. The discussions complement the technical papers presented during the workshop and provide a unique opportunity for extensive interactions between authors and delegates and are a highlight of the workshop. All presentation materials received are included in the proceedings. The full workshop proceedings were also video-recorded and are available at the LBNL main library. Copies can also be ordered from LBNL Video Production Services.

The high regard in which the workshop was held by the research community is attested to by the nearly 50 participants from a variety of U.S. and foreign institutions who attended it.

Special thanks are owed to the team of scientists from the European Synchrotron Radiation Facility (ESRF): Per Spanne, Anatoly Snigirev, Irina Snigireva, Carsten

Raven, and Andreas Koch. Thanks also to all the CMT workshop invited speakers for their excellent scientific contributions and keen scientific insights into the CMT technique and its potential applications. Gratitude must also be expressed to others who made major contributions to the success of the CMT workshop: the LBNL Conference Coordination Group, Audio-Visual Services, the Technical and Electronic Information Department (TEID), and the administrative support staff in the LBNL Advanced Light Source (ALS) and Earth Sciences Division.

1996 High Resolution CMT Workshop Coordinators

Erika Schlueter

Earth Sciences Division

Fred Schlachter

Advanced Light Source

E.O. Lawrence Berkeley National Laboratory

February 1997

FINAL PROGRAM[08/08/96]

High Resolution X-Ray CMT Workshop

Lawrence Berkeley National Laboratory

Dates: August 12 - 13, 1996

Location: Bldg. 66 - Auditorium

Monday August 12:

7:45 - 8:20	Registration and Continental Breakfast	
8:20 - 8:30	Introductory Remarks	Brian Kincaid/Fred Schlachter (ALS)
8:30 - 8:55	CMT for Materials Science	John Kinney (LLNL)
9:00 - 9:25	CMT for Biomedical and other Applications	Per Spanne (ESRF)
9:30 - 9:55	High Resolution IVEM Tomography of Biological Specimens	David Agard/John Sedat (UCSF)
10:00	Break	
10:30 - 10:55	CMT for Transport in Porous Media	Larry Schwartz (Schlumberger-Doll)
11:00 - 11:25	Video, Transport in Porous Media CMT Results	Larry Schwartz (Schlumberger-Doll)
11:30 - 11:55	CMT for Soil Science Applications	Volker Clausnitzer/Jan Hopmans (UCD)
12:00	Lunch/ALS Visit & XM-1 X-ray Microscope Demo.	All/John Brown (LBNL)
2:00 - 2:25	Computerized Microtomography for New Applications	Al Thompson (LBNL)/Gene Ice (ORNL)
2:30 - 2:55	Video, New Applications CMT Results	Al Thompson (LBNL)/ Gene Ice (ORNL)
3:00 - 3:25	The Solid - State Signaling Pathway from Extracellular Matrix to Nuclear Matrix: The Critical Role of Three-dimensional Architecture at the Cellular Level	Sophie Lelievre (LBNL)
3:30	Break	
4:00 - 5:30	Discussion: user driven microtomography applications and radiation requirements	All
6:00 - 7:00	Reception	The Claremont
7:00 - 9:00	Dinner	The Claremont

FINAL PROGRAM[08/08/96] (continued)

High Resolution X-Ray CMT Workshop

Lawrence Berkeley National Laboratory

Dates: August 12 - 13, 1996

Location: Bldg. 66 - Auditorium

Tuesday August 13:

7:45 - 8:30	Continental Breakfast	
8:30 - 8:55	Bragg-Fresnel Optics: New Fields of Applications	Anatoly Snigirev (ESRF)
9:00 - 9:25	Phase Contrast Imaging with Coherent High Energy X-rays	Irina Snigireva (ESRF)
9:30 - 9:55	Reconstruction Methods for Phase Contrast Tomography	Carsten Raven (ESRF)
10:00	Break	
10:30 - 10:55	Holography and Tomography	Malcolm Howells (ALS)
11:00 - 11:25	High Resolution X-ray Microtomography of Biological Samples: Requirements and Strategies for Satisfying Them	Billy Loo/Stephen Rothman (UCSF)
11:30 - 11:55	High Resolution X-ray CMT: Reconstruction Methods	Keenan Brown (UCSF)
12:00	Lunch	
1:30 - 1:55	Requirements on High Resolution Detectors	Andreas Koch (ESRF)
2:00 - 2:25	Dose-fractionation Theorem in 3-D Reconstruction (Tomography)	Robert Glaeser (UCB/LBNL)
2:30 - 2:55	Post-processing Methods of Rendering and Visualizing 3-D Reconstructed Tomographic Images	Steven Wong (UCSF)
3:00	Break	
3:30 - 3:55	Neural Network and Its Application to CT Imaging	M. Nikravesh/Tadeusz Patzek (UCB)
4:00 - 4:25	X-ray Microtomography of Porous Media at BNL	Betsy Dowd (BNL)
4:30 - 5:30	Discussion: technical challenges and strategies towards achieving high resolution ($\sim 1\mu$m) tomography	All
5:30 - 5:40	Adjourn	Erika Schlueter/Fred Schlachter

LIST OF PARTICIPANTS

High Resolution X-Ray CMT Workshop

David A. Agard
Dept. of Biochemistry & Biophysics
University of California, San Francisco
S-964
San Francisco, CA 94143
(415) 476-2521
(415) 476-1902
agard@msg.ucsf.edu

Mark S. Amman
Lawrence Berkeley National Lab.
MS 70A-3363
1 Cyclotron Road
Berkeley, CA 94720
(510) 486-5638
(510) 486-5857
mark_amman@lbl.gov

David Attwood
Lawrence Berkeley National Lab.
MS 2-400
1 Cyclotron Road
Berkeley, CA 94720
(510) 486-4463
(510) 486-4955
dtattwood@lbl.gov

Tom Breunig
University of California, San Francisco
P.O. Box 0758
707 Parnassus Ave.
San Francisco, CA 94143
tbreunig@earthlink.net

Keenan Brown
Physics Research Laboratory
University of California, San Francisco
389 Oyster Point Boulevard
So. San Francisco, CA 94080
(415) 502-4495
(415) 742-0146
keenan@itsa.ucsf.edu

Jon E. Burger
Department of Petroleum Engineering
Stanford University
65 Green Earth Sciences
Stanford, CA 94305
(415) 723-6348
(415) 725-2099
jeb@pangea.stanford.edu

Chris Cann
Physics Research Laboratory
University of California, San Francisco
389 Oyster Point Boulevard
So. San Francisco, CA 94080
(415) 476-5026
(415) 476-0146
chris@imatron.com

Volker Clausnitzer
University of California, Davis
Davis, CA 95616
(916) 752-1372
(916) 752-5262
vclausnitzer@ucdavis.edu

Luc Derrendinger
University of California, Berkeley
145 Hilgard Hall
Berkeley, CA 94720
(510) 643-9951
(510) 643-5098
flocsim@nature.berkeley.edu

Betsy A. Dowd
Brookhaven National Laboratory
Building 725D
Upton, NY 11973
(516) 344-7092
(516) 344-3238
dowd@bnl.gov

Amitabh Garg
University of California, Berkeley
338 Hearst Mining Building
Berkeley, CA 94720
(510) 642-6286
(510) 642-3805
garg@patzek.berkeley.edu

Robert M. Glaeser
Lawrence Berkeley National Lab.
Donner Lab.
1 Cyclotron Road
Berkeley, CA 94720
(510) 642-2905
(510) 486-6488
rmglaeser@lbl.gov

Waleed S. Haddad
Lawrence Livermore National Lab.
P.O. Box 808
L-437
Livermore, CA 94551
(510) 422-6172
(510) 422-1796
haddad3@llnl.gov

David L. Haupt
Lawrence Livermore National Lab.
7000 East Avenue
Livermore, CA 94551
(510) 422-0242
(510) 422-2118
haupt1@llnl.gov

Jan Hopmans
Dept. of Land, Air and Water Resources
University of California, Davis
Hydrology Program
123 Veimeyer Hall
Davis, CA 95616
(916) 752-3060
(916) 752-5262
jwhophans@ucdavis.edu

Malcolm Howells
Advanced Light Source
Lawrence Berkeley National Lab.
MS 2-400
1 Cyclotron Road
Berkeley, CA 94720
(510) 486-4949
(510) 486-7696
mrhowells@lbl.gov

Gene Ice
Oak Ridge National Lab.
P.O. Box 2008
Room B260 4500 S
Oak Ridge, TN 37831
(423) 574-2744
(423) 574-7659
gei@ornl.gov

Galina Ishkhanova
Lawrence Berkeley National Lab.
MS 70A-3317
1 Cyclotron Road
Berkeley, CA 94720
(510) 486-7837
(510) 486-7152
gvishkhanova@lbl.gov

Brian Kincaid
Advanced Light Source
Lawrence Berkeley National Lab
MS 80-101
1 Cyclotron Road
Berkeley, CA 94720
(510) 486-4810
(510) 486-4773
bmkincaid@lbl.gov

John Kinney
Lawrence Livermore National Lab.
7000 East Avenue
Livermore, CA 94551
(510) 422-6669
(510) 423-7040
kinney3@llnl.gov

Andreas Koch
ESRF
BP 220
Grenoble, France
33-76-88-22-68
33-76-88-25-42
koch@esrf.fr

Yang-Mo Koo
Department of Material Science
POSTECH
Pohang, Kyungbuk South 790-800
82-562-279-2142
82-562-279-2399
koo@vision.postech.ac.kr

Anthony R. Kovscek
Earth Sciences Division
Lawrence Berkeley National Lab.
MS 90-1116
1 Cyclotron Road
Berkeley, CA 94720
(510) 486-5926
(510) 642-3805
kovscek@garnet.berkeley.edu

Sophie A. LeLièvre
Lawrence Berkeley National Lab.
MS 83-101
1 Cyclotron Road
Berkeley, CA 94720
(510) 486-4368
(510) 486-5586
lelivr@lbl.gov

Billy W. Loo, Jr.
Lawrence Berkeley National Lab.
MS 2-400
1 Cyclotron Road
Berkeley, CA 94720
(510) 486-7328
bwloo@lbl.gov

C. William McCurdy
Computing Sciences
Lawrence Berkeley National Lab.
1 Cyclotron Road
Berkeley, CA 94720
(510) 486-4283
(510) 486-4300
cwmccurdy@lbl.gov

Christopher R. Mitchell
ARACOR
425 Lakeside Drive
Sunnyvale, CA 94086
(408) 733-7780
(408) 732-1996
mitchell@aracor.com

Masoud Nikravesh
Earth Sciences Division
Lawrence Berkeley National Lab.
1 Cyclotron Road
Berkeley, CA 94720
(510) 486-7728
(510) 642-3805
mnikravesh@lbl.gov

Howard Padmore
Advanced Light Source
Lawrence Berkeley National Lab.
MS 2-400
1 Cyclotron Road
Berkeley, CA 94720
(510) 486-5787
(510) 486-7696
padmore@lbl.gov

J.R. Patel
Advanced Light Source
Lawrence Berkeley National Lab.
1 Cyclotron Road
Berkeley, CA 94720
(510) 486-6698

Tad W. Patzek
MSME
University of California, Berkeley
Evans Hall #591
Berkeley, CA 94720
(510) 643-5834
(510) 642-3805
patzek@patzek.berkeley.edu

Dale L. Perry
Lawrence Berkeley National Lab.
MS 90-1116
1 Cyclotron Road
Berkeley, CA 94720
(510) 486-4819
(510) 486-5686
dlperry@lbl.gov

Carsten Raven
ESRF
BP. 220
Grenoble, France 38043
33-76-88-22-61
33-76-88-27-85
raven@esrf.fr

Dale Sayers
Physics Department
North Carolina State University
Raleigh, NC 27695
(919) 515-4453
(919) 515-4496
sayers@pymvds.physics.ncsu.edu

Fred Schlachter
Advanced Light Source
Lawrence Berkeley National Lab.
MS 80-101
1 Cyclotron Road
Berkeley, CA 94720
(510) 486-4892
(510) 486-6499
fred_schlachter@lbl.gov

Erika M. Schlueter
Lawrence Berkeley National Lab.
MS 90-1116
1 Cyclotron Road
Berkeley, CA 94720
(510) 486-7154
(510) 486-5686
emschlueter@lbl.gov

Ross D. Schlueter
Lawrence Berkeley National Lab.
MS 46-161
1 Cyclotron Road
Berkeley, CA 94720
(510) 486-7405
(510) 486-4873
rdschlueter@lbl.gov

Lawrence M. Schwartz
Schlumberger-Doll Research
Old Quarry Road
Ridgefield, CT 06877
(203) 431-5210
(203) 438-3819
schwartz@ridgefield.sdr.slb.com

Horst D. Simon
Lawrence Berkeley National Lab.
MS 50B-4230
1 Cyclotron Road
Berkeley, CA 94720
(510) 486-7377
(510) 486-4300
hdsimon@lbl.gov

Anatoly Snigirev
ESRF
BP 220
Grenoble, France 38043
33-76-88-26-27
33-76-88-25-42
snigirev@esrf.fr

Irina Snigireva
ESRF
BP 220
Grenoble, France 38043
33-76-88-23-60
33-76-88-25-42
snigirev@esrf.fr

Per Spanne
ESRF
BP 220
Grenoble, France F-38043
33-768-82-647
33-768-82-542
spanne@esrf.fr

Ralph Steininger
Forschungszentrum
Postfach 3640
Eggenstein, Germany 76344
49-7247-82-6173/6171
49-7242-82-6172
ragt@anka.fzk.de

Diane E. Stott
National Soil Erosion Research Lab.
Perdue University
USDA-ARS
1196 Soil Building, Perdue
West Lafayette, IN 47907
(317) 494-6657
stottd@soils.ecn.purdue.edu

Al Thompson
Lawrence Berkeley National Lab.
1 Cyclotron Road
Berkeley, CA 94720
(510) 486-5590
(510) 486-4550
acthompson@lbl.gov

Tetsu K. Tokunaga
Lawrence Berkeley National Lab.
MS 90-1116
1 Cyclotron Road
Berkeley, CA 94720
(510) 486-7176
(510) 486-5686
tktokunaga@lbl.gov

Tamara Welcome
Computing Sciences
Lawrence Berkeley National Lab.
1 Cyclotron Road
Berkeley, CA 94720
(510) 486-4897
(510) 486-4300
tswelcome@lbl.gov

Heinz Weyer
Paul Scherrer Institut
Villigen, Switz. CH-5232
41-56-310-3494
41-56-310-3151
weyer@psi.ch

Stephen T.C. Wong
University of California, San Francisco
Room 158
530 Parnassus Avenue
San Francisco, CA 94142
(415) 476-6542
(415) 502-3217
steven_wong@radmac1.ucsf.edu

Jure J. Zaninovich
Lawrence Berkeley National Lab.
MS 70A-3363
1 Cyclotron Road
Berkeley, CA 94720
(510) 486-7542
(510) 486-5857
jure@ux5.lbl.gov

DISCUSSION SESSIONS

DISCUSSION (8/12/1996) - CMT WORKSHOP

"User Driven Microtomography Applications and Radiation Requirements"

Moderator: Per Spanne - ESRF

Per: Let's start this last session of the day which is going to be a discussion. The topic is "*User driven microtomography applications and radiation requirements.*" I start by making a couple of comments on this: I am coming from an institution (ESRF) where we are supposed to be user driven and 85% of our beamtime is devoted to outside users. I think that microtomography is a tool. It is not a science in itself, but a tool that we are going to use to solve scientific problems. I also think that it is important to realize that this is a tool in a whole arsenal of different microscopy techniques and it is complementary to all other microscopy techniques. It does not replace anything; it does not really compete, but it has certain advantages which other methods do not have. You could easily ask "Why do we even bother doing it at a resolution of one micron?" There are many applications where we can use its nondestructive nature, where the sample preparation would actually change the sample in such a way that we cannot answer the questions that we have. With those remarks I let you say something about this. I do not really know what all the user driven applications are because most of all the work (CMT) except for a bit of technical developmental work is user driven. Does anybody want to make any comment or say anything provocative?

Al Thompson teased me before his talk because I said it was important to talk about those things that were challenging and difficult to achieve and he finally said that after all, I did not mentioned anything and only presented results. So I will pay him back by telling him that he started his talk by saying that he was not going to present any results and that he ended his talk by presenting results. So I call that real fast progress. Is there anyone that wants to say anything about user driven applications? What do you want? I know what I want. My goal was to make a 256 cubed tomographic volume at 10 Hz, collect the data, reconstruct and display and update the display at 10 Hz. I think that is possible. Now after talking to Al I decided to update

the requirements so now I say I am going to do a 1024 cube instead of 256. Of course that is going to be very difficult, but I think that there are very interesting developments going on in the East Coast at Stony Brook with respect to the reconstruction and display part. Kaufman at N.Y. State University at Stony Brook is developing something that he calls "the cube" which is a display machine. He said at a lecture that instead of storing the data in real space he was going to store it in Fourier space. I said 'wow', then we have the reconstruction automatically, because if we can store the data in Fourier space and he can display it, that essentially means that he is taking the inverse Fourier transform of the data. That is exactly what we do when we do Fourier reconstruction. So maybe this is not just a dream, but something that is going to be possible to realize within 5 to 10 years, I would guess. There is a user requirement for materials scientists. I think that John Kinney touched that issue. Also Al Thompson is studying for example crack propagation in modern composite materials in real time. We cannot study fluid flow in real time, for the reasons that I mentioned earlier because if we have a 10 Hz update, the sample will spin with 10 revolutions per second which is significant. So what do you want? We heard one speaker who wanted 50 μm spatial resolution.

Ralph Steininger: Can CMT be used to study problems in coal production?

Per: Of course, you can put anything into the beam you use for microtomography, but it is not always possible to visualize what you want. You are severely detection task limited and you always have to keep in mind what it is that you want to see and so as a user you have to choose your x-ray microscopy method in general and I do not know if microtomography is specially good for what you want to do.

Fred Schlachter: May I present two viewgraphs? Not to worry, this is not a talk, but I would like to emphasize the point that I hope I made during the Advanced Light Source (ALS) tour and that is that third generation light sources have high brightness. Brightness is not an intuitive concept; that is why I want to show these viewgraphs. The point here is that if you are trying to fill a tea cup and you have

(a) a rain cloud. You can make a lot of water but it does not necessarily go in the cup very efficiently. Obviously using (b) a sprinkling can is better and using (c) a tea pot of course is the best. The analog would be for a laboratory x-ray source, '(a)' would be a light bulb '(b)' would be a First/Second generation light source, and '(c)' would be a third generation light source. So, what has the progress been? You have probably all seen this viewgraph from Scientific American where the vertical axis is brightness and the units are photons per second per unit source size per unit solid angle per unit bandwidth and what it means is putting photons into a small spot. The progress here for many years if you look at the blue line is quite flat and then with the advent of light sources the brightness has gone up several orders of magnitude. With the exception of computation and information science it is very rare to have any technology that goes up orders of magnitude per decade and that is the opportunity that we have here. So when you are thinking about applications, think about what previously was done on homogeneous samples is now done on heterogeneous samples or on small samples where the only useful photons are the ones that illuminate the sample. So in a porous medium, for example, if it were a small sample or small pore sizes that you are looking at, this is the opportunity. Now I also want to remind you that the light source is only one component of this and it is increasing very dramatically. The next component is detectors and one of the talks this morning emphasized the developments at the European Synchrotron Radiation Facility (ESRF) and the comparable developments here of very high speed, high resolution imaging detectors. One of the later talks emphasized the sample handling at a particular beamline here "the x-ray microscope," where the sample could be placed to a 100 nanometers repositioning accuracy. The third area of course where there has been enormous progress is in data acquisition and processing. We heard about 3 Gigabyte data sets and so on. So, we have had progress in all three areas: in the x-ray source, in the detectors, and in the data acquisition and processing and that is the opportunity. That is all I want to say. I will be glad to answer any questions regarding the Advanced Light Source (ALS) and third generation light sources.

Per: Thank you. More comments?

Howard Padmore: Here is a question to people here about microtomography: What is the ultimate spatial resolution of the technique? The presentations which have been made today work in one particular mode which is a plane wave transmission mode. I was particularly wondering whether people have thought about other point source geometries where you can take advantage of the superb microfocussing techniques that we now have available such as Bragg-Fresnel optics and zone plates. Perhaps we ought to talk a little bit about the ultimate spatial resolution of this technique, because it seems to me that right now it is disconnected at a few microns level from other types of x-ray microscopies which have already achieved angstrom resolution.

Anatoly Snigirev: If you are talking about high energy x-rays (energies more than 6 keV) you can employ Bragg-Fresnel optics but I am sure that during the next 10 years we will stay at a spatial resolution no better than 0.1 microns first of all due to technological limits in the production. And secondly you would have no contrast from the elements smaller than 0.1 microns with this energy even applying holography or phase contrast imaging. This is the limit I think for the next 10 years because it is quite difficult to make the optics smaller than 0.1 microns fringe size for high energy x-rays. It is not comparable with soft energy x-rays. You can forget about absorption at this resolution because there is no absorption. You can apply the phase contrast technique. For carbon base materials with a size of 0.1 microns you can get a few percent contrast at 10 kev. This is the limit, and there is no technique better than phase contrast at the moment.

Howard: We are interested in studying microelectronics structures.

Anatoly: But for that you can use other techniques such as topography, high resolution diffraction techniques.

Howard: We would be interested in aluminum cubes which might be say 20 or 50

microns on edge. So in that case there might be a possibility of imaging with high contrast perhaps down to 1000 angstrom resolution.

Anatoly: So then you need to use Bragg diffraction. This is the easiest way and most sensitive to make stress analysis. So you should have a monochromator and a double crystal spot and you can apply this tomography technique to treat the data somehow.

Howard: But there are two problems: One is physical motion of the aluminum interconnect which attract within a SiO_2 structure and physically you can actually see the structure move. Secondly, there is another problem which is due to stressing individual micrograins in the structure. This second one is being attacked by various people here by using microdiffraction.

Anatoly: For that you can combine this double crystal geometry with the micro-probe technique, which is what we did for the Siemens people when we used this for a laser structure analysis and it is possible of course.

Howard: But we are dealing with three dimensional reconstruction techniques at very high resolution and not plane wave. So you are limited by the resolution of your detector in that case. Is that right?

Anatoly: Yes, if you use the plane wave you are limited by the resolution of the detector but you can use a focused beam and it is going to be 0.1-0.3 microns so you can scan this easily.

Howard: The only example I know of right now, and perhaps you can correct me, of that technique being applied in x-rays is by some people in the soft x-ray group at Stony Brook (Janos Kirz's group), who did a test experiment using about 20 angstrom radiation looking at some artificial structure. It was a very small structure

as well. It was a tomographic reconstruction where you had x-ray scanning and you had formation of a microprobe using a zone plate and I think they achieved a 3D reconstruction of about 10 angstrom resolution. But nothing similar has been done at harder energies I think.

Anatoly: At submicron resolution not yet.

Howard: My question was really to motivate the discussion on what are really the intrinsic resolution determining factors in different energy regions for microtomography. Right now for high energy photons, one seems to be the resolution of the detector if you use the conventional plane wave approach.

Anatoly: Yes, the only way is to use a point source, to have some magnification, and this can be done with the optics as well, or you need to optic after the object and to magnify the image and this is possible with Bragg-Fresnel optics to have a 0.5 micron resolution. We want to go in this direction. It is the only way to have submicron resolution with high energy x-rays.

Howard: Are people working on optics as magnifiers?

Anatoly: No, I do not believe that it will work.

Howard: Because people are getting to take 0.3 microns as the actual size of a microcapillary.

Anatoly: Don Bilderbeck got this result with 500 angstrom resolution.

Howard: That was a single capillary. But I am talking about polycapillaries.

Anatoly: That is not optics it is just a collimator. It will never work like the imaging optics.

Howard: But it can be used as image expander.

Anatoly: No, if you are looking at the surface in inner capillaries the slope error or different deffects are higher than microradians scale for high energy x-rays and you need microradian accuracy of this kind of optics. So, you can forget the capillary like an imaging optic. Even a mirror is difficult to polish with the quality better than one microradian so how can you polish a capillary? It is impossible. So I do not believe in this kind of optics. It is not even optics, right?

Howard: We can talk about it off-line, but I mean that the x-rays are contained within a single element of the polycapillary array, you do not have to focus with the thing. You just use it as a beam expander.

Anatoly: Did you see the image of the capillary at the ESRF for example. It looks like a mess. It is not a spot, it is something different.

Howard: Maybe we need a pencil and paper to explain each other's point.

John Kinney: I guess I have been drinking too much coffee, but once it comes out of the capillary it is diverging with a critical angle at least of the reflection and so you are talking about measuring volume now and not doing point source imaging like a scan of a fluorescense map in 2D. I think that is one of the issues. The second issue with integrated circuits is that you have to have very good friends in the integrated circuits community because they usually give you a chip that has all the gold and then they say "well, we may have a 'delam,' can you find it?" We say we will take the gold off and then they say "no, we cannot, this is the only one we think that has

a 'delam' there." So there you sit. You have something that is gold and something sitting right next to it that is silicon and it is very hard...

Howard: That is a very interesting point. One of the problems that we have in general in microscopy treatments, is a general form of microscopic problem is that a microelectronics manufacturer will give you a circuit, and like you say, it is almost impossible to find the point which the manufacturer is interested in on that circuit. So one of the things that we are building in, at their request, (and we have a number of collaborations with Intel Corporation on this point) is absolute fiducialization of samples and absolute encoding of the sample in the sample holder to sub-resolution precision and that in some cases is a more severe problem than actually forming a microimage in the first place.

John: Can I show one picture? This is a typical package that we get from the manufacturer that is sitting on a Kovar backing with silver epoxy. This is a radiograph and this is the best we can do in a tomogram. We are not really set up very well. These are 5 μm Al onto Si. The mechanism for contrast here I think cannot be the micron-thick Al coating Si. One of the prime sources of the contrast here, we think, is reflection at certain angles and reflection looks like absorption so most of the data, most of the information is not in the planar view. It comes as the sample rotates to the point we are looking at the edge of the sample. And you can pull out another case. This is a case where the contrast on the edge of the Al here is a barrier coating. That is a 70 nanometer barrier coating, so I am tempted to say we have 70 nanometer resolution but unfortunately if you map this out we have 2 microns instead of 70 nanometers. So I think you can do these varied structures but I am not convinced that tomography is the best way to do it. I think it is an Al Thompson's case here where laminography or planar methods might give you more information. I think that maybe it is that we do not have any capital equipment money but everybody talks about hardware and all that. One of the things I think it is important to emphasize is also what you do with three-dimensional data and why do you take three-dimensional data. It is a huge amount of storage. One of the volumes we talked about was 3 Gigabytes of vol-

ume and then we store hundreds of samples and why? What is the advantage of 3D? One of the things that I still think we need to investigate more of are applications of three-dimensional imaging because we are all trained, if you are in material sciences, to do electron microscopy and two-dimensional analysis of data and this is the story of flatland. You are sitting on flatland. Have you heard the story of flatland? It is a hundred year old story about a 2D world populated by polygons and a square is visited by a sphere who lifts him off the surface of flatland and he can see his 3D counterpart, a cube, and then he comes back to flatland and he tries to convince everybody that there is a third dimension and he is branded heretic and he is put in jail and even looses the memory of what the cube looked like. So I think that one of the things, that when we start thinking in 3D data, what you are going to have to ask yourself is "can I convince the people who really want to know structural information that we should give them 3D data," because once they find out how difficult it is to handle it, and even with the nice array processors, even with an alpha workstation to handle a $2000 \times 2000 \times 2000$ array for your data analysis, the question is do you really need this information? And I think that scenario is what you have to be careful about.

Howard: I agree with that. Just to take the example of the microelectronics industry a little bit further: you have a whole array of different imaging techniques. One is to use an electronmicroscope; you look at image changes which are injected into the surface. You very often know exactly where there is a fault or something going wrong or something strange happening in a circuit. So one of the things that we would like to do is to be able to have a three-dimensional image of just that local area. So the fiducialization, being able to go to exactly to a 1 μm spot or a $(10\ \mu\text{m})^3$ area around the fault region is very important. What we are doing in other areas right now is that is we think we know that area, we actually microcleave the area and then with other x-ray microscope probes or electron probes we look at local surface chemistry in that area. So perhaps sometimes you do not need 1024^3 arrays of data, you just need sparse sets of data around something that is already identified.

John: I think that you can do that now because you can take advantage of some

other weird effect. If you have this barrier interface you can actually reflect inside that interface. And now you will see for example if you look at something dead online you can see very nice effects because light is reflected at the surface of these cracks.

Howard: Another point of very high resolution is that a lot of structures we have started to look at now, because of the shift of the microelectronics industry from Al Si and SiO_2 technology, to replace dielectric with high temperature analogs of polymides. The whole structure becomes very low Z. We are interested in the structure of the Si-Al, polymide interface and so this possibly opens up a way to do tomography at much longer wavelengths because we do not have very absorbent structures there involved.

Per: I would like to comment on your statement that somebody had made a 100 nanometer resolution tomogram. I claim that this is wrong. Nobody has achieved that. It was done as a tomography experiment at Stony Brook and if you look into the data you first of all find that, they undersample in angle and secondly you realize that with the zone plate you are focusing, you are creating a divergent beam which blows up significantly in the sample and I think that if you only take that into account, which means that you only have this 100 nanometer resolution in a focal spot. If you take that into account, you will end up with something at best 0.6 microns, if I remember the numbers correctly, and if you take the care to look at the data that was presented, the only frame that gives really good tomographic section is the plane that is perpendicular to the rotation axis. You can see that the rectangular structure is very badly distorted; it is almost an ellipse. So they might have reached, perhaps, slightly below a micron but definitely not an order of magnitude lower. I think this is one of the main problems with these focusing methods. In all of them the beam expands in the sample as it passes through because the beam has a finite extent. It is the divergence of the beam that counts if you look at the submicron capillaries. Stony Brook's experiment is a tomography experiment but it is not correct to say with a 100 nanometer resolution.

Anatoly: I think that they are right to write this paper and cite these numbers. How they measure it is defined in the paper. Nobody could repeat this experiment in the future I am sure, but still the paper is published and we should use this result as a reference.

Per: Yes, but if you clearly can show that the resolution is not submicron, I do not think that is correct to say we can achieve this.

Howard: A comment about detectors. I have been to a few talks today and some people have made some comments about limitations of the current generation of CCD detectors. I am not sure that people are aware of this or if it is even particularly applicable, but there is a new generation of x-ray detectors based on individual pixels. We have a program here at LBNL for protein crystallography to develop and to use this new type of detector. The difference in comparison to a regular CCD is that under each sensing element of the detector there is a single preamplyfier-amplyfier discriminator and prescalar and each individual element is its own separate counting channel. So our aim is to produce an array which has several thousand elements. The elements right now are 150 μm^2. We only make right now 16×16 arrays. This is the basic building block of much larger detectors that will be made in the next couple of years. The specifications of these types of pulse counting detectors is that they count about 1 MHz per channel per second. So they can handle very high data rates and you do buffering on the chip so you do not have to read out at that rate; you can pre-scale by any factor that you want. You may be able to just read it out every second or every 10 s or every 100 ms. We are particularly interested in this for dynamic experiments where we are actually reading out detectors "on the fly" in real time, rather than reading out CCD's on a serial basis. So I think this will become fairly accessible technology in the next 2 or 3 years.

Per: What is the pixel size at the moment state-of-the-art if you want high resolution?

Howard: State-of-the-art I guess is here at LBNL and is 150 μm. I think there is shorter prospects of going down to 100 μm. The microelectronics is under 1 pixel. We are actually fairly conservative now, as we are only using about one quarter of the area of 1 pixel for the microelectronics and we are using a Hewlett Packard 0.65 micron metallization process. So in the future if we go to 0.35 μm then we will potentially be able to go down to a few microns pixel size.

Per: That is a very exciting development and will be able to play a big role in medical imaging in the long run.

Howard: The one that we are developing right now is for medium energy x-rays (10-12 keV). That is really limited by the type of detector front end that you use. The current version is a Silicon pin diode array, which is then bonded onto an applications-specific integrated circuit which has microelectronics under each pixel. We are working on detector arrays made of Cadmium-Zinc telluride. We have actually made one of these. The only problem over and above using Silicon is that they are much more fragile. Those are designed to work up to 30 keV. It is a much higher Z-material and you can work up to a much higher energy.

Per: One thing if we really want to go down to 0.1 microns we need to put an effort into the movement of the stages. We need a controlled environment to be able to reach the accuracy and precision we need when we do tomography. Well, after all, we need to rotate the sample, but it's technically possible.

David Haupt: I think that Sandia Corporation in Florida has recently put up a set of stages supposely certified for around a 25 nanometer repetition that certainly gets you into the ball part. The problem that I have noticed for a long time is that everybody doing tomography is basically dealing with a light microscope. We are taking an image off the scintillator of some type and blowing it up onto the camera and you are not going to do much better than 0.6 microns operating like that. I

think that probably the finest microscope objective made is a Zeiss with a numerical aperture around 1.43 or so. It is going to have to be done with true x-ray optics so that you can really accomplish it, I think.

Per: We will hear more about x-ray optics and detectors tomorrow. So, if nobody else wants to say anything, we close this discussion. Thank you very much.

DISCUSSION (8/13/1996) - CMT WORKSHOP

"Technical Challenges and Strategies towards Achieving 1-μm CMT"

Moderator: Ross Schlueter - LBNL

Ross: I have a couple of items to start the ball rolling. I would like to know if someone could comment on how the different optimum x-ray energies for various experiments/applications might affect the choice of optics, detectors, etc. In particular, for example, how would a 7 keV experiment and a 10's of keV experiment be compatible with one set of beam optics, detectors, etc?

Tom Breunig: At lower energies what you need to use for light conversion is going to be different than what you are going to need at higher energies. Thickness is going to play a role in what you have there, total stopping power is going to come into play as well as if you are going to try to get extremely high magnifications on a small sample we see from a lot of the medical applications dose sensitivity comes into play. The whole detector package has to really kind of reflect what you are trying to image. If you are trying to do phase contrast imaging what you need there is very different from what you need for straight transmission.

Ross: So, if you have a different set of users here from the biomedical community and for someone that wants to measure frog legs and someone who wants to measure the Berea sandstone, we have to have different beamlines set-up to do the experiments?

Tom: The basic beamline set-up can be the same, e.g., a monochromator with multiple silicon crystals for doing things. What is going to change is the detector package. If you need extremely high spatial resolution, as was mentioned yesterday, the staging for positioning the sample becomes very critical. It is a question of if you are looking at a large object, i.e., a rock versus something very fine, i.e., the holy grail for the biological stuff at 10 or 20 nanometer scale, then the size of the field becomes very

important.

Per Spanne: I believe that you not only need to tailor your detector to your detection task, but I think you need to choose the source out from your detection task too, so microtomography should not be concentrated at the ALS, APS, or NSLS, it should be driven in all places. My management at the ESRF has asked me if we should build a microtomography beamline at the ESRF and I have said not yet, I need to know how big the user community is. Also because I want to go to different beamlines because they have different optics and different characteristics and the sample range is enormous. We are talking about of a couple of hundreds eV's up to 50 keV and there is no universal equipment that is going to handle all of those things at the same time. It is a compromise: detector resolution and energies, always a compromise.

Tom: We have seen that people want more divergent geometries, while some others want more parallel geometries. So just based on that alone the source characteristic you need is going to have to be variable, in which case the investment is huge, or there will have to be multiple facilities that are each tailored to a certain range of applications.

Waleed Haddad: I would like to extend it into the area of x-ray optics as well, which also has to be tailored for the imaging application, especially as it connects in with the original subject of the discussion which is to push below one micron resolution, in which case you really need to do something with x-ray optics. For example, in the case of zone plates you certainly need to design the zone plates specifically for the energy range that you are using, in terms of the materials that are chosen and the geometry of the zone plate. And it may in fact connect in with the choice of the source because if you wanted to use a zone plate to produce a microfocus for a scanning probe type of experiment you want to have a coherent source which points you towards the use of an undulator or something like that. And of course if you are using mirrors or something like that to produce focus, they have to be designed for the specific energy range. So it also pertains to the x-ray optics as well.

Andreas Koch: I would like to make a comment about detectors. I don't think it is a question of a compromise just between technical specifications, but also between the time you want to spend to get a device (a detector) and the money you want to spend. So my question to the community is what are you willing to pay and how long do you want to wait for for it, and even more so, are you willing to follow up different approaches. We could imagine to have a short-term developing project which is not very risky, where you know what you get in a certain time, and on the other hand you could imagine in parallel to do some ambitious development project where you really do not know what will come out. Are you really willing to finance it, I would like to know.

Anatoly Snigirev: For example, if you want to build a beamline dedicated to tomography specifications for tomography at 1 μm resolution at 10 keV it is quite attractive to use an undulator source without a monochromator, but if somebody wants to use mirrors, I want to show you the image of multilayers and mirrors so this is one example so we can easily use this high resolution film 1 micron to achieve. But you have to be very careful with this kind of optics. This is just paper that you put in the beam so you have to be very careful with the filters that you want to put in the beam with 1 micron tomography. For example, this is 20 μm Aluminum foil it was done for a few months at the bending magnet at the ESRF. It is slightly melted. So it seems to me, you can see a lot of artifacts afterwards in your imaging facility if you put in such a filter. Concerning the monochromators, if your monochromator is not polished correctly, you can see these microscratches. They are 1 micron but becoming larger if you move it further. So, it is really a nice image you can obtain at the tomographic facility. Now, concerning the mirror once again and yesterday we discussed this point can we use these mirrors "to expand" the image. With the mirrors it is in principle possible, but this is the best available mirror, 70 cm long. It is polished one microradian slope error and less than 1 Angstrom roughness, but you can see a lot of thin fringes coming from low frequency modulated surface of the mirror. This as done at 12 keV. So you have to be very careful with this kind of thing, even if you have the

best mirror from General Optics. If you have this image, let's say this holographic image, and if you want to transfer this image to the mirror and if mirror is after the sample it is not so bad, it works. But if the mirror is before the sample you can see it degrades the appearance of the beam. So, in principle the mirror can be used to transfer the image and to expand the image, but the acceptance of the mirror is limited. So it can be used to fix the resolution of the CCD detector. Concerning the multilayers, (this is a multilayer), so it has completely spoiled the imaging facility. So I am not sure that multilayer can be used as an imaging device. This is a best multilayer, the same General Optics stuff and multilayer tungsten silicon made at the ESRF. So, I am not so optimistic about this. And concerning the sources, I just want to show you one demostration. We do not need the ESRF for phase contrast imaging. These are from my colleages in my former Russian Institute. They use a Microflex generator, so they use a silicon crystal 3 microns in this direction, what we use for phase contrast imaging, and they put in some fibers and they easily observe these tomographic images of the different hairs. In principle in some cases you can build this facility in the laboratory. So you can see a lot of things using this microfocusing generated in the laboratory. So this I want to comment concerning the optics requirement. And a last point - Yesterday we discussed for microelectronics structures how to probe the different layers and this coherent imaging can be used. This is an example of the SiO_2. If you use some simple topography image you have this contrast from the SiO_2. But if you move this detector further away, I mean 0.5 of a meter, probably you can see this holographic image due to the streaks you introduce in the Bragg refractive layers and probably this is one of the ways to scan this structure. To change the Bragg angle you can probe this structure in the depth if you have a multilevel system and this coherent imaging can help you a lot. So this is another example of this SiO_2. Now you can have a holographic image of different layers of SiO_2. This is one of the ways, but it is not completely tomography in this particular case.

Ross: Another question that I wanted to ask the community is that here at LBNL we have this new supercomputer center called NERSC. I would like to know as we

go to higher resolution if someone could comment on the need for supercomputers in either data collection, storage, data processing, reconstruction, visualization, or post processing.

Bill Loo: I am not really familiar with the Thinking Machine but I know one of the machines here and I think the actual name of the company is "Maspar." I forget how many processors it is, a few thousand processors each with its own memory and it is good for processing array type of data. So essentially tomographic type of data is a good candidate for this type of computer. I think this was here before the NERSC Center was moved here so there are other computers in addition that I do not know about.

David Haupt: We were approached by some people a few years ago in trying to raise interest in our using it. They had realized that they had to come up with more local work orders or they had to go somewhere else. The problem that we ran into was that there was going to be very substantial software development cost and we really did not have tomographic algorithms and things like that already in place on the machine. They had all kinds of magnetic hybrid code type stuff. There were some people at Los Alamos that had software but for a slightly different machine. So there is a possibility that this stuff can be rounded up within the system but I suspect that there is still going to be software development involved. We more or less decided that it was cheaper and easier to keep upgrading our own workstations. We have an alpha model 900 now and we find that gets done most of the things that we need to do if not the same hour, at least overnight. They had a few people at Livermore (Joe Huang) I think, that was getting good use of those supercomputers for his work. I really do not know much of that facility though. It was kind of isolated from us.

Tom: Part of the concept, the need for the possibility of using the supercomputing facilities: if you are going to have a user facility on site dedicated to tomography, you either have to send people home with the raw data and let them deal with reconstructing it or set up the facility so that once the data is collected it gets fully

reconstructed on site either locally on a workstation or by submitting it to the supercomputer facility and sending the user home with a large 3D volume set. That would be the real use of the supercomputing facility: sending the user home with that data taken care of and then it is up to them to deal with analyzing what they have.

Bill: I would like to make a comment about the usefulness of the supercomputer facility. For the kind of experiment that I would like to do, like I was showing at the end of my presentation, the automatic segmentation, where I am collecting population statistics. That kind of information is not really useful on just one image. Really what I would like to be able to do is to do a similar kind of analysis on hundreds or thousands of images and then we are talking about 3D data sets. And if you have one 3D data set you might be willing to wait overnight or even a couple of days to reconstruct it, but if you are reconstructing hundreds or thousands you cannot wait overnight on each one. So that is a potential application area for supercomputing.

Per: I think you have to be careful when you start discussing this computer topic because it is easy to go beyond the reconstruction, but I do not think you should do it. My advice is to leave to the user to do the analysis. You could perhaps implement some good reconstruction algorithms and do it for him/her but if you go beyond that you are going to need big stuff. And with the CCD detectors today, it is enough work to do the reconstructions. At the ESRF, the management has decided that we are not really going to do the reconstructions other than in the case for "in house" research.

Larry Schwartz: I will just make a comment. When you get involved in using a supercomputer, you will be sharing it with many other users so the apparent increase in clock speed will be rapidly diminished. So many groups just find that it is more useful to get a really strong dedicated work station so that they can write a special purpose software for it and use that as their machine. For massively parallel computing, the codes are not terribly difficult to write, but you quickly get into situations where there are a lot of people using the machine and there are hundreds or thousands

of processors that have to be partitioned and you may get, for example, 50 processors for two hours next Wednesday.

David: The NERSC at the Lawrence Livermore National Laboratory (LLNL) machine was designed to handle an enormous user load distributed essentially worldwide. There were big microwave satellite links into it so it does have a tremendous capability to handle multiple users so that may not be quite such a problem. I am really not an expert on it but most of what I know about it I read in the Lab newsline and by talking to several other people. It probably would not be as unpleasant an experience as running "batch mode" on an old IBM 360 was.

Larry: That was before my time.

David: Are you kidding me? As far as a user facility capability regarding an imaging beamline, it would be nice to have in such a facility the best monochromator and collimation equipment that modern technology can provide. As far as what kind of equipment is in the hutch where the users access it, I think it might be nice to have a very high quality state-of-the-art CCD camera and excellent optics for imaging scintillation detectors, but leaving it to the user to provide their own individual detector or scintillator. They would be somewhat constrained, but I think they would probably be able to design something that would fit the existing hardware. Possibly also you can provide a good set of stages and again, assuming it came from a company like Newport or Huber, that people could have the drawings on hand to design their own individual sample apparatus to fit. We certainly see a lot of that at Stanford Synchrotron Radiation Facility (SSRL) where people show up with boxes of little goodies that they have designed and they put them in place and proceed to work. Regardless of what kind of computer facility is available, we would never consider leaving the facility without the raw scanned data on tape. If there were further facilities for instantaneous reconstruction and so on, we probably would make use of that, but if we got home and decided that anything looked funny we probably would end up doing it all over again in that case.

Ross: I have one more item that I would like to give those of you who are out of town guests, that were not speakers, the opportunity to tell us what your CMT application or interest is. Ralph, John, or Diane?

Diane Stott: Basically what my interest is looking at the interior structure of soil aggregates with aggregation size anywhere between 50 μm and 2 mm in diameter average. The first step in soil crusting and surface sealing is the breakdown of soil aggregates that leads to soil erosion and what we are trying to determine is how management impacts soil aggregation, how the aggregates form during time because some of this happens seasonally, how organics that are present in the soil impact the aggregation process since it is a biological process, and there is no way right now that we can look at in-situ what is happening inside an aggregate. We only see the exterior, we can look at the aggregate visually and see what the exterior is like. We also have no way that we can look at the interior structure and be able to test that same aggregate on terms of slakeing and mechanical breakdown. And that is the biggest use I can see of CMT, is being able to look at that interior structure and still have that intact aggregate to test slakeing and mechanical breakdown.

Ross: Are there any other topics that anyone else would like to bring up before we close? If not then I will turn the closing ceremonies over to Erika Schlueter and Fred Schlachter.

SESSION I: MONDAY AUGUST 12, 1996

The *In Vivo* Microscope

three–dimensional characterization of skeletal structures with microscopic resolution

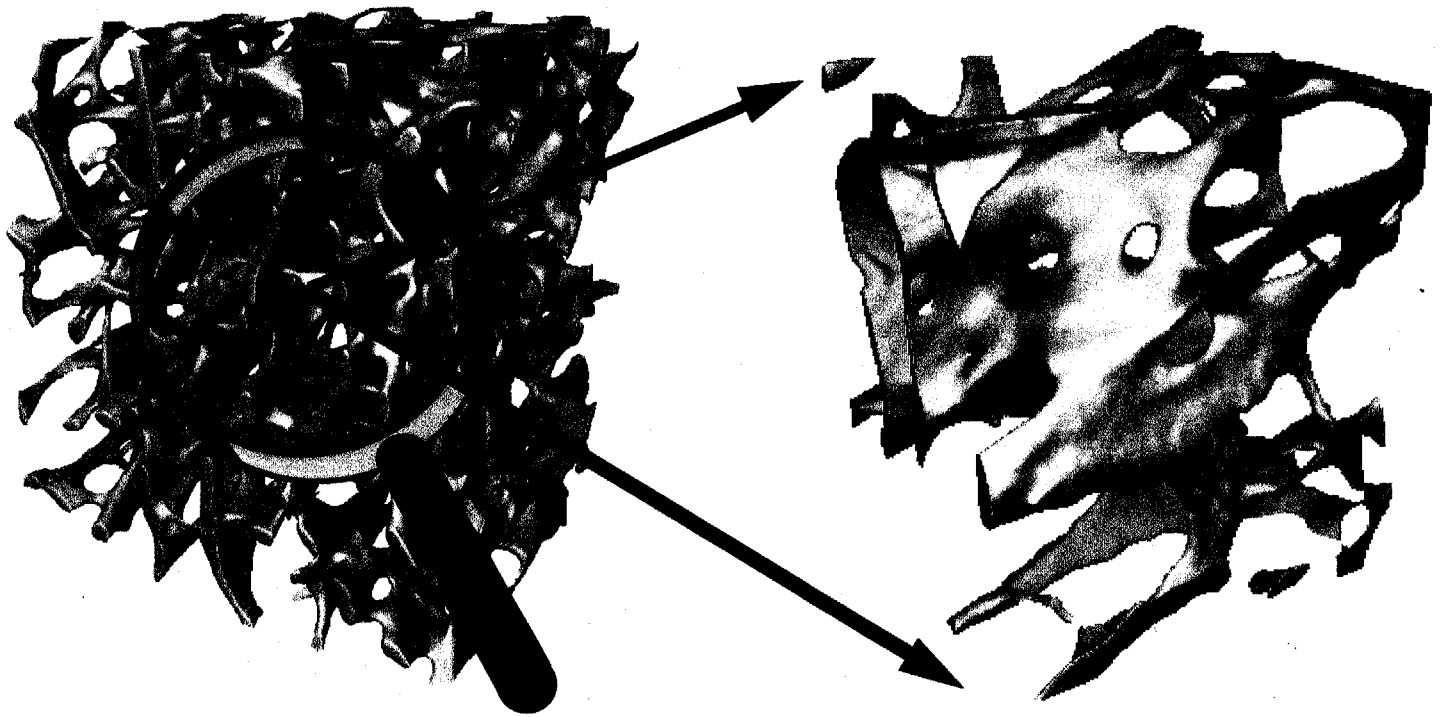

human proximal tibia **higher magnification view**

(9 μm voxels)

John Kinney

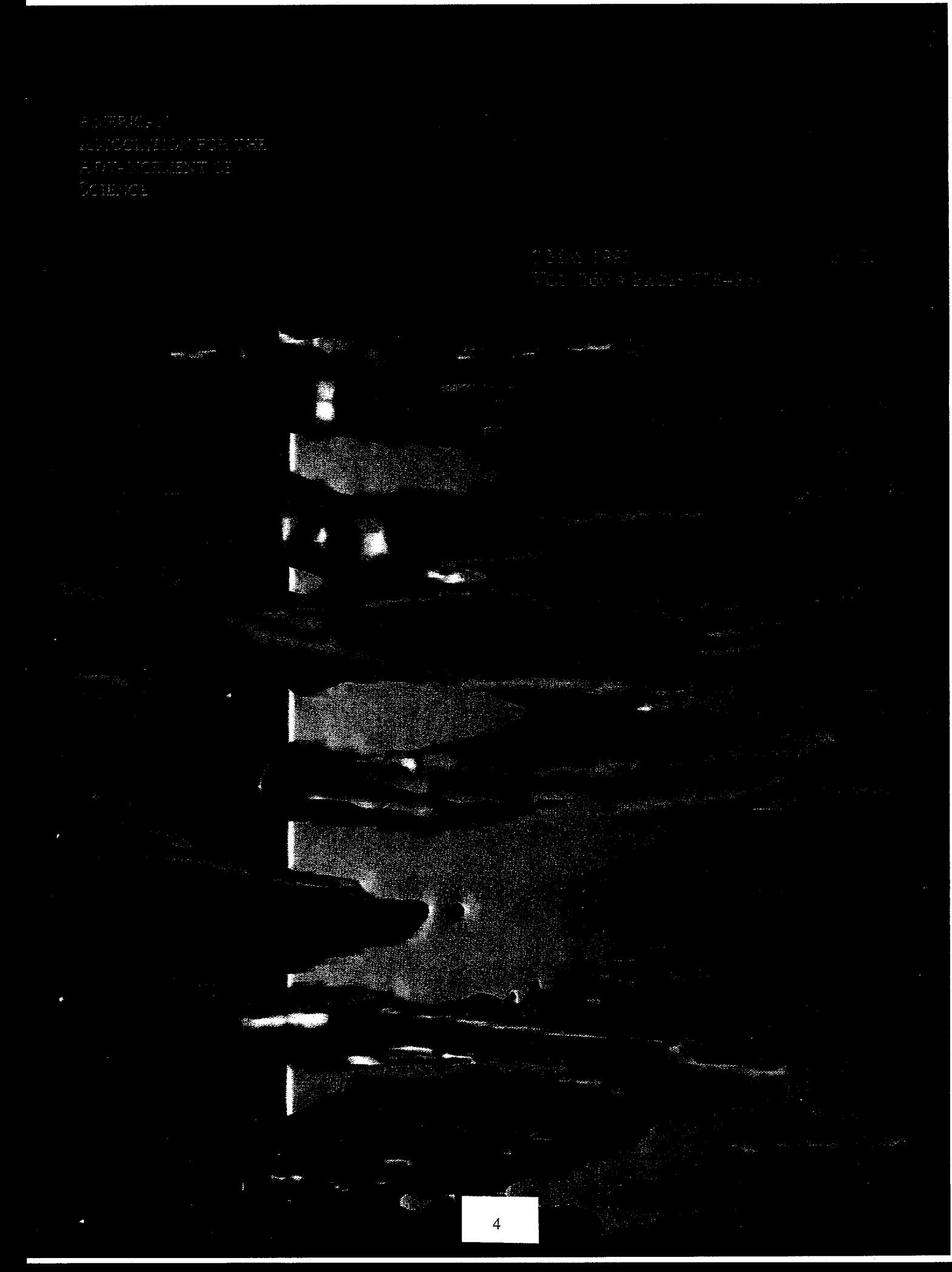

JOURNAL OF BONE AND MINERAL RESEARCH
Volume 10, Number 2, 1995
Blackwell Science, Inc.

In Vivo, Three-Dimensional Microscopy of Trabecular Bone

J.H. KINNEY,[1] N.E. LANE,[2] and D.L. HAUPT[1]

ABSTRACT

Osteoporosis, which is correlated with low bone mass and increased bone fragility, is responsible for about 1.2 million fractures per year in the United States. We have used the three-dimensional (3-D), X-ray tomographic microscope to image the trabecular bone architecture of the proximal tibias of six Sprague–Dawley rats in vivo. Three of these rats were then ovariectomized to induce estrogen depletion, and three remained as controls. Five weeks later, the tibias were reimaged. The ovariectomized rats lost approximately 65% of their trabecular bone volume as compared with an insignificant change in the control rats. The connectivity density of the trabecular bone, as measured by the Euler characteristic, was linearly correlated with trabecular bone volume, even in the ovariectomized rats. Hypoestrogenemic bone loss manifested itself in greatly reduced connectivity and fewer trabecular elements, but not in thinning of trabeculae. The ability to microscopically image sequential changes in the 3-D architecture of trabecular bone in vivo will allow exploration of the earliest stages of hypoestrogenemic bone loss and to more rapidly test the effectiveness of new clinical treatments for this major public health problem.

INTRODUCTION

OSTEOPOROSIS IS A DISEASE characterized by bone fragility that results in fractures. One third of women older than 65 will have osteoporotic fractures.[1,2] These fractures, which often occur with little or no trauma, have largely been attributed to reduced bone mass. Accordingly, research in osteoporosis has focused on those factors that affect bone mass, such as estrogen deprivation, age, and physical activity. Furthermore, treatments to control osteoporosis have been largely based on trying to maintain or increase skeletal mass.[3] However, significant overlap exists between the bone mass of normal and osteoporotic populations.[4] This overlap has led a number of investigators to search for factors other than low bone mass, such as structural properties and bone quality, to help explain the abnormal susceptibility to fractures among osteoporotics. Much of this research has focused on the trabecular bone.[5–8]

Trabecular bone is made up of an interconnected structure of curved plates and struts. Parfitt[5] pointed out that one of the age-related changes that accompanies bone loss is a decrease in the number of these trabecular elements. He and his colleagues found, in transiliac biopsies from normal subjects, that trabecular bone volume decreased with age. This decrease in bone volume appeared to be due to a loss in the number of trabeculae, as opposed to a thinning of trabecular elements. The authors suggest that the elimination of trabecular connections would be expected to reduce the mechanical strength of the bone out of proportion to the loss of tissue. Others have made similar observations.[6–10]

Currently, histomorphometry is used as a method for quantifying three-dimensional (3-D) structures from planar sections. It allows estimates of the volume fraction of trabecular bone (BV/TV) and surface areas of trabeculae. With an appropriate model it is also possible to calculate the trabecular separation (Tb.Sp), thickness (Tb.Th), number (Tb.N), and other features required to explain bone formation, resorption, and architecture.[11] However, it is impossible with histomorphometry to determine the true number, true shape, or interconnectedness of trabeculae

[1]Lawrence Livermore National Laboratory, Livermore, California.
[2]University of California at San Francisco, San Francisco, California.

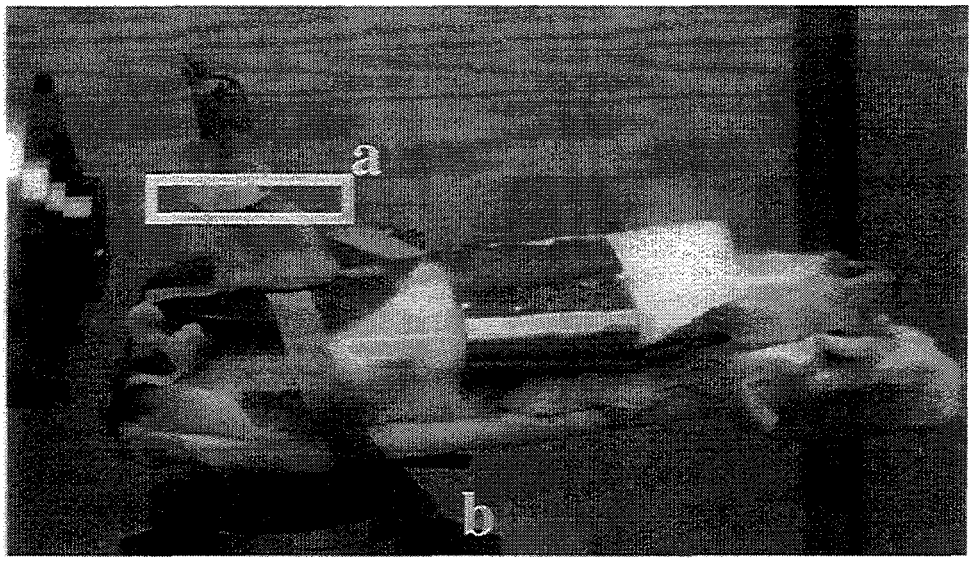

FIG. 1. An anesthetized rat with hind limb immobilized being scanned with the in vivo microscope. The scanned region is shown by the window marked "a." The rat is secured to the rotating stage, "b," and is shielded with lead foil. Part of the foil has been removed for greater clarity. The X-ray camera is to the left of the image.

short of serially sectioning much of the sample.[12] DeHoff et al.[13] established that the spacing between consecutive sections must be between 1/3rd to 1/10th the intercept length of the features of interest to determine topological properties such as connectivity between objects. In the tibial metaphysis of the rat, where the trabecular length scales are often less than 150 μm, this would require serial sections with spacings between 15 and 50 μm from the diaphysis to the growth plate. Such detailed sectioning is time consuming, artifact prone, and destructive. Hence, 3-D analyses of heterogeneous trabecular structures are rarely undertaken.[14]

Another method for reconstructing 3-D images of a structure is X-ray computed tomography (CT). Because little or no sample preparation is required for CT, tomographic methods provide a cost-effective alternative to serial sectioning. An important achievement in X-ray CT occurred with the development of the 3-D "cone" beam scanner.[15] Investigators reported using a 3-D cone-beam microtomography system to image the trabecular bone architecture in small samples of human tibias and vertebrae ex vivo with a stated spatial resolution of 60 μm.[16,17] A resolution of 60 μm, however, although acceptable for characterizing the connectivity of human trabeculae, may be insufficient for studies in small animals like the rat, where the trabecular widths average about 50 μm and trabecular separations average 150 μm or less. Furthermore, Smith and Silver[18] have reported that 3-D images from cone beam scanners are inevitably distorted away from the central slice because the single-orbit cone beam geometry does not provide a complete data set. These distortions and associated loss of spatial resolution have been particularly evident in samples containing plate-like structures, even when the cone beam angle is less than 6.5°.[18] Nevertheless, investigators have reported relatively high spatial resolution (30 μm) when imaging small specimens with this method.[19]

Synchrotron radiation sources, because of their high brightness and natural collimation, have allowed the development of CT systems that have spatial resolutions approaching 1 μm.[20] With synchrotron CT, it is possible to use parallel beam imaging geometry, thus avoiding the distortions and loss of resolution inherent in cone beam methods. One such high resolution CT instrument is the X-ray tomographic microscope (XTM).[21–23] Bonse et al.,[20] using an XTM at a synchrotron storage ring, have demonstrated the ability to make distortionless images of human trabecular bone in small (1 mm diameter) samples with 8 μm resolution. In this study, we have successfully used the XTM to image the 3-D structure and mineral density of trabecular bone in vivo, demonstrating that the instrument can detect microscopic changes in the trabecular bone structure and connectivity in ovariectomized rats, an important animal model for hypoestrogenemic bone loss.

MATERIALS AND METHODS

For this experiment, the proximal tibias of five, female, Sprague–Dawley, retired breeder rats (6 months old at start of study) were imaged in vivo with the XTM. A sixth rat was not imaged at this time. The radiation source was the 31-pole, X-ray wiggler beamline 10-2 at the Stanford Synchrotron Radiation Laboratory. The radiation from the wiggler was made nearly monochromatic at 25 keV by using a single crystal silicon (220) monochromator. A combination of pixel binning and demagnification of the charge-coupled device (CCD) detector reduced imaging times to less than 30 minutes/animal. Shuttering of the direct beam reduced actual exposure times to less than 2.5 minutes.

The animals were anesthetized with Xylazine (13 mg/kg) and Ketamine (87 mg/kg) for 50 minutes. While the animals

were unconscious, they were secured to a rotating platform and their right hind limbs were elevated into the X-ray beam, splinted rigidly in place to eliminate motion artifacts, and scanned (see Fig. 1). The scanned region contained both cortical and metaphyseal trabecular bone in the proximal tibia from approximately 1.5 to 3.5 mm distal to the growth plate (see Fig. 2a). On the day following the initial scans, three rats were chosen at random and ovariectomized by the dorsal approach. Five weeks after ovariectomy, all six animals were imaged a final time with the same imaging parameters.

The animals tolerated the procedure well. Dosimetry provided an upper bound to the amount of radiation each animal received. No animal received more than 90 rad of radiation, and this dosage was confined to a narrow band about 2 mm high in the X-ray target zone. We believe that the radiation had no measurable effect on bone development, as reflected by the normal growth of bone and cartilage in the two irradiated control animals. Previous work on vertebrae in rat tails showed that a 500 rad dose of radiation in 1-week-old rats stunted growth very little.[24] In humans, radiation doses below 2500 rad showed no signs of capital femoral epiphyseal slippage or epiphyseal abnormalities.[25] Thus, we anticipate that a 90 rad dose to older rats, especially when performed away from the epiphysis, will cause no measurable effects. We are taking steps to further reduce the radiation exposure levels.

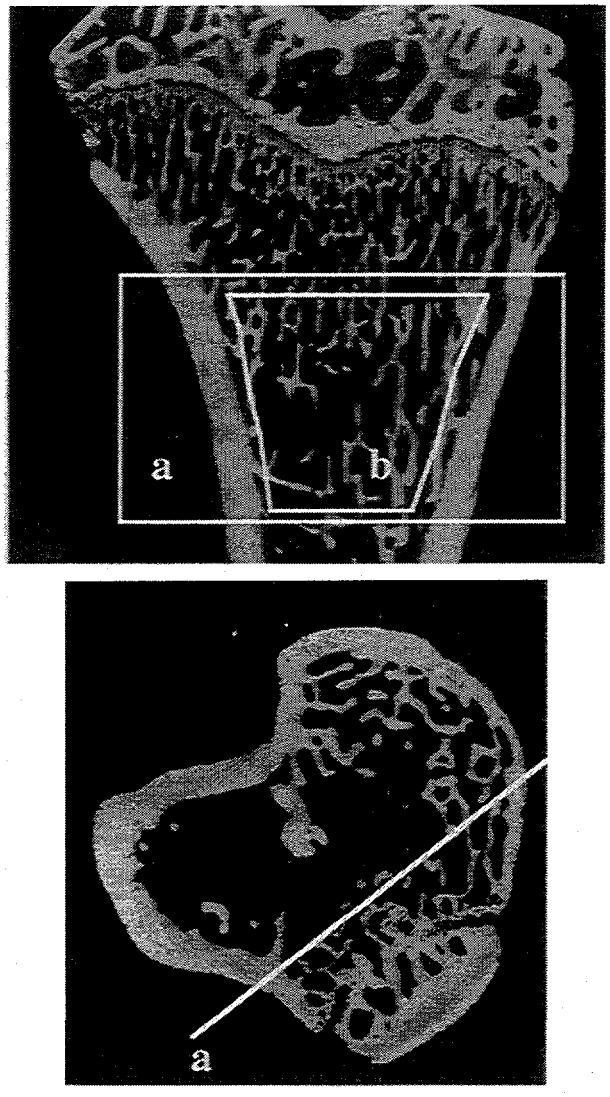

FIG. 2. XTM images of single sections of the proximal tibia. (a) frontal section showing the region of tibia scanned for this in vivo study. The large window, "a," is the region over which the three-dimensional images (Fig. 3) were acquired. The trapezoidal area, "b," is the region within this window where the conventional morphometric parameters were measured for Table 1. (b) a transverse section through the metaphysis. The line "a" is the position of the plane used to create the frontal section in (a).

Once the radiographic projection data were acquired, the 3-D images of the tibia were reconstructed by Fourier-filtered backprojection on a computer workstation.[22] The 3-D reconstructions required approximately 1 h to perform. Because the reconstructions could be performed separately, a single 8 h shift of beam time was more than sufficient to image the six animals.

The volumetric data were analyzed by two methods. In the first method standard morphometry was performed on vertical image-reconstructed sections from the XTM data taken across the medial/lateral extent of the tibias (see Fig. 2). The cortical bone on both sides of each section was removed approximately 0.5 mm inward from the endosteal surface. Closed contours were fitted to the interfaces between the trabecular bone and the marrow. B_A, the total perimeter length of the contours (mm) per section area (mm^2), was used to obtain the surface area, S_V, according to the relation

$$S_V = \frac{4B_A}{\pi}.$$

The fraction of pixels lying inside the contours per unit section area A_A was equated directly to the volume fraction of trabecular bone. These two measured values of area and perimeter were then used to calculate the trabecular width, separation, and number with the plate model.[11]

In the second method, cluster analysis was performed on the trabecular bone structures in the 3-D images.[26] Cluster analysis identified all of the trabecular bone that was continuously interconnected and also any isolated structures that were disconnected from the surrounding cortical bone and trabecular structure. Cluster analysis, therefore, provided a direct measure of β_0 and β_2, the topological variables that quantify both the number of isolated bone fragments and the number of imbedded pores. For the interconnected cluster, the connectivity, β_1, was determined by the relationship $\beta_1 = \beta_0 - \chi + \beta_2$ where χ is the Euler–Poincaré characteristic calculated with the method described by Feldkamp et al.[17] The connectivity is a topological property of a structure that enumerates the times that connections can be separated without disconnecting the structure.

After the second scan the animals were sacrificed and the imaged tibias were sent to Creighton University Center for

Hard Tissue Research for 2-D histomorphometry. Standard methods, published elsewhere, were utilized.[29]

RESULTS

Figure 3 shows 3-D images of a portion of the proximal tibia of the same rat just prior to ovariectomy and 5 weeks after surgery. A major loss of trabecular bone has occurred in the 5 weeks following ovariectomy. In addition, the 3-D images show a significant change from an interconnected plate- and strut-like structure to one that is mostly disconnected struts. Also, dangling (or dead-end) trabecular elements are seen only in the ovariectomized animals. These dangling elements, although still contributing to the total bone mass, most probably do not contribute significantly to the stiffness or strength of the bone.

Figure 4 shows a small region of trabecular bone in an ovariectomized rat at higher magnification. Of particular interest is the small trabecular fragment that is isolated from the surrounding bone and supported only by marrow. We have only observed trabecular fragments such as this in ovariectomized animals, where they account for about 1.5% of the total trabecular bone volume. These isolated trabecular fragments, as well as the more significant fraction of dangling trabecular bone, may be responsible for the overlap in bone mass between individuals with osteoporotic fractures and individuals without fractures.

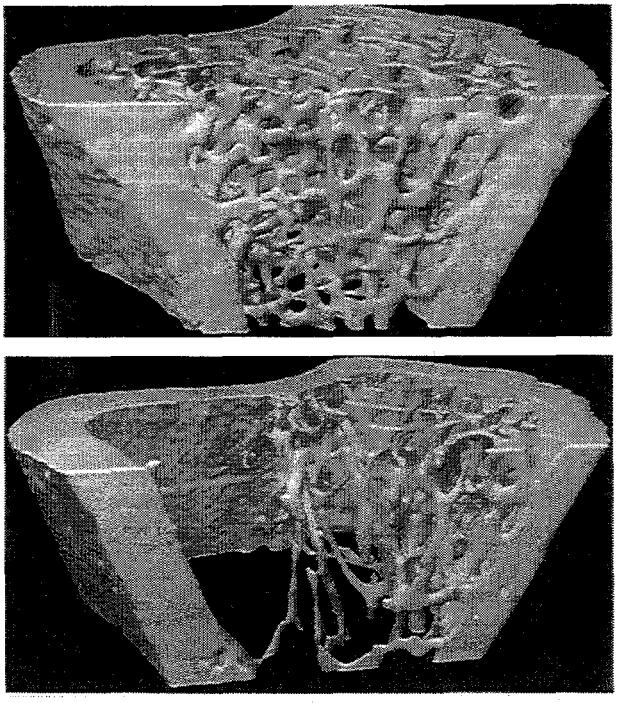

FIG. 3. Three-dimensional visualization of a subset of the trabecular bone in the proximal tibia of a female rat imaged (a) just prior to ovariectomy and (b) 5 weeks after ovariectomy. The trabecular bone volume decreased by approximately 65% following the ovariectomy. In addition, the plate-like structures have been highly resorbed, leaving behind disconnected strut-shaped structures.

Table 1 shows the results from the morphometric approach to XTM data analysis listing the measured values of BV/TV and calculated values of Tb.Sp, Tb.Th, and Tb.N. We compare the XTM results of the control and ovariectomized groups after the final scan with the results from conventional histomorphometry performed on the same limbs. In addition, we list the values given by Li et al.[27] for age-similar, nonovariectomized female Sprague–Dawley rats. It should be noted that we did not calculate Tb.Th, Tb.Sp, and Tb.N for the ovariectomized rats at 5 weeks because the plate model was clearly no longer valid.

Five weeks after ovariectomy, we recorded a 60% decrease in the trabecular bone volume, similar to the magnitude reported in other studies from histomorphometric analyses.[28,29] The bone loss recorded with conventional histomorphometic methods on the same bones was 58%, in very good agreement with the XTM results. The connectivity density (β_1 normalized to the analysis volume) as a function of volume percent bone is shown in Fig. 5. The measured connectivity density of the rat is much greater than that reported for human bone.[14,16,17] The higher connectivity density can be explained by the smaller intercept lengths in rat bone than in human bone.

DISCUSSION

The morphometric parameters measured with the XTM (Table 1) are in good agreement with those observed in age-similar animals with conventional methods. In addition, with the exception of trabecular spacing, the XTM mea-

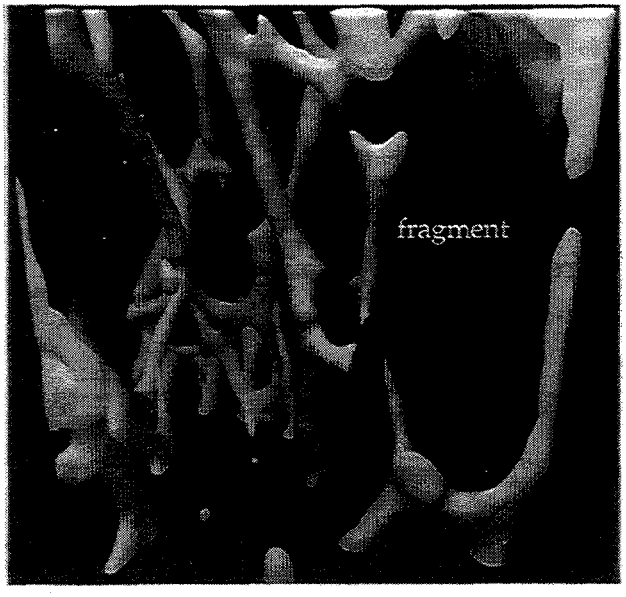

FIG. 4. In vivo image of a small region of trabecular bone in an ovariectomized rat. A small trabecular fragment, isolated from the surrounding bone, is supported only by marrow. Other, smaller fragments can also be seen in this image. Five weeks following ovariectomy, these isolated fragments account for only about 1.5% of the total remaining trabecular bone.

TABLE 1. HISTOMORPHOMETRY RESULTS

Sample	BV/TV %	Tb.Th (μm)	Tb.Sp (μm)	Tb.N (/mm)	Number of samples
Li et al.	23.5 ± 4.7	47.4 ± 3.6	160.6 ± 40.3	5 ± 1	6
Pre-OVX	23.0 ± 2.5	54.0 ± 4.3	193.4 ± 20.6	4 ± 0.4	5
Control (5 weeks)	23.4 ± 5.3	49.6 ± 5.7	168.5 ± 51.7	4.8 ± 1.1	3
OVX (5 weeks)	9.2 ± 5.6				3
Control[a] (5 weeks)	21.3 ± 8.3	63.7 ± 11.8	307.7 ± 64.1	3.3 ± 0.7	3
OVX[a] (5 weeks)	8.9 ± 3.3				3

[a] Values determined with conventional histomorphometry.

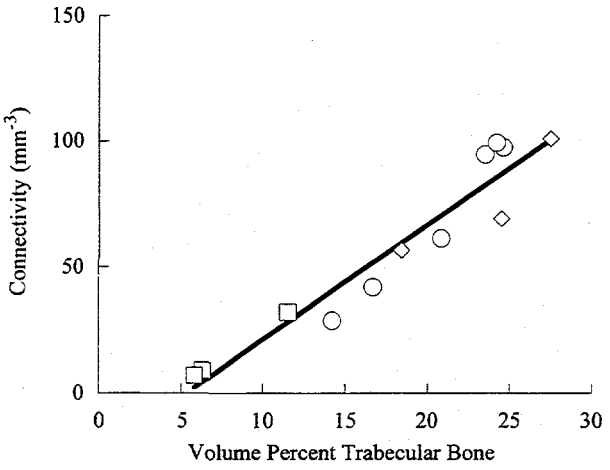

FIG. 5. The connectivity density/mm^3 as a function of volume-percent trabecular bone. The open circles are the connectivity density of the rats prior to ovariectomy. Five rats were initially imaged; the sixth data point was provided (the value at 14% bone volume) from a second scan on one rat of a region 2 mm more distal than that initially scanned. The open diamonds represent the connectivity densities of the nonovariectomized control rats 5 weeks after the initial scan. The open squares are for the ovariectomized rats 5 weeks following ovariectomy.

surements are consistant with conventional histomorphometry of the identical bones. The higher average value of the trabecular spacing determined with conventional histomorphometry may be due to the larger examination area. The histomorphometry slide covered a range from approximately 1.5 mm distal to the growth plate to approximately 5.5 mm distal. Because the histomorphometry section sampled the trabecular bone farther from the growth plate than we did with the XTM, it is more likely to reveal higher average trabecular spacings.

The linear correlation we observed between connectivity density and trabecular volume is significant ($p < 0.001$; $R^2 = .91$) over a range from 5 to 25 vol. %. We are aware of three other published reports showing the relationship between connectivity density measured in three dimensions and trabecular bone volume.[14,16,30] Two of these studies were of human bone.[14,16] Goldstein et al. reported a significant linear correlation between bone volume and connectivity density with positive values for the Euler characteristic at low bone density (negative connectivity).[16] Other investigators have commented that a positive Euler characteristics may be due to measurement artifacts.[14] These investigators suggested, from analysis of their own data, that the connectivity density is correlated more with architecture than with bone volume, as the connectivity density is a topological, not a metric, measure of the microstructure.

We avoided measurement artifacts that might influence the calculated Euler characteristic by using smoothing and percolation algorithms that have an effect similar to Odgaard's and Gundersen's artifact suppression methods.[14] Our computed Euler characteristics remained negative throughout the density range. Unlike Odgaard and Gundersen, however, our connectivity density is linear with trabecular volume and goes to zero at a small positive value of bone density (it would be unlikely that connectivity density should go through the origin, since, by definition, the connectivity of a simply connected structure having finite mass is zero). Also, the linear relationship between bone volume and connectivity density was preserved after major hypoestrogenemic bone loss. A similar observation has been reported in the L2 vertebrae of ovariectomized canines.[30]

Our data were obtained from approximately the same position in each animal; position variability in the connectivity density, therefore, is minimal. The overall linear relationship observed in our data is most likely a true reflection of the way in which trabeculae are distributed in bone. Bone mass is increased or decreased by either adding or subtracting connections. Though this linear relationship is preserved at 5 weeks postovariectomy, it remains to be determined if it is manifest in the earliest stages of hypoestrogenemic bone loss.

The sharp loss in connectivity density that we observed is a direct measurement of what time-consuming, multiple sectioning methods have only been able to infer indirectly: hypoestrogenemic bone loss leads to a removal of trabecular plates (connections) more than it leads to a thinning of surviving trabeculae.[11] From our data, trabecular connections are lost at a 4.5 times greater rate than the bone volume decreases. However, our data have been taken at only two points in time when a considerable amount of bone loss has occurred. The sequential changes in connectivity immediately following ovariectomy must be measured

to establish the significant time markers at which the connectivity of trabeculae are irreversibly lost.

CONCLUSION

In summary, we have developed an in vivo technique for imaging trabecular bone structure in three dimensions. Our initial results substantiate that the number of trabecular interconnections (connectivity density) decreases linearly with trabecular bone volume. The linear correlation between connectivity density and bone volume is preserved even after significant hypoestrogenemic bone loss. The XTM will allow us to quantify microscopic changes in trabecular bone architecture resulting from estrogen deficiency. With the XTM, we will be able to evaluate therapies and conditions that affect bone structure. Osteoporosis is a disease of bone fragility, and, if the key to understanding fragility is to understand the trabecular microstructure, in vivo X-ray tomographic microscopy will significantly advance our understanding of this important public health problem.

ACKNOWLEDGMENTS

This work was performed under the auspices of the US Department of Energy (DOE) under Contract W-7405-Eng-48. Financial support was provided by the Laboratory-Directed Research and Development Program, Lawrence Livermore National Laboratory. The authors express their appreciation to D. B. Kimmel (Creighton University, Omaha, NE) for the histomorphometry, G. W. Marshall, Jr. and S. J. Marshall (University of California, San Francisco, CA) for technical discussions, to W. N. Massey (Lawrence Livermore National Laboratory, Livermore, CA), to T. M. Breunig and M. C. Nichols (Sandia National Laboratories) for reviewing the manuscript, and to S. Newton (University of California, San Francisco, CA). The in vivo measurements were performed at the Stanford Synchrotron Radiation Laboratory (SSRL). SSRL is supported by DOE, Chemical Sciences Division.

REFERENCES

1. Riggs BL, Melton LJ III 1986 Involutional osteoporosis. NEJM **314:**1676–1686.
2. Phillips S, Fox N, Jacobs FJ, Wright WE 1986 The direct medical costs of osteoporosis for American women ages 45 and older. Bone **9:**271–279.
3. Riggs BL, Melton LJ 1992 The prevention and treatment of osteoporosis. NEJM **327:**620–627.
4. Recker RR 1989 Low bone mass may not be the only cause of skeletal fragility in osteoporosis. Proc Soc Exp Biol Med **191:** 272–274.
5. Parfitt AM, Mathews CHE, Villanueva AR, Kleerekoper M, et al. 1983 Relationships between surface, volume, and thickness of iliac trabecular bone in aging and in osteoporosis. J Clin Invest **72:**1396–1409.
6. Kleerekoper M, Villanueva AR, Stanciu J, et al. 1985 The role of three-dimensional trabecular microstructure in the pathogenesis of vertebral compression fractures. Calcif Tissue Int **37:**594–597.
7. Aaron JE, Makins NB, Sagreiya K 1987 The microanatomy of trabecular bone loss in normal and aging men and women. Clin Ortho **215:**260–271.
8. Mellish RWE, Garrahan ENJ, Compston JE 1989 Age-related changes in trabecular width and spacing in human iliac crest biopsies. Bone Miner **6:**331–338.
9. Weinstein RS, Hutson NE 1987 Decreased trabecular width and increased trabecular spacing contribute to bone loss with aging. Bone **8:**137–142.
10. Mosekilde L 1986 Age-related changes in vertebral trabecular architecture assessed by a new method. Bone **9:**247–250.
11. Parfitt AM 1983 The physiologic and clinical significance of bone histomorphometric data. In: Recker RR (ed.) Bone Histomorphometry: Techniques and Interpretation. CRC Press, Boca Raton, FL, pp. 143–224.
12. Weibel ER 1989 Measuring through the microscope: Development and evolution of stereological methods. J Microscopy **155:**393–403.
13. DeHoff RT, Aigeltinger EH, Craig KR 1972 Experimental determination of the topological properties of three-dimensional microstructures. J Microscopy **95:**69.
14. Odgaard A, Gundersen HJG 1993 Quantification of connectivity in cancellous bone, with special emphasis on 3-D reconstructions. Bone **14:**173–182.
15. Feldkamp LA, Davis LC, Kress JW 1984 Practical cone-beam algorithm. J Opt Soc Am **A1:**612–619.
16. Goldstein SA, Hollister SJ, Kuhn JL, Kikuchi N 1990 The Mechanical and Remodeling Properties of Trabecular Bone. In: Mow C, Ratcliffe A, Woo SL-Y (eds.) Biomechanics of Diarthrodial Joints, Vol. 2. Springer-Verlag, New York, pp. 61–81.
17. Feldkamp LA, Goldstein SA, Parfitt AM, et al. 1989 The Direct Examination of Three-Dimensional Bone Architecture In Vitro by Computed Tomography. J Bone Miner Res **4:**3–11.
18. Smith CR, Silver MD 1994 Comparison between single slice CT and volume CT. In: Czichos HCH, Schnitger D (eds.) International Symposium on Computerized Tomography for Industrial Applications, Bundesministerium des Innern, Bundesanstalt fur Materialforschung und-prufung, Berlin, Germany, 8–10 June, 1994 (in press).
19. Layton MW, Goldstein SA, Goulet RW, et al. 1988 Examination of subchondral bone architecture in experimental osteoarthritis by microscopic computed axial tomography. Arthritis Rheum **31:**1400–1405.
20. Bonse U, Busch F, Gunnewig O, et al. 1994 3D computed x-ray tomography of human cancellous bone at 8μm spatial resolution and 10^{-4} energy resolution. Bone Miner **25:**25–38.
21. Kinney JH, Lane NE, Majumdar S 1992 Noninvasive, three-dimensional histomorphometry using x-ray tomographic microscopy. J Bone Miner Res **7S:**136.
22. Kinney JH, Nichols MC 1992 X-ray tomographic microscopy (XTM) using synchrotron radiation. Ann Rev Mater Sci **22:** 121–152.
23. Kinney JH, Breunig TM, Starr TL, et al. 1993 X-ray tomographic study of chemical vapor infiltration processing of ceramic composites. Science **260:**789.
24. Kember NF, Coggins J 1967 Changes in the vascular supply to rat growth cartilage during radiation injury and repair. Int J Radiat Biol **12:**143–151.
25. Silverman CL, Thomas PRM, McAlister WH, et al. 1981 Slipped femoral capital epiphyses in irradiated children: Dose, volume and age relationships. Int J Radiat Oncol Biol Phys **7:**1357–1363.
26. Hoshen J, Kopelman R 1976 Percolation and cluster distribu-

tion. I. Cluster multiple labeling technique and critical concentration algorithm. Phys Rev B **15**:3438–3445.
27. Li XJ, Jee WSS, Ke HZ, et al. 1991 Age related changes of cancellous and cortical bone histomorphometry in female Sprague–Dawley rats. Cells Mater **S1**:25–35.
28. Wronski TJ, Dann LM, Scott KS, Cintron M 1989 Long-term effects of ovariectomy and aging on the rat skeleton. Calcif Tissue Int **45**:360–366.
29. Lane NE, Coble T, Kimmel DB 1990 The effect of naprosyn on cancellous bone in ovariectomized rats. J Bone Miner Res **10**:1029–1035.
30. Goldstein SA, Goulet R, McCubbrey D 1993 Measurement and significance of three-dimensional architecture to the mechanical integrity of bone. Calcif Tiss Int **53**(S4):S127–S133.

Address reprint requests to:
Dr. J. H. Kinney, L-356
Lawrence Livermore National Laboratory
P.O. Box 808
Livermore, CA 94550

Received in original form January 18, 1994; in revised form August 20, 1994; accepted August 20, 1994.

Nuclear Instruments and Methods in Physics Research A 347 (1994) 480–486
North-Holland

NUCLEAR INSTRUMENTS & METHODS IN PHYSICS RESEARCH Section A

The X-ray tomographic microscope: three-dimensional perspectives of evolving microstructures

J.H. Kinney [a,*], D.L. Haupt [a], M.C. Nichols [b], T.M. Breunig [b], G.W. Marshall, Jr. [c], S.J. Marshall [c]

[a] *Lawrence Livermore National Laboratory, Livermore, CA 94551, USA*
[b] *Sandia National Laboratories, Livermore, CA 94551, USA*
[c] *University of California, San Francisco, CA 94143, USA*

Recent advances in X-ray tomography using synchrotron radiation enable three-dimensional microscopic images to be obtained nondestructively from relatively large samples. With both increased sample size and improved spatial resolution, it is now possible to quantify experimentally-induced microstructural and microchemical changes in materials as they occur in situ, in vitr, and even in vivo. With the X-ray tomographic microscope, we have begun to improve our understanding of the processing of ceramic matrix composites, bone loss in osteoporosis, and the development of caries lesions in teeth.

1. Introduction

Complex, heterogeneous microstructures occur naturally. Examples can be found in teeth and bone, which are complex composites with organic and mineral phases. Heterogeneous microstructures can also be synthesized to achieve materials with tailored properties. Examples of synthesized microstructures include continuous-filament metal and ceramic matrix composites. Predicting the properties of materials possessing heterogeneous microstructures, or understanding and optimizing the synthesis of these materials, is complicated by the difficulty of obtaining three-dimensional microstructural characterization.

Stereology is a method for estimating three-dimensional structures from planar sections [1]. With stereological methods, it is possible to estimate volume fractions and surface areas of pores, inclusions, second phases, and other features found in heterogeneous microstructures. However, it is impossible with stereology to determine the number, true shape, or interconnectedness of such microstructural features, short of serially sectioning the entire sample [2]. DeHoff et al., in a sintering study, established that the spacing between consecutive sections must be on the order of 1/3 to 1/10 the length of the feature of interest in order to determine topological properties such as the connectedness between objects [3]. Such detailed sectioning is time consuming, artifact-prone, and destructive. Hence, three-dimensional analyses of heterogeneous microstructures are rarely undertaken.

X-ray computed tomography (CT) is a method for reconstructing three-dimensional images of a structure from a finite number of radiographic images. Because little or no sample preparation is required, tomographic methods provide a cost-effective alternative to serial sectioning. Until the advent of accessible synchrotron radiation sources, however, the spatial resolution of X-ray CT (with a few exceptions [4] has been limited to 50–100 μm in nonmedical applications [5,6]. Synchrotron sources, however, because of their brightness, have allowed CT systems to be developed that have spatial resolutions approaching 1 μm and better – sufficient resolution to begin effective microstructural imaging in three dimensions [7,8]. We have called these high-resolution methods that use synchrotron radiation *X-ray tomographic microscopy* to emphasize the distinction between microtomography and what is definitely microscopic imaging [9].

The most important advantage of X-ray tomographic microscopy over serial sectioning methods is that tomographic methods are nondestructive. This means that the same sample can be characterized many times. It is possible to characterize samples in situ, in vitro, and in some cases, in vivo and observe how microstructures evolve in response to processing, degradative environments, or mechanical loading. Each sample, in essence, provides its own baseline. Sample-to-sample variations that might cloud the interpretation of a sequence of events are compensated for by the use of repeated measurements on the same sample.

We have developed and used the X-ray tomographic microscope (XTM) on the 31 pole, hard-X-ray beamline 10-2 at Stanford Synchrotron Radiation Laboratory [10]. The XTM has evolved from the designs described by others to include capabilities for imaging large samples under a variety of conditions [7,8,11]. The types of microstructural information that can be obtained from the

* Corresponding author.

Elsevier Science B.V.
SSDI 0168-9002(94)00427-9

instrument may be described with respect to an application in ceramic matrix composites in which the XTM is used to quantify the evolution of porosity during chemical vapor infiltration [12]. In addition, biomedical applications are being pursued, including characterization of the internal structural materials of teeth and bone and their responses to demineralization processes such as dental caries (decay) and osteoporosis.

2. The X-ray tomographic microscope

The XTM uses monochromatic synchrotron radiation to measure with great precision the X-ray attenuation coefficient as a function of position in a sample. In practice, the linear attenuation coefficient, α, is averaged over a finite-sized volume element (voxel) in the sample. Because α depends on both average atomic number and density, differences in composition and concentration throughout the sample give rise to variations in α different voxels. These differences in α provide the contrast for forming an image.

This concept is illustrated in Fig. 1, where an arbitrary sample containing two phases (A and B) is shown as being partitioned into voxels. These voxels, each containing a measured value of α, fill a cubic array $A(x, y, z)$. Cross-sectional images may be examined by displaying single slices in the x, y plane (shown) or vertical cuts in the x, z or y, z planes. Three-dimensional images may also be displayed using volumetric rendering algorithms. Metric and topological parameters that describe the heterogeneous microstructure of the object can be obtained using methods to be described later.

The linear X-ray attenuation coefficient, α, in a voxel at $r_{x,y,z}$ in a sample is determined from a finite set of X-ray attenuation measurements (projection data) taken at different angles. The projection data $[I(x', y')]$ are the transmitted X-ray intensities that reach a position-sensitive detector after passing through the sample. These data are given by

$$I = \int S(E)\left[\exp\left(-\int \alpha(x, y, z, E)\, \mathrm{d}l\right)\right] \mathrm{d}E, \qquad (1)$$

where $S(E)$ is the energy spectrum of the X-ray source and $\alpha(x, y, x, E)$ specifies the energy and material dependence of the linear attenuation coefficient. The line integral is taken along a straight path $\mathrm{d}l$ through the sample. For nearly monochromatic radiation with energy E_0, $S(E)$ can be approximated by a delta function, and Eq. (1) reduces to the familiar form of the Radon transform [13]:

$$\ln\left(\frac{I_0}{I}\right) = \int \alpha(x, y, z, E)\, \mathrm{d}l. \qquad (2)$$

Measurements of the attenuation through the sample as a function of angle are used to numerically invert Eq. (2) to solve for $\alpha(x, y, z, E_0)$. As long as the detector has sufficient spatial resolution to discriminate between closely-space ray paths, the reconstruction voxels can be made arbitrarily small. As the voxels become smaller than the size of the features of interest, the spatial resolution

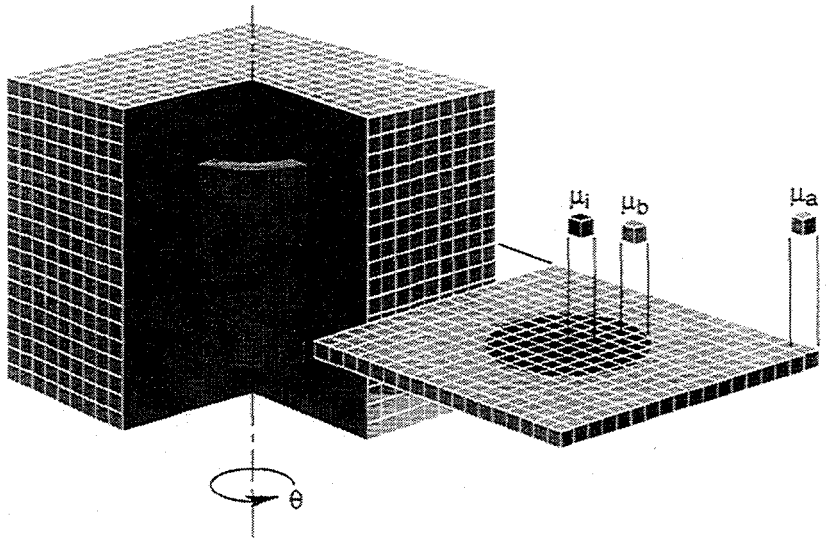

Fig. 1. The XTM provides a quantitative measure of the linear attenuation coefficient within individual volume elements in a slice plane through the sample. Three-dimensional images are obtained by stacking these slice planes into a three-dimensional volume. Because the detector accumulates the data for each slice plane simultaneously, data for the volume can be obtained at speeds greater 2 s per slice.

becomes sufficiently high to be able to perform microstructural analysis. This increase in resolution with decreasing voxel size is illustrated in Fig. 2, where a single cross-sectional slice of the greater trochanter of a rat (a bony projection on the proximal femur) has been imaged with ever finer resolution. Fig. 2a approximates the resolution obtainable with the best of medical CT scanners (250-$\times$250-$\times$500-μm voxels); Fig. 2b approximates the resolution obtainable with a typical industrial high-resolution scanner (100-$\times$100-$\times$100-μm voxels); Fig. 2c approximates the resolution obtainable with high-resolution microtomography system (50-$\times$50-$\times$50-μm voxels); and Fig. 2d is the resolution achieved with the XTM running in the low-resolution mode (17-$\times$17-$\times$17-μm voxels). Clearly, as the voxel size becomes smaller, the number of resolvable microstructural features increases.

The XTM uses a single-crystal silicon monochromator to select the X-ray energy. The energy chosen is sample-dependent, and an energy that will optimize the signal to noise in the images is used. This energy selection criteria represent a compromise between too much attenuation at low energy and loss of contrast at high energy [14]. A specially-designed scintillator screen is used to convert the X-rays into visible light. Presently, the XTM uses a single crystal of $CdWO_4$ for this purpose. The crystal is highly polished and coated with an antireflective layer to reduce blurring that might be caused by reflections from the surface. The visible light produced by the X-rays is projected onto the CCD using variable-magnification optical lenses. These lenses were specially designed for a large field of view and high spatial resolution with minimal distortion.

A two-dimensional CCD array detector is used to convert the visible light from the scintillator into position-sensitive electronic signals required for tomographic reconstruction. The CCD array allows the simultaneous collection of both multiple ray paths and multiple slices for a given orientation of the sample, which increases the efficiency of the tomographic measurements. The CCD is cooled thermoelectrically to temperatures below -40°C to reduce dark current and readout noise. The optimal temperature for operation is CCD-dependent, and must be established by making careful measurements of resolution and charge-transfer efficiency. Finally, the CCD is read

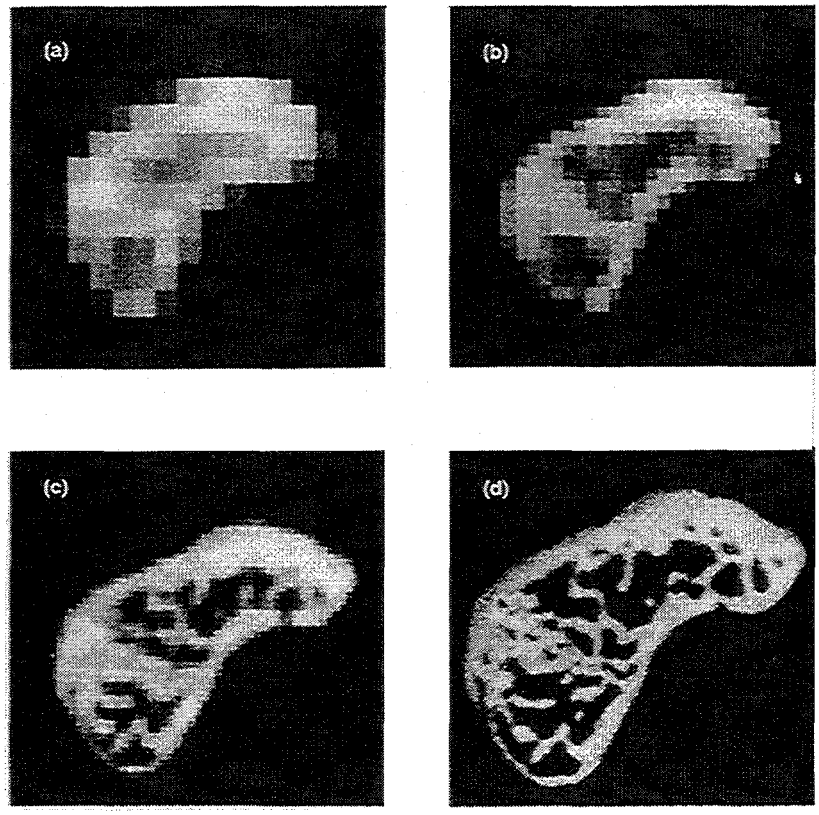

Fig. 2. XTM images of the greater trochanter off of the proximal femur of the rat with decreasing voxel size: (a) voxel is 250$\times$250$\times$500 μm (typical of medical CT), (b) voxel size is 100$\times$100$\times$100 μm (typical of industrial CT), (c) voxel size is 50$\times$50$\times$50 μm (typical of microtomography), and (d) voxel size is 17$\times$17$\times$17 μm (typical of the XTM in low-resolution mode).

out as 12-bit data in slow scan manner, thereby greatly reducing the noise and significantly increasing the linear range of the detector.

To obtain three-dimensional images, a sample is positioned on the rotating stage. The sample is initially translated out of the X-ray path, and an image is obtained of the incident X-ray beam. This reference image, taken without the sample, provides the values for $I_o(x', y')$ in Eq. (2). Next, the sample is placed between the X-ray path and the scintillator, and another image, the projection image, is acquired. The projection image provides the value for $I(x', y')$ at a given angular orientation. The ratios of the logarithms of the reference image and the projection image provide values of the integrated attenuation along the individual ray paths. By rotating the sample in discrete angular increments through 180°, sufficient data are obtained from the two-dimensional projection images to reconstruct them into a three-dimensional image of the attenuation coefficients of each of the voxels in the structure. This procedure, known as reconstruction from projections, can be performed in any number of ways [13]. For our applications, we choose to reconstruct by Fourier-filtered back-projection.

3. Methods of data analysis

The reconstruction produce large volumes of attenuation data. Of the numerous methods for analyzing these data to obtain microstructural information, perhaps the simplest is to display slices or cuts through the object as images (as in Fig. 2a, b, c, and d). Alternatively, the entire data set can be rendered as a three dimensional object and viewed from all orientations. As informative as visual inspection can be, it does not provide quantitative information. In addition, if one considers that many data sets will consist of literally thousands of slices, direct viewing of every orientation of the sample and relating them to each other become problematic.

We have extended many of the two-dimensional techniques from stereology to analyze the three-dimensional XTM data. In particular, we calculate the volume fractions (V_v) and surface areas (S_v) of different phases. In addition to these stereological parameters, we quantify microstructural features that can be determined only from three-dimensional analyses. These include the number of particles (N_v) and their distribution within the sample (correlation lengths), the interconnectedness of features, and the true shape and size of the particles. Quantification is facilitated because the three-dimensional image data are in digital format.

We illustrate the power of XTM as a three-dimensional tool for characterizing microstructures by considering an application to the processing of continuous-filament, ceramic-matrix composites. Chemical vapor infiltration (CVI) is an important technology for fabricating SiC ceramic-matrix composites [15]. In CVI, a vapor precursor of the matrix material, methyltrichlorosilane (MTS), is passed through a network of reinforcing fibers at elevated temperature. The MTS dissociates, and the SiC matrix phase deposits on the fibers. As matrix growth progresses, avenues for gas transport become more tortuous and begin to close off, eventually stopping the infiltration process. Pore closure determines the final density of the composite.

CVI technology must be improved if continuous fiber ceramic composites are to realize their full potential. Fabrication costs must decrease, and residual porosity must be reduced and controlled. Improvements will require a better understanding and how processing variables and fiber architecture (the orientation of the fibres and the type of arrangement, or weave) ultimately control the composite's microstructure. This understanding has been frustrated by a lack of good microstructural data showing the evolution of composite microstructure during CVI [16]. This lack of microstructural data is largely the result of the difficulty in trying to reconstruct the three-dimensional pore networks with two-dimensional analytical methods.

We are using the XTM to study CVI. In a recent experiment, three-dimensional images of woven SiC fiber samples (performs) mounted in specially-designed infiltration chambers were made prior to infiltration with MTS. After the uninfiltrated preforms were imaged, the samples were placed into a 975°C furnace and infiltrated for 3 h. After infiltration, imaging was repeated. This procedure of infiltration followed by imaging was repeated at 3-h intervals until, because of pore closure, vapor flow through the composite could no longer be achieved. In this manner, consolidation of the composite specimens was quantified as a function of infiltration time.

Within the fiber bundles (tows), where pore sizes can be much smaller than the spatial resolution of the instrument, consolidation was measured by equating the average attenuation coefficient in a supervoxel (an assemblage of adjacent voxels that average over several micropores) to the amount of SiC that had been deposited. Prior to infiltration, when the composite is a two-phase mixture of fibers and pores, the volume fraction of porosity, V_v, can be determined from the measured attenuation coefficient averaged over the supervoxel:

$$V_v = 1 - \frac{\langle \alpha \rangle}{\mu_f \rho_f}, \tag{3}$$

where $\langle \alpha \rangle$ is the measured averaged attenuation coefficient, and μ_f and ρ_f are the calculated (or independently measured) mass attenuation coefficient and density of the individual fiber strands. The initial value of the porosity is used to solve for the subsequent porosity during the course of infiltration. In this manner, the porosity can be measured as a function of infiltration time with X-rays of a single energy.

In an independent study, it was established that the

supervoxel approach produced volume-fraction values that were indistinguishable from those obtained with conventional destructive sectioning techniques [17]. Fig. 3 shows the consolidation of the first 10 plies of a 0/90 preform as a function of infiltration time. These results are in excellent agreement with model predictions that show the fiber tows being consolidated rapidly at the outset of CVI.

A similar approach can be used to quantify the mineral (hydroxyapatite) concentration in dentin: the hard, calcified tissue beneath the enamel layer in teeth. Of interest in these studies are the changes in mineral density that occur during caries growth (cavity formation). A relationship has been derived that relates the attenuation data measured with XTM to the concentration of the mineral phase in dentin (C_m) with good accuracy [18]:

$$C_m = \frac{\alpha_d - 0.28}{3.38}, \tag{4}$$

where α_d is the measured attenuation coefficient, and the measurements are made with 25 keV X-rays. With this relationship, it is possible to map the three-dimensional distribution of the mineral phase in dentin and to quantify caries-induced changes in mineral concentration.

We have designed and used a specimen cell for in vitro studies of caries growth. The cell is a cylindrical lexan vessel, 8 mm in diameter. A dentin specimen, approximately 3 to 4 mm wide and 2 to 3 mm thick with the enamel removed, is placed in the vessel, and caries growth is simulated by submerging the specimen in a buffered gel (pH ≈ 4). The XTM acquires three-dimensional images of the lesion as it evolves in the gel and quantifies both the amount of mineral phase removed and the mineral density gradients that evolve during demineralization. In this manner, it is possible to rapidly evaluate the effectiveness of

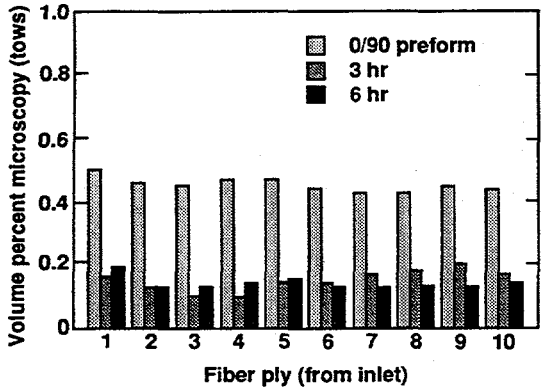

Fig. 3. Tow porosity in the first 10 plies of a 0/90 preform quantified in situ with the XTM: uninfiltrated preform, 3 h infiltration, and 6 h of infiltration. Tows are fully consolidated in the first six to seven plies by the end of 3 h of infiltration. Plies farther from the vapor inlet become fully consolidated between 3 to 6 h of infiltration. The gradient is consistent with gas-depletion effects on the deposition process.

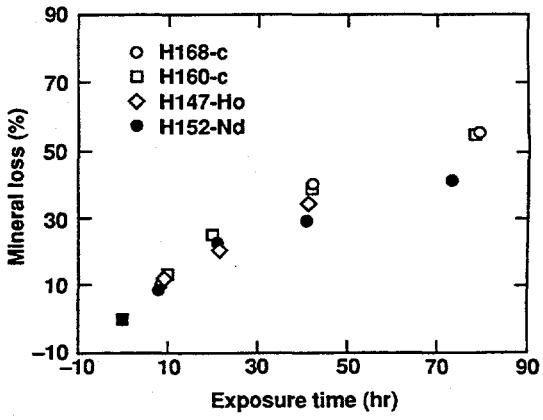

Fig. 4. Percentage of the mineral phase removed from a 0.85-mm-thick dentin sample, as a function of exposure to caries-simulating broth (pH = 4). Two controls (unlased samples) are compared to Nd:YAG-treated and Ho:YAG-treated samples. Data are obtained in vitro with the XTM.

caries treatments and improve our understanding of lesion formation in dentin.

In a recent experiment, we use the in vitro caries cell to evaluate the effectiveness of laser surface modification as a method for inhibiting caries growth in dentin. In this experiment, dentin samples were treated with two different laser wavelengths: Nd:YAG at 1.06 μm and Ho:YAG at 2.1 μm. The demineralization was measured as a function of time in caries solution. The treated samples were then compared with unlased controls. Fig. 4 shows the percentage of the mineral phase removed as a function of time in the gel for two controls: an Nd:YAG treated sample and an Ho:YAG treated sample. These data are from a recent experiment and are included in this paper only to show that the XTM is useful for studies of this kind. Until all of the data are analyzed, it is not possible to evaluate the effectiveness of laser treatments at these wavelengths.

These examples show how volume fractions and concentrations can be measured with voxel averaging methods. As the voxel size becomes smaller than the features of interest, direct measurement of surface area also becomes possible. The surface area per sample volume, S_v can be estimated by fitting contours to the phase boundaries in two dimensions and measuring the total perimeter length per unit area, B_A From stereology,

$$S_v = \frac{4}{\pi} B_A. \tag{5}$$

Because our data are three-dimensional, however, S_v can also be measured by integrating over a three-dimensional mesh fitted to the structures of interest. The advantages of the first method are the ease in fitting two-dimensional contours and the direct relationship of surface areas determined in this manner to conventional stereological approaches. The advantage of the three dimensional method

is that the result is not a two-dimensional approximation, but a direct, three-dimensional measurement.

In more complex applications, it is possible to count all isolated (nonconnected) particles in a sample. Identifying isolated particles and correctly enumerating them in a large volume set (> 100 million voxels) should be a computationally intensive task. Thanks to an efficient cluster-labeling algorithm developed by Hoshen and Kopelman [19], however, it is possible to label and count all of the isolated features in a large volume set quite rapidly on a standard workstation. In this method of counting, particles of type A are composed entirely of voxels (called *sites* in ref. [19]) containing attenuation coefficients unique to the type A particle. The algorithm performs a single pass through the data, giving each cluster of type A voxels a unique label. In those cases where two or more previously isolated clusters merge, the higher numbered clusters are relabled as belonging to the lowest number in the newly merged cluster. A cluster may be considered as being face-connected only, or edge and corner connections may also be included.

We have use the HK algorithm to count the number of pores that become isolated (closed off from the infiltration) during consolidation of the ceramic matrix composite during CVI. Ideally, the number of isolated pores would be minimal because porosity can weaken the composite. Prior to infiltration, there are no isolated pores, as they are all interconnected. As infiltration proceeds, pores close off and become isolated from the infiltrating vapor mixture. The number of isolated pores increases until, near the completion of infiltration, the number of isolated avalanches. At this point, there are no longer any percolating (continuous) clusters, and infiltration ceases.

We are interested in knowing if the topological properties of the pore network can be used to explain the onset of pore avalanche. A similar study of sintering showed a strong correlation between decreased interconnectedness and increased isolated porosity [3]. However, in that study, the method for measuring the connectedness (the number of connections or pathways between pores) was developed for serial sectioning and did not lend itself to computer methods. Feldkamp described a method for calculating the connectedness of three-dimensional structures, which is straightforward to implement on a computer [20]. The algorithm computes the Euler–Poincareé characteristic for a network, X, which is a topological number describing the number of connections, or branches, minus the number of nodes. For the volume sets from the CVI data, we calculated $\beta_1 = 1 - X$, where β_1 is the first Betti number: the number of branches that must be cut to form a disconnected, or isolated, structure. For example, a simply-connected pore network, or Caley tree, has $\beta_1 = 0$. Closure of any pathway or branch in a simply-connected pore network will produce an isolated pore.

Fig. 5 shows preliminary results from a combined cluster/connectivity analysis. The number of pores is represented by the left abscissa, and the connectivity (β_1) is represented by the right abscissa. A sharp break occurs in both curves at about 75% fractional density. A sudden decrease in the number of connections toward a more simply connected network is associated with a simultaneous increase in the number of isolated pores. This correlation between connectivity and porosity may lead to new techniques of optimizing fiber architectures for chemical vapor infiltration processing.

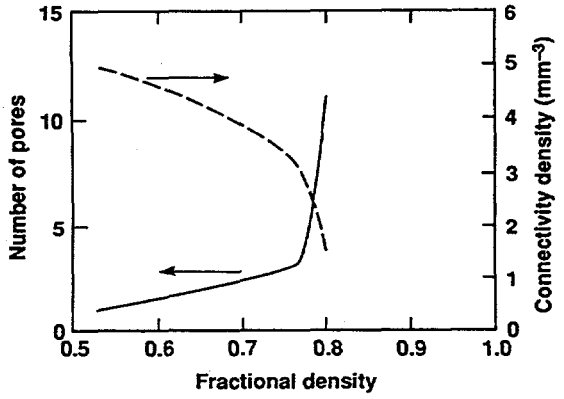

Fig. 5. The connectivity density and the number of pores in a 0/45 ceramic matrix composite at different stages in its consolidation. Initially, only one interconnected pore permeates the entire sample. As infiltration proceeds and the fractional density of the composite increases, pores gradually become isolated. The connectivity density only gradually decreases during early stages of consolidation. However, at a critical density, the connectivity density rapidly decreases as vapor pathways close off. This is accompanied by an avalanche in isolated pores. Infiltration ceases shortly thereafter.

4. Conclusion

We have described the X-ray tomographic microscope that we have designed for imaging microstructures in three dimensions. Although the XTM can be used with conventional X-ray sources, it is truly microscopic only when used with synchrotron radiation.

The XTM's application in advanced composites and mineralized tissues has been described. Methods for following the evolution of microstructure with in vitro and in situ imaging cells have been demonstrated. A large number of specially designed cells can be envisioned. Sandia National Laboratories, California, has designed an in situ load frame to use with the XTM. With this load frame, it should be possible to image the nucleation and growth of cracks in composites. At Lawrence Livermore National Laboratory, we have designed and begun using a stage for imaging cancellous bone structure in small animals in vivo. This stage will allow us to quantify sequential changes

in cancellous bone resulting from estrogen deficiency, microgravity environments, or immobilization.

We anticipate that the next generation of high-brightness synchrotron radiation sources will make the use of X-ray optics practical, allowing the XTM to achieve even higher spatial resolution. Nevertheless, even with the current spatial resolution, the XTM is already making valuable contributions to those studies that require a three-dimensional understanding of microstructure.

Acknowledgments

Funding for the development of the XTM for composites research has been obtained, in part, from the Department of Energy, Advanced Industrial Materials Program ED38-02. Additional applications to mineralized tissues have been funded, in part, from the National Institutes of Health, National Institute for Dental Research grant P01 DE 09859. Lawrence Livermore National Laboratory is operated by the University of California for the U.S. Department of Energy under contract W-7405-ENG-48. Sandia National Laboratories, California, is operated by Martin Marietta for the Department of Energy. Stanford Synchrotron Radiation Laboratory is supported by the U.S. Department of Energy, Chemical Sciences Division.

References

[1] E.R. Weibel, J. Microsc. 155 (1989) 393.
[2] E.B. Vedel-Jensen, Ann. Inst. Statist. Math. 3 (1991) 455.
[3] R.T. DeHoff, E.H. Aigeltinger and K.R. Craig, J. Microsc. 95 (1972) 69.
[4] J.C. Elliott and S.D. Dover, J. Microsc. 126 (1982) 211.
[5] W.A. Ellingson, M.W. Vannier and D.P. Stinton, in: Characterization of Advanced Materials, eds. W. Altergath and E. Henneke (Plenum, New York, 1991) p. 9.
[6] G.Y. Baaklini, R.N. Yancey and S.M. Swickard, Cer. Eng. Sci. Proc. 14 (1993) 473.
[7] B.P, Flannery, H. Deckman, W. Roberge and K.D'Amico, Science 237 (1987) 1439.
[8] U. Bonse, Q. Johnson, M. Nichols et al., Nucl. Instr. and Meth. A 246 (1986) 43.
[9] J.H. Kinney, S.R. Stock, M.C. Nichols, U. Bonse and T.M. Breunig, J. Mater. Res. 5 (1990) 1123.
[10] J.H. Kinney, Q.C. Johnson, R.A. Saroyan, M.C. Nichols and U. Bonse, Rev. Sci. Instr. 60 (1989) 2475.
[11] J.H. Kinney, M.C. Nichols, Ann. Rev. Mater. Sci. 22 (1992) 121.
[12] J.H. Kinney, T.M. Breunig, T.L. Starr et al., Science 260 (1993) 789.
[13] G.T. Herman, 1980 Image Reconstruction form Projections: The Fundamentals of Computerized Tomography (Academic Press, New York).
[14] L. Grodzins, Nucl. Instr. and Meth. 206 (1983) 541.
[15] T.M. Bessmann, B.W. Sheldon, R.A. Lowdon and D.P. Stinton, Science 253 (1991) 1104.
[16] G.B. Freeman, T.L. Starr and T.C. Elston, in MRS Symp. Proc. 168 (1990) 49.
[17] T.M. Breunig, M.C. Nichols, J.H. Kinney and D.L. Haupt, Cer. Eng. Sci. Proc. 14 (1993) 500.
[18] J.H. Kinney, G.W. Marshall and S.J. Marshall, Scanning Microscopy (submitted).
[19] J. Hoshen and R. Kopelman, Phys. Rev. B 15 (1976) 3438.
[20] L.A. Feldkamp, S.A. Goldstein, A.M. Parfitt et al., J. Bone Miner Res. 4 (1989) 3.

Computed microtomography:

Techniques and biomedical applications

Per Spanne
ESRF
Grenoble, France

Principle of computed tomography

Why synchrotron radiation

Contrast mechanisms

Instrumentation

Real time CMT

Applications : Biomedical
Fluid flow modelling

New possibilities

Advantages with monoenergetic x-rays:

Less beam hardening artefacts

Better quantitative accuracy

Optimized imaging time

Minimized absorbed dose

Contrast mechanisms:

Attenuation - atomic number and density

Fluorescence - elemental mapping

XAFS, XANES - chemical speciation

Compton scattered photons

Coherently scattered photons

Phase shift - low attenuation objects

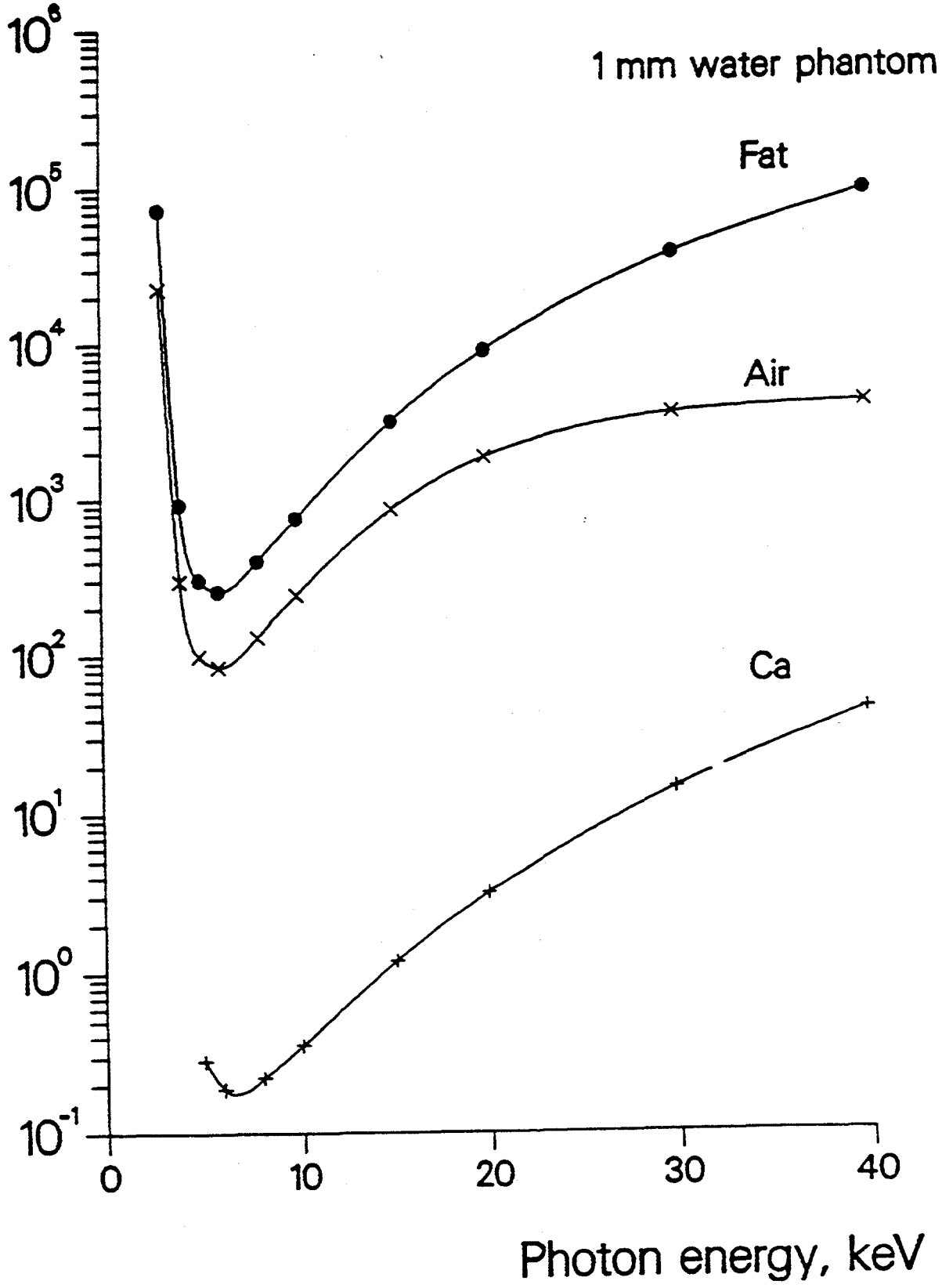
Absorbed dose, Gray
1 mm water phantom
Fat
Air
Ca
10^6
10^5
10^4
10^3
10^2
10^1
10^0
10^{-1}
0
10
20
30
40
Photon energy, keV

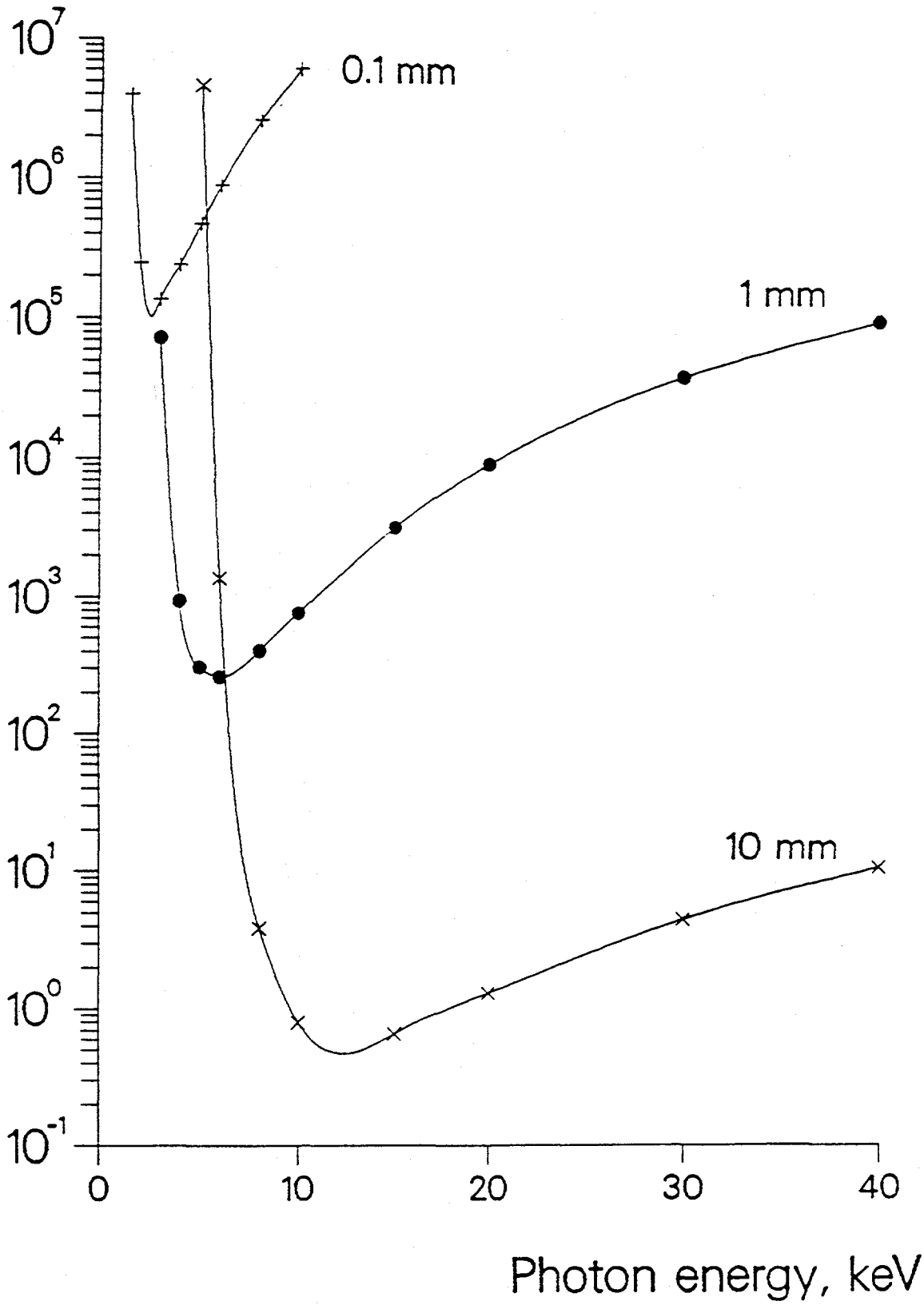
Absorbed dose, Gray
10^7
10^6
10^5
10^4
10^3
10^2
10^1
10^0
10^{-1}
0.1 mm
1 mm
10 mm
0
10
20
30
40
Photon energy, keV

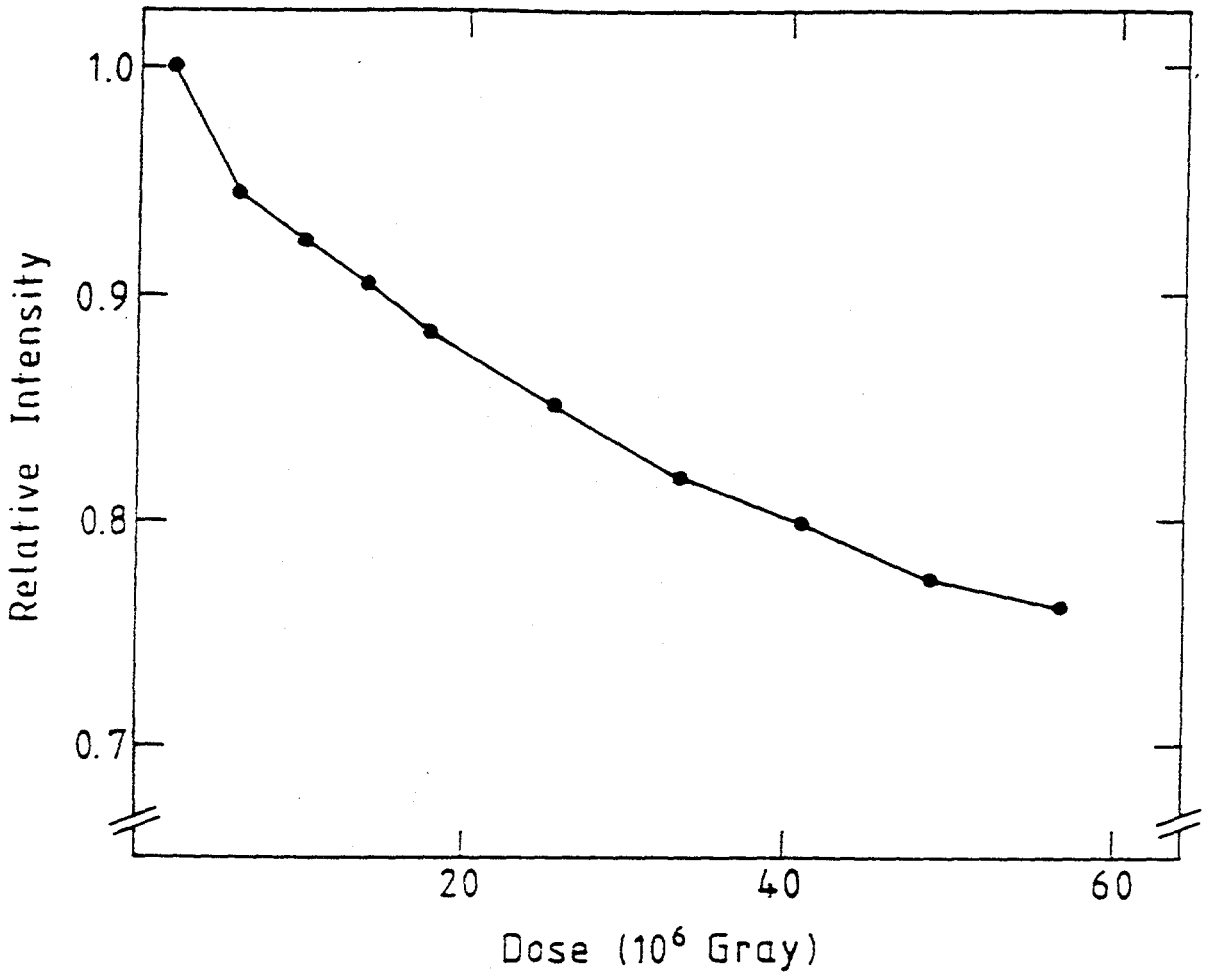

Fig. 8. The relative number of scattered X-rays from a skin sample as a function of the absorbed dose. The line is drawn to guide the eye.

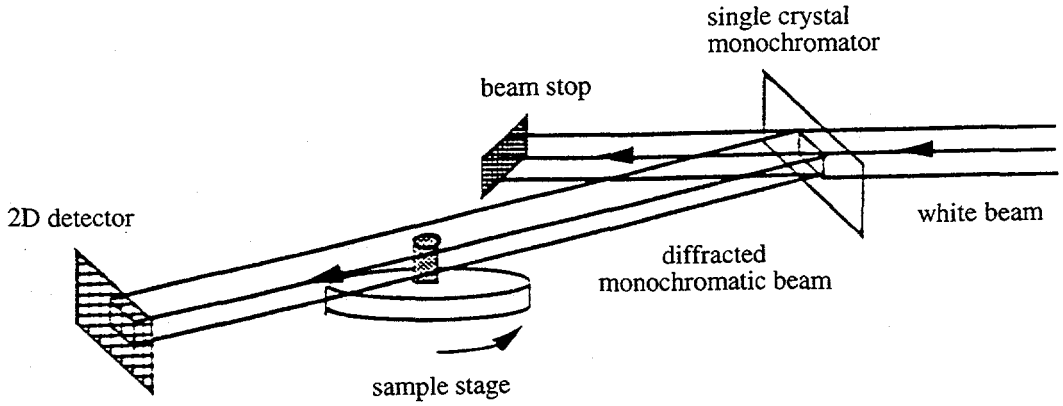

Schematic of the 3D CMT instrument.

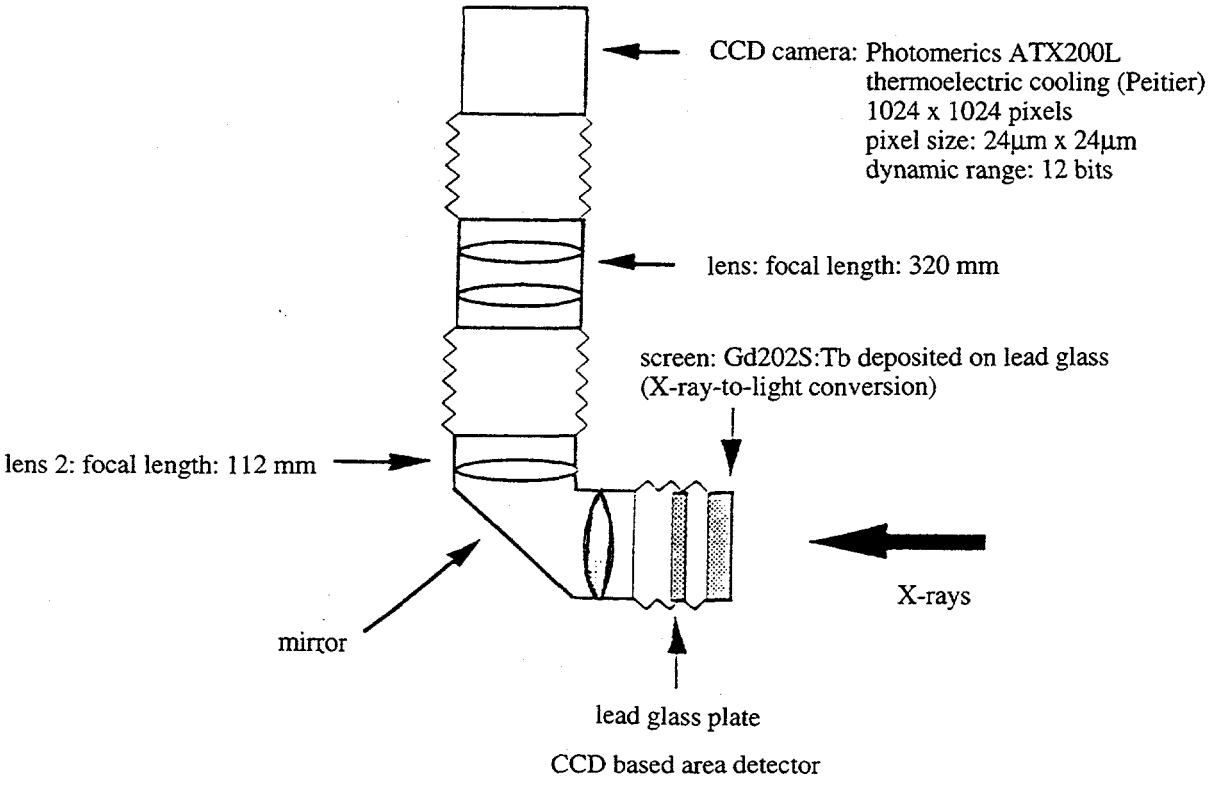
CCD camera: Photomerics ATX200L
thermoelectric cooling (Peitier)
1024 x 1024 pixels
pixel size: 24µm x 24µm
dynamic range: 12 bits
lens: focal length: 320 mm
screen: Gd202S:Tb deposited on lead glass
(X-ray-to-light conversion)
lens 2: focal length: 112 mm
X-rays
mirror
lead glass plate
CCD based area detector

High Performance ESRF Camera Head

High pixel rate, High Dynamic Range, 1 Million 19 μm2 pixels
200 ms Readout Time

J.C. Labiche, J.Segura, D. Van Brussel, J.P. Moy and the cooperation of
J.Cerrai, J. Clement and S. Gibney

Sept 95

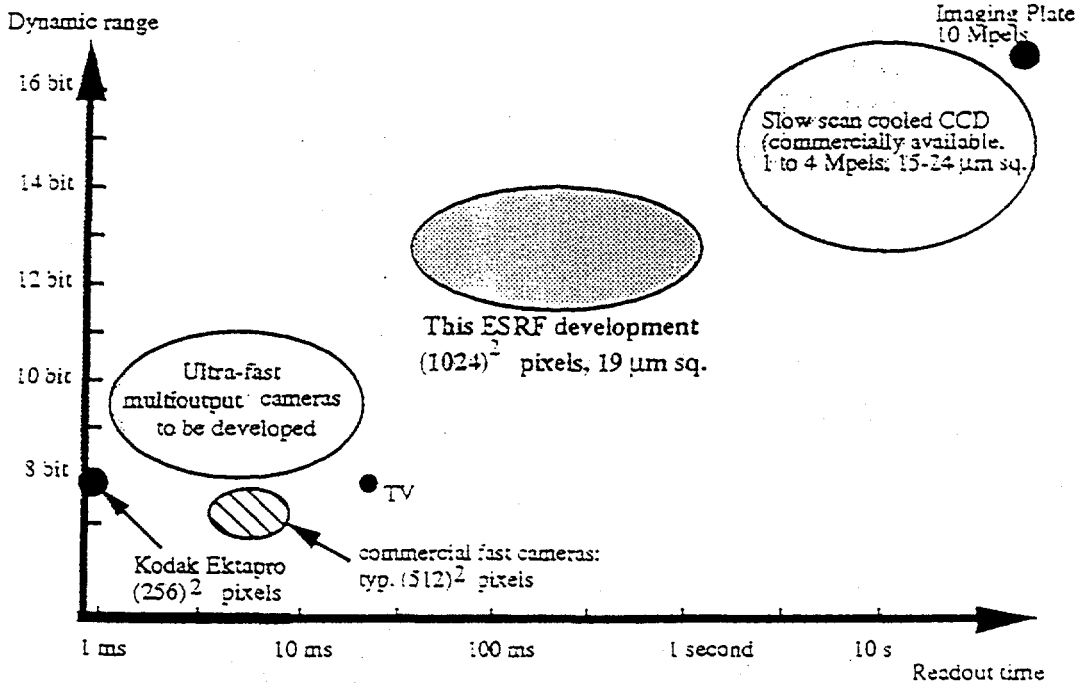

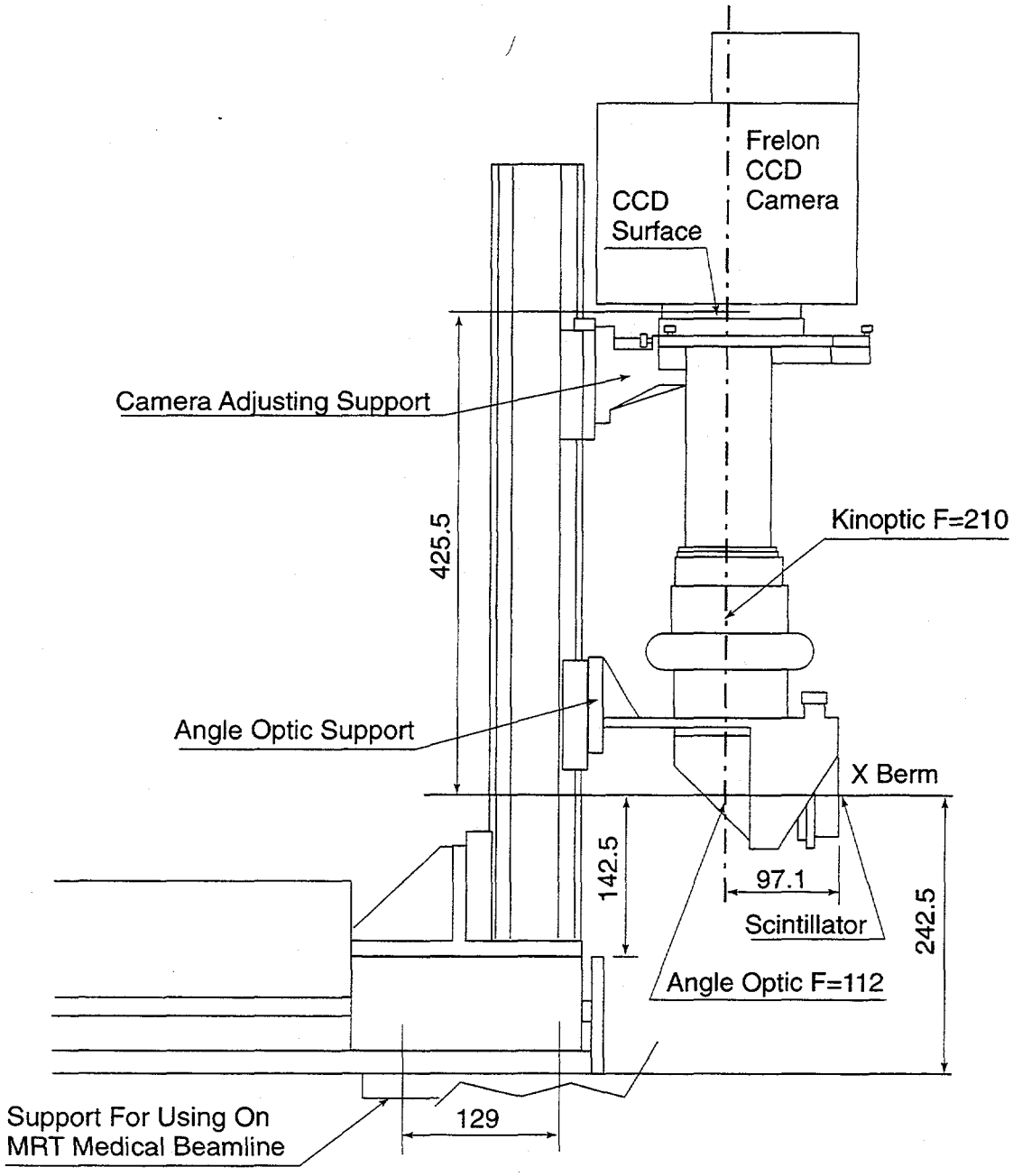

0mm SCALE: 2-5 250		NAME	DATE
	DRN	J.BORREL	8-07-96
	CKD		
BL 14 MRT-1017 MEDICAL FRELON DETECTOR F=210 ASSEMBLY	APPO.		
	ISO STANDARD CDL SURFACE FINISH: CDL LINEAR TOL: CDL ANGULAR TOL:		
EUROPEAN SYNCHROTRON RADIATION FACILITY BP 220 38043 GRENOBLE CEDEX-FRANCE TEL. 76-88-20-00 FAX 76-88-20-20	ASSY.		
A1	17.56.1000		

CONCEPTUAL DESIGN FOR HIGH-SPEED COMPUTED MICROTOMOGRAPHY AT THE ADVANCED PHOTON SOURCE

W. B. Lindquist
Department of Applied Mathematics and Statistics
State University of New York, Stony Brook, NY

A. E. Kaufman
Department of Computer Science
State University of New York, Stony Brook, NY

P. Spanne and K. W. Jones
Department of Applied Science
Brookhaven National Laboratory, Upton, NY

J. V. Smith, M. L. Rivers, and S. R. Sutton
Department of the Geophysical Sciences
The University of Chicago, IL

Real Time Computed Tomography System

GOAL:

Data collection, reconstruction and display for a

256x256x256

element volume

at a refresh rate of

10 Hz.

Raw data from CMT:

One slice:

Typically $1024 \times 1024 \times \frac{\pi}{2}$ words

For volume consisting of 1024 slices:

Approximately 3 Gbyte array

Reconstruction today:

SNARK filtered backprojection

Parallel processing using PVM

- Now 16 computers
- Average of 36 s per 1024^2 slice
- 10^9 voxels in 10 h

Improvements within the next 3 months:

Implementation and parallellisation of the linogram method will increase speed by a factor of 8

Alternative algorithm can perhaps give another factor of 2

BEREA SANDSTONE

(for Erika Schlueter, LBNL)

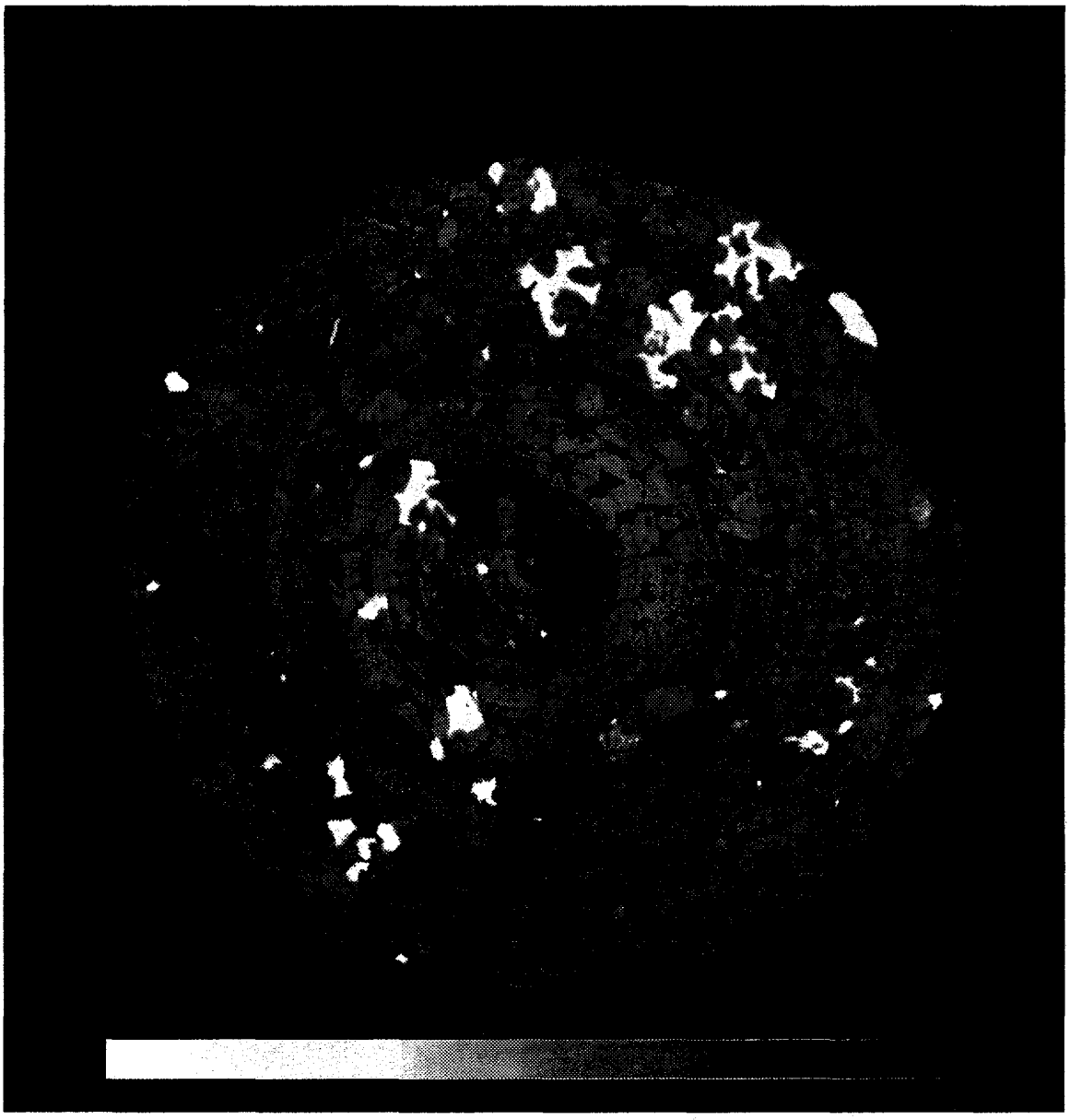

(6 μm voxels - 5 mm diameter)

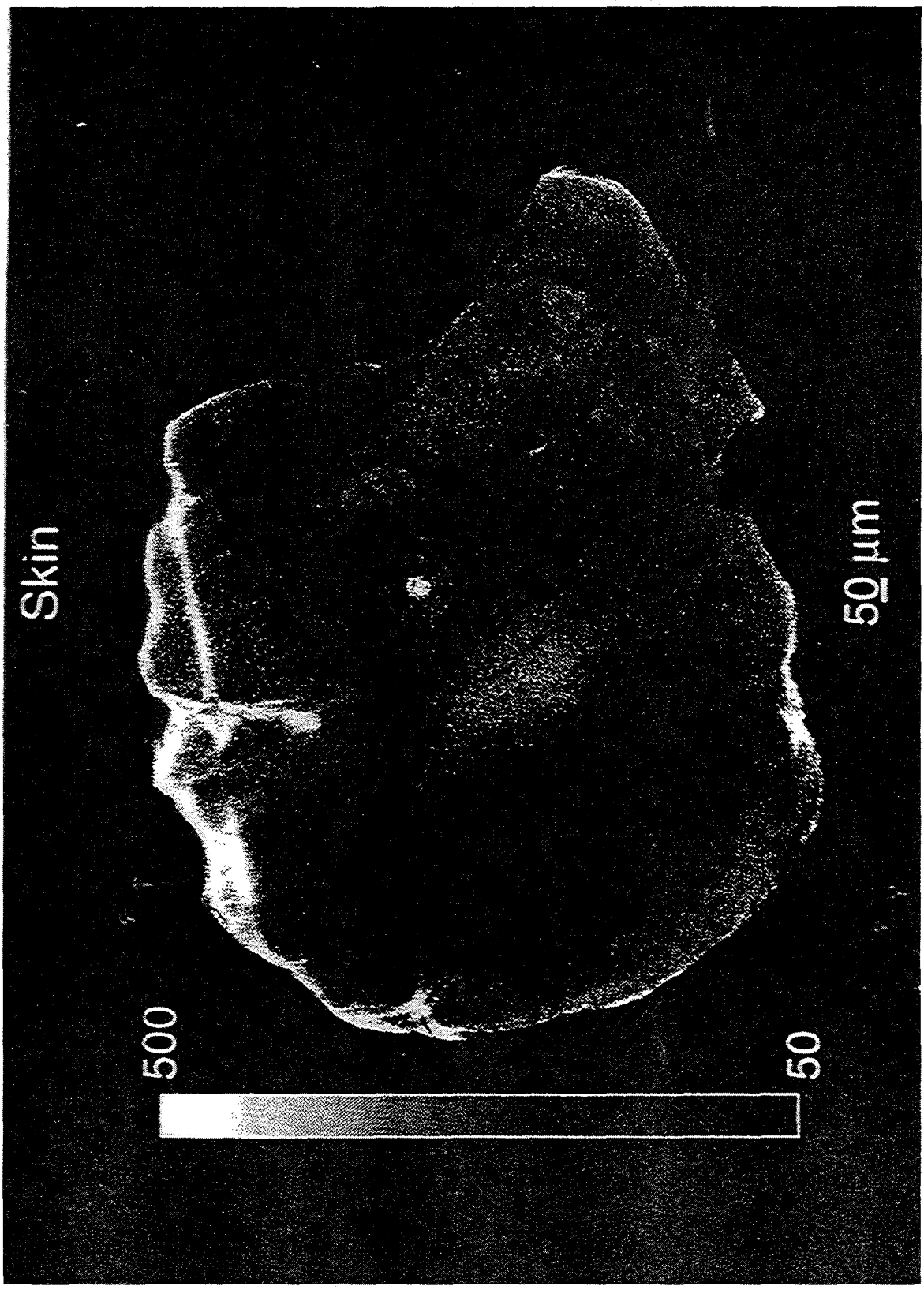
Skin
500
50
50 µm

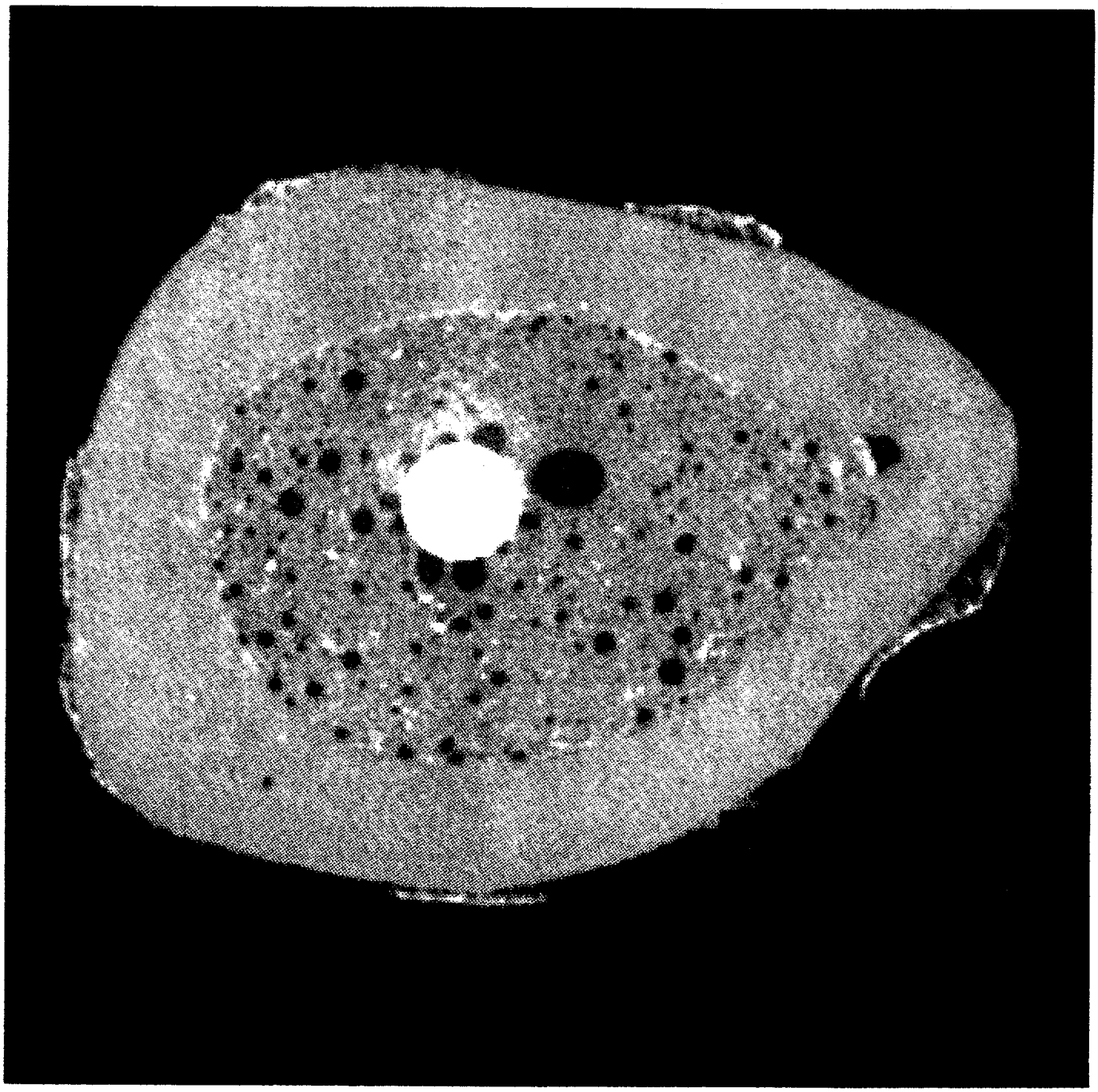

3D reconstruction of a human vertebra sample

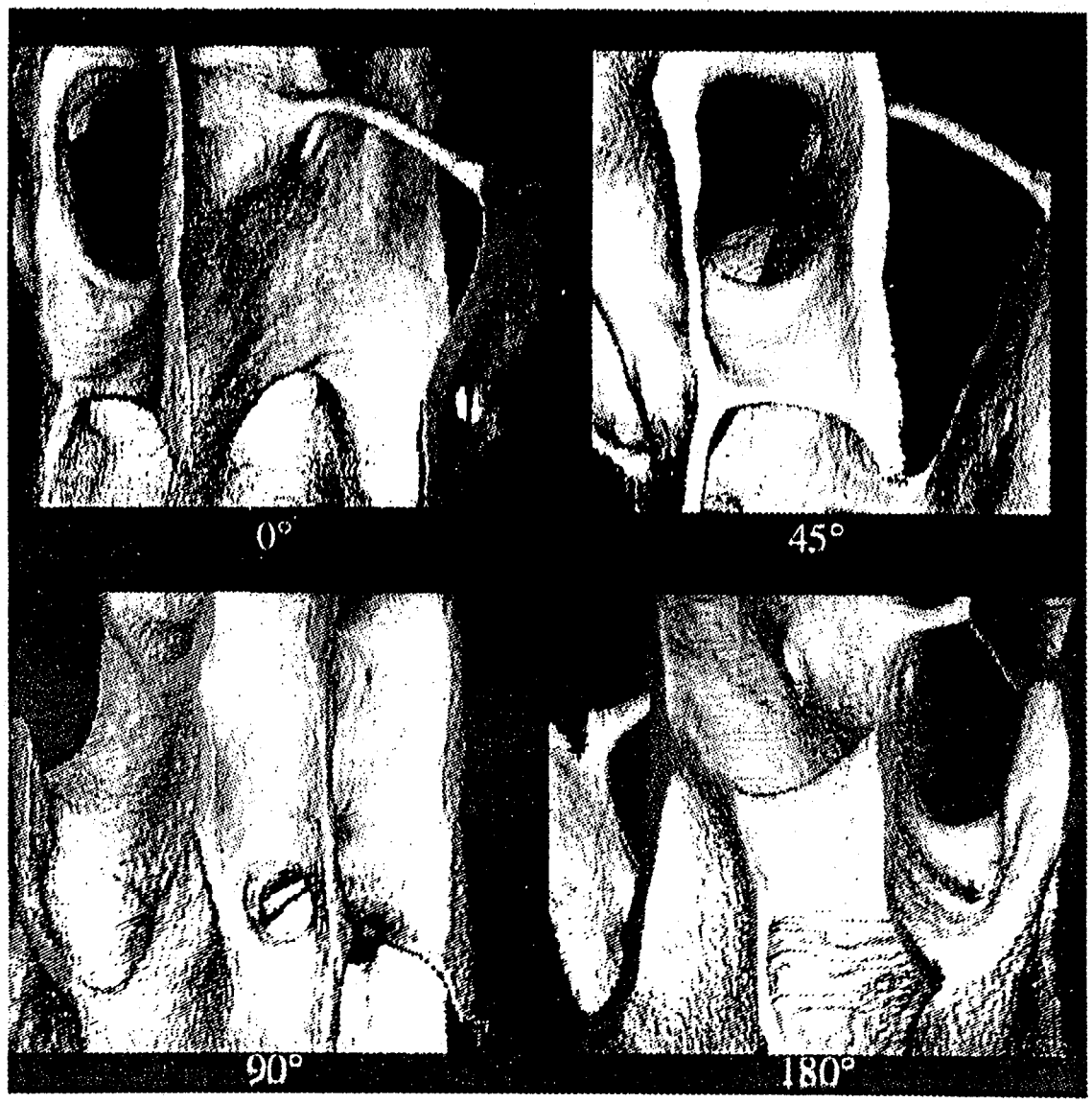

M. PATEYRON
F. PEYRIN

Creatis

3D microtomographic reconstruction of a human vertebra sample

1 mm

M. PATEYRON
F. PEYRIN

Creatis

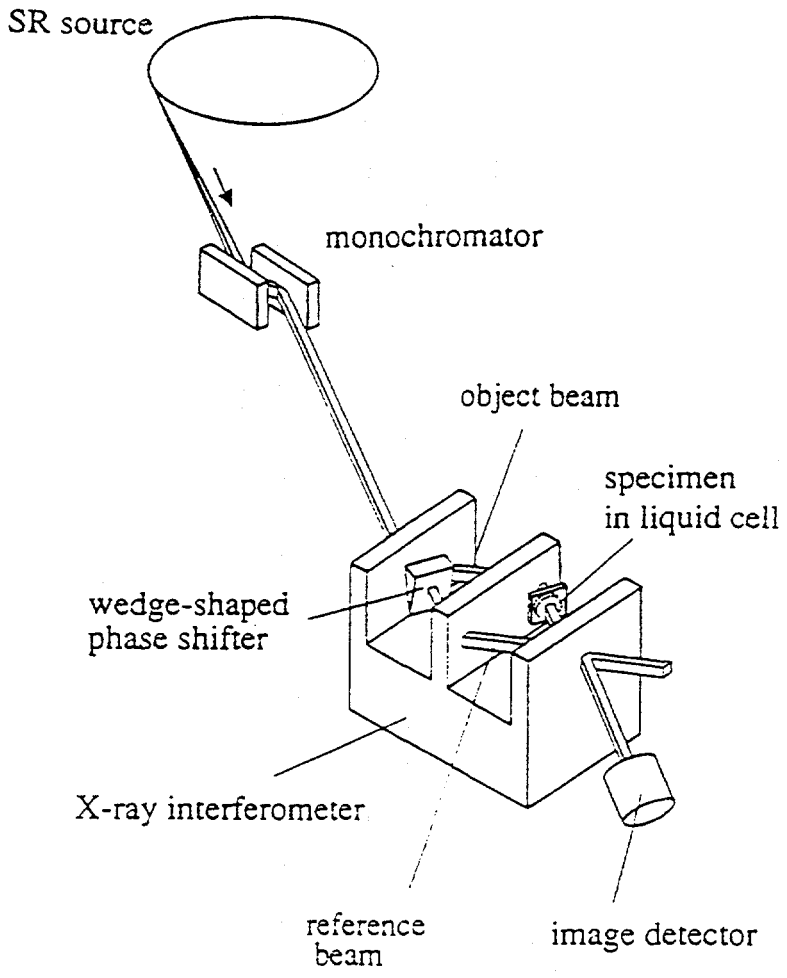

FIG. 2. Experimental setup for phase-contrast radiography. When the incident x-ray beam to an x-ray interferometer, which is cut from a silicon perfect crystal, satisfies the Bragg diffraction condition, an object beam and a reference beam are created. A specimen which is put in a liquid-filled cell is inserted in the object beam path. For quantitative analysis of an interference pattern, a wedge-shaped phase shifter is inserted in the reference beam path. The interference pattern is detected by an x-ray image detector and x-ray films.

C. Raven, A. Snigirev, I. Snigireva, A. Suvorov, P. Spanne

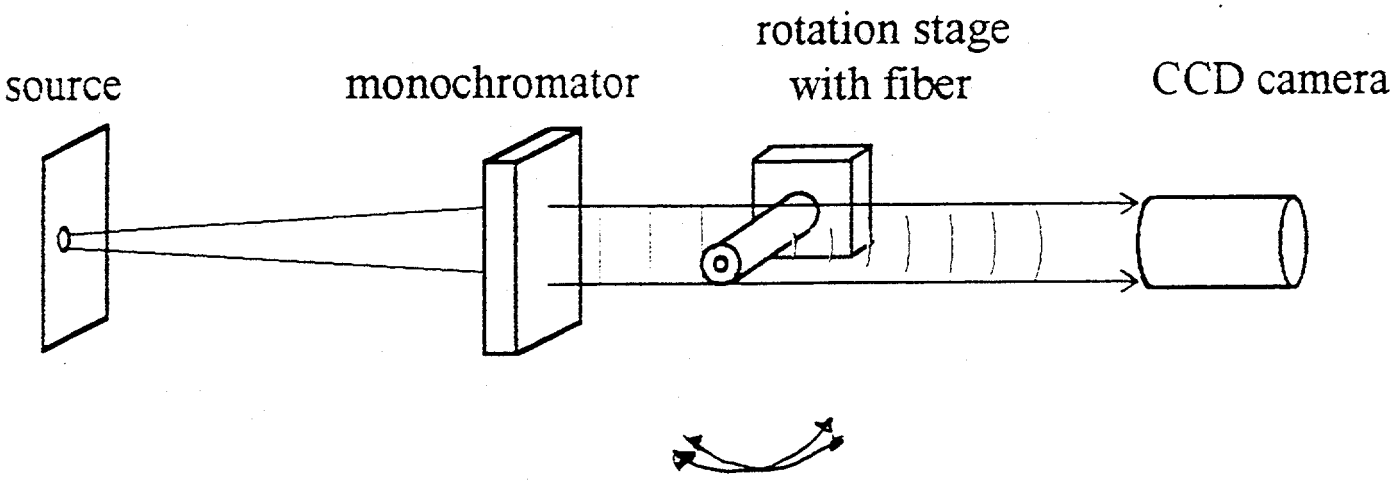

Phase imaging: Human Vertebra - E=19 keV

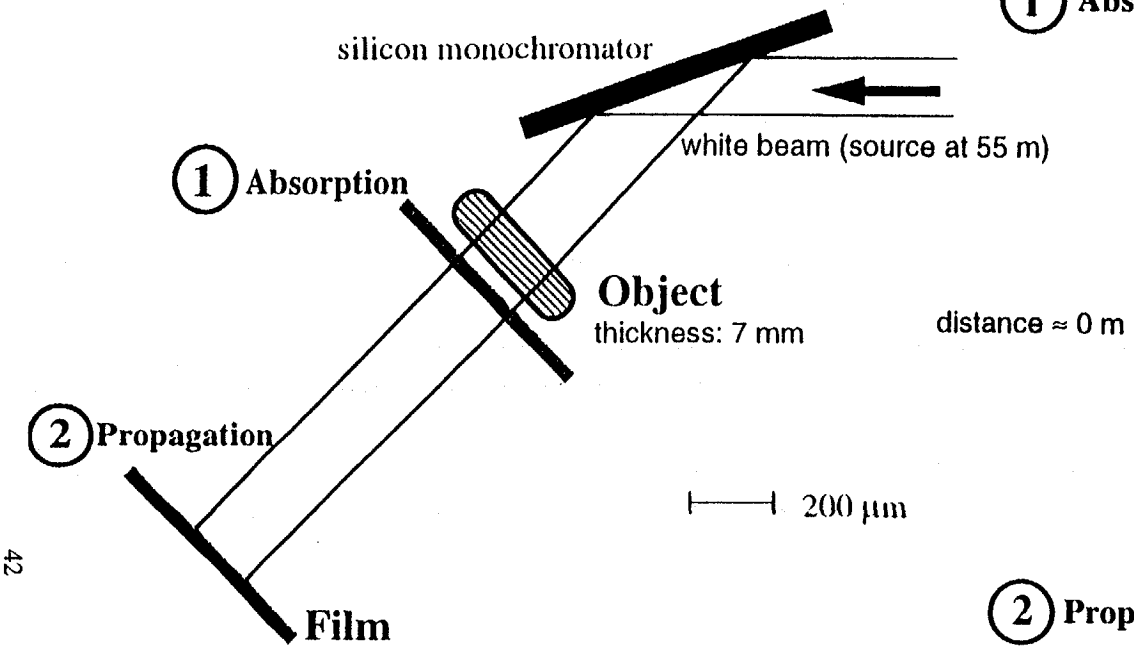

distance ≈ 0 m

1 Absorption

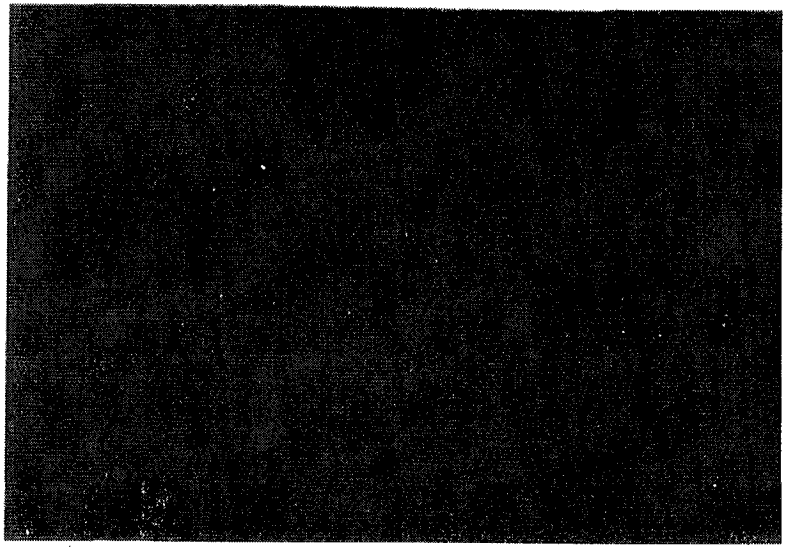

2 Propagation

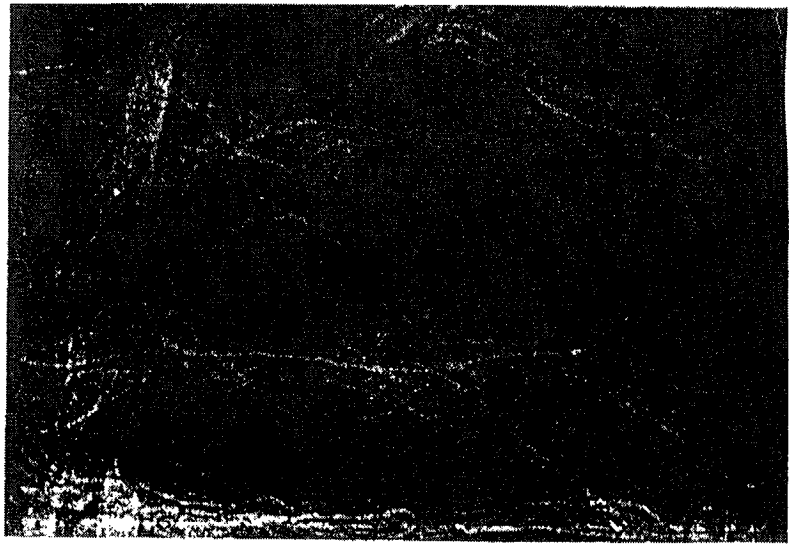

Peter CLOETENS
Murielle PATEYRON

distance = 1 m

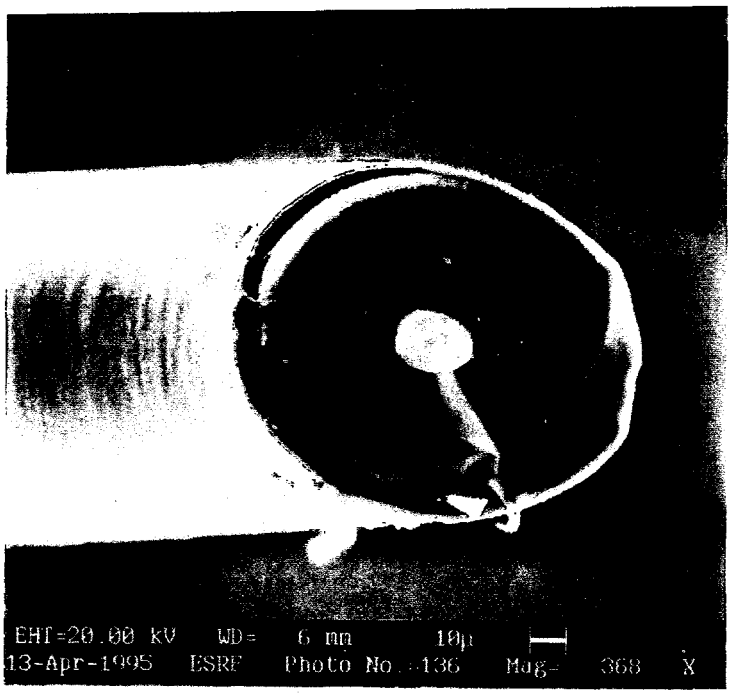
EHT=20.00 kV WD= 6 mm 10µ
13-Apr-1995 ESRF Photo No.:136 Mag= 368 X

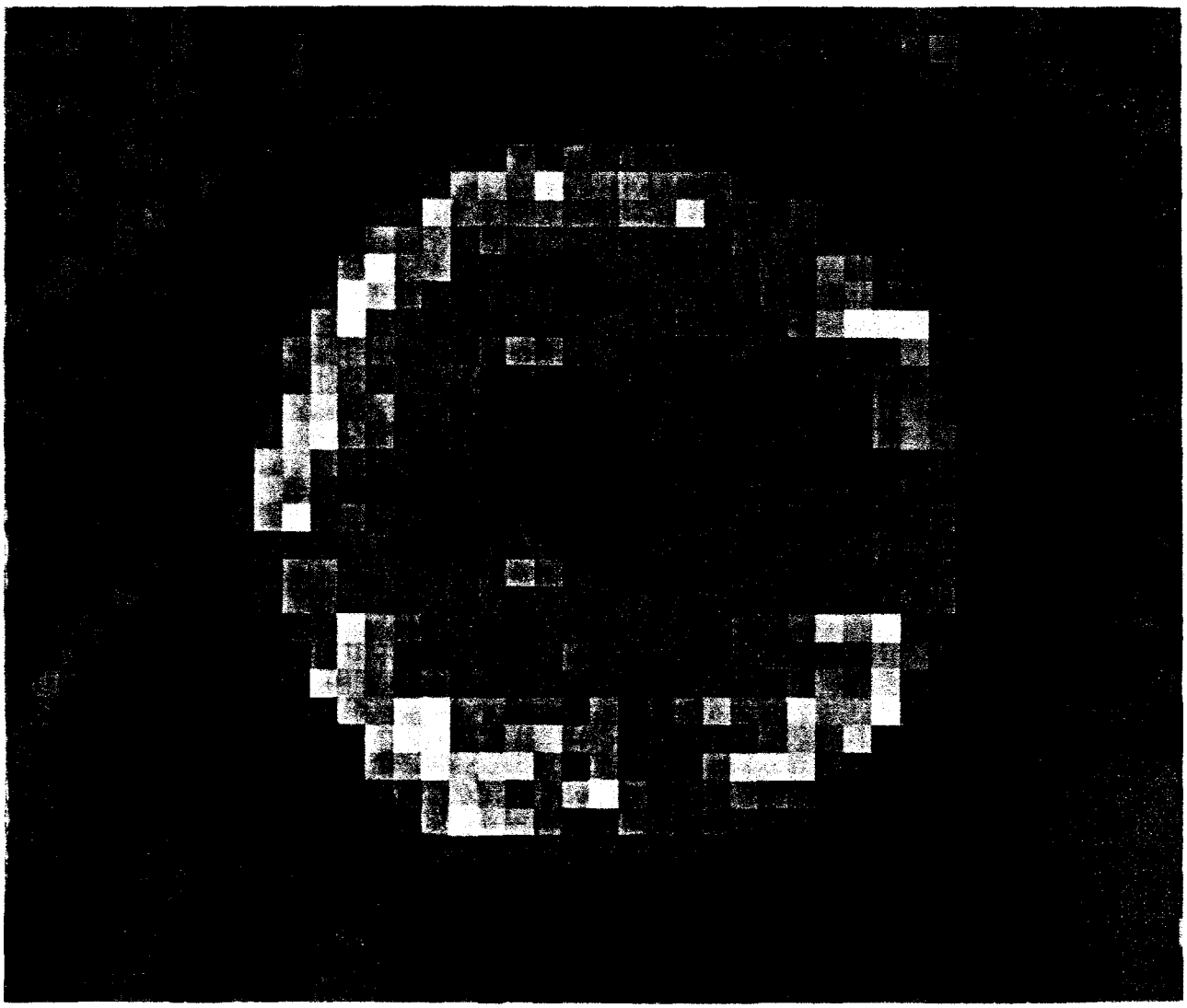

High Resolution IVEM Tomography of Biological Specimens

John W. Sedat and David A. Agard*

Department of Biochemistry and Biophysics and *Howard Hughes Medical Institute, University of California at San Francisco, San Francisco CA 94143-0448

Electron tomography is a powerful tool for elucidating the three-dimensional architecture of large biological complexes and subcellular organelles. The introduction of intermediate voltage electron microscopes further extended the technique by providing the means to examine very large and non-symmetrical subcellular organelles, at resolutions beyond what would be possible using light microscopy. Recent studies using electron tomography on a variety cellular organelles and assemblies such as centrosomes (Moritz et al.,1995a,b), kinetochores (McEwen, 1993) and chromatin (Woodcock, 1994), have clearly demonstrated the power of this technique for obtaining 3D structural information on non-symmetric cell components. When combined with biochemical and molecular observations, these 3D reconstructions have provided significant new insights into biological function.

Although the information that tomography provides is unique, its use as a general tool in the biological community has been limited due to the complexities involved in data collection and processing. To obtain reasonable resolution on thick biological samples requires the collection of a large number of tilted views of the same sample (typically > 100) at fine tilt intervals (< 1.5°) covering an angular range in excess of ± 60°. Because it is impossible the make the sample perfectly eucentric, specimen tilting results in both an X-Y translation and an alteration in focus. Thus each image has to be re-centered and re-focused. In addition, the images must be converted to digital form and precisely aligned with one another before the reconstruction can be calculated.

This is an extremely exacting and labor-intensive procedure. Recently, efforts have been made to simplify parts of tomography through the development of automated data collection systems (Dierksen et al, 1992; Koster et al,1993). These systems automate the tilting, translating, focusing and picture-taking steps that make up a typical data collection. If done manually, this process is both time-consuming due to the large number of images needed to be collected and also, suboptimal because of the high dose to which the sample is exposed during the execution of these actions. With an automated data collection a marked reduction in both time and dose is achieved (Fung et al, 1996; Braunfeld et al,1994; Koster et al, 1992) improving the quality of the data collected.

Our approach to simplifying and integrating the entire process has been to combine all aspects of a tomographic study: data collection, reconstruction, and image interpretation within one system (for a more complete discussion, see Fung et. al., 1996). With our system, both data collection and reconstruction are automated to make tomography more approachable to the average user. Ease, reliability and speed have been emphasized.

Instrumentation: Our current system is built around a Philips EM430 Intermediate Voltage TEM (300 kv LaB_6) with a Phillips C400 microscope/computer interface unit providing a link to all the TEM's functions. Images are acquired through a prototype 12 bit/pixel cooled (-35° C) slow scan CCD camera attached to a Photometrics controller (Thompson CCD chip 1024^2 pixels and 19 x19 um) with a readout rate of 2×10^5 pixels/s. Imaging control, display and processing were built around a Personal IRIS 4D35 (Silicon Graphics, Sunnyvale) workstation. For fast image acquisition and cross-correlation calculations, we use a 4 processor Shamrock array processor providing 320 Mflops (SKY Computers Inc.).

Image Positioning and Focusing Fundamental for automated tomography is the ability to dynamically correct for the positional and focus offsets that result from imperfect specimen eucentricity. To minimize beam dosage, very short exposures (~ 0.1s) are used for all correction functions. Cross correlation between the current test image taken after a tilt change, and the last good image immediately reveals the amount and direction of image translation. Both image and beam deflection coils are energized so as to precisely re-center the image. In a manner analogous to the built-in wobbler used to aid in manual focusing, the cross correlation error between two images taken with the beam tilted first + then - ~ 1mrad reveals the distance that the same is away from true focus. The energization of the objective lens is then altered to set the desired underfocus level.

In an effort to make the process more robust, we have developed functions to monitor the behavior of the data collection. Values such as tilt, maximum or minimum intensity, and image shift displacements are all checked to make sure each of the values falls within an expected range, otherwise, an error message is sent and the data collection is paused until further operator instructions. Problems can be dealt with either by using a function to resume the next action, or by using a function which goes back to previous sections in order to redo their collection. Microscope and computer failures which can completely halt the data collection do happen occasionally. For such

situations, a recovery function was installed to restore the reference section and all environment conditions to the last saved image.

More General Functions For a tomography system to be complete, additional functions which permit ease in scanning and aid in image analysis are needed. We have incorporated functions to permit computer optimization of sample eucentricity, to interactively shift the image center , as well as a stereo viewing function to automatically acquire stereo pairs of an image. To aid in recording larger areas than permitted by the limitations of the CCD field, a montage function has also been added. The montage function takes a series of partially overlapping views in order to construct a larger combined image.

Data Processing Once a data stack is collected, the tilt projection views making up the stack are processed to ensure that their alignment and mass density distribution are consistent with the 3D object from which they were derived. Only then can the entire set of tilt projection views be used to reconstruct a 3D model of the specimen. To maximize the automation of the processing steps, a pipeline was installed so that parameters and files created or modified in one module are automatically updated as input to the next module. Furthermore, each module was optimized so that the number of input parameters and files entered by the user are kept to a minimum. In the best case, only the name of the data stack, the approximate size and number of the beads used for alignment, and the reconstruction volume are strictly required. Options to switch to an interactive mode are also provided for in each module.

The next step is to obtain the parameters to perform a mass normalization of the data i.e. to convert the image intensity to a measure of mass density. Once calculated, these parameters along with the alignment parameters, are applied to the original data stack before the actual reconstruction begins. One reconstruction method or a combination of methods is then chosen as a means to construct our 3D density map from the collected tilt data. We have two reconstruction algorithms: EWBP(Elliptical Weighted Back-Projection) which is a linear method, and TAPIR (Tomographic Alternating Projection Iterative Reconstruction) which is non-linear and iterative. EWBP computes the weighted back-projection reconstruction. Besides the conventional r-weighting function, EWBP contains an elliptical-square weighting function to allow for arbitrary projection tilting geometry and proper reconstruction scale (i.e., the scale of the reconstruction corresponds to that of the projections). The other reconstruction algorithm TAPIR uses an iterative method to compare the reconstruction with the original data while incorporating some boundary conditions. Simply, TAPIR tries to

minimize the difference between the reconstruction and the projections with constraints such as positivity and Z-boundedness. Positivity and boundedness provide strong constraints for removing reconstruction artifacts due to the missing wedge (finite tilt range). TAPIR also attempts to minimize the limited detector problem which arises when the specimen area is larger than the detector.

References

Braunfeld, M. B., Koster, A. J., Sedat, J. W., and Agard, D. A. (1994) *J. Microscopy* **174**(2), 75-84.

Dierksen, K., Typke, D., Hegerl, R., Koster, A. J., AND Baumeister, W. (1992) *Ultramicroscopy* **40**, 71-87.

Fung, J.C., Liu, W., deRuijter,W.J., Chen.H., Abbey,C.K., Sedat, J.W., and Agard, D.A. (1996) *Journal of Structural Biology* **116**:181-189.

Horowitz, R. A., Agard, D. A., Sedat, J. W., and Woodcock, C. L. (1994) *J. Cell Biol.* **125**(1)1-10.

Koster, A. J., Chen, H., Sedat, J. W., and Agard, D. A. (1992) *Ultramicroscopy* **46**, 207-227.

Koster, A. J., Braunfeld, M. B., Fung, J. C., Abbey, C. K., Han, K. F., Liu W., Chen, H., Sedat, J. W., and Agard, D.A. (1993) *MSA Bulletin* **23**(2), 176-188.

McEwen, B. F., Arena, J. J., Frank, J., and Rieder, C. L. (1993) *J. Cell Biol.* **120**(2), 301-312.

Moritz, M., Braunfeld, M. B., Fung, J. C., Sedat, J. W., Alberts, B. M, and Agard, D. A. (1995) *J. Cell Biol.*,**130**:1149-1159.

Moritz, M., Braunfeld, M. B., Sedat, J. W., Alberts, B. M, and Agard, D. A. (1995). *Nature* **378**:638-640.

X-ray Microtomography

What Can We Learn About Reservoir Rocks and the Interplay Between Physics and Geometry

Larry Schwartz

Schlumberger-Doll Research, Ridgefield, CT, USA

1) Models and Measurements of Pore and Grain Geometries

   Granular and Image Based Models

   Synchrotron X-Ray Microtomography

2) Calculation of Transport Properties

   Electrical and Fluid Flow - Single Phase Transport

   Multi-Phase Transport

3) Challenges for the Future - Two Component Pore Spaces

   Interfacial Transition Zone in Mortar

   Micro-Porosity in Carbonates

Collaborators:

F. Auzerais
J. Dunsmuir (Exxon)
E. Garboczi (NIST)
N. Martys (NIST)
T. Ramakrishnan
D. Rothman (MIT)

References:

B. P. Flannery, H. W. Deckman, W. G. Roberge, and K. L. D'Amico, Three dimensional X-ray microtomography, Science **237**, 1439 (1987).

P. Spanne, J. F. Throvert, C. J. Jacquin, W. B. Lundquist, K. W. Jones, and P. M. Adler, Syncrotron computed microtomography of porous media: topology and transports, Phys. Rev. Letters, **73**, 2001 (1984).

F. M. Auzerais, J. Dunsmuir, B. B. Ferréol, N. Martys, J. Olsen, T. S. Ramakrishnan, D. H. Rothman, and L. M. Schwartz, Transport in Sandstone: A study based on three dimensional microtomography, Geophysics Res. Lett. **23**, No. 7, 705 (1986).

ADCO/SA64/9148_3/SEM

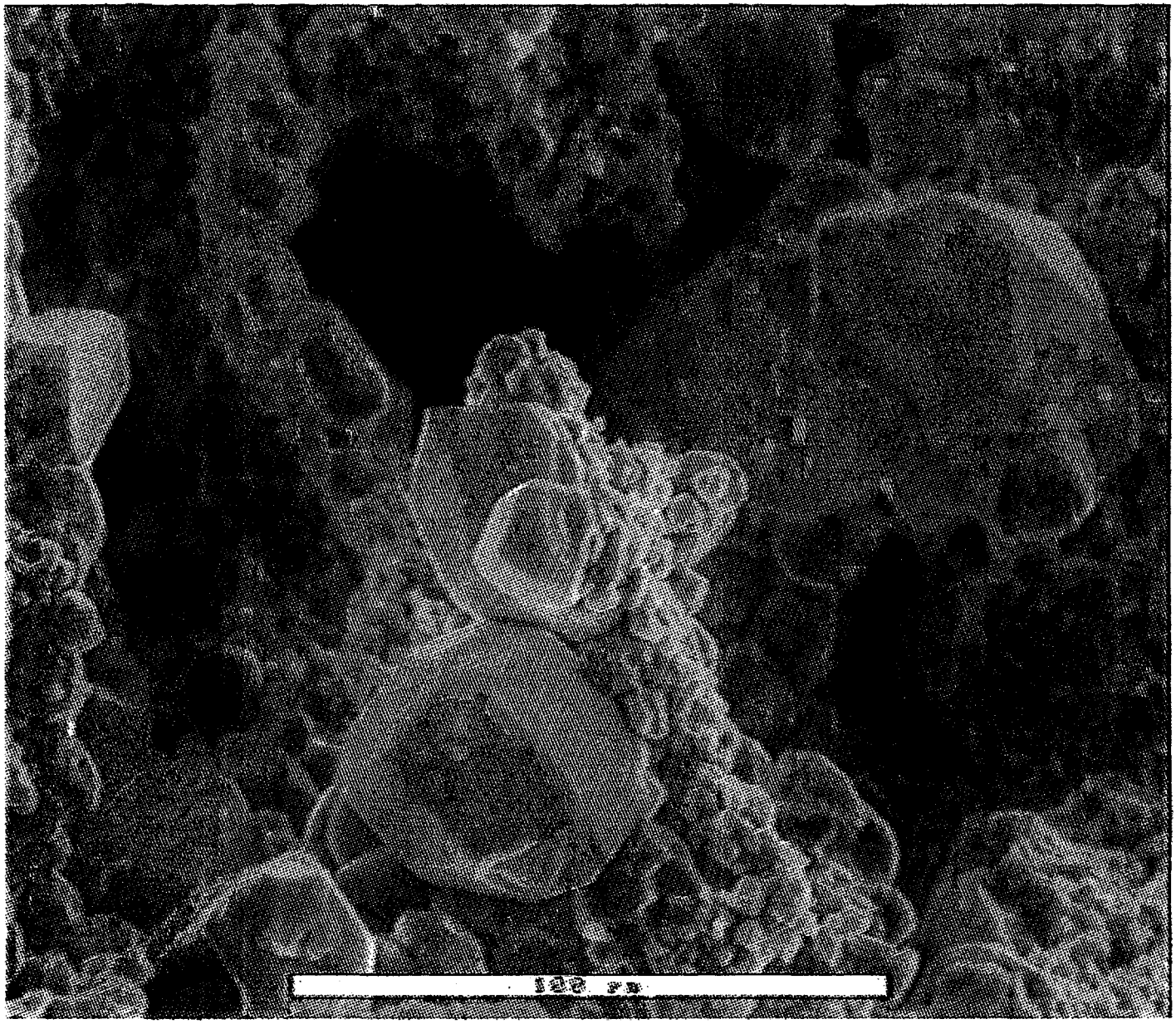

Three Dimensional X-ray Microtomography

B. P. Flannery, H. W. Deckman, W. G. Roberge, and K. L. D'Amico,
Science **237**, 1439 (1987).

Source-Detector Arrangement:

Conventional Medical CT Scanner

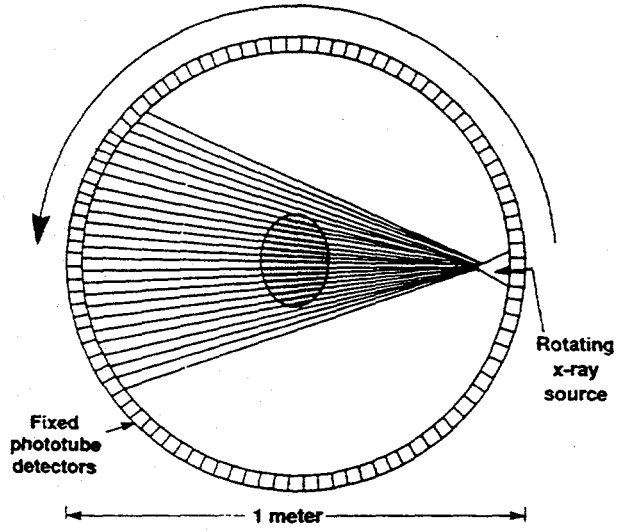

X-ray Microtomography

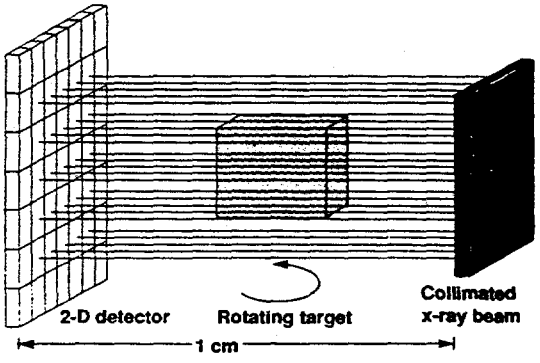

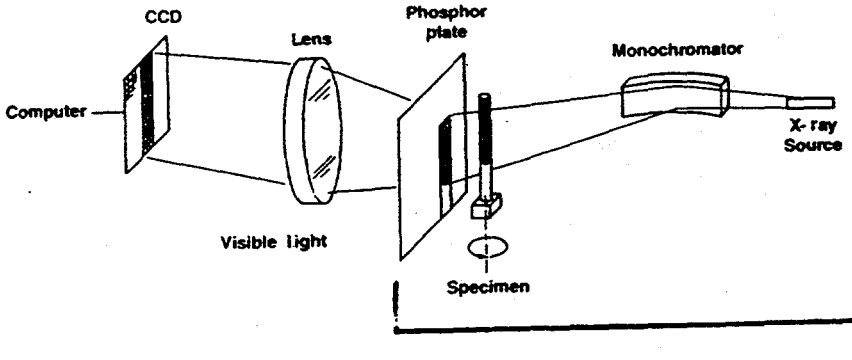

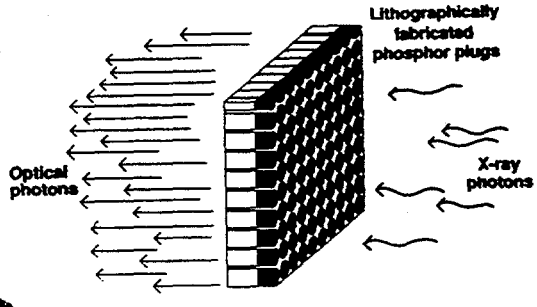

Cellular Phosphor Plate
[1 μm cell spacing]

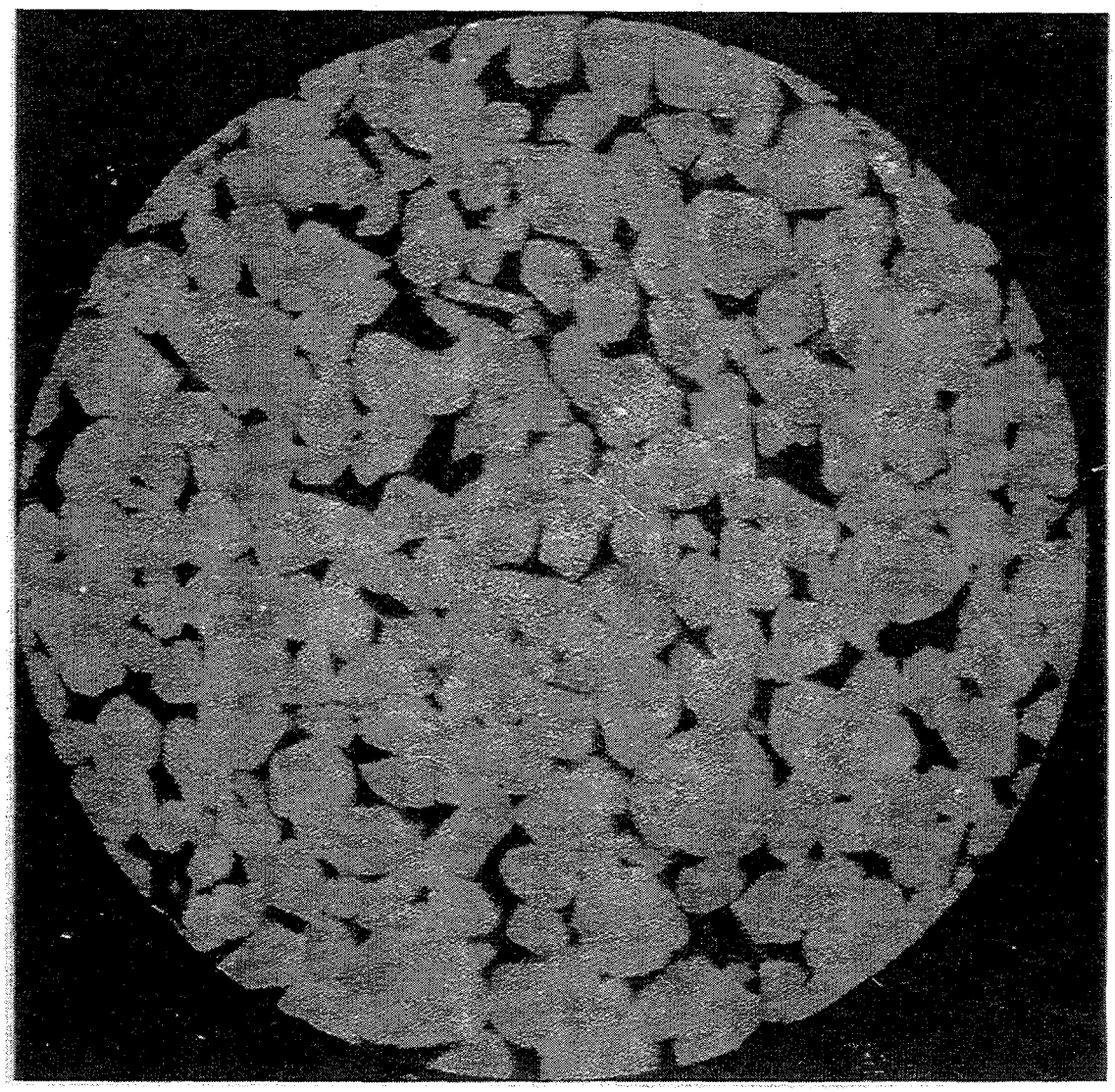

f2b78.ps

How do we Convert Data to a Binary Representation (Pores and Grains)?

1) Bin data into 400 levels and store the intensity function, $p(i)$

2) Find three parameters: Threshold (T) and Two Grey Levels (A and B)

that minimize the error function

$$E = \int_0^T (i - A)^2 p(i)\, di + \int_T^{400} (B - i)^2 p(i)\, di$$

with respect to A, B, and T

3) This is equivalent to an iterative solution for T

$$T = (A + B)/2$$

where A and B are the means of the distributions separated by T.

$$A = \frac{\int_0^T ip(i)\, di}{\int_0^T p(i)\, di} \quad \text{and} \quad B = \frac{\int_T^{400} ip(i)\, di}{\int_T^{400} p(i)\, di}$$

4) Result: $\phi_{MT} = 0.154$; while $\phi_{exp} = 0.152$ (He intrusion)

Reference: A. Magid, S. R. Rotman, A. M. Weiss, IEEE Trans. Systems, Man, and Cybernetics, **20**, 1238-39 (1989)

Diffusion Simulations of Conductivity

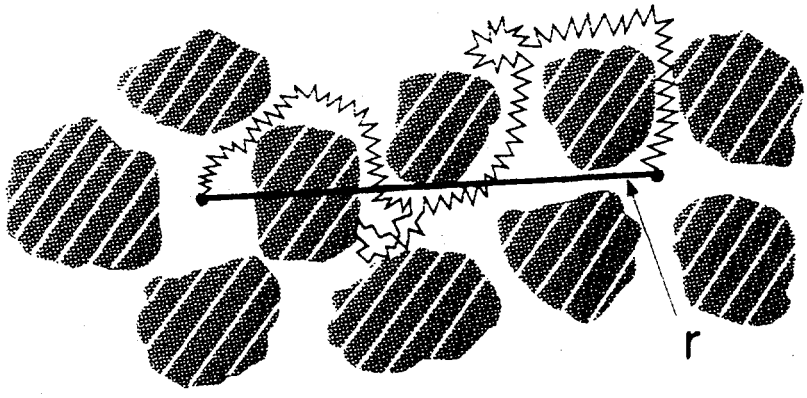

(1) Standard Diffusion

$\sigma = \phi D$

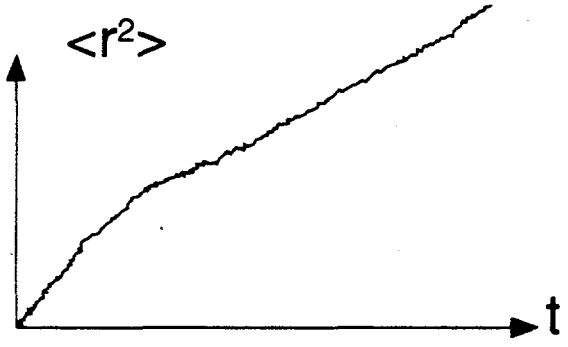

(2) Weak Applied Bias

$J \sim \sigma E$

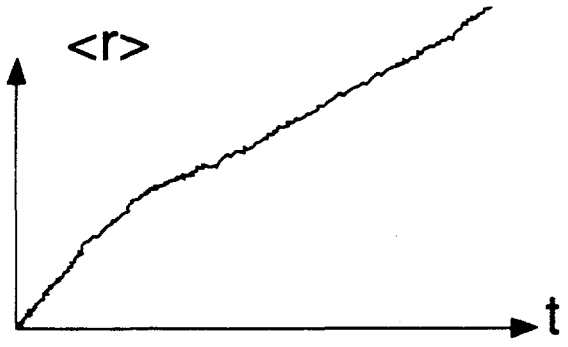

$$\text{Formation Factor } F = \frac{\sigma(\phi = 1)}{\sigma(\phi)}$$

VISCOUS FLUID FLOW IN POROUS MEDIA

(1) Definition of Permeability: Darcy Equation

$$\vec{V} = \frac{k}{\eta}\vec{\nabla}p$$

η: Fluid Viscosity

$\vec{V}$: Macroscopic Fluid Velocity

p: Pressure

k: Permeability

(2) Proper Thing to Do: Solve Stokes Equation

$$-\vec{\nabla}p + \eta\nabla^2\vec{u} = 0\,; \quad \vec{\nabla}\cdot\vec{u} = 0$$

Where $\vec{u}(\vec{r}\,)$ is the Microscopic Fluid Velocity

(3) Note: k has the Dimensions of Area; Depends on Length Scale

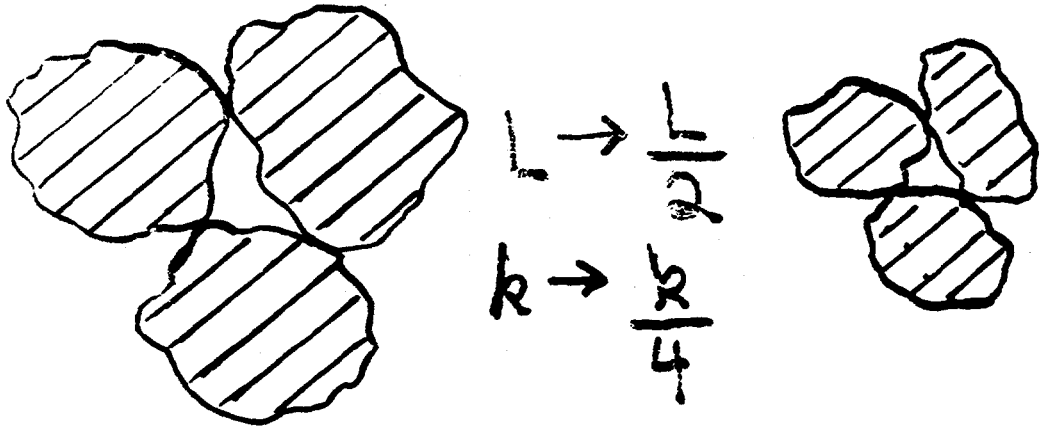

Geophysical Research Letters

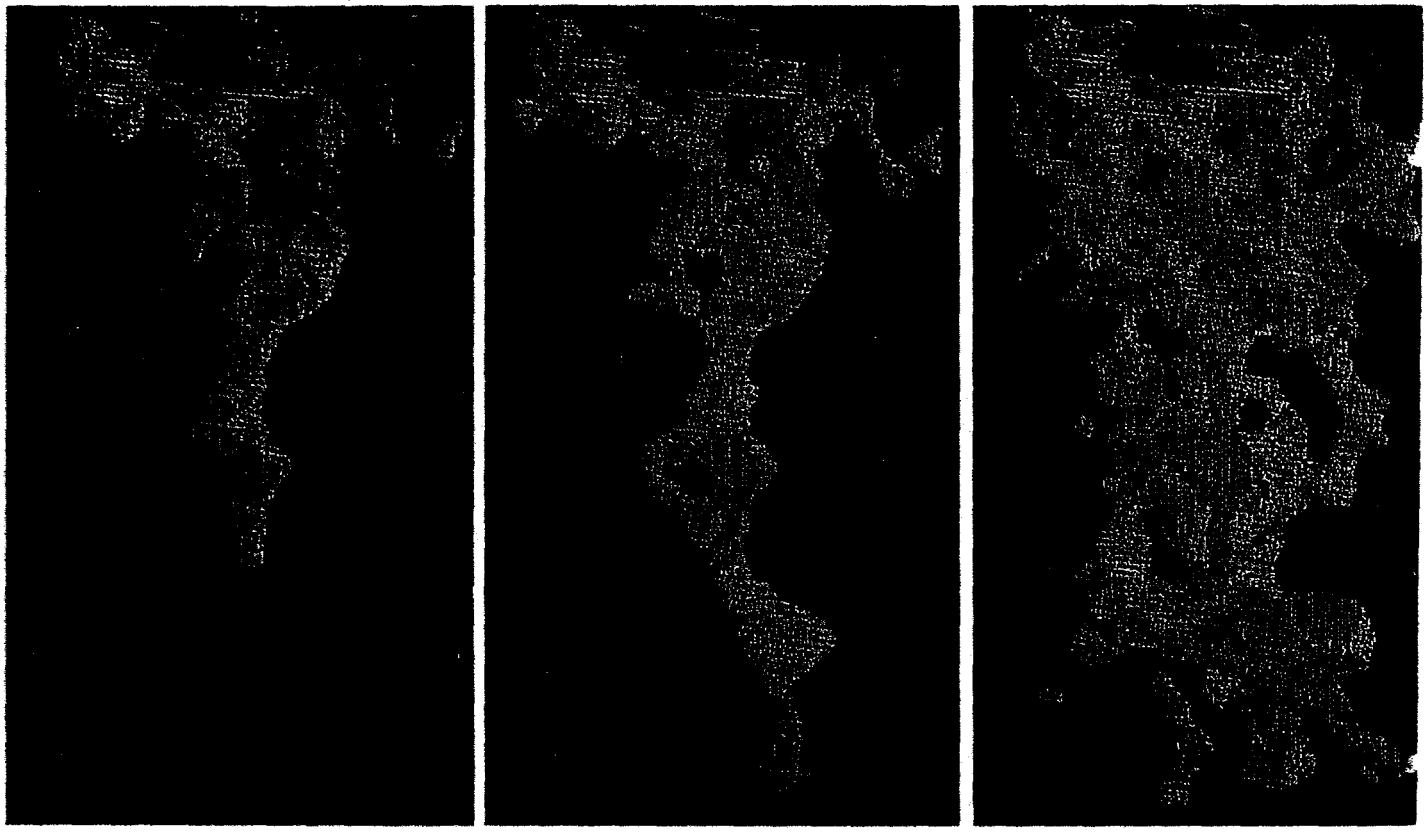

APRIL 1, 1996

Volume 23 Number 7

AMERICAN GEOPHYSICAL UNION

Fountainbleau Sandstone

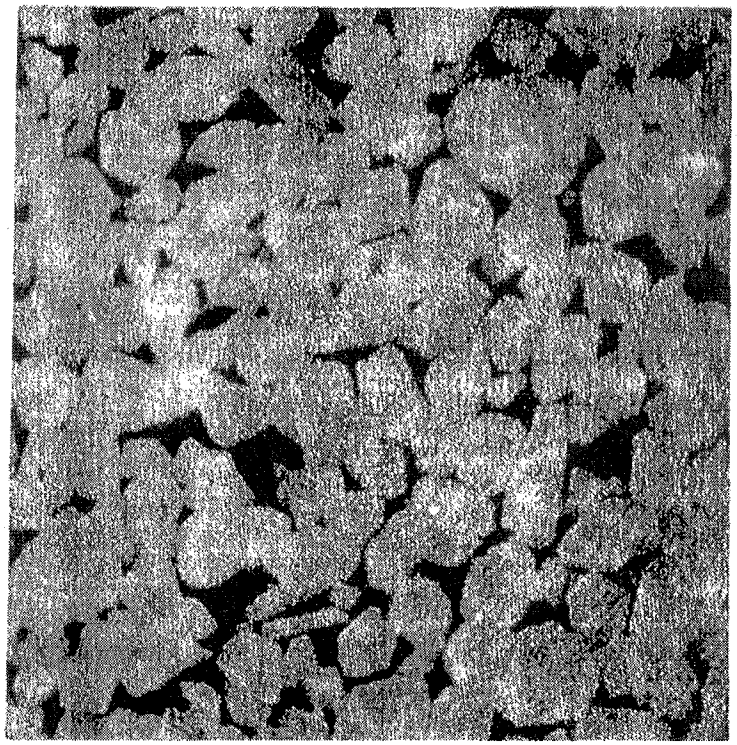

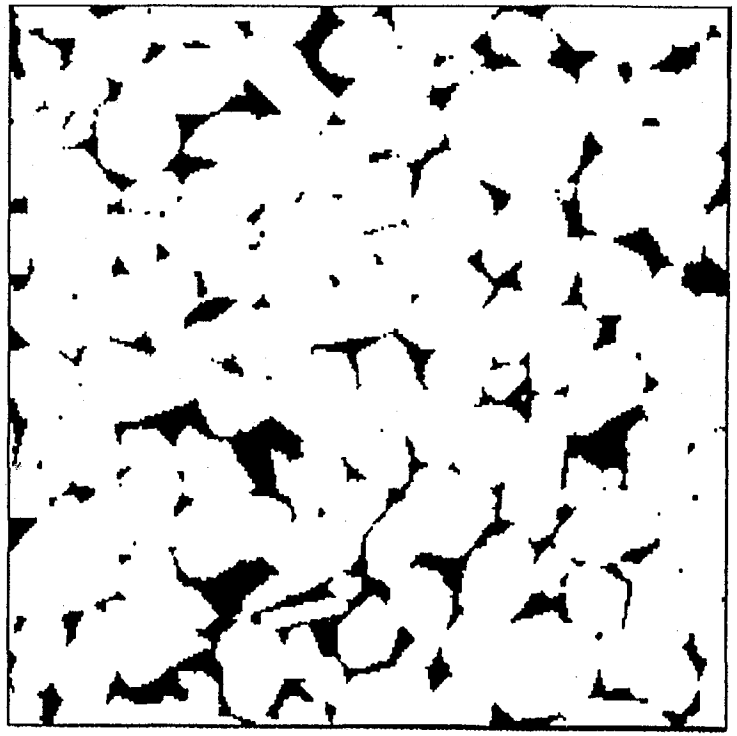

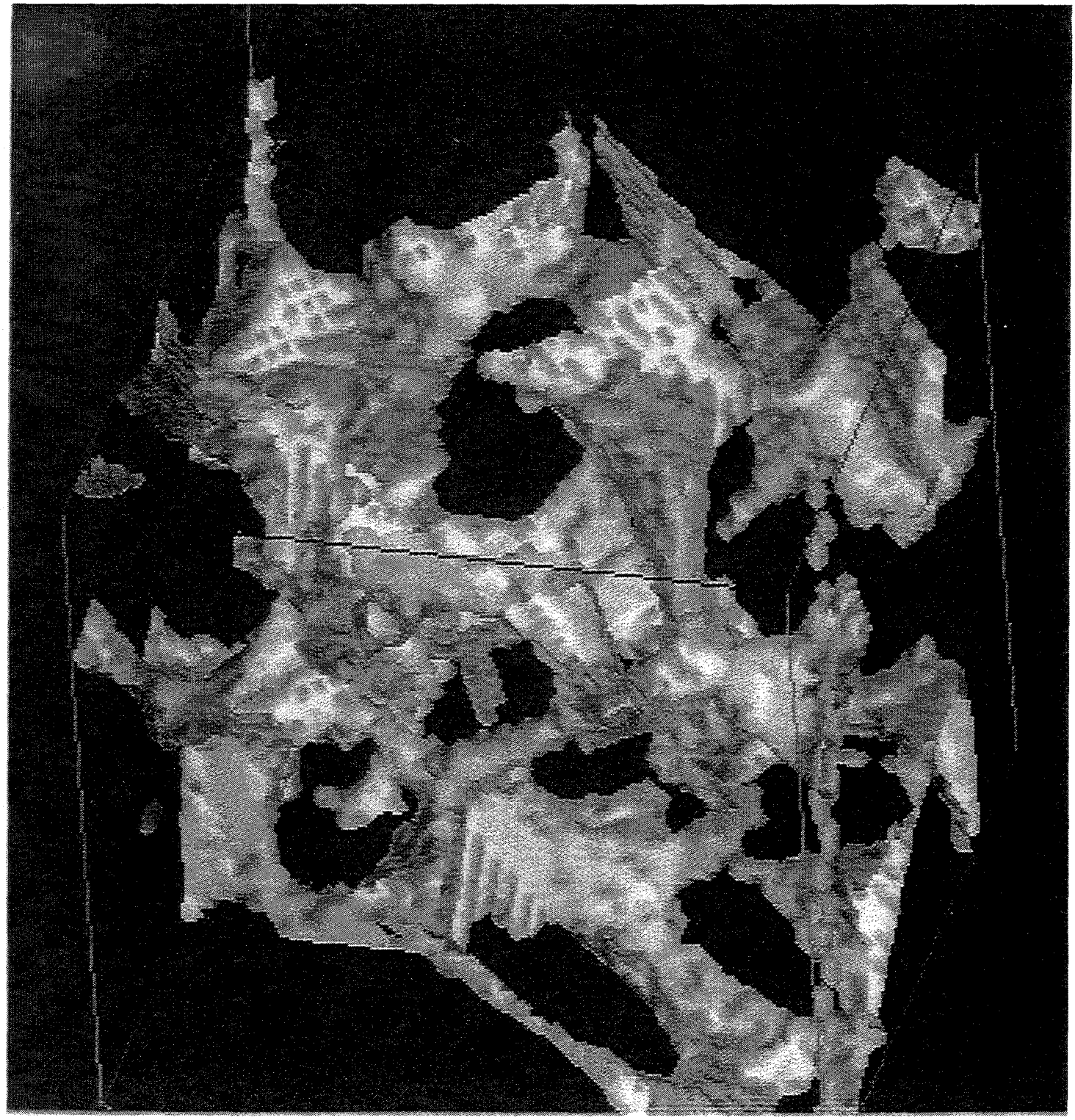

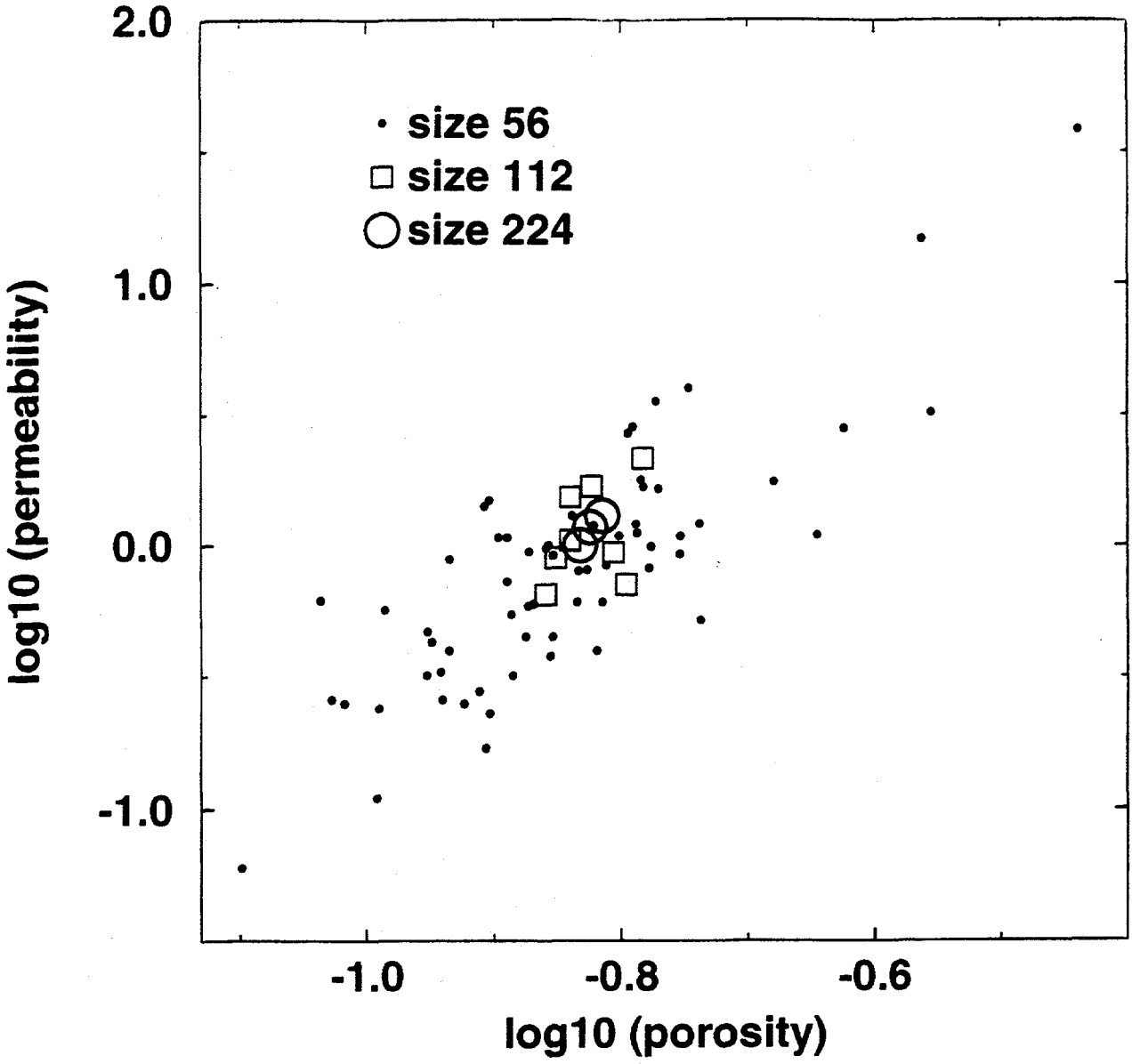
2.0
1.0
0.0
-1.0
log10 (permeability)
size 56
size 112
size 224
-1.0
-0.8
-0.6
log10 (porosity)

	ϕ (%)	$\frac{V_p}{S}$ (μm)	F	k (μm)^2	k_{ro}^0	S_{rw}
Measured	15.2	9.6	25.6	1.1	0.92	0.03
Calculated (Sample 1)	16.8	10.4	36.0	1.0 (FD) 1.2 (LB)	0.84 (I) 0.90 (II)	0.53
Calculated (Sample 2)	15.0	8.9	28.6	1.3 (FD)	—	—
Calculated (Sample 3)	14.6	8.7	32.7	1.0 (FD)	—	—

Table 1: Measured and calculated values of porosity ϕ, pore-volume-to-surface ration V_p/S, formation factor F, permeability k, endpoint relative permeability k_{ro}^0, and residual saturation S_{rw}. In the permeability column, FD and LB denote values computed by finite-difference and lattice-Boltzmann methods, respectively. The endpoint relative permeabilities were computed from both nonwetting invasion (Type I) and constant saturation (Type II) simulations.

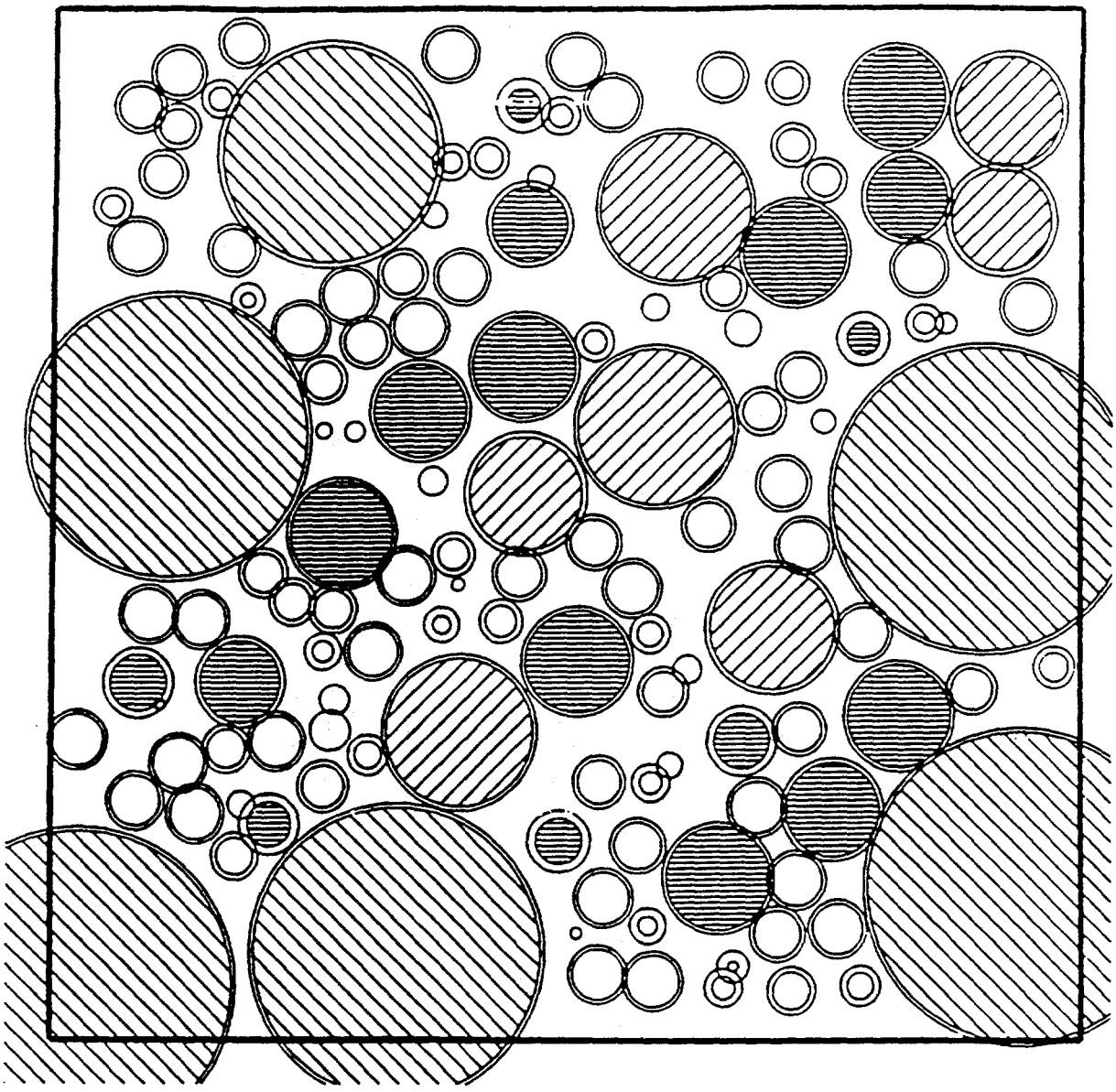

TABLE I. Size distribution for aggregate sand grains in a typical mortar. The second and third columns give, respectively, the volume and numerical fractions of the four size populations.

Grain Diameter (μm)	Volume Fraction	Numerical Fraction
3000	0.354	0.00718
1500	0.232	0.0376
1000	0.224	0.1226
500	0.190	0.8324

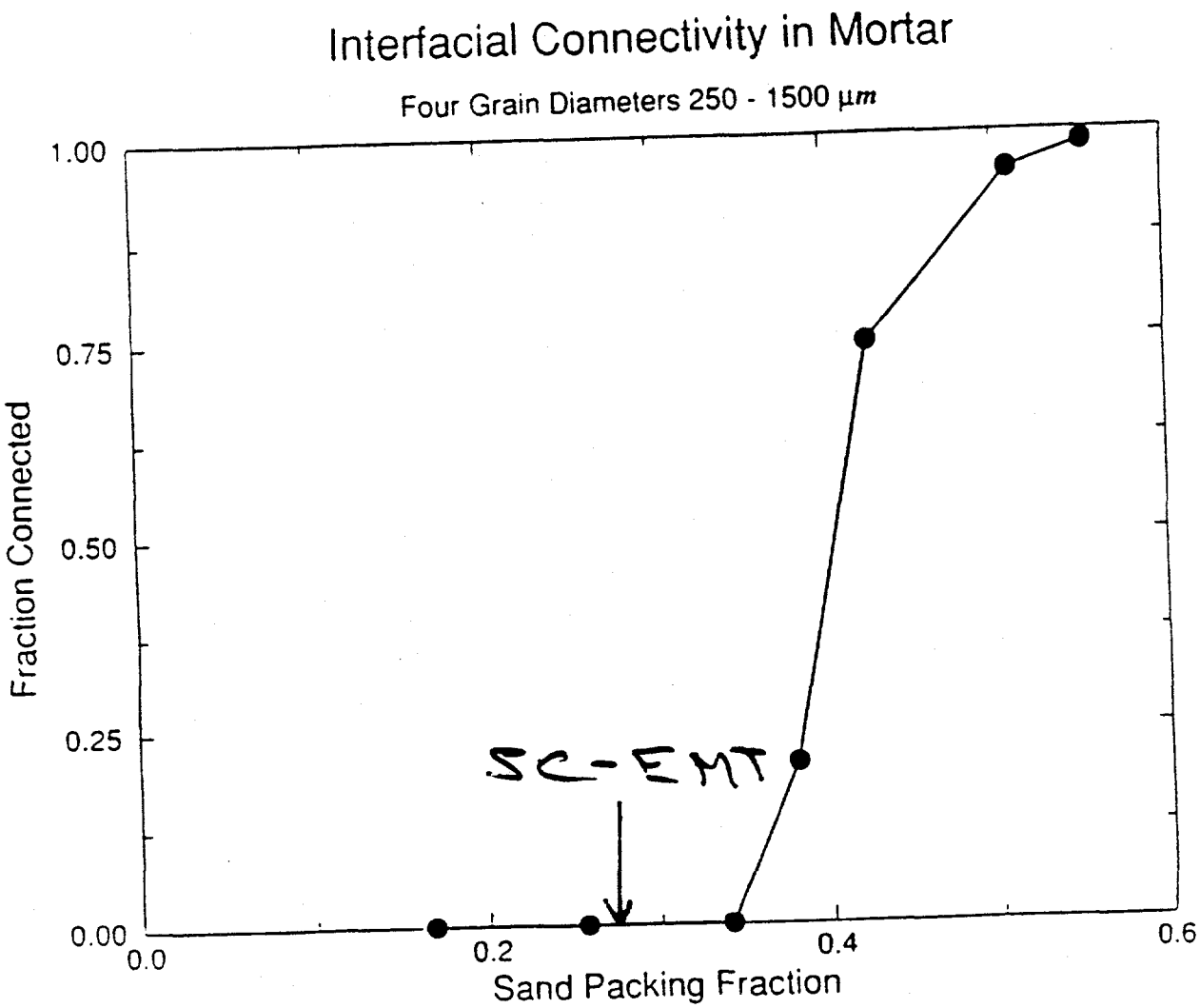
Interfacial Connectivity in Mortar
Four Grain Diameters 250 - 1500 μm
1.00
0.75
0.50
0.25
0.00
Fraction Connected
0.0
0.2
0.4
0.6
Sand Packing Fraction
SC-EMT

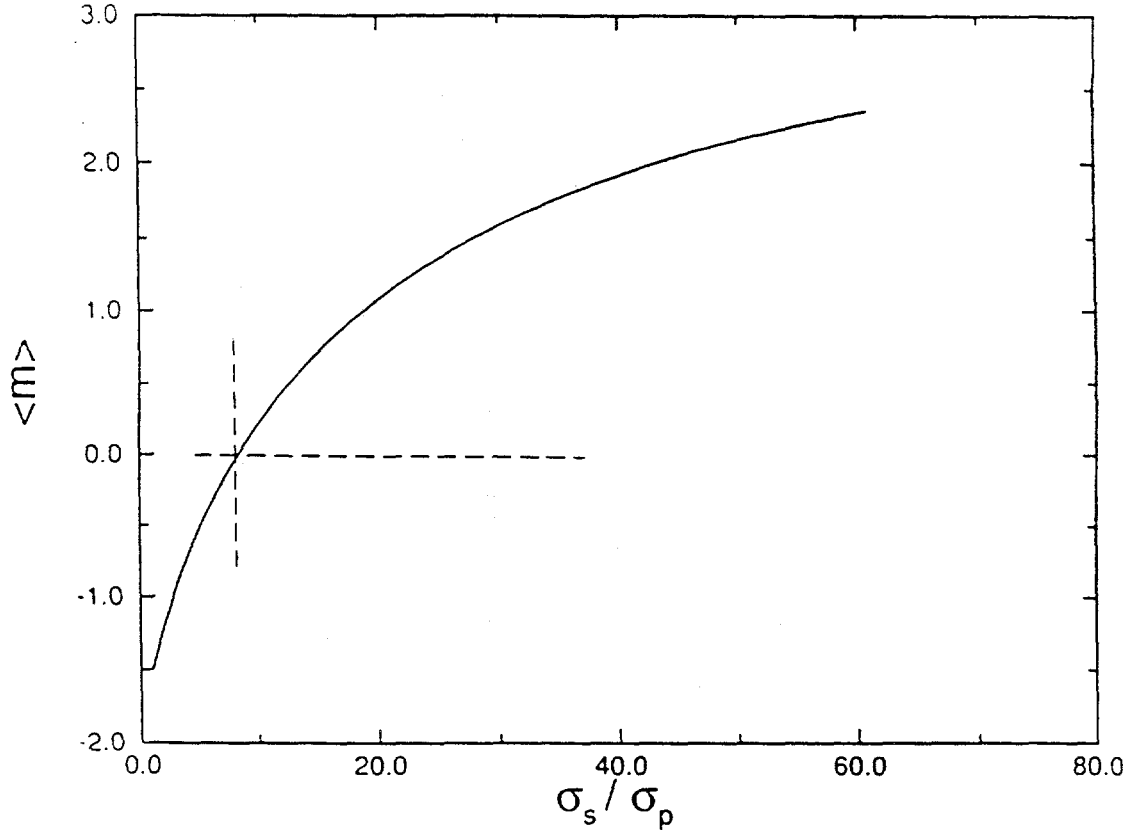
3.0
2.0
1.0
0.0
-1.0
-2.0
<m>
0.0
20.0
40.0
60.0
80.0
σ_s / σ_p

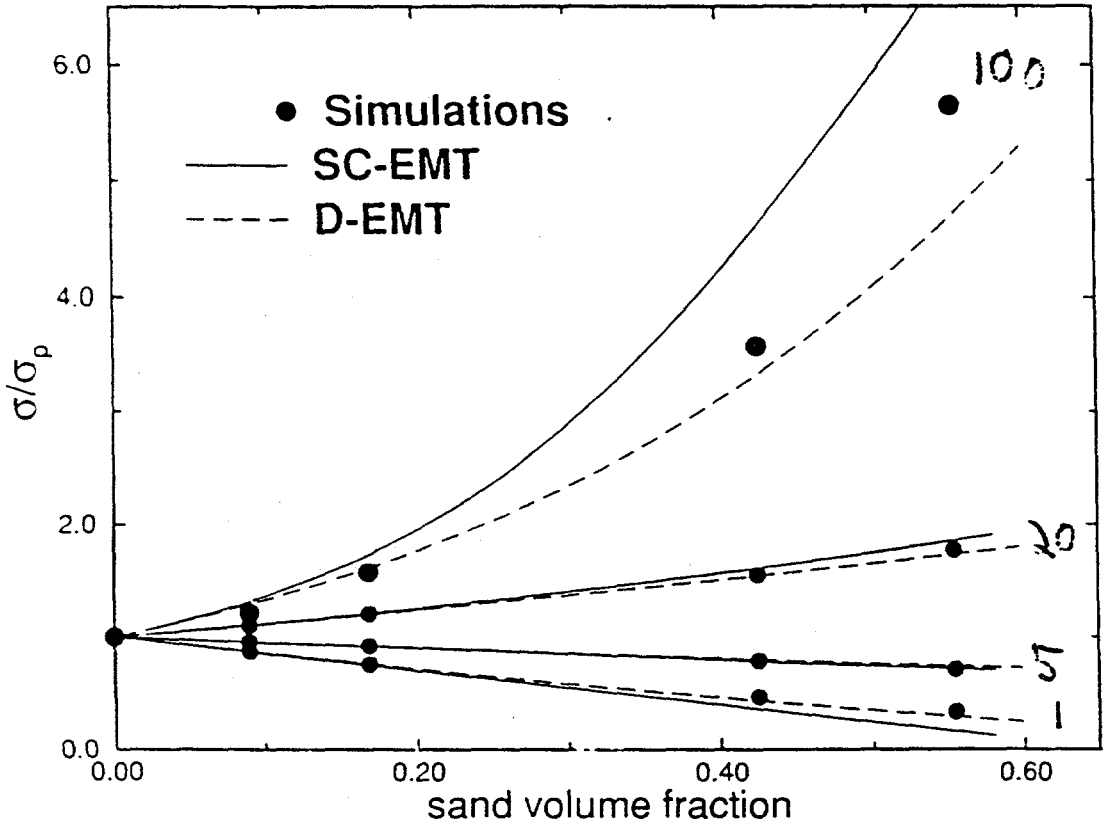
Simulations
SC-EMT
D-EMT
6.0
4.0
2.0
0.0
σ/σ_p
0.00
0.20
0.40
0.60
sand volume fraction
10
20
5
1

-- FLUID SATURATED ROCK --

MAGNETIC RELAXATION → PORE LENGTH SCALES

Two Mechanisms
- Bulk Relaxation
- Surface Relaxation ← $\rho = \frac{h}{\mathcal{L}_s}$

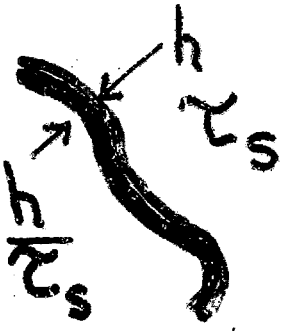

Spherical Pore - Radius a - Two Characteristic Time Scales:

$$\tau_D \equiv \frac{a^2}{D} \text{ (Diffusion)} \qquad \tau_\rho \equiv \frac{a}{\rho} \text{ (Wall Relaxation)}$$

Fast Diffusion: $\frac{\rho a}{D} < 1$ *Slow Diffusion*: $\frac{\rho a}{D} > 1$

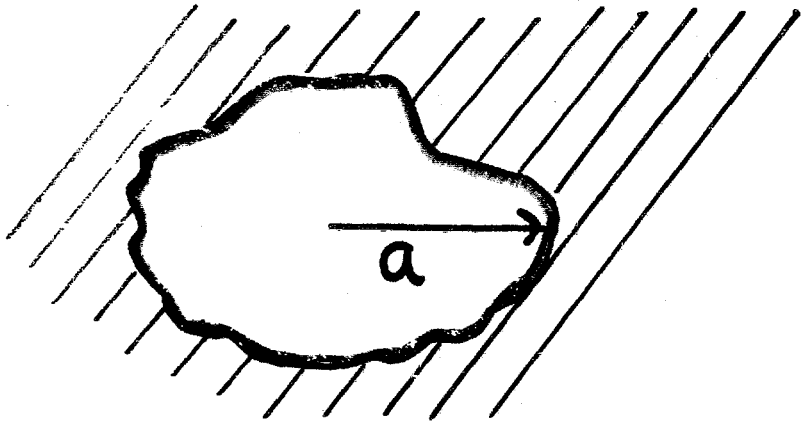

Link to Permeability

is Remote (At Best)

BUT - ρ is *Unknown* - Crucial in *Fast Diffusion* Regime

Physical principle

NMR relaxation time T_2 ⟷ pore-body size

$$\frac{1}{T_2} = \rho \frac{S}{V} + \frac{1}{T_{2b}}$$

- ρ: surface relaxivity
- S/V: surface area / volume
- T_{2b}: NMR relaxation of bulk fluid

Data transformation

Advantage: clarity of thinking

NMR relaxation curve

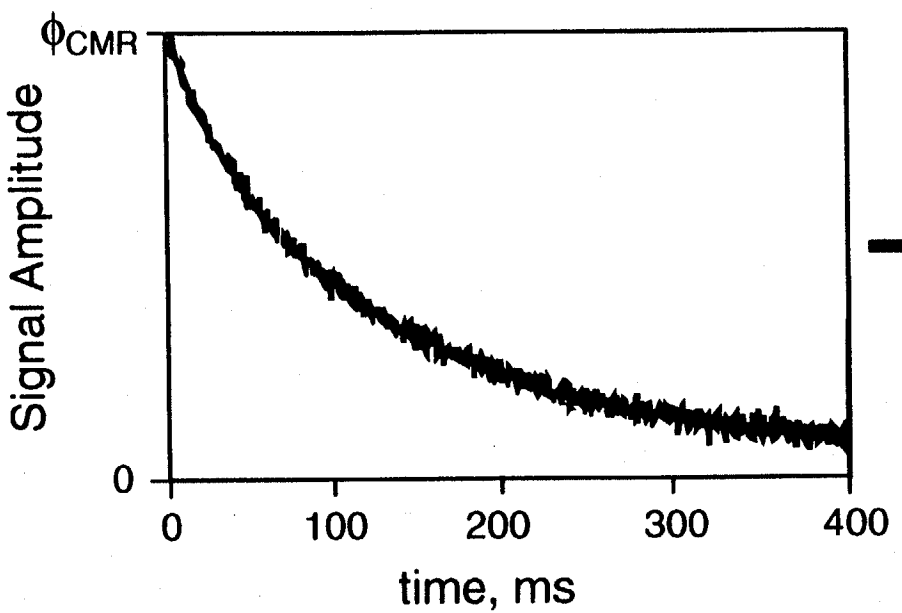

T2 spectrum

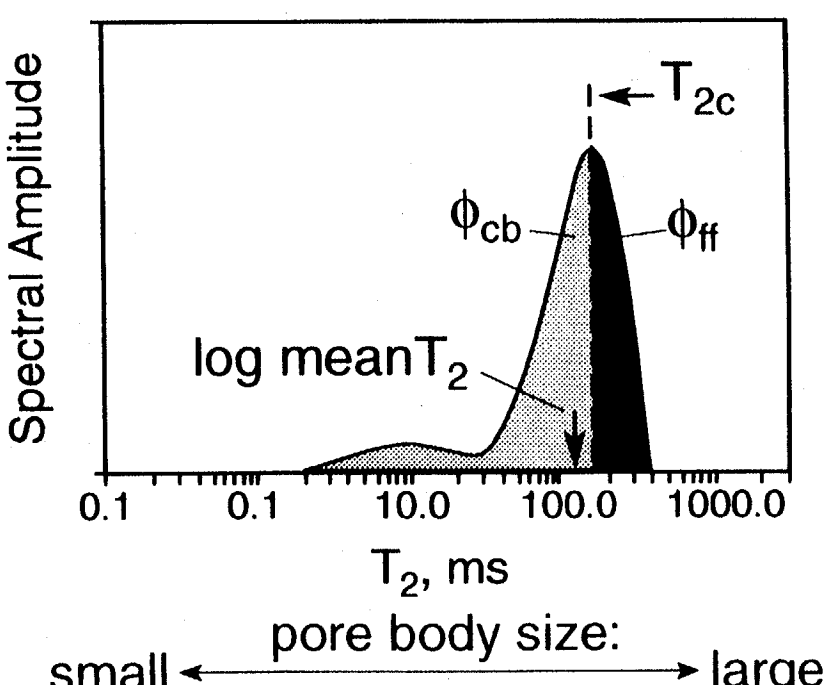

MICRITE(Calcite Crystal)

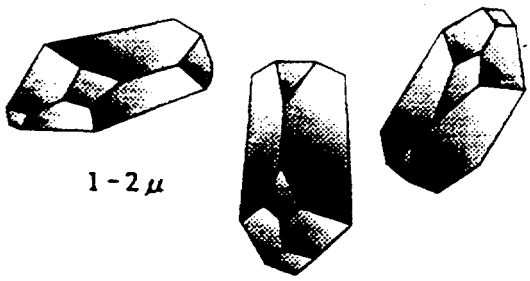

MICRITE PARTICLE

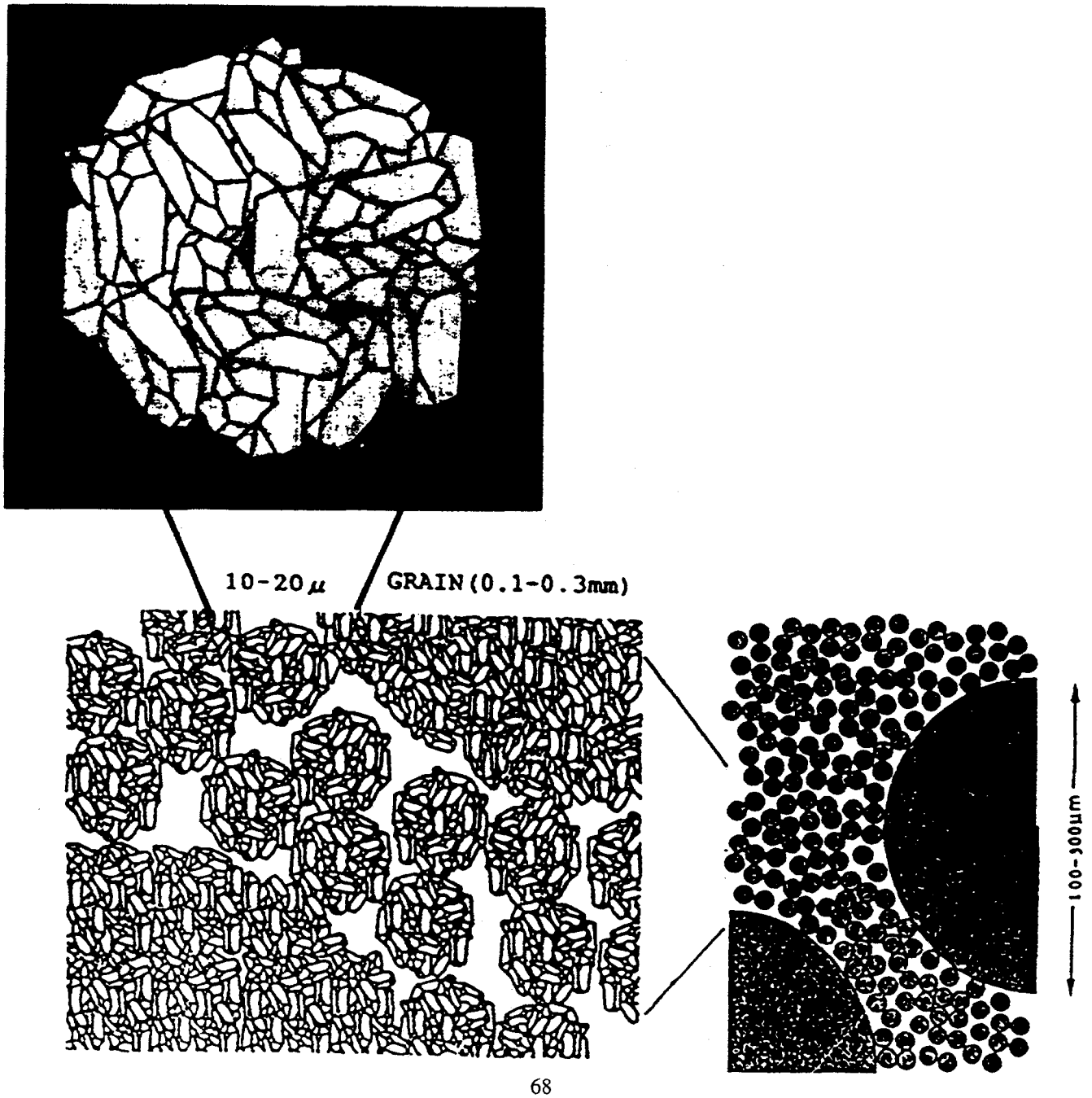

Grain Consolidation Model

Simple Cubic Lattice

R = 1.0

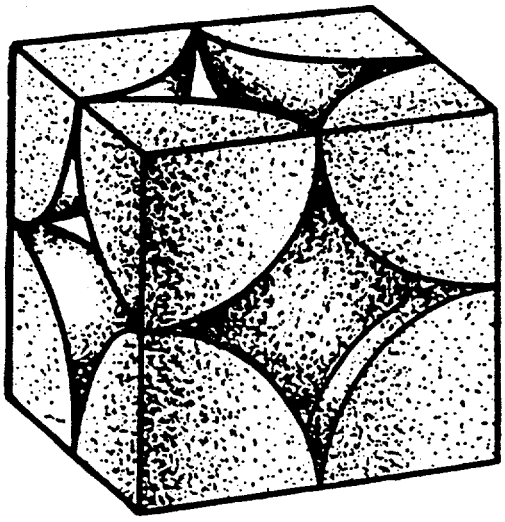

R= 1.2

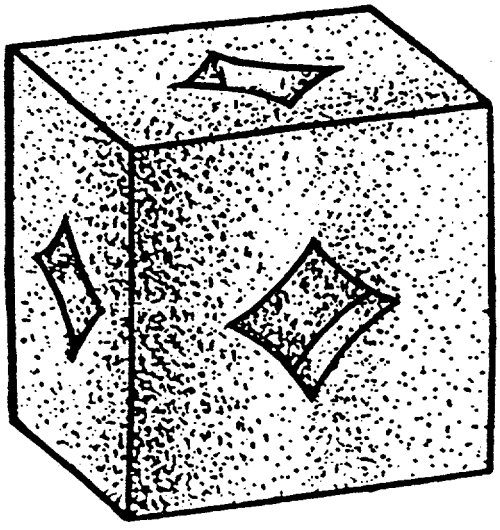

Microporous Grain Consolidation Model

$A/a = 40;\ \phi = 0.202$

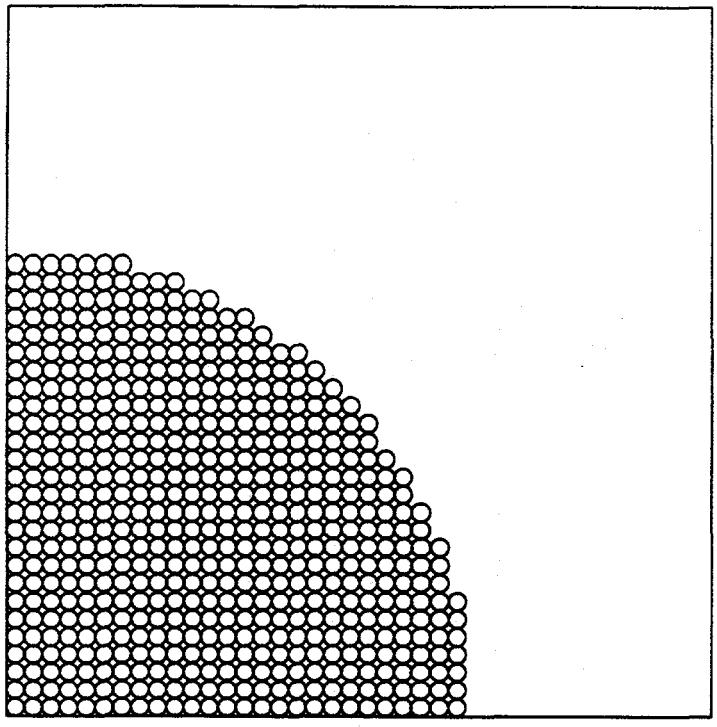

Pore Section

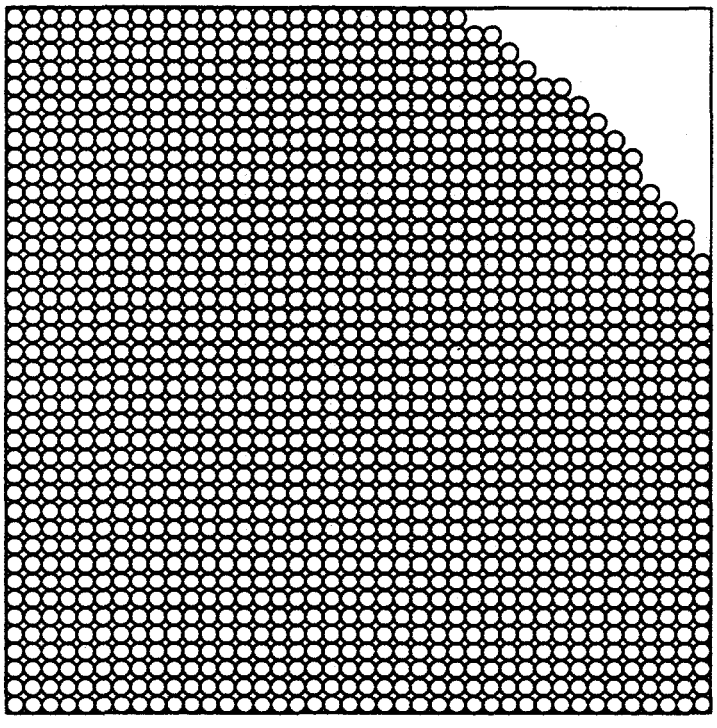

Throat Section

Combined Intergranular and Micro-Porosity

$A/a = 40;\ \phi_{micro} = 0.20,\ \phi_{inter} = 0.05;\ \alpha = 0.50$

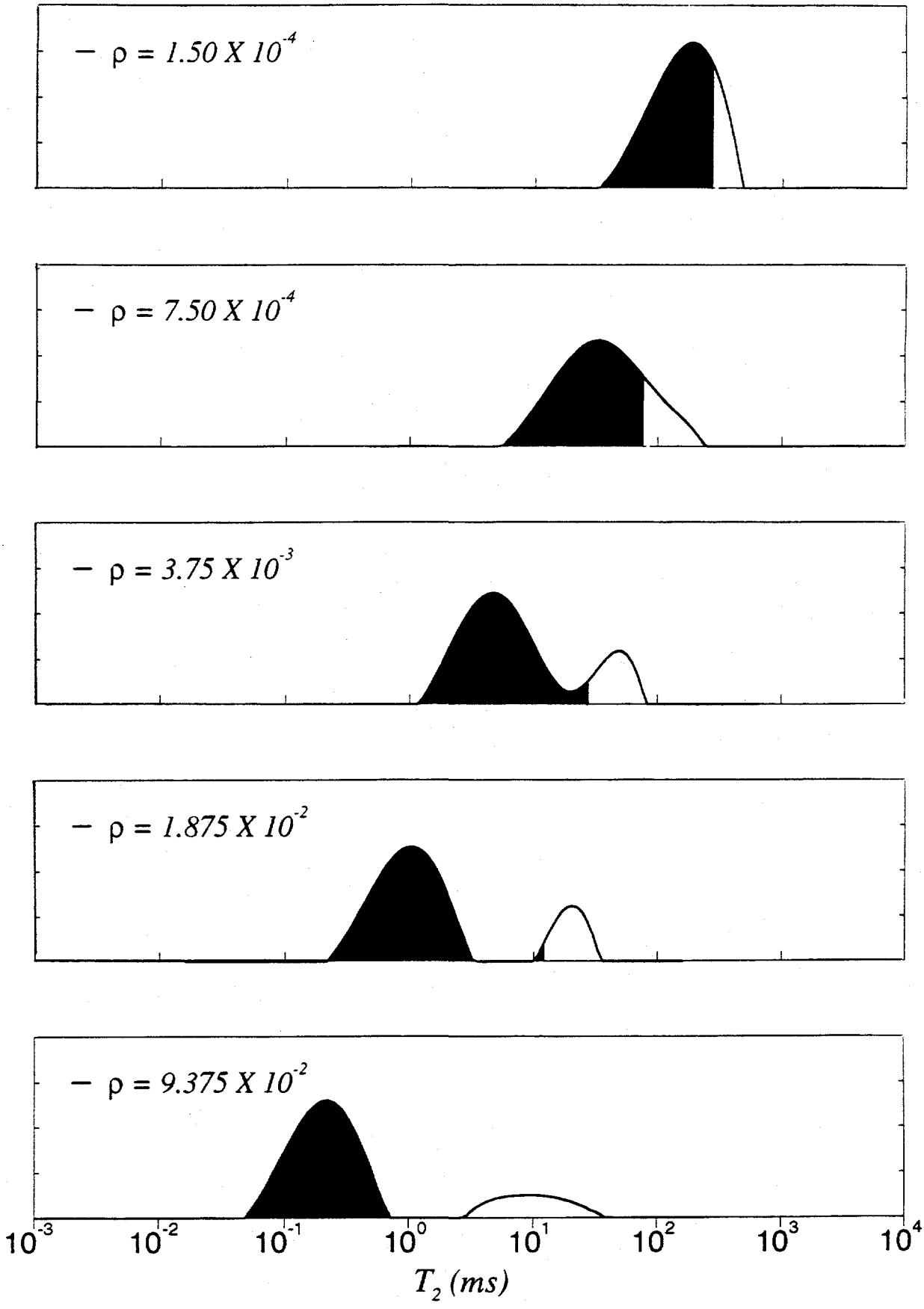

Components of the T_2 Distributions

A/a = 100; $\phi_m = 0.153$, $\phi_i = 0.157$

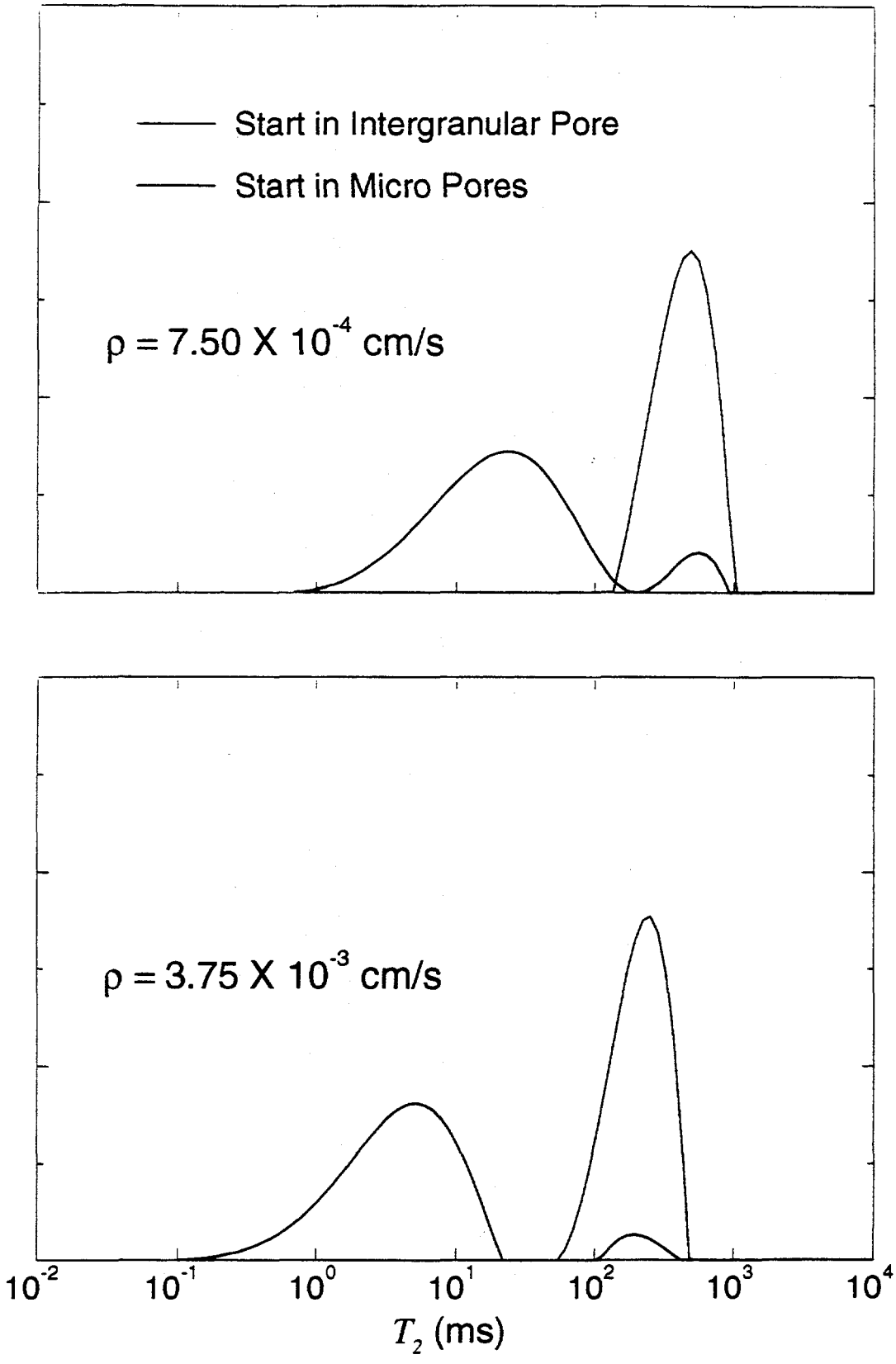

Crystalline Dolomites

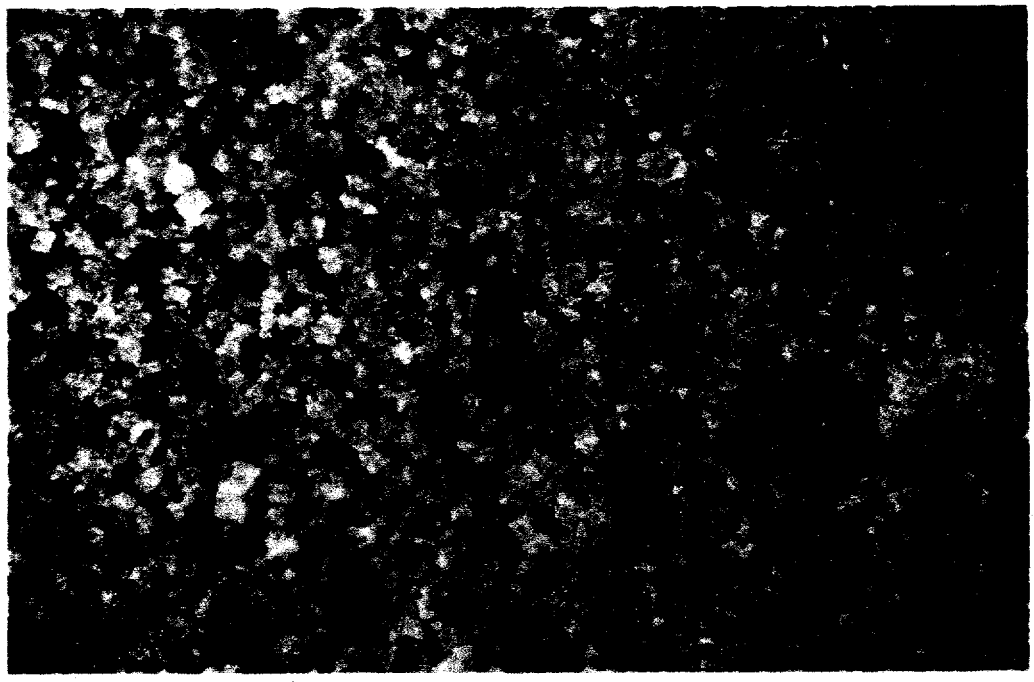

Magnification 36x

500 μ

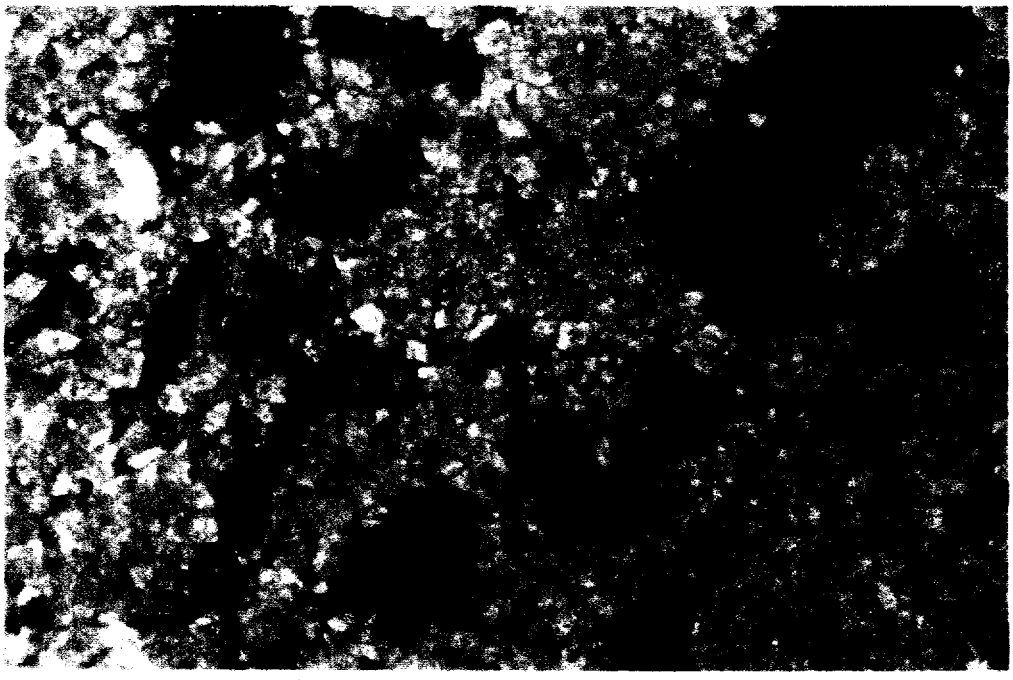

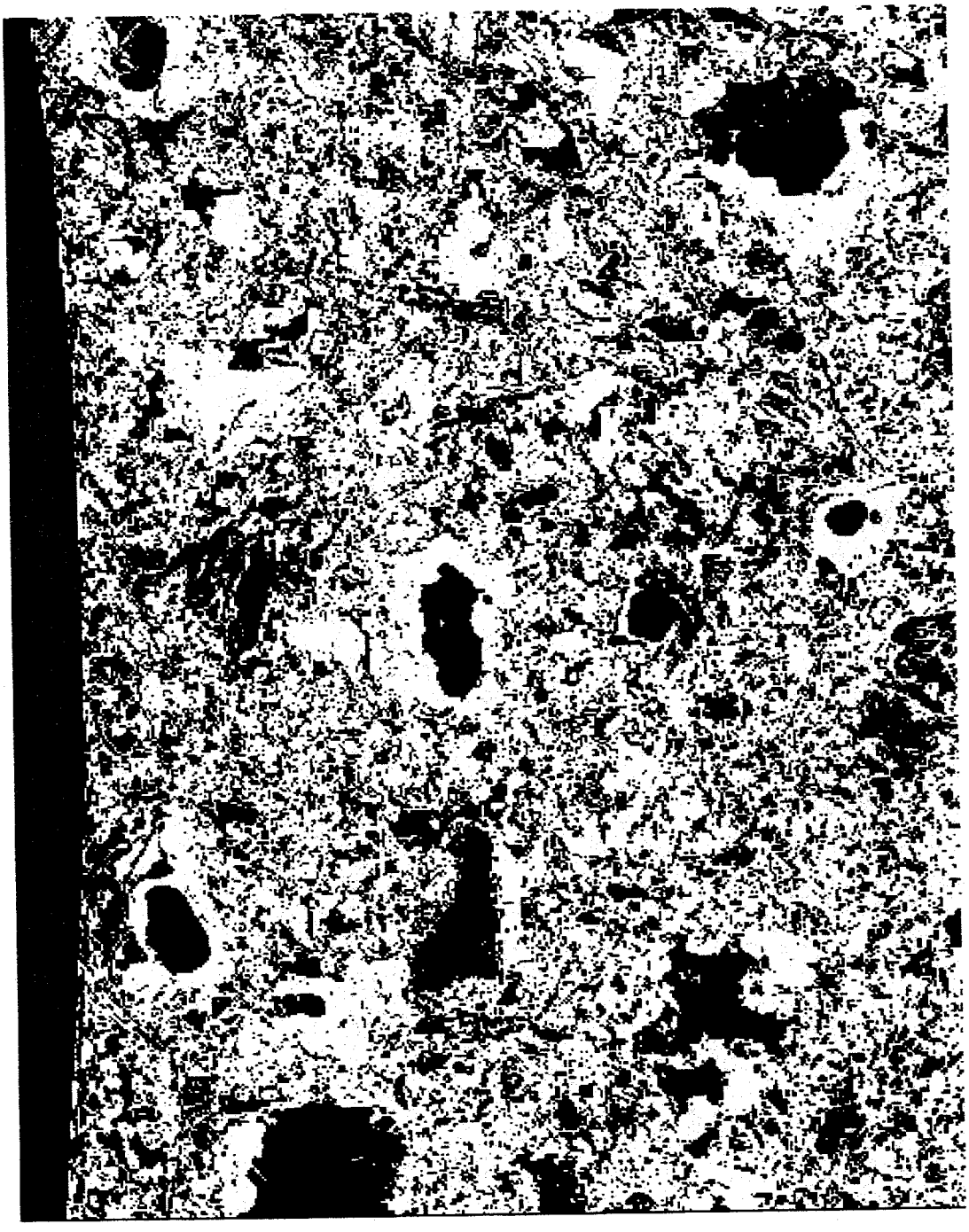

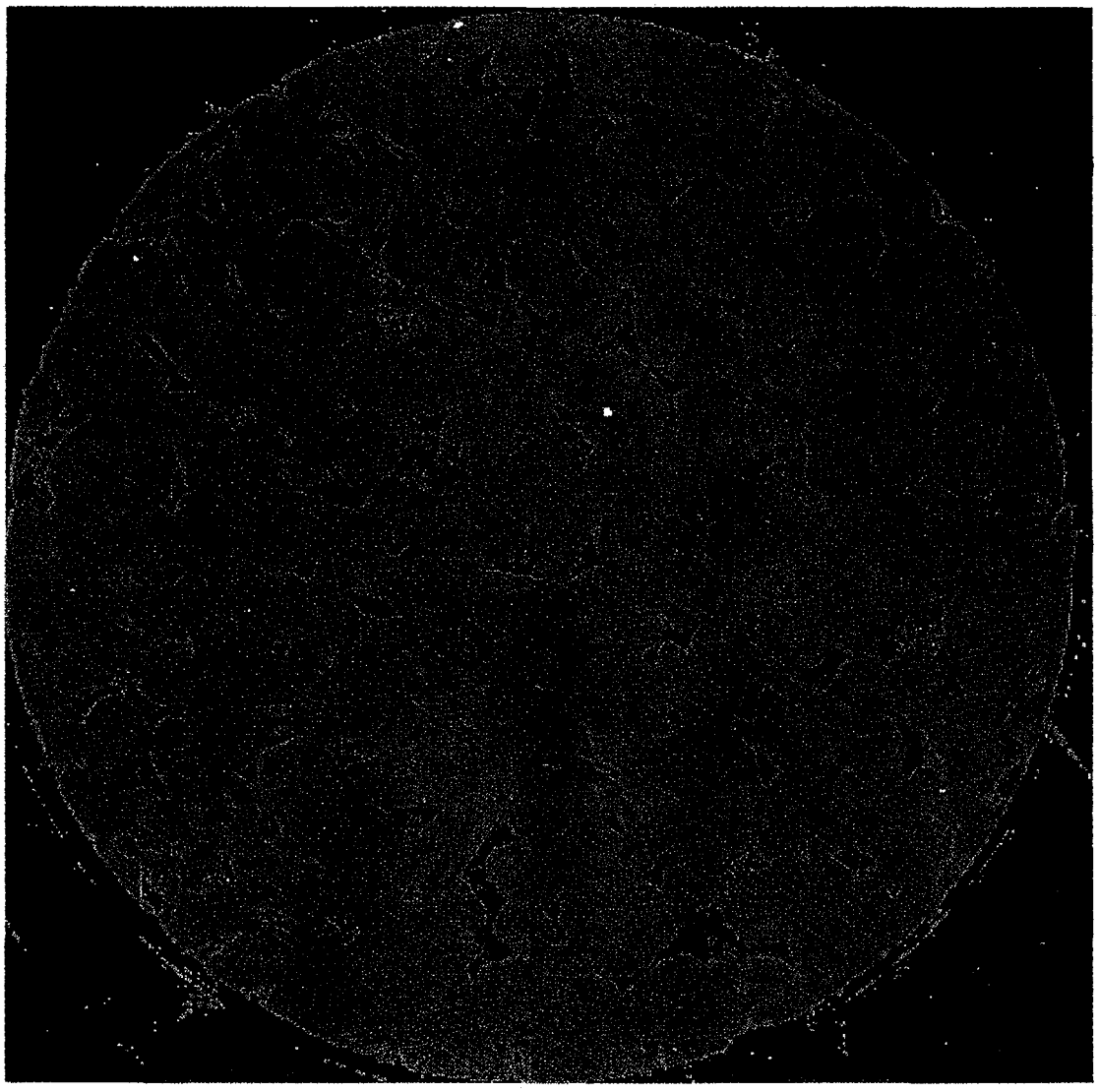

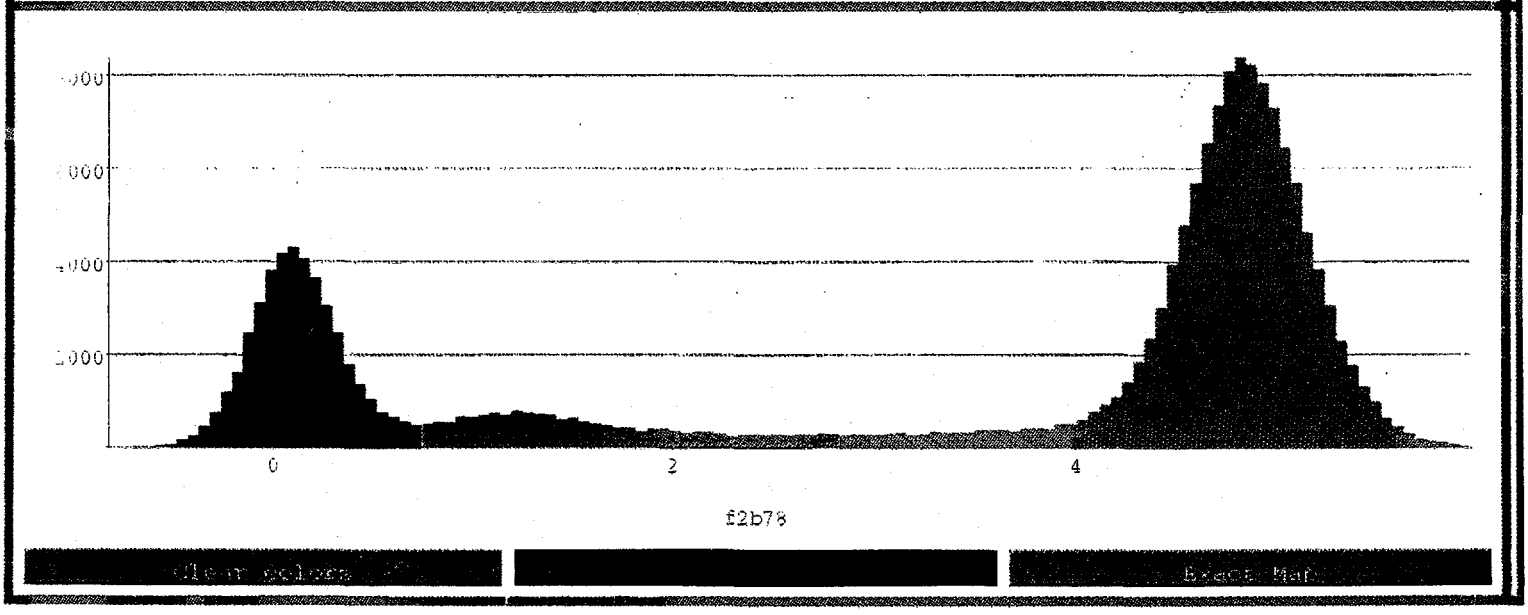

f2b78_c.ps

AMERICAN ASSOCIATION FOR THE ADVANCEMENT OF SCIENCE

SCIENCE

18 SEPTEMBER 1987 $2.50
VOL. 237 • PAGES 1389–1544

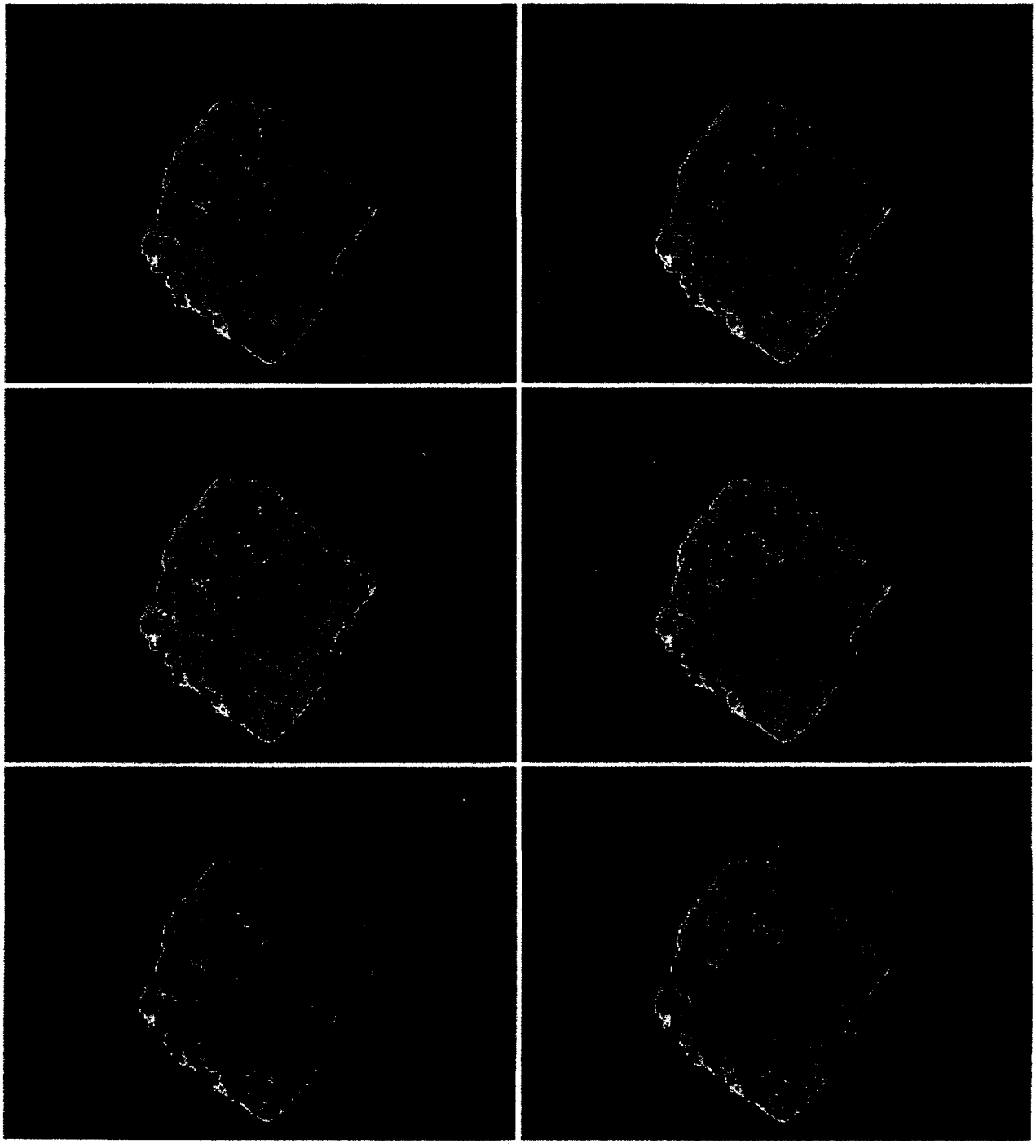

CMT for Soil Science Applications

Volker Clausnitzer and Jan W. Hopmans
University of California, Davis

The CT technique was introduced into the soil sciences by Petrovic et al. (1982) who measured soil bulk density. Changes in soil water content in both space and time were determined by Hainsworth and Aylmore (1983), Crestena et al. (1985), and Hopmans et al. (1992). The ability of CT to monitor displacement concentrations was first demonstrated by Vinegar and Wellington (1987) and by Steude et al. (1990). For a compilation of recent soil-related tomography studies, see Anderson and Hopmans (1994).

Today, x-ray computed microtomography (CMT) provides us with the ability to noninvasively measure porous-media properties at a scale approaching 10 μm. In contrast, traditional measurement techniques are either destructive or else invasive while still providing only locally limited information. Because the output from x-ray CT is directly related to density and atomic number, it is well suited for phase identification and concentration measurements.

This information is especially valuable when evaluating macroscopic flow and transport equations derived from the microscopic (or "point") equations through volume averaging. While the point equations are based on first principles and the laws of continuum mechanics, practically useful macroscopic equations are typically obtained only at the expense of more limiting assumptions and may also require empirical constitutive relations. The limits of applicability for a macroscopic model have therefore to be carefully investigated in terms of homogeneity, isotropy, length-scale, and geometric considerations. For example, consider the transport of a dilute dissolved species by diffusion and hydrodynamic dispersion. The appropriate microscopic equation for this case is

$$\frac{\partial c}{\partial t} + \nabla \cdot (c\,\mathbf{v}) = \nabla \cdot (D\,\nabla c).$$

Given the velocity field **v**, boundary and initial conditions, and the coefficient of molecular diffusion D, it will predict the solute concentration in space and time, $c(\mathbf{x}, t)$, where **x** is the location vector. The volume-averaged, macroscopic version of the equation is

$$\varepsilon \frac{\partial \overline{c}}{\partial t} + \overline{\mathbf{v}} \cdot \nabla \overline{c} = \mathbf{D} : \nabla\nabla \overline{c},$$

where ε and **D** are porosity and total dispersion tensor, respectively, and the bar indicates intrinsic averages, i.e., values that are averaged with respect to the liquid phase over a

representative volume. Within resolution limits, x-ray CT can potentially provide exhaustive description of pore-space geometry and the $c(\mathbf{x}, t)$ field, and consequently, of ε and $\overline{c}(\mathbf{x}, t)$. In addition to being noninvasive, c-measurements by CT also avoid the problem of flux-weighted sampling which is inherent to any physical sampling or collecting method. Given the velocity field **v** and the CT information, the suitability of the macroscopic equation, including the selected constitutive model for **D** (which physically is a function of pore space geometry and **v**), can be evaluated. If the spatial description of the system is exhaustive, the CT data can also help identifying the optimum size of the representative averaging volume, i.e., the size at which the value of the averaged quantity becomes largely independent of the size.

To be useful, the chosen CT method has to be able to capture a sufficiently large domain in a sufficiently short period of time with sufficient resolution and accuracy. We investigated the suitability of x-ray microtomography for studying solute transport in porous media at approximately 20 μm spatial and 20 min time resolution using a 125-kV microfocus cone-beam scanner (10 μm spot size) at Scientific Measurement Systems, Inc., Austin, Tex.

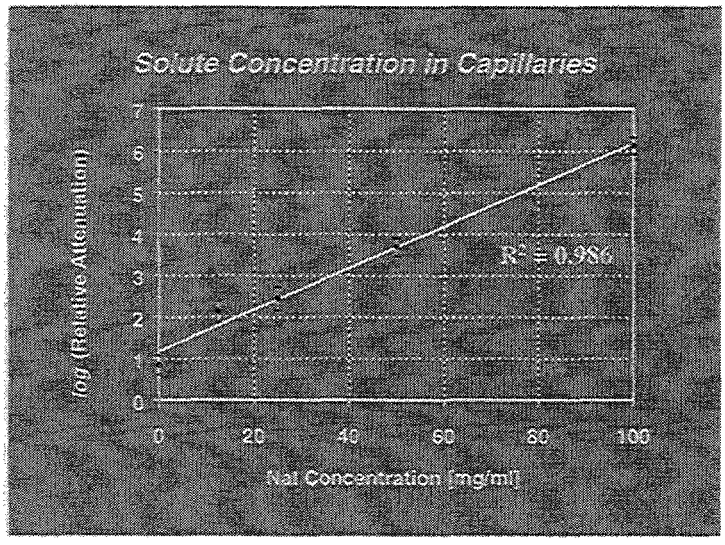

Fig. 1 X-ray attenuation vs. solute concentration

After establishing that the chosen scanner configuration permitted the measurement of solute concentration inside of pores—represented by 0.5-mm glass capillaries—with adequate accuracy (Fig. 1), we observed the breakthrough of 10%-NaI solution in an initially water-saturated pack of 0.5-mm glass spheres (average porosity = 0.47). A 90-min pulse was moved through the system at a steady flow rate of 100 μl/hr. Individual 3D data sets of attenuation values were acquired in 20-min intervals, each encompassing the complete circular cross section of 4.5 mm diameter over a 0.5-mm vertical range, 20

mm below the inflow (Fig's. 2 and 3). Before introducing the NaI, a reference scan of the water-saturated sample was obtained.

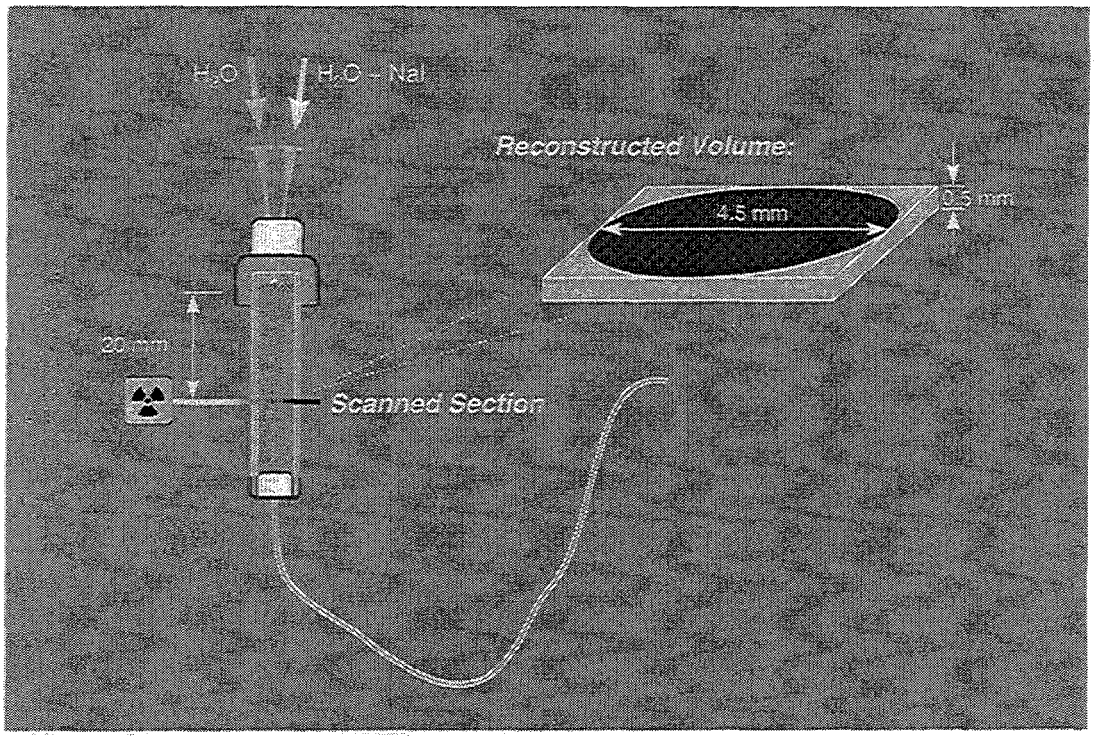

Fig. 2 Miscible-displacement experiment

For each scan, the spatial distribution of the iodide was inferred from the attenuation values after subtracting the reference scan. For quantitative analysis, the top horizontal cross-section was divided into 16 segments by imposing a rectangular grid.

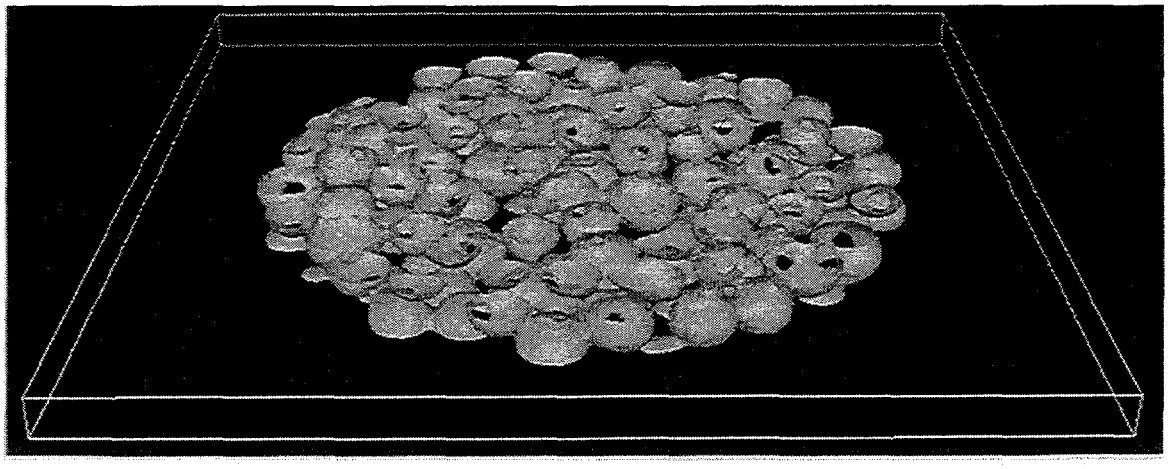

Fig. 3 Iso-attenuation representation of the glass-air interface in the dry porous medium

The results indicate that the method clearly discerned differences in the breakthrough between the 16 individual cross-sectional portions (Fig. 4).

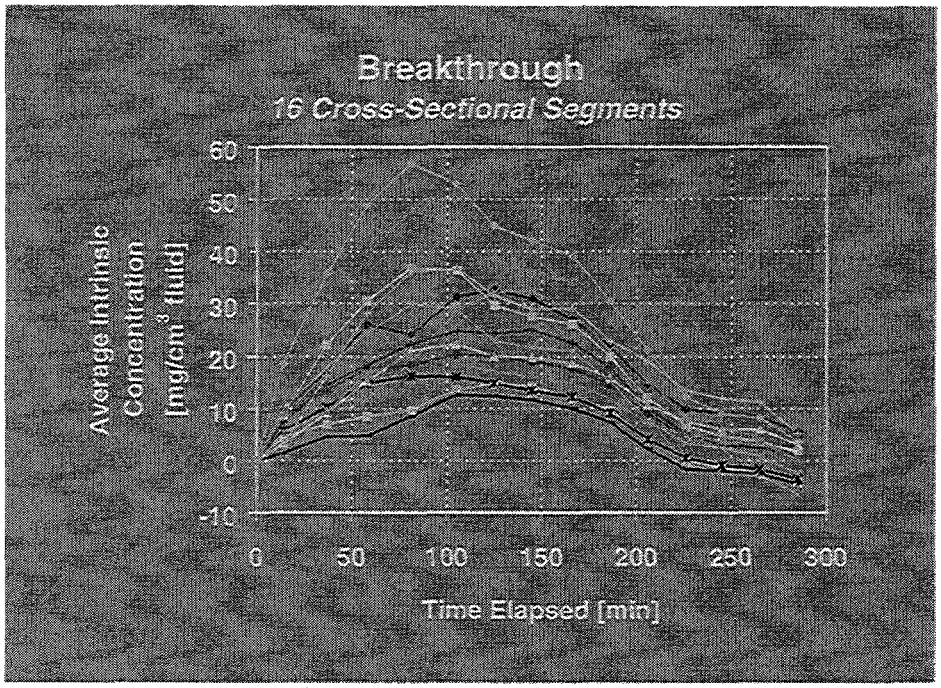

Fig. 4 Local breakthrough curves

The lower limit on the size of these portions is controlled by the noise in the attenuation values after reconstruction. Smaller portions would contain too few voxels to identify a significant above-noise reading. To achieve true pore-scale observation capability at reasonable acquisition times, the photon flux rate in the optimum energy range will have to be improved.

$$M_{solute,total} = \int_t \int_{A_{\perp,liquid\,phase}} v\,c\,dA\,dt$$

$$M_{solute,total} \approx \sum_{i=1}^{all\ segments} \left[\sum_{k=1}^{all\ scans} c_{i,k} (\Delta t)_k \right] v_i\, A_{\perp,liquid\,phase,i}$$

For a mass-balance computation, liquid-phase cross sections for each segment were obtained from reference scan (H_20-saturated sample), and vertical components v_i of the local pore-water velocities were estimated from individual peak-arrival times. Based on these assumptions, 86% of the introduced solute were accounted for in the scans.

The results to date are very encouraging as they demonstrate the applicability of x-ray CMT for quantitative investigation of flow and transport in porous media. To further exploit the potential of CMT, our next step will be to observe the complete vertical flow range of similar breakthrough experiments. Variations in breakthrough are caused by local variations in flow velocity and in flow path geometry. Because these mechanisms are represented by the total dispersion tensor **D**, a complete three-dimensional set of local breakthrough measurements will be very valuable in evaluating proposed models for this critical parameter.

REFERENCES

Anderson, S. H., and J. W. Hopmans, Eds., Tomography of Soil-Water-Root Processes, Soil Science Society of America, Special Publication No. 36, 1994.

Crestana, S., S. Mascarenhas, and R. S. Pozzi-Mucelli, Static and dynamic three-dimensional studies of water in soil using computed tomographic scanning, *Soil Sci.,* 140(5): 326-332, 1985.

Hainsworth, J. M. and L. A. G. Aylmore, The use of computer-assisted tomography to determine spatial distribution of soil water content, *Aust. J. Soil Res.,* 21:435-443, 1983.

Hopmans, J. W., T. Vogel, and P. D. Koblik, X-ray tomography of soil water distribution in one-step outflow experiments, *Soil Sc. Soc. Am. J.,* 56(2):355-362, 1992.

Petrovich A. M., J. E. Siebert, and P. E. Rieke, Soil bulk density analysis in three dimensions by computed tomographic scanning, *Soil Sc. Soc. Am. J.,* 46:445-450, 1982.

Steude, J. S., C. P. Sullivan, R. C. Chaney, M. McKee, and L. E. O'Shea, Tracer experiments in saturated sand by computed tomography and inductively coupled plasma, in: K. B. Hoddinott and R. O. Lamb, eds., Physico-chemical aspects of soil and related materials, Am. Soc. for Testing and Materials STP 1095, Philadelphia, p. 171-184, 1990.

Vinegar, H. J., and S. L. Wellington, Tomographic imaging of three-phase flow experiments, *Rev. Sci. Instrum.,* 58(1):96-107, 1987.

Computerized Microtomography for New Applications

A. Thompson
LBNL

G. Ice
ORNL

The advent of high brilliance synchrotron sources has stimulated the development of advanced x-ray microtomography and has made it possible gain new insights into materials properties. However, materials research problems challenge existing tomographic techniques. High spatial resolution is required to identify and characterize microstructure in real materials. Good elemental sensitivity is required to study the effects of microalloying. Three-dimensional crystal texture, strain and phase information is required to understand advanced materials. In addition, materials samples can include a wide range of elements, can come in unfavorable geometries, and sometimes will require dynamic measurements of their three dimensional structure.

One challenge for x-ray microtomography, is the measurement of low concentrations with good spatial resolution and high elemental sensitivity. In several alloy systems, the addition of 10 to 100 ppm can have a major effect on ductility, impact resistance, creep-rupture strength, radiation stability or weldability. For example in Fe_3Al and iridium alloys, weld properties are sensitive to ppm of Zr and Th. The study the 3-dimensional distributions in microalloy samples, will require fluorescence tomography techniques. Fluorescence tomography has been applied to tomography of plasma confinement in fusion devices, and some proof-of-principle experiments for fluorescence x-ray microtomography have been performed with simple phantoms and low Z (biological) samples. For example Paul Boisseau completed a dissertation in 1978 under Lee Grodzins which used x-ray fluorescence microtomography to study the iron distribution in a honey bee.

Another challenge to standard x-ray microtomography is the study of elemental distributions in planar structures where elemental sensitivity is required in one or two dimensions, but the spatial sensitivity in all three dimensions is not required. For example, the elemental distribution through the thickness of a plastic rocket fuel liner was recently needed to study the effect of elemental contamination on the liner adhesive properties. Because of the small concentrations, standard tomographic techniques were not possible. Depth profiling was accomplished by crossing the x-ray sensitive volume with the incident beam. This technique allows three dimensional elemental distributions to be built up with good resolution in two dimensions (determined by the transverse beam dimensions) and with poor resolution in the third dimension. Similarly, total-external-reflection techniques can be used to depth profile the elemental distribution with nanometer depth resolution in smooth samples, and standing wave techniques can be use to study surface contamination with sub-angstrom resolution on perfect single crystals.

For a large class of materials, crystalline structure, strain and texture are critical to the materials properties. Recent work has now demonstrated the possibility of extending x-ray microdiffraction to the study of three dimensional crystallographic distributions. Efforts are now underway at the APS, ALS, SSRL and NSLS to further develop x-ray microdiffraction and x-ray microdiffraction tomography. The measurement of strain and texture in three dimensions will have important applications to the study of high J_c high T_c superconductors, the study of second phase distributions and texture in composite materials, and the study of crack and void evolution in structural and electronic materials.

Another frontier for x-ray tomography is the development of dynamic or real-time measurements. Gunivier and Stock have recently studied crack propagation by observing the evolution of a crack through repeated cycling of the specimen. By monitoring the evolution of cracks, phases, diffusion, void growth and other microstructural properties it will be possible to greatly extend our understanding of materials properties.

Although there are many challenging materials samples where more powerful microtomography techniques are needed, for some specimens, existing techniques provide very valuable new information. One almost ideal specimen is an advanced nuclear fuel sphere for intrinsically safe reactor fuel. These small spheres are composed of a nuclear fuel kernel surrounded by buffer layers of graphite and a containment barrier of SiC. X-ray tomography allows a nondestructive evaluation of the sphere to study defects, inhomogeneities and interfaces. Not only do the tomographic measurements avoid the contamination problems associated with traditional sectioning methods, but because the tomographic measurements are nondestructive it is possible to study the evolution of the spheres through various environmental insults such as simulated melt downs.

THE SOLID-STATE SIGNALING PATHWAY FROM EXTRACELLULAR MATRIX TO NUCLEAR MATRIX: THE CRITICAL ROLE OF THREE-DIMENSIONAL ARCHITECTURE FOR FUNCTIONAL DIFFERENTIATION.

Sophie Lelièvre and Mina J. Bissell.
Life Sciences Division, Lawrence Berkeley National Laboratory,
1 Cyclotron Road, Bldg 83-101, Berkeley CA 94720.

Organs comprise specific organization of cell populations surrounded by an extracellular jelly which includes fibrous and globular proteins called the extracellular matrix (ECM) (figure 1). Cells are able to communicate with each other through specific cell-cell interactions. Cell-ECM interactions also transduce messages which participate in the regulation of cell behavior. Some of these messages ultimately reach the level of the genome in the nucleus and induce the activation or inactivation of specific genes. Such signaling is the basis for cell differentiation, a process by which cells start out with the same genetic information in the DNA of their nuclei and change into distinctly different specialized tissues and organs which make up a functional organism. Understanding cell differentiation is the Holy Grail of cell biology! Cell biology encompasses the study of cells as living entities that interact with their microenvironment, take on specialized shapes, size and functions, and organize into communities (morphogenesis). While most of the functions of the various tissues of the organism are now known, the role played by tissue structure and organization in the regulation of such functions remains obscure. Clarifying the relationships between structure and function at the cellular level is one of the keys which should allow us to answer fundamental questions regarding the determination of cell and tissue phenotypes as well as their alteration in different pathologies.

Breast cells are useful experimental subjects for cell biologists because the mammary gland is one of the few tissues that undergoes dramatic changes in form and function after adulthood. The study of breast cells has permitted the determination of the importance of cell-ECM interactions and cell structure in the regulation of cell phenotypes. In particular, Bissell and collaborators showed that the ECM was critical for the induction of cellular differentiation in the mammary gland, leading to the lactating phenotype through specific ECM component and cell receptor (integrins) interactions (1). They also demonstrated that ECM-dependent cell shape control was critical for cell differentiation and they proposed that cellular structure was part of the message necessary for the completion of such differentiation (2-3). Cellular structure is determined by the ECM-induced organization of cells into clusters and the specific distribution of internal components of the cellular architecture, which are both events of a process called morphogenesis. Their results led them to define not the cell, but the cell plus its ECM as the smallest functional unit of tissues (3-4). How do these differences in cell shape and structure relate to function in various tissues?

Already we know a lot about the composition of cellular structure. At the surface of the cells specific components (receptors) are in contact with components of other cells or with ECM protein fibers. These cellular components are connected within the cell to various elements of the cytoskeleton. These elements comprise filamentous proteins whose arrangement depends on cell shape and on cell-ECM and cell-cell interactions. Cytoskeletal elements participate in cell shape and cell movements. They are also involved in transmission of biochemical signals which cascade toward internal cellular targets. The overall cytoskeleton constitutes a network of fibers connected by some of its components to the peripheral part (lamina) of the nuclear skeleton called the nuclear matrix (figure 2). The nuclear matrix is also described as a network of filamentous components which may organize nuclear bodies associated with DNA replication and gene expression (5). Interestingly the chromatin which represents the higher level of DNA organization has been shown to be associated with the nuclear matrix through specific DNA sequences (6). The physical continuity between the ECM, the cytoskeleton and the nuclear matrix has been demonstrated using a technique involving the preparation of cell skeleton/nuclear matrix and the visualization of interconnected elements of the cellular architecture by electron-microscopy (7). Moreover, the modulation of cell phenotype has been shown to be associated with alterations of the different elements of cellular architecture. Together these data support the existence of a solid-state signaling pathway which comprises the ECM, the ECM receptors, the cytoskeleton, the nuclear matrix and the chromatin (figure 2) and which has been proposed to be the basis for the regulation of gene expression and cell differentiation (8).

In order to unravel the relationship between cell structure and function, an increasing number of studies are now investigating cellular architecture in a biophysical context. One of the aims is to understand how local changes in the ECM produce alterations of cell and nuclear shape. This is based on the fact that changes in cell shape are commonly associated with alterations of nuclear structure (9) which in turn appear to be required for changes in nuclear functions including gene expression. Ingber and collaborators have introduced the concept of tensegrity (tensional integrity) several years ago. They studied the transmission of mechanical signals in ECM-directed blood vessel growth and differentiation (10), by applying a mechanical stress directly to cell surface receptors using a magnetic twisting device. They argued that mechanical stresses must be transmitted over structural elements

that are physically interconnected (tensegrity). The concept of a solid-state ECM-driven signaling pathway could be integrated with such a model. For example, it has been shown that only adhesion receptors such as the beta-1 integrin receptor-induced focal adhesion formation will support a force-dependent stiffening response to a cell surface applied mechanical stress. Therefore integrins can be considered as mechano-chemical receptors transmitting physical signals to the cytoskeleton and nuclear matrix (11). The fact that certain cytoskeletal components are capable of polymerization/depolymerization (e.g., actin, tubulin) implies that the system can be dynamic (12), whereas cytoskeletal components such as the cytokeratins, which are static may provide an element of mechanical integrity which defines cell organization and permits structured morphogenetic movements (13). These cytoskeletal properties could play an important role during the organization of cells into defined structures. Ingber and Folkman (14) showed that extracellular attachment points predominated ECM-driven morphogenetic activity. There is an equilibrium between cellular tension and ECM resistance, and forces generated from one part of the system will generate a feedback reaction. Therefore cell-generated forces of tension can organize ECM into a structure that directs the behavior of single cells and provides the positional information necessary for the organization of multicellular structures (for a review see 15).While the cytoskeleton has been shown to participate in ECM signaling, the role of the nuclear matrix in such signaling still requires elucidation. Certain forces generated by the ECM and transmitted to the cytoskeleton might elicit a resistance response by the nuclear matrix. We can for example envision such a phenomenon to occur at the level of the lamina which underlines nuclear shape and whose distribution may be perpendicular to forces emanating from the ECM and/or the cytoskeleton (figure 3). If it is feasible that intracellular feedback forces might partly derive from the intrinsic resistance inherent to nuclear matrix structure the evidence is still lacking. Nuclear matrix structural components implicated in the mediation of ECM-directed gene regulation might be different from nuclear matrix components which are involved in change in nuclear shape. It has been proposed that ECM-induced changes in cell shape and nuclear shape result from the action of mechanical tension that is generated within the cytoskeleton via a filament sliding mechanism (16). Bending or sliding between cytoskeletal filaments rather than the stretching of the filaments themselves is also proposed to be responsible for the compliance of cells (17). Parallel to tensional events, biochemical signals may cooperate and add the subtle alterations in cytoskeletal and nuclear matrix organization necessary for specific gene regulation during

differentiation. It has been proposed that a change in the scaffold topology of the cell cytoskeleton provides a mechanism for the regulation of cellular biochemistry (18). For example, it was suggested that focal contacts (ECM/cell or cell/cell interactions) may activate signaling molecules bound to the cytoskeletal network (e.g., protein kinases implicated in the phosphorylation of proteins). Moreover, various kinases have been shown to be associated with the nuclear matrix and it has been proposed that phosphorylation of specific nuclear matrix proteins could alter their association and/or organization within the nucleus and correlate with fundamental events which modulate cells phenotype (19).

How ECM-induced mechanical and biochemical signals cooperate to direct the expression or repression of specific genes remains to be determined. More particularly the repercussion of such signals on chromatin structure has to be analyzed. However such an investigation requires the identification of structural elements of the nuclear matrix which participate in ECM signaling and the development of new high resolution technique to analyze the intricate 3-dimensional organization of the nucleus.

Recently the study in our laboratory of a human breast tumor progression series has allowed for the analysis of changes in cellular architecture (including nuclear architecture) when phenotypically normal cells become tumorigenic. This work is included in the context of cancer as a disease of cellular organization and structure (20) and aims to participate in the battle against breast cancer by helping to understand tumor progression and to identify new therapeutic markers for cancer treatment. The studies were done by culturing cells in physiologically relevant conditions where the cells are embedded in a 3-dimensional extracellular matrix. This culture system enables the cells to form pluricellular structures encompassing complex cell-cell and cell-ECM interactions. Moreover, it allows for the discrimination between functionally normal and tumor cells (21). Functionally normal breast cells undergo morphogenesis (they growth arrest and form alveoli-like structures) whereas tumor cells do not undergo morphogenesis (they form disorganized spheroids including actively proliferating cells). Using the 3-dimensional culture system we were able to show that an alteration in cytoskeletal architecture was critical for the onset of tumorigenesis (Weaver et al., in preparation). Moreover, using cell skeleton/nuclear matrix preparations performed directly on cell cultures (in situ), we were able to identify a nuclear matrix structural component whose distribution is dependent upon

ECM signaling in functionally normal cells. The distribution of this nuclear matrix component is altered when the cells become tumorigenic. Interestingly, its distribution in tumor cells does not seem to depend on cell-cell and cell-ECM interactions anymore. This suggests that some interconnections in the 3-dimensional network of cellular architecture have been modified when the cells became tumorigenic. Hopefully this nuclear matrix component, as well as other nuclear matrix components under investigation in our laboratory, will facilitate the establishment of the link between ECM signaling and the regulation of gene expression through the modulation of nuclear and chromatin structures.

To achieve this aim, we now have to study the interactions of different elements of cellular architecture. Such a study undertaken at the nuclear level will require new methods of investigation using high resolution techniques. Our ideas about cell architecture are shaped by the technology available for examining the cells. So far thin section electron microscopy permits the study of nuclear structure at a 2-dimensional level with no possible reconstruction in a 3-dimensional context. Utilization of immunofluorescent markers permits the simultaneous study of up to three different parameters of the cellular architecture using confocal microscopy. The 3-dimensional reconstruction of images of complete cell clusters using a specific computer analysis program is also possible. However not all the components of the cellular architecture can be analyzed simultaneously and the resolution is limited. We hope that high resolution X-ray computed microtomography will open up new avenues for the study of 3-dimensional organization of tissue architecture. More specifically we need to study the 3-dimensional interactions of nuclear structural elements using cell skeleton/nuclear matrix preparations in situ. The technique of visualization must allow for the analysis of the connective distribution of nuclear elements as thin as 30 nm diameter in pluricellular structures representing several dozens of microns, but in which we can make sections which would fit with the maximum thickness authorized by the instrument utilized for the investigation. We propose the challenge, you give us the instrument: it is a deal !

Acknowledgments:

The Human breast tumor progression series was kindly provided by our collaborator Dr. Ole W. Peterson (Denmark). We thank Drs. Valerie Weaver and Carolyn Larabell (Lawrence Berkeley National Laboratory, Berkeley, CA) who are active participants in the work involving the human

breast tumor progression series presented in this article. This work was primarily supported by the U.S. Department of Energy, Office of Health and Environmental Research (contract DE-AC03-76-SF0098) to M.J. Bissell. S. Lelièvre is supported by a research fellowship from the International Agency for Research on Cancer, The World Health Organization.

References:

1. Streuli CH, Schmidhauser C, Bailey N, Yurchenko P, Skubitz APN, Roskelley C, Bissell MJ. *J. Cell Biol.*, 129: 591-603, 1995.

2. Bissell MJ and Barcellos-Hoff M-H. *J. Cell Sci. Suppl.*, 8: 327-343, 1987.

3. Roskelley CD, Desprez P-Y, Bissell MJ. *Proc. Natl. Acad. Sci. USA*, 91: 12378-12382, 1994.

4. Bissell MJ and Hall HG. *In*: The mammary gland (Neville M and Daniels C, eds), pp. 97-146, Plenum Press Publishing, New York, 1987.

5. Nickerson JA, Blencowe BJ, Penman S. *Int. Rev. Cytol.*, 162A: 67-123, 1995.

6. Gasser SM and Laemmli UK. *EMBO J.*, 5: 511-518, 1986.

7. Fey EG, Wan KM, Penman S. *J. Cell Biol.*, 98: 1973-1984, 1984.

8. Bissell MJ, Hall HG, Parry G. *J. Theor. Biology*, 99: 31-68, 1982.

9. Ingber DE, Madri JA, Folkman J. *In Vitro Cell Develop. Biol.*, 23: 387-394, 1987.

10. Ingber DE. *Curr. Opin. Cell Biol.*, 3: 841-848, 1991.

11. Wang N, Buttler JP, Ingber DE. *Science*, 260: 1124-1127, 1993.

12. Morita M, Kurihara H, Maemura K, Yoshizumi M, Nagai R, Yazaki Y. *Circulation Res.*, 75: 630-636, 1994.

13. Singh S and Gupta PD. *Epith. Cell Biol.*, 3: 79-83, 1994.

14. Ingber DE and Folkman J. *J. Cell Biol.*, 109: 317-330, 1989.

15. Vernon RB and Sage EH. *Am. J. Pathol.*, 147: 873-883, 1995.

16. Sims JR, Karp S, Ingber DE. *J. Cell Sci.*, 303: 1215-1222, 1992.

17. Gittes F, Mickey B, Nettleton J, Howard J. *J. Cell Biol.*, 120: 923-934, 1993.

18. Ingber DE and Jamieson JD. *In*: Gene expression during normal and malignant differentiation (Anderson LC, Gahmberg CG, Ekblom P, eds), pp. 13-32, Academic Press, Orlando, 1985.

19. Weaver VM, Carson CE, Walker PR, Chaly N, Lach B, Raymond Y, Brown DL, Sikorska M. *J. Cell Sci.*, 109: 45-56, 1996.

20. Pienta KJ, Partin AW, Coffey DS. *Cancer Res.*, 49: 2525-2532, 1989.

21. Petersen OW, Rønnov-Jessen L, Howlett AR, Bissell MJ. *Proc. Natl. Acad. Sci. USA*, 89: 9064-9068, 1992.

FIGURE LEGENDS.

Figure 1. **Tissue organization: schematic example of the mammary gland.**
Mammary epithelial cells (EC) are organized in alveoli-like structures and surrounded by a specific type of extracellular matrix called basement membrane (BM). Some mesenchymal cells (MC) are distributed around the alveolus. Endothelial cells (ENC) which form the blood vessel are also surrounded by a basement membrane. The various pluricellular structures are embedded in the jelly-like substance of the extracellular matrix (ECM), which is composed of fibrous and globular proteins. ECM composition depends on the tissue-type. (N: nucleus of the epithelial cell; nuclei are represented in gray in all cell types; L: lumen of the alveolus where mammary epithelial cells secrete milk proteins during lactation).

Figure 2. **Model of the solid-state signaling pathway**: the postulated minimum required unit for tissue-specific function, the cell plus its ECM (model modified from Bissell et al., 1982, and Bissell and Barcellos-Hoff, 1987). NM: nuclear matrix, L: lamina; NE: nuclear envelope; A: actin microfilament; IF: intermediate filament; T: microtubules; ECM: extracellular matrix. Specific cell-ECM interactions direct the reorganization of the internal cell architecture (schematic square). A, IF, and T are elements of the cytoskeleton. Regulatory proteins directing cytoskeletal remodeling and facilitating interconnections between ECM receptors and cytoskeletal elements are not represented.

Figure 3. **Diagram representing transmission of ECM-induced mechano-chemical signals through the cell architecture (solid-state signaling).** Hypothetically, the tension-inducing signals transmitted through pathway A may be resisted at the level of the nuclear structure (e.g., at the level of the peripheral lamina (L), which is part of the nuclear matrix and part of the nuclear envelope). Another pathway (B) may permit the transmission of signals inside the nuclear matrix and lead to the modification of nuclear functions. NM: nuclear matrix; (p) nuclear pores; (pm) plasma membrane.

Fig.1

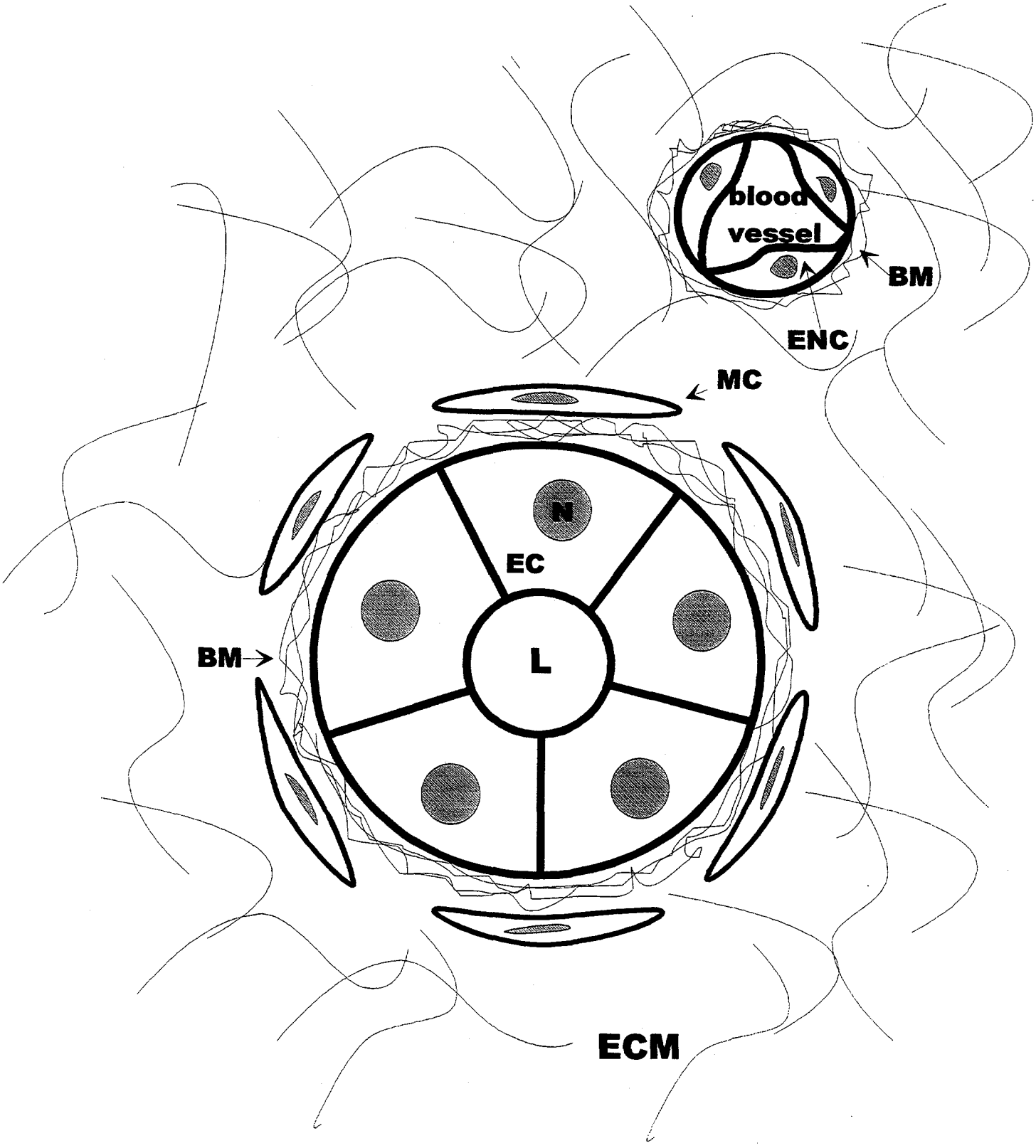

Fig.2

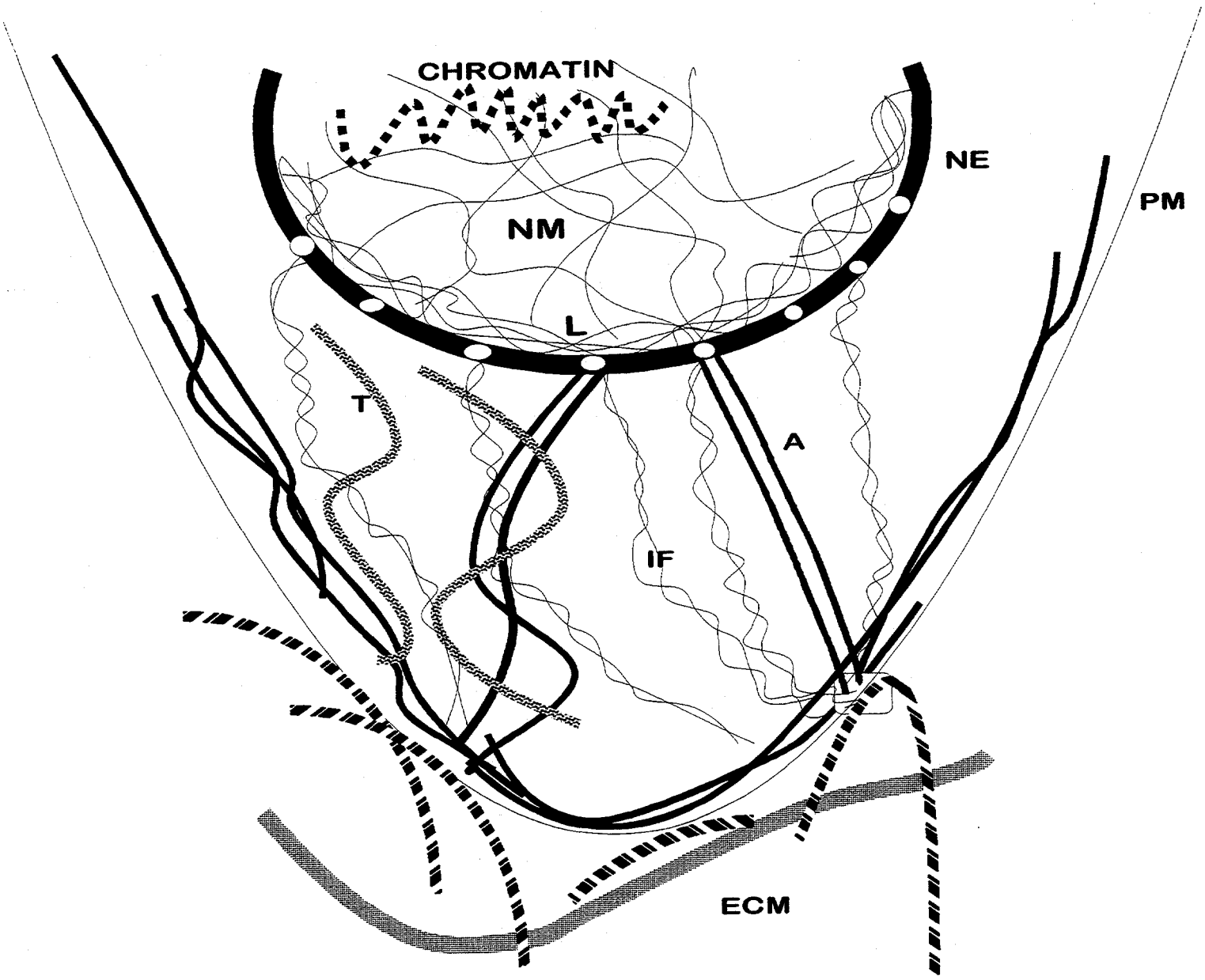

Fig.3

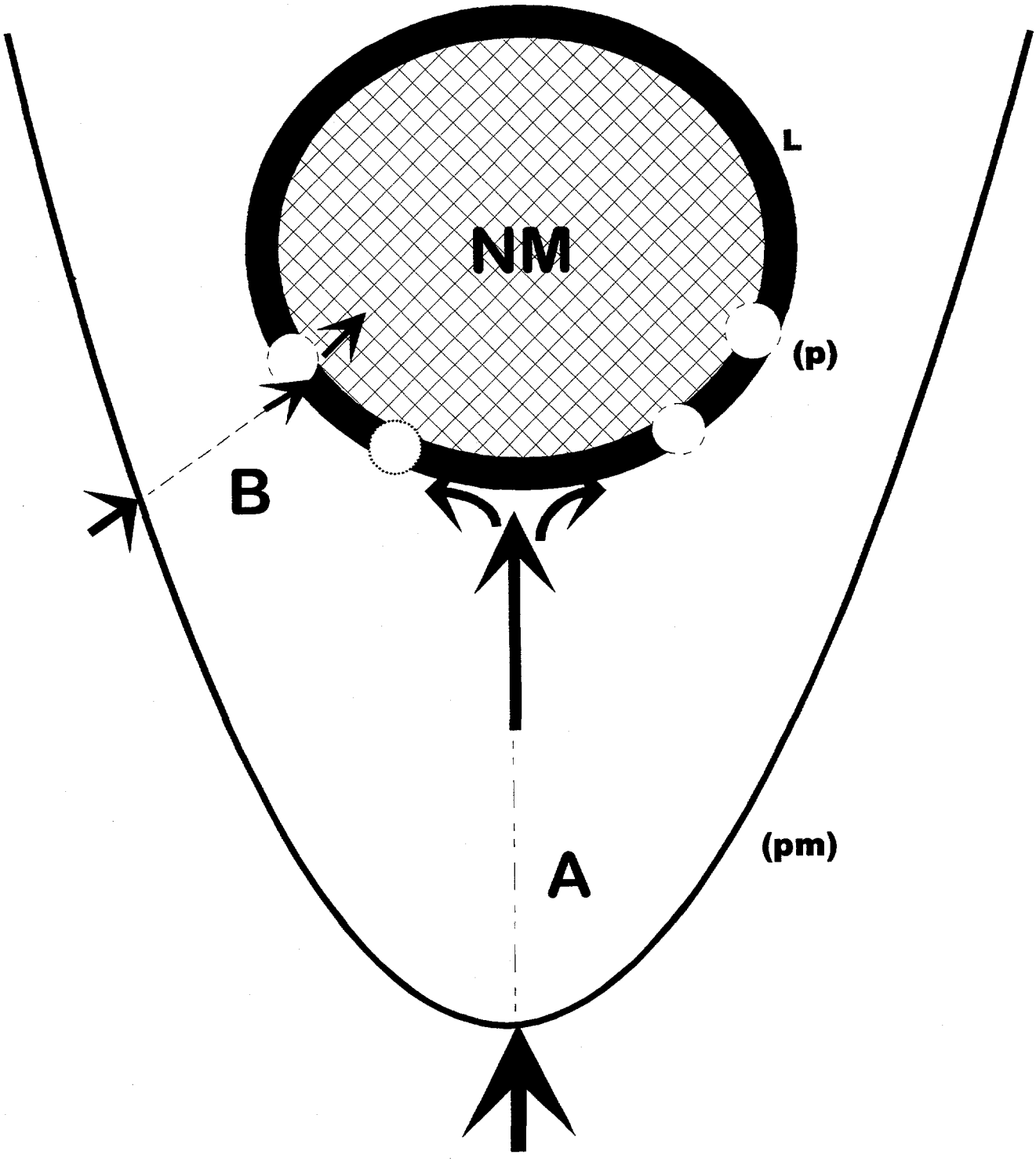

SESSION II: TUESDAY AUGUST 13, 1996

Bragg-Fresnel Optics: New Field of Applications.

Anatoly Snigirev, ESRF, B.P. 220, 38043 Grenoble, France

Abstract

Bragg-Fresnel Optics shows excellent compatibility with the third generation synchrotron radiation sources such as ESRF and is capable of obtaining monochromatic submicron focal spots with 10^8-10^9 photons/sec in an energy bandwidth of 10^{-4}-10^{-6} and in a photon energy range between 2-100 keV. New types of Bragg-Fresnel lenses like modified, ion implanted, bent and acoustically modulated were tested. Microprobe techniques like microdiffraction and microfluorescence based on Bragg-Fresnel optics were realised at the ESRF beamlines. Excellent parameters of the X-ray beam at the ESRF in terms of low emittance and quite small angular source size allow for Bragg-Fresnel optics to occupy new fields of applications such as high resolution diffraction, holography, interferometry and phase contrast imaging.

1. Introduction

Among the focusing elements for hard X-rays (> 6 keV) Bragg-Fresnel Optics shows excellent compatibility with the third generation synchrotron radiation sources such as ESRF. In addition to a beam of extremely high brilliance, these X-ray sources are characterised by very small source size. A typical source size at the ESRF is 50-100 μm, that at the source -to-sample distance of 50 m gives an angular source aperture of about 1-2 μrad. The coherence preservation is precisely, an essential feature which is required of the focusing optics. The Bragg-Fresnel optics (BFO) is a combination of Bragg reflectionfrom the crystal and diffraction by Fresnel structure grooved into crystal. As evident from creating principles, the BFO is coherent optics and this is the only focusing optics that is able to preserve the coherence of the incoming beam. As a coherent focusing element Bragg-Fresnel optics allows to realise along with standard microprobe the new field of applications such as high resolution diffraction, ultra small angle scattering, holography, interferometry and phase contrast imaging.

BFO was put forward in the Institute of Microelectronics Technology Russian Academy of Sciences ten years ago [1]. Since that time a lot of efforts has been spent on both BFO technology development and on experimental and theoretical research on the BFO performance [2-6]. It is clear that in general Fresnel zone structure on the surface of the flat crystal has an elliptical shape. Unfortunately, all attempts to obtained reasonable focusing properties for this type of the BFL failed due to low efficiency (~10%), an existence of zero order of diffraction, and shadowing effect in the diffraction plane. A remarkable study was done on BFL with the slope zones [7], but further optimisation of the profile structure is needed. At present two types of Bragg-Fresnel lenses (BFL) are mainly used [8-9]: linear BFL in sagittal geometry (Fig. 1–2) and circular BFL in backscattering (Fig. 3-4).

2. BFO : principles, performance

Bragg-Fresnel crystal optics is based on a superposition of Bragg diffraction by a crystal and dispersion by a Fresnel structure, which is patterned on the surface or grooved into the crystal. Unlike the transmission FZP the Bragg-Fresnel lens (BFL) is working in reflection. Its main advantage is that the various possibilities of beam transformation arising from the specific properties of Fresnel structures now become accessible to the high energy x-ray range. The wave reflected by the lower surface of the BFL zone structure gains an additional phase shift π, as compared to that reflected by the upper surface. So far BFL is a purely phase element, since upon diffraction of the X-ray wave on the BFL zone structure no amplitude modulation of the reflected wave is observed. Moreover BFL phase shift for a certain reflection is independent on the energy and is determined by the structure height only [8]. Diffraction efficiency of the BFL is very closed to the theoretical performance and is about 40% . The limiting spatial resolution that can be obtained in BFO is given by the width of the outermost zone of the zone structure. Present technologies permit to achieve fractions of a micron.

2.1 Linear BFL

A linear BFL in sagittal geometry (Fig. 1-2) on a flat substrate produces one-dimensional focusing of X-rays [8]. The phase properties of a linear BFL structure do not depend on the

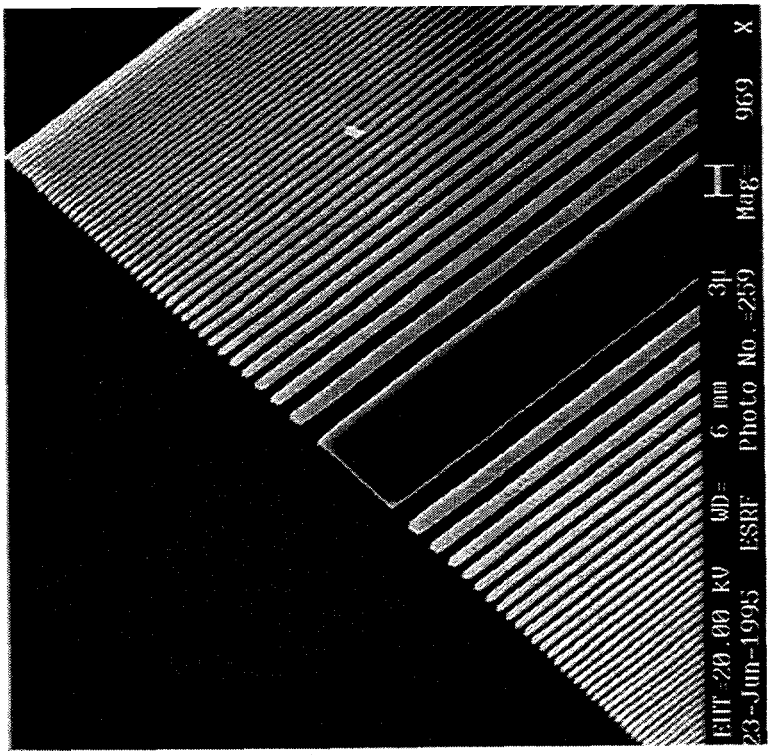

Fig. 1 SEM image of linear Si based Bragg-Fresnel Lens: aperture 150 µm, outermost zone width 0.3 µm, focal distance at 8 keV 25 cm.

energy. Therefore the same lens can be designed for a wide energy range determined only by Bragg's low. Tests of linear BFL were done at the undulator source and wiggler sources. It was shown that linear BFL is capable of focusing white radiation in the range from 2 to 100 keV[10]. The focal spot of 0.8 μm with intensity 10^8 - 10^9 photons/sec for linear BFL was measured at 8 keV and was limited by the source size according the demagnification ratio [11].

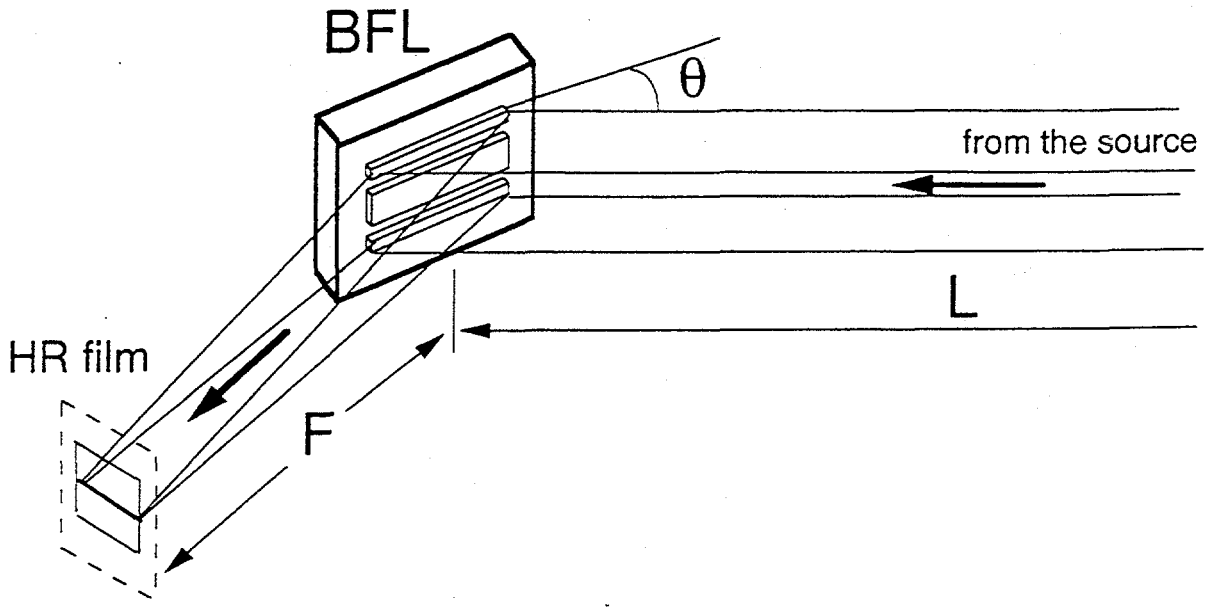

Fig. 2 Schematic sketch of the principle of the focusing by means of linear BFL in sagittal geometry

A limitation of the one dimensional focusing by linear BFL can be easily overcome by applying Kirckpatrick-Baez geometry [12] or cylindrical bending of the BFL [13-14]. The experiment was carried out at the Optics beamline (D5) at the ESRF. The focusing properties of the curved BFL were tested at energies 18 keV and 28 keV. The intensity in the focal plain of the BFL was measured by means of 2D mapping with 1μm pinhole paired with scintillating detector or Si PIN diode. In accordance with demagnification factor and X-ray source size the focal spots of 2*4.5 μm^2 at 18 keV and of 3*6.5 μm^2 at 30 keV were measured. The comparison of the X-ray integral intensities in the focus spot by the flat and curved linear BFL with same parameters was carried out. A gain by the factor of up to 100 in the focal flux was obtained.

To improve the resolution and to increase the focal flux the BFL may be completed with the third and fifths order structures which, increase the total aperture of the BFL by a factor of 3 and 5 respectively [15]. To perform the experiment linear BFL on Si (111) substrate with first and third order structures was fabricated with the following parameters: total aperture A = 380 μm, lens length L = 8 mm, outermost zone width Δr_n = 0.3 μm, focal distance F = 0.25 m at E = 8 keV. The measured focal spot size was in a good agreement with the limitations given by the source size and demagnification factor.

To increase the absolute intensity in the focal spot of a BFL it is to change the crystal reflectivity, i.e. to modify the crystal lattice. An enhancement of the BFL focal flux of up to 15% due to crystal lattice deformations was demonstrated already with ion implanted BFL[16]. However, due to the complicated scattering of the implanted ions inside micron or submicron size crystal features which make up the BFL relief, the implantation technology destroys the peripherical zones of the BFL more than increases the intensity in the focus.

2.2 Circular BFL

A circular BFL in backscattering (Fig. 3-4) produces two-dimensional focusing at fixed X-ray energies determined by Bragg's low for the different reflection orders [9, 17].

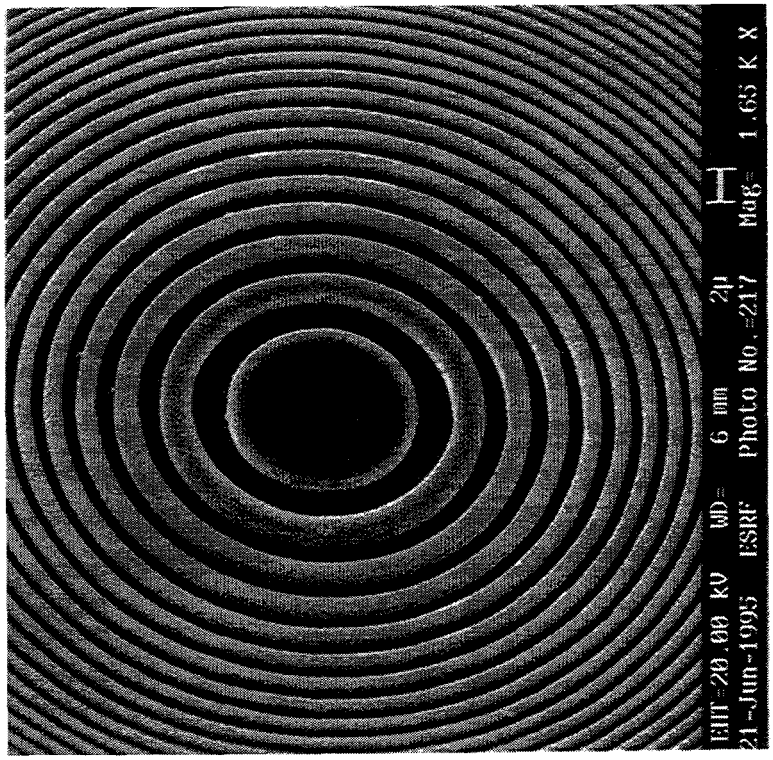

Fig. 3 SEM image of the Ge based circular Bragg-Fresnel Lens: outermost zone width 0.15 μm, aperture 100 μm, focal distance at 8 keV 10 cm.

Therefore, it is not possible to tune the energy. It was shown that the imaging can be made with significant diffraction efficiency of the BFL in the energy range of about 2 keV-18 keV when the reflections were varied from Si-111 to Si-999 [9, 17]. The focal spot of 0.7 μm with intensity 10^7 - 10^8 photons/sec for circular BFL was obtained at 10 keV [18].

The phase BFL gives a high efficiency focusing of monochromatic X-rays however no more than a small fraction of the total intensity of a white source is gathered into the focus. To increase the absolute intensity in the focal spot the ultrasonic modulation of crystals which BFL is based on was applied [19]. The influence of an ultra sonic modulation of the Bragg-Fresnel lens as a tunable instrument to vary the radiation flux at the focal spot was studied (Fig. 5). The reflectivity and integral intensity of the crystal substrate depend on the frequency and amplitude of the exited ultra sonic wave. The intensity in the focal plain of the BFL was measured by means of 2D mapping with 10 μm pinhole paired with scintillating detector or Si PIN diode. A gain by the factor of up to 3 in the focal flux was obtained.

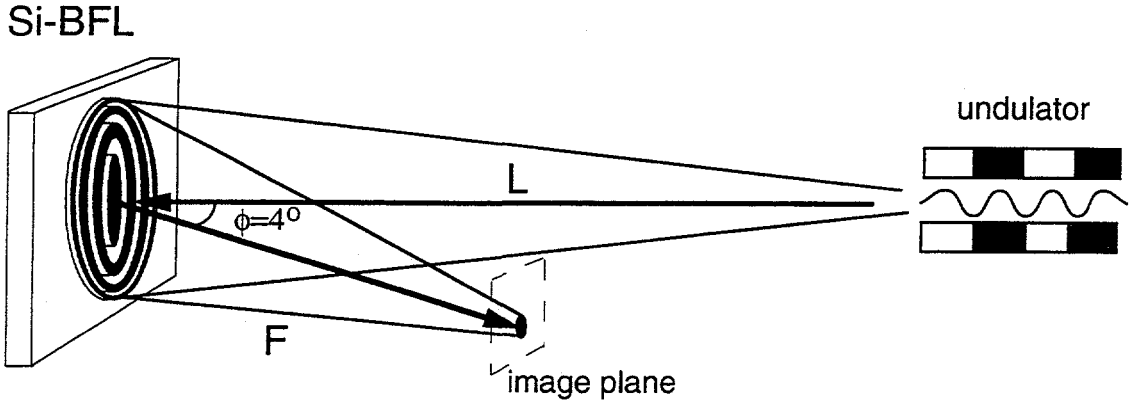

Fig. 4 Schematic layout for principle of focusing using circular BFL in backscattering geometry.

2.3 Elliptical Multilayer BFL

For some applications the degree of monochromatisation obtained by Bragg-Fresnel lenses is too high. This is the case especially for circular BFLs used in back reflection geometry. This problem can be overcome by using an elliptical Bragg-Fresnel lenses based on multilayers [20-21]. Elliptical multilayer lens (Fig. 5) with aperture 140 μm * 18 mm was tested at the ESRF Optics beamline. The focal length was 40 cm at 12.4 keV. The outermost zone width which

determines the resolution was 0.3 μm. A focal spot of 1.3 * 5 μm^2 and a flux 10^8 photons / sec was reached.

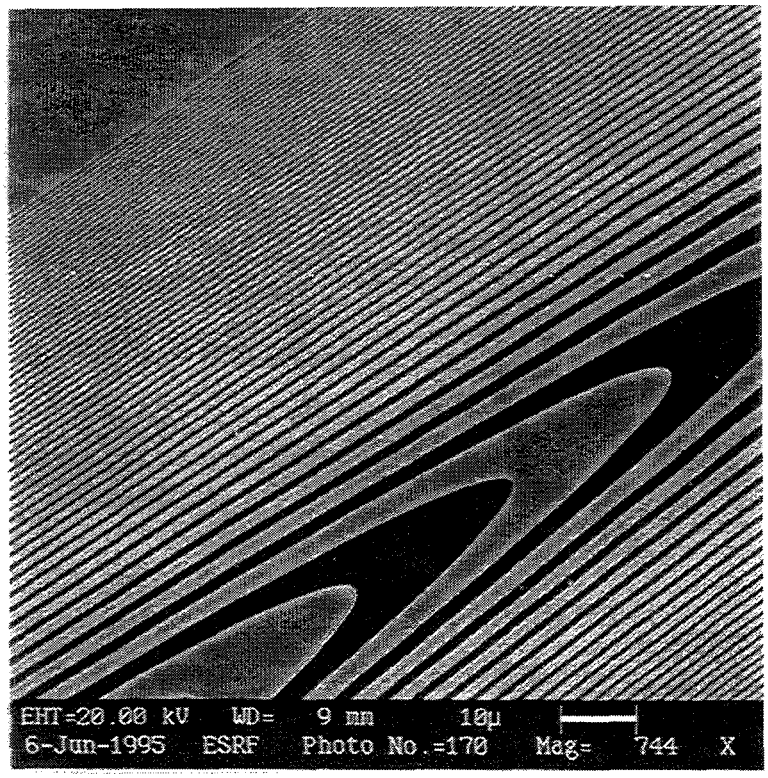

Fig. 5 SEM image of the elliptical W / Si multilayer BFL: length 18 mm width 140 μm, outermost zone width 0. 3 μm

3. Applications

It is evident that a combination of microfocusing x-ray optics with the high brilliance x-ray beams provided by the third generation synchrotron radiation sources like ESRF opens up new capabilities to develop hard x-ray microimaging and microprobe techniques.

3.1 Microprobe

3.1.1 Microfluorescence

A varied program of experiments using X-ray microbeam produced by BFLs for fluorescence imaging and elemental distribution was carried out. The experiments have been performed at different undulator and bending magnet beamlines at the ESRF. Applications of the developed fluorescence microprobes for elemental distributions in volcanic rocks, Antarctica micrometeorites, bone specimens and human hair slices were demonstrated [20-22].

3.1.2 SAXS camera

The attractive feature of proposed BFL-based camera is the fact that one can measure down to the smallest angles without using a complicated collimation system: defining and guard apertures (slits). The performance of the BFL-based SAXS camera has been designed and tested at the Microfocus beamline [23]. The diffraction patterns from the turkey tendon collagen were detected on the Molecular Dynamics image plate. The first 25 meridional reflections were resolved. Thus, small-angle scattering is possible from a sample on the scale of a few μm and can be extended to the subμm range. These open the possibility for new applications of SAXS, in particular in the area of surfaces and interfaces.

3.1.3 High pressure diffraction

It is evident that microbeam is very desirable for high pressure experiments, especially when diamond cells have to be transparent for x-rays and very little amount of sample is involved in the measurement [24]. A range of samples were investigated at 26 keV, but more important results were obtained on oxygen at very high pressures (up to 108 GPa).

3.2 High resolution diffraction

Single crystal Bragg-Fresnel lens is acting as a focusing monochromator producing cylindrical wave front - a sagittally focused beam remains a very parallel in meridional plane. This focusing monochromator can be applied in high resolution diffraction technique: double- and triple-crystal diffractometry for a detailed study of nearly perfect semiconductor crystals with topological surface structure. High angular resolution can be easily achieved using an asymmetrically cut BFL crystal, so standing wave technique with lateral resolution of about 1μm is also feasible.

3.2.1 Double crystal stress analysis

A turbine blade of the nickel-base super alloy CMSX-6 which was subjected to service in an accelerated mission test for several hundred hours was investigated at different positions along several (100) and (001) sections. The local lattice parameters were determined from the locally measured line profiles of the (004) and (400) Bragg reflections using BFL based diffractometry set-up with high lateral and angular resolution. The analysis of the data shows that lattice parameter distributions is determined mostly by the centrifugal stresses and the high material temperatures, and further details will be published soon [25].

3.2.2 Double crystal diffractometry

The microfocus X-ray diffraction measurements were carried out at the Optics beamline in (+n, -n) setting consisting of a Si (111) Bragg-Fresnel lens and the sample [26]. Using this set-up III/Y heterostructures grown by different selective area epitaxy techniques (planar and

embedded selective area MOVPE and MOMBE) were investigated. The samples were test structures of InGaAs and InGaAsP layers grown on an InP (001) substrate that was partially masked with SiO_2 fields and laser/waveguide devices laterally integrated on an InP (001) wafer. In order to determine the lattice mismatch close to the boundaries of the layer / oxide and laser / waveguide boundary, rocking curve scans with micrometer step width were performed. The lattice distortions of the III/Y - heterostructures show changes at the boundaries in the range of 5 μm to 100 μm depending on the selected process.

3.3 Imaging techniques

3.3.1 Imaging of the self-luminous objects

The circular BFL was applied for imaging of the self-luminous objects such as the undulator source [27-28]. Two optical geometry's have been tested at the energy 8 keV. In a first set-up the image formed by the long focus (F = 1.25 m) BFL as an objective lens has been vertically enlarged by asymmetrically reflected Si-422 crystal with magnification 15 that corresponds to asymmetry factor. The enlarged image was recorded by X-ray CCD camera having a resolution of 30 μm FWHM. In a second set-up classical telescope geometry was applied when two BFLs were used in tandem. The first objective forms a real inverted image, which was examined using the second short focus BFL (F = 0.25 m), the eyepiece. The second focal plane of the objective nearly coincided with the first focal plane of the eyepiece and a 100 μm pinhole was installed in this plane in order to spurs the zero diffraction order for better image contrast. The image was recorded by X-ray CCD placed at 1.5m distance from the second lens. The computer recorded images for both optical set-ups were treated and the deduced values of the emittance are in a good agreement with other estimates.

3.3.2 Phase contrast microscopy

Usual principle of the microscopy based on amplitude contrast which arises through differences in the absorption length from material to material. From this concept x-ray imaging microscopy is practically impossible for hard x-rays. It is well known that the contrast of the sample to be imaged can be enhanced considerably by using phase contrast. Zernicke type phase contrast microscopy was realised in soft x-ray domain. In principle the same approach can be apply for hard x-rays using BFO or zone plates. But we suggested to use another way. High level of collimation and coherency of the X-ray beam provided by the ESRF sources make it possible to develop phase sensitive technique [29-31]. High energy X-ray phase contrast microscopy based on the Bragg-Fresnel optics with submicrometer resolution was demonstrated [32]. An X-ray image of the free-standing gold grid was observed at 9.5 keV using a circular Bragg-Fresnel lens in backscattering geometry. The fine 0.5 μm gold grid was clearly seen not only in the open areas of the supporting mesh but also underneath the 3 μm

bars. A contrast of more than 20% was measured. Crystal BFL works like a normal imaging lens, so it magnifies the phase-contrast image of the object. Moreover, the depth of the image field was experimentally measured to be almost infinite, this confirms a partially coherent illumination as in laser microscopy.

3.3.3 Microtomography

Considering the small divergence and coherent properties of the beam evident benefits might be achieved in the development of phase contrast tomography. The first results on phase-contrast tomography were obtained at 50 keV recently [33]. For phase contrast tomography with parallel illumination the resolution is determined by the resolution of the detector: at present this is 5-10 μm for high resolution X-ray cameras and 1 μm for high resolutions films. The use of additional optics like a Bragg-Fresnel lens installed after the object should lead to a 0.1 μm resolution.

Bragg-Fresnel optics is quite promising for normal absorption tomography with the pencil beam with sub-micrometer resolution. It is practically impossible to produce sub-μm beam with collimation systems owing the diffraction broadening.

3.3.4 Holography and interferometry

First holograms from the organic fibres and boron fibre were recorded at the ESRF with X-rays in the energy range from 10 till 60 keV. Preliminary numerical reconstruction's of these holograms with a modified Genzberg-Saxon algorithm show encouraging results. However, in Gabor holography the spatial resolution is limited by the detector resolution to 1-10 μm. To achieve higher resolution, Fourier transform holography seems to be a promising alternative. Here the object wave interfere with a spherical reference wave rather than a plane wave as in the Gabor set-up. We propose to utilise a Bragg-Fresnel lens to obtain a point source for the spherical reference wave. The resolution will then be limited by the size of the focal spot, thus by the outermost zone width of the Bragg-Fresnel zone plate.

References

1. V. V. Aristov, A. A. Snigirev, Yu. A. Basov, A. Yu. Nikulin, AIP Conf. Proc., 147, 253, (1986).

2. V. V. Aristov, Yu. A. Basov, S. V. Redkin, A. A. Snigirev, V. A. Yunkin, Nucl.Instrum.& Methods A261, 72, (1987).

3. V. V. Aristov, Yu. A. Basov, G. N. Kulipanov, V. F. Pendyurin, A. A. Snigirev, A. S. Sokolov, Nucl. Instrum.& Methods A274, 390, (1989).

4. V. V. Aristov, Yu. A. Basov, A. A. Snigirev, Rev. Sci. Instrum., 60, 1517, (1989).

5. V. Aristov, S. Kuznetsov, A. Snigirev, Inst. Phys. Conf. Ser. No130, 543, (1992).

6. E.Aristova. C.David, A.Freund, Ya.Hartman, B.Kaulich, A.Snigirev, V.Yunkin, in X-Ray Microscopy IY, Eds. V.V.Aristov, A.I.Erko, 617, (Bogorodskii Pechatnik, Chernogolovka, Moscow region, Russia, 1994).

7. V. V. Aristov, Yu. A. Basov, A. A. Snigirev, V. A. Yunkin, Rev. Sci. Instrum., 63, 586, (1992).

8. V. V. Aristov, Yu. A. Basov, T. E. Goureev, A. A. Snigirev, T. Ischikawa, K. Izumi, S. Kikuta, Jpn. J. Appl. Phys., vol.31, 2616, (1992).

9. Yu. A. Basov, T. L. Pravdivtseva, A. A. Snigirev, M. Belakhovsky, P. Dhez, A. Freund, , Nucl. Instrum.& Methods A308, 363, (1991).

10. A. Snigirev, Rev. Sci. Instr, 66(2), 2053, (1995).

11. S. M. Kuznetsov, I. I. Snigireva, A. A. Snigirev, P. Engström, C. Riekel, Appl.Phys.Lett. 65 No 7, 827, (1994).

12. U. Bonse, C. Riekel, A. A. Snigirev, Rev. Sci. Instrum.,63, 622, (1992).

13. Ya. Hartman, A. Freund, I. Snigireva, A. Snigirev, to be published.

14 Bent BFL

15 M. J. Simpson, A. G. Michette, Opt.Acta, **31**, 403 (1984).

16 A. Suvorov, A. Snigirev, I. Snigireva, E. Aristova, Rev. Sci. Instrum., 67(5), 1733, (1996).

17. E. Tarasona, P. Elleaume, J. Chavanne, Ya. M. Hartman, A. A. Snigirev, I. I. Snigireva, Rev. Sci. Instr., 65(6), 1959, (1994).

18. A. Snigirev, I. Snigireva, P. Engström, S. Lequien, A. Suvorov, Ya. Hartmann, P. Chevallier, F. Legrand, G. Soullie, M. Idir, , Rev. Sci. Instr., 66(2), 1461, (1995).

19. A. Souvorov, I. Snigireva, A. Snigirev, E. Aristova, Ya. Hartman, to be published.

20 V.V. Aristov, S. V. Gaponov, V. M. Genkin, Yu. A. Gorbatov, A. I. Erko, V. V. Martynov, L. A. Matveeva, N. N. Salaschenko, Sov. Journ. Exp. and Thor. Phys. (JTEPh) Letters, 44(4), 265, (1986).

21. A. Erko, Yu. Agafonov, L. A. Panchenko, A. Yuakshin, P. Chevallier, P. Dehz, F. Legrand, Optics Com., 106, 146, (1994).

22. P. Chevallier, P. Dehz, F. Legrand, M. Idir, G. Soullie, A. Mirone, A. Erko. A. Snigirev, I. Snigireva, A. Suvorov, A. Freund, P. Engström, J. Als-Nielson, A. Grübel, , Nucl. Instrum.& Methods, A354, 584, (1995).

23. A. A. Snigirev, I. I. Snigireva, C. Riekel, A. Miller, L. Wess, T. Wess, Journal de Physique IV, Vol.3, C8,Suppl.JP III, N12, 443, (1993).

24. M. Hanfland, D. Hausermann, A. Snigirev, I. Snigireva, Y. Ahahama, M. Mcmahon, ESRF Newsletters, No22, 8, (1994).

25 H. Biermann, B. V. Grossmann, S. Mechsner, H. Mughrabi, T. Ungar, A. Snigirev, I. Snigireva, A. Souvorov, M. Kocsis and C. Raven, to be published.

26. A. Iberl, M. Schuster, H. Göbel, B. Baur, R. Matz, A. Snigirev, I. Snigireva, A. Freund, B. Lengeler, H. Heinecke, J. Phys. D: Appl. Phys., 28, A200, (1995).

27. Ya. Hartman, E. Tarazona, P. Elleaume, I. Snigireva, A. Snigirev, Journal de Physique IY, Colloq.C9, vol.4, C945, (1994).

28. Ya. Hartman, E.Tarazona, P. Elleaume, I. Snigireva, A. Snigirev, Rev. Sci. Instrum., 66(2), 1978, (1995).

29. A. Snigirev, I. Snigireva, A. Suvorov, M. Kocsis, V. Kohn, ESRF Newsletters, No24, 23, (1995).

30. A. Snigirev, I. Snigireva, V. Kohn, S. Kuznetsov, I. Schelokov, Rev. Sci. Instrum., 66(12), 5486, (1995).

31. A. Snigirev, I. Snigireva, V. Kohn, S. Kuznetsov, Nucl. Instrum. & Methods, A370, 634, (1996).

32. A. Snigirev, I. Snigireva, P. Bösecke, S. Lequien, to be published in Optics Commun.

33. C. Raven, A. Snigirev, I. Snigireva, P. Spanne, A. Suvorov, V. Kohn, to be published in Appl. Phys. Letters.

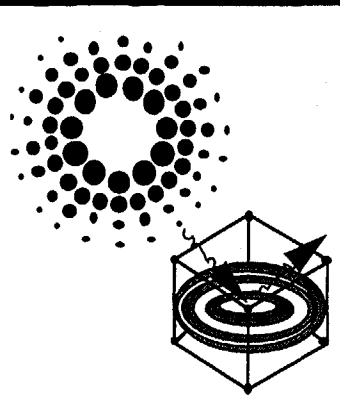

Bragg-Fresnel Optics
New Fields of Applications

Irina SNIGIREVA

ESRF, Grenoble, France

- Introduction
- Performance of Bragg-Fresnel Optics
- Applications
- Future perspectives

Workshop on Computed Microtomography, ALS/LNBL, Berkeley, August12-13, 1996

Focusing Optics for Hard X-rays
Energy: (2) 6 - 30 (100) keV

	KINEMATICAL FOCUSING BENT MIRROR OR CRYSTAL			DYNAMICAL FOCUSING			CAPILLARY OPTICS	FRESNEL OPTICS	BRAGG-FRESNEL OPTICS
				Indenbom 1974	Afanas'ev,Kohn 1977	Petrashen', Chukhovsky 1976	Kreger 1948	Baez 1952	Aristov et al 1986
	mirror	multilayer	crystal	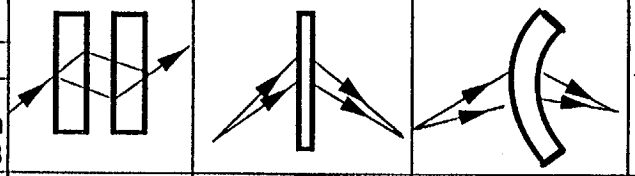			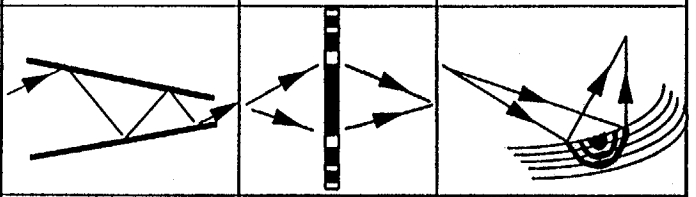		
	Kirkpatrick, Baez 1948	Underwood, Barbee,Frieber 1986	Johann, Johansson 1931-1933						
angular apperture	10^{-3}	10^{-3}	10^{-4}	$10^{-4} - 10^{-5}$			10^{-3}		
resolution	5μm Suzuki et al 1992	5μm Underwood et al 1988	~~10~~5μm Van Lageveld 1992	≤10μm Suvorov et al	10μm Aristov	8 μm Kushnir et al.	0.05 Bilderback et al 1994	0.6μm Yun et al 1992	0.5-0.7 Snigirev et al 1994-95

Iida 0,8μm

A. Thomson 1μm 1995

4.5μm

0.5μm

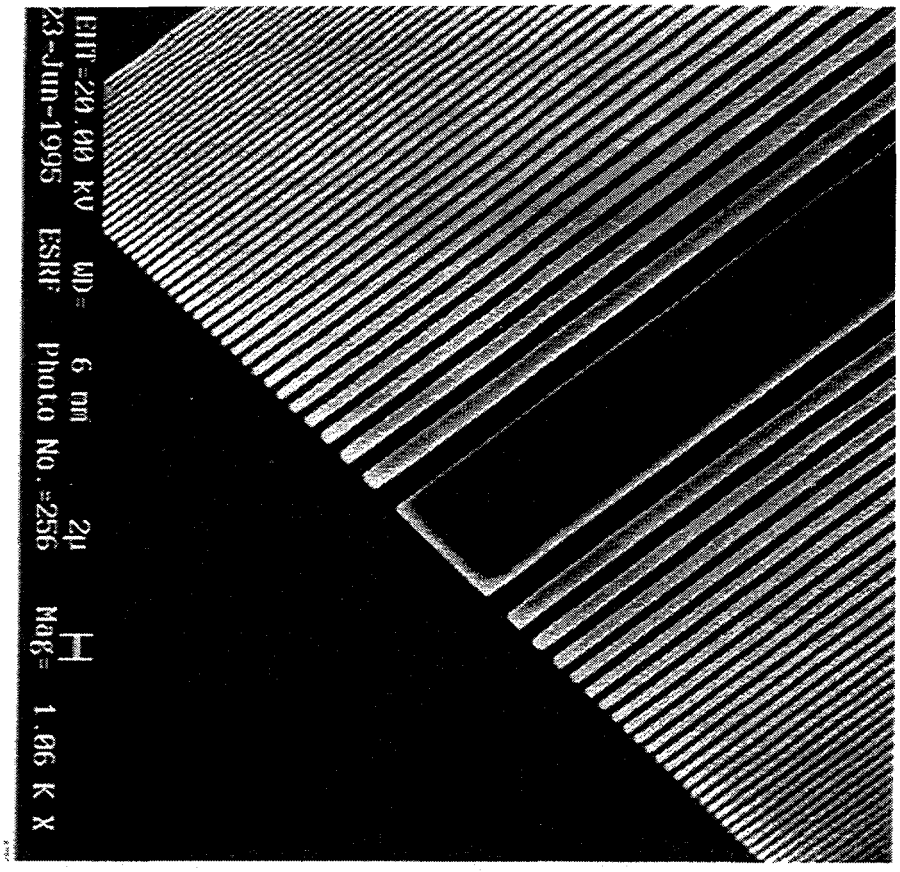

Linear BFL

Si (111)

$A = 200\ \mu m$

$\Delta r_n = 0.3\ \mu m$

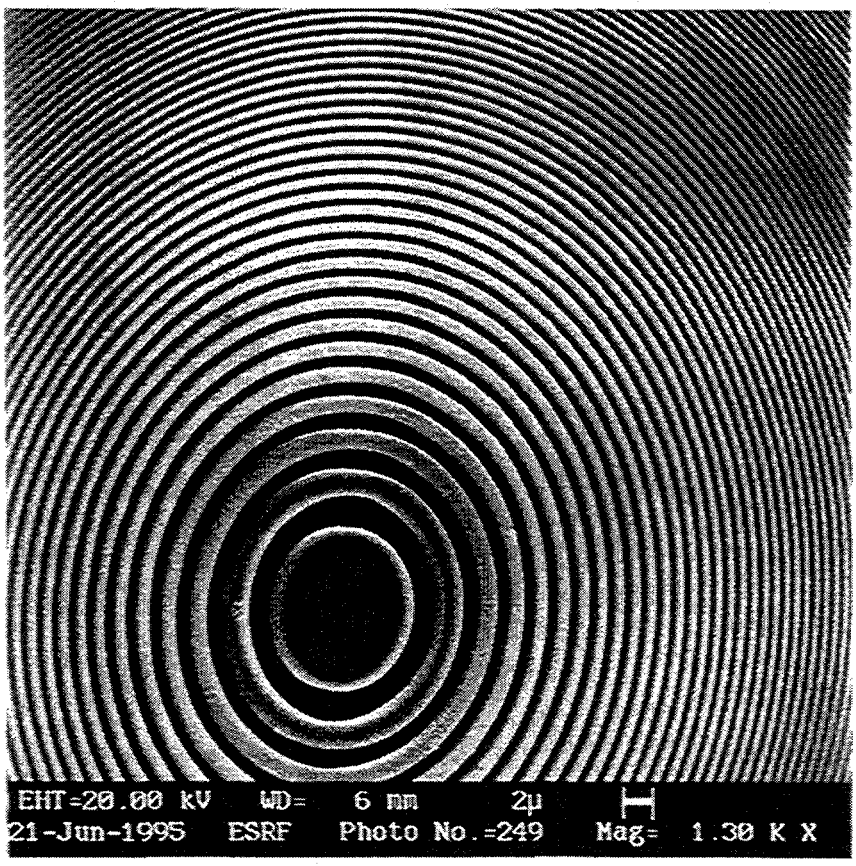

Circular BFL

Ge(111)

$A = 200\ \mu m$

$\Delta r_n = 0.15\ \mu m$

Bragg-Fresnel Multilayer lens

E=12.4keV (λ=1Å)
Δr_n=0.3µm
F=40cm

56 W/Si periods
length 18mm
width 136µm

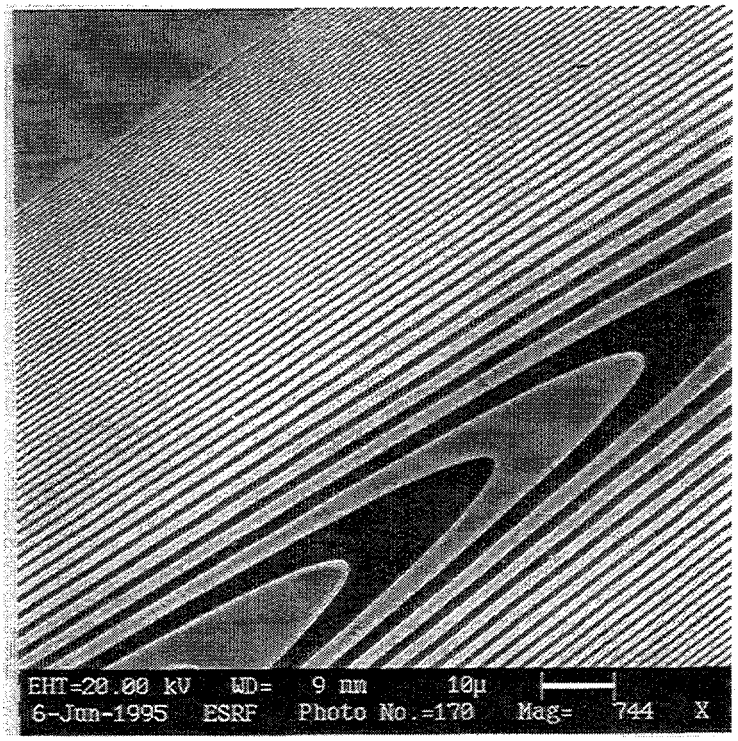

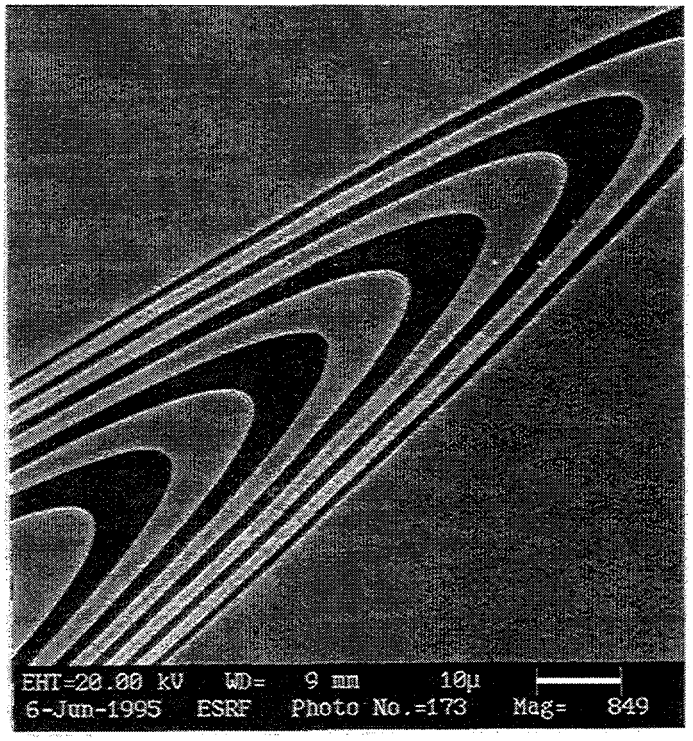

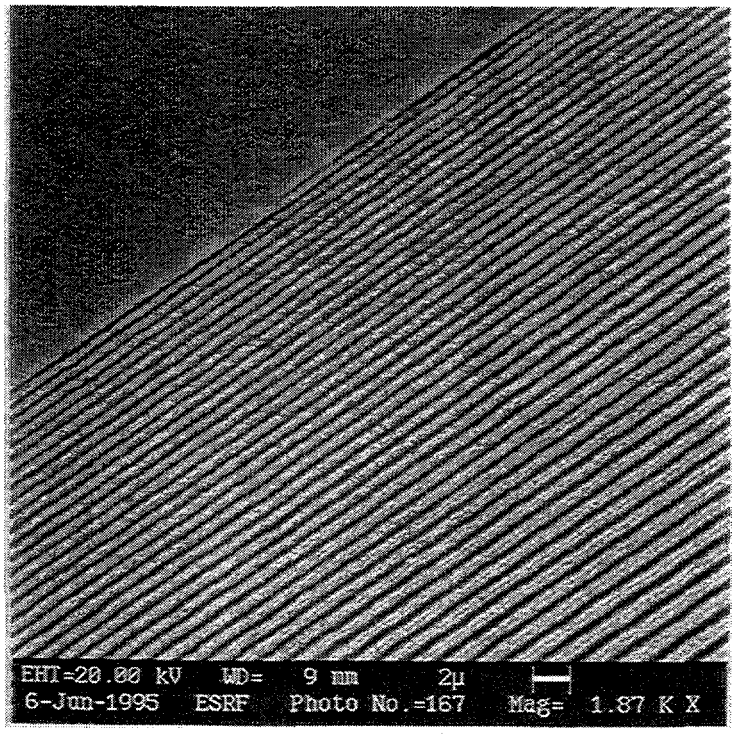

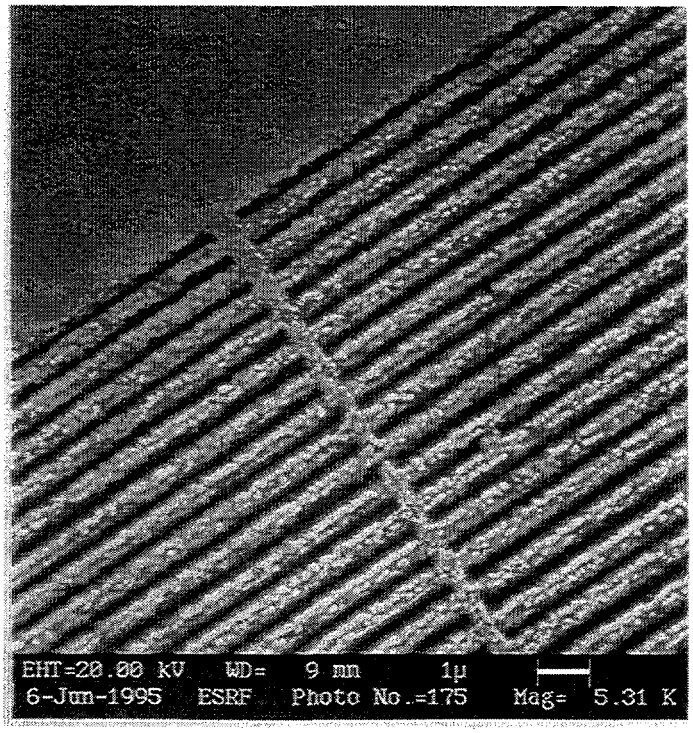

Fluorescence Knife-edge mesurements of the BFL microfocus beam

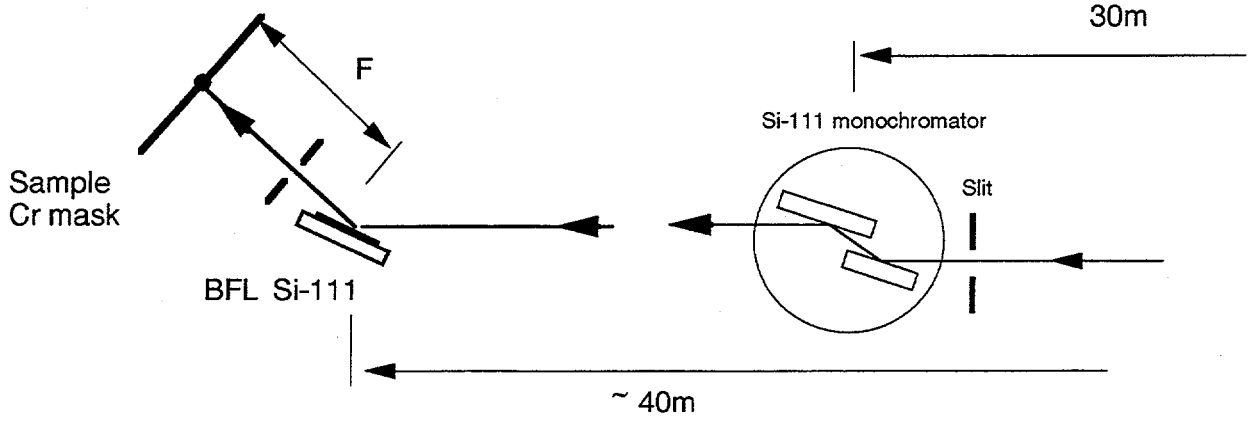

TOP VIEW

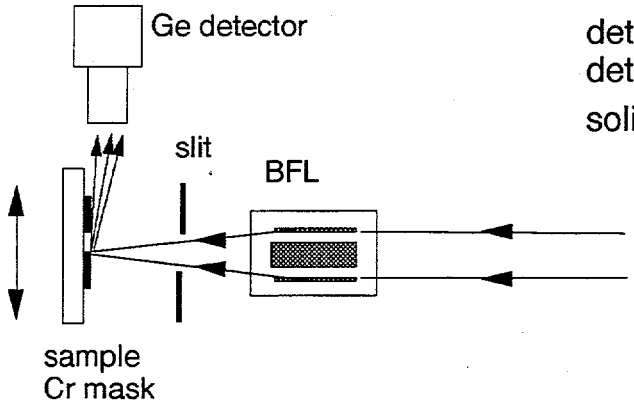

detector-to-sample distance - 7cm
detector window ~ 10mm∅
solid angle ~ 2×10^{-3} steradians

E=15keV λ=0.8A
BFL Si-111 F=0.18m
Cr-strip 8μm

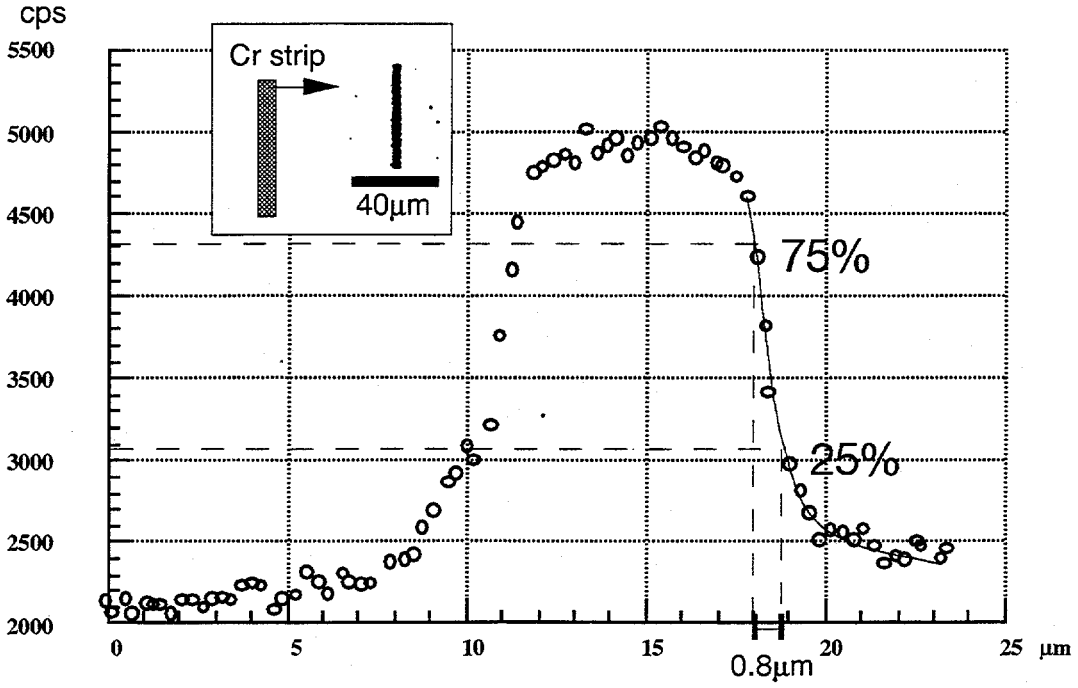

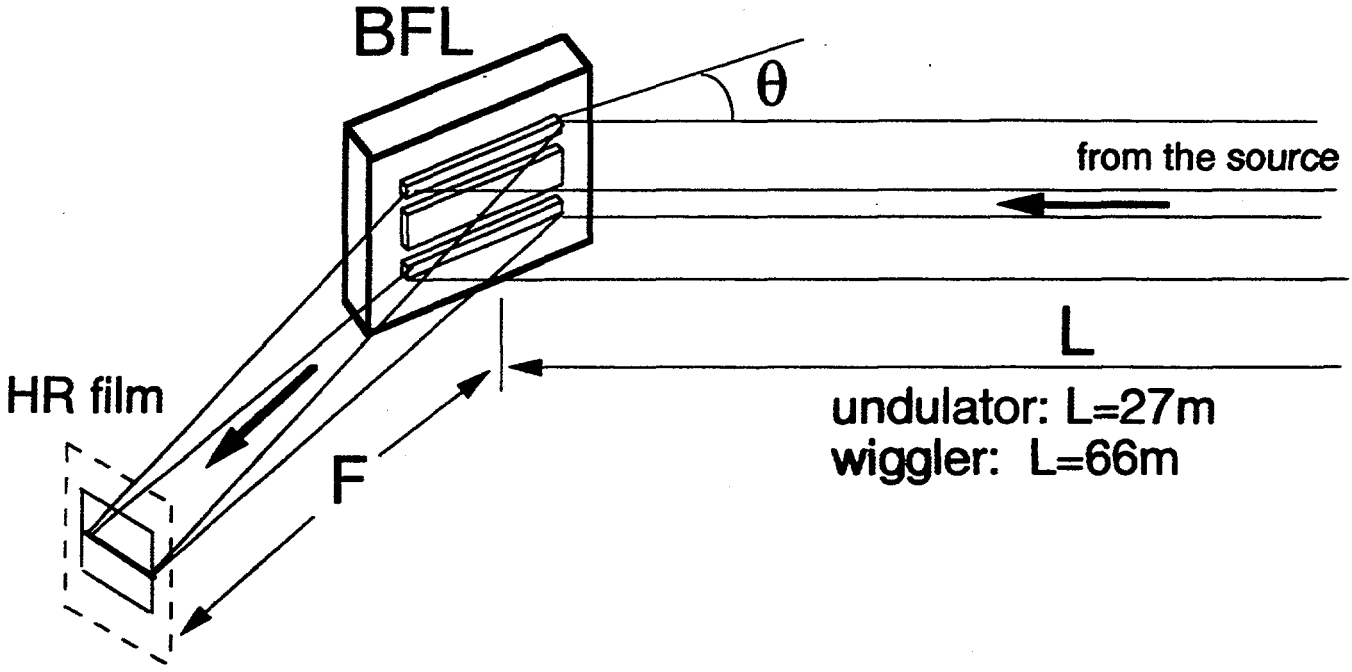

source	undulator ID-13 low-β		wiggler ID-15 high-β	
E=8keV θ=14° F=0.1m	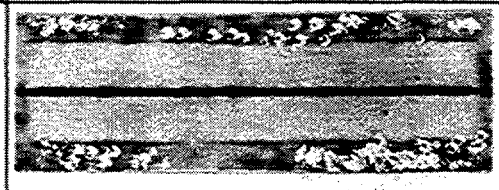		E=37 keV θ=3° F=0.47m	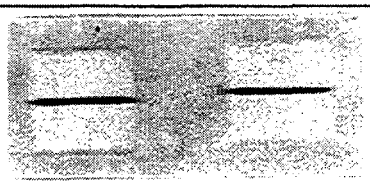
E=10keV θ=11° F=0.13m	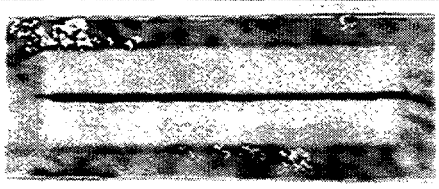		E=54 keV θ=2.1° F=0.67m	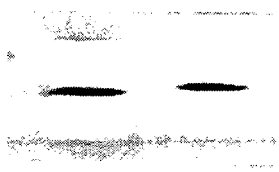
E=16 keV θ=7° F=0.2m	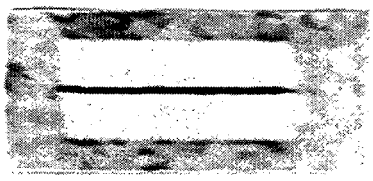		E=60 keV θ=1.9° F=0.75m	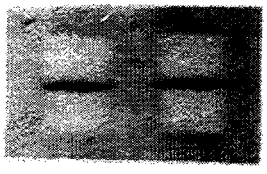
E=22 keV θ=5° F=0.28m	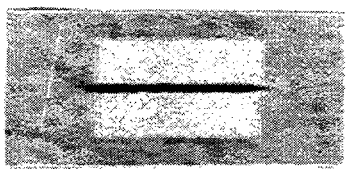		E=80 keV θ=1.4° F=1m	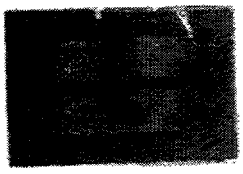
E=28 keV θ=4° F=0.35m	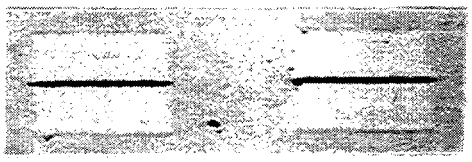		E=93 keV θ=1.2° F=1.2m	 50μm

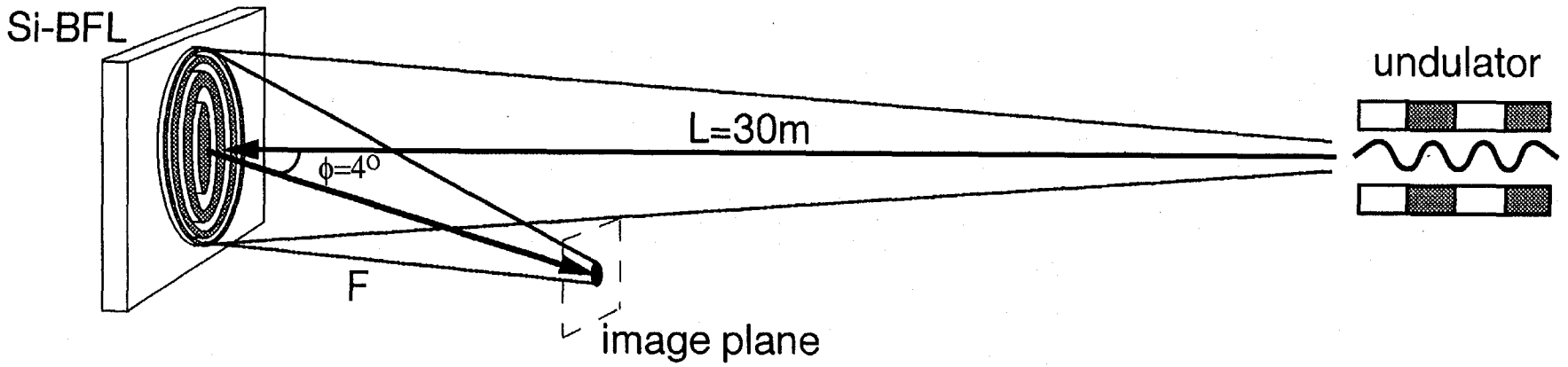

Si-333	Si-444	Si-555	Si-777	Si-888	Si-999
E=**5.9keV**	E=**7.9keV**	E=**9.9keV**	E=**13.9keV**	E=**15.8keV**	E=**17.8keV**
λ=2.09Å	λ=1.57Å	λ=1.25Å	λ=0.89Å	λ=0.78Å	λ=0.7Å
F=0.37m	F=0.49m	F=0.61m	F=0.86m	F=0.98m	F=1.1m
Gap=40mm	Gap=50mm	Gap=25.2mm	Gap=31mm	Gap=34.2mm	Gap=38.3mm
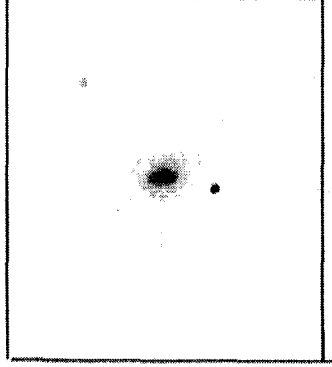	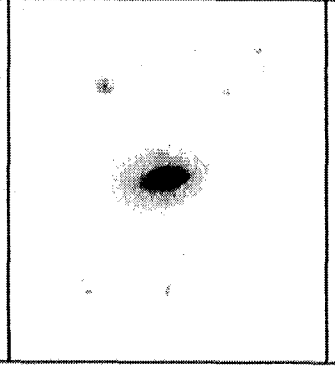	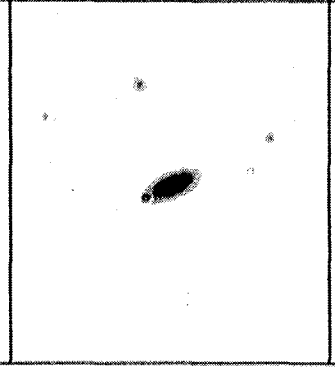	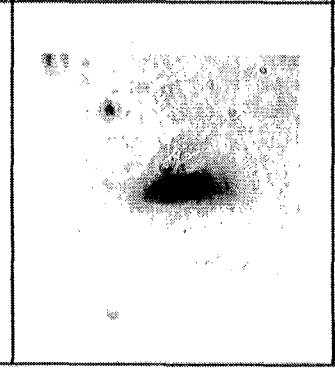	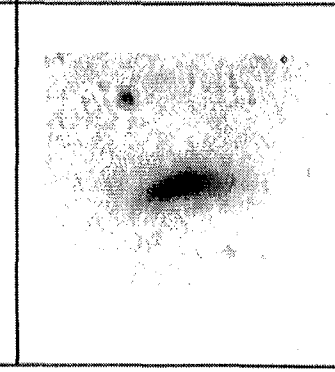	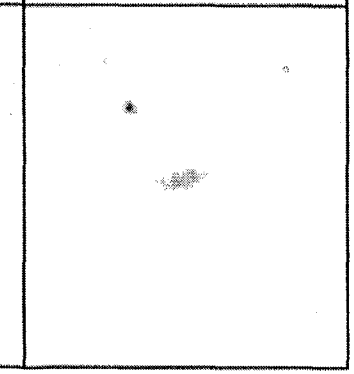

50μm

TESTING OF SUB-MICROMETER FLUORESCENCE MICROPROBE BASED ON BRAGG-FRESNEL CRYSTAL OPTICS AT THE ESRF

A. Snigirev, I. Snigireva, P. Engström, S. Lequien,A. Suvorov, P. Chevallier, F. Legrand, G. Soullie
M. Idir
ESRF, LURE, IMT RAS,LSA

subm. to SRI-94, to be published in Rev.Sci.Instr.

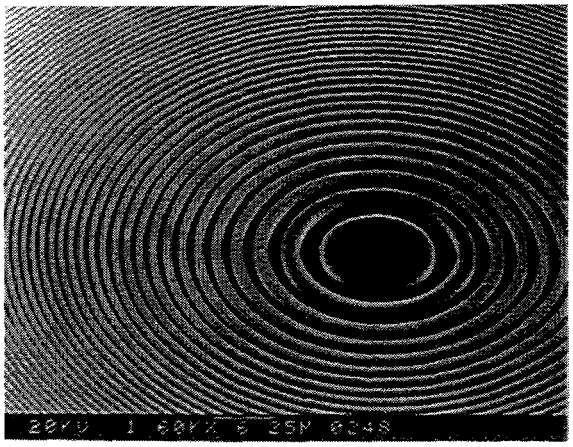

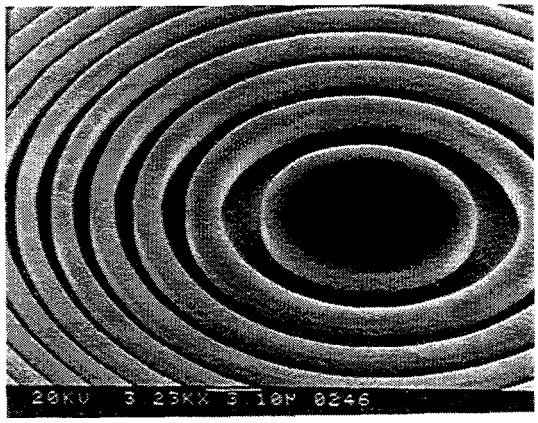

Germanium Phase Circular Bragg-Fresnel Lens

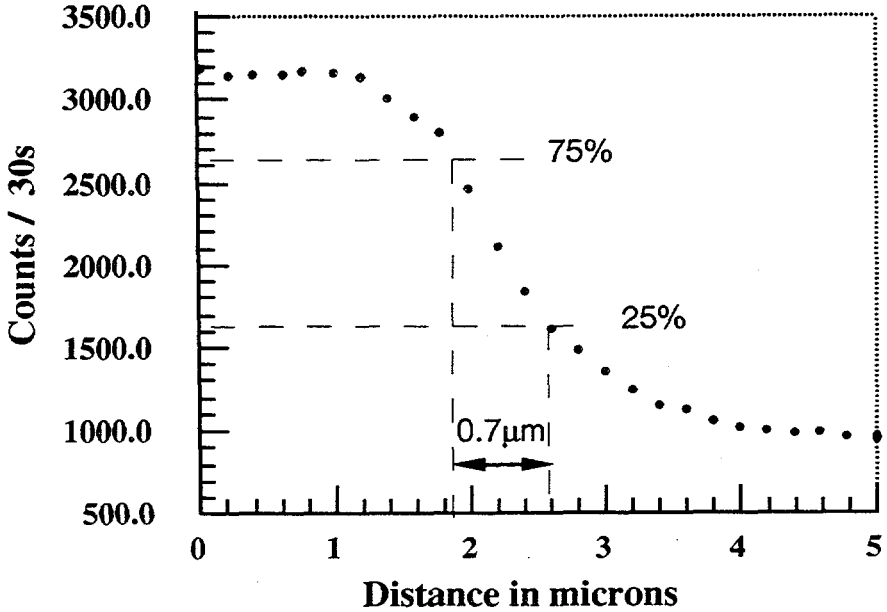

Measured flux
in the focal spot

~10^7-10^8 ph/s

Experimental variation of Cr Kα - fluorescence signal

upon scanning a Cr - strip pattern

Ge BFL

$r_n = 100\ \mu m$

$\Delta r_n = 0.14\ \mu m$

Number of zones 144

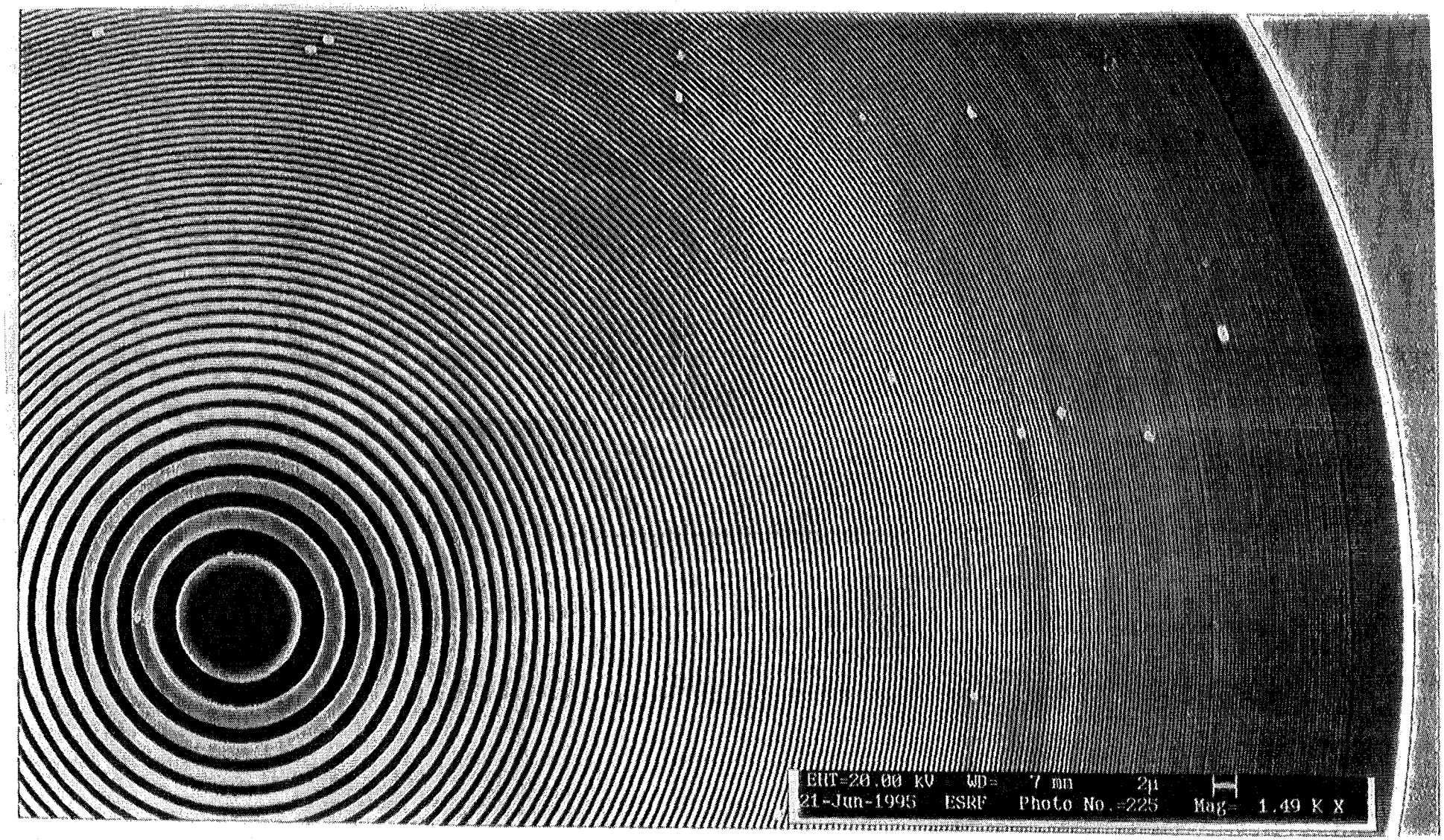

Composed Bragg-Fresnel Lens

A. Snigirev, I. Snigireva, A. Souvorov,
F. Legrand, C. Raven (ESRF, France)
Ya. Hartmann, V. Yunkin, (IMT, Russia)

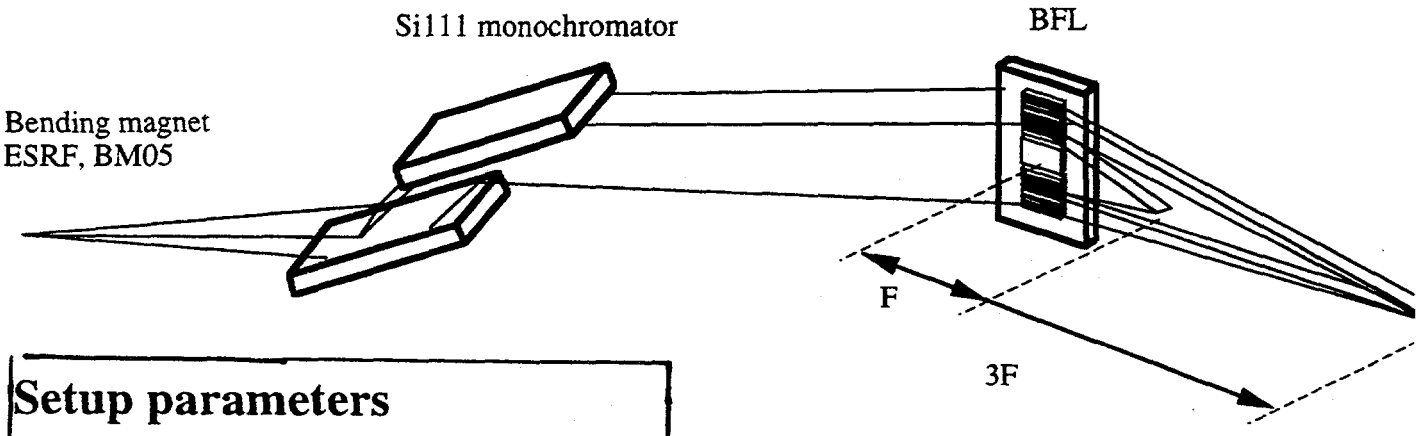

Setup parameters

E=10keV
Si111-based linear BFL 1+3 orders
F_{BFL}=31cm
BFL aperture = 380μm
θ_B = 11.4°

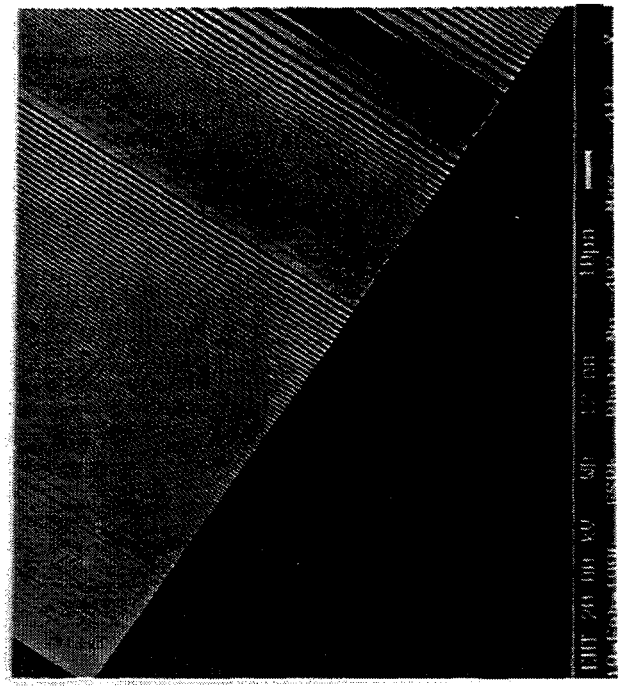

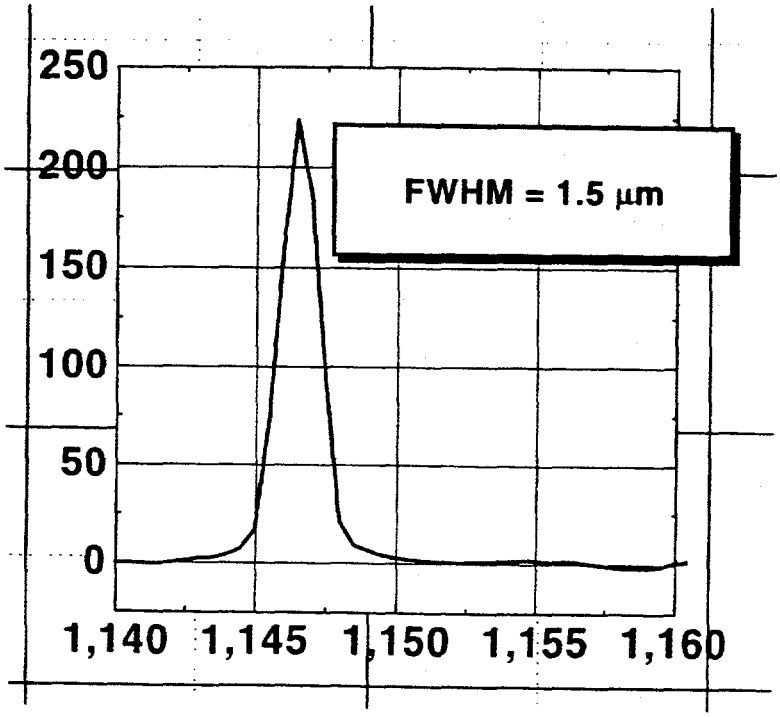

Si(111) BFL

$A = 400\mu m$

$\Delta r_n = 0.2\mu m$

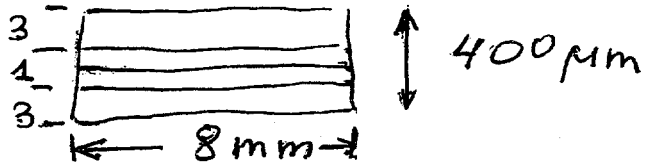

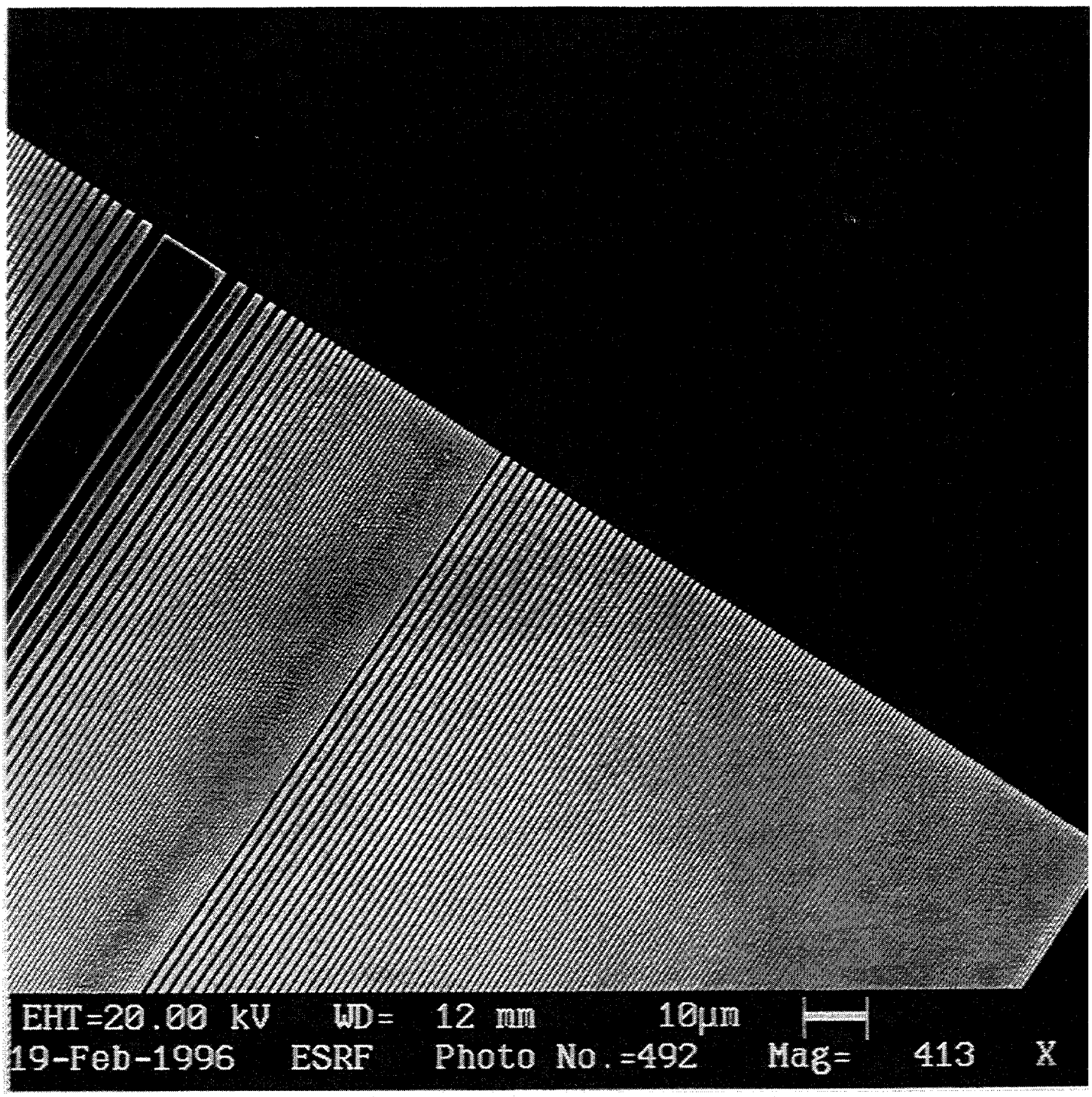

"Matreshka"

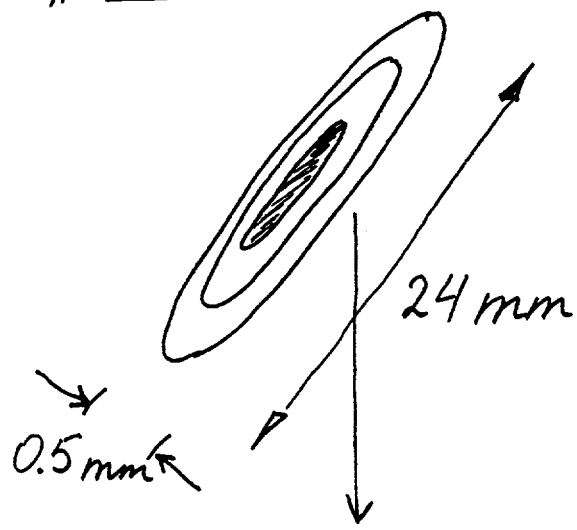

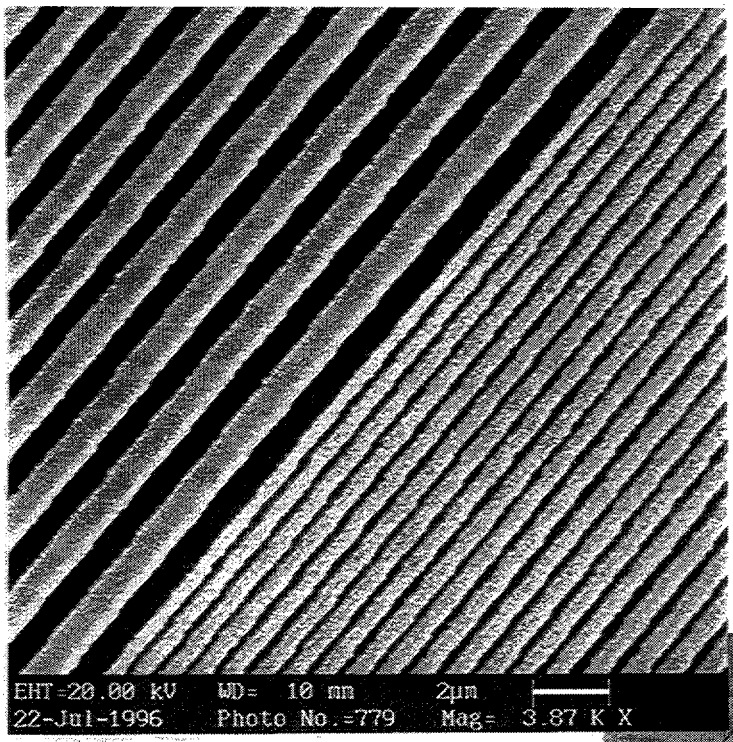

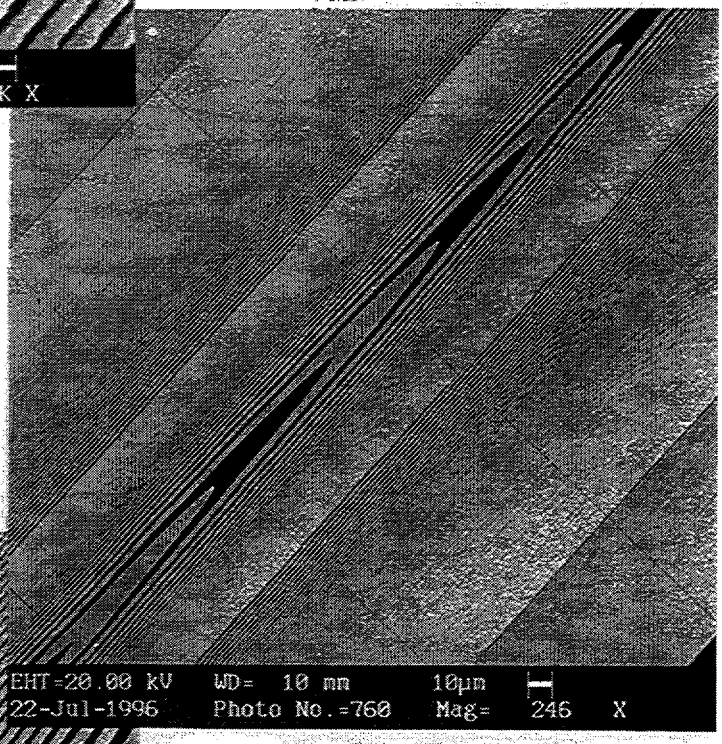

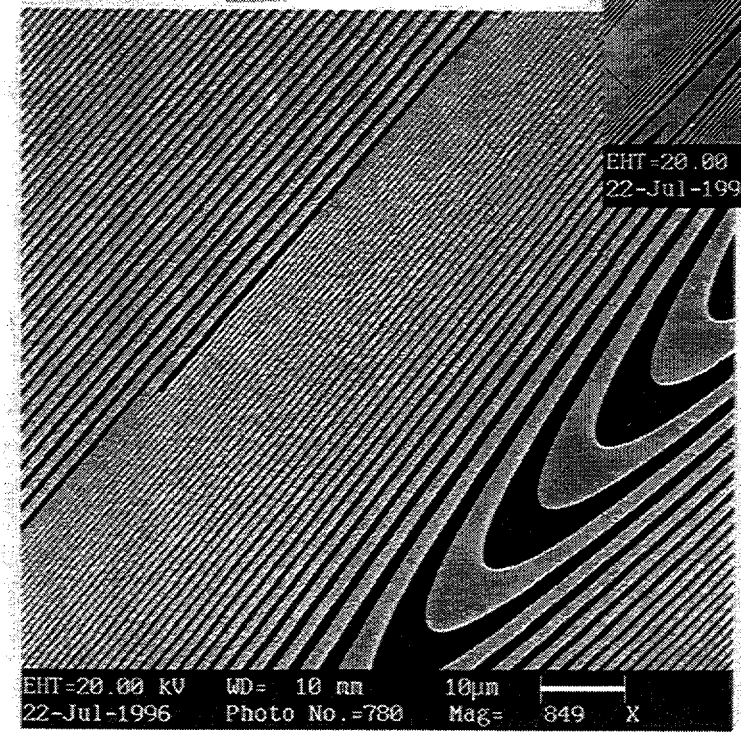

Compound multylayer lens

Si BFL „Composed"

A = 1 mm !

1 mm

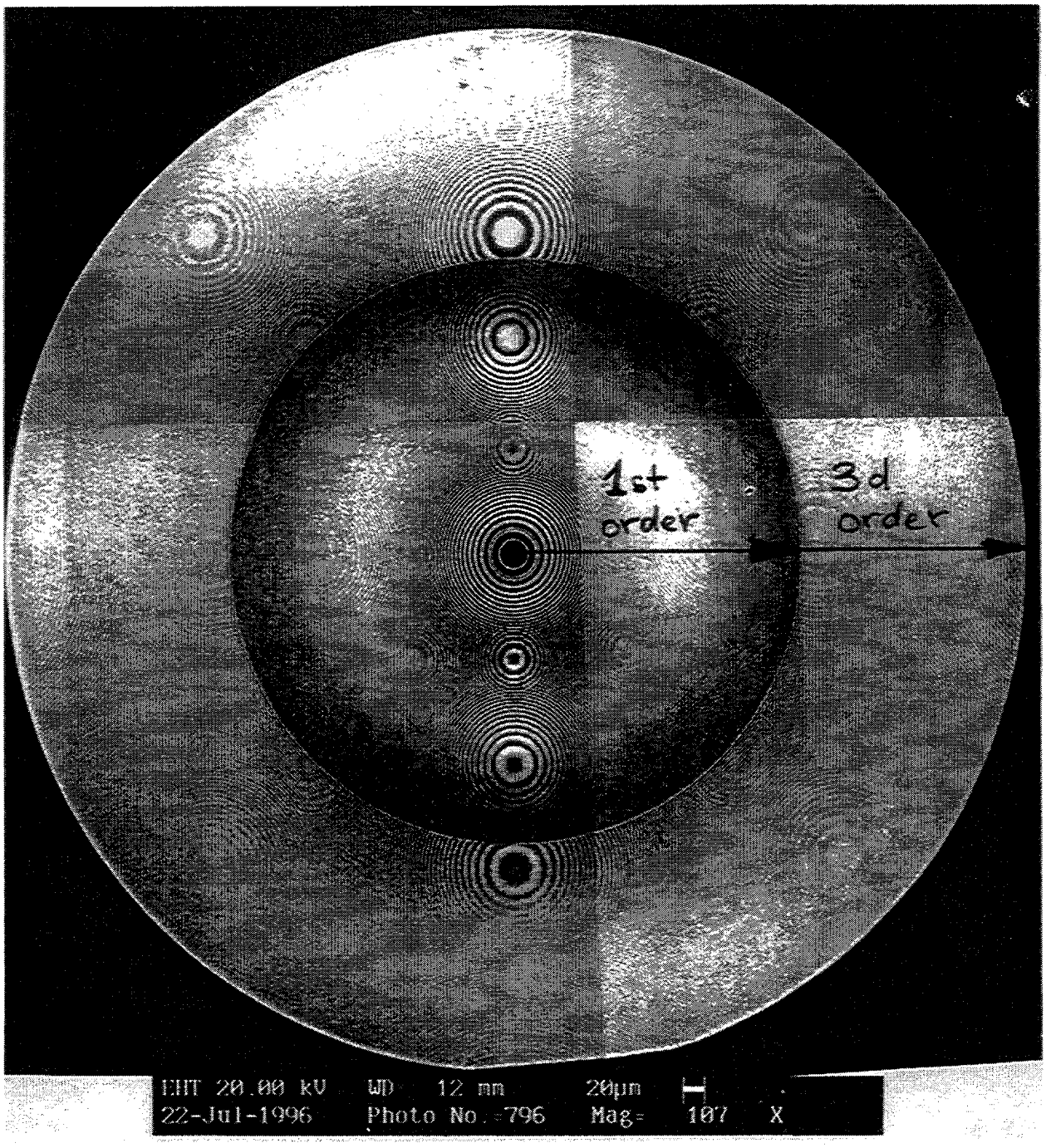

2-D focusing by curved linear BFL

A. Snigirev, I. Snigireva, A. Souvorov (ESRF, France)
Ya. Hartmann, V. Yunkin, (IMT RAS, Russia)

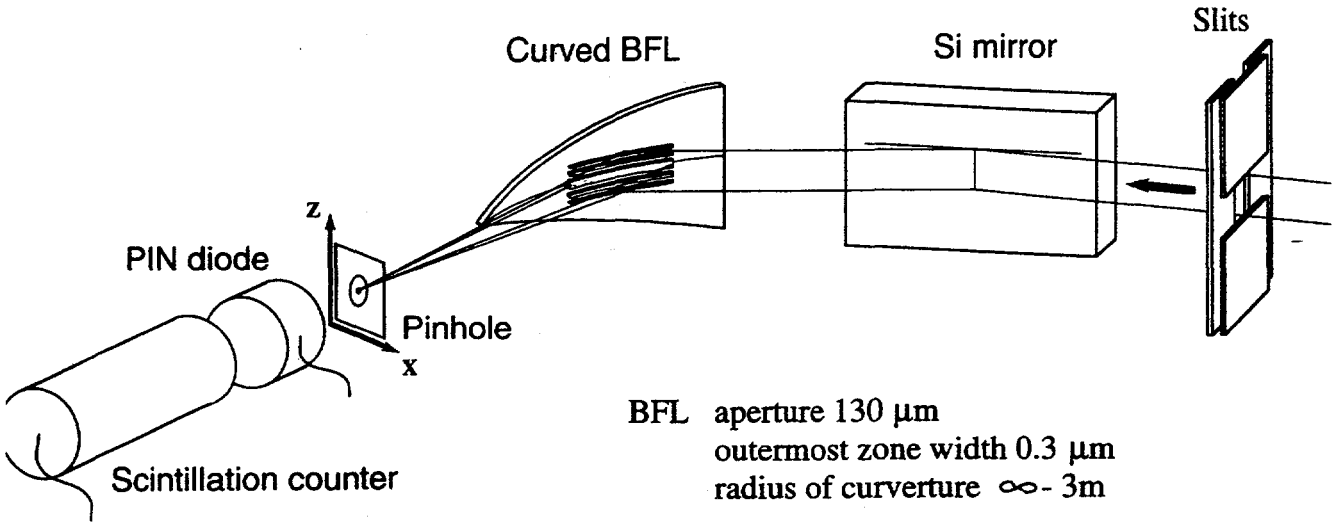

BFL aperture 130 μm
outermost zone width 0.3 μm
radius of curverture ∞- 3m

	measured BM	expected ID
energy (keV)	10 - 30	6 - 60
resolution	3 * 5 μm^2	1 * 5 μm^2
flux (ph/s)	10^{8}	10^{10}-10^{11}
focal distance	0.3 - 0.9 m	

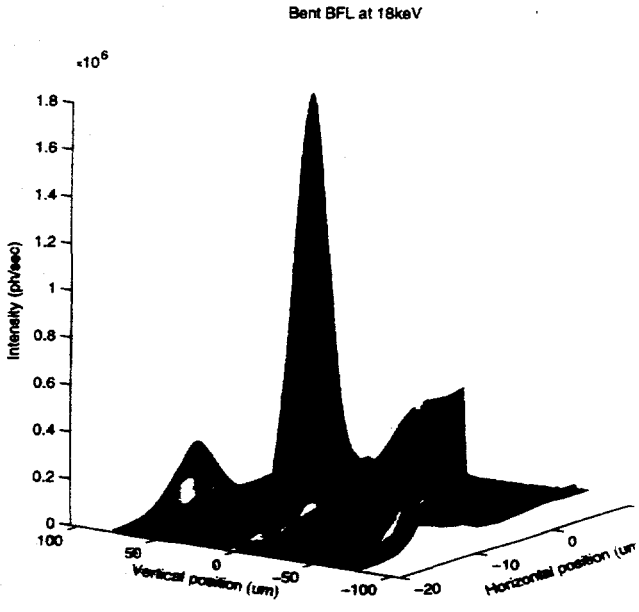

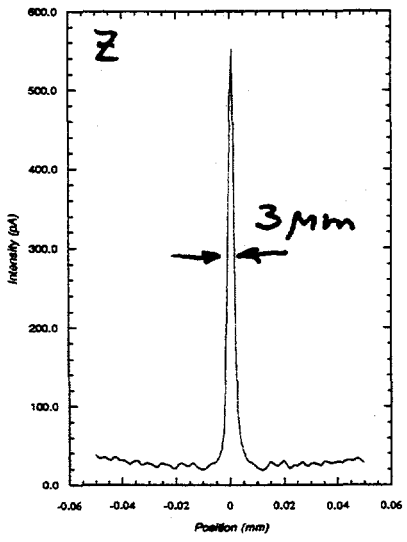

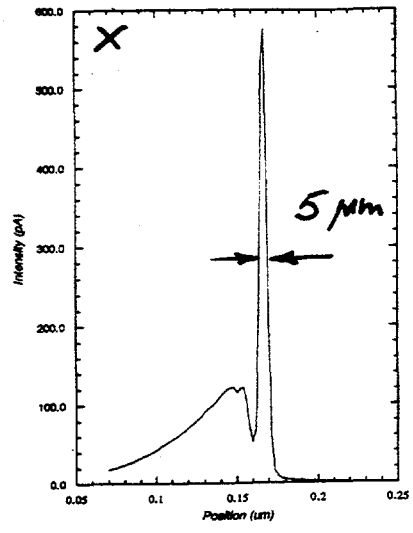

BFL acoustics excitation for light gathering power enhancement

A. Snigirev, I. Snigireva, A. Souvorov (ESRF, France)
Ya. Hartmann, E.Aristova, (IMT RAS, Russia)

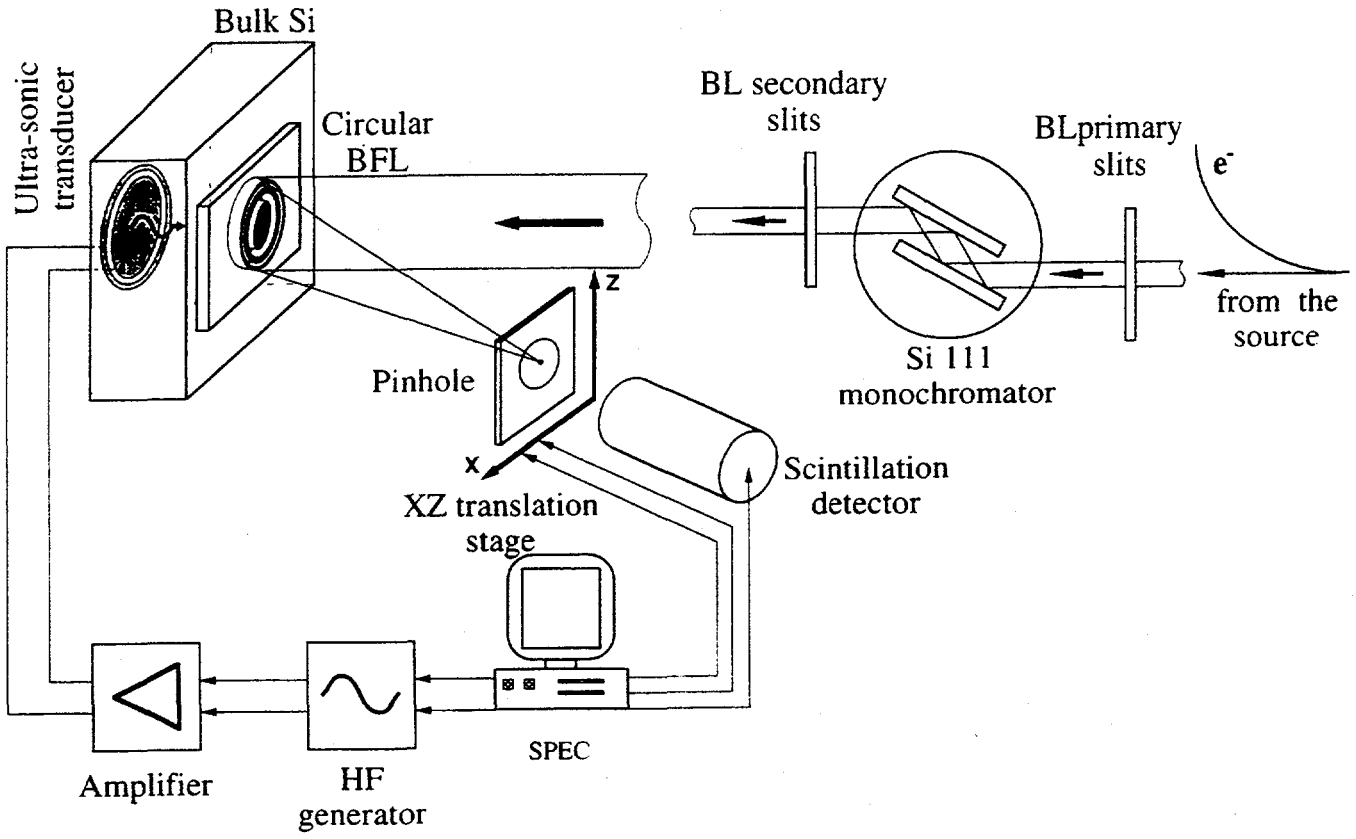

no acoustics

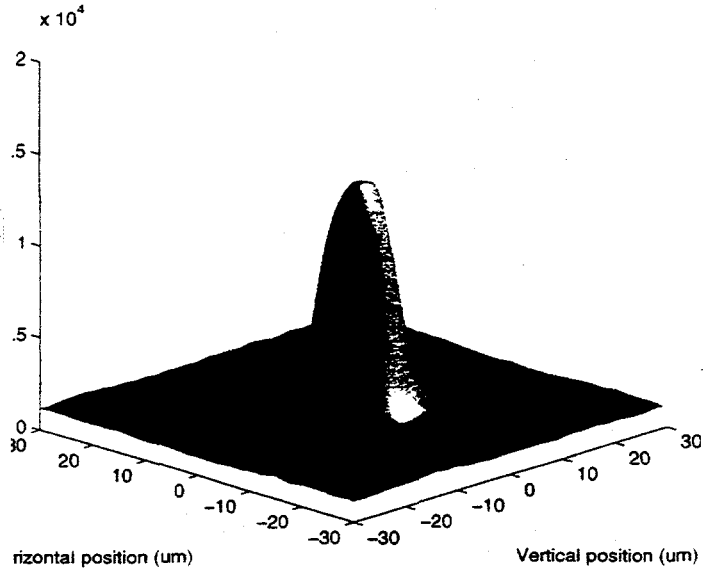

acoustics, 12 MHz

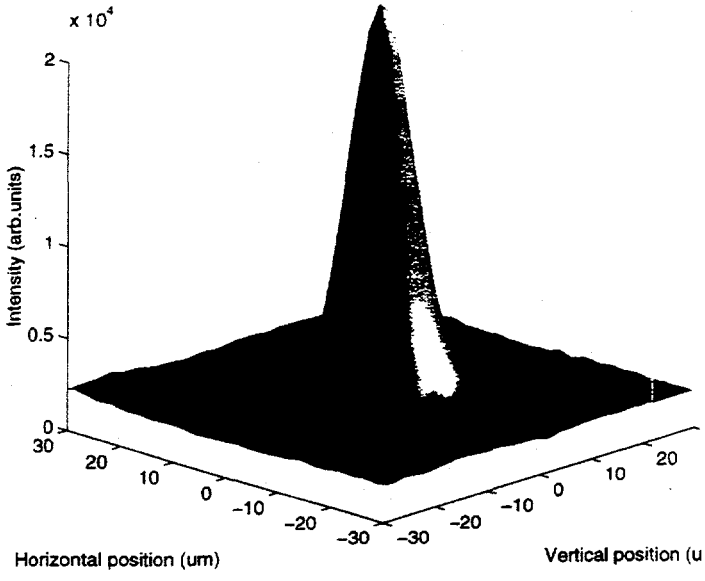

Microbeam parameters

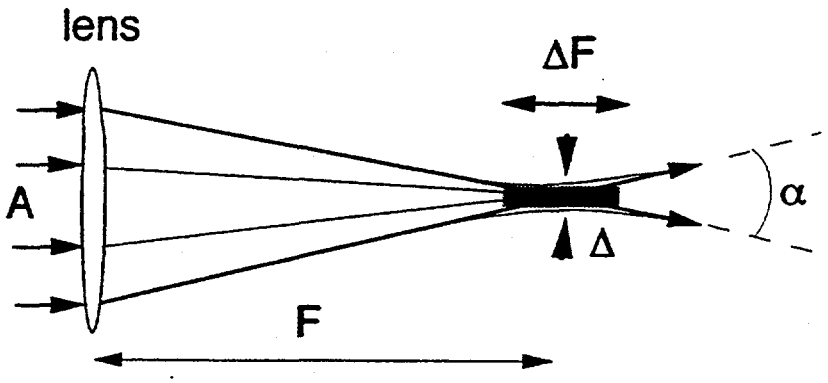

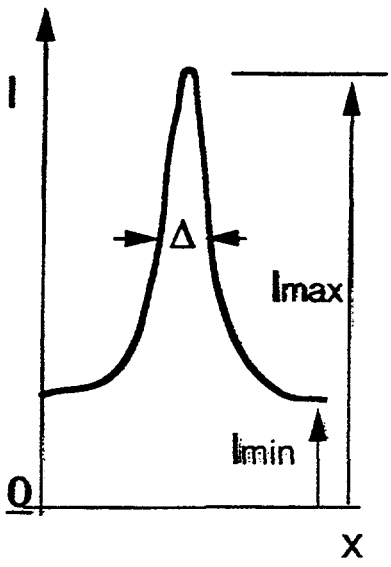

BFL	linear	circular
coherence preservation !	yes	yes
energy tunability	yes 2-100keV	no 2-6-8-10-14-16-18...
bandpath ΔE/E	10^{-4}	10^{-5}-10^{-7}
resolution: Δ=S/M =100μm/1000 Δ~Δr_n	0.1μm 0.3μm	0.14μm
angular divergence: α=λ/Δr_n=A/F	10^{-4} -10^{-3}	10^{-4} -10^{-3}
depth of field ΔF=Δ/α=	1-5 mm	1-5 mm
efficiency	40%	40%
gain 100μm→0.3μm 0.1	300 1000	10^5 10^6
flux ph/s	10^9 (10^{11})	10^7-10^8 → (10^9)
focus (working) distance	0.1m - 1m	0.1m - 1m

high β
10^{10} n

ML BEL $10^{11} \div 10^{12}$
BW ~ 1%

Applications of Bragg-Fresnel Crystal Optics

Energy range: 2-100keV
Resolution: at present <1μm in future ~ 0.1μm
Efficiency: ~40% ~70%

X-ray **microprobe** linear/2D

- **μ-fluorescence**

- **microdiffraction**
  - **high pressure**
  - **small angle scattering**

- **high resolution diffraction**
  multicrystal diffractometry
  standing wave
  microtopography

Imaging

- **beam emittance monitor**
  - beam position monitor
- **phase contrast microscopy**
  - microtomography
  - microinterferometry/ holography/ speckle

E = 10 keV
spot size < 2 μm
divergence ~ $4 \cdot 10^{-4}$ rad

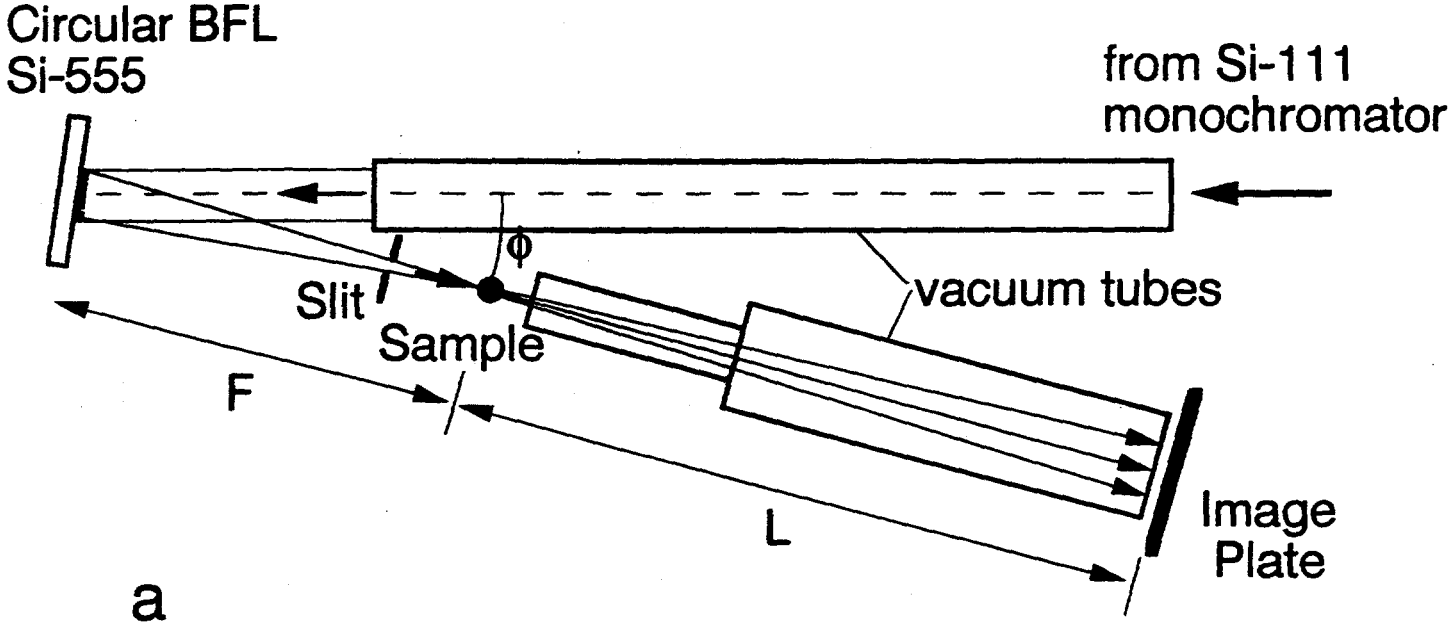

a

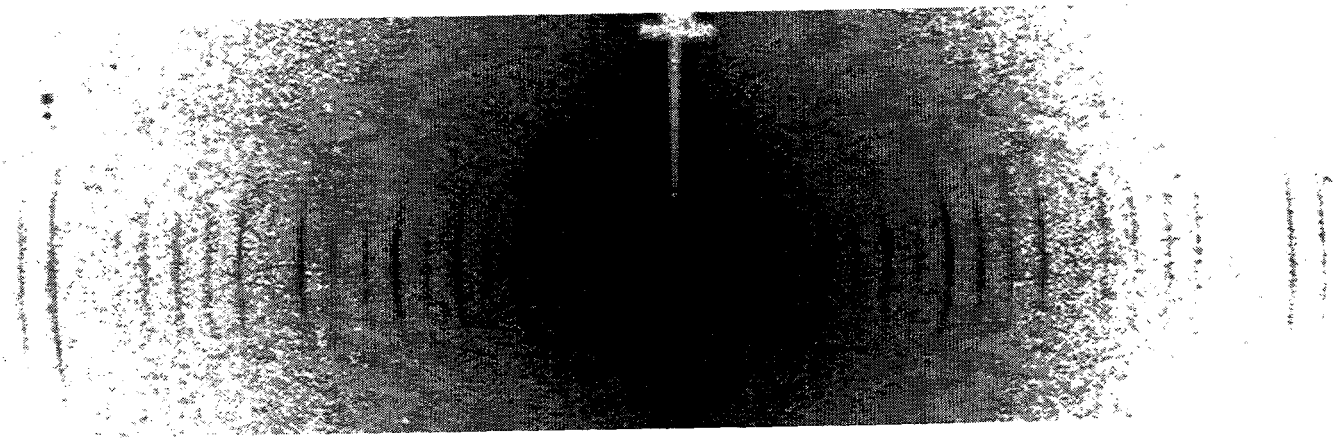

b

Schematic layaut of the BFL-based SAXS camera: deviation from normal incidence, $\phi=6^{o}$; focal distance, F=0.62 m; distance sample-to-detector, L=1.3 m (a). Low-angle X-ray diffraction pattern of the turkey tendon collagen obtained in BFL-based SAXS camera using Molecular Dynamics image plate (b).

High Pressure Microdiffraction with Bragg-Fresnel Lens

M. Hanfland, D. Hausermann, A. Snigirev, I. Snigireva *(ESRF)*
T. Ahahama *(Himeji Institute of Technology, Japan)*
M. McMahon *(University of Edinburg, U.K.)*

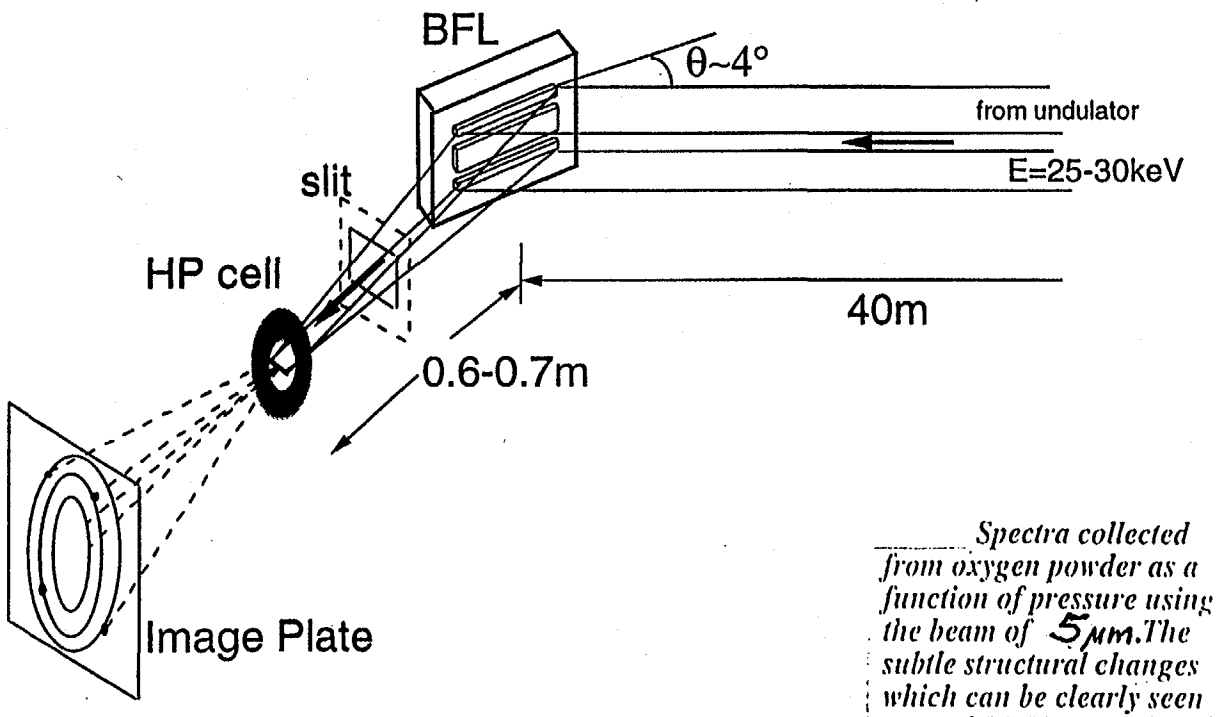

Spectra collected from oxygen powder as a function of pressure using the beam of 5μm. The subtle structural changes which can be clearly seen around 90 GPa (900 kbar) coincide with the so-called molecular metallisation transition observed in optical studies. These are the first structural data collected from a light element at such high pressures.

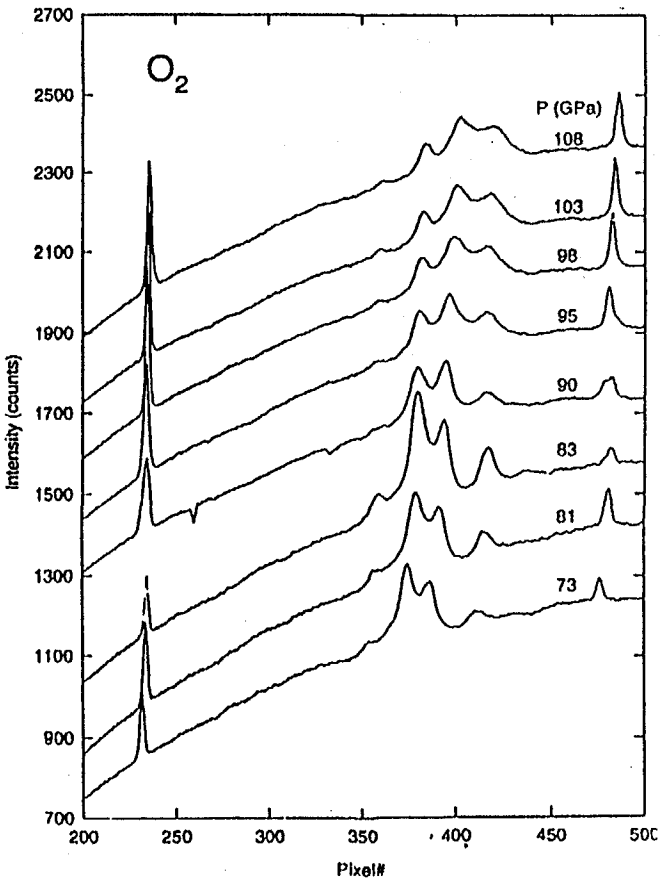

Microdiffraction with Bragg-Fresnel Lens

H. Biermann *(Erlangen-Nürnburg University, Germany)*
T. Ungar *(Ëotvös University, Budapest, Hungary)*
M. Kocsis, C. Raven, A. Suvorov, I.Snigireva, A.Snigirev *(ESRF)*

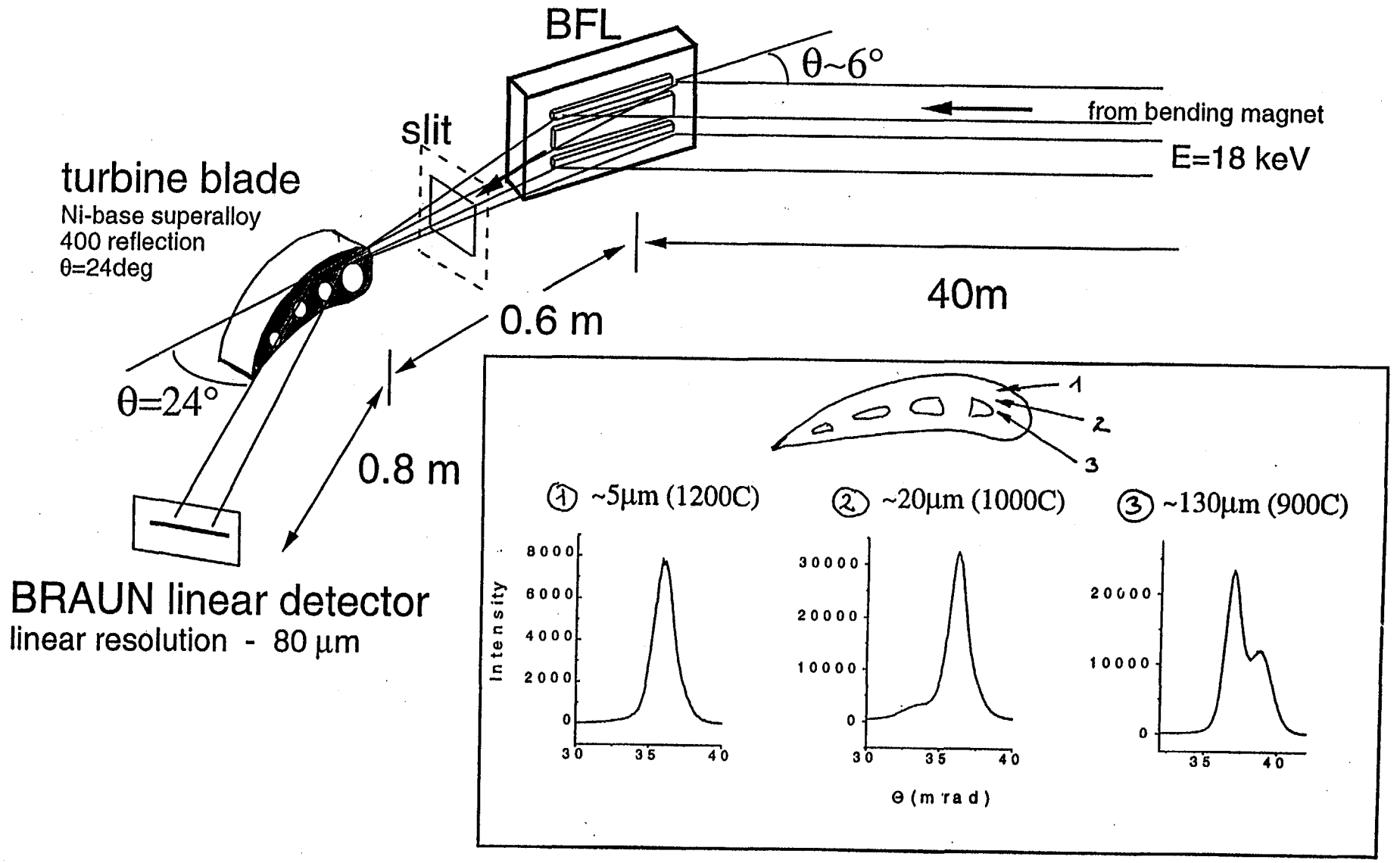

Microfocus double crystal diffractometer based on a linear BFL

ESRF, Optics Beamline

A. Snigirev, I. Snigireva, A. Freund, B. Lengeler
ESRF

A. Iberl, M. Schuster, B. Baur, H. Göbel
SIEMENS

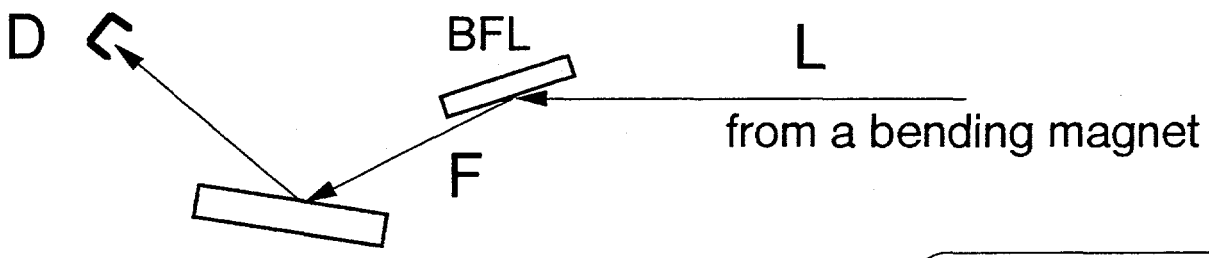

L = 40 m
F = 0.3 m
E = 12 keV
res. ~ 2 μm

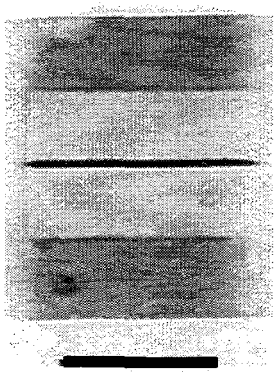

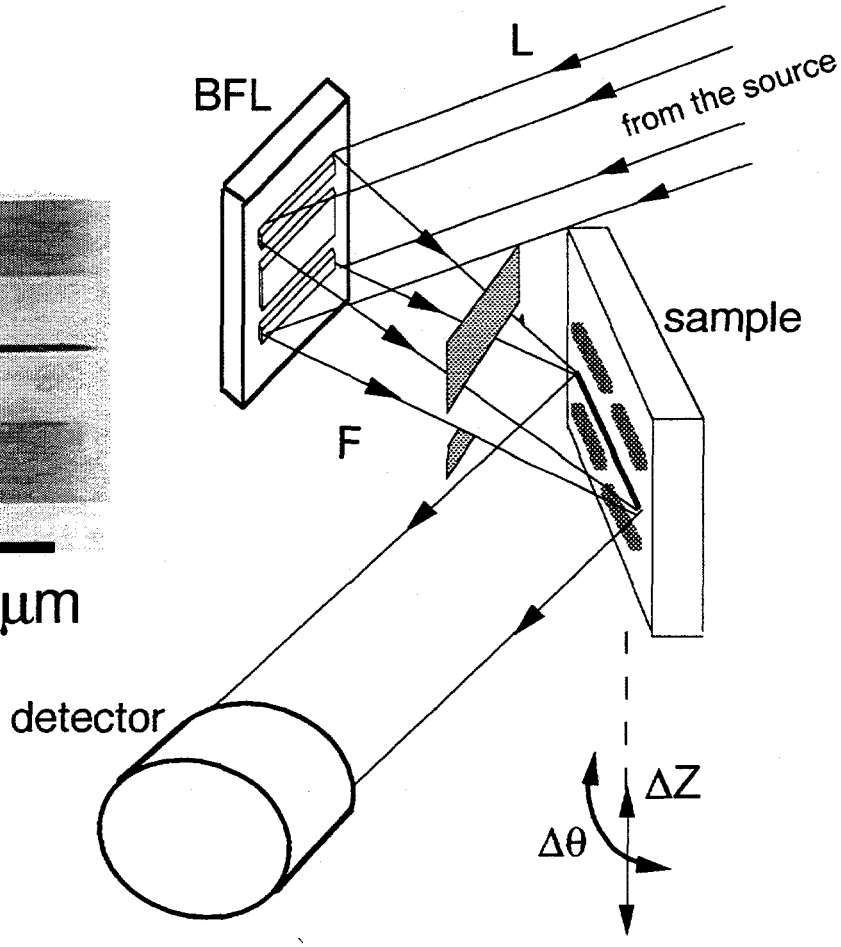

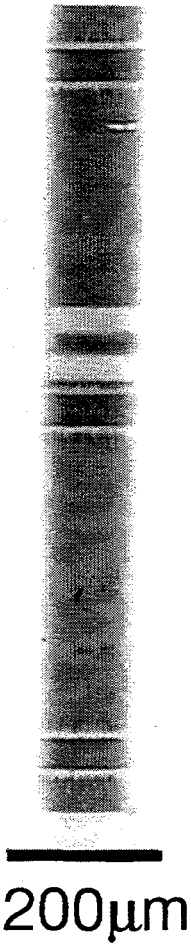

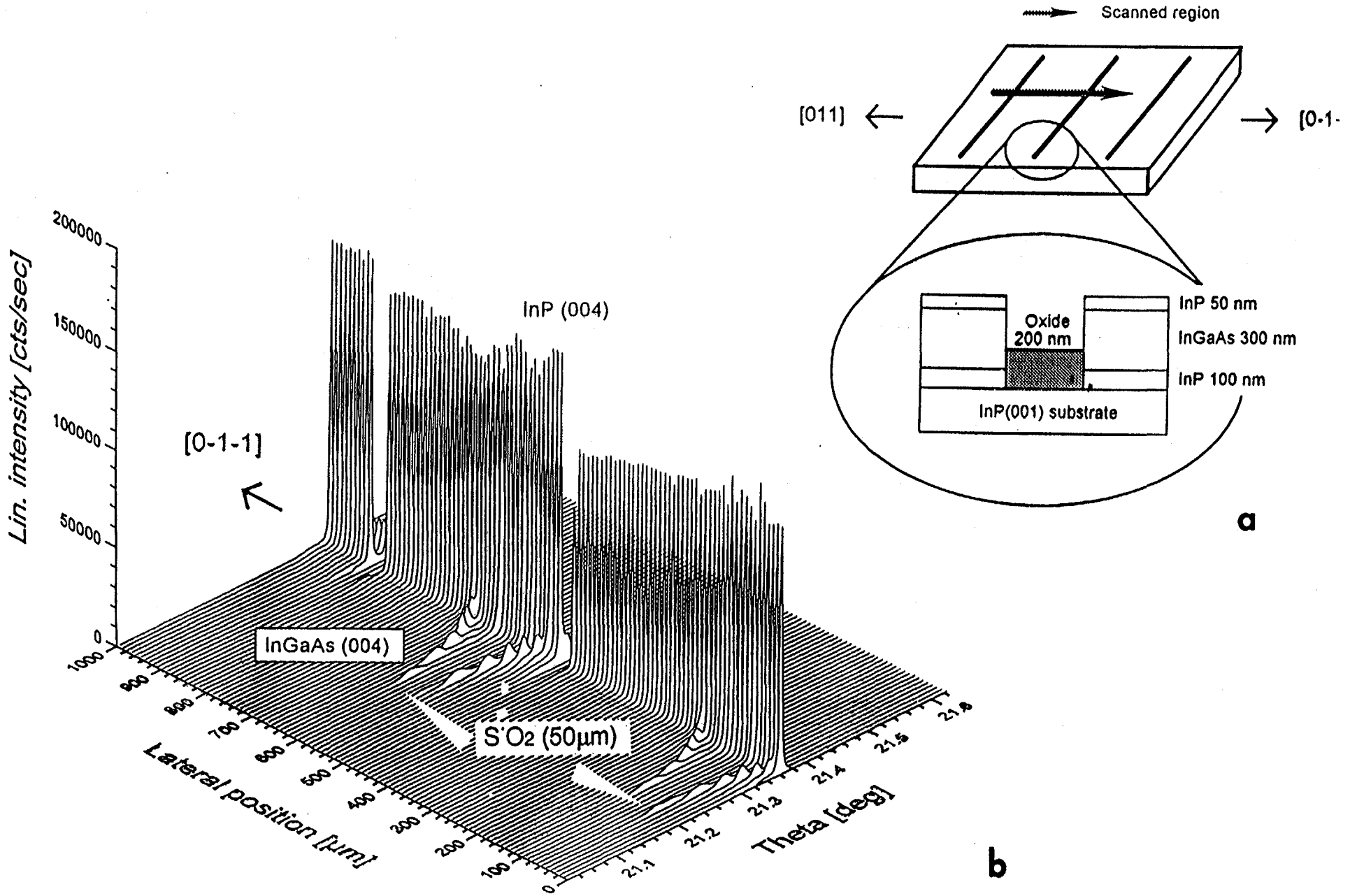
Scanned region
[011]
[0-1-
InP 50 nm
Oxide
200 nm
InGaAs 300 nm
InP 100 nm
InP(001) substrate
a
Lin. intensity [cts/sec]
200000
150000
100000
50000
0
[0-1-1]
InP (004)
InGaAs (004)
SiO2 (50µm)
Lateral position [µm]
1000
900
800
700
600
500
400
300
200
100
0
Theta [deg]
21.1
21.2
21.3
21.4
21.5
21.6
b

2D imaging of the undulator source ID6 by phase circular BFL

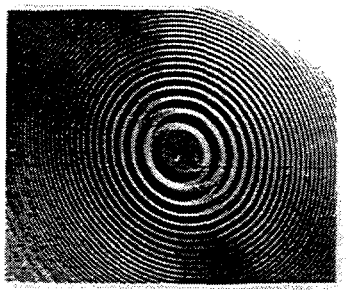

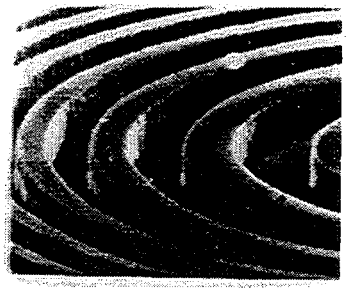

$A = 200\,\mu m$

$r_1 = 9\,\mu m$

$\Delta r_n = 0.3\,\mu m$

$h = 4\,\mu m$

Si-333 BFL

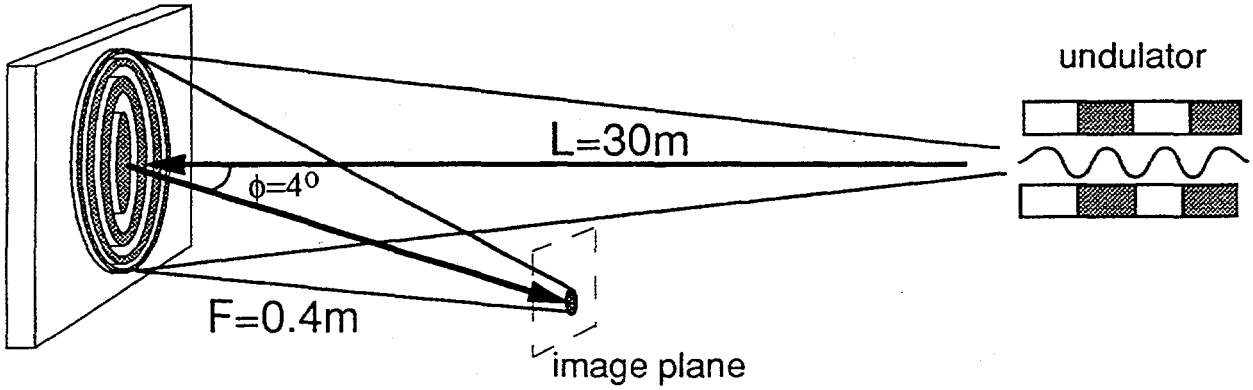

E=6keV $\lambda = 2.09\,\text{Å}$ $\theta = 88.5^\circ$

GAP 40mm 45mm 50mm

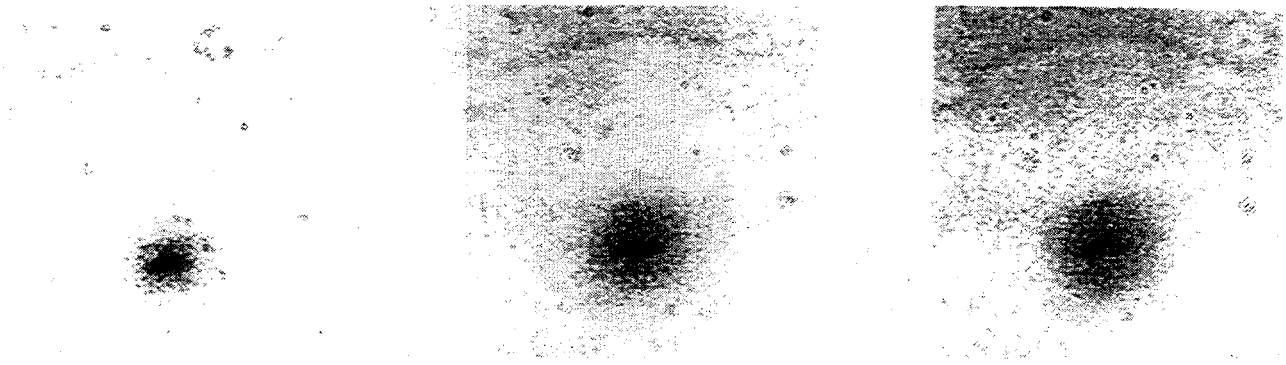

50μm

Si-444 BFL

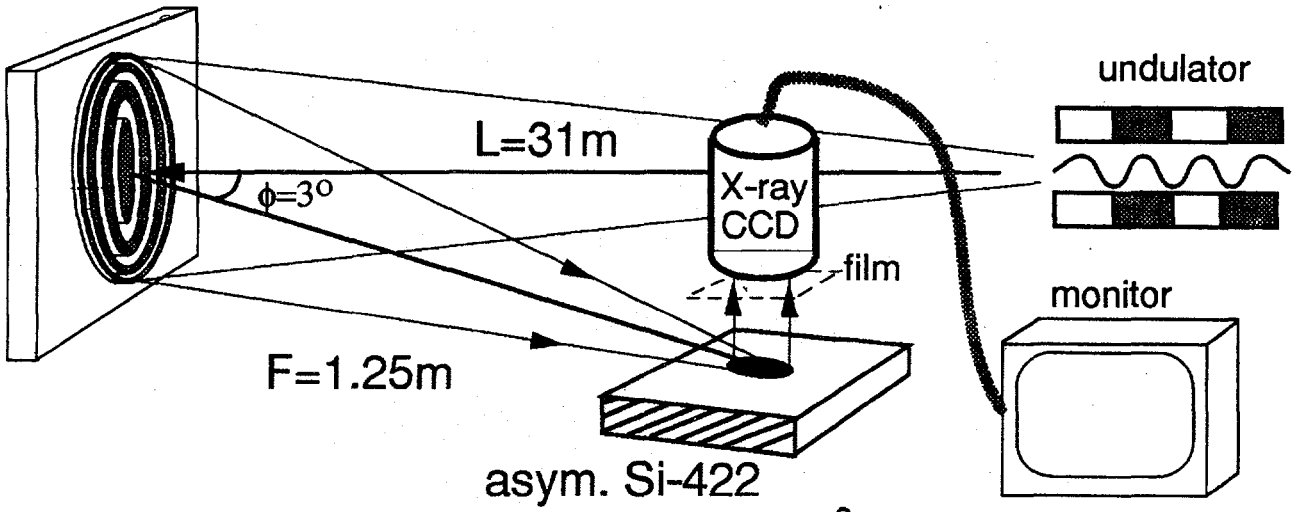

E=7.92keV λ=1.55Å Θ= 88.5°

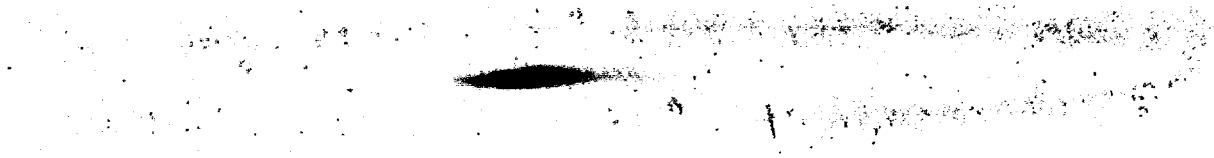

X-ray HR film image 500μm

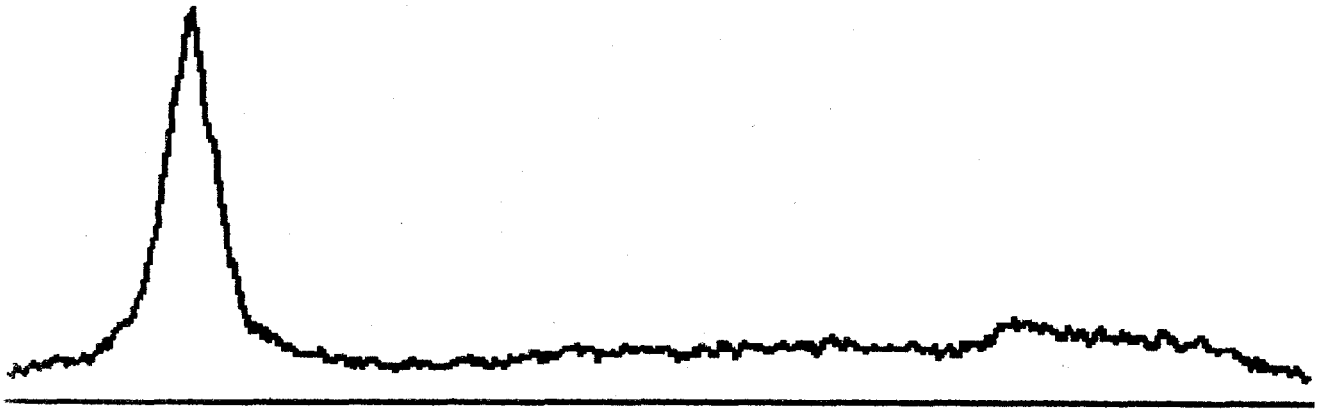

X-ray CCD image 1mm

Image of the Electron Beam through the X-Telescope

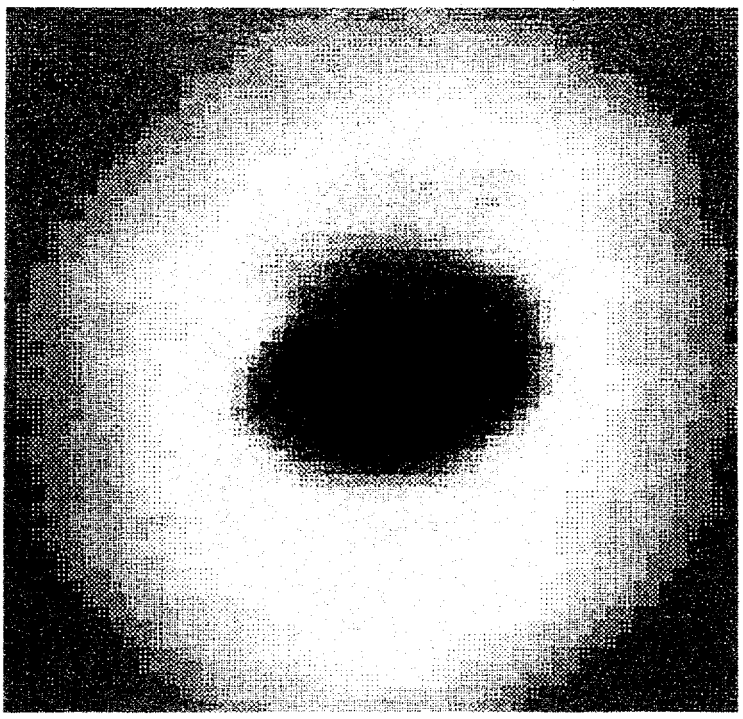

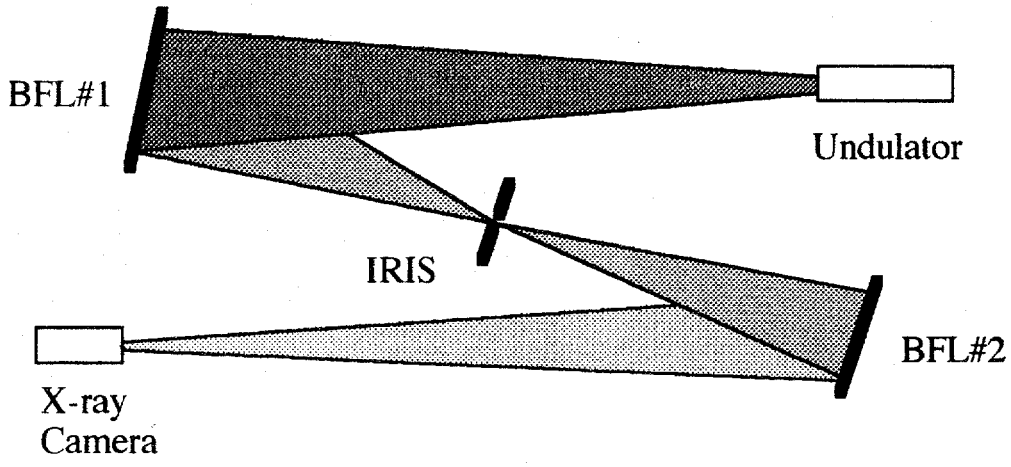

Electron	Energy = 6.05 GeV, Current = 90 mA, BetaX = 27 m, BetaZ = 13 m
Undulator	Per. = 42 mm, Field = 0.054 T, K = 0.20, L = 1680 mm
BFL#1	31 m from ID, Foc.= 1.25 m, Diam .= 400 μm, E = 7.91 keV
Iris	1.20 m from BFL #1, Diam = 100 μm
BFL#2	1.58 m from BFL#1, Foc. = 0.25 m, Diam = 120 μm
X-ray Camera	1.75 m from BFL#2, Pixel = 11μm, Res.FWHM = 30μm

10 keV Sub-μ Transmission X-ray Microscopy at the ESRF BL4

Snigirev A., Snigireva I., Bösecke P., Lequien S.

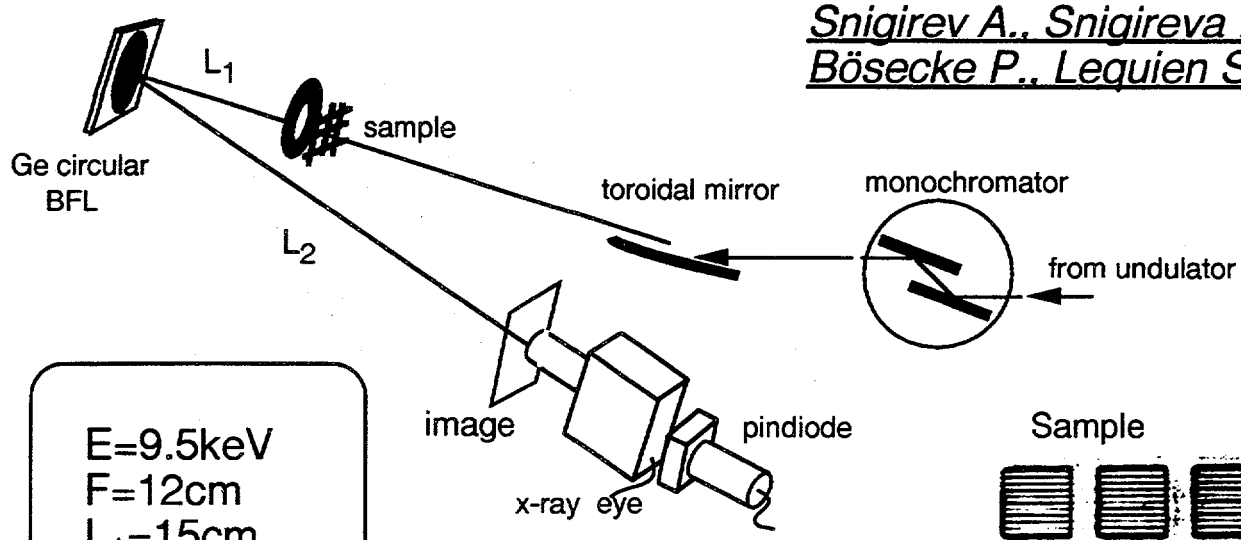

E=9.5keV
F=12cm
L_1=15cm
L_2=60cm

Sample

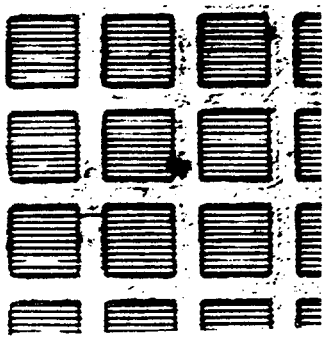

15μm

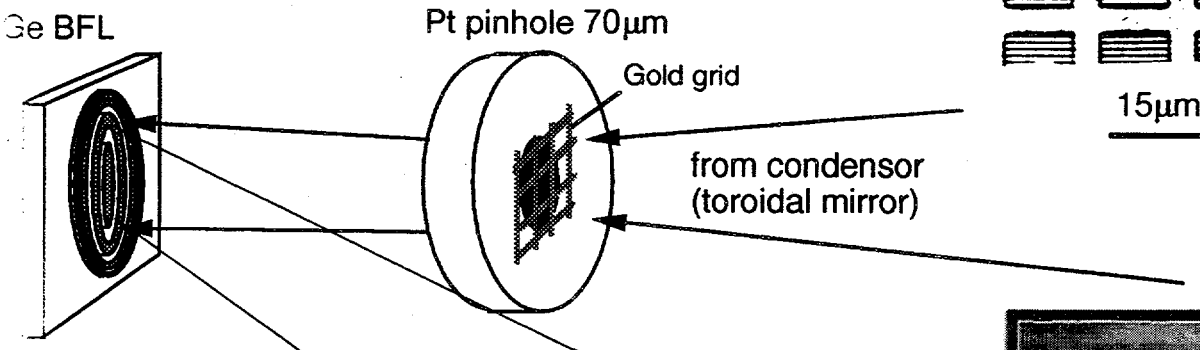

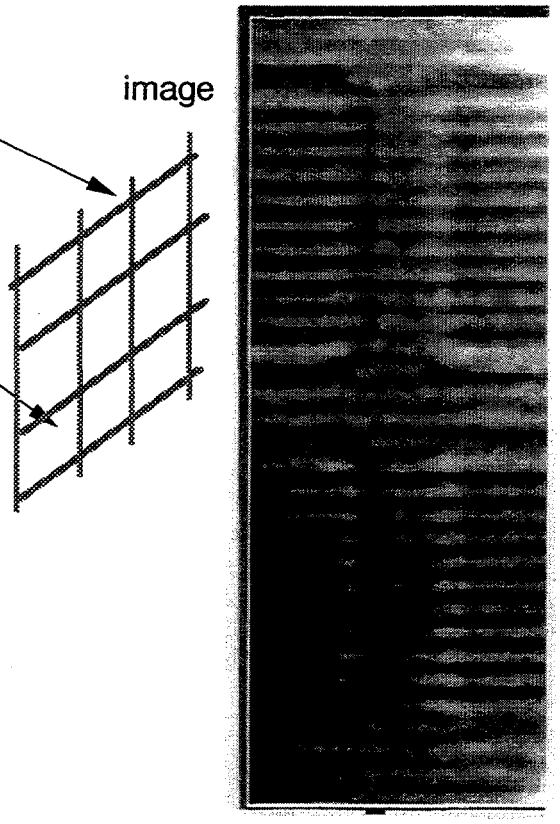

X-ray image
magnification M=4
resolution ~ 0.5μm

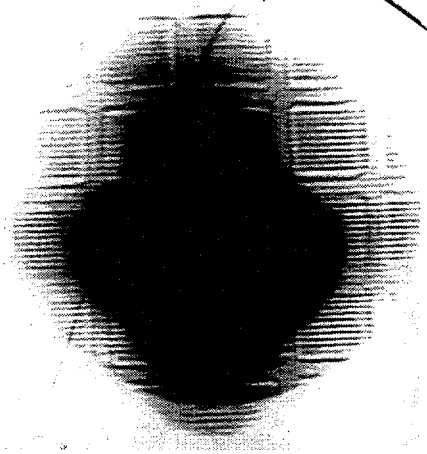

BFO - based

X-ray microscopes suitable for 3D imaging

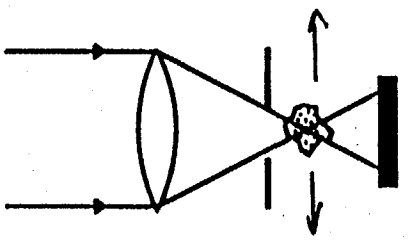

0.1 μm → 100 μm

1 μm → 1 mm

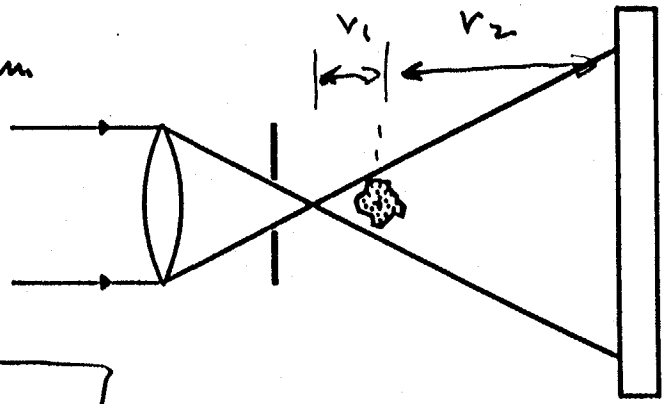

$M = \frac{r_2}{r_1}$

Scanning

resolution

0.1 - 0.3 μm

Projection (Gabor in-line holography)

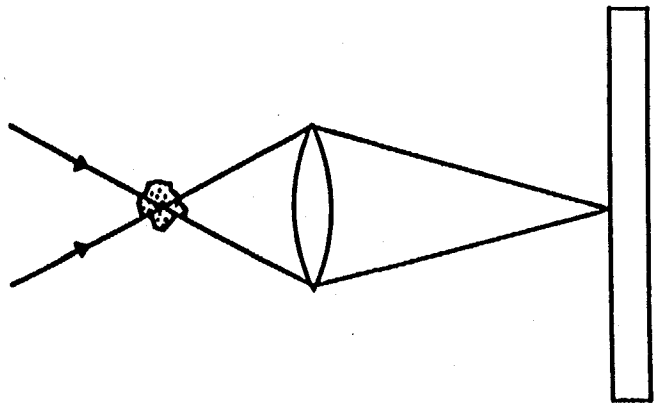

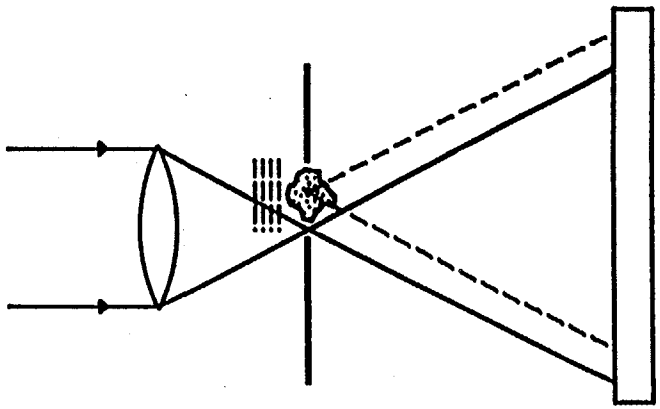

Imaging

Holographic (Fourier)

Phase contrast imaging with coherent high energy X-rays.

Irina Snigireva ESRF, B.P. 220, 38043 Grenoble, France

1. Introduction

X-ray imaging concern high energy domain (>6 keV) like a contact radiography, projection microscopy and tomography is used for many years to discern the features of the internal structure non destructively in material science, medicine and biology. In so doing the main contrast formation is absorption that makes some limitations for imaging of the light density materials and what is more the resolution of these techniques is not better than 10-100 μm. It was turned out that there is no way in which to overcome 1μm or even sub-μm resolution limit except phase contrast imaging.

It is well known in optics that the phase contrast is realised when interference between reference wave front and transmitted through the sample take place. Examples of this imaging are: phase contrast microscopy suggested by Zernike and Gabor (in-line) holography. Both of this techniques: phase contrast x-ray microscopy [1] and holography [2] are successfully progressing now in soft x-ray region.

For imaging in the hard X-rays to enhance the contrast and to be able to resolve phase variations across the beam the high degree of the time and more importantly spatial coherence is needed. Because of this it was reasonable that the perfect crystal optics was involved like Bonse-Hart interferometry [3-6], double-crystal and even triple-crystal set-up using Laue and Bragg geometry with asymmetrically cut crystals [7-16].

2. Phase contrast imaging based on perfect single crystals

2.1 Phase contrast imaging with Bonse-Hart interferometer

First time imaging was realises by M. Ando and S. Hosoya [4], and then very successfully developed by A. Momose [5-6].

Advantages:

- refractive index mapping
- high absolute sensitivity

Shortcomings:

- high absorption due to relatively thick crystals
- spatial resolution is limited by the Bormann fan (~30 μm)
- energy tunability for given interferometer is limited
- lack of space for sample environment

2.2 Phase contrast imaging with multicrystal set-up: Laue or Bragg case

There are different schemes using analyser crystal in Laue or Bragg cases that have specific names as "schlieren" (K. Goetz, M. Kalashnikov, Yu. Mikhailov, G. Sklizkov, S. Fedotov, E. Förster, P. Zaumseil, 1978 [7-8]); "dispersion" (V. Ingal, E. Beliaevskaya, 1991 [9-11]); "refraction" (K. Podurets, V. Somenkov, S. Shilstein,, 1986 [12-14]); "phase-contrast" (T. Davis, D. Gao, T. Gureev, A. Stevenson, S. Wilkins, 1995 [15-16]).

Advantages:

- can be realised using laboratory sources

Shortcomings:

- resolution limited by extinction depth (length) 5 - 10 microns
- contrast lost due to beam filtering by crystal analyser.

3. Phase contrast using in-line holography set-up at the ESRF.

3.1 Experimental conditions at the ESRF

Third generation sources such as ESRF make possible to realise phase contrast techniques for high energy X-rays using Gabor in - line holography set - up [13-16]. Taking into consideration the optical set-up of the typical beamline at the ESRF (source size ~100 μm, large source to object distances ~50m and presence of the Si monochromator as the first optical element) one can easily estimate that the provided spatial coherence is about 100 μm, that is sufficient to observe an interference patterns from samples up to 100 μm in size.

The idea of phase contrast imaging in the transmission geometry can be explain in the following way. It is easy to show when nearly parallel monochromatic X-ray beam impinges on the surface of a practically transparent light density specimen there will always be an apparent deviation from the rectilinear X-ray propagation - the segments of the wave front will be deflected due to refraction on the sample edge-air interface slope. Further interpositioning of the deflected coherent rays will course the strong interference at the certain distance. Rough estimations for the energy 10-50 keV show that the angle of deflection is about 10^{-5}-10^{-6}rad. and 5-10 microns intersection of the beam may occur at the 1 m distance from the sample.

3.2 Results on phase contrast imaging

The experimental set-up used at the ESRF beamlines for imaging different low density materials is shown in Fig. 1. The 6 - 60 keV radiation from the source (undulator, wiggler or bending magnet) was selected using Si monochromator.

Three imaging areas can be determined: shadow or outline image, Fresnel zone fringes and Fraunhofer zone fringes (Fig. 2). The distance for outline imaging can be varied from few millimeters to few centimeters depending on the object size. The distances for Fresnel zone fringes for 1 μm; 10 μm and 100 μm samples for light, soft and hard X-rays are displayed in

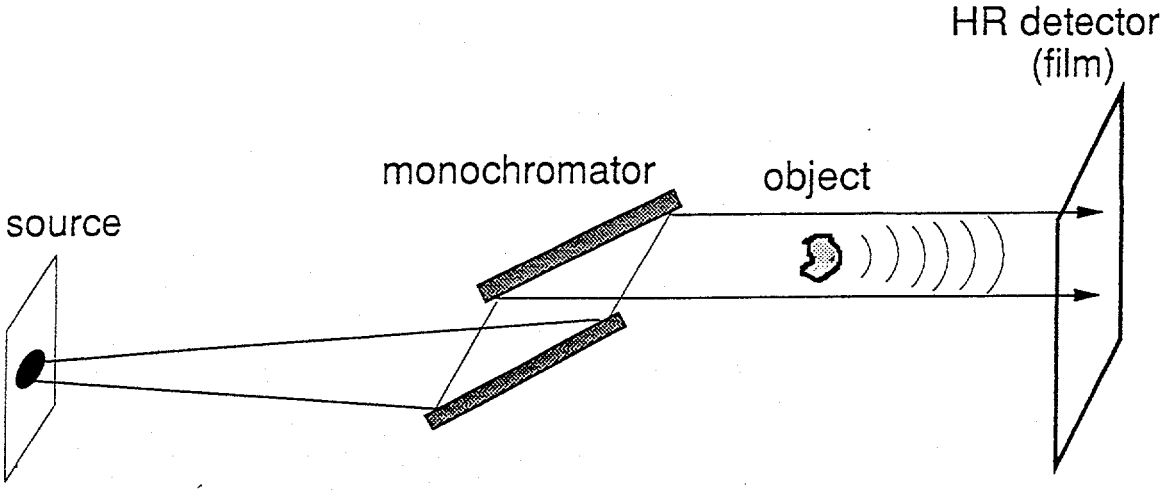

Fig. 1 Schematic display of the experimental set-up, where distance from the source to the object was 40 m and distance from the object to the detector varied from 0 to 200 cm.

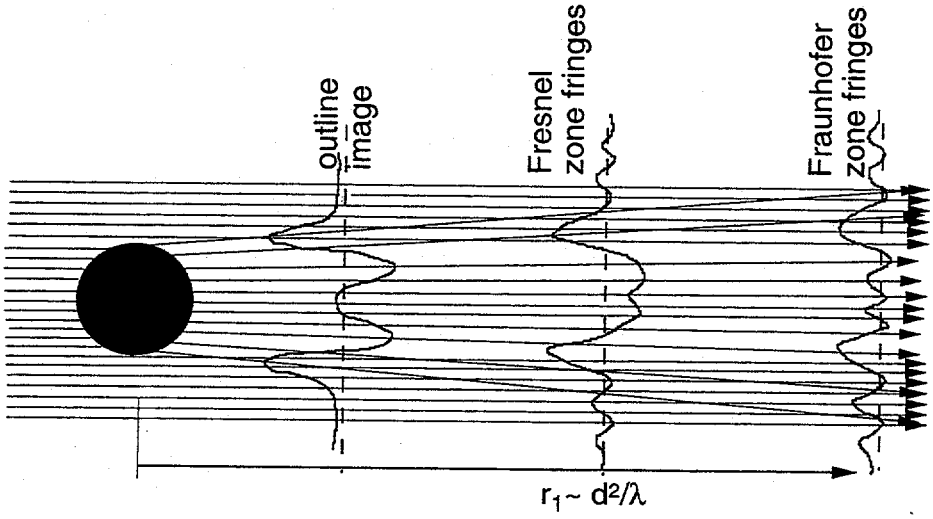

	object (d, μm)	$r_1 = d^2/\lambda$
light	1	2 μm
$\lambda = 0.5\mu m$	10	200 μm
	100	20 mm
soft x-rays	1	1 mm
$\lambda > 10Å$	10	0.1 m
	100	10 m
hard x-rays	1	10mm
$\lambda < 1$ Å	10	1 m
	100	100 m

Fig. 2 Principle of X-ray phase contrast imaging generated by interference of the diffracted beams with unscattered wavefield. Three imaging areas are defined: outline imaging (just after the object; Fresnel and Fraunhofer diffraction zones. Comparison of the Fresnel zone distances (r_1) for light, soft X-rays and hard x-rays are given in the table for 1, 10, 100 μm (d) carbon-based samples.

table. As it is seen for high energy X-rays we are always in the Fresnel region for imaging 1 - 100 μm objects.

The phase contrast X-ray images of the boron fiber 100 μm in diameter with tungsten core of about 15 μm are shown in Fig. 3. Outline image of the fibers borders at short distances from the fiber and the fine interference pattern at larger distances (~50 cm) are clearly seen.

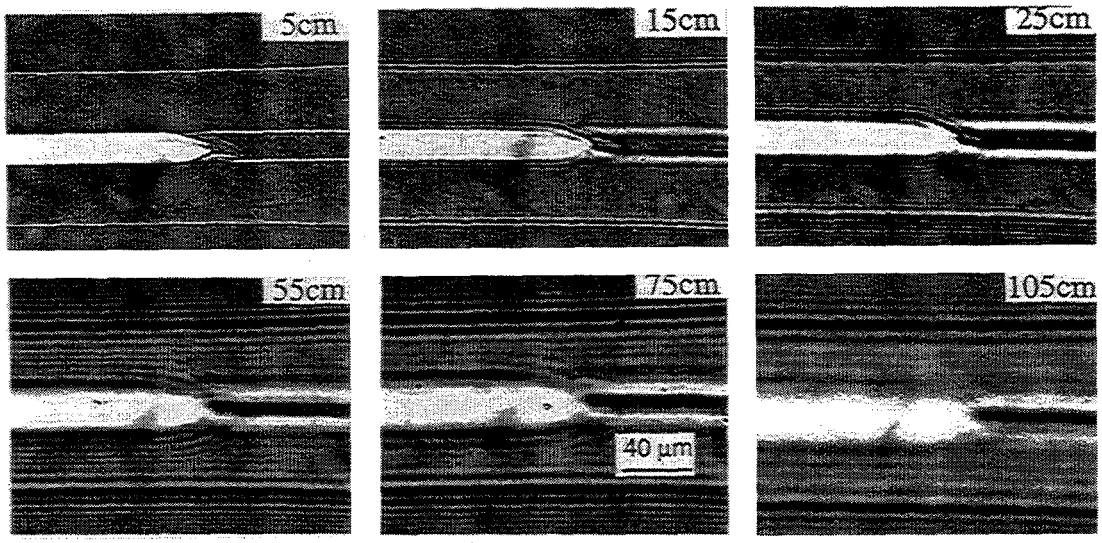

Fig. 3 Holograms from the boron fiber with tungsten core recorded at 12 keV energy. fiber-to-film distance are from 5 to 105 cm.

A comparison between amplitude and phase contrast at 18 keV energy was done. Fig. 4(a-b) show a seashell Foraminifer "*Operculina ammonoides*" imaged in amplitude and phase contrast modes [17]. It may be advantageous to use both modes, phase and amplitude contrast, for taking images.

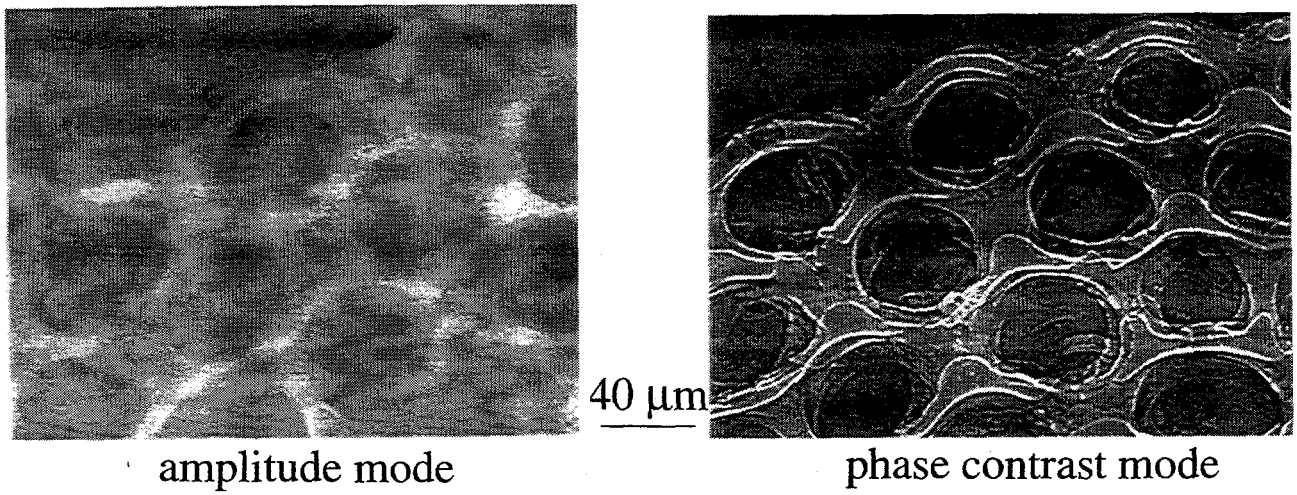

Fig. 4 Image of seashell Foraminifer "*Operculina ammonoides*" taken with 18 keV X-rays in amplitude and phase contrast modes.

Theoretical analysis given in [18], shows that the carbon based fibers of 0.1 μm diameter are detectable with 2% contrast at 10 keV. Since the contrast behaviour is linear with the X-rays wavelength one can predict the same values for 2-3% contrast for 1μm fiber at 100 keV.

4. Phase contrast tomography

Phase contrast imaging is very attractive for phase contrast tomography due to the following features:

- experimental simplicity (straightforward technique)
- energy tunability (5 - 60 keV)
- large space for sample environment
- spatial resolution is only limited by the detector
- no need for monochromator, undulator beam can be used directly
- short exposure (recording) time

Phase contrast imaging in outline region and Fresnel (holographic) region can be used for two types of phase contrast tomography: outline and holographic.

4.1 Outline tomography

Outline imaging (detector is close to the sample) can be applied for outline phase contrast tomography. Taking images at different angles and applied then standard will provide cross - sectional information of the interfaces and borders in the sample. The first results on this type of phase-contrast tomography [21] were obtained at 50 keV recently (Fig. 5). More examples and detailed consideration are presented in C. Raven contribution (this proceedings).

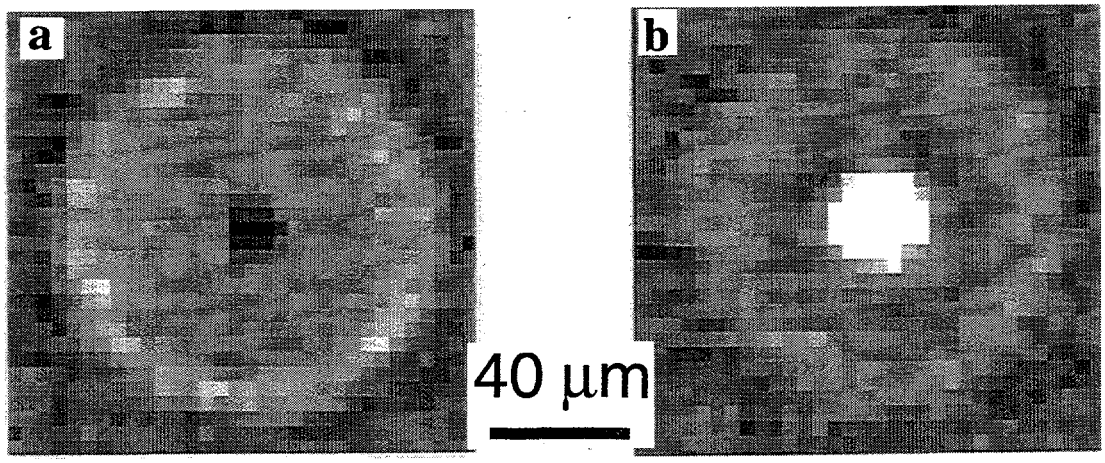

Fig. 5 (a) reconstructed cross-section of the boron fiber with the tungsten core and (b) without (hollow) obtained by a filtered backprojection algorithm.

4.2 holographic tomography

For holographic tomography set of holographic images in Fresnel region at different angles of view is recorded. From each projection the phase profile or in other words integrated phase shift over the projection is reconstructed. Then the obtained set of reconstructed profiles is putted in standard tomographic algorithm for reconstruction the diffractive index in the cross section. The most critical step in this technique is the reconstruction of the phase profile from holograms.

5. Requirements to the optics

Phase contrast imaging based on high spatial coherency of the X-ray beam impose special requirements for the optics and all elements of the optical set-up to be installed in the beampath.

It was shown that the rough surface of the Be windows is mainly responsible for the intensity variation in the beam [20]. To avoid this problem Be foils have to be polished. It should be noted that the same requirements must be fulfilled for any filters used at the beamlines

For the first time was demonstrated that the mirrors, that are the best available for the modern technology, give rise to deterioration of the coherent properties (or produce speckle structure) of the beam delivered at the third generation synchrotron radiation sources [22]. In the case of using of mirror, it should be installed in horizontally deflected set-up.

We proposed a holographic technique to characterise the coherence preservation by the mirrors and multilayers [23]. The X-ray interference pattern from the well known calibrated transparent sample like a round fiber can be used to characterise the coherence of the beam including the source and all optical elements installed. It was shown that mirrors deteriorate the source coherence, while the multilayer completely destroyed a coherence of the radiation in the vertical direction.

6. Bragg-Fresnel optics for phase contrast imaging

For phase contrast imaging techniques in the in-line holography set-up the resolution is determined by the resolution of the detector: at present this is 5-10 μm for high resolution X-ray cameras and 1μm for high resolution films. The use of additional optics like a Bragg-Fresnel lens installed after the object should lead to a 0.1 μm resolution [24-26]. First experimental tests of the imaging properties of the BFO were performed at the ESRF [27]. Crystal BFL works like a normal imaging lens, so it magnifies the phase-contrast image of the object.

Bragg-Fresnel optics is quite promising for normal absorption tomography with the pencil beam with sub-micrometer resolution. It is practically impossible to produce sub-μm beam with collimation systems owing the diffraction broadening.

7. Conclusion

In conclusion we would like to mention that straightforward experimental set-up proposed allows one to obtain phase contrast imaging at any beamline at the ESRF. Phase contrast imaging is therefore expected to be useful for investigating the microstructure inside biological specimens, and organic materials enables the separation of a specific inhomogeneity or inclusions from the matrix. Specimen size and thickness can have large ranges depending on the applications.

Future developments is needed on:

- reconstruction technique
- optics:
    - coherence preservation (monochromator and mirrors)
    - Zernike type microscope based on Bragg-Fresnel optics
    - magnification with Bragg-Fresnel optics μm and sub-μm resolution
- detectors with resolution 1 μm.

References

1. G. Schmahl, D. Rudolph, P. Gutmann, G. Schneider, J. Thieme, B. Niemann and T. Wilhein, Synchrotron Radiation News, vol.7, No.4, 19, (1994).

2. M. R. Howells and C. J. Jacobsen, Synchrotron Radiation News Compendium, vol.1-3, p. 411, (1994).

3. U. Bonse and M. Hart, Appl. Phys. Lett., 6, 155, (1965).

4. M. Ando, S. Hosoya, in Proc. 6th Intern. Conf. on X-ray Optics and microanalysis, eds. G. Shinoda, K. Kora and T. Ichinokawa, page 63, (Univ. of Tokio Press, Tokio, 1972).

5. A. Momose, T. Takeda and Y. Itai, Rev. Sci. Instrum., 66(2), 1434-1436, (1995).

6. A. Momose, T. Takeda, Y. Itai, K. Hirano, Nature Medicine, 2, 473, (1996).

7. K. Goetz, M. Kalashnikov, Yu. Mikhailov, G. Sklizkov, S. Fedotov, E. Förster, P. Zaumseil, Preprint Nr. 159, FIAN UdSSR, (1978).

8. E. Förster, K. Goetz, P. Zaumseil, Kristall and Technik, 15, 937, (1980).

9. E. A. Belyaevskaya, V. P. Epifanov, V. N. Ingal, Russian Patent No 2012872, priority 14. 05. 1991.

10. V. N. Ingal and E .A. Beliaevskaya, J. Phys. D: Appl. Phys., 28, 2314, (1995)

11. V. N. Ingal and E. A. Beliaevskaya, to be published in Physika Medica.

12. N. Mitrofanov, K. Podourets, V. Somenkov, A. Tyugin, P. Chistyakov, S. Shilshtein, Soviet Patent No 1402871, priorety 13. 11. 1986.

13. V. A. Somenkov, A.K. Tkalich, S. S. Shilshtein, J. Tech. Phys., 61, 197, (1991).

14. A. A. Manushkin, N. L. Mitrofanov, K. M. Podurets, V. A. Somenkov and S. S. Shilstein, Proc. of 2nd European Symposium "X-Ray Topography and High Resolution Diffraction", page 147, (Berlin, Germany, September 1994).

15. T. J. Davis, D. Gao, T. E. Gureyev, A. W. Stevenson and S. W. Wilkins, Nature, vol.373, 595-598, (1995).

16. T. J. Davis, , D. Gao, T. E. Gureyev, A. W. Stevenson and S. W. Wilkins, Phys. Rev. Lett., 74, 3173, (1995).

17. A. Snigirev, I. Snigireva, A. Suvorov, M. Kocsis, V. Kohn, ESRF Newsletters, No24, 23, (1995).

18. A. Snigirev, I. Snigireva, V. Kohn, S. Kuznetsov, I. Schelokov, Rev. Sci. Instrum., 66(12), 5486, (1995).

19. P. Cloetens, R. Barret, J. Baruchel, J.-P. Guigay, M. Schlenker, J. Phys: Appl. Phys., 29, 133, (1996).

20. A. Snigirev, I. Snigireva, V. Kohn, S. Kuznetsov, Nucl. Instrum. & Methods, A370, 634, (1996).

21. C. Raven, A. Snigirev, I. Snigireva, P. Spanne, A. Suvorov, V. Kohn, to be published in Appl. Phys. Letters.

22. I. Schelokov, O. Hignette, C. Raven, A. Snigiev, I. Snigireva, A. Souvorov, SPIE conf. Proc. conf. 2508, (1996).

23. A. Snigirev, Proc. of 10th ICFA Beam Dynamics Panel Workshop, page WG2 103, (Grenoble, France, January 1996).

24. A. Snigirev, Rev. Sci. Instr, 66(2), 2053, (1995).

25. Ya. Hartman, E.Tarazona, P. Elleaume, I. Snigireva, A. Snigirev, Rev. Sci. Instrum., 66(2), 1978, (1995).

26. A. Snigirev, I. Snigireva, P. Engström, S. Lequien, A. Suvorov, Ya. Hartmann, P. Chevallier, F. Legrand, G. Soullie, M. Idir, , Rev. Sci. Instr., 66(2), 1461, (1995).

27. A.Snigirev, I.Snigireva, P.Bosecke, S.Lequien to be published in Opt.Commun..

Phase Contrast Imaging with Coherent High Energy X-rays

Applications in Microtomography

A.Snigirev

ESRF

- What is phase contrast and why do we need it?

  how does phase contrast work in high energy X-rays?

- Phase contrast imaging using in-line holography geometry

  Peculiarities of the ESRF beam,

  First experimental results

- Future perspectives

Workshop on Computed Microtomography, ALS/LNBL, Berkeley, August12-13, 1996

$$n = 1 - \delta + i\beta$$

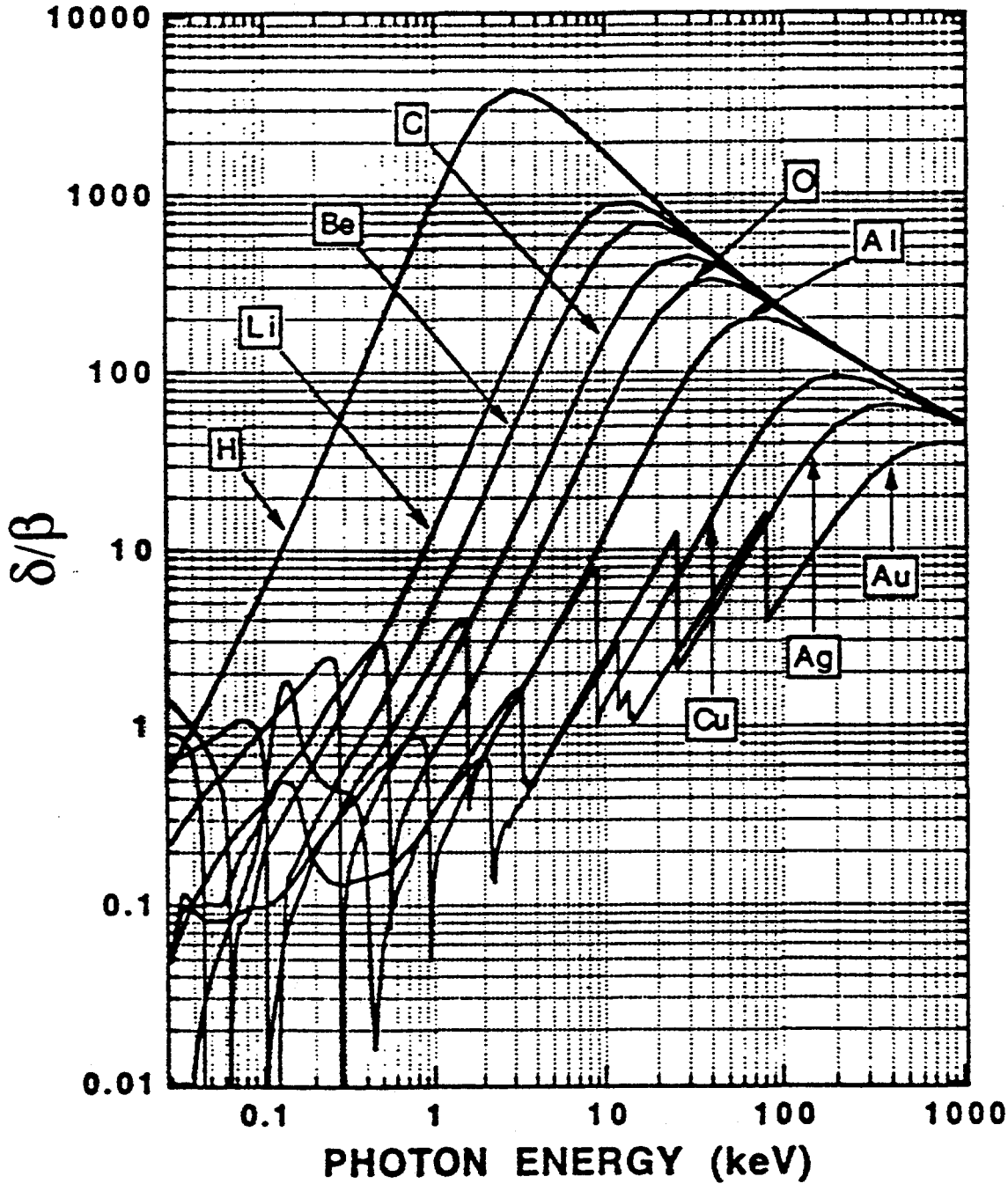

For light elements, the phase-shift cross section is almost a thousand times larger than the absorption cross section.

What is phase contrast?

Snigirev, ESR

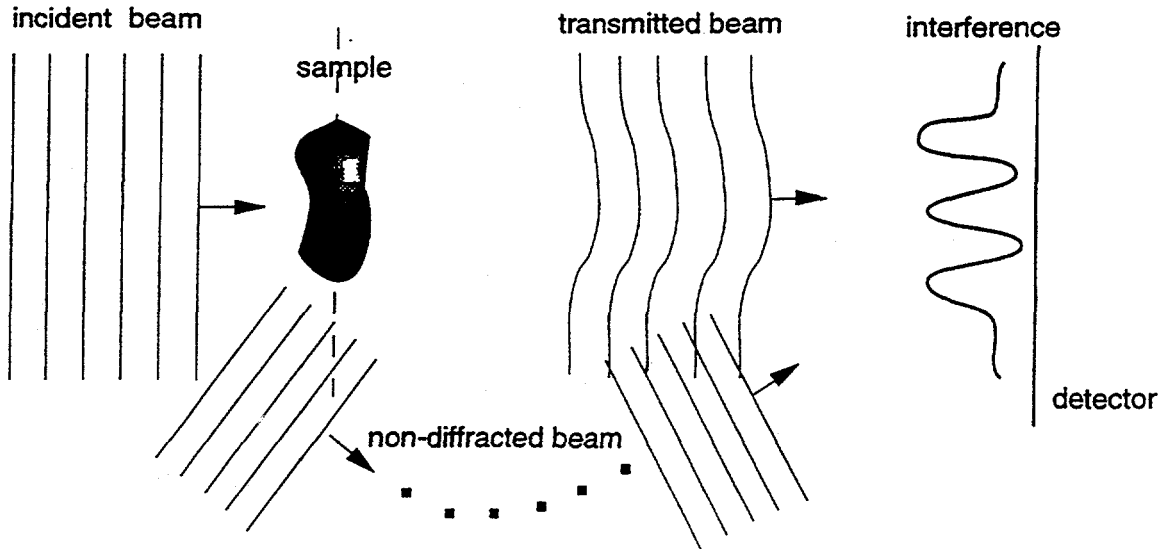

Phase contrast method consist in

- separating the diffracted and non diffracted parts of the light

- treating them differently

- recombining them under conditions such that they produce controlled visible intereference effects

light

- Phase contrast light microscopy	Zernike, 1935
- In-line holography	Gabor, 1948

soft X-rays

- Phase contrast microscope	Schmahl et al., 1988
- X-ray holographic microscopy	Aoki et al. 1972 Howels(ALS), Jacobsen(BNL), Polack (LURE)
- X-ray Fourier holography	McNulty & Kirz, 1992

hard X-rays

- interferometer	Bonse & Hart, 1965
- phase contrast imaging & tomography	Ando & Hosya, 1972; Momose, 1995

- phase contrast based on multicrystal setup

"schlieren"	Goetz, Kalashnikov, Mikhailov, Sklizkov, Foerster, Zaumseil, 1978;
"refraction"	Shilstein & Podurets, 1986;
"dispersion"	Ingal & Beliaevskaya, 1991;
"phase-contrast"	Davis, Gao, Gureev, Stevenson, Wilkins , 1995

Phase contrast imaging

- Phase contrast microscopy *(Zernike, 1935)*
- In-line holography *(Gabor, 1948)*

Soft X-rays (E < 1 keV)

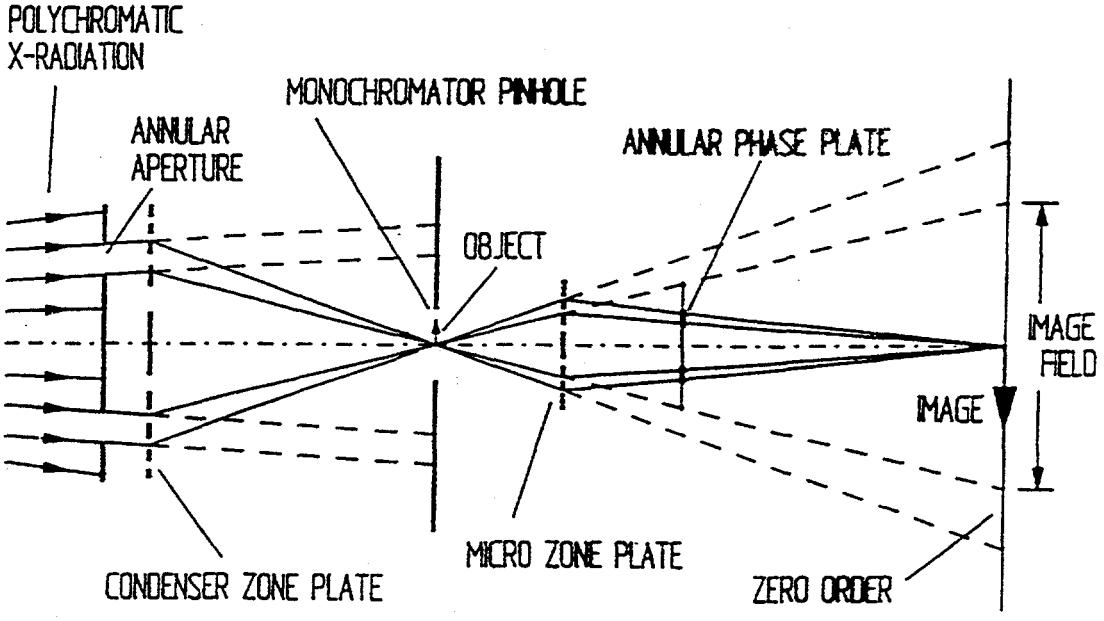

Phase contrast X-ray microscope
(Schmahl, Rudolph, Guttmann, 1988)

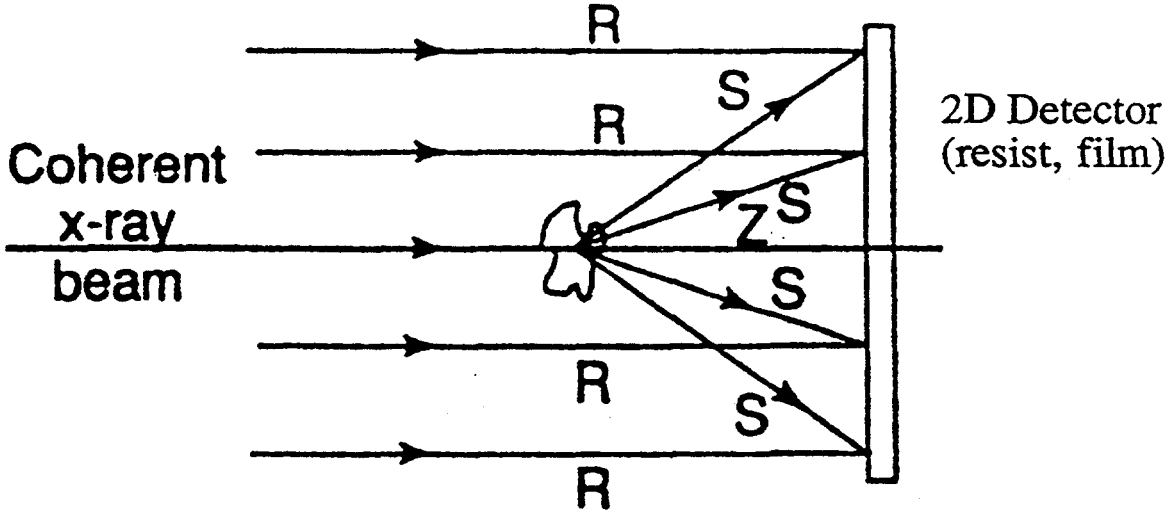

X-ray in-line holography
(Aoki, Ichikara, Kikuta, 1972)

Howells (ALS)
Jacobsen (Stony Brook
Polack (LURE)

Phase contrast using interferometer

Bonse-Hart Interferometer

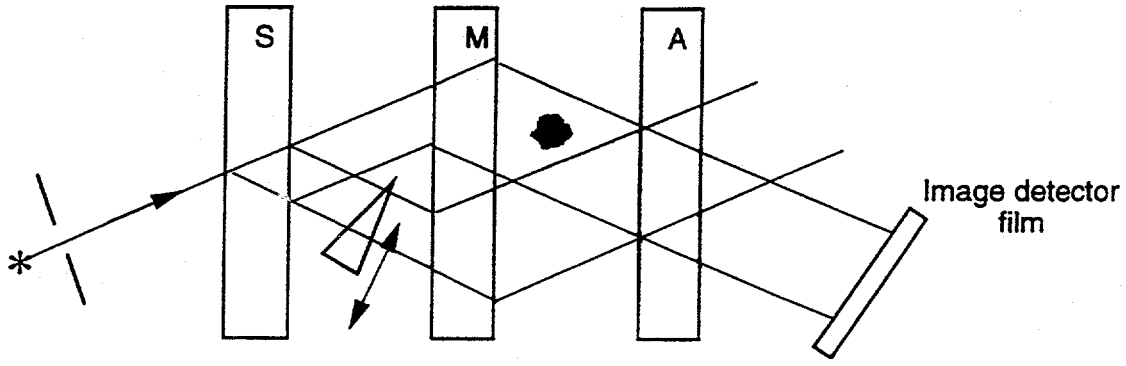

M.Ando and S.Hosoya, 1972
A.Momose, 1995

U. Bonse, (1996) at ESRF

Advantages

- refractive index mapping
- high absolute sensitivity

Shortcomings

- relatively thick crysals (1mm) - high absorption
  10^5ph/s/mm^2 at BM Photon Factory (Momose)

- spatial resolution is limited by the Borrmann fan
  30 μm (according to Momose)

- energy tunability for given interferometer is limited
  11 - 18 keV / 0.7 - 1.3 Å (Momose)

- lack of space for sample environment
  pressure, temperature etc.

Multicrystal setup: Laue (I) or Bragg case (II)

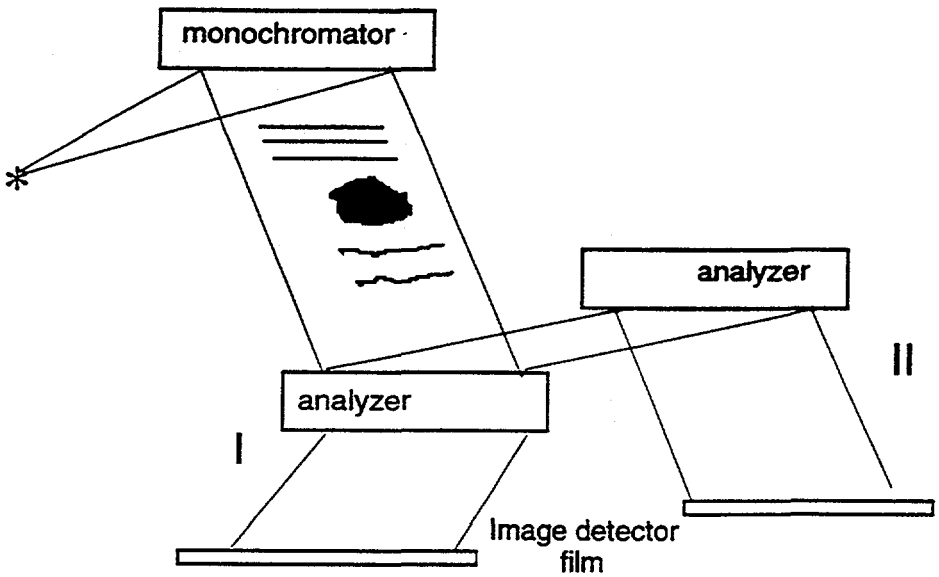

I *V.Ingal and E.Belyaevskaya, 1991*
II *S.Shilstein and V.Somenkov, 1986*
T.Davis, T.Gureev, D.Gao, A.Stevenson, and S.Wilkins, 1995

"schlieren"	Goetz, Kalashnikov, Sklizkov, Foerster, Zaumseil, 1978;
"refraction"	Shilstein & Podurets, 1986;
"dispersion"	Ingal & Beliaevskaya, 1991;
"phase-contrast"	Davis, Gao, Gureev, Stevenson, Wilkins , 1995

Advantage:

can be realised using laboratory source

Shortcomings:

resolution limited by extinction depth (length) 5 - 10 microns

contrast lost

Experimmental conditions at the ESRF BL

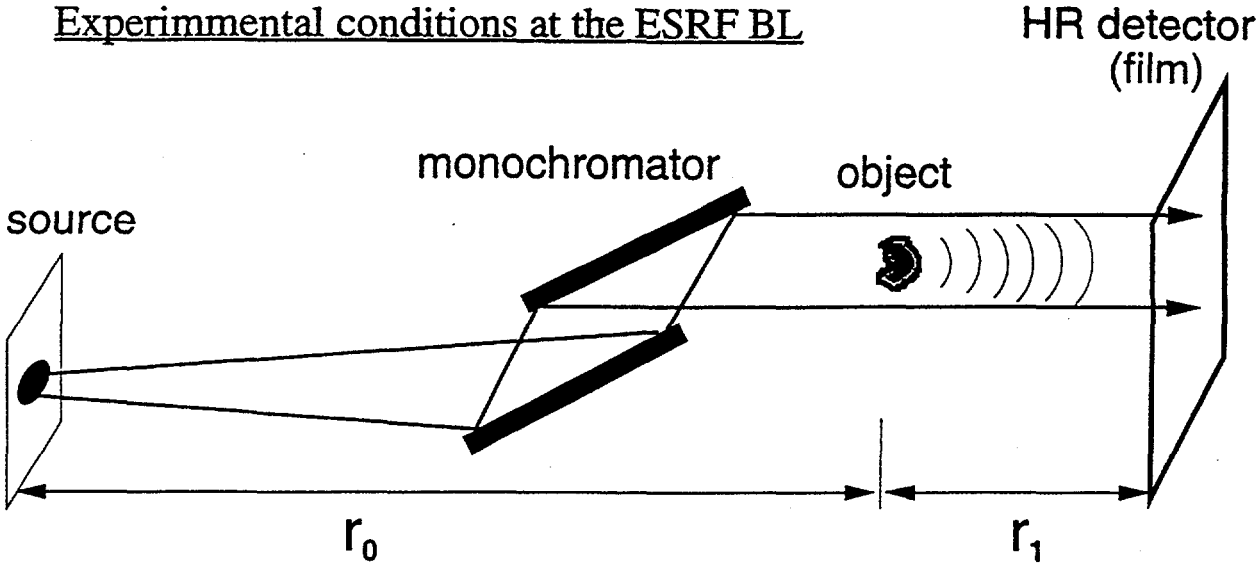

source size: s ~ 100μm

source-to-sample distance: r_0 ~ 50m ⇒ spatial coherence

⇓

angular source size: ~ 2μrad $\lambda r_0/s = 50\mu m$ (λ=1Å)

1% coupl. s ~ 50μm

angular source size: $\phi = s/r$ ~ 1μrad !

1. $\phi < \Delta\Theta$ (width of the rock. curve Si monochr.)

2. $\phi \sim \Delta n \sim 10^{-5}$ -10^{-6} (refractive index decrement)

⇓

spatial coherence

λ/ϕ = 100μm (λ=1Å)

Coherence is the set of experimental conditions to observe an interference pattern, which we wish to study.

Snigirev A., ICFA Jan. 1996

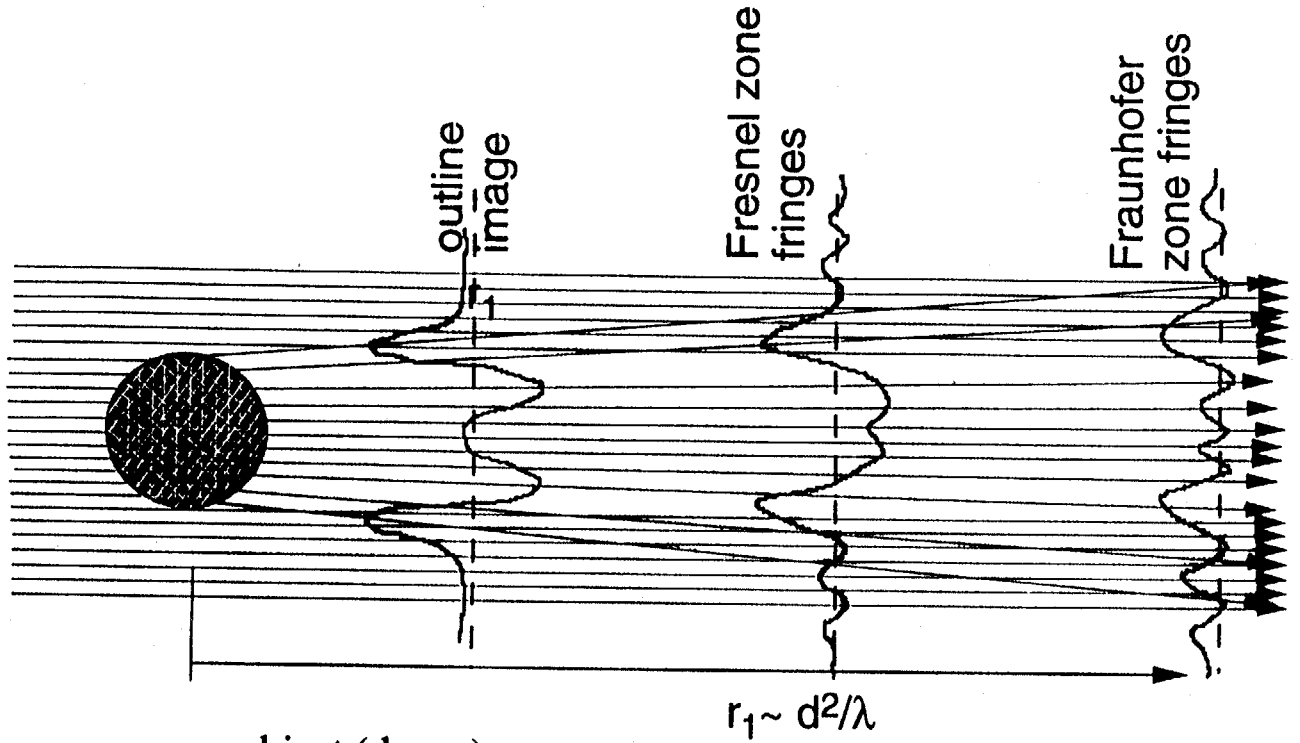

		object (d, μm)	$\phi = 2\pi\delta d/\lambda$	
light	$\lambda = 0.5\mu m$	1	2 μm	
		10	200 μm	
		100	20 mm	
soft x-rays	$\lambda > 10Å$	1	1 mm	0.8 π
		10	0.1 m	8 π
		100	10 m	80 π
hard x-rays	$\lambda \leq 1$ Å	1	10mm	0.08 π
		10	1 m	0.8 π
		100	100 m	8 π

Hard x-rays

(1) λ is 10÷10000 smaller

(2) no absorption

(3) perfect monoch - single crysta

(4) Dynamical diffraction theory

Boron tube

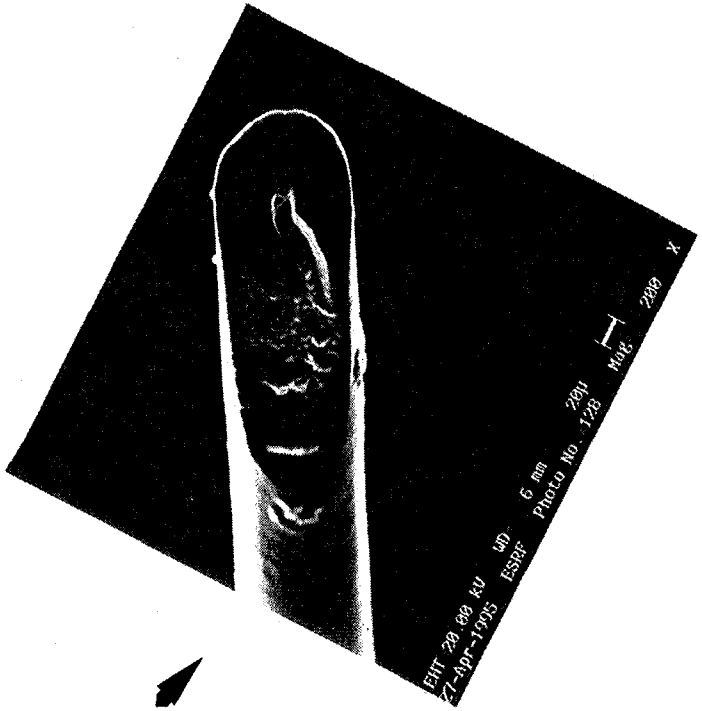

S E M image

X-ray Phase Contrast
Imaging at 15keV

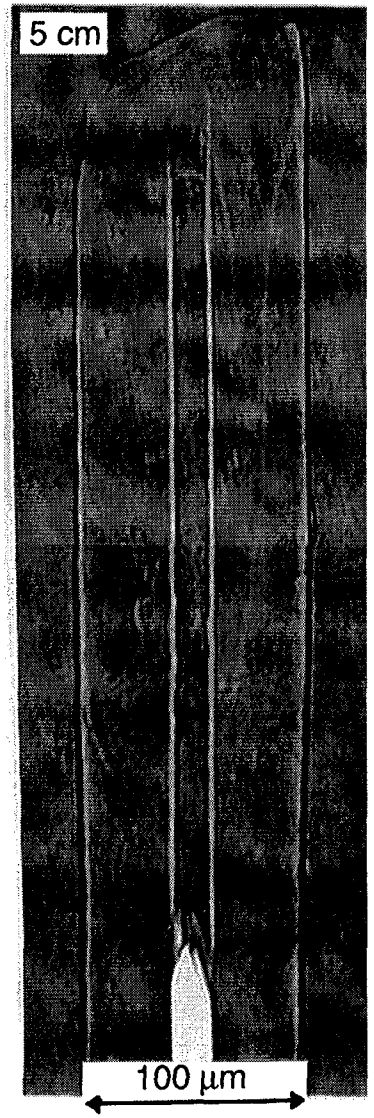

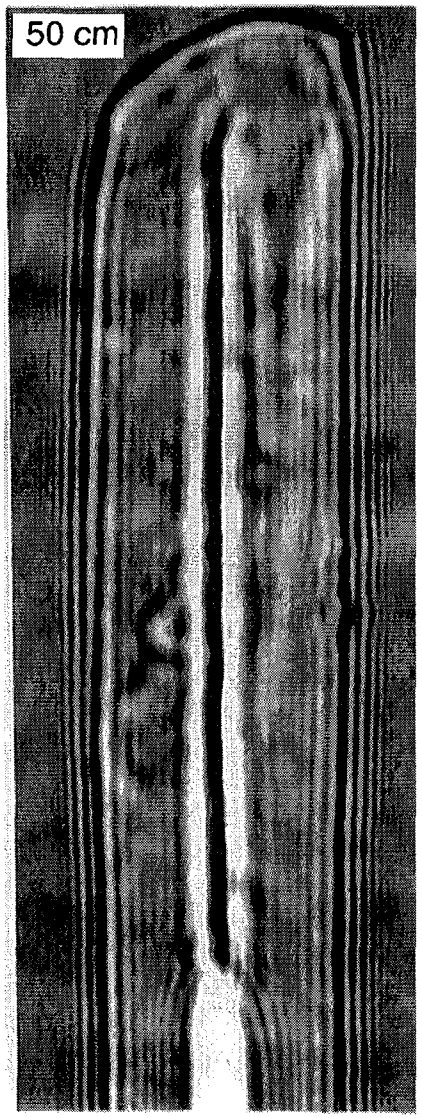

X-ray phase contrast imaging of Boron fiber at 50keV

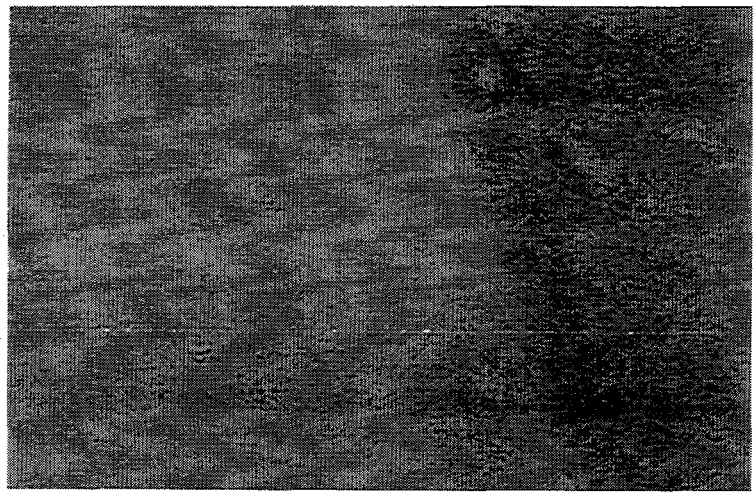

0 cm

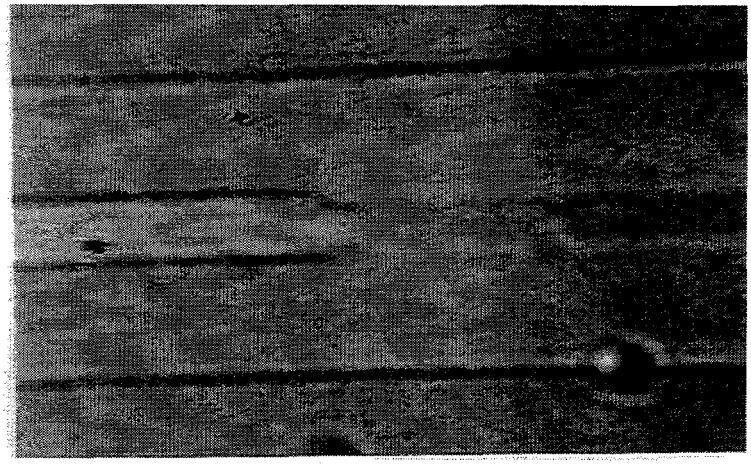

100 cm

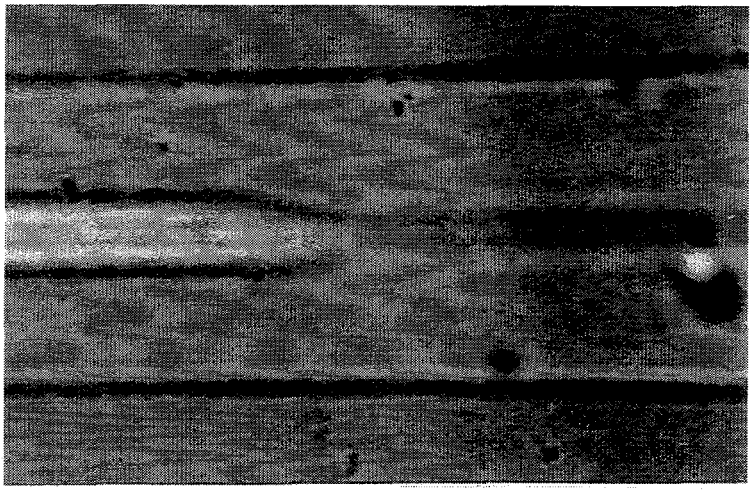

200 cm

40μm

X-ray imaging of seaweed Valonia ventricose at 20keV energy

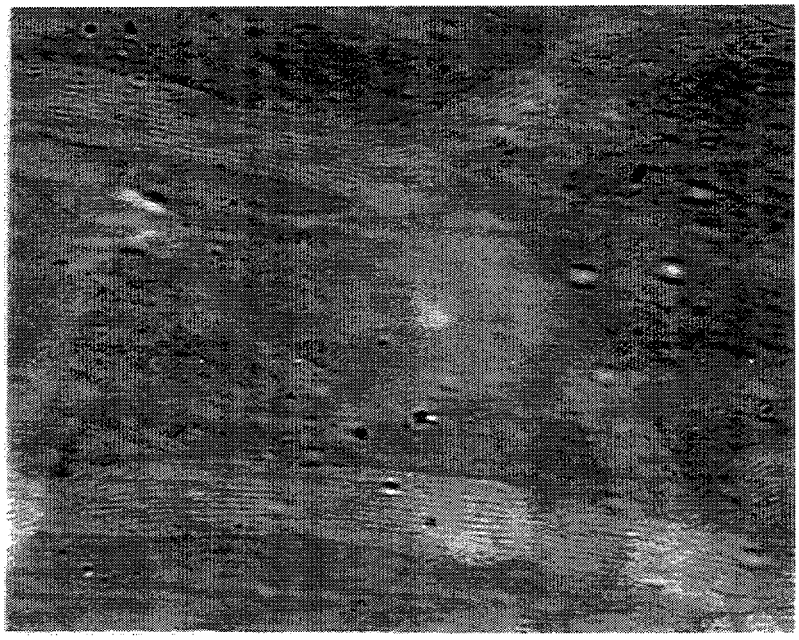

image in amplitude mode

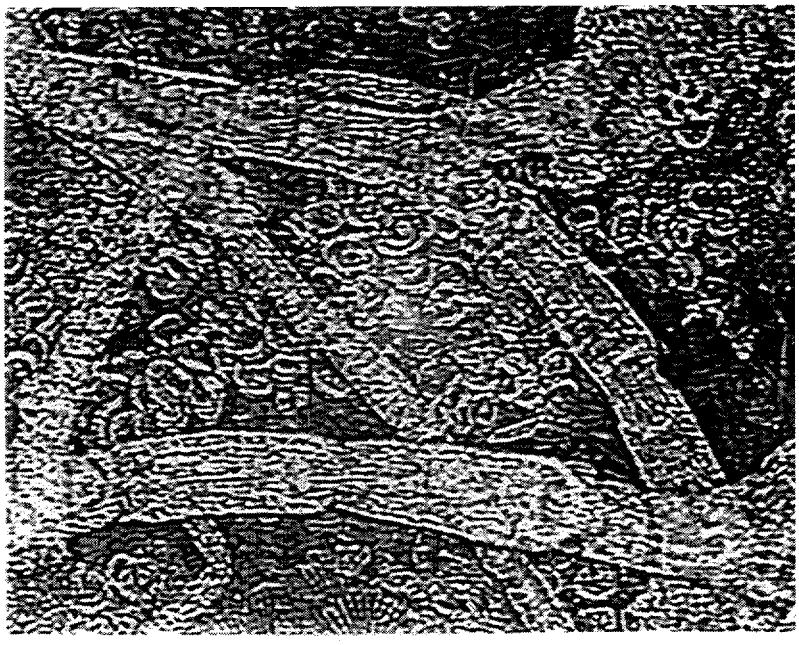

image in phase contrast mode

500 μm

X-ray phase contrast imaging

Seaweed *Valonia ventricosa*

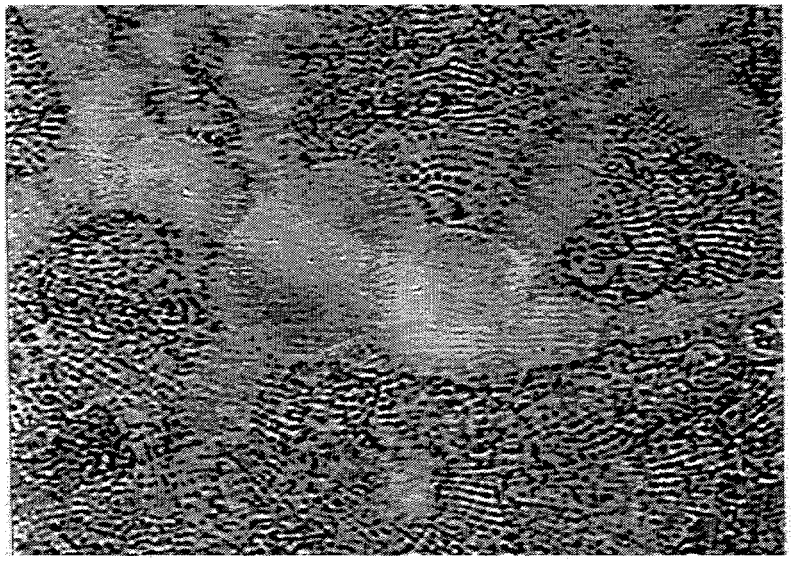

200 μm

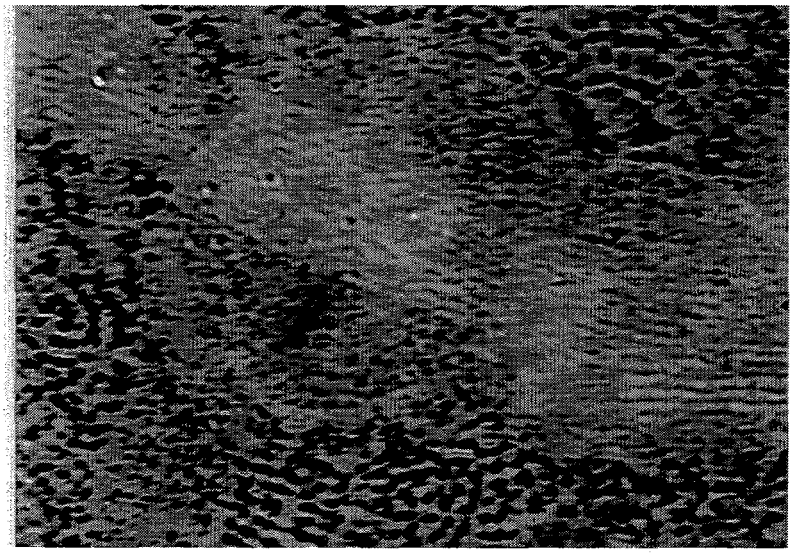

100 μm

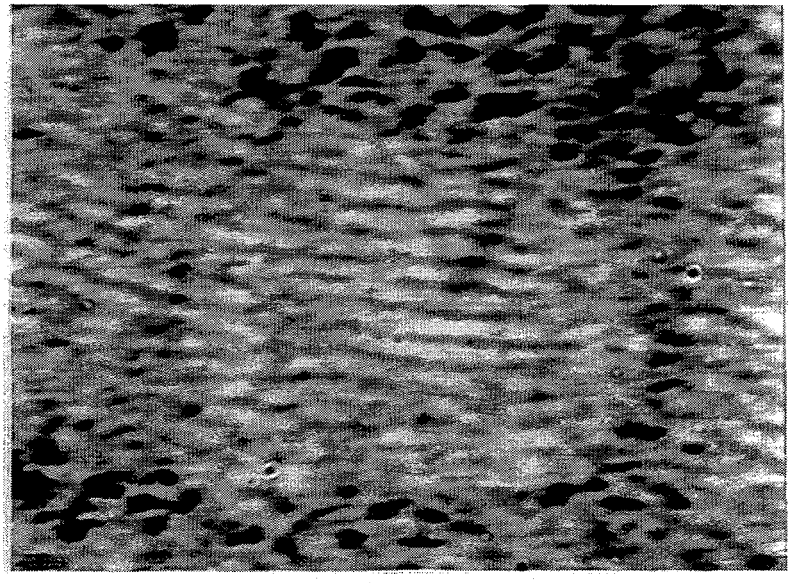

40 μm

Phase contrast imaging at 18 keV

foraminiferal shell
„Operculina ammonoides"

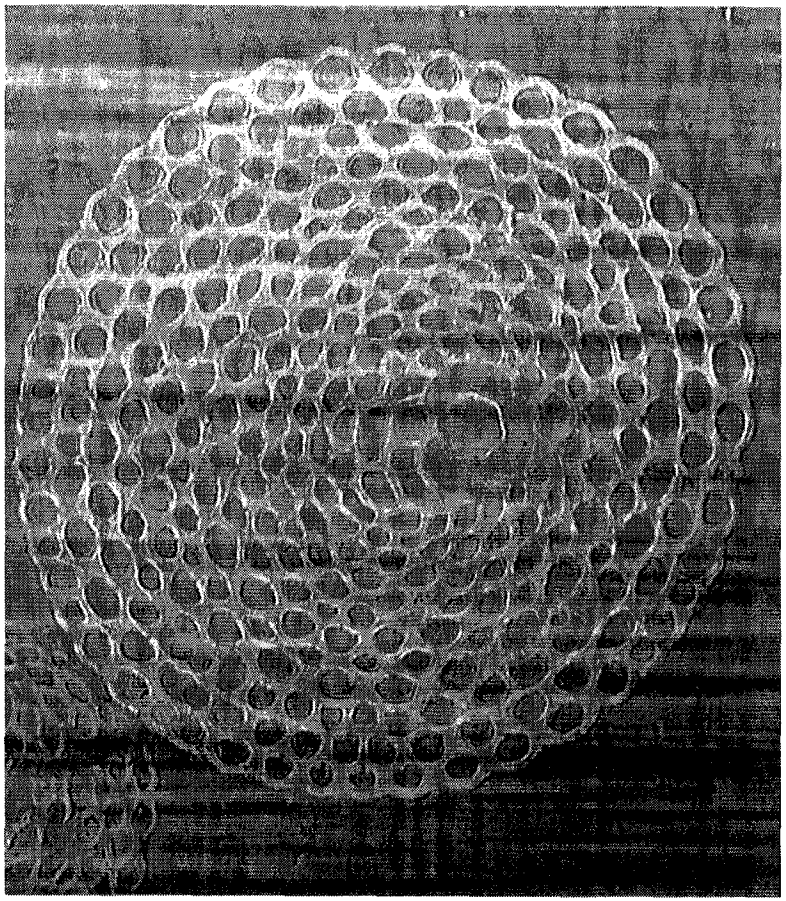

200 µm

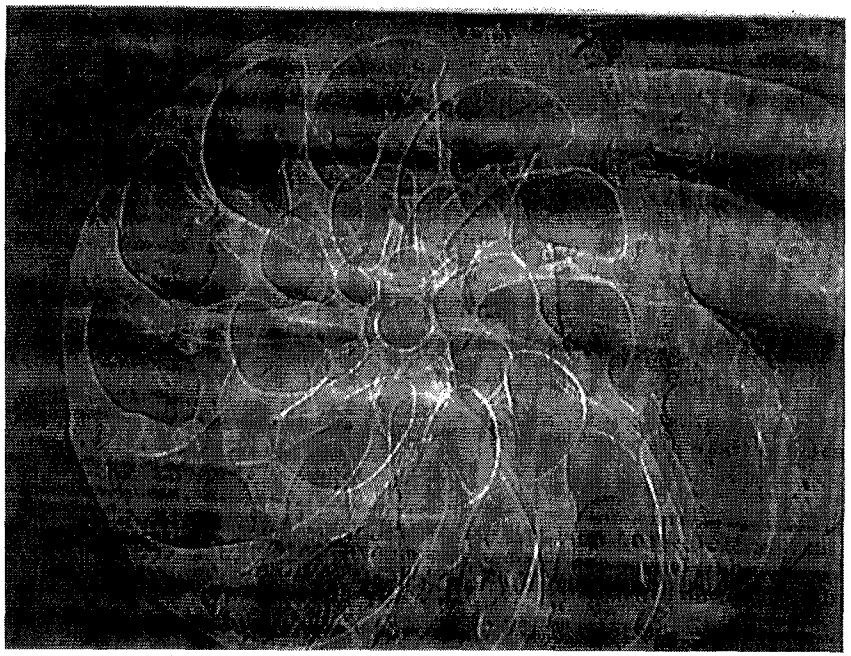

100 µm

foraminiferal shell „Operculina ammonoides"

18 keV

1 mm

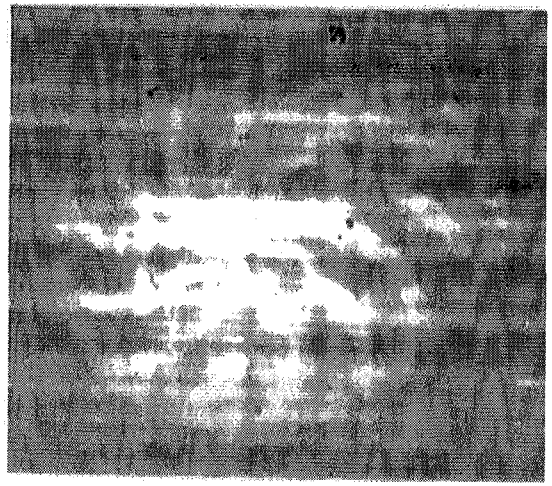

0

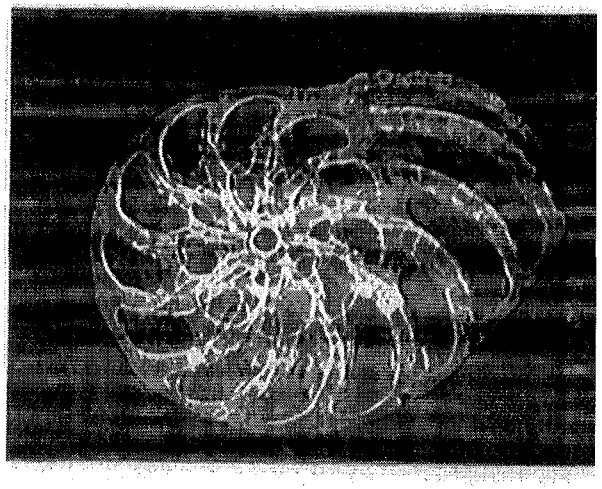

10 cm

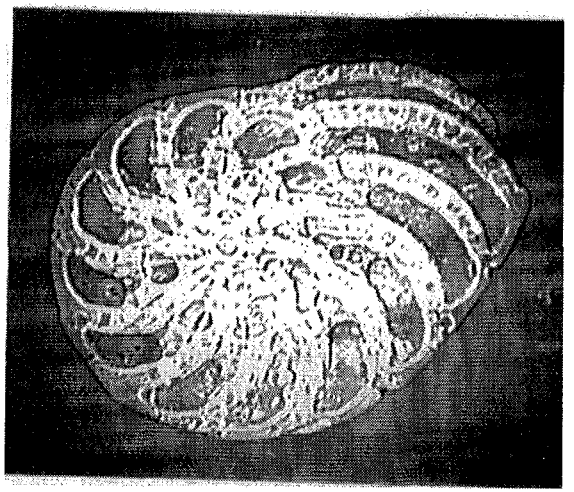

40 cm

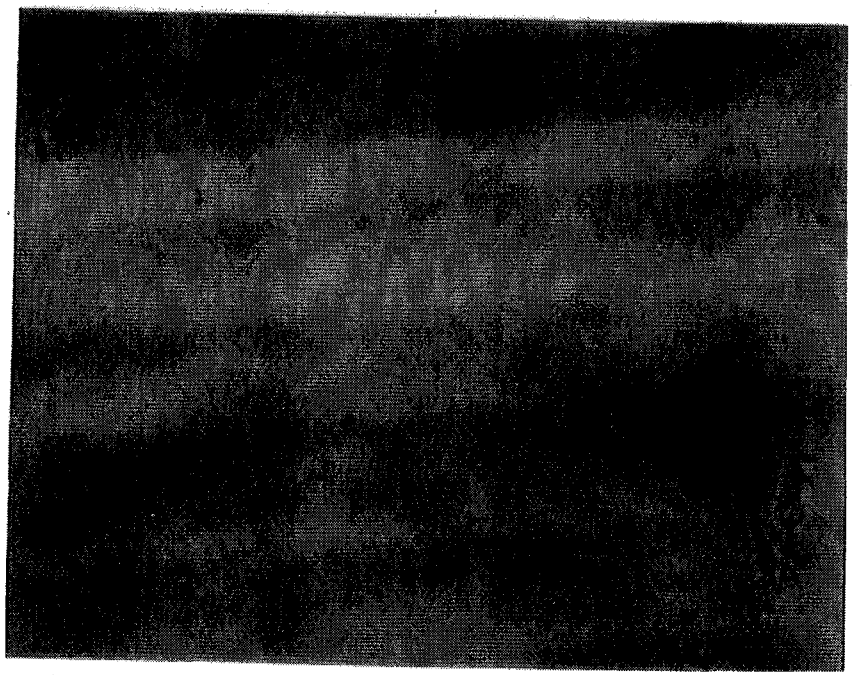

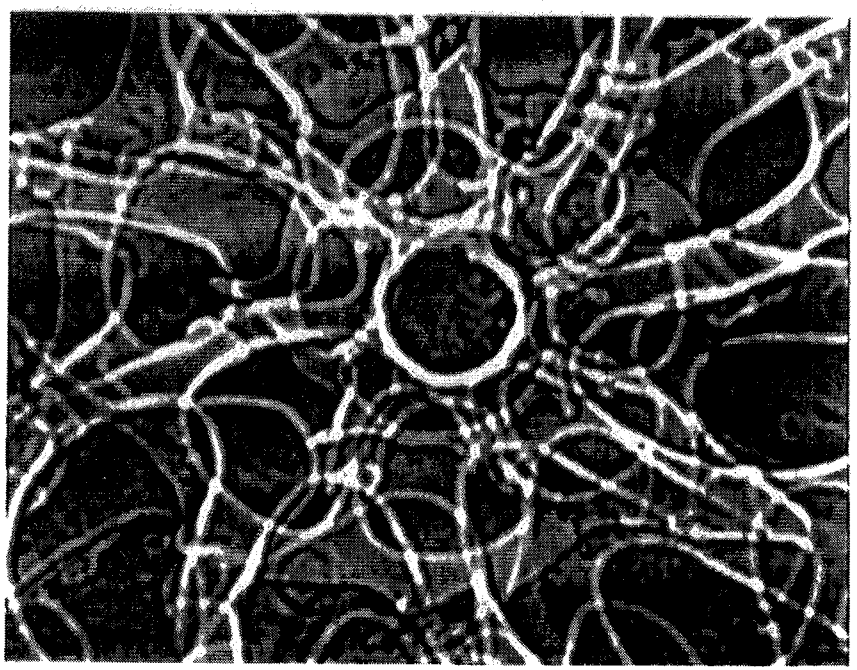

BEREA SANDSTONE

(for Erika Schlueter, LBNL)

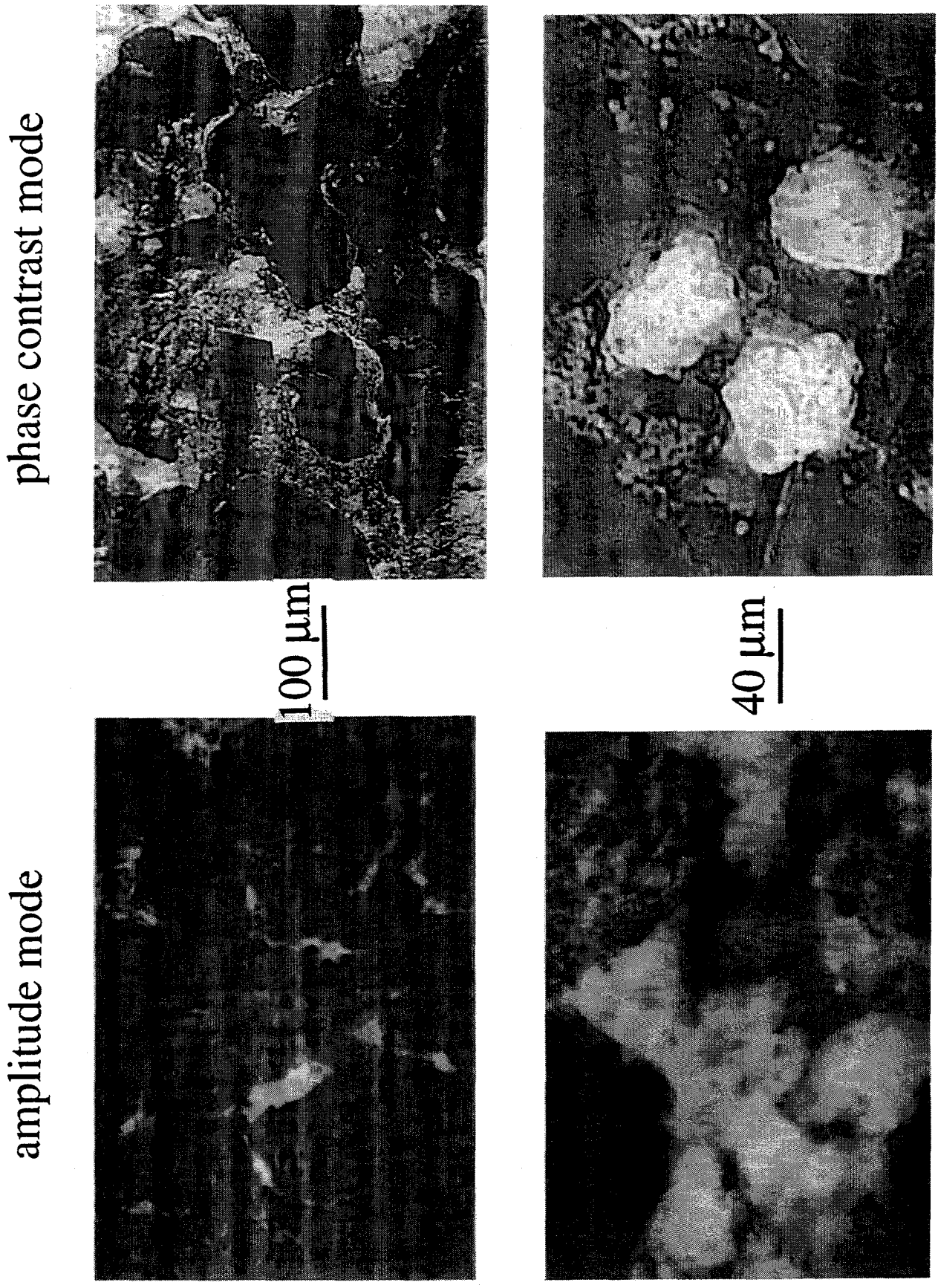

Computed Tomography

- record projections at different angles

$$g(x,y,z) \mapsto P(r,\theta,z)$$

- reconstruct 3d data set by

  Filtered Backprojection

  ➡ Fouriertransformation

  Algebraic Reconstruction (ART)

  ➡ linear inverse problem

Experimental setup

60 keV !

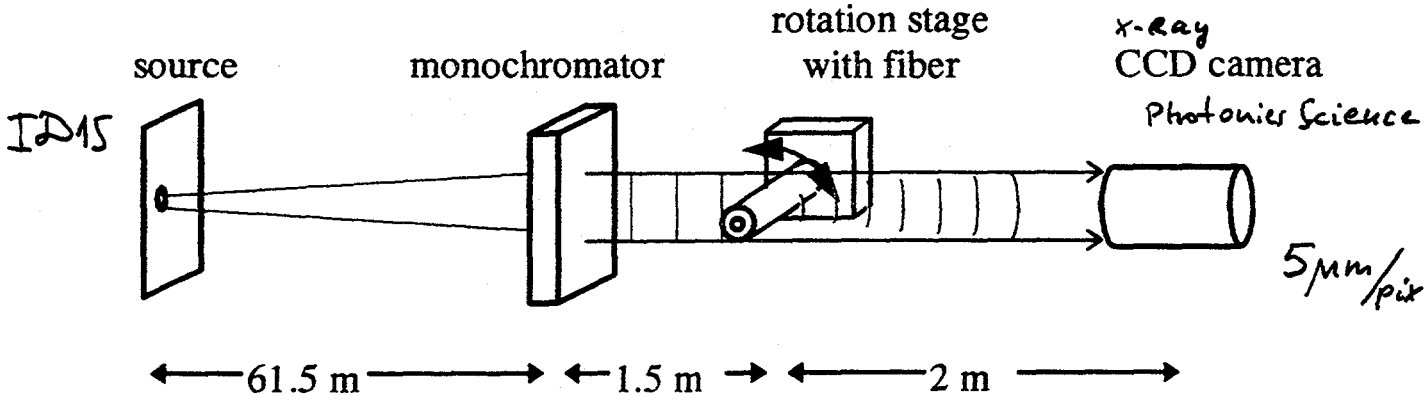

Phase-Contrast Microtomography

Interference pattern recorded from different angles of view were used to obtain cross-section images of the boron fiber by means of a standard tomographic algorithm.

Instead of the high resolution film we used a CCD camera with pixelsize of 5 µm. The images were recorded with a 50 keV beam in 2 m distance from the fiber. ID15 (ESR

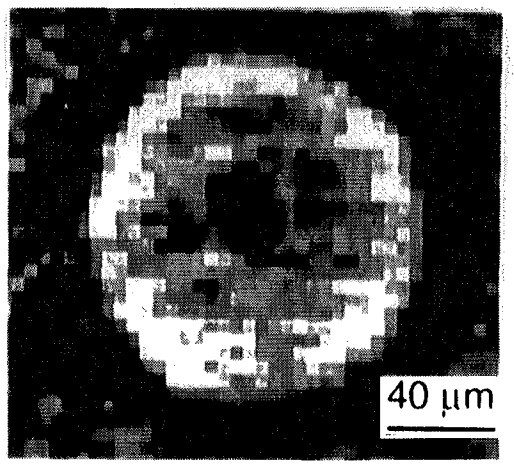

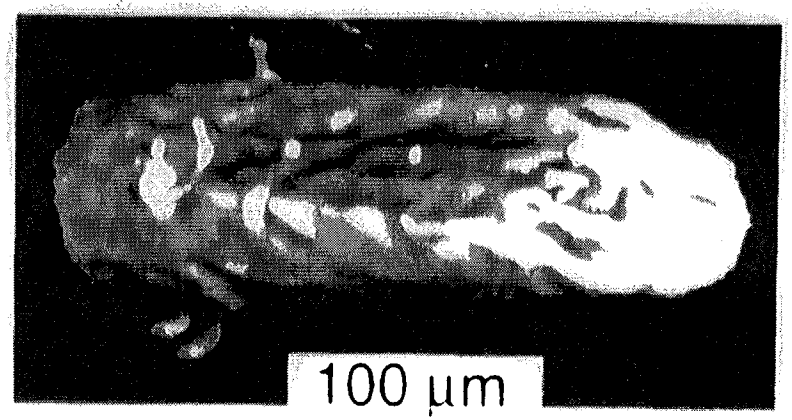

Reconstructed cross-section of the boron fiber without the tungsten core (hollow core). The cross-section was calculated from 61 images.

Rendered 3D image of the fiber tip. The etched core (15 µm) is still seen, even with the lower resolution of the camera compared to high resolution film.

C. Raven, I. Snigireva, V. Kohn, P. Spanne, A. Snigirev

Contrast parameter

$$C = I_{max} - I_{min} / I_{mid}$$

$$C = 2\pi\gamma\lambda d = \varphi$$

where $\gamma = \delta / \lambda^2$

d = 0.1μm

λ = 1.24 Å (E=10 keV)

$\delta = 4.7 * 10^{-6}$ (carbon)

$\gamma = 3.05 * 10^{14}$

$C = 2\%$

---

d = 1μm

λ = 0.124 Å (E = 100keV)

$C = 2 - 3\%$

detectable $\varphi \approx \frac{2\pi}{100}$

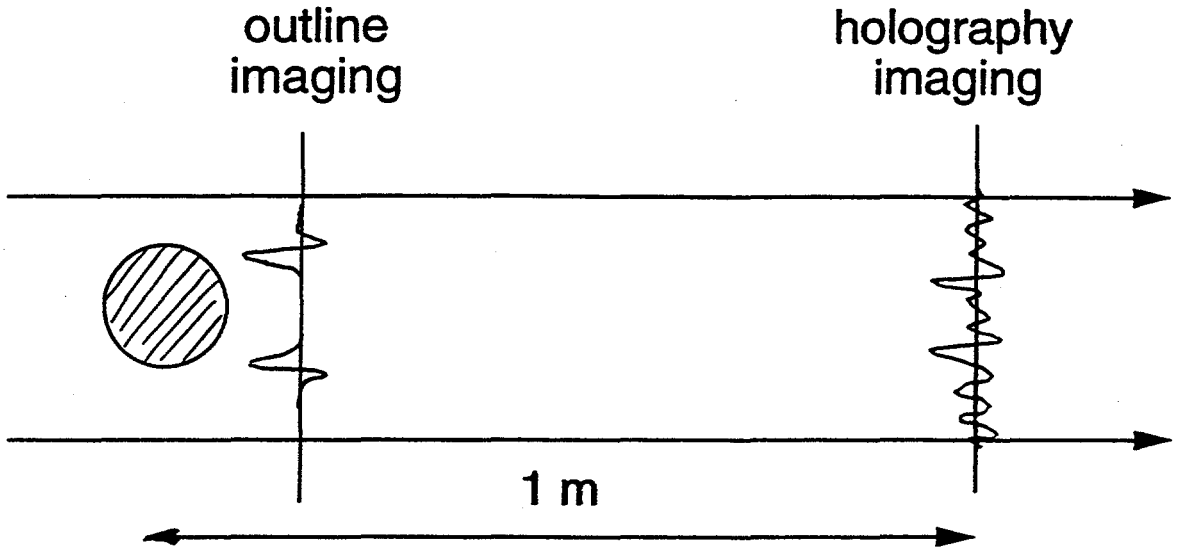

$\lambda = 1\text{Å}$

1 μrad

1 μm resolution

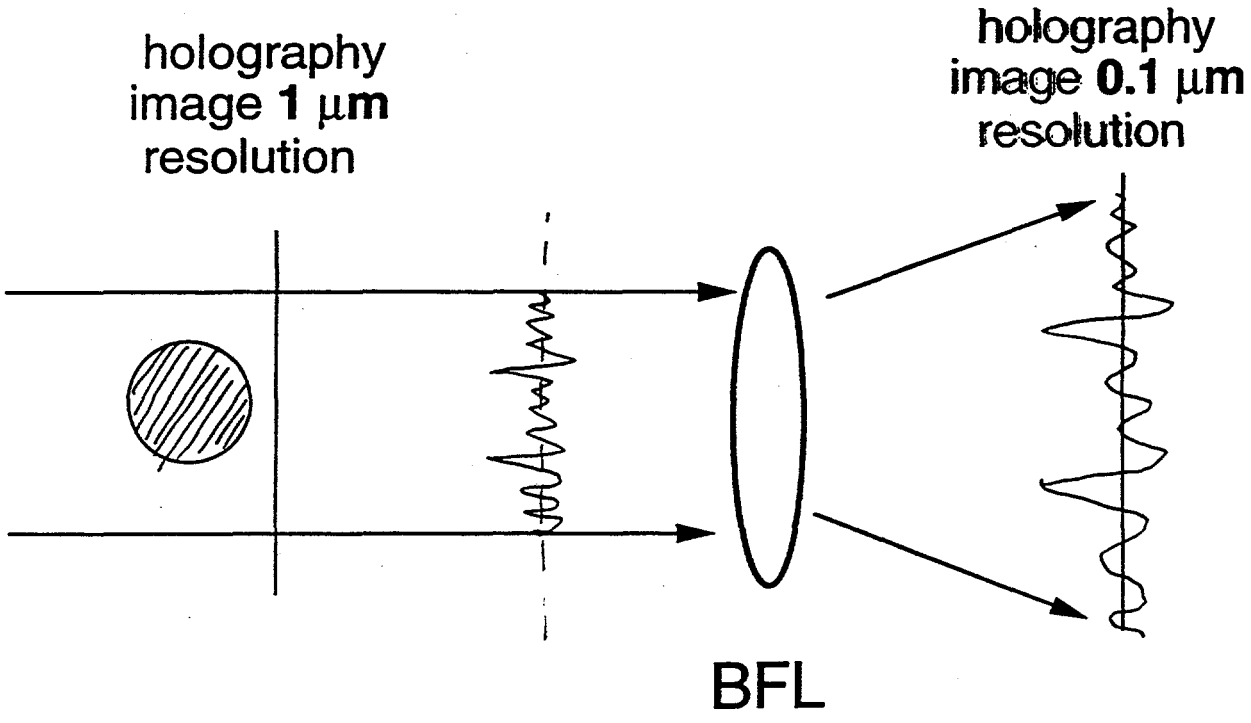

Phase contrast using in - line holography geometry

Attractive features

- experimental simplicity / straightforward technique
- energy tunability 5- 50 (100) keV
- large space for sample environment
- spatial resolution is only limited by detector (source)
- no needs for monochromator
  - undulator beam can be used
  - short exposure (recording) time

Shortcomings

At present!

- it is difficult to interpret the images quantitatively
- lack of reconstruction technique

Applications to various heterogeneous materials:

biological samples,
soil,
advanced materials,
Htc superconductors,
ceramics,
injection moulding composites,
ferrofluids,
filters, paper,
video tapes etc.

Reconstruction Methods for Phase-Contrast Tomography

Carsten Raven

July 21, 1996

1 Introduction

Phase contrast imaging with coherent x-rays can be distinguished in outline imaging and holography, depending on the wavelength λ, the object size d and the object-to-detector distance r. When $r << d^2\lambda$, phase contrast occurs only in regions where the refractive index fastly changes, i.e. at interfaces and edges in the sample. With increasing object-to-detector distance we come in the area of holographic imaging. The image contrast outside the shadow region of the object is due to interference of the direct, undiffracted beam and a beam diffracted by the object, or, in terms of holography, the interference of a reference wave with the object wave (Fig.1). Both, outline imaging and holography, offer the possiblity to obtain three dimensional information of the sample in conjunction with a tomographic technique. But the data treatment and the kind of information one can obtain from the reconstruction is different.

2 Tomography in Outline Mode

When the phase-contrast images are recorded close to the object, contrast occurs only at edges and interfaces in the form of sharp peaks in intensity. In a crude approximation, this intensity distribution can be seen as the projection of thin absorbative layers in an otherwise transparent object. The thin layers are exactly there located where interface in the real object are (Fig. 2).

Taking images from different angles of view and process them with a standart tomographic algorithm will give cross-sectional information of the

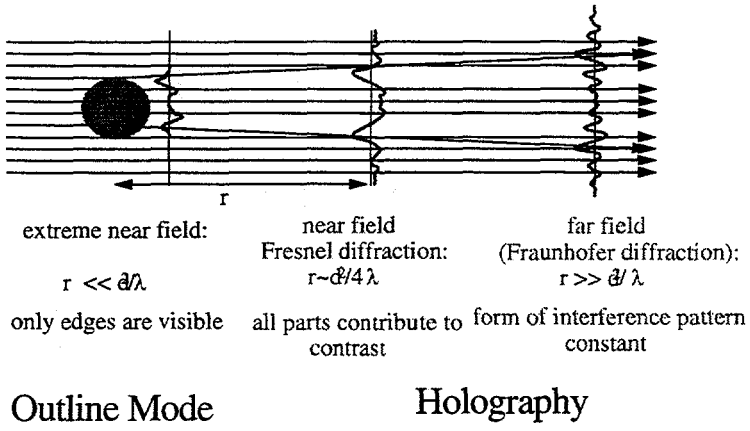

Figure 1: Image formation. The intensity distribution is a function of the object-to-detector distance.

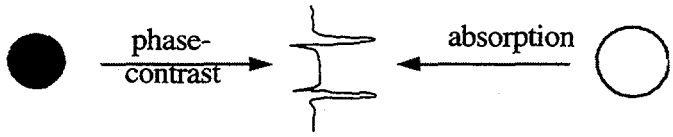

Figure 2: Phase-contrast images in outline mode can be modeled by a transparent objects in absorption mode having thin absorbative layer where interface in the real object are.

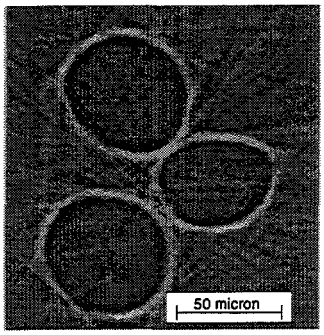

Figure 3: tomographic reconstruction of three hairs in outline mode.

interfaces in the sample. The method of outline-mode tomography differs from absorption tomography in the way the images are corrected for inhomogenities in the background. Where in the latter

$$\ln \frac{N_{in}}{N_d} = \frac{4\pi}{\lambda} \int_{\text{ray}} \beta(x,z) ds \tag{1}$$

is used as input data for the tomographic reconstruction to calculate the absorption index β, in outline mode tomography the flatfield $I_0$is substracted from the phase-contrast image I_ϕ to account for background noice and inhomogenities. In Fig.**3** the tomographic reconstruction of three fibers is seen. 200 outline images were recorded on Kodak high resolution X-ray film and scanned into an image processing routine, which realigned the images,substracted the flatfield images and sharpened the peaks by means of a differentiation and a thresholding filter.

3 Holographic Tomography

Reconstruction of the cross sectional refractive index distribution from holograms involves one step more. Prior to the tomographic reconstruction, each

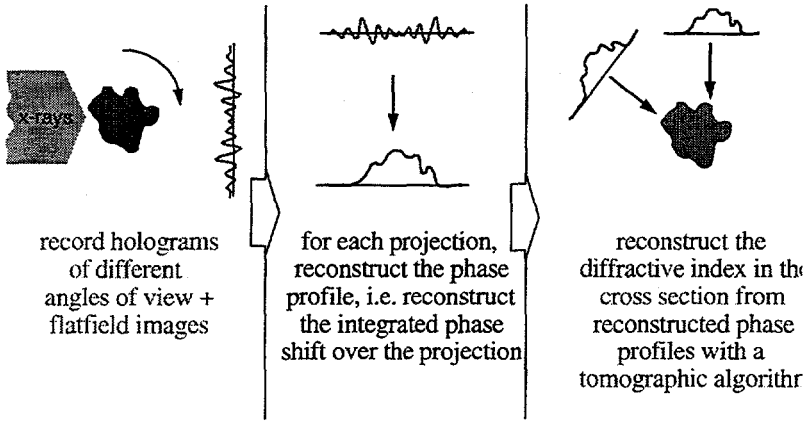

Figure 4: Principle of holographic tomography. Prior to the tomographic reconstruction, the phase profiles must be reconstructed numerically from the holograms for each angle of projection

phase profiles, i.e. the line integral over the phase shift inside the sample

$$\theta(\tilde{x}) = \frac{2\pi}{\lambda} \int_{-d/2}^{d/2} \delta(\tilde{x}, z) dz. \tag{2}$$

must be reconstructed from a hologram. This set of (holographically) reconstructed phase profiles serves then as input for the tomography algorithm to obtain cross-sectional information (Fig 4).

4 Phase Reconstruction from Holograms

The most critical step in holographic tomography is the reconstruction of the phase profile from holograms. We tested the feasibility of different reconstruction and phase-retrieval algorithms and the best choice seems to be a modified Gerchberg-Saxton algorithm, which iteratively propagates the wavefield between the object and the detector plane back and forth, satisfying in both planes constrains given by the measured hologram and an a-priori knowledge of the outer sample-size. A schematic diagram of one iteration step is shown in Fig. 5. Convergence to the real phase profile is provided only for a certain range of values for the source size, the wavelength and the outer size of the object play. The smaller the source size, the

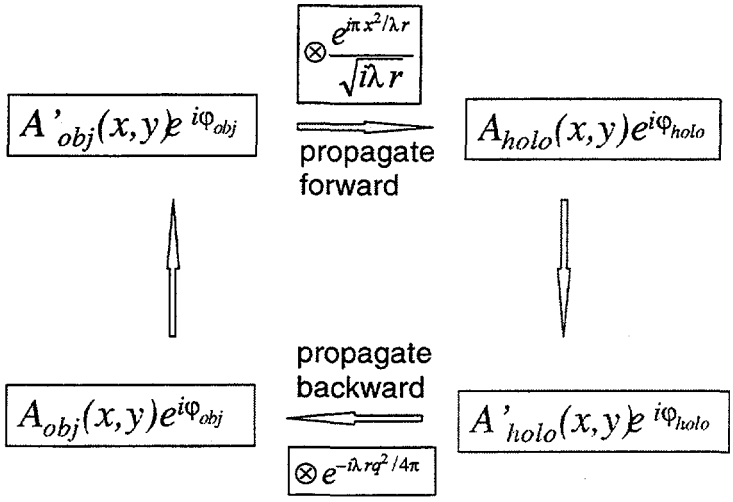

Figure 5: one iteration step in the modified Gerchberg-Saxton algorithm

higher the coherence and the better the spatial resolution. The lower the wavelength, the larger the interference pattern and thus the less the demand on detector resolution. Even under optimal conditions (simulations with a perfectly homogenous beam, no noise, no detector aberrations) the maximal object size with which the algorithm still converges is limited to $\lesssim 100$ μm for a 10 keV beam in the moment. Fig.6 shows that the reconstructed phase profile 'creeps' to the real phase profile beginning from the border of the object. The larger the object size the more iteration steps are necessary to achieve convergence. Rather major improvements have to be made on the reconstruction algorithm to overcome this problem of limited object size.

5 Spatial Resolution

Fig.7 shows the calculated and the reconstructed cross-section of the diffractive index of a fiber bundle. Fig. 8 shows that improving the detector resolution to better than 2 μm does not improve the quality of the reconstructions further as long as the improvement in detector resolution is not accompanied by a decrease in source size. A brief listing with the major issues limiting the spatial resolution of holographic tomography is given in Fig. 9.

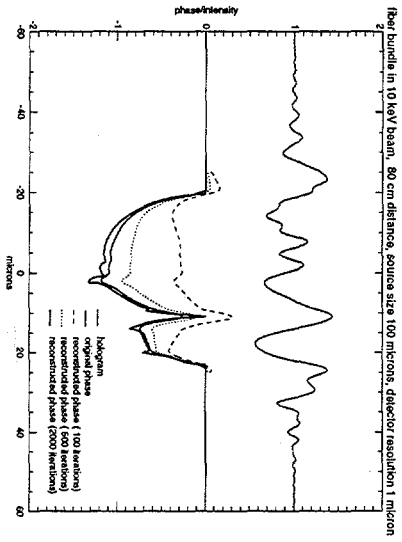

Figure 6: iterative reconstruction of the phase profile. In this simulation the hologram was calculated from the ideal phase profile and then the phase profile was reconstructed from the hologram iteratively

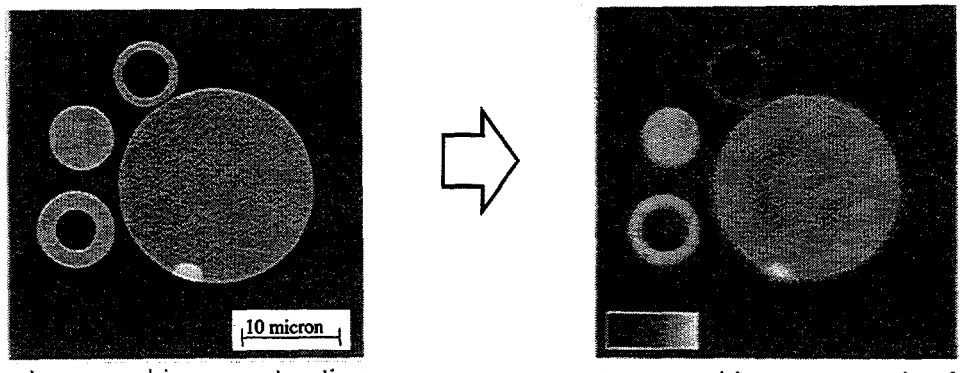

Figure 7: calculated and reconstructed phase profiles were used to calculate these cross-sections. The blurring is due to the source size rather than due to detector limitations.

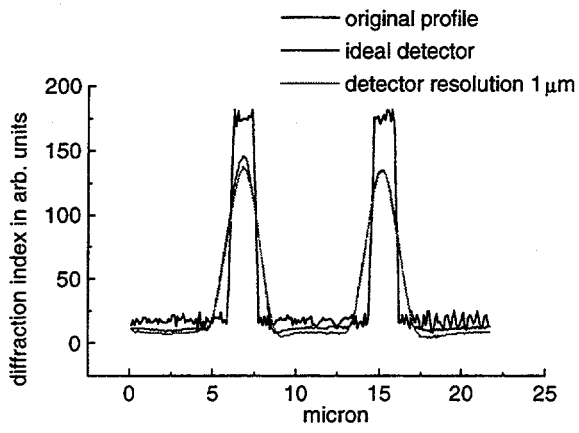

Figure 8: improving the detector resolution beyond 1 μm does not improve the image quality due to the then limiting source size

	today	future	limiting
source size:	80 μm	50 μm	beam emittance, vertical coupling
demagnification factor:			
object-to-detector distance	1 m	50 cm	reconstruction algorithm
source-to-object distance	40 m	50 m	length of beamlines
	= 2.5 μm	= 0.5 μm	
detector resolution:			
high resolution film	1 μm	1 μm	cornsize, dynamic range
CCD - camera	8 μm	2 μm	fluorescence screen
max. object size:	100 μm	500 μm	reconstruction algorithm
beam inhomogenities			
vacuum windows			surface finish of windows
optical elements in the x-ray beam			surface roughness

Figure 9: The most important parameters which are limiting the spatial resolution in holographic imaging and tomography

6 References

A. Snigirev et al., Rev. Sci. Instrum. **66** (12),5486-5492 (1995)
C. Raven et al., Apl. Phys. Lett. (to be published)
R. Gerchberg, W.O. Saxton, Optik **35**, 237-46 (1972)
J. Fienup, Opt. Engin. 19, 297-305 (1980)

Reconstruction methods for phase-contrast tomography

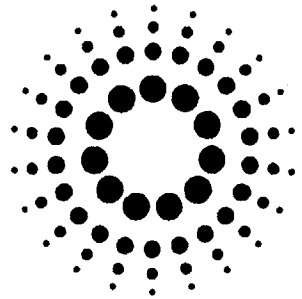

Workshop on
High Resolution X-ray Computed Tomography
LBNL, Berkeley, CA
August 12-13, 1996

Carsten Raven
European Synchrotron Radiation Facility,
Grenoble, France

Summary

Image Formation with Coherent X-rays

- phase contrast imaging in outline mode
- holography

Tomography in Outline Mode

Phase Reconstruction from Holograms

Holographic Tomography

Spatial Resolution

Coherent Properties of X-ray Beams at the ESRF

source size s ~ 100 μm
source distance R ~ 40 m
monochromaticity $\Delta\lambda/\lambda \sim 10^{-4}$ (with Si monochromator)

transversal coherence length $\Delta l = R\lambda / s \sim 25$ μm
longitudinal coherence length $\lambda^2/\Delta\lambda \sim 1$ μm

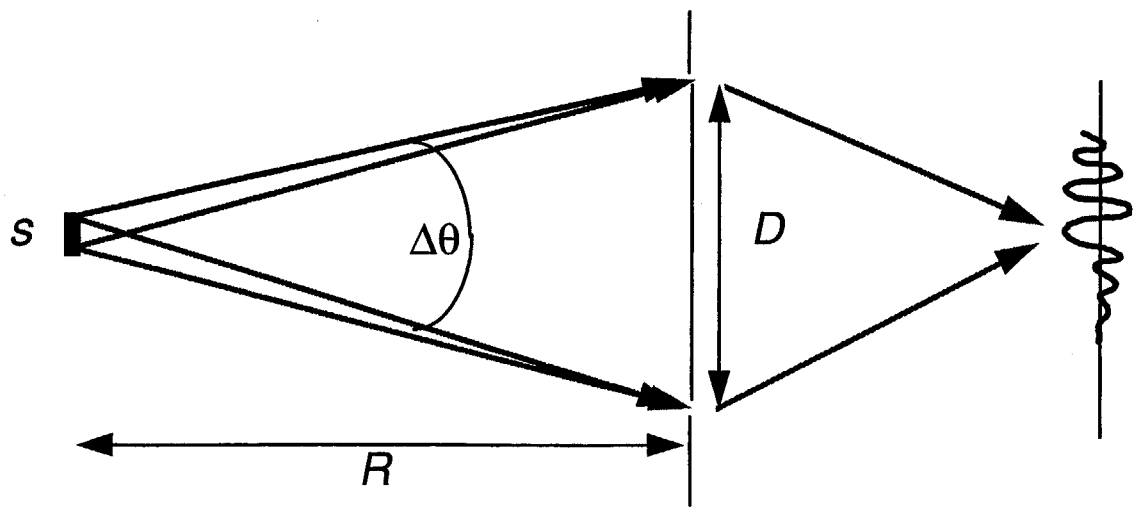

Interference if: $D < \Delta l$

or: $\Delta\theta \leq \frac{\lambda}{s}$

Image Formation

- superposition of the scattered wave with the undeflected incoming wave
- intensity distribution is a function of the object-to-detector distance:

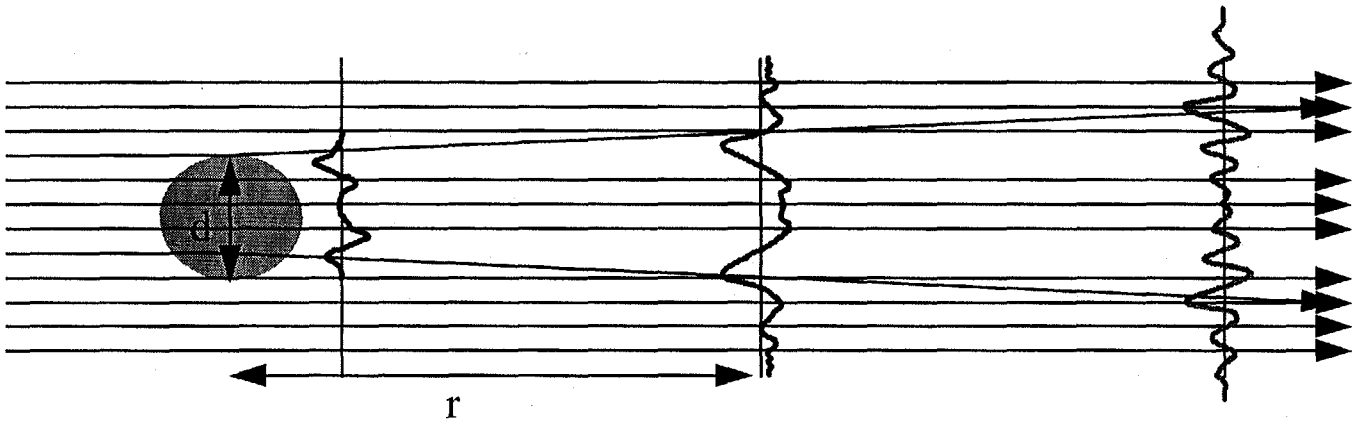

extreme near field:	near field Fresnel diffraction:	far field (Fraunhofer diffraction):
$r << d^2/\lambda$	$r \sim d^2/4\lambda$	$r >> d^2/\lambda$
only edges are visible	all parts contribute to contrast	form of interference pattern is constant

Outline Mode

Holography

Tomography in Outline Mode

Reconstruction of outline images

- Idea: phase-contrast images <=> absorption images of a hollow shell
- we will see the 3d distribution of edges and interfaces in the sample
- same tomographic reconstruction algorithms as for absorption tomography

Different preprocessing of the data

- in absorption tomography: use ln (I_0/I_θ) as input data: flatfield correction
- in outline-mode tomograpy:use $I_\theta - I_0$ as input data: flatfield substraction
  filter the projections with a differentiation filter

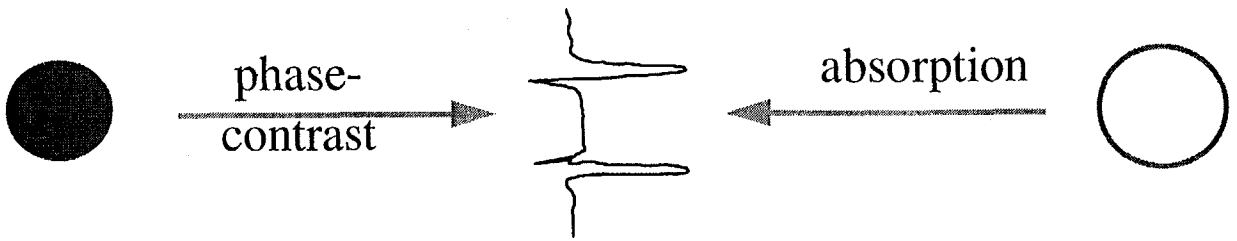

Tomography in Outline Mode

- Three hairs in a 20 keV beam, 8 cm recording distance
- 200 projections recorded on high resolution film (~ 1 μm)
- flatfield substraction (1)
- filtering with differential filter
- tomographic reconstruction with a convoluted backprojection algorithm (2)

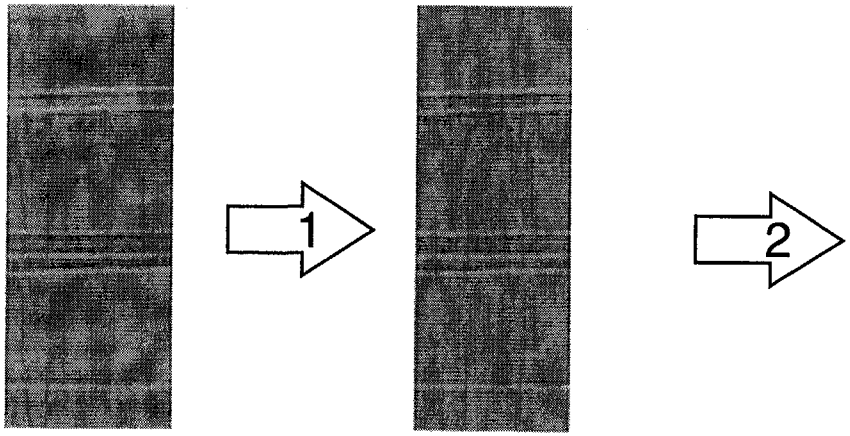

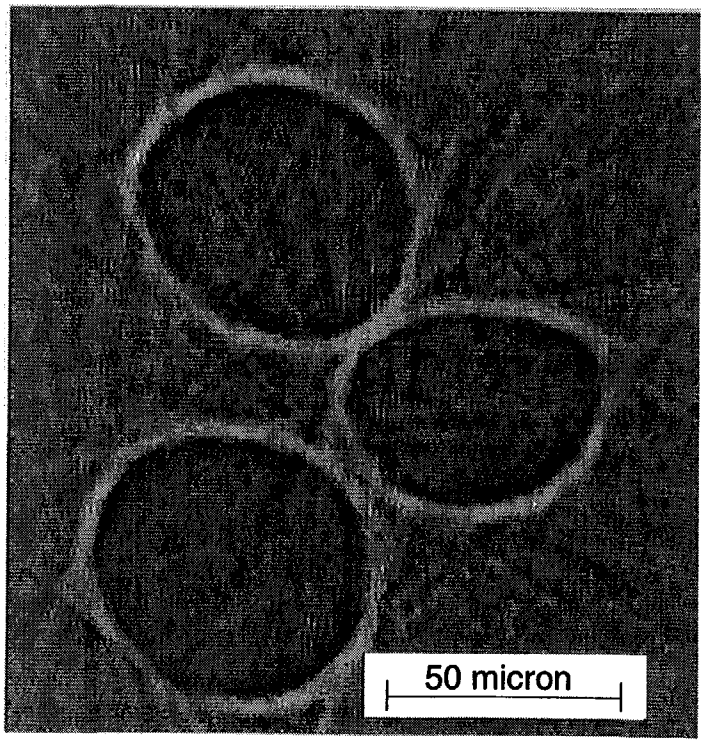

High-Resolution Tomography

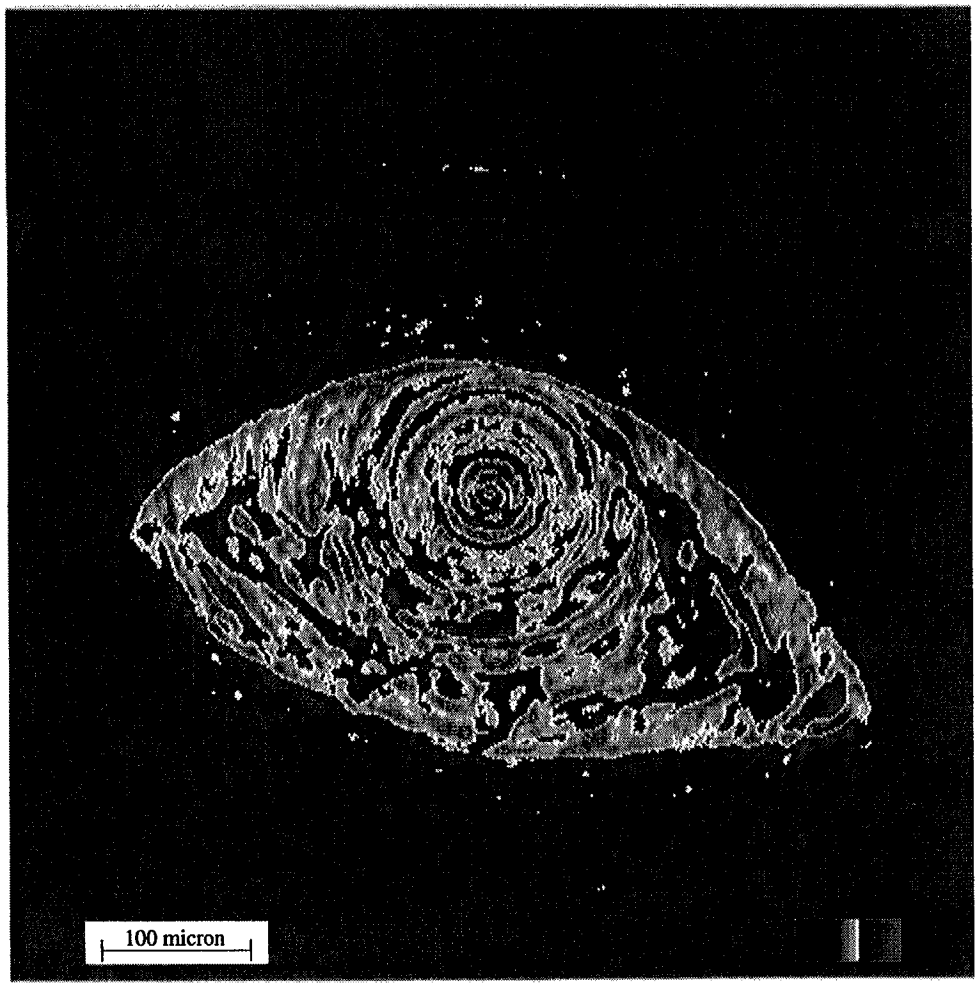

reconstruction of 400 phase-contrast images of foraminifer shell

images taken with a high-resolution slow-scan CCD camera

25 keV and 8 cm distance

resolution ~ 5 μm

recording time 30 sec per image

Holographic Tomography

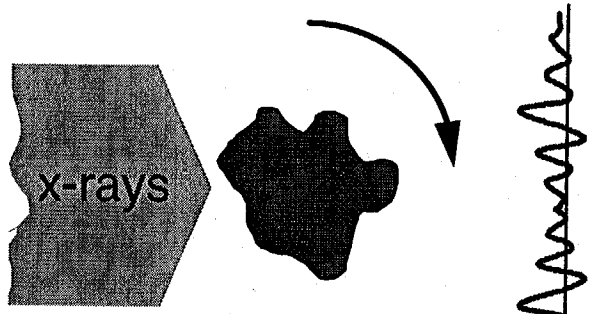

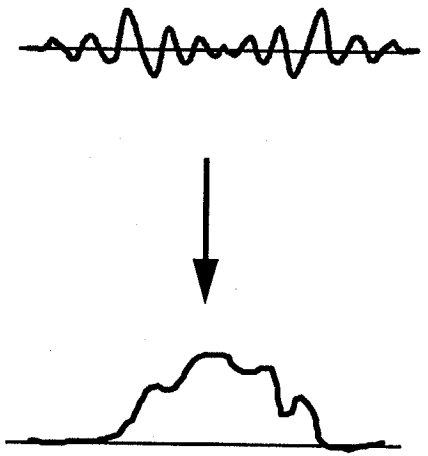

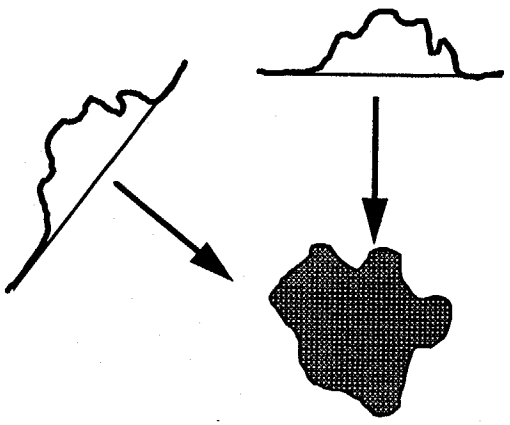

record holograms of different angles of view + flatfield images

for each projection, reconstruct the phase profile, i.e. reconstruct the integrated phase shift over the projection

reconstruct the diffractive index in the cross section from reconstructed phase profiles with a tomographic algorithm

Optical Reconstruction of Holograms

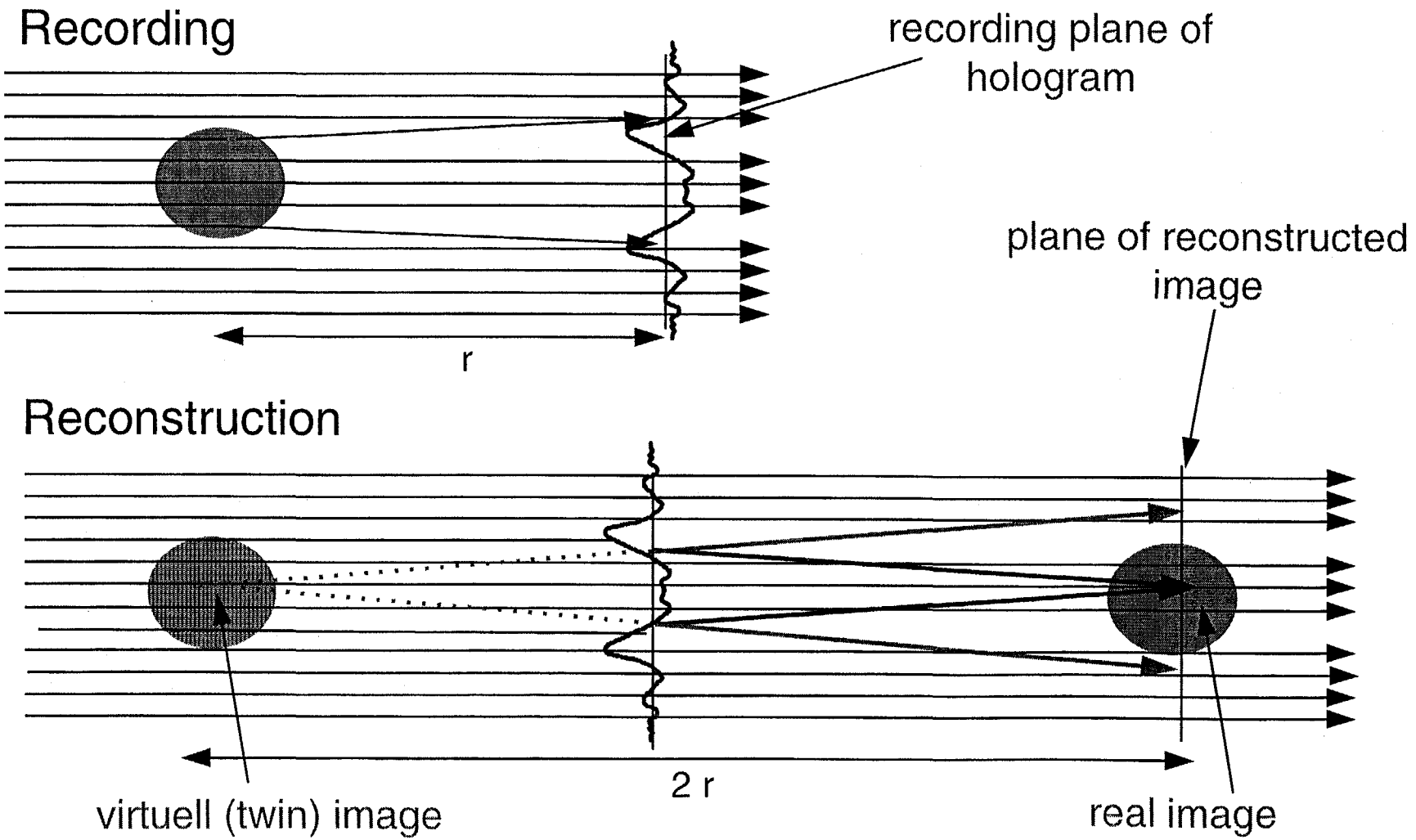

Numerical Reconstruction: an iterative method

- goal: to reconstruct the complex wave field in the object plane
  - known: amplitude of the wavefield in the object plane (by an absorption measurement)
  - known: modulus of the wavefield in the detector plane (hologram)
  - known: propagator function between both planes
  - unknown: phase of the wavefield in the object plane (given by the refractive index distribution in the sample)

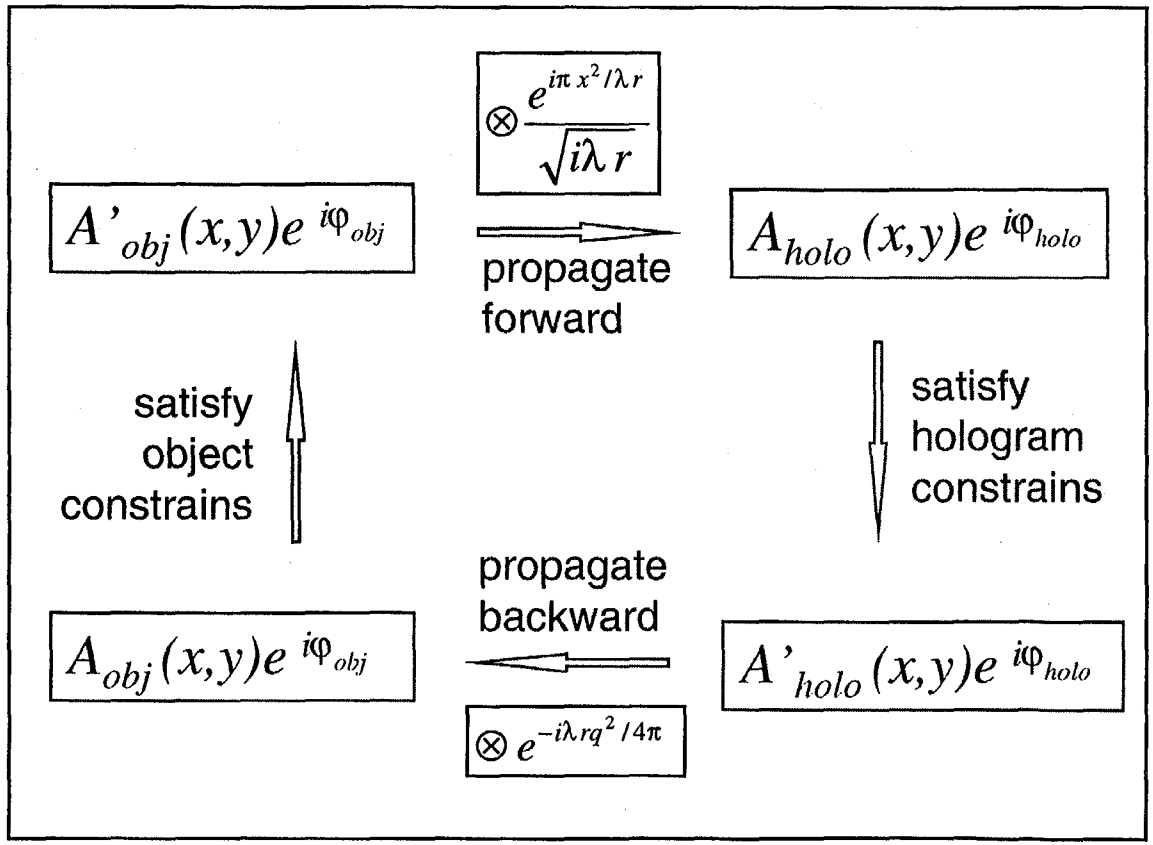

Testing the Algorithm

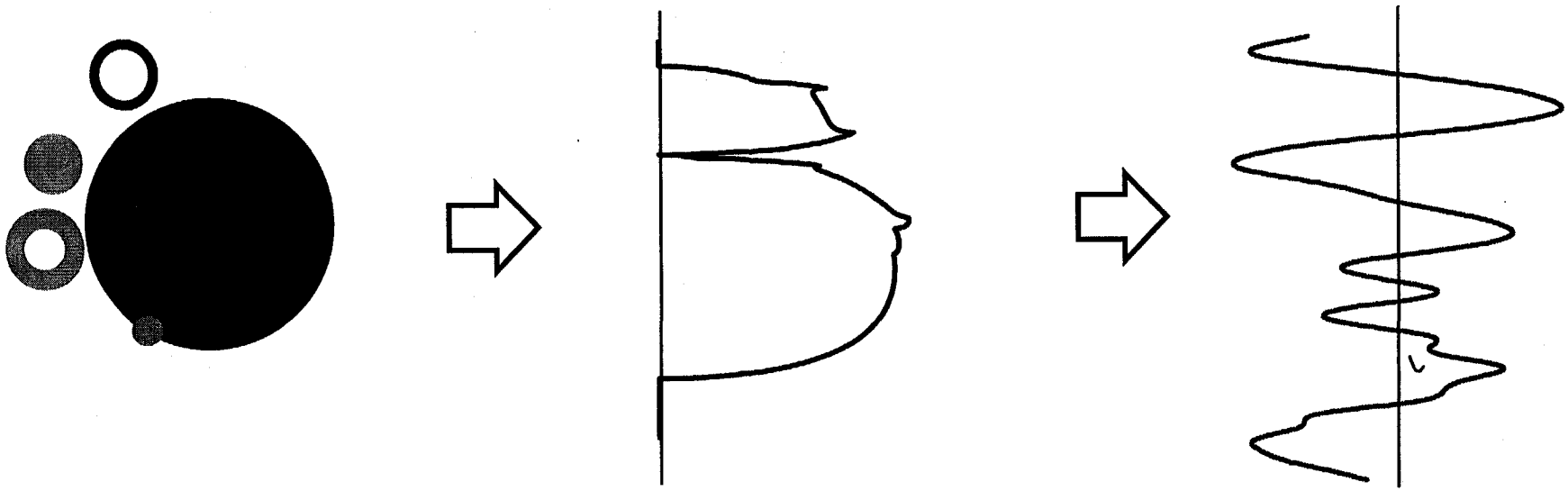

simulate
phase object δ *(x,z)*

- 5 fibers of 3 different materials (B, C, Si)
- diameters between 5 and 30 μm

calculate
phase profile

$$\varphi(x) = -\frac{2\pi}{\lambda}\int dz\,\delta(x,z)$$

calculate
hologram

$$e^{i\varphi(x)} \otimes \frac{e^{i\pi x^2/\lambda r}}{\sqrt{i\lambda r}}$$

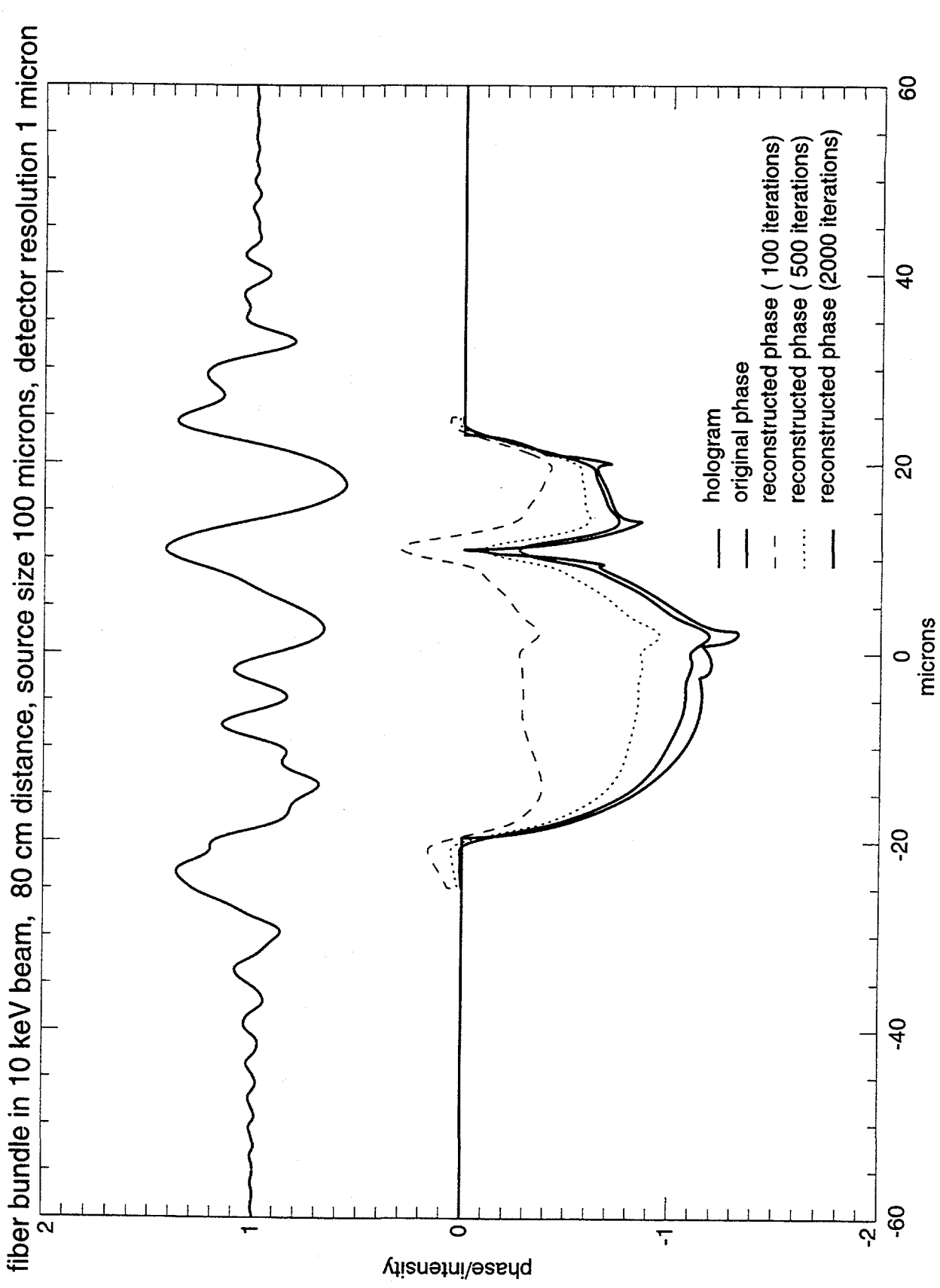
fiber bundle in 10 keV beam, 80 cm distance, source size 100 microns, detector resolution 1 micron
phase/intensity
microns
hologram
original phase
reconstructed phase (100 iterations)
reconstructed phase (500 iterations)
reconstructed phase (2000 iterations)
2
1
0
-1
-2
-60
-40
-20
0
20
40
60

Tomographic Reconstruction of Simulated Holograms

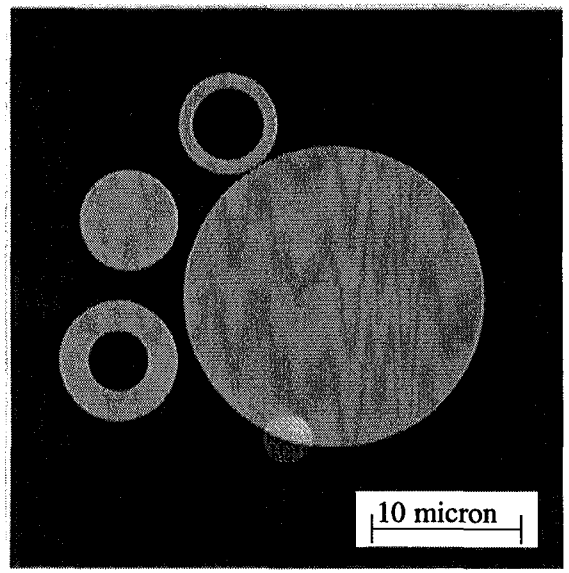

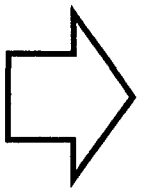

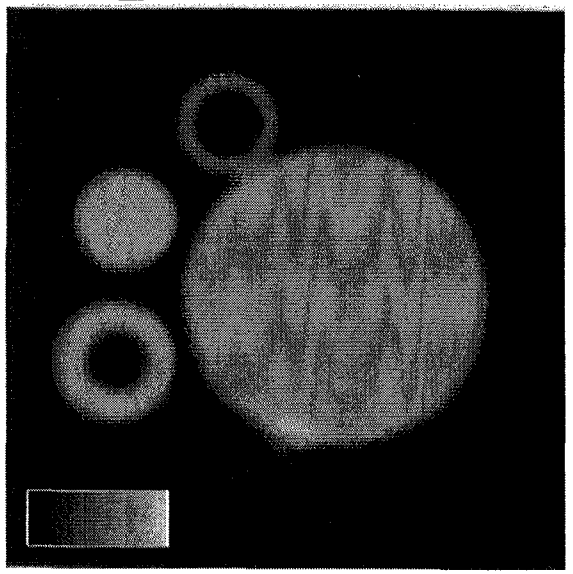

tomographic reconstruction from calculated phase profiles

tomographic reconstruction from reconstructed phase profiles

Parameters of Simulation:
- 10 keV beam
- 80 cm distance
- 100 μm source size
- 1 μm detector resolution

1. Calculation of 200 holograms for 200 different directions of projection
2. Reconstruction of the phase profile by means of an iterative method
3. Tomographic reconstruction of the cross section with a filtered backprojection algorithm

Spatial Resolution

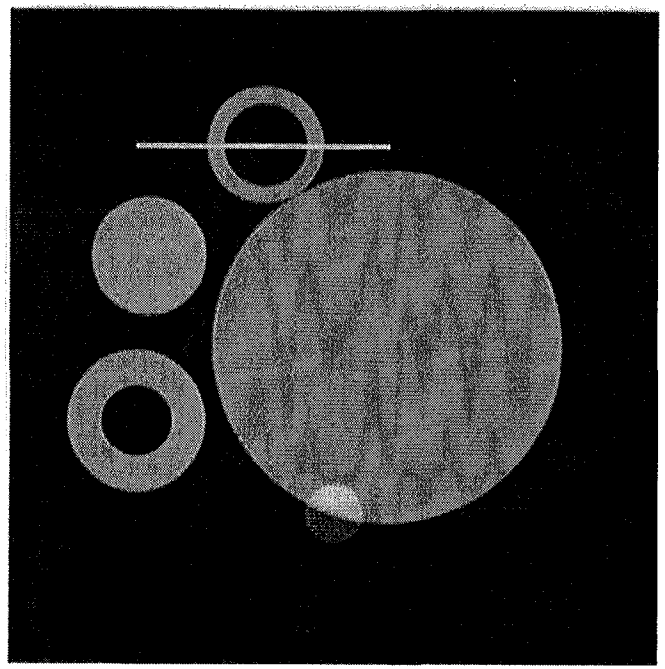

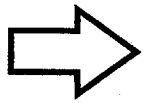

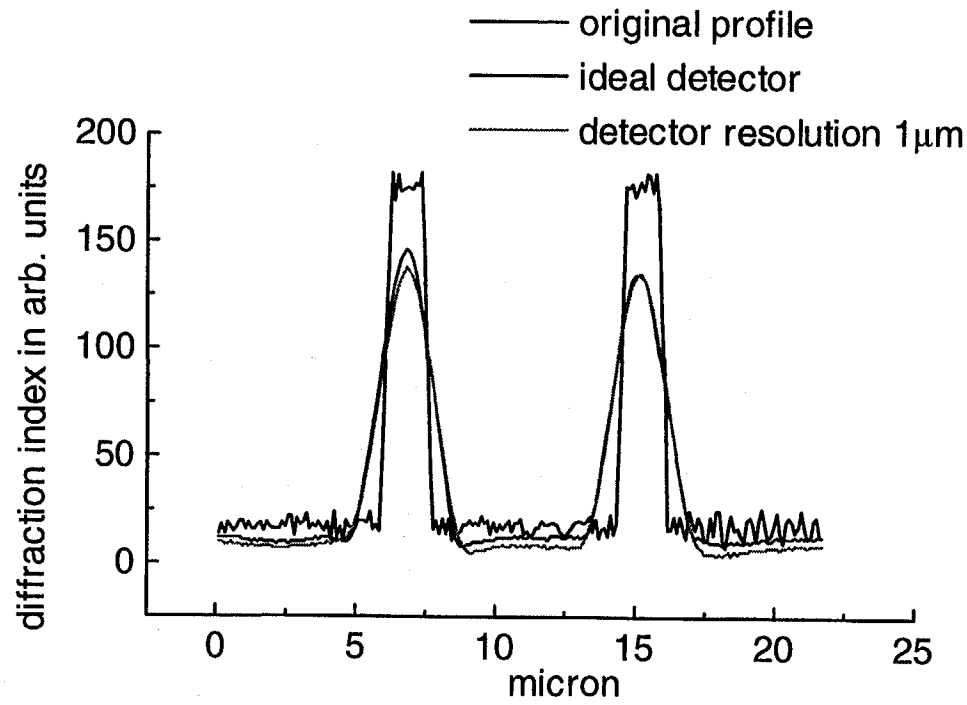

it's not only the detector!

Limits

	today	future	limiting
source size:	80 μm	50 μm	beam emittance, vertical coupling
demagnification factor:			
object-to-detector distance	1 m	50 cm	reconstruction algorithm
source-to-object distance	40 m	50 m	length of beamlines
	= 2.5 μm	= 0.5 μm	
detector resolution:			
high resolution film	1 μm	1 μm	cornsize, dynamic range
CCD - camera	8 μm	2 μm	fluorescence screen
max. object size:	100 μm	500 μm	reconstruction algorithm
beam inhomogenities			
vacuum windows			surface finish of windows
optical elements in the x-ray beam			surface roughness

X-Ray Gabor Holography

Steve Lindaas and Malcolm Howells
Advanced Light Source
Lawrence Berkeley National Laboratory

Brandoch Calef and Dan Pinkas
University of California at Berkeley

Chris Jacobsen
Physics Department
SUNY at Stony Brook

Supported by:
DOE Alexander Hollander post-doctoral Fellowship (SL). Presidential Faculty Fellowship (CJ), the NSF Grant No. BIR-9316594, and the DOE Grant No. DE-FG02-89ER60858.

dp.sl/titlepage/8-96

DIFFRACTION TOMOGRAPHY VIA SOFT X-RAY HOLOGRAPHY

- **HISTORY**
- **HOLOGRAPHY EXPERIMENTS**
- **READOUT**
- **RADIATION DOSE LIMITATIONS**
- **SXR DIFFRACTION TOMOGRAPHY: PRINCIPLES**
  - **Born approximation**
  - **Rytov approximation**
- **PROGRESS IN IMPLEMENTATION**
  - **Cryoholography experiments**
  - **Results**
- **PROGRESS IN TWIN-IMAGE SUPPRESSION**

X-RAY HOLOGRAPHY: HISTORY

1948	**Invention of holography D. Gabor**
1952	**Suggestion to record holograms with x-rays and reconstruct the image with visible light, A. Baez**
1960's	**Invention of the laser and off-axis holography but failure to do x-ray holography with good resolution**
1972	**First hologram made with SR (Aoki and Kikuta 1972), recognition of the spatial coherence advantages of SR**
1980's	**Gabor holography at submicron radiation at Orsay and Brookhaven** **• Undulators** **• Resists**
1990's	**Fourier-transform x-ray holograms and 3D reconstructions (McNulty, Trebes, Haddad)** **Atomic-force-microscope readout (Lindaas)** **Hard x-ray Gabor holography (ESRF)**

X-ray Holography: Results of Denis Joyeux (Institut d'Optique, CNRS) and Francois Polack (LURE, CNRS)

SEM of silica skeleton of diatom

Interference micrograph of a hologram recorded at 100 Å.

Image reconstructed using a 6320 Å laser (48 × 63 μm^2 field).

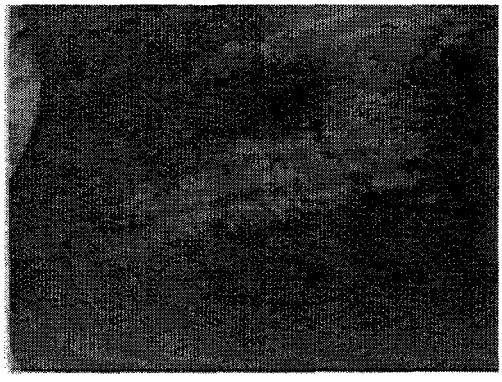

X-ray Gabor (in-line) Holography

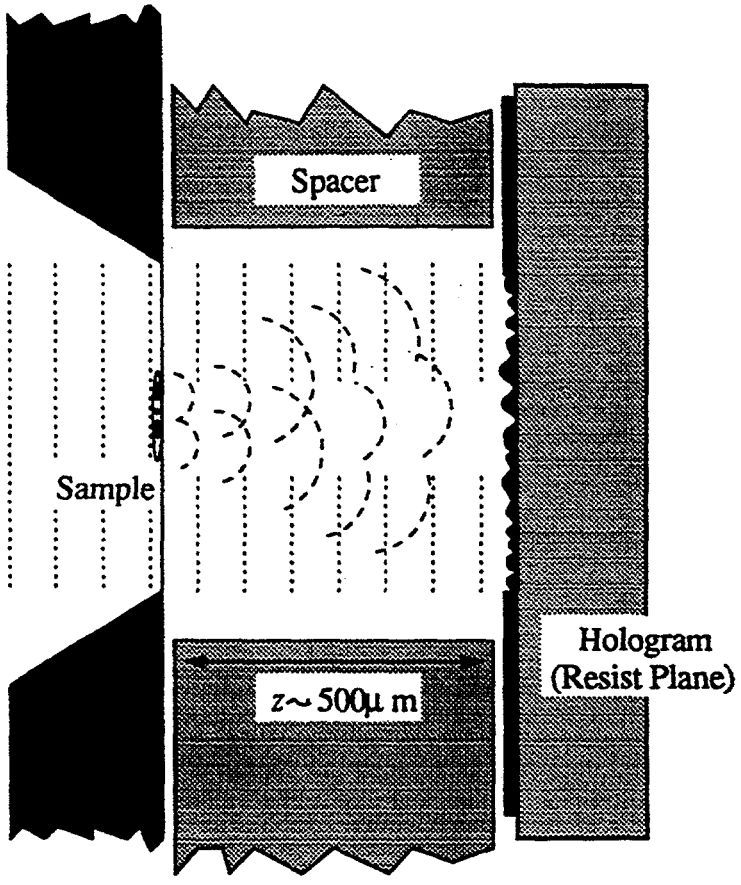

- No pre-focusing (no imaging optics)
- Multimode
- Resolution potential
- Compatible with one-shot imaging
- Numerical reconstruction:
  - Aberration-free
  - Simultaneous phase and amplitude images obtained
- o Disadvantage: Twin-image artifact

THE TWIN IMAGE SIGNAL

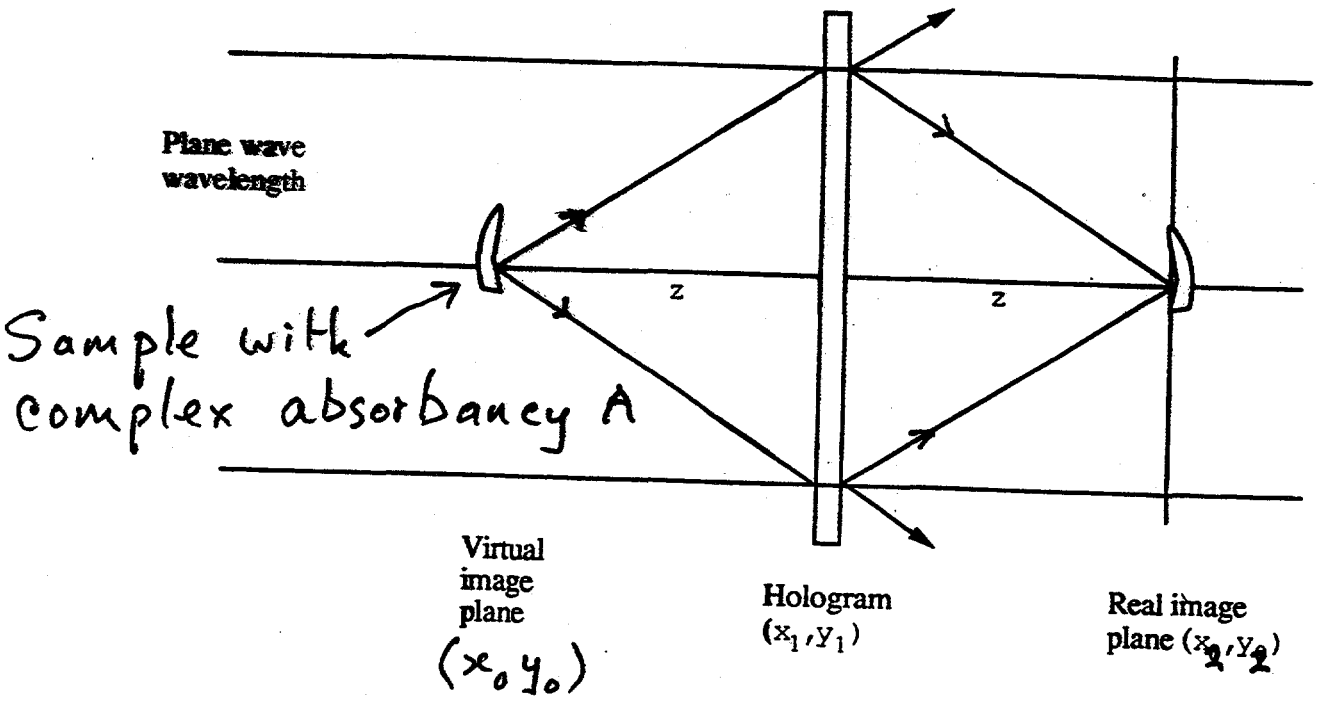

At the hologram the intensity $I_H(\mathbf{x}_1) = \left| r\,(1 - A(\mathbf{x}_0)) \otimes \frac{1}{i\lambda z}\, e^{\frac{i\pi|\mathbf{x}_0|^2}{\lambda z}} \right|^2_{\mathbf{x}_1}$

Now reconstruct with the original reference wave - the field at the real image plane is

$$E(\mathbf{x}_2) = r^3 \left\{ 1 - A(\mathbf{x}) \otimes \frac{1}{2i\lambda z} e^{\frac{i\pi|\mathbf{x}|^2}{2\lambda z}} \Big|_{\mathbf{x}_2} - A^*(\mathbf{x}_2) + \ldots \right\}$$

Leads to the correct real image plus a second hologram at distance $2z$

Scanning Force Microscopy

Steve Lindaas

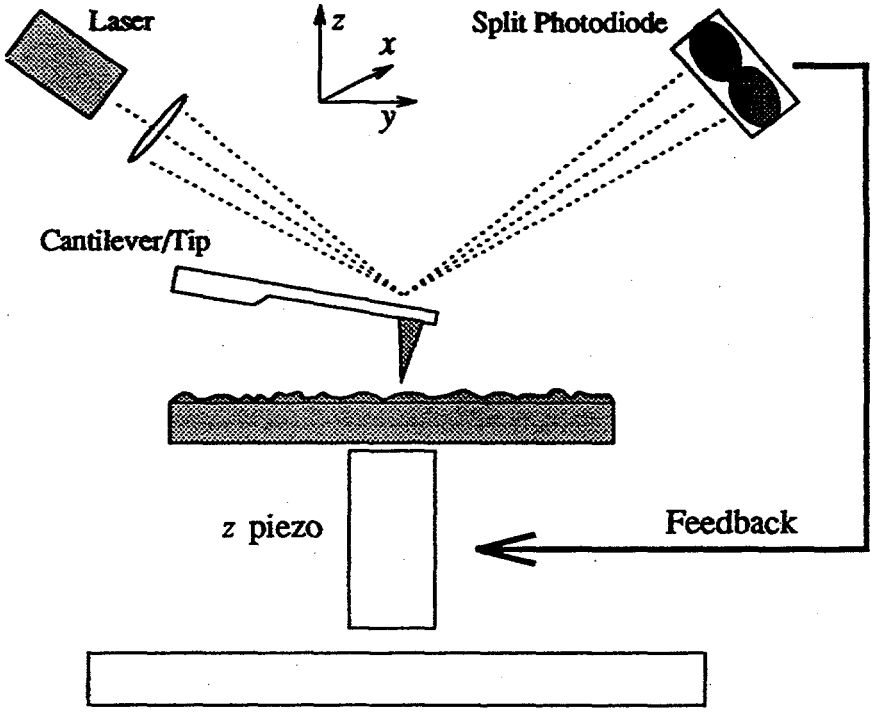

Weak Cantilever < 0.1 N/m
Typical Deflection < 1μm

Contact and Noncontact Operating Modes

Atomic Force Microscope

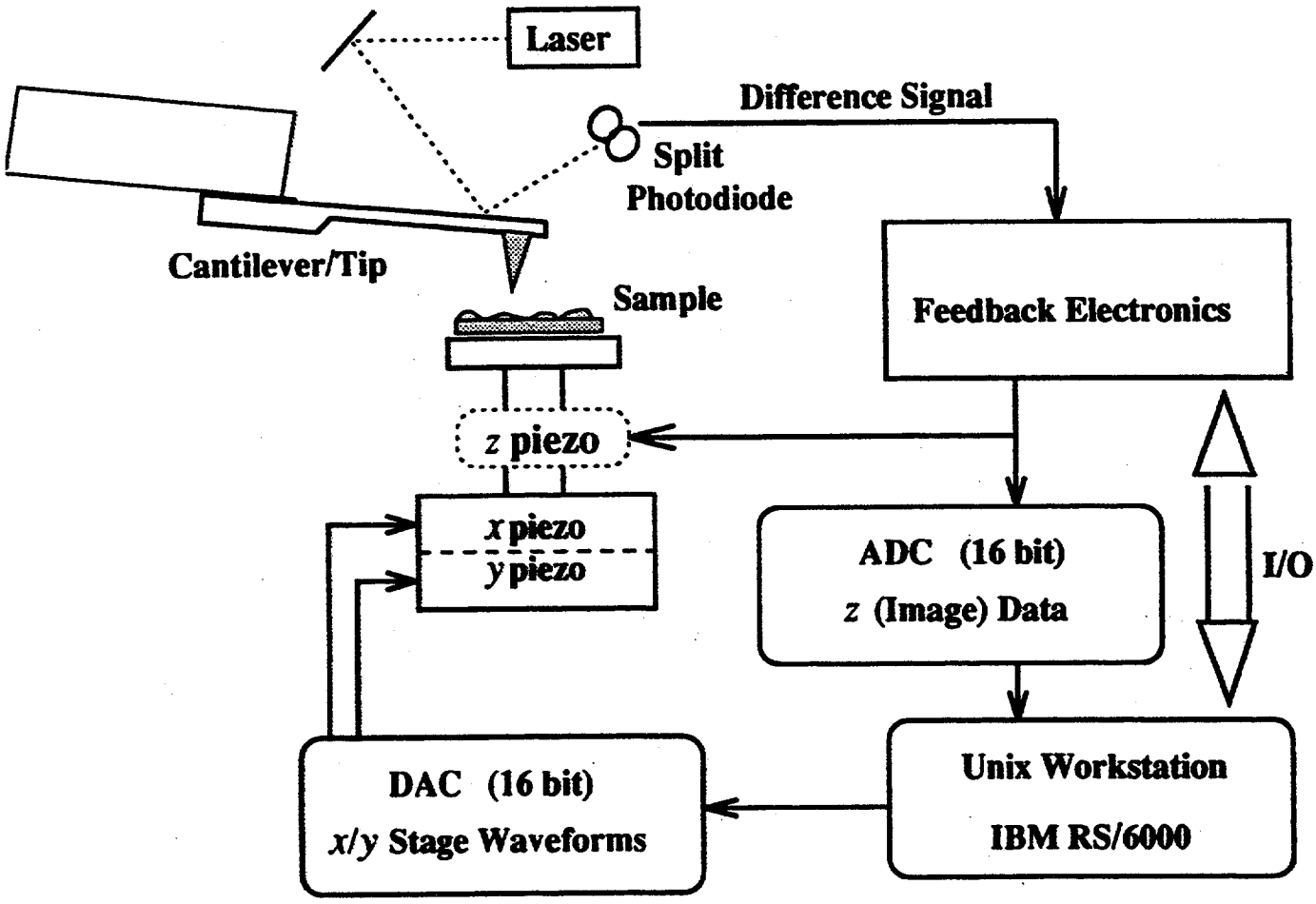

Custom Features:

- Linear stage - bettter than 5 parts in 10^4
- Large scan field
- Controlled by UNIX workstation
  - No limits on size of dataset
  - Computational power

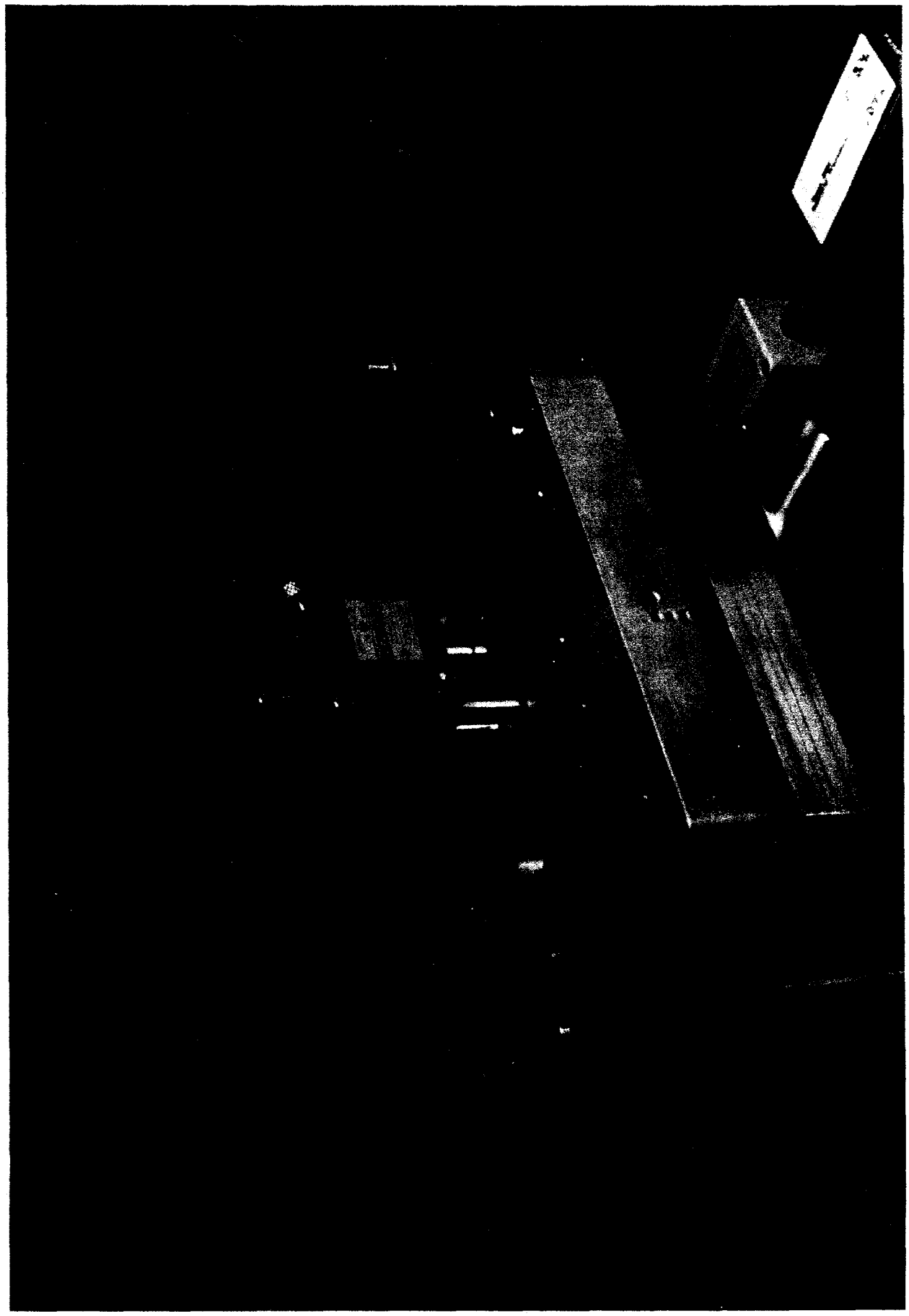

Atomic Force Microscope

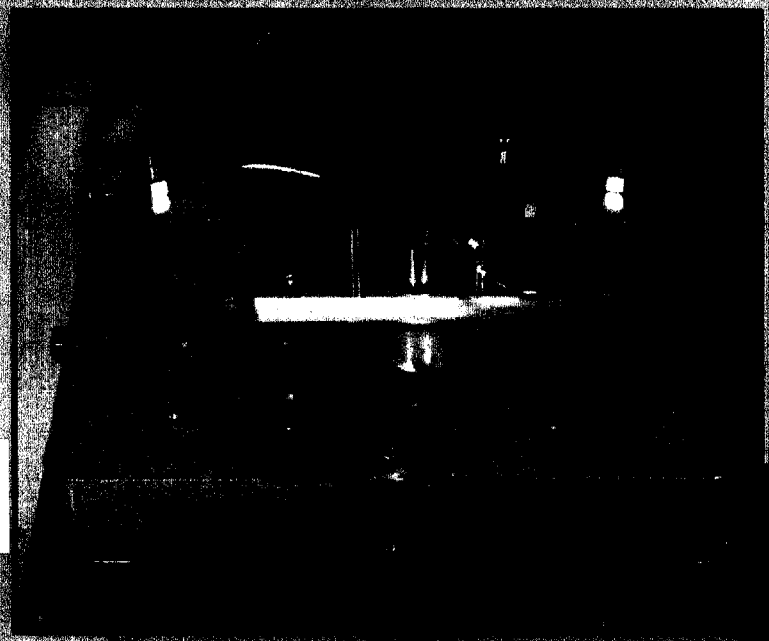

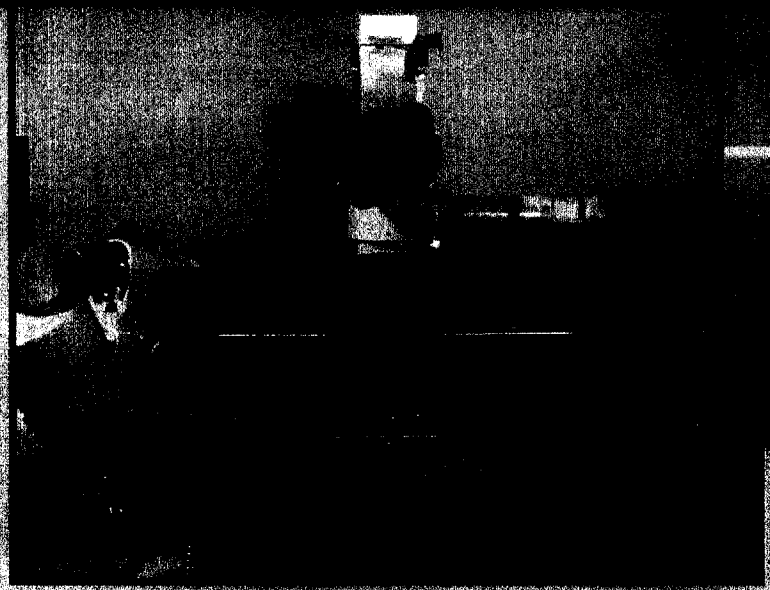

ag.sl/afm/8-96

Gabor x-ray holography using photoresists

S. Lindaas and M. Howells, Advanced Light Source, Lawrence Berkeley Laboratory
C. Jacobsen and A. Kalinovsky, Stony Brook Physics

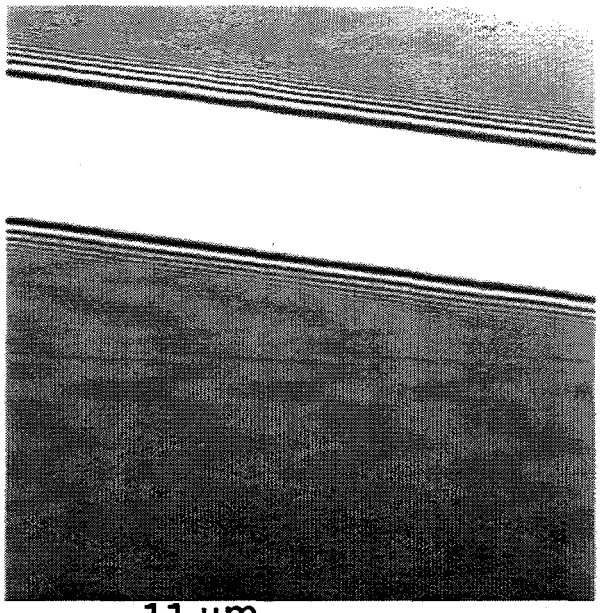

(400 pixels × 0.15μm)^2

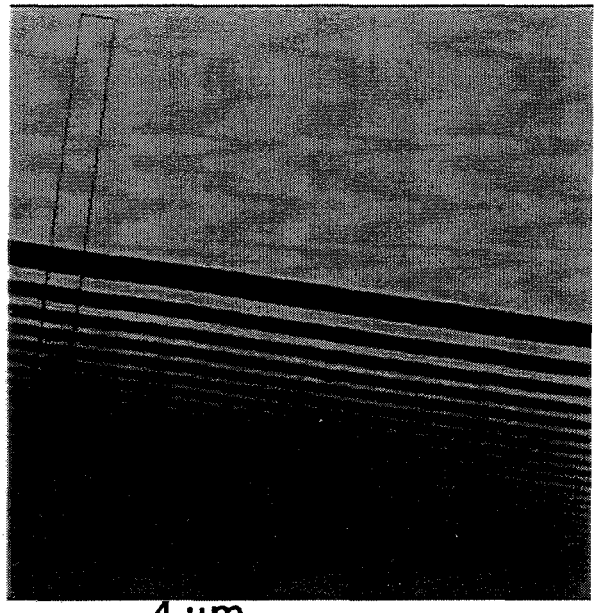

(512 pixels × 0.04μm)^2

Gold wire (diameter = 12μm) exposed on PMMA using λ = 1.89 nm x-rays.

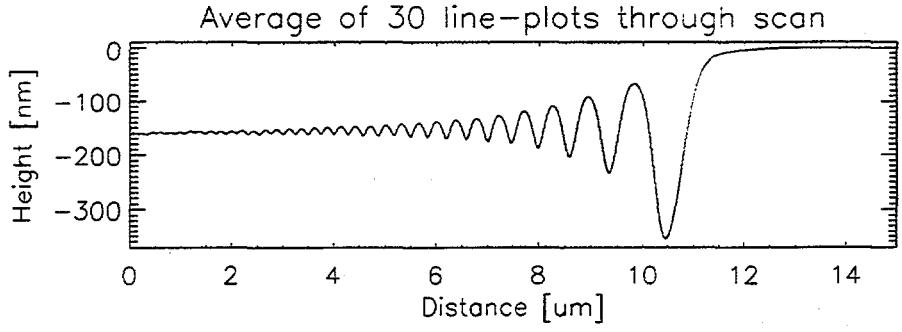

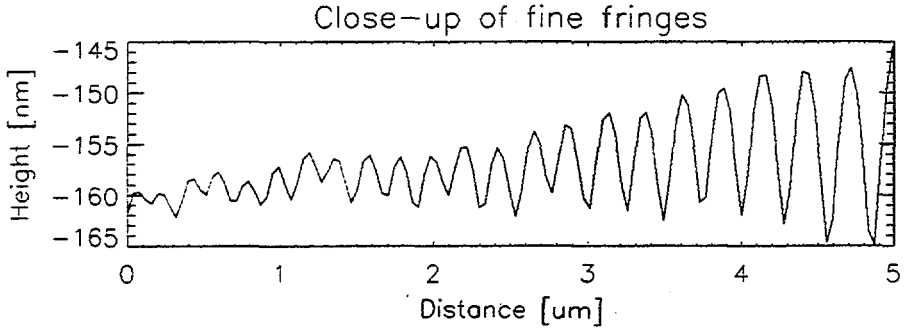

Resoluition Test — Diatom

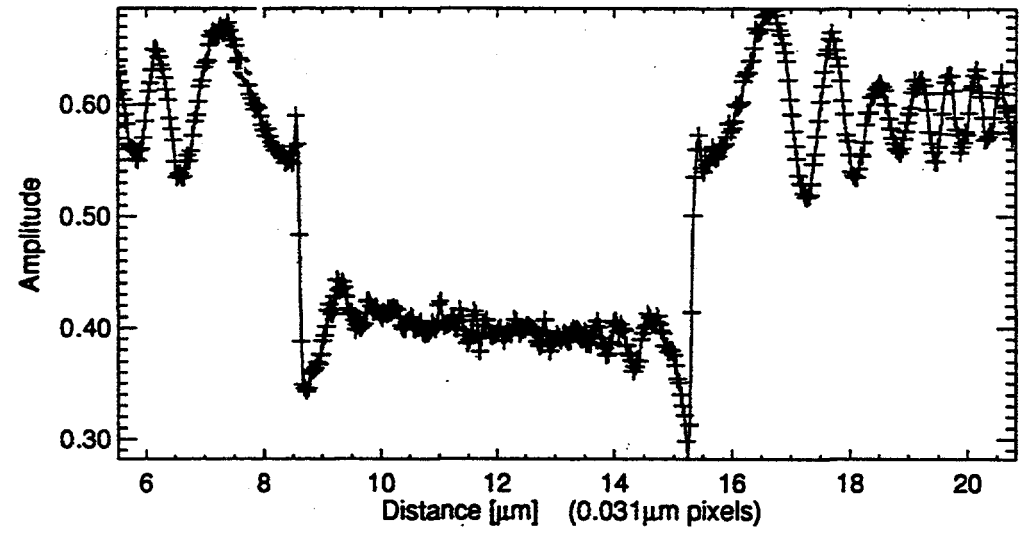

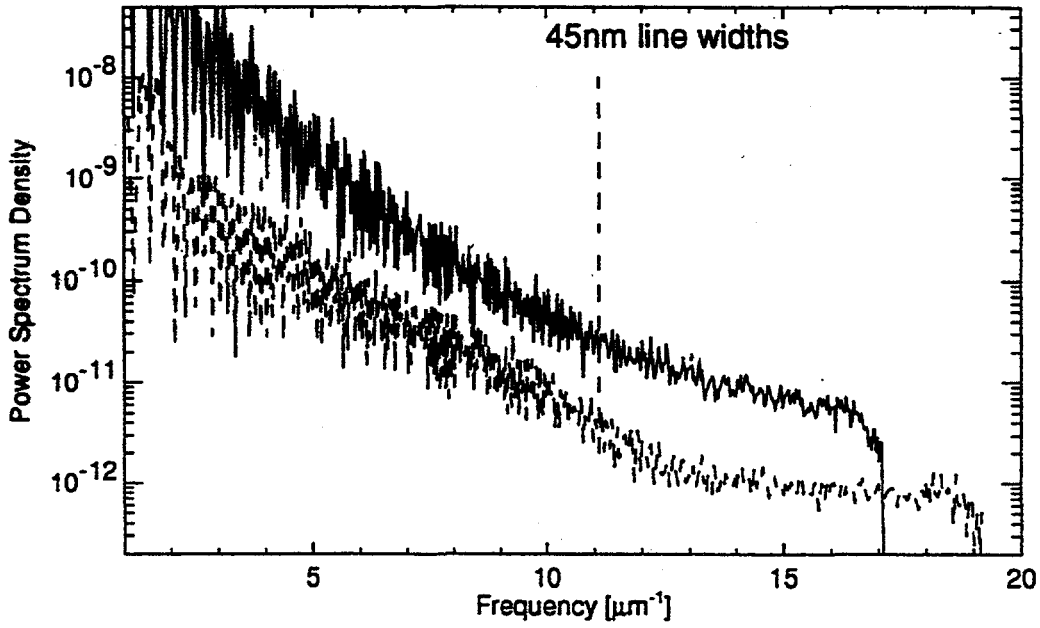

X-Ray Gabor (in-line) Holography

S. Lindaas†, M. Howells†, C. Jacobsen‡ and A. Kalinovsky‡ († LBL, ‡ Stony Brook)

Comparative microscopy on critical point dried NIL cell.

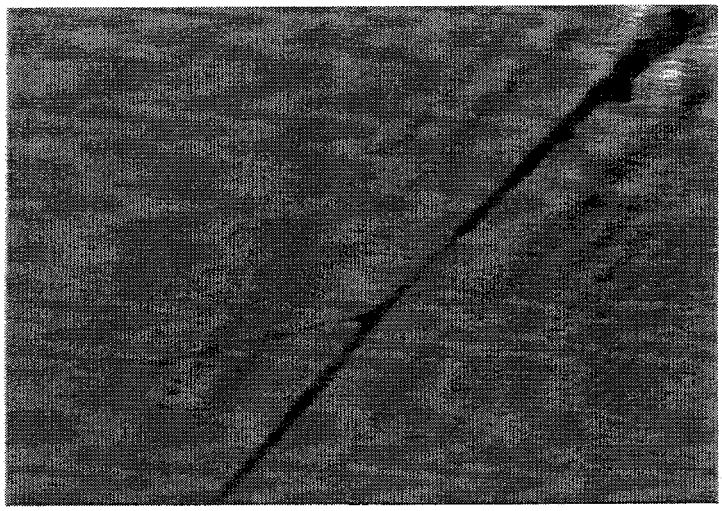

X-ray image:

Recorded in photoresist ($z = 415\,\mu m, \lambda = 1.89\,nm$) and scanned using a custom atomi force microscope.

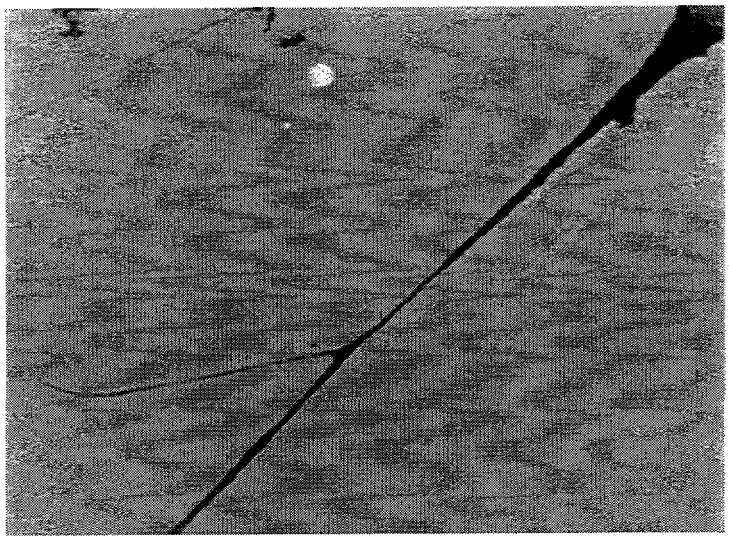

TEM image:
magnified 3000×

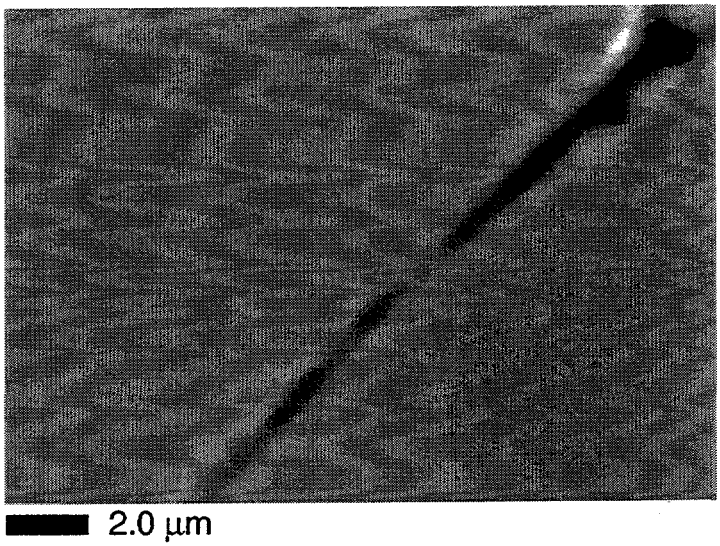

Optical image:
100×, N.A. = 0.90 objective

LIMITATIONS DUE TO RADIATION DOSE

- **Single hologram with resolution 200-400 Å: $> 10^8$ rads**
  slow imaging of natural material not possible

- **Can image fixed or dried material**

- **Can image frozen hydrated samples at LN_2 temperature including multiview diffraction tomography experiments: (10^{10} rads allowed)**

- **Can use a pulsed source for single-view imaging of natural material**

- **The ultimate possibility: single-shot, multiview tomography, (needs a high-gain free-electron laser)**

DIFFRACTION IN THE BORN APPROXIMATION

(Mott and Massey 1950)

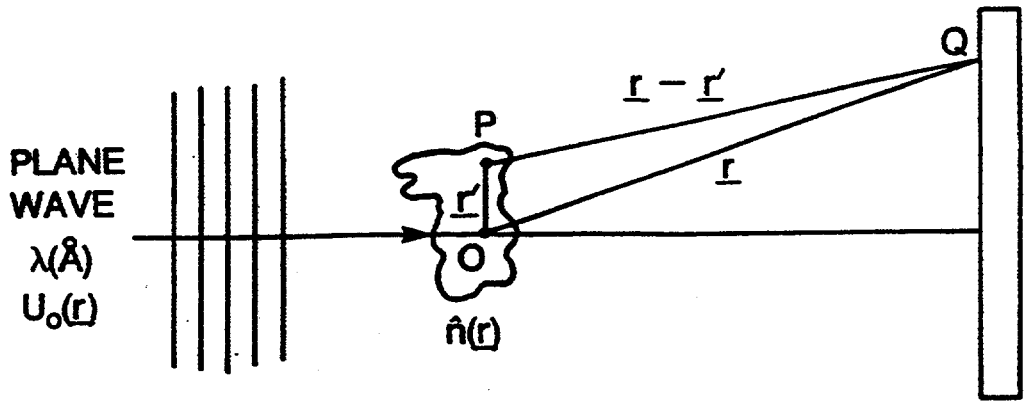

Free space: $\nabla^2 U_0 + k_0^2 U_0 = 0$

Medium of index n: $\nabla^2 U + k_0^2 U = \left(1 - n^2\right) k_0^2 U$

$(k = n k_0)$

Substitute: $U = U_0 + U_1 \qquad n = n_0 + n_1$

Now subtract the free-space form and drop second order small quantities

$$\nabla^2 U_1 + k_0^2 U_1 = -2 k_0^2 n_1 U_0$$

At Q we now get:

$$U_1 = -\frac{k_0^2}{4\pi} \int_{obj} \frac{e^{ik_0|\mathbf{r}-\mathbf{r}'|}}{|\mathbf{r}-\mathbf{r}'|} n_1 U_0 \, d^3\mathbf{r}'$$

Green's function — Scattering potential

Approximations: $n_1 \ll n_0$ **Always OK for x-rays (n_0=1)**

$U_1 \ll U_0$ **Weak scattering and weak absorption**

If these are valid: $U_1 \left(\equiv U_S^B\right) \cong$ **the measured scattered field**

X-RAY VALIDITY: **HARD X-RAY: VALID**

SOFT X-RAY: NOT VALID

DIFFRACTION IN THE RYTOV APPROXIMATION

(Tatarski 1961, Devaney 1986)

Helmholz equation: $\nabla^2 U + k_0^2 U = \left(1 - n^2\right) k_0^2 U$

Substitute: $U = e^{\psi}$

Ricatti equation: $\nabla^2 \psi + (\nabla \psi)^2 + k_0^2 = \left(1 - n^2\right) k_0^2$

Substitute: $\psi = \psi_0 + \psi_1 \qquad n = n_0 + n_1$

Now subtract the free-space form and drop second order small quantities

$$\nabla^2 (U_0 \psi_1) + k_0^2 (U_0 \psi_1) = -2 k_0^2 n_1 U_0$$

This is the same as before with

$$U_1 = U_0 \psi_1$$

Approximations: $n_1 << n_0$ **Aways OK for x-rays (n_0=1)**

$|\nabla \psi_1| << |\nabla \psi_0|$ **but** $\psi_0 = ik_0 r$ **so** $|\nabla \psi_0| = k_0$

So the validity condition for the Rytov approximation is

$|\nabla \psi_1| \lambda << 2\pi$

phase
change
per λ

X-RAY VALIDITY: **HARD X-RAY: VALID**

SOFT X-RAY: VALID

Optical Properties of Biological Materials at 3 nm

	Water	Protein	DNA	Lipid	Carbohydrate
Index real part (δ)[a]	0.0010	0.0015	0.0017	0.0012	0.0017
Index image part (β)[a]	0.000047	0.00057	0.00076	0.00038	0.00039
Phase change per wavelength ($2\pi\delta$) rad	0.0063	0.0094	0.011	0.0078	0.011
Attenuation per wavelength ($4\pi\beta$)	0.00059	0.0072	0.0095	0.0048	0.0049
Absorption length (μm)	5.1	0.42	0.32	0.36	0.61
Phase change per absorption length ($\delta/2\beta$) rad	10.7 (2.1 per μm)	1.3	1.1	1.62	0.2

[a]The complex refractive index is taken to be $1-\delta-i\beta$.

SOLUTION TO THE INVERSE PROBLEM

Born Approximation:

$$U_s^B(\underline{r}) = \frac{k_o^2}{2\pi} \iiint_{\text{object}} \frac{\exp ik_o |\underline{r} - \underline{r}'|}{|\underline{r} - \underline{r}'|} \hat{n}_1(\underline{r}') U_o(\underline{r}') \, d^3\underline{r}'$$

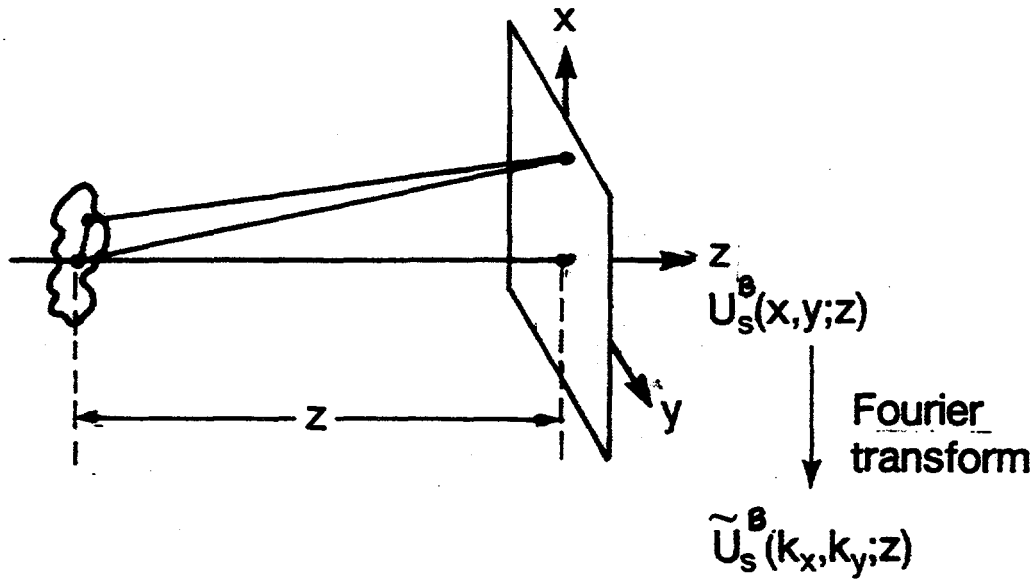

$$\tilde{n}_1(\underline{K}) = \frac{ik_z}{\pi} \exp\left[-ik_z z\right] \tilde{U}_s^B(k_x,k_y;z)$$

$$\underline{K} = \underline{k} - \underline{k}_o \quad , \quad k_z = \sqrt{k_o^2 - k_x^2 - k_y^2}$$

Wolf 1969

GENERALIZED PROJECTION-SLICE THEOREM

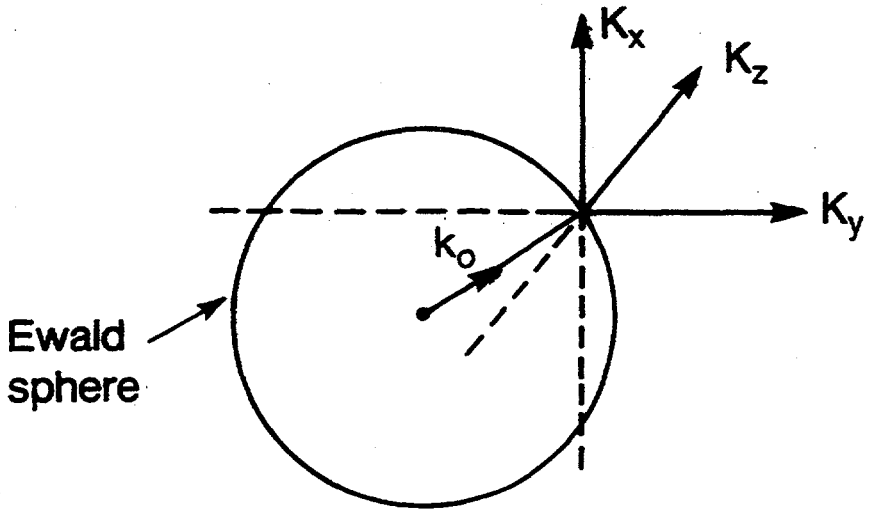

XBL 8611-9949

EXPERIMENTS

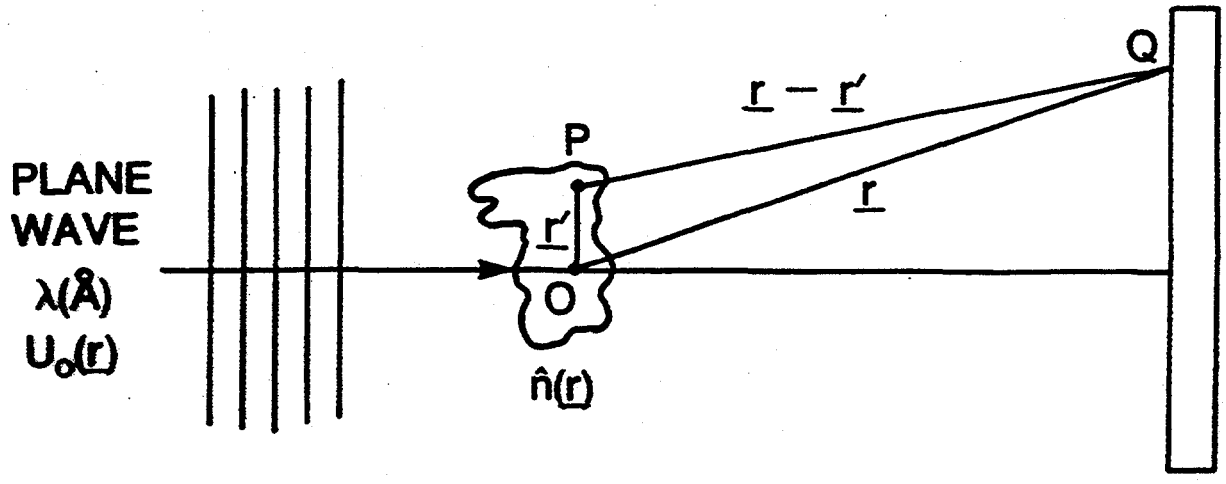

At each view we measure:

$$U = Ae^{iS}$$
$$U_0 = A_0 e^{iS_0}$$

Note <u>the phases are needed</u>: holography provides an approach to this

Two ways to derive $U_1\left(U_S^B\right)$ from the measured data

Born:

$$U_1 = U - U_0$$
$$= Ae^{iS} - A_0 e^{iS_0}$$

Rytov:

$$U_1 = U_0 \psi_1$$
$$= A_0 e^{iS_0}\left\{\ln\frac{A}{A_0} + i(S - S_0)\right\}$$

Either way the Generalised-Projection-Slice Theorem (or a more modern equivalent) could then be used to get $n_1(\mathbf{r})$.

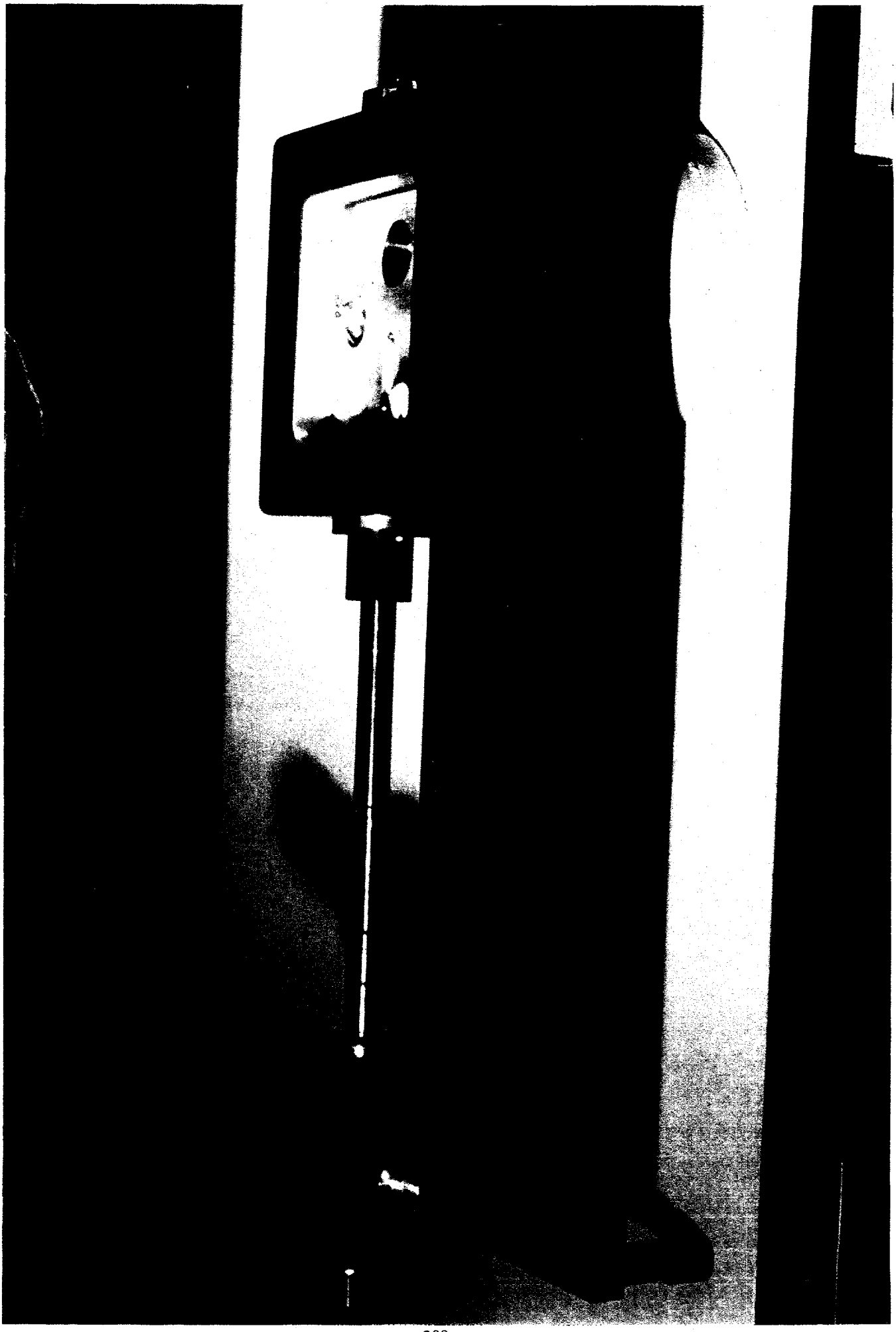

Cryo-Holography Sample Holder

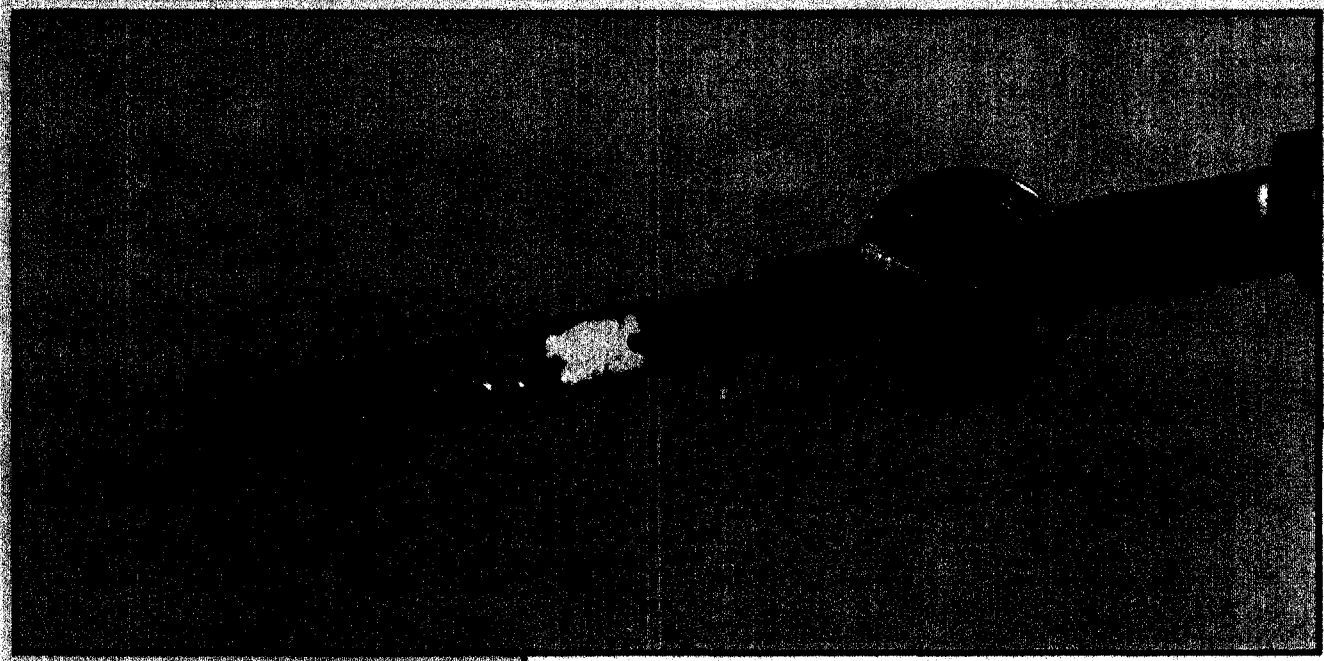

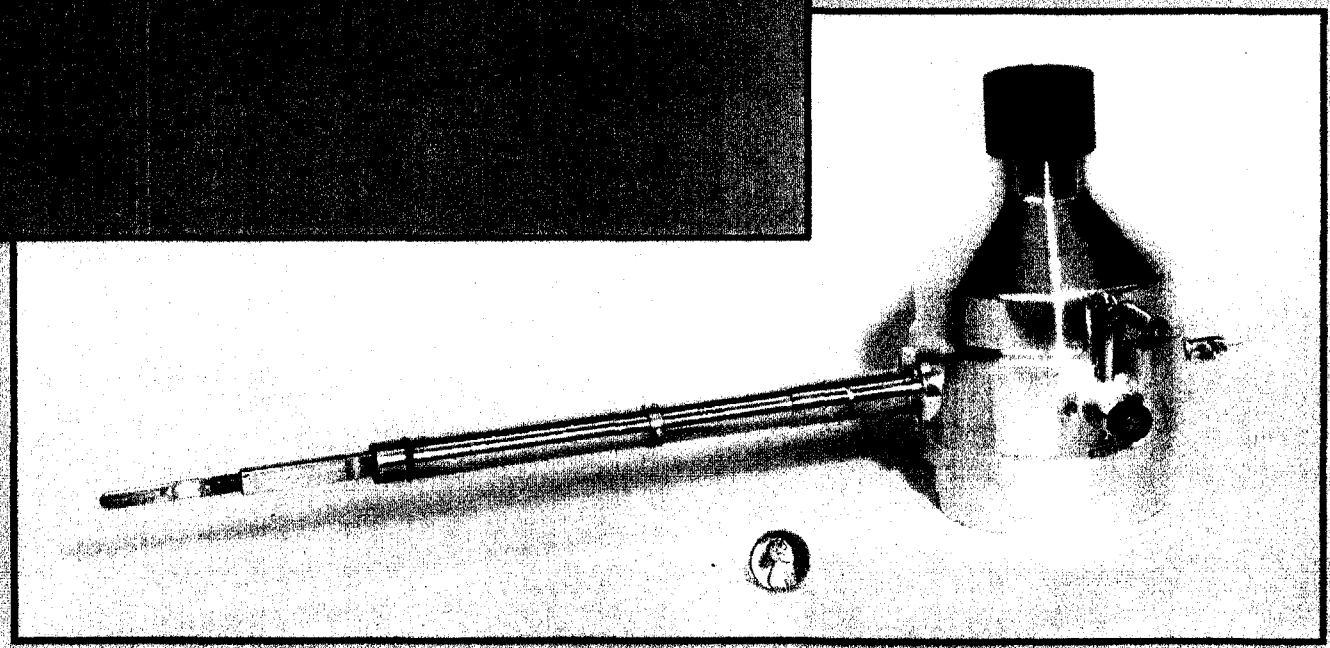

ag.sl/holder/8-96

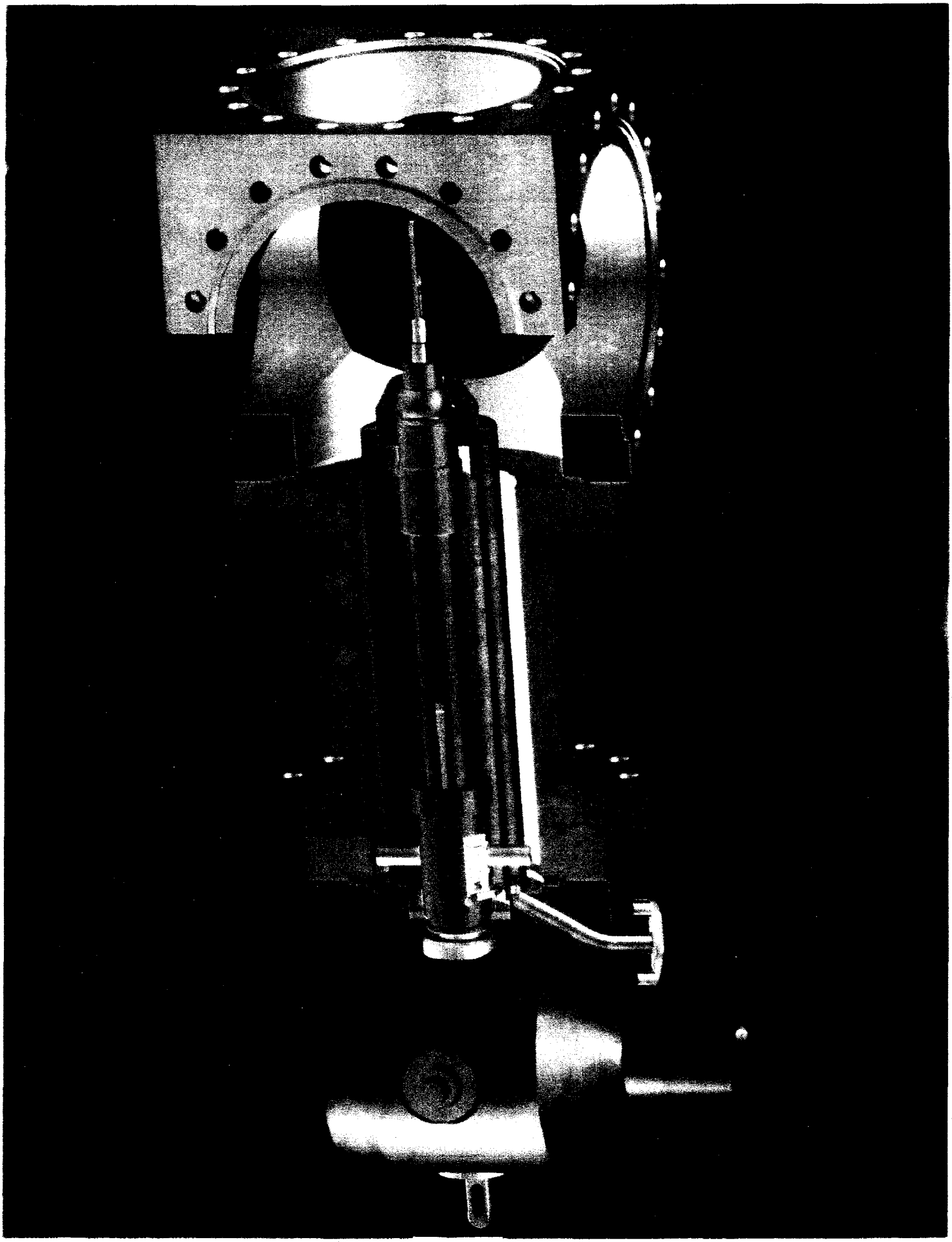

Cryo-Holography at NSLS X1A

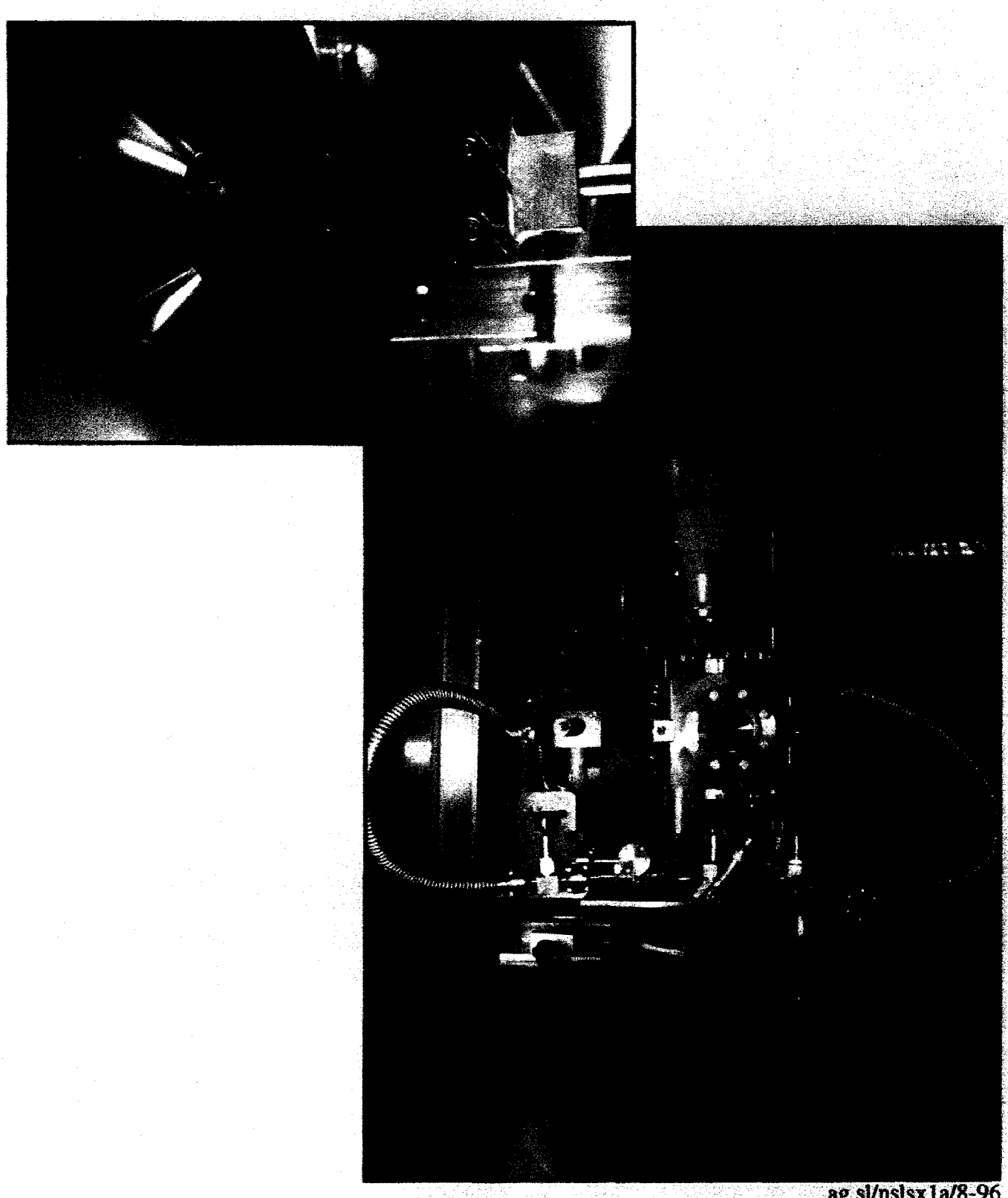

ag.sl/nslsx1a/8-96

Cryo-Holography Chamber

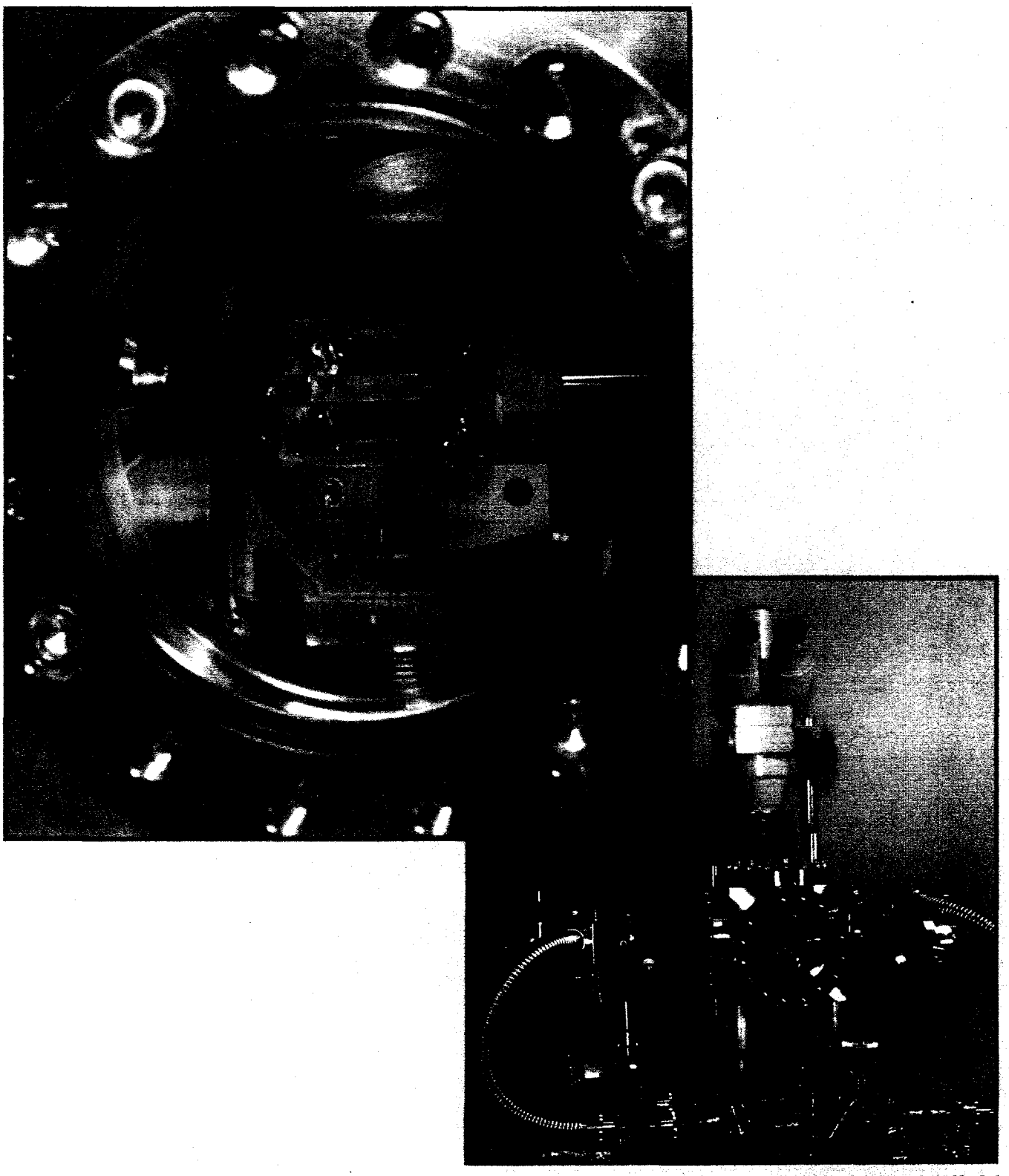

ag.sl/cryochamber/8-96

Cryo-Holograms of Malaria infected RBC

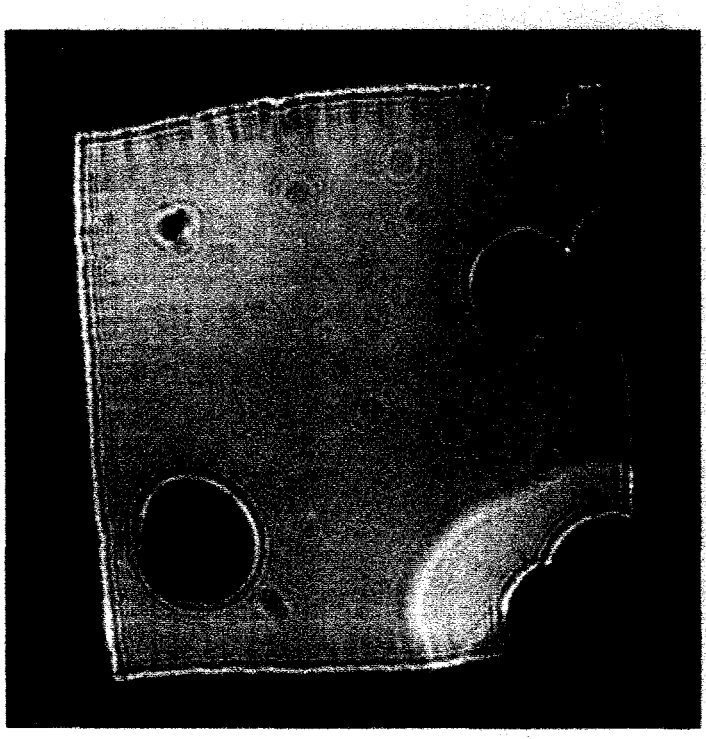

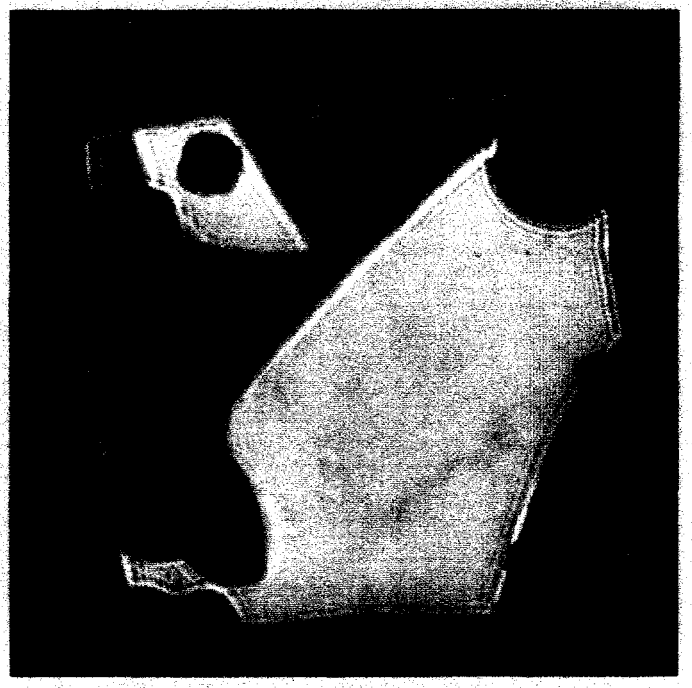

10μm

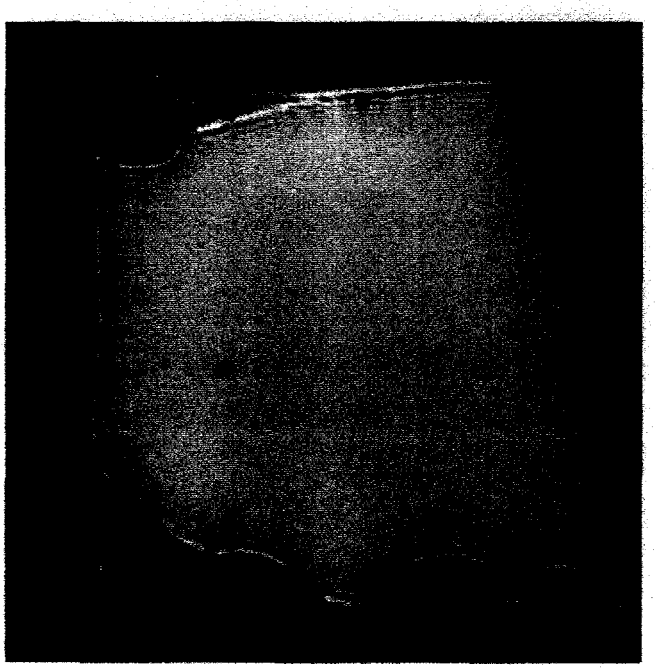

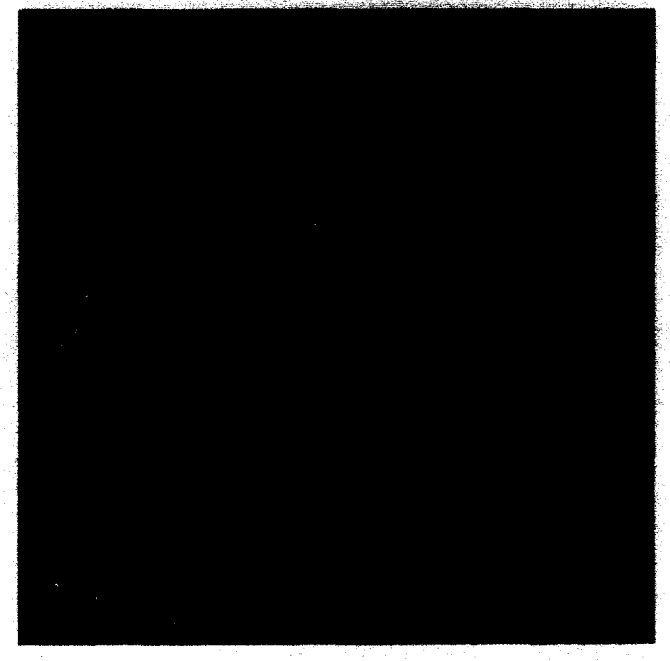

Cryo-Holograms of Malaria infected RBC

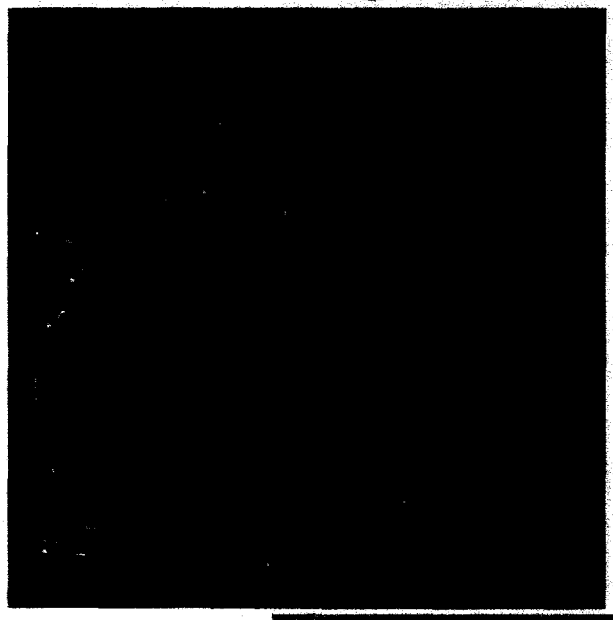

10μm

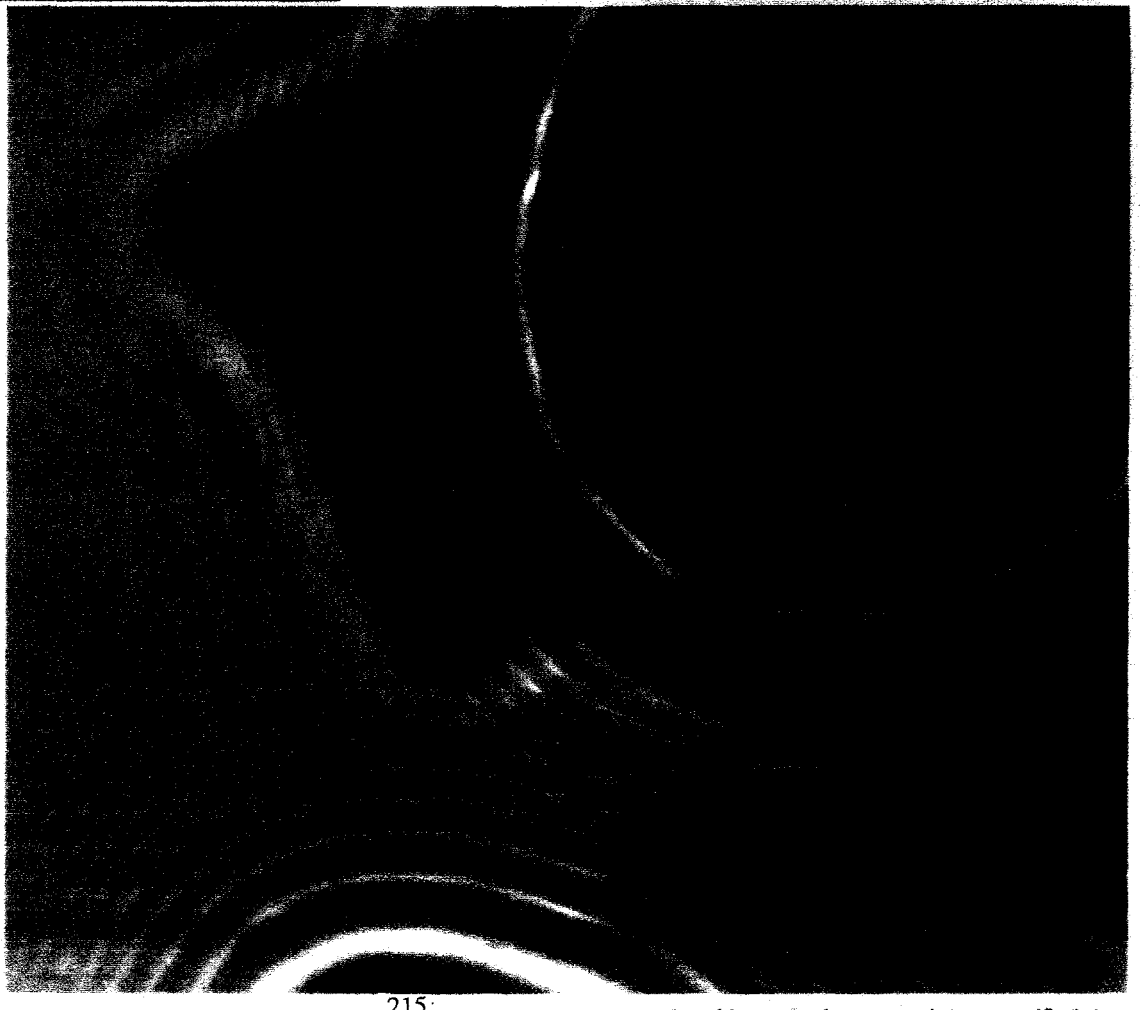

2μm

X-Ray Gabor Holography — Geometry

Recording

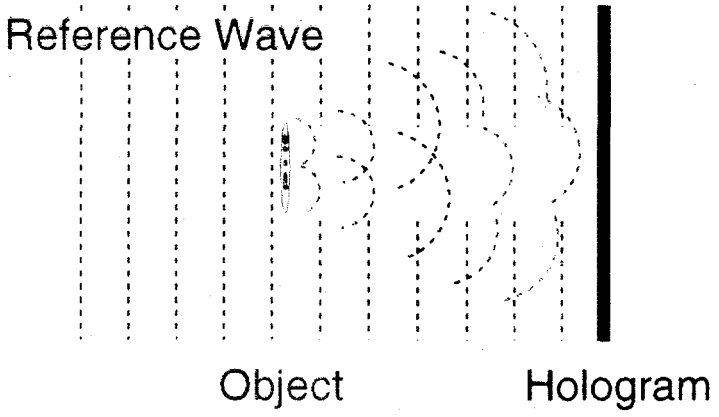

Reconstruction

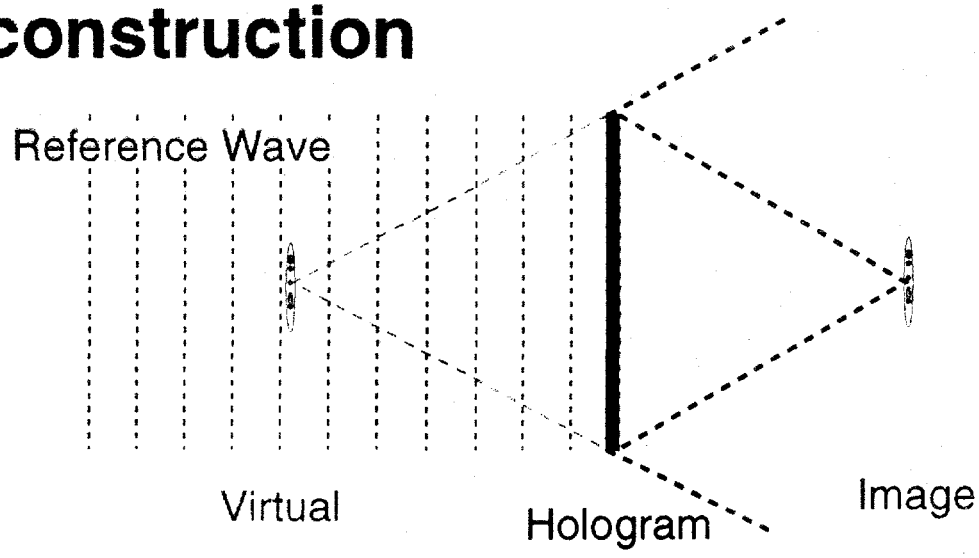

Twin-image Suppression of Model

Brandoch Calef

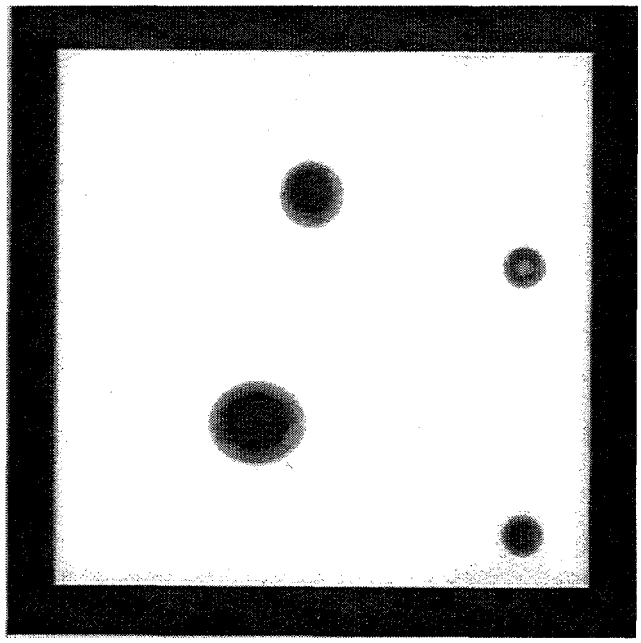

Model

8 μm

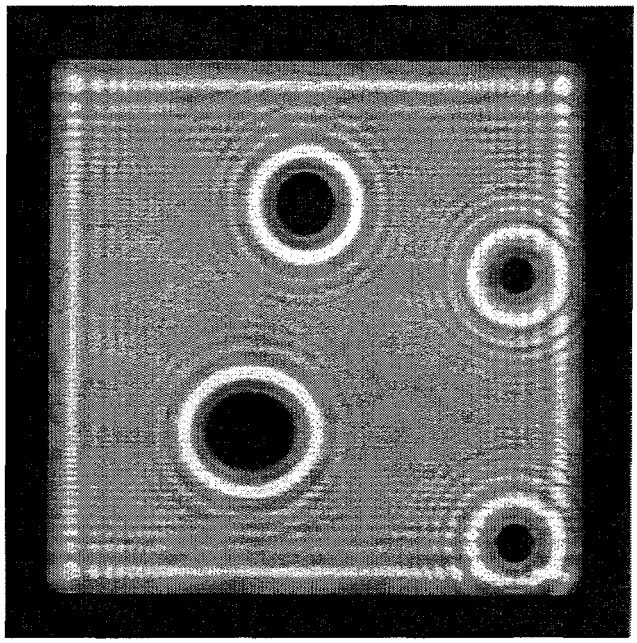

N=1

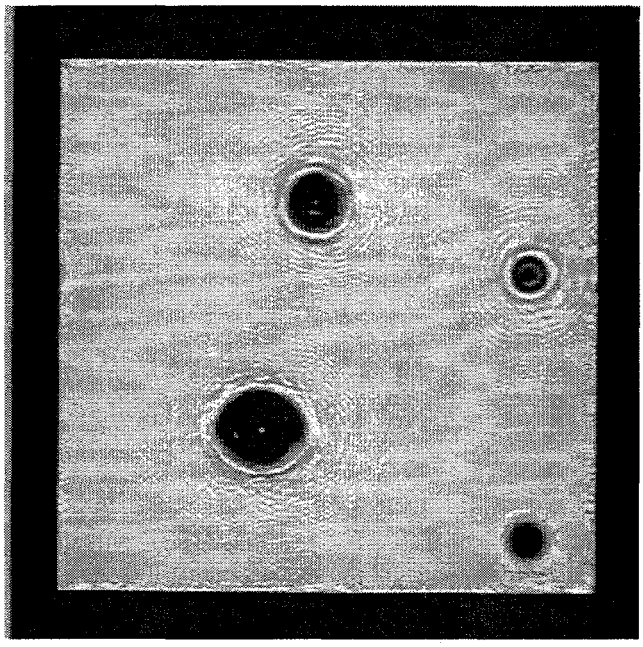

N=80

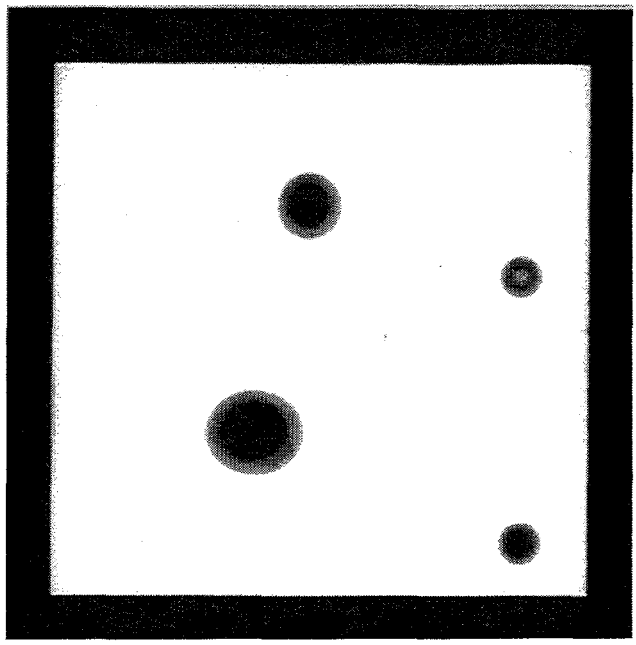

N=2000

Twin-image Supression Error in Model

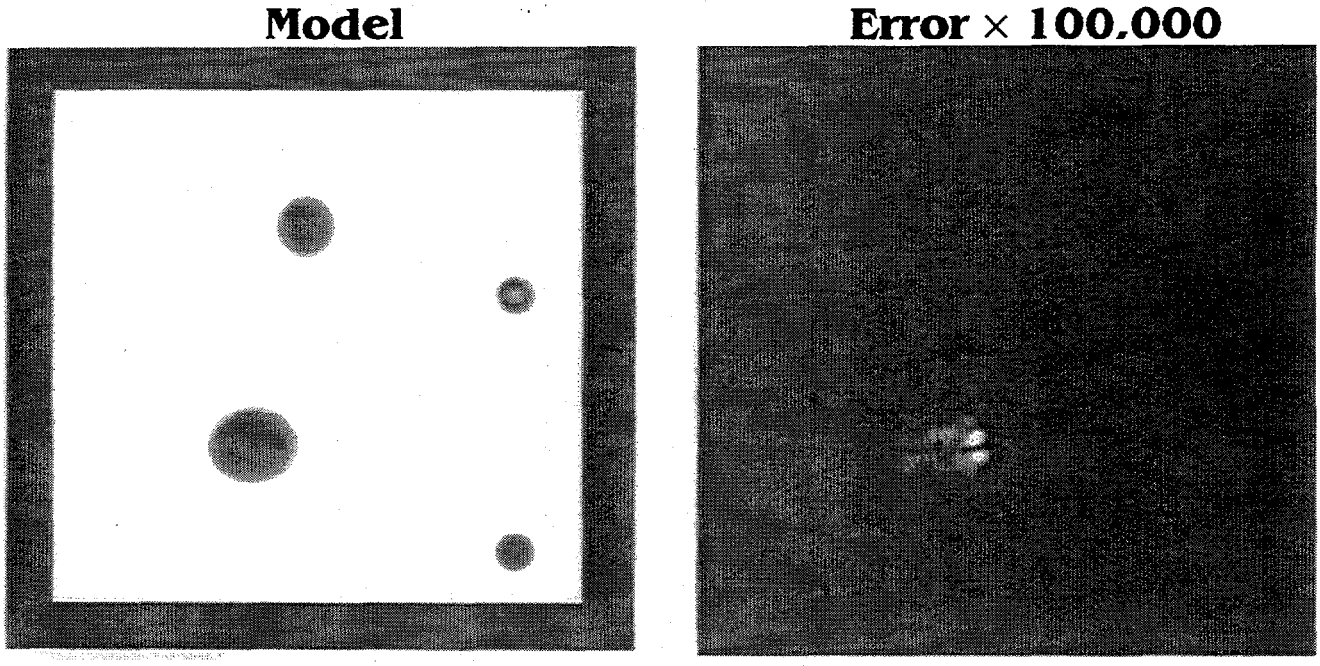

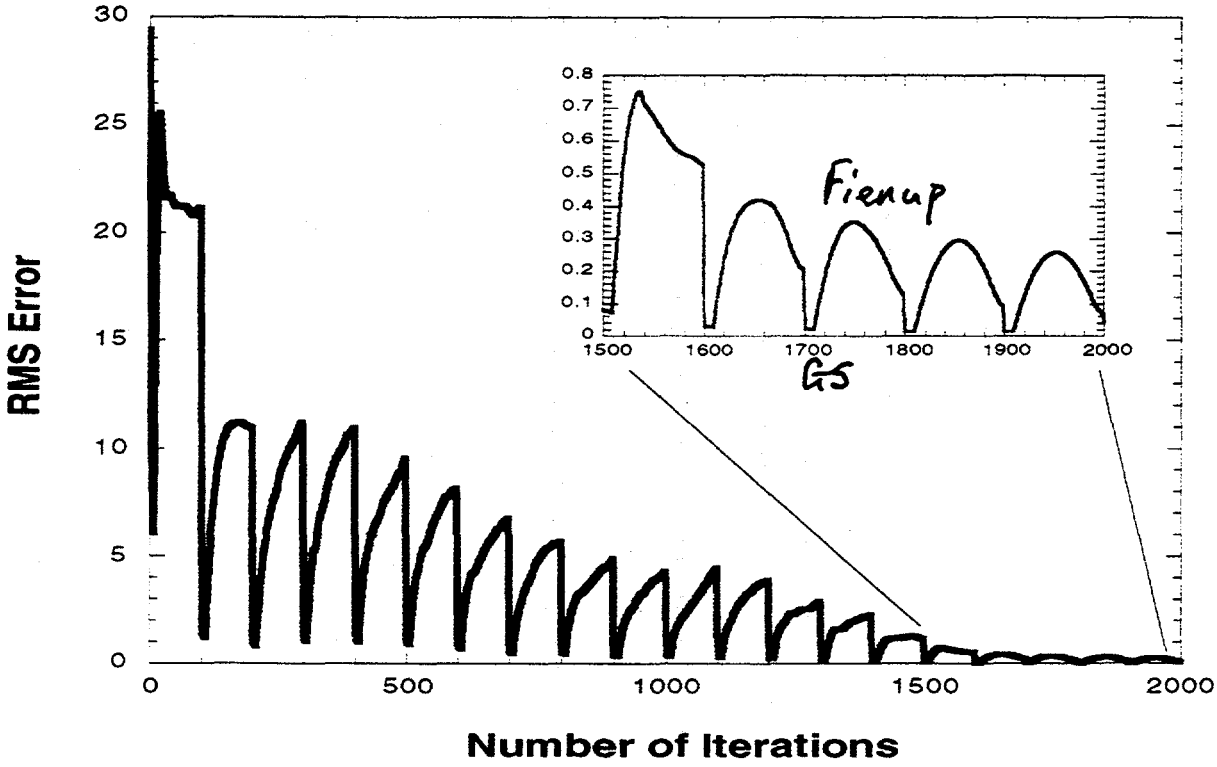

dp.sl/modeltwinerror/8-96

PROJECTIONS ON TO CONVEX SETS

(Stark 1987)

An image of *n* pixels can be regarded as a vector in *n*-space

A set of such vectors (images) is convex if for any x_1 and x_2 in the set the point

$$x = \lambda x_2 + (1-\lambda)x_1 \quad (0 \le \lambda \le 1)$$

is also in the set

- **Set of all vectors with certain components equal to zero is convex**

SUPPORT CONSTRAINT

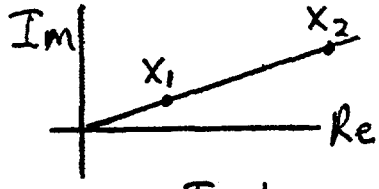

- **Set of all vectors with prescribed phases is convex**

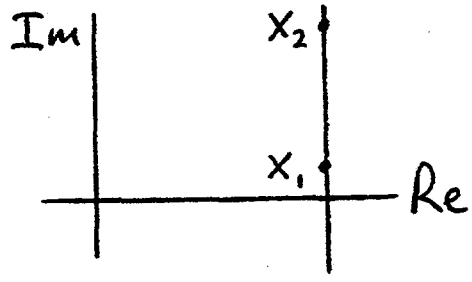

- **Set of all vectors with prescribed real parts is convex**

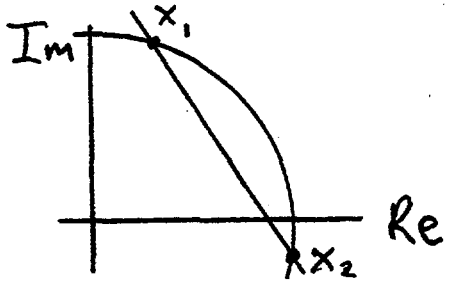

- **Set of all vectors with prescribed amplitudes is NOT convex**

When the constraints are convex and a solution exists, convergence to it is assured

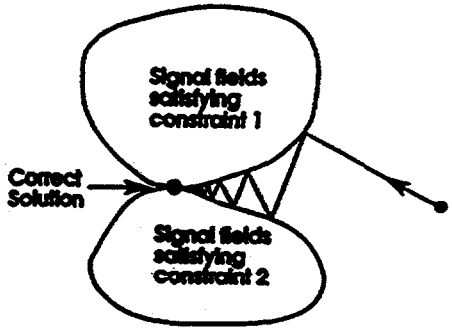

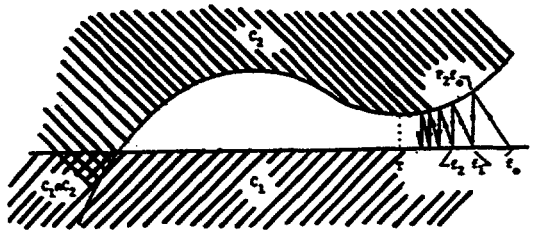

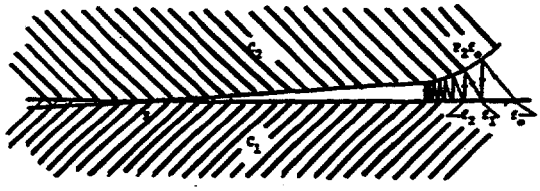

A. Devaney
1995

Phase Retrieval

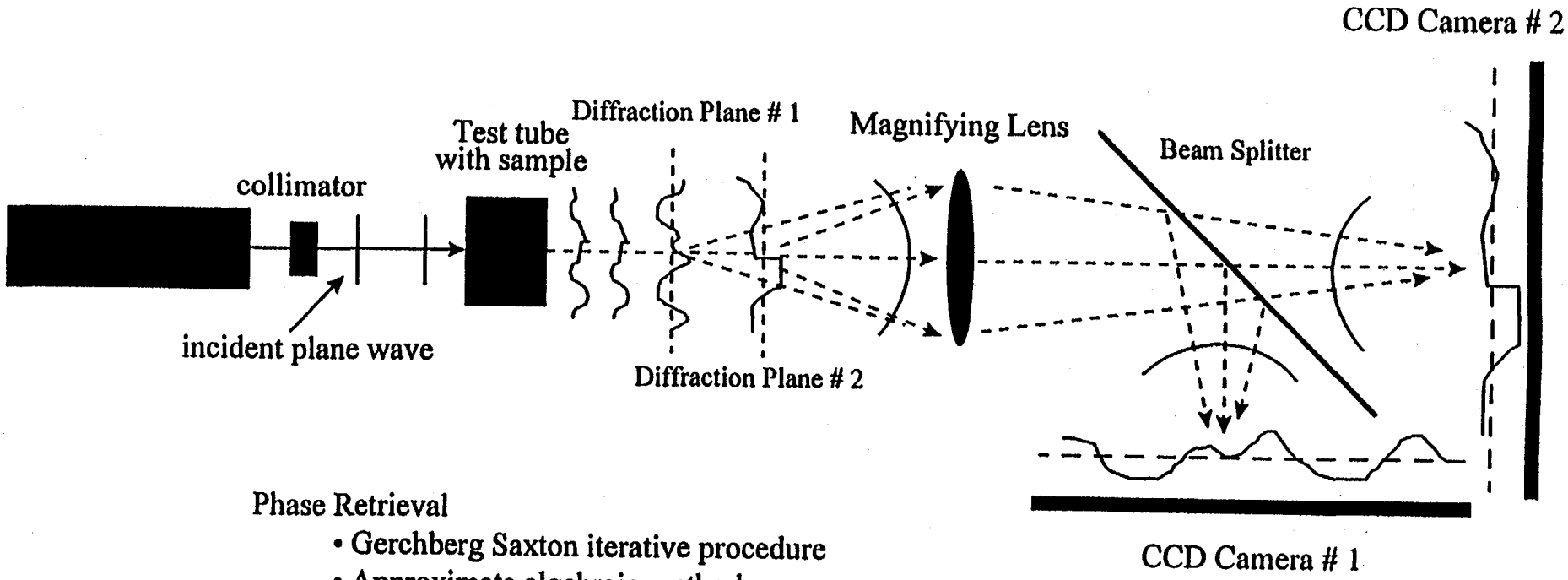

Phase Retrieval

- Gerchberg Saxton iterative procedure
- Approximate algebraic method

Diffraction tomography (DT) generates quantitative image of real and imaginary parts of object's index of refraction distribution from complex (amplitude and phase) distribution of field

12/8/95

Cryo-Hologram of Malaria Infected RBC

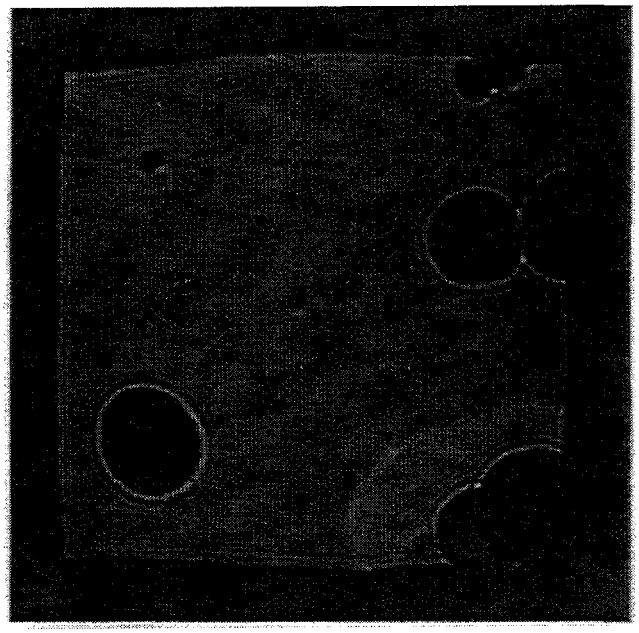

λ=2.4nm z=340μm

(2048×2048) (21nm)^2

10 μm

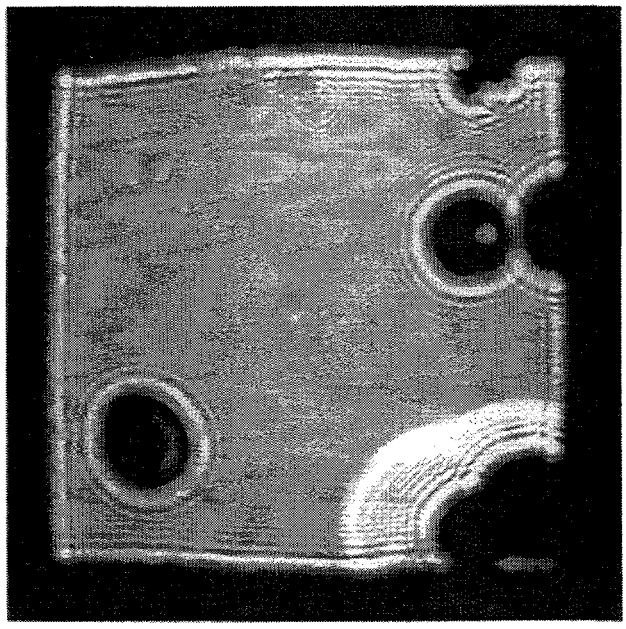

N=1

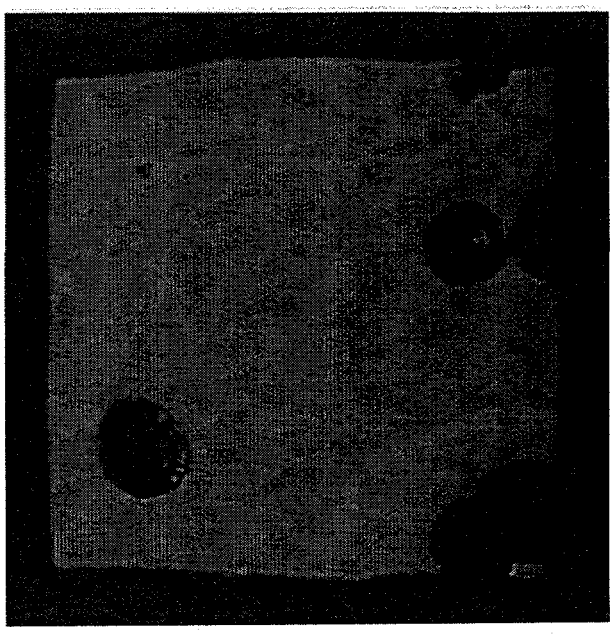

N=1025

High resolution x-ray microtomography of biological samples: requirements and strategies for satisfying them

Billy W. Loo, Jr.[1,2,3] and Stephen S. Rothman[1,3,4]

1. Bioengineering Graduate Group, University of California, San Francisco and Berkeley
2. School of Medicine, University of California, Davis
3. Ernest Orlando Lawrence Berkeley National Laboratory, Berkeley, California
4. Departments of Physiology and Stomatology, University of California, San Francisco

Introduction: Biological soft x-ray microscopy

High resolution x-ray microscopy has been made possible in recent years primarily by two new technologies: microfabricated diffractive lenses for soft x-rays with about 30 - 50 nm resolution, and high brightness synchrotron x-ray sources.

X-ray microscopy occupies a special niche in the array of biological microscopic imaging methods[1,2]. It extends the capabilities of existing techniques mainly in two areas: a previously unachievable combination of sub-visible resolution and multi-micrometer sample size, and new contrast mechanisms.

Because of the soft x-ray wavelengths used in biological imaging (about 1 - 4 nm), XM is intermediate in resolution between visible light and electron microscopies. Similarly, the penetration depth of soft x-rays in biological materials is such that the ideal sample thickness for XM falls in the range of 0.25 - 10 μm, between that of VLM and EM. XM is therefore valuable for imaging of intermediate level ultrastructure, requiring sub-visible resolutions, in intact cells and subcellular organelles, without artifacts produced by thin sectioning.

Many of the contrast producing and sample preparation techniques developed for VLM and EM also work well with XM. These include, for example, molecule specific staining by antibodies with heavy metal or fluorescent labels attached, and sectioning of both frozen and plastic embedded tissue. However, there is also a contrast mechanism unique to XM that exists naturally because a number of elemental absorption edges lie in the wavelength range used. In particular, between the oxygen and carbon absorption edges (2.3 and 4.4 nm wavelength), organic molecules absorb photons much more strongly than does water, permitting element-specific imaging of cellular structure in aqueous media, with no artificially introduced contrast agents (Figure 1). Thus even living cells can be imaged, depending on radiation dose. This natural contrast can also be exploited at shorter wavelengths using phase contrast[3,4].

Some of the x-ray microscopes now in operation around the world produce images directly in digital form. This greatly facilitates quantitative imaging and computational image reconstruction. For three-dimensional imaging applications requiring the capabilities of XM, an obvious extension of the technique would therefore be computerized x-ray microtomography (XMT)[5,6].

I. Resolution requirements

A consideration of the requirements demanded of XMT must take into account what can be accomplished using more readily available VLM methods, weighed against the advantages of imaging with x-

rays. Three-dimensional VLM is generally accomplished by confocal microscopy or wide field microscopy with digital reconstruction by deconvolution of the lens point spread function[7]. Fluorescence imaging is required to achieve the highest resolutions. In most cases, resolutions of about 0.2 μm laterally and 0.5 μm axially can be expected, for sample thickness up to a few tens of micrometers. The newest developments in VLM techniques are pushing the resolution limit to about 0.1 μm in all three dimensions, although to achieve these extreme resolutions ideal optical conditions are required that constrains the types of samples that can be examined, and how they are prepared.

Given this, it is reasonable to require that XMT resolutions be 0.1 μm or smaller in all three dimensions. This corresponds roughly to the dimensions of internal features of important intracellular compartments and organelles, such as mitochondria, Golgi apparatus, and membrane bound storage and secretion vesicles. Many such compartments have complicated three-dimensional topologies that are beyond the ability of current methods to measure[8]. XMT has the potential to allow visualization of such structures, and even quantitation of their contents, in as close to their natural state as possible.

II. Achieving high resolution in three dimensions — strategies and tradeoffs

Focusing of x-rays is accomplished by the diffraction of the radiation by the small structural features of a diffractive optical element, called a zone plate, consisting of alternately transparent and opaque concentric rings. The lateral resolution of the lens is roughly the same as the size of its smallest feature, the width of the outermost zone, currently limited by the fabrication process to about 30 nm[9]. Because the wavelengths used are much smaller than the zone plate resolution, the numerical aperture is low and the depth of focus is much longer than the lateral resolution, typically about 1 - 10 μm. The relatively long depth of focus compared to the sample thickness means that each 2-D image is a projection of axial sample structure onto a plane. This makes tomography the method of choice for reconstructing 3-D structure, as opposed to the optical sectioning used for 3-D VLM.

The entire sample must be in focus to achieve a good projection of sample structure. This occurs when the depth of focus is at least as large as the sample. For zone plates the depth of focus is proportional to the square of the outermost zone width divided by the illuminating wavelength. Thus, a balance must be achieved between resolution, wavelength, and sample size: imaging larger samples requires either lower resolution or shorter wavelength. For example, at 2.4 nm wavelength, nearly the shortest wavelength at which good absorption contrast exists between protein and water, an 80 nm resolution zone plate has a depth of focus of 11 μm while a 50 nm resolution zone plate could be used to image a 4 μm sample with corresponding focal depth.

A stronger constraint on resolution is radiation dose to the sample, which is proportional to about the fourth power of the 3-D resolution. In the above example, achieving 50 nm resolution in 3-D would thus require roughly 7 times the radiation dose that 80 nm resolution would for the same statistical significance in the image, while 40 nm resolution would require 16 times the dose. As a result, high resolution XMT will likely require freezing of biological samples to cryogenic temperatures, or some similar means of protection against radiation damage. A conservative estimate of the dose that can be withstood by frozen biological samples is about 2 - 5 x 10^7 Gray (J/kg), based on the dose at which x-ray diffraction patterns from frozen protein crystals are lost[10]. The dose required to detect by Rose's criterion (signal to noise ratio of 5) a single 80 nm cube of protein at a concentration of 100 mg/mL in the middle of a 10 μm

water layer is 2 x 10^6 Gy. The dose is the energy absorbed per unit mass by the sample, which depends on three parameters: sample density, sample thickness, and a wavelength dependent absorption coefficient. Increases in any of these results in lower transmission through the sample, and therefore requires stronger illumination and higher dose to obtain images of equal statistical quality.

Consequently, for a given wavelength and acceptable dose, resolution can be increased by decreasing sample thickness. This can be accomplished by sectioning thick samples, or by imaging samples that are naturally thin such as cultured cells. Similarly, thicker samples can be imaged more optimally at shorter wavelengths, where the absorption coefficients are generally lower. At wavelengths shorter than 2.3 nm, there is no longer good absorption contrast between protein and water. This means that other contrast mechanisms must be used at these wavelengths, but it also means that dose absorbed by the sample can be significantly lower. Examples of other contrast mechanisms include naturally occurring phase contrast, or artificially added contrast agents such as heavy metals or luminescent labels that emit visible light upon x-ray excitation[11]. A barrier to imaging with short wavelengths is that the diffraction efficiency of zone plates is lower for shorter wavelengths. Manufacturing zone plates that are efficient at short wavelengths is therefore a technical problem that needs to be resolved for best performance.

III. Instrumental requirements

Other components are needed for XMT in addition to appropriate sources, optics, and detectors, primarily related to mounting and positioning of the sample. A sample rotation stage is necessary for obtaining views from multiple angles because most x-ray microscopes are end stations on synchrotron beamlines, so the optical axis cannot be moved about the sample. The main challenge is to engineer the stage in such a way that the sample holder, which can be quite complicated and large, can be rotated through as large an angle as possible in order to facilitate a good reconstruction.

As mentioned above, radiation doses in XMT generally require that samples in aqueous media be frozen, so the sample stage must include equipment for cryofixation. One advantage of XM over EM is that the sample can be in air rather than vacuum, but this means that condensation of humidity onto the cryostage must be prevented, such as by surrounding the sample area with a dry gas chamber.

In addition, samples must be mounted on substrates that are transparent to soft x-rays. Thin membranes of polymer or silicon nitride under 100 nm thick are usually used for this purpose. These membranes must be supported by frames such as metal grids or silicon wafers, because their fragility makes them difficult to fashion into free standing structures.

Given the number of components and optics in the vicinity of the sample, some of them possibly bulky, it is likely that for practical considerations, the range of rotation of the sample must be restricted to less than a full circle. This necessitates the use of specialized algorithms to reconstruct the image.

IV. Computational strategies and requirements

Many algorithms have been developed to solve the tomographic reconstruction problem. The most efficient of these from a computational standpoint take advantage of analytical properties of the projection process that allow inversion of the measurements using Fourier transforms. However, they are not well

suited to dealing with high noise levels, which may be present when lower illumination intensity is used to reduce radiation dose, or with missing data as in the limited angle tomography problem. Certain iterative algorithms are useful in these cases because they are designed to provide a good statistical estimate in the presence of noise, and allow incorporation of prior knowledge about the sample to compensate for cases in which data is missing[12].

The most computationally expensive operations in tomographic reconstruction are projection and backprojection, the operations that transform between object and projection spaces. For each 2-D axial slice, a projection or backprojection operation involves a number of arithmetic operations proportional to the number of angular views times the number of ray projections per view times the number of pixels intersected by each ray. The Fourier inversion methods require only one backprojection. However, the iterative methods may require one projection and one backprojection operation per iteration.

These operations are equivalent to a sparse matrix multiplication, with the number of nonzero elements in the transition matrix roughly equal to the cube of the width of the slice in pixels, for a typical angular sampling. Thus for a 256 x 256 pixel axial slice, the transition matrix (using floating point values) would require about 70 megabytes of memory to store. Assuming each slice in the volume can be processed independently, with a small multiplicative factor added when there is cross-talk between slices, the computational cost is on the order of 10^{10} arithmetic operations per iteration for reconstructing a 256 x 256 x 256 volume. (At a voxel size of 40 nm, the total field of view in this case would be a cube 10 μm on a side.) A good iterative algorithm may converge within about 30 iterations. A computer of relatively modest expense should be able to perform such a full volume reconstruction within several hours.

Aside from the reconstruction process itself, computational tools are needed to analyze volumetric data and extract measurements automatically to allow processing of a sufficient number of images for statistical significance. Examples of such tools are algorithms to segment and compile statistics on attributes of objects of interest[13].

V. Current status, and developments at LBNL

The results of computer simulations have indicated the feasibility of high resolution XMT of biological samples at tolerable radiation doses[6,14] (Figures 2-3). Experimental imaging of an artificial test object has been a technical proof of principle[5]. However, XMT of biological samples at sub-visible resolution has not yet been demonstrated. The authors' work on two view x-ray stereomicroscopy has come the closest so far to achieving this goal[15,16].

One of the newest high resolution biological x-ray microscopy facilities has been contructed and operating at the Advanced Light Source (ALS) synchrotron at Lawrence Berkeley National Laboratory (LBNL)[17]. The authors have been using this microscope to do quantitative imaging of pancreatic tissue in their investigation of cellular secretory mechanisms (Figure 4). Work is in progress to implement cryofixation and sample rotation in this and a number of other x-ray microscopes around the world. In addition, a scanning x-ray microscope for biological samples has been proposed that would take full advantage of the high brightness of the ALS. Such an instrument would be ideal for XMT because the scanning geometry allows imaging with lower dose due to the lack of optics between the sample and the detector.

VI. Conclusion

X-ray microscopy has begun to provide a new view of biological samples. By extending its view to three-dimensions, x-ray microtomography has the potential to become a truly powerful method for elucidating complex cellular ultrastructure. X-ray microscopes are in operation around the world that could be modified into XMT instruments using existing or readily implementable technologies. Continual progress is being made in overcoming the remaining obstacles to optimal performance.

VII. References

1. J. Kirz, C. Jacobsen, and M. Howells, "Soft X-ray microscopes and their biological applications," *Quarterly Reviews of Biophysics*, Vol. 28, No. 1, pp. 33-130, 1995.

2. S.S. Rothman, K.K. Goncz, and B.W. Loo, Jr., "Following protein transport with the high resolution x-ray microscope," in *X-Ray Microscopy III*, ed. by A.G. Michette, G.R. Morrison, and C.J. Buckley, pp. 373-383, Springer-Verlag, Berlin, 1992.

3. M.R. Howells, "Contrast mechanisms in x-ray microscopy," in *X-Ray Microscopy III*, ed. by A.G. Michette, G.R. Morrison, and C.J. Buckley, pp. 373-383, Springer-Verlag, Berlin, 1992.

4. G. Schmahl, *et. al.*, "Phase contrast x-ray microscopy," *Synchrotron Radiation News*, Vol. 7, No. 4, pp. 19-22, 1994.

5. W.S. Haddad, *et. al.*, "Ultrahigh-resolution x-ray tomography," *Science*, Vol. 266, No. 5188, pp. 1213-1215, 1994.

6. B.W. Loo, Jr., J.K. Brown, and S.S. Rothman, "X-ray microtomography: three-dimensional reconstruction methods for x-ray microscopy of biological samples," in *Three-Dimensional Microscopy: Image Acquisition and Processing II*, Proceedings SPIE Vol. 2412, ed. by T. Wilson and C.J. Cogswell, 1995.

7. *Handbook of Biological Confocal Microscopy*, ed. by J. Pawley, 2nd ed., Plenum Press, New York, 1995.

8. K. Tanaka, A. Mitsushima, H. Fukudome, and Y. Kashima, "Three-dimensional architecture of the Golgi complex observed by high resolution scanning electron microscopy," *Journal of Electron Microscopy Technique*, Vol. 17, No. 1, pp. 15-23, 1991.

9. E.H. Anderson and D. Kern, "Nanofabrication of zone plates for x-ray microscopy," in *X-Ray Microscopy III*, ed. by A.G. Michette, G.R. Morrison, and C.J. Buckley, pp. 373-383, Springer-Verlag, Berlin, 1992.

10. R. Henderson, "Cryo-protection of protein crystals against radiation damage in electron and x-ray diffraction," Proceedings of the Royal Society of London B, Vol. 241, pp. 6-8, 1990.

11. A. Irtel von Brenndorff, M.M. Moronne, C. Larabelle, P. Selvin, and W. Meyer-Ilse, "Soft x-ray stimulated high resolution luminescence microscopy," in X-Ray Microscopy IV, ed. by A.I. Erko and V. Aristov, Bogorodski Peschatnik, Chernogolovka, 1994.

12. L. Kaufman, "Maximum likelihood, least squares, and penalized least squares for PET," *IEEE Transactions on Medical Imaging*, Vol. 12, No. 2, pp. 200-214, June 1993.

13. B.W. Loo, Jr., B. Parvin, and S.S. Rothman, "Two- and three-dimensional segmentation for measurement of particles in the analysis of microscopic digital images of biological samples," in *Three-Dimensional Microscopy: Image Acquisition and Processing III*, ed. by C.J. Cogswell, G.S. Kino, and T. Wilson, Proceedings SPIE Vol. 2655, 1996.

14. B.F. McEwen, K.H. Downing, R.M. Glaeser, "The relevance of dose-fractionation in tomography of radiation-sensitive specimens," *Ultramicroscopy*, Vol. 60, No. 3, pp. 357-373, 1995.

15. B.W. Loo, Jr., S. Williams, S. Meizel, and S.S. Rothman, "X-ray stereomicroscopy: high resolution 3-D imaging of human spermatozoa in aqueous suspension with natural contrast," *Journal of Microscopy*, Vol. 166, No. 2, pp. RP5-RP6, 1992.

16. B.W. Loo, Jr., *et. al.*, "High resolution x-ray stereomicroscopy: true three-dimensional imaging of biological samples," in *Soft X-Ray Microscopy*, Proceedings SPIE Vol. 1741, pp. 393-401, 1993.

17. W. Meyer-Ilse, *et. al.*, "New high-resolution zone-plate microscope at Beamline 6.1 of the ALS," *Synchrotron Radiation News*, Vol. 8, No. 3, pp. 29-33, 1995.

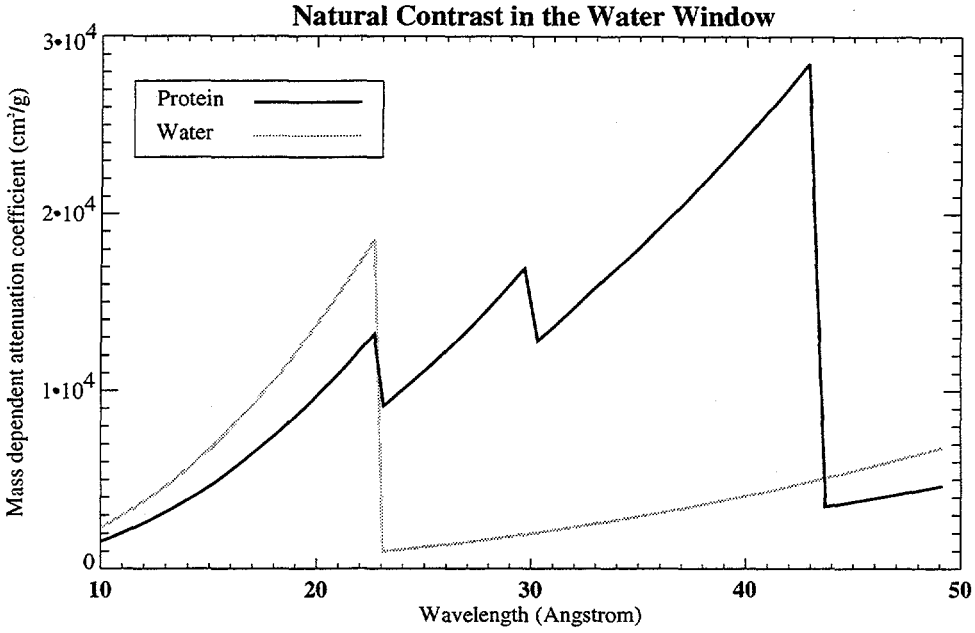

Figure 1: Protein absorbs x-rays much more strongly than does water in the "water window" wavelength range

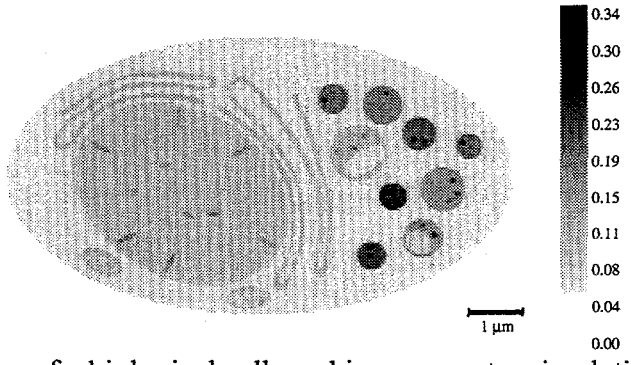

Figure 2: Digital phantom of a biological cell used in a computer simulation of XMT. The pixel values represent density (in g/cm^3) of protein. The smallest point-like features are 80 nm across. Reproduced with permission from [6].

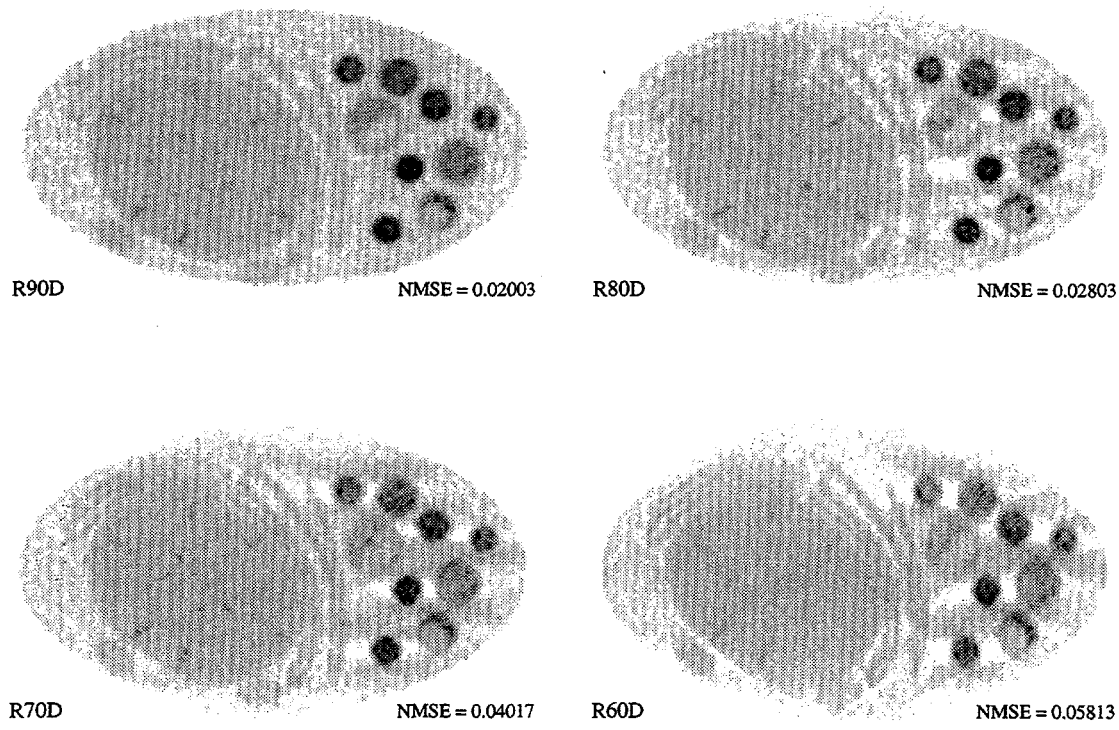

Figure 3: Simulated tomographic reconstruction of the phantom in Figure 2 with various restrictions on the range of view angles. Reconstructions by an iterative algorithm are shown for the angular ranges: ±90°, ±80°, ±70°, ±60°. Both photon shot noise and blurring due to the point spread function of an 80 nm resolution zone plate lens are simulated. X-ray wavelength is 2.4 nm. The average dose to the sample, set at a level sufficient to resolve barely the 80 nm features, is 9 x 10^6 Gray. Reproduced with permission from [6].

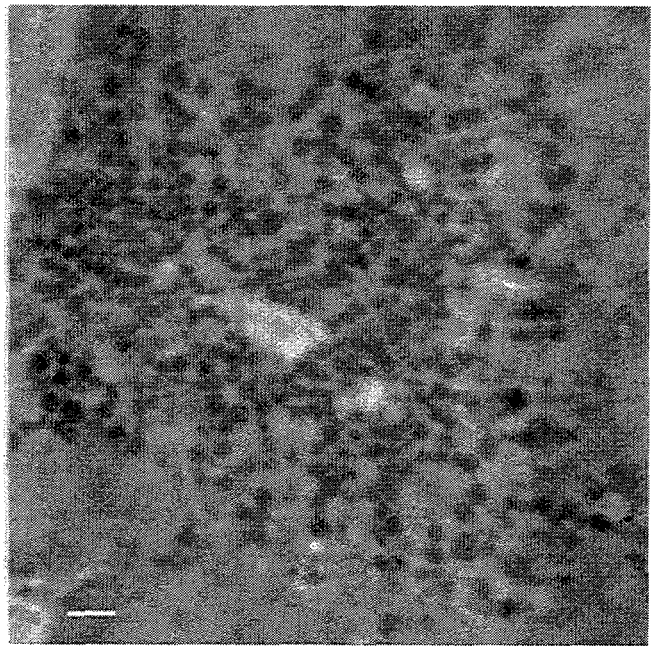

Figure 4: High resolution x-ray micrograph of a 0.75 µm section of rat pancreatic tissue. The image shows many zymogen granules surrounding a ductal space. This image is a mosaic of several images with smaller field of view. Scale bar = 2 µm.

High Resolution X-Ray Microtomography of Biological Samples: Requirements and Strategies for Satisfying Them

Billy W. Loo, Jr.[1,2,3]

Stephen S. Rothman[1,3,4]

1. Bioengineering Graduate Group, University of California, San Francisco and Berkeley
2. School of Medicine, University of California, Davis
3. Lawrence Berkeley National Laboratory
4. Departments of Physiology and Stomatology, University of California, San Francisco

UCSF

UCB

L·B·N·L

High Resolution X-Ray Microtomography of Biological Samples: Requirements and Strategies for Satisfying Them

- Introduction to biological soft x-ray microscopy
- 3-D Resolution
  - Requirements
  - Strategies
- Instrumental requirements
- An XMT simulation
- Computational requirements
  - Reconstruction
  - Analysis

UCSF
UCB

Principles of x-ray microscopy

Where does x-ray microscopy fit in?

	Visible light	**X-ray**	**Electron**
Wavelength	~ 500 nm	2 - 4 nm	< 0.1 nm
Resolution	~ 250 nm	~ 50 nm	~ 0.5 nm
Penetration	10's-100's μm	~ 10 μm	< 0.1 μm
Sectioning required?	No	No	Yes
Stains required?	No	No	Yes
Living cells?	Yes	Yes	No
Quantitative densitometry	No	**Yes**	No

Diffractive X-Ray Lens: Fresnel Zone Plate

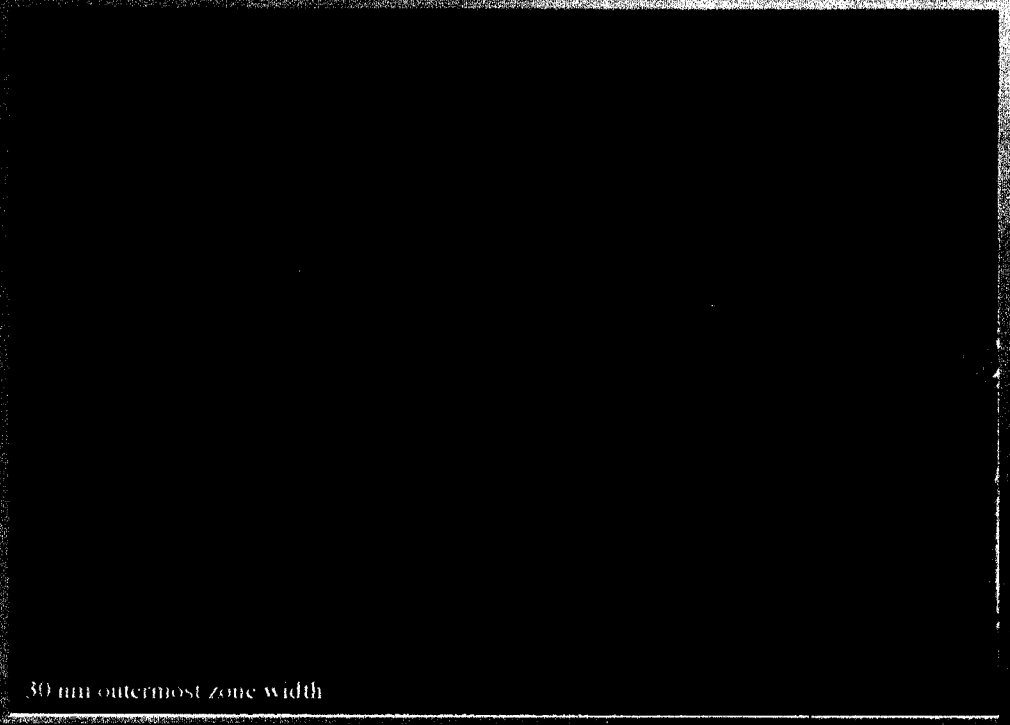

30 nm outermost zone width

UCSF
UCB

L·B·N·L

"Natural Contrast"

Attenuation Coefficients in the "Water Window"

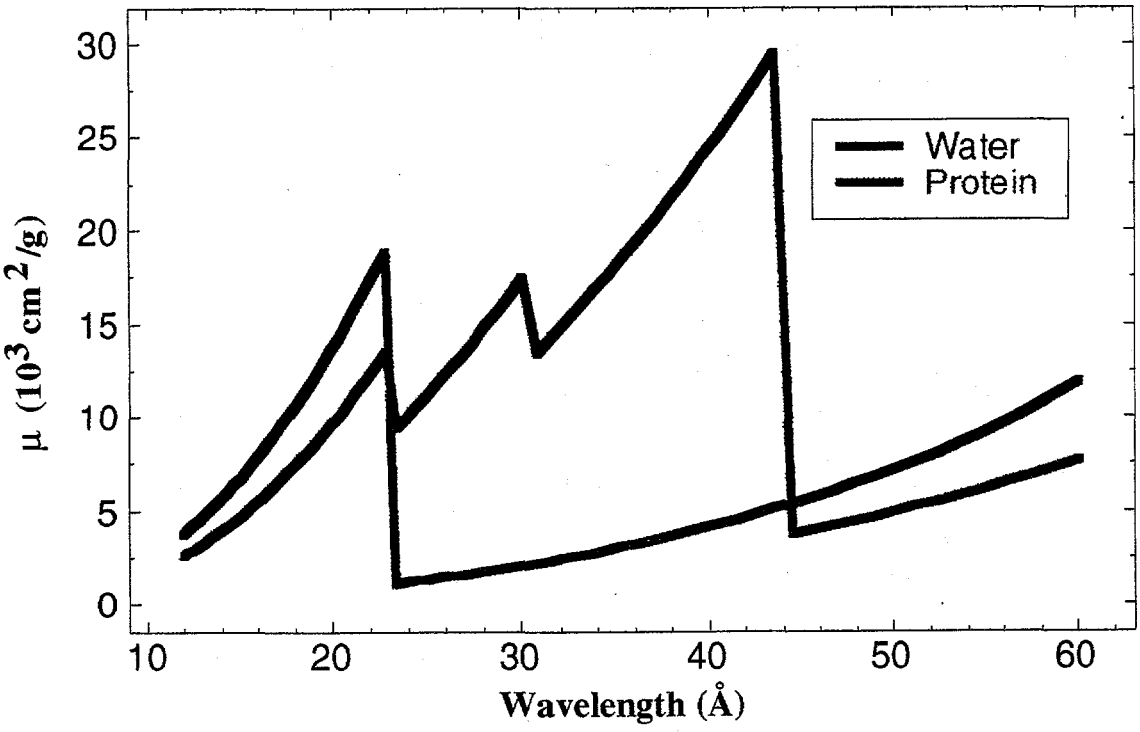

High Resolution Zone-Plate Microscope XM-1 at the ALS

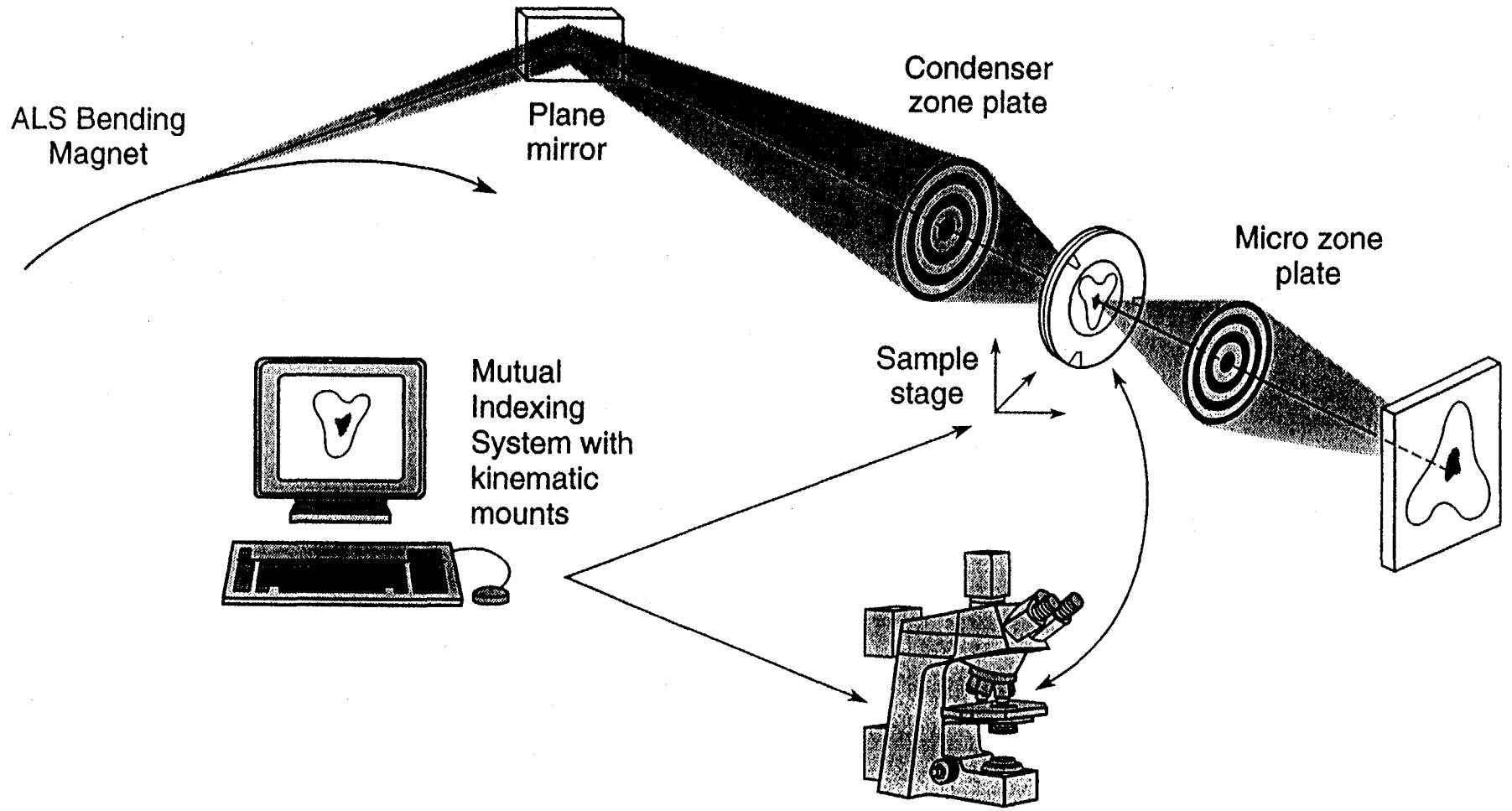

XBD 9510-04714.ILR

X-ray Microscopes at the Advanced Light Source (ALS)

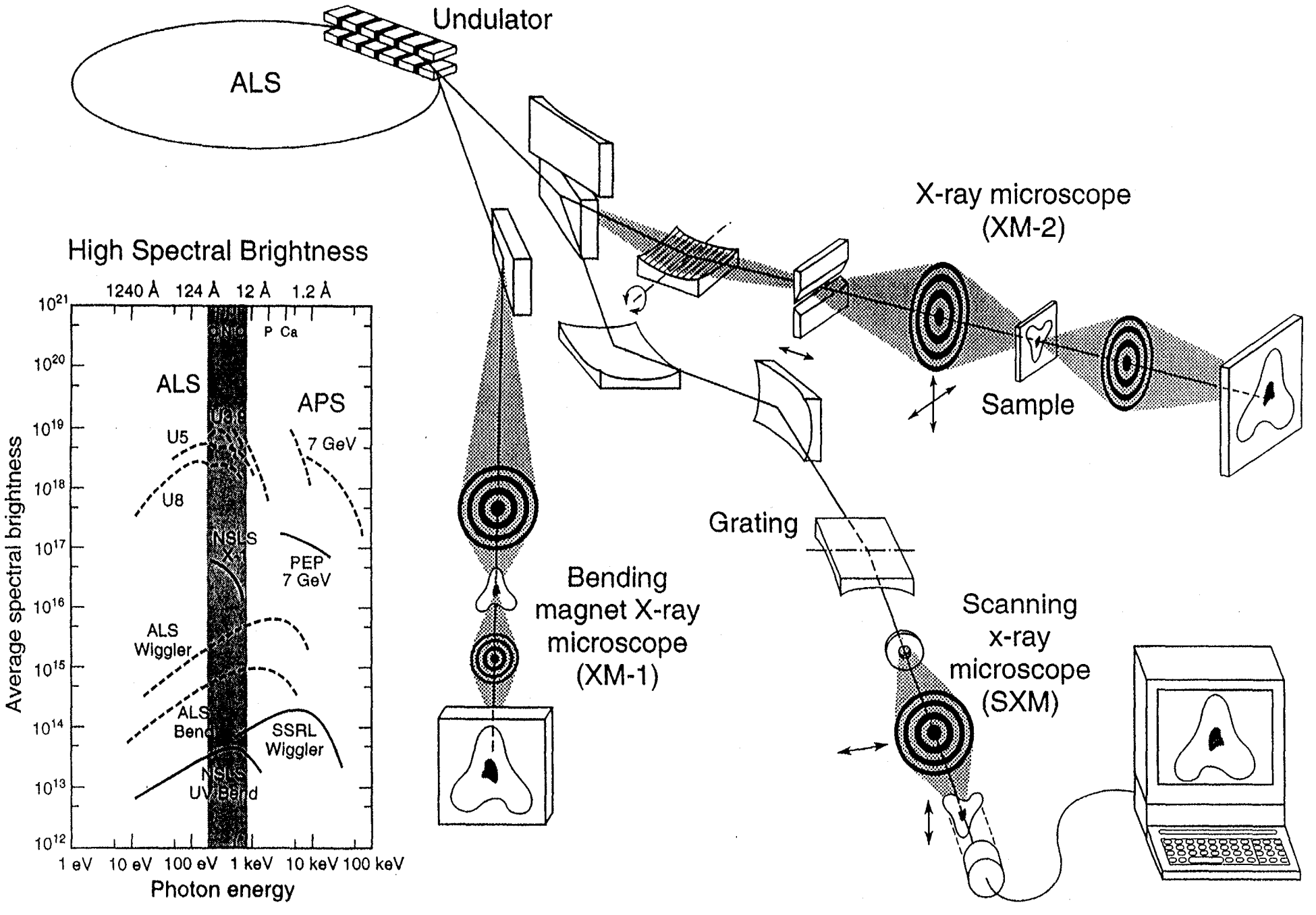

XBL 942-5690

XM-1 Images

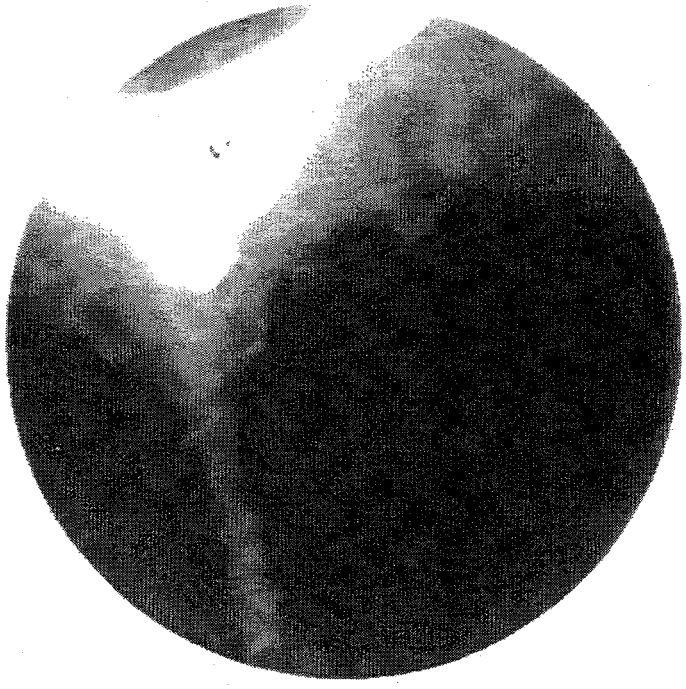

Rat pancreatic acinar cells

Human spermatozoon

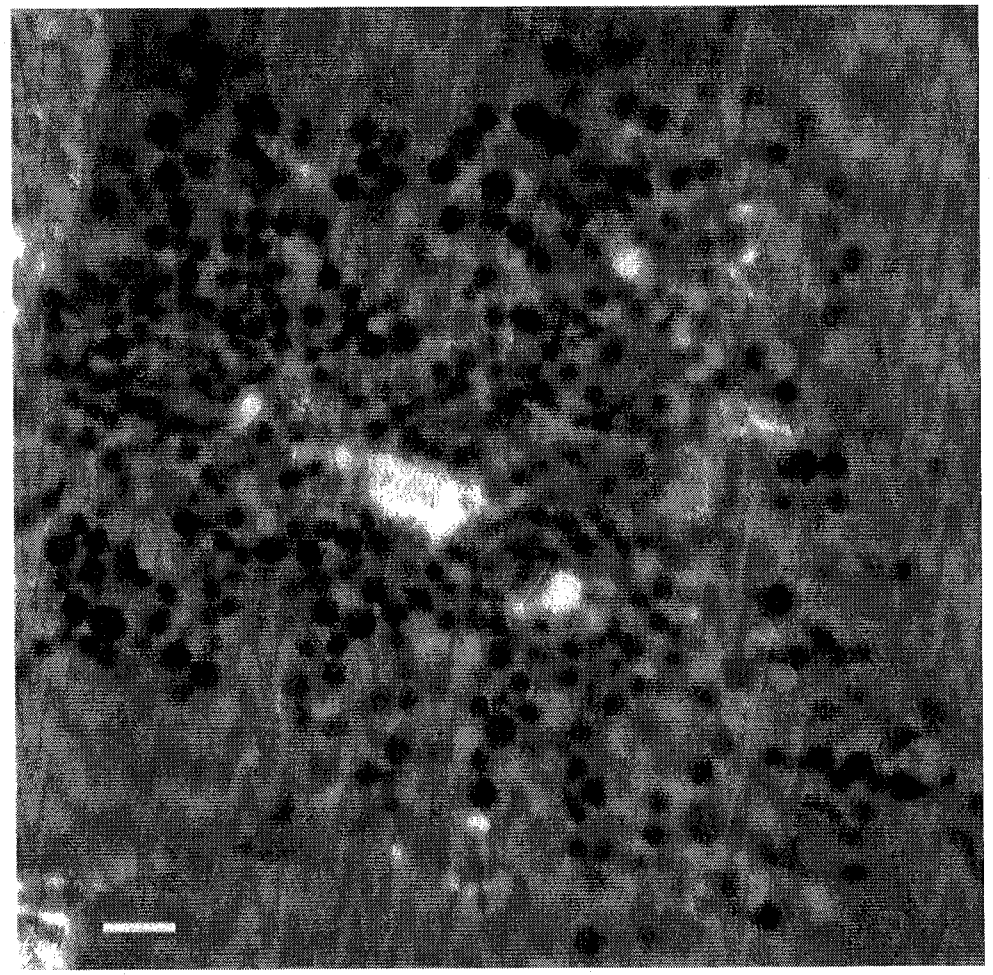

XM-1 image of plastic section of rat pancreatic acinus. Scale bar = 2.0 μm.

Billy W. Loo, Jr., Aaron J. Lee, and Stephen S. Rothman

Resolution

- Requirements - Limit of Detection
  - 3-D VLM resolution: ~0.2 μm lateral, 0.5 μm axial
  - Newest VLM methods approach 0.1 μm in 3-D
  - Can start to measure internal features of important intracellular compartments and organelles
- Strategies - choosing a right combination of:
  - Zone plate resolution
  - Sample thickness
  - Wavelength
  - Contrast mechanism
- Main constraint: Radiation dose

Fig. 8-7: Electron micrograph of pancreatic acinar cell
from B. Alberts, *et. al.*, *Molecular Biology of the Cell*, 2nd ed.,
Garland Publishing, Inc., New York, 1989.

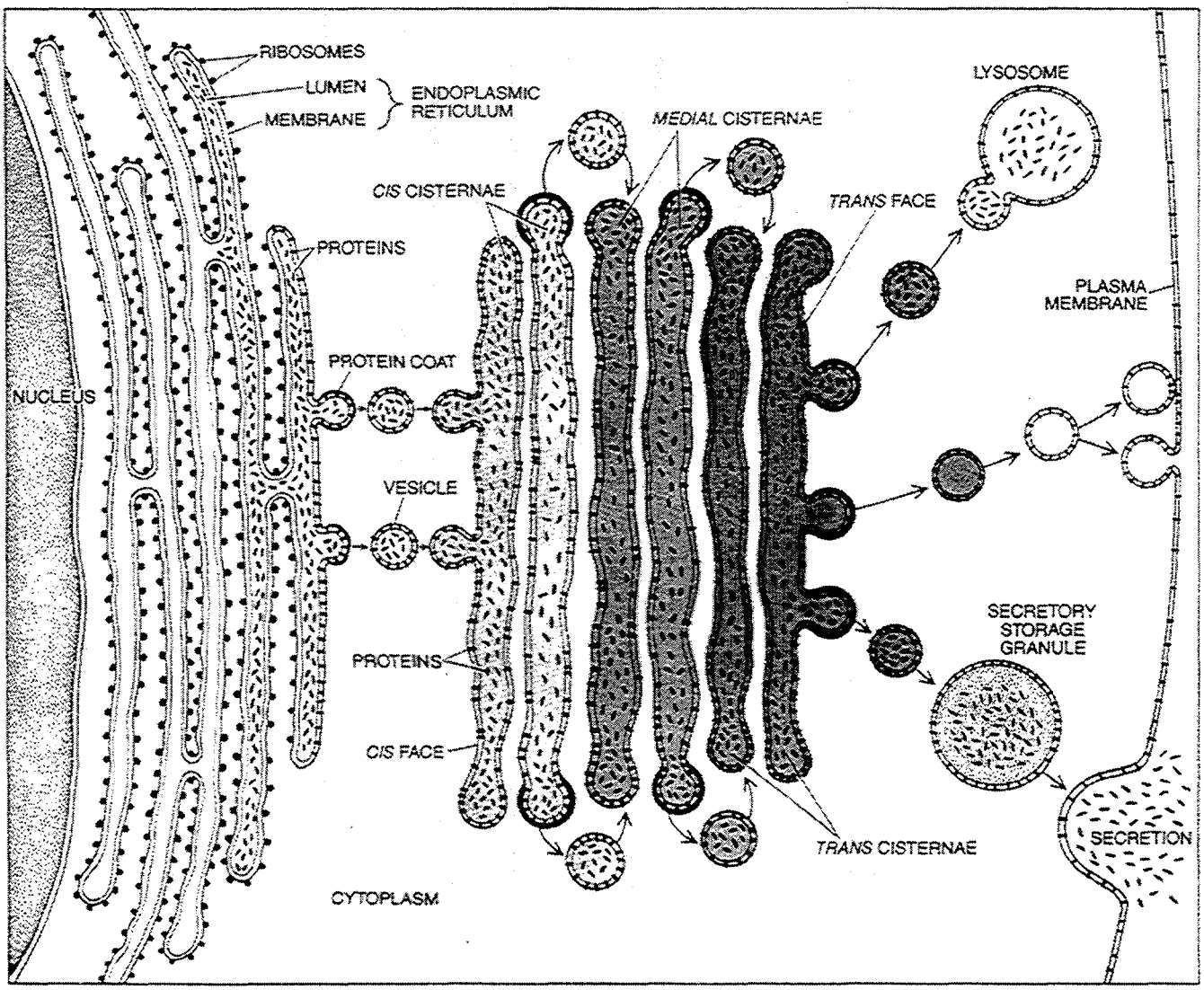

from J.E. Rothman, "The compartmental organization of the Golgi apparatus," *Scientific American*, **253**(3), Sept. 1985.

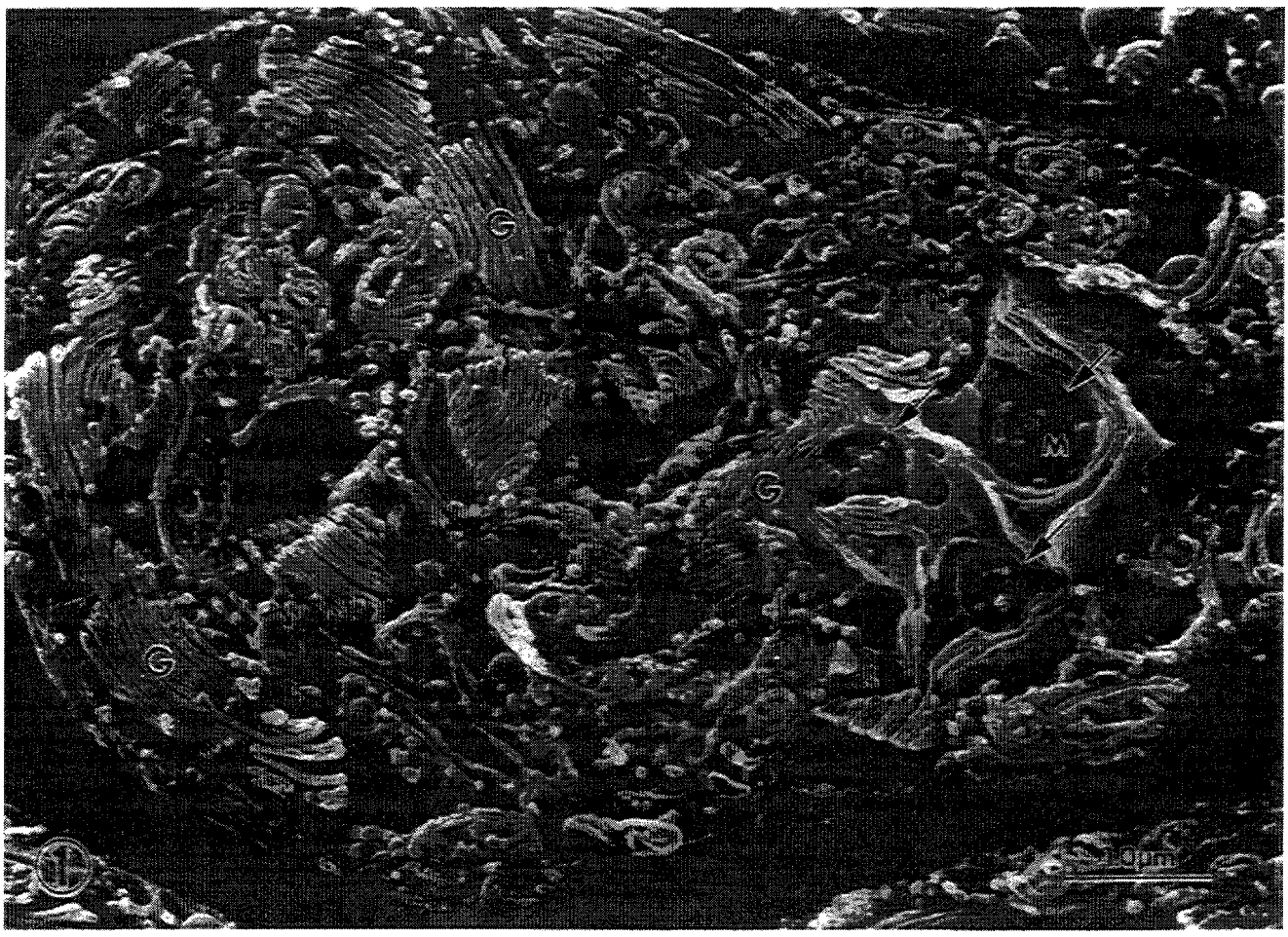

Fig. 1: High resolution scanning electron micrograph of cleaved rat epididymal cell from K. Tanaka and H. Fukudome, "Three-dimensional organization of the Golgi complex observed by scanning electron microscopy," *Journal of Electron Microscopy Technique*, **17**(1), 1991.

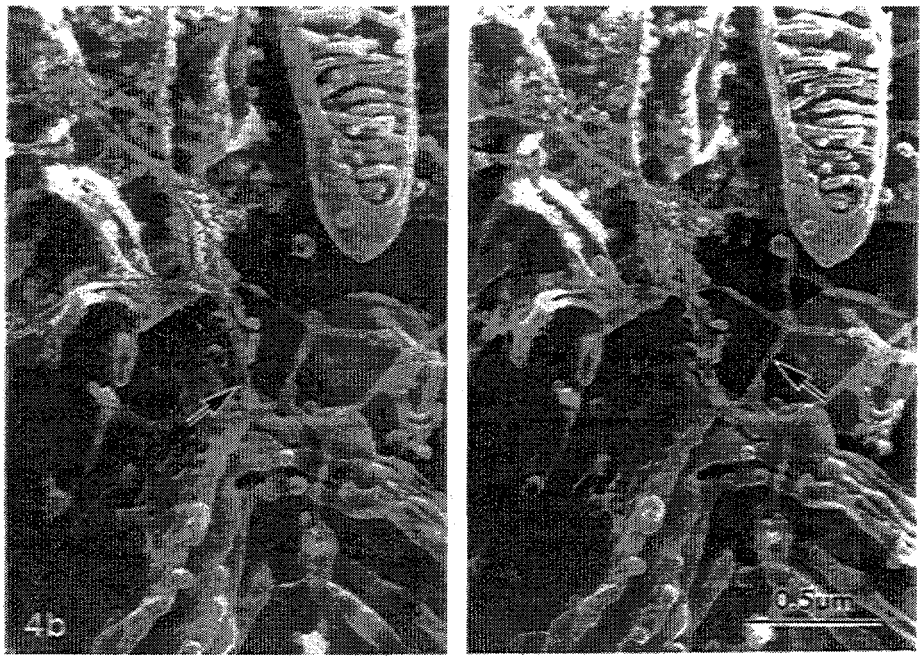

Fig. 4b: Connections between ER and Golgi in nerve cell from rat spinal cord

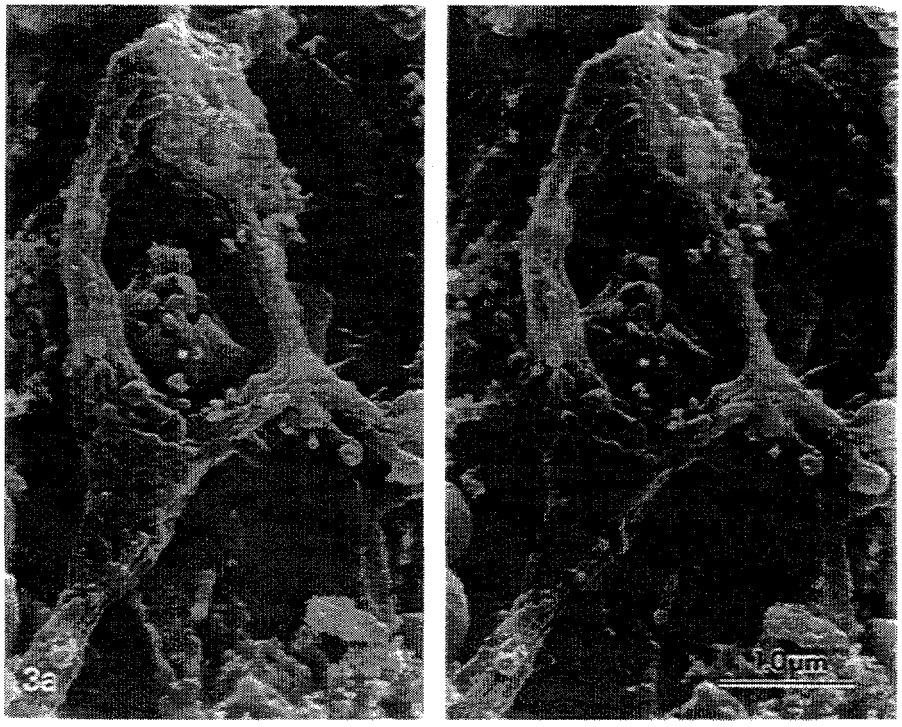

Fig. 3a: Helically wound Golgi stack in rat extraorbital lacrimal gland cell
from K. Tanaka, A. Mitsushima, H. Fukudome, and Y. Kashima, "Three-dimensional architecture of the Golgi complex observed by high resolution scanning electron microscopy," *Journal of Submicroscopic Cytology*, **18**(1), 1986.

Zone Plate Focal Properties

Outermost zone width:

Resolution:

Depth of focus: (FW 0.8 × Max)

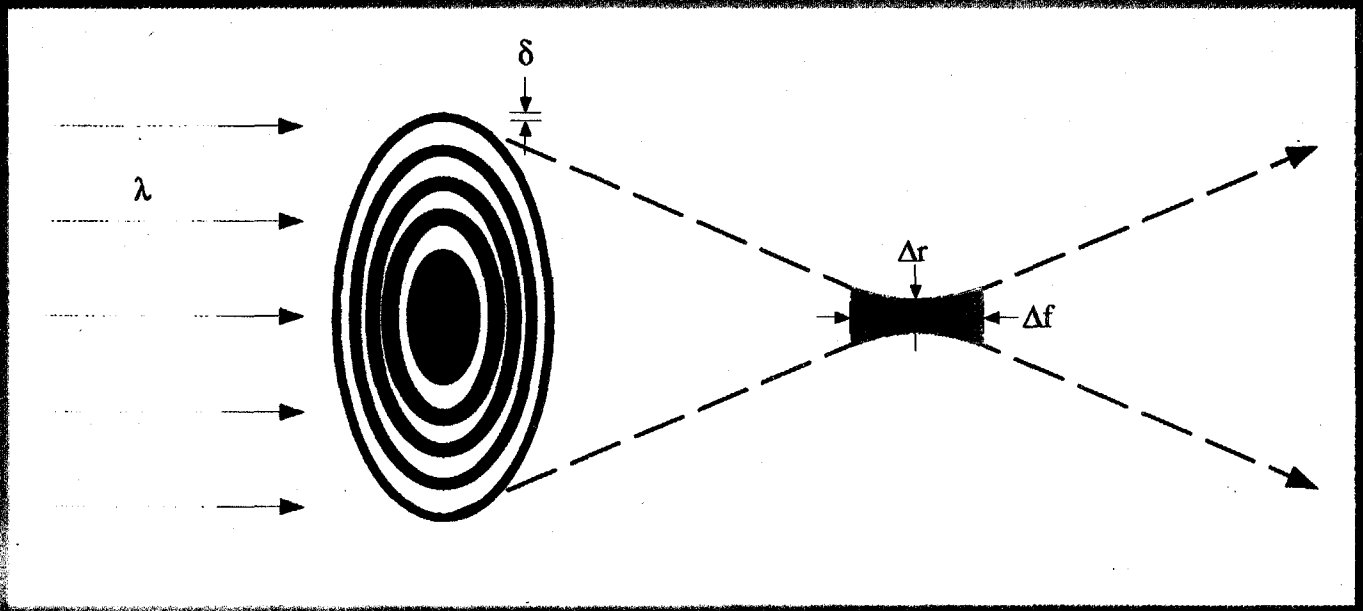

UCSF
UCB

L·B·N·L

Factors Affecting Radiation Dose

- Absorbed dose:

  $I_{abs} = I_0 (1 - e^{-\mu t})$

  ρ sample density

  μ wavelength dependent absorption coefficient

  t sample thickness

- Relationship to resolution: Dose ~ $1/\lambda^3$
- Strategies:
  - Choice of sample thickness
  - Choice of contrast mode and wavelength

UCSF
UCB

L·B·N·L

Estimated Limits Imposed by Radiation Dose

- Dose above which diffraction patterns are lost for x-ray crystallography of frozen, hydrated protein crystals: $2 - 5 \times 10^7$ Gray
- "Critical dose" for electron microscopy at 1.0 nm resolution: 1.0^8 Gray
- Dose required to detect (S/N = 5) an 80 nm cube of protein at 100 mg/ml in the middle of a 1.0 μm water layer: 2×10^9 Gray

UCSF
UCB

L·B·N·L

Contrast Mechanisms in XM

- Natural contrast
  - Element specific contrast due to organic molecules in biological samples
  - Amplitude (absorption) contrast — wavelengths in the "water window"
  - Phase contrast
- Artificial contrast agents
  - Stains
  - Heavy metals
  - Luminescent probes

UCSF
UCB

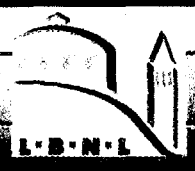

Terbium-Polychelate Labeled Polymerized Tubulin

X-ray Transmission

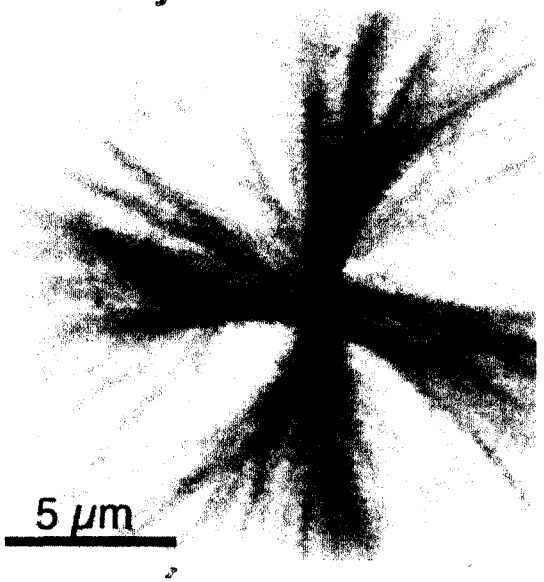

Tb Luminescence

Brookhaven
STXM

EM Transmission

Tb X-ray Fluorescence

NCEM

M. Moronne and R. Glaeser, Innovative Microscopies

Instrumental Requirements for XMT

- Optics
  - Efficient for short wavelengths
  - Long working distance
- Rotational sample stage
  - Large angles of rotation
  - Must accomodate sample holders
  - Allow sample scanning
- Cryofixation apparatus
  - Dry gas chamber
- Miscellaneous
  - 3-D resolution test objects

UCSF
UCB

L·B·N·L

WET CELL SAMPLE HOLDER FOR BIOLOGICAL MICROSCOPY

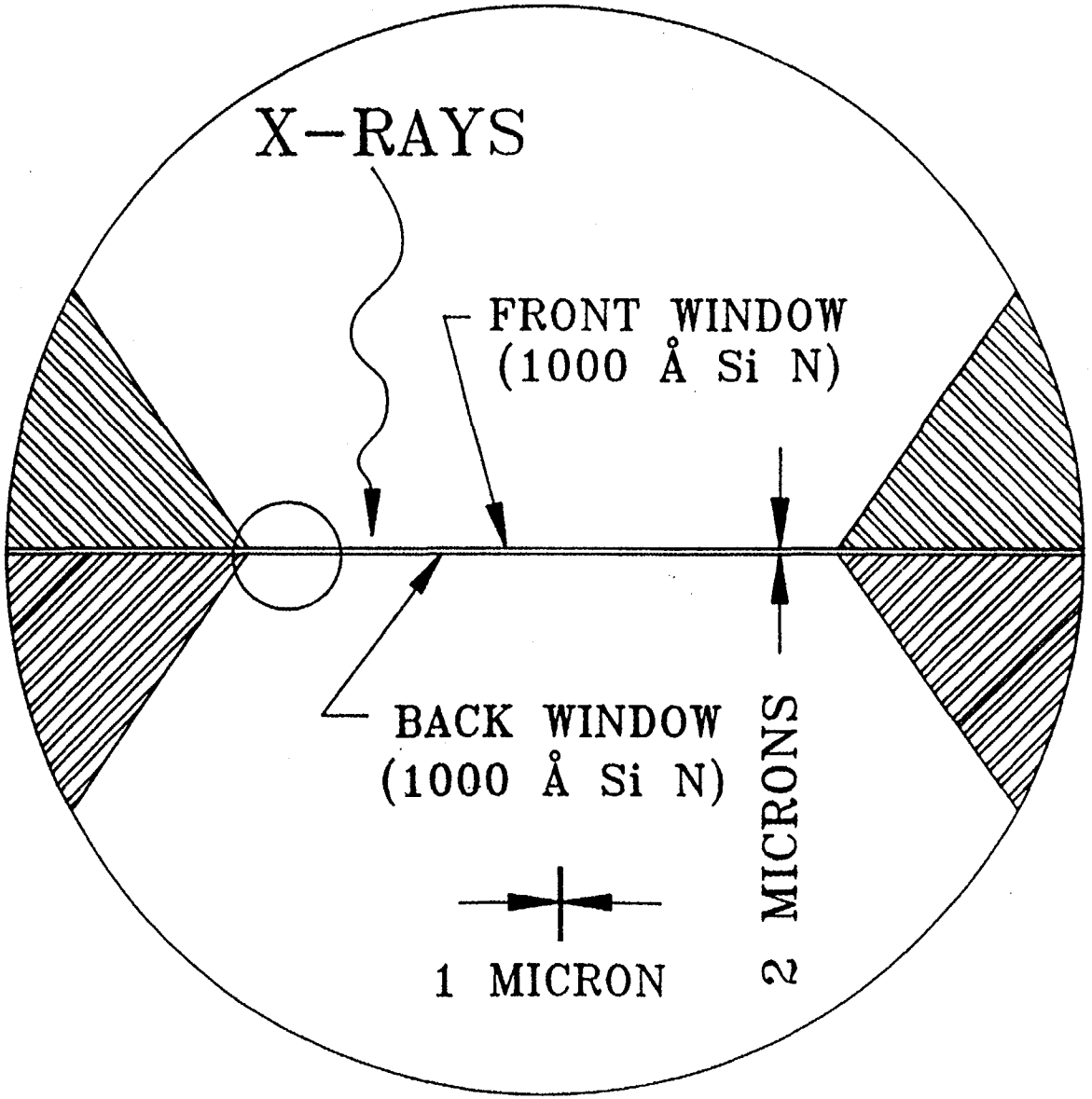

CLOSE UP VIEW OF WINDOWS AND GRANULES

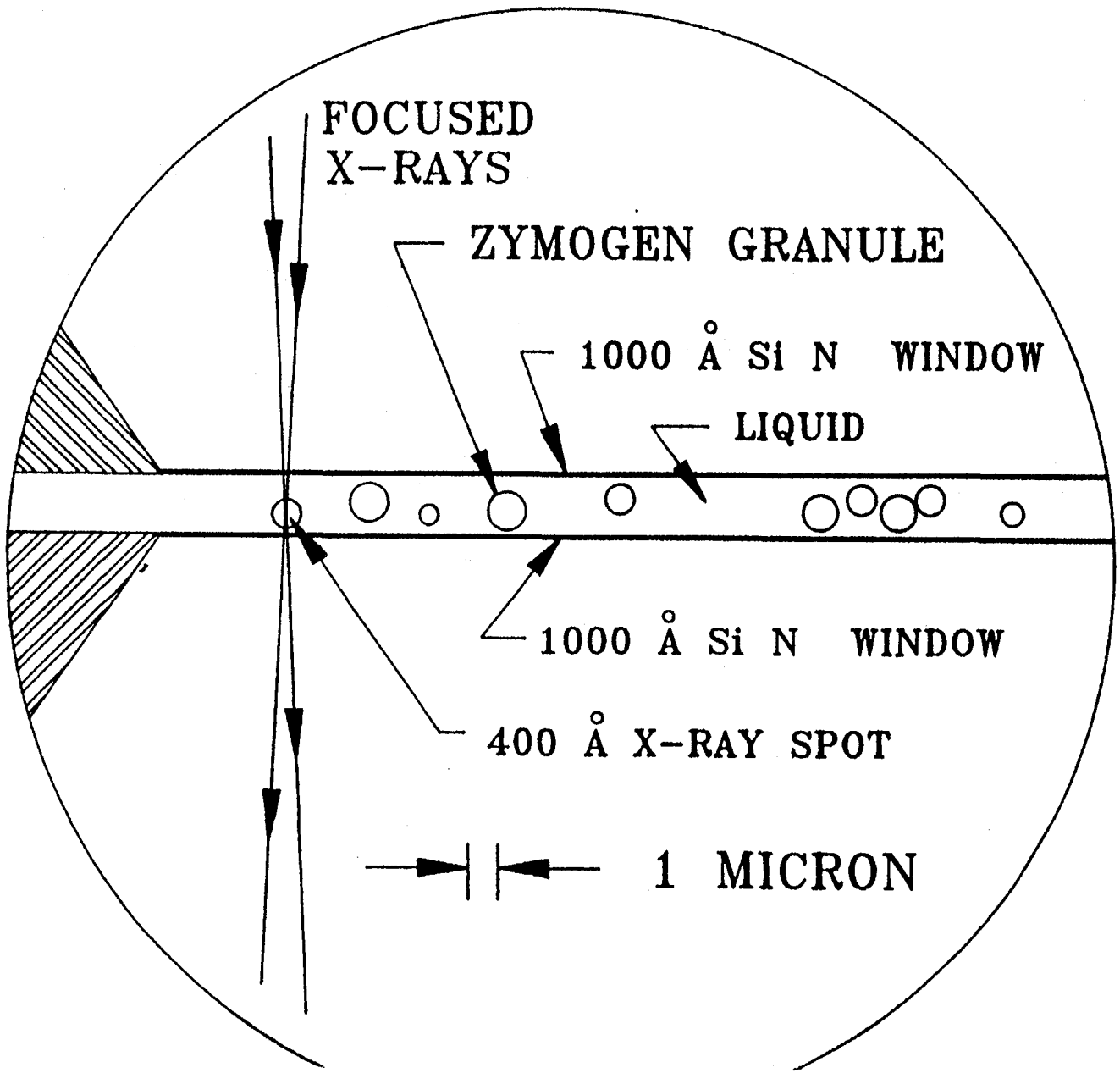

Simulation: A Sample XMT Problem

- Digital phantom
  - An X-Z slice of a "cell" with features as small as 80 nm
- Simulation parameters:
  - Cell is in 5 μm thick water layer, with no stains
  - Protein absorption contrast only
  - Restricted tilt angle
  - Blurring due to lens point spread function
  - Sufficient illumination to detect an 80 nm protein feature at 80 mg/ml contrast
  - Analysis of absorbed radiation dose

UCSF
UCB

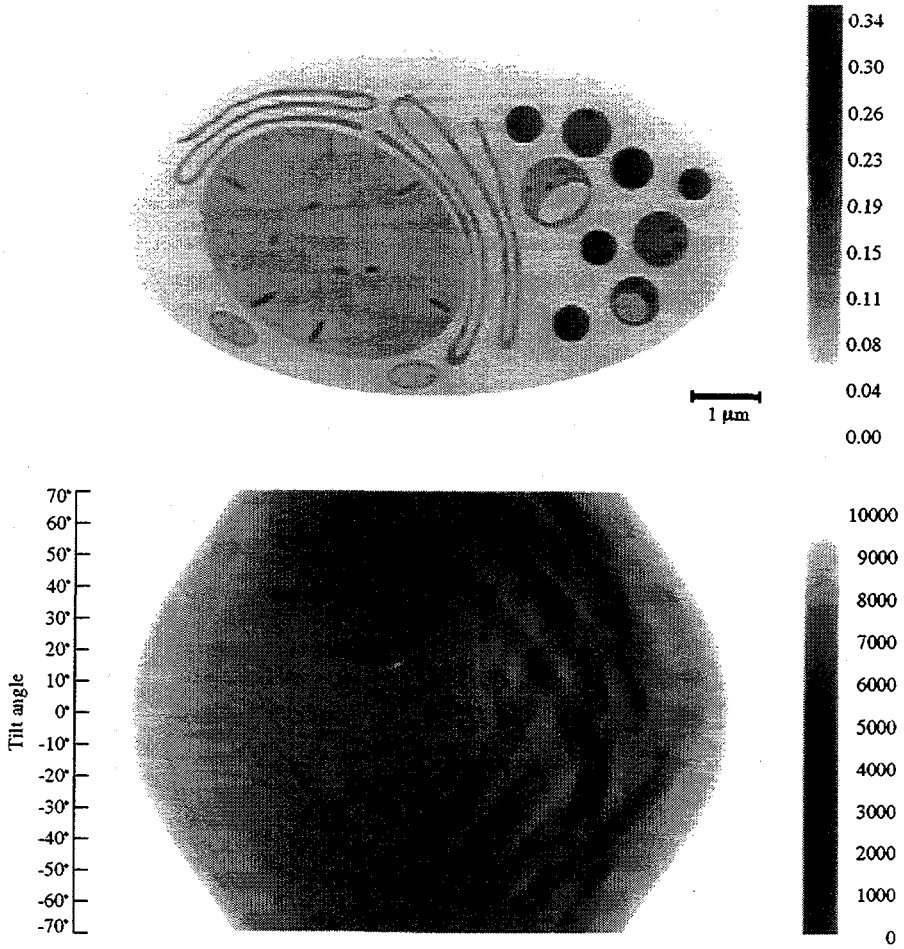
0.34
0.30
0.26
0.23
0.19
0.15
0.11
0.08
0.04
0.00
1 µm
Tilt angle
70°
60°
50°
40°
30°
20°
10°
0°
-10°
-20°
-30°
-40°
-50°
-60°
-70°
10000
9000
8000
7000
6000
5000
4000
3000
2000
1000
0

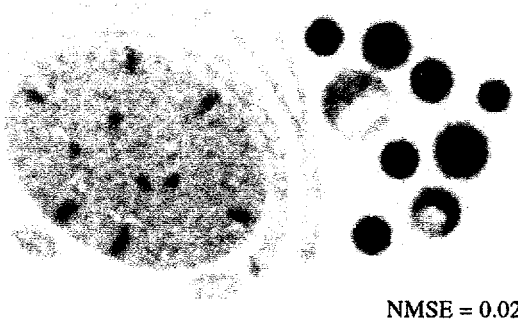

R90D NMSE = 0.02003

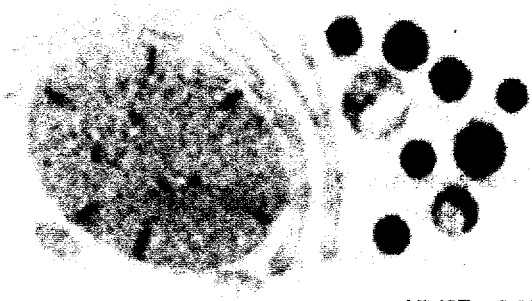

R80D NMSE = 0.02803

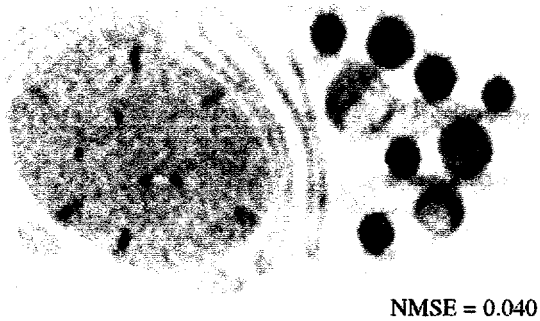

R70D NMSE = 0.04017

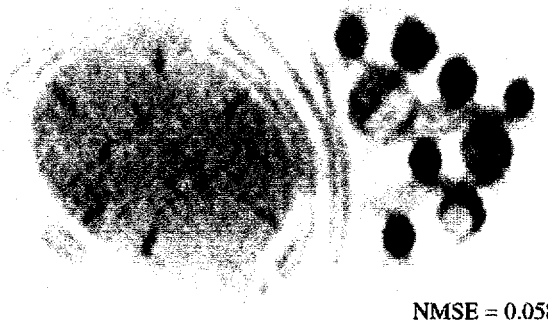

R60D NMSE = 0.05813

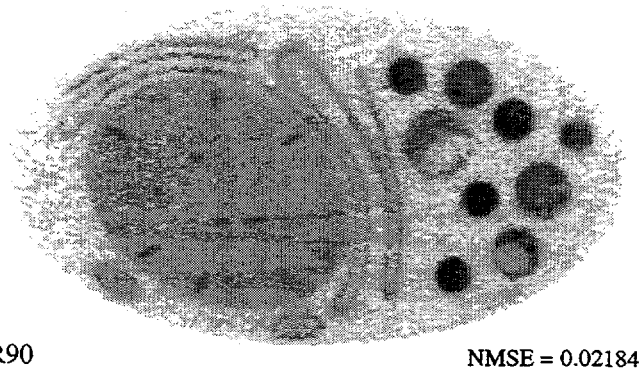

R90 NMSE = 0.02184

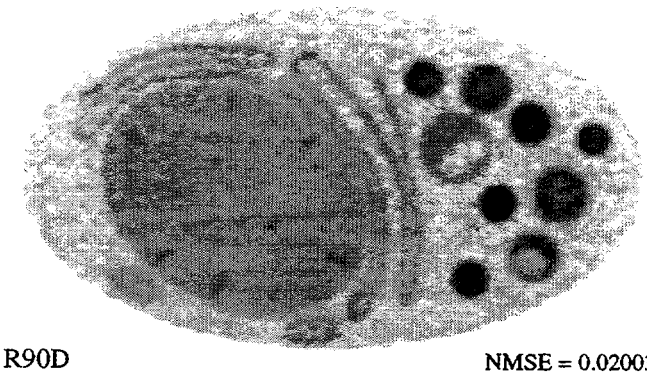

R90D NMSE = 0.02003

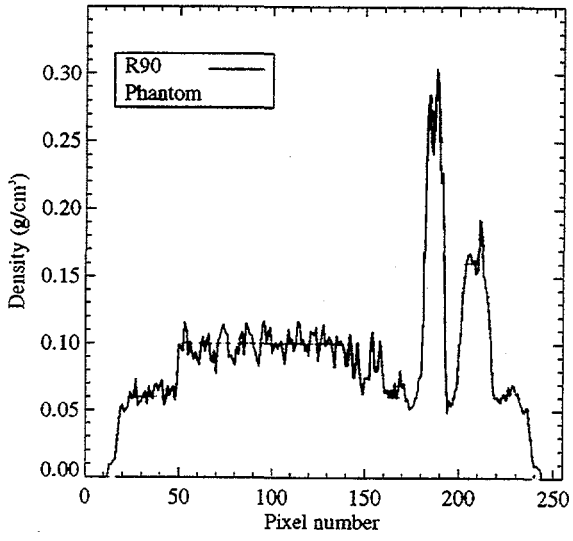

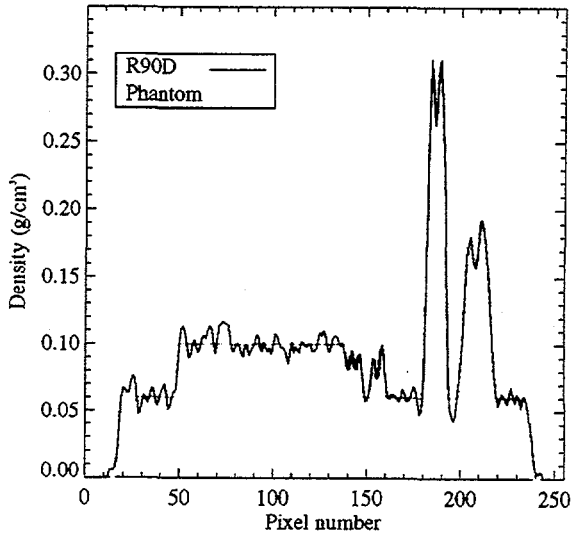

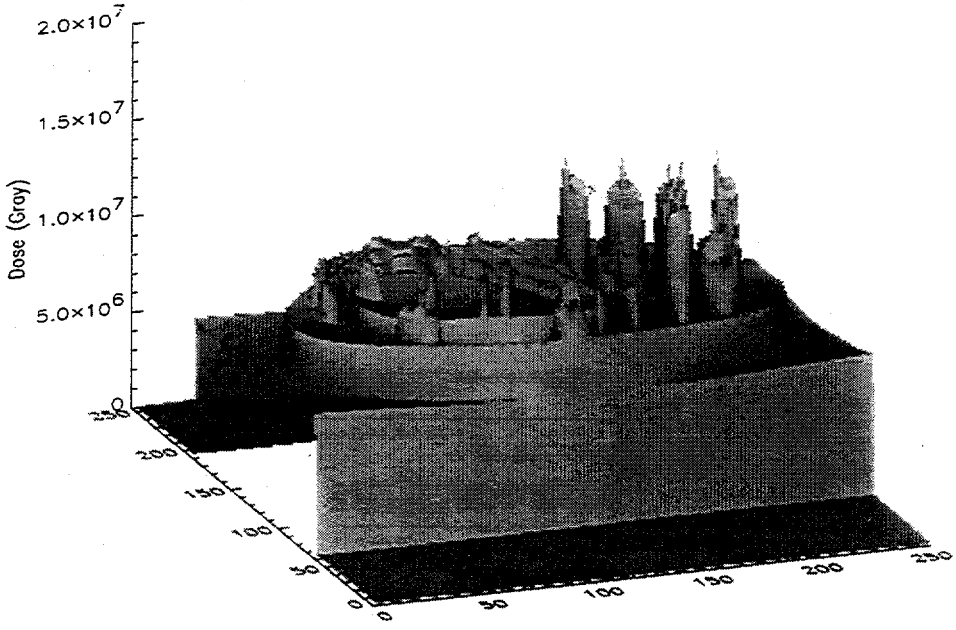
Dose (Gray)
2.0x10^7
1.5x10^7
1.0x10^7
5.0x10^6
0
250
200
150
100
50
0
0
50
100
150
200
250

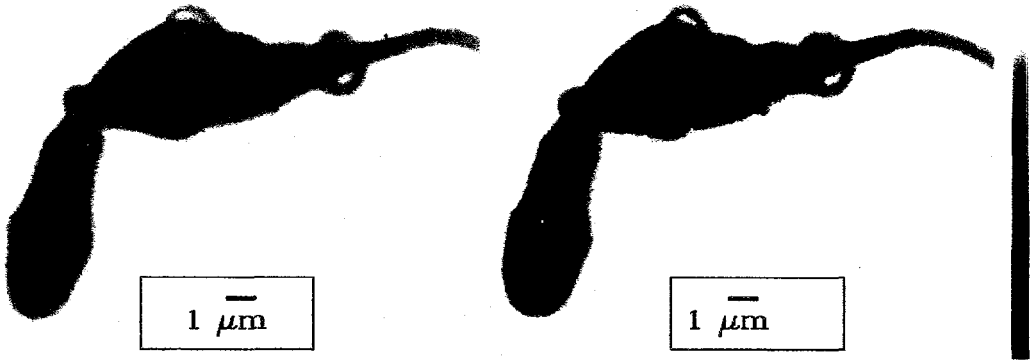

Fig. 1: Stereo image pair of human spermatozoa
from B.W. Loo, Jr., S. Williams, S. Meizel, and S.S. Rothman,
"X-ray stereomicroscopy: high resolution 3-D imaging of human spermatozoa
in aqueous suspension with natural contrast," *Journal of Microscopy*, **166**(2), 1992.

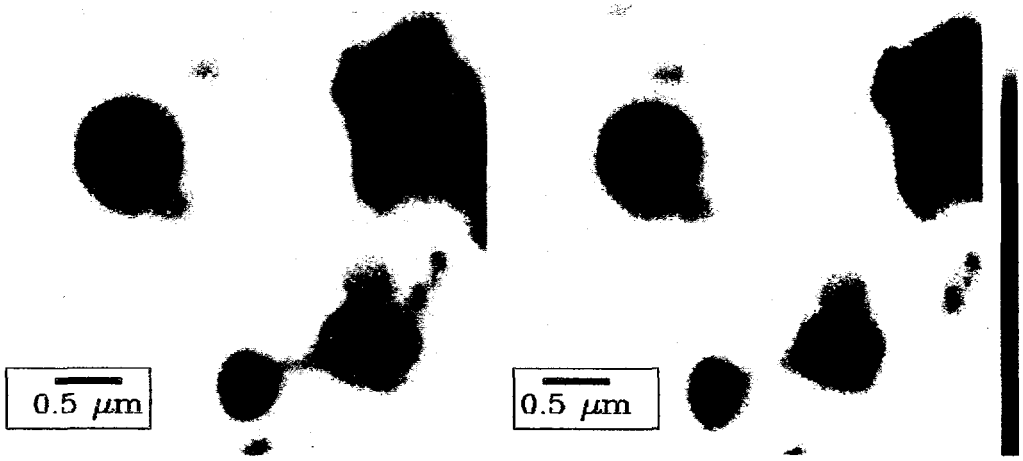

Plate 5: Stereo image pair of rat pancreatic zymogen granule
from B.W. Loo, Jr., *et. al.*, "High resolution x-ray stereomicroscopy:
true three-dimensional imaging of biological samples," in *Soft X-Ray Microscopy*,
Proceedings SPIE vol. 1741, 1993.

Computational Requirements

- Iterative reconstruction
  - Better noise properties
  - Can incorporate constraints and prior knowledge
- Hardware requirements for a typical problem size (256 × 256 × 256 pixels):
  - Storage: > 140 MB RAM
  - Processing: ~10^{10} arithmetic operations / iteration
- Analysis tools:
  - 3-D image visualization
  - 3-D image segmentation and measurement

UCSF
UCB

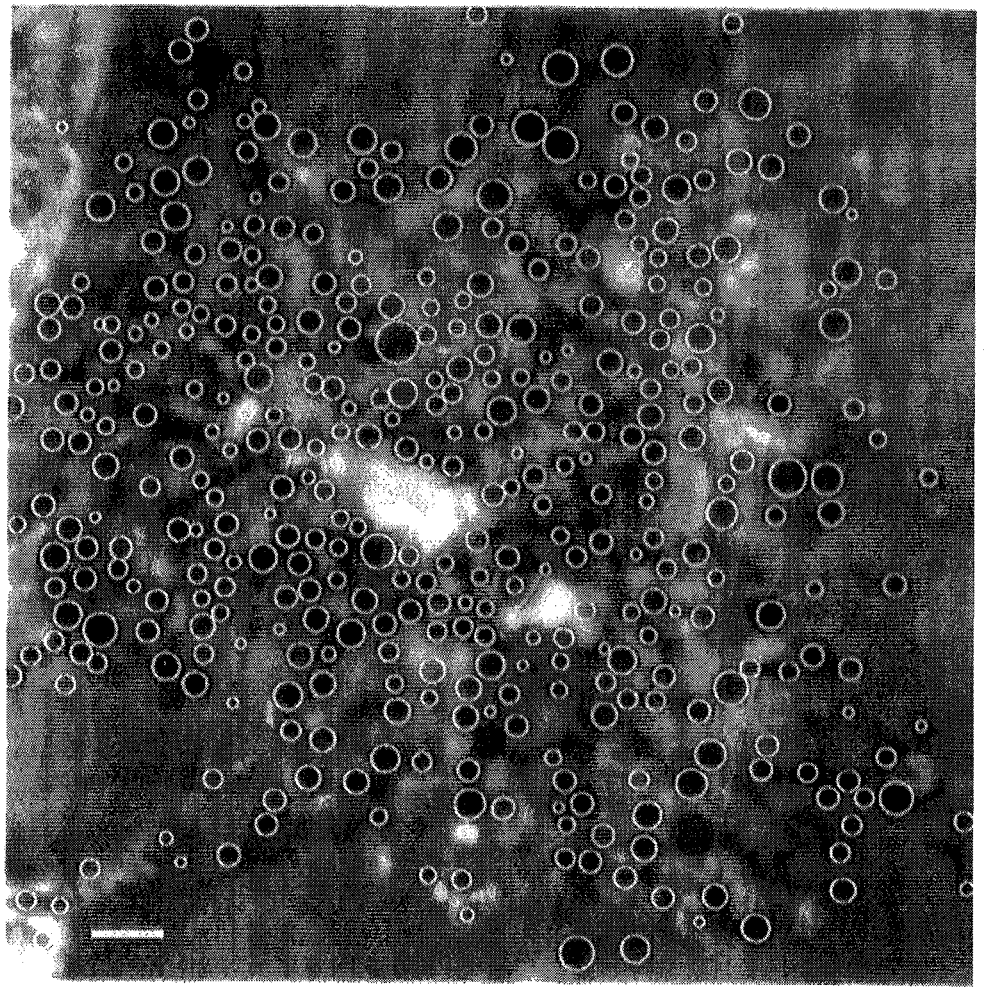

Automatic segmentation of zymogen granules. Scale bar = 2.0 μm.

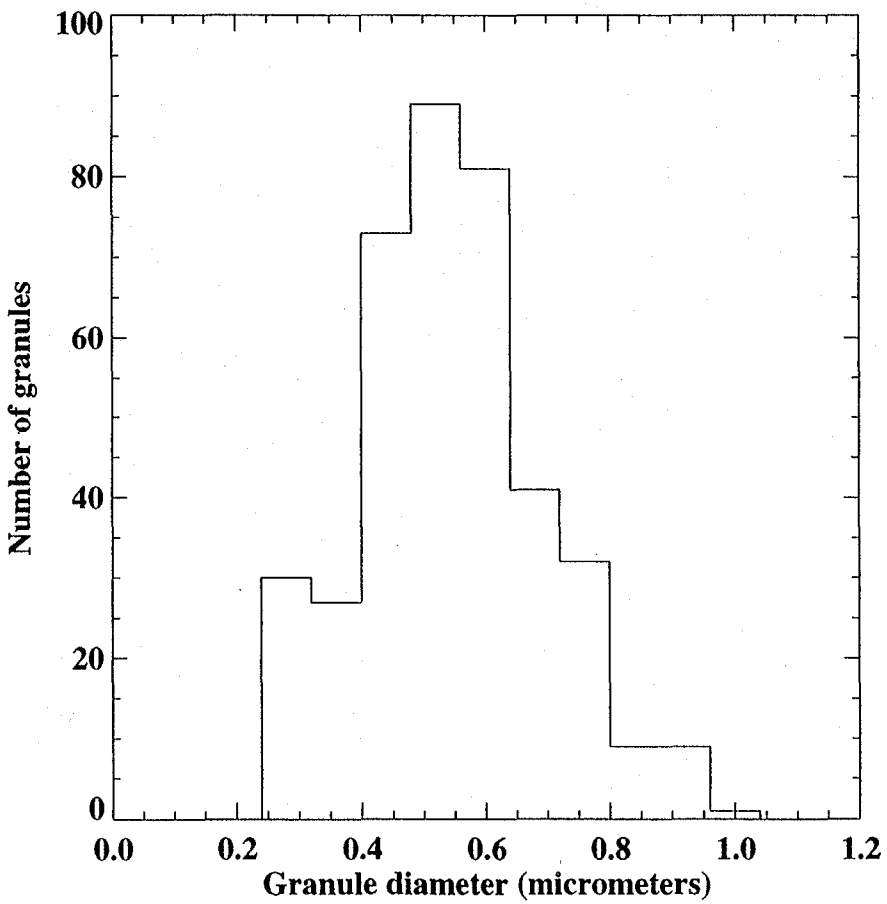
100
80
60
40
20
0
Number of granules
0.0
0.2
0.4
0.6
0.8
1.0
1.2
Granule diameter (micrometers)

Conclusions

- XMT can provide a new and unique means of visualizing and quantitating cellular ultrastructure
- Existing x-ray microscopes can be modified into XMT instruments with current technology
- Optimal performance requires additional advances that are within reach

UCSF
UCB

High Resolution X-ray Computed Microtomography

J. Keenan Brown
UCSF Department of Radiology
and the
UCSF/UCB Bioengineering Graduate Group

Abstract: This paper qualitatively discusses the primary characteristics of methods for reconstructing tomographic images from a set of projections. These reconstruction methods can be categorized as either "analytic" or "iterative" techniques. Analytic algorithms are derived from the formal inversion of equations describing the imaging process, while iterative algorithms incorporate a model of the imaging process and provide a mechanism to iteratively improve image estimates. Analytic reconstruction algorithms are typically computationally more efficient than iterative methods; however, analytic algorithms are available for a relatively limited set of imaging geometries and situations. Thus, the framework of iterative reconstruction methods is better suited for high accuracy, tomographic reconstruction codes.

I. Introduction

Numerous methods have been used to reconstruct tomographic images, representing the distribution of attenuators within planes through an object, from sets of x-ray transmission projections through the object(1-3). Generally, these reconstruction methods can be classified as either an "analytic" or an "iterative" approach. Analytic reconstruction algorithms are derived by starting with a mathematical model that predicts the set of projections that would be measured given a particular object geometry (i.e., material types and distributions). The model equations are then inverted to give an expression for an object geometry in terms of the set of projections. Analytic reconstruction algorithms are simply techniques for numerically evaluating the inverse model equations. These algorithms can be computationally efficient. Unfortunately, the needed inverse relationship has only been derived for a limited number of projection geometries.

An alternative reconstruction strategy is provided by iterative reconstruction techniques. As with analytic reconstruction methods, iterative methods start from a mathematical model of the projection imaging process. Iterative algorithms, however, use this model explicitly to calculate the set of projections expected for a given *image estimate* of the object. The calculated projections are then compared with a measured set of projections for a particular object, and then the image estimate is updated based on discrepancies between the calculated and measured projections. The projection-comparison-update cycle is repeated iteratively until the calculated and measured projections in some sense "match." Since the inverse of the mathematical projection model is not explicitly needed in iterative algorithms, the projection model can include many details that are typically ignored in analytic algorithms. Improvements in the accuracy of the projection model can result in superior reconstructed tomographic image quality. However, improvements in image quality must be weighed against the computational burden of iterative algorithms since a single projection-comparison-update cycle frequently requires more computer time than a full analytic reconstruction from the same projection data set.

II. Analytic Reconstruction Algorithms

Perhaps the most common class of analytic reconstruction algorithms for transmission computed tomography (TCT) are the filtered backprojection (FBP) algorithms. These algorithms divide the reconstruction process into three steps: (1) weighting the projections, (2) filtering the projections, and (3) backprojecting the projections. One of the attractive aspects of filtered backprojection algorithms from a computational perspective is that projections acquired from different angular views of an object can be processed independently. Thus, the reconstruction can take place concurrently with the acquisition of projection data, and reconstructed images can be viewed almost immediately after acquiring the projection data.

As noted previously, analytic reconstruction algorithms, including FBP, have been derived for a limited number of idealized projection geometries. Most TCT scanners are designed to closely approximate these idealized geometries so that FBP or other analytic reconstruction techniques can be used with the system. While these compromises have proved adequate in many medical TCT imaging situations, applications arise that require higher resolution, accuracy and/or precisision than can be achieved with these systems.

Several physical aspects associated with TCT imaging are commonly neglected in the formulation of analytic reconstruction algorithms. Examples include: (1) beam hardening, (2) truncation, (3) projection measurement noise, (4) object motion, and (5) finite source focal spot size and detector size. Although the manifestation of neglecting these aspects of transmission imaging in the reconstruction process varies, generally doing so results in images with reduced contrast and resolution, and can result in artifactual image structures such as streaks.

III. Iterative Reconstruction Algorithms

In theory, the physical characteristics of TCT imaging noted above that are not considered in typical FBP implementations can be treated using iterative reconstruction techniques. This is possible as long as the imaging and object characteristics are well enough defined to construct an accurate model of the projection imaging process in the iterative code. While this advantage of iterative reconstruction methods has been recognized for many years, these techniques are not routinely exploited for transmission imaging due to the computational burden of iterative reconstruction methods.

The runtime for iterative reconstruction methods is determined by several factors including: (1) the complexity of the projection model, (2) the optimization algorithm used, and (3) the number of iterations required to satisfy the particular set of stopping conditions. Roughly, the minimum time per iteration is approximately the time to reconstruct the data using an FBP code. Depending on the optimization algorithm used, it is likely that at least 10 iterations, and perhaps several hundred, may be required to satisfy the stopping conditions. Qualitatively, this implies that iterative codes require at least an order of magnitude more time to reconstruct a data set on a given system than is needed by FBP. Obviously, increasing the complexity of the projection model will increase the runtime for the reconstruction.

IV. Summary

Analytic and iterative tomographic reconstruction methods have complimentary characteristics, and the availability of both techniques on the LBNL Computed Microtomography system would be advantageous. Several analytic reconstruction methods are well established and computationally efficient. These techniques generally deliver good image quality for a broad range of imaging circumstances. However, iterative methods can provide superior image contrast and resolution, and better quantitative accuracy and precision, at the expense of computational efficiency.

V. References

1. HH Barrett and W Swindell, "Radiological Imaging, The Theory of Image Formation, Detection, and Processing", Volume 2, Academic Press, New York, 1981.

2. AC Kak and M Slaney, "Principles of Computerized Tomographic Imaging", IEEE Press, New York, 1988.

3. K Lange and R Carson, "EM Reconstruction algorithms for emission and transmission tomography," *J. Comput. Assist. Tomogr.* **8**:306-16 (1984).

High Resolution X-ray Computed Microtomography

J. Keenan Brown

Dept. of Radiology, UCSF
and the
UCSF/UCB Bioengineering Graduate Group

Outline

I. The Transmission CT Reconstruction Problem

II. Analytic and Iterative Reconstruction Strategies

III. Filtered Backprojection

IV. Scanner Design Considerations

V. Iterative Reconstruction Methods

Transmission CT Sinogram

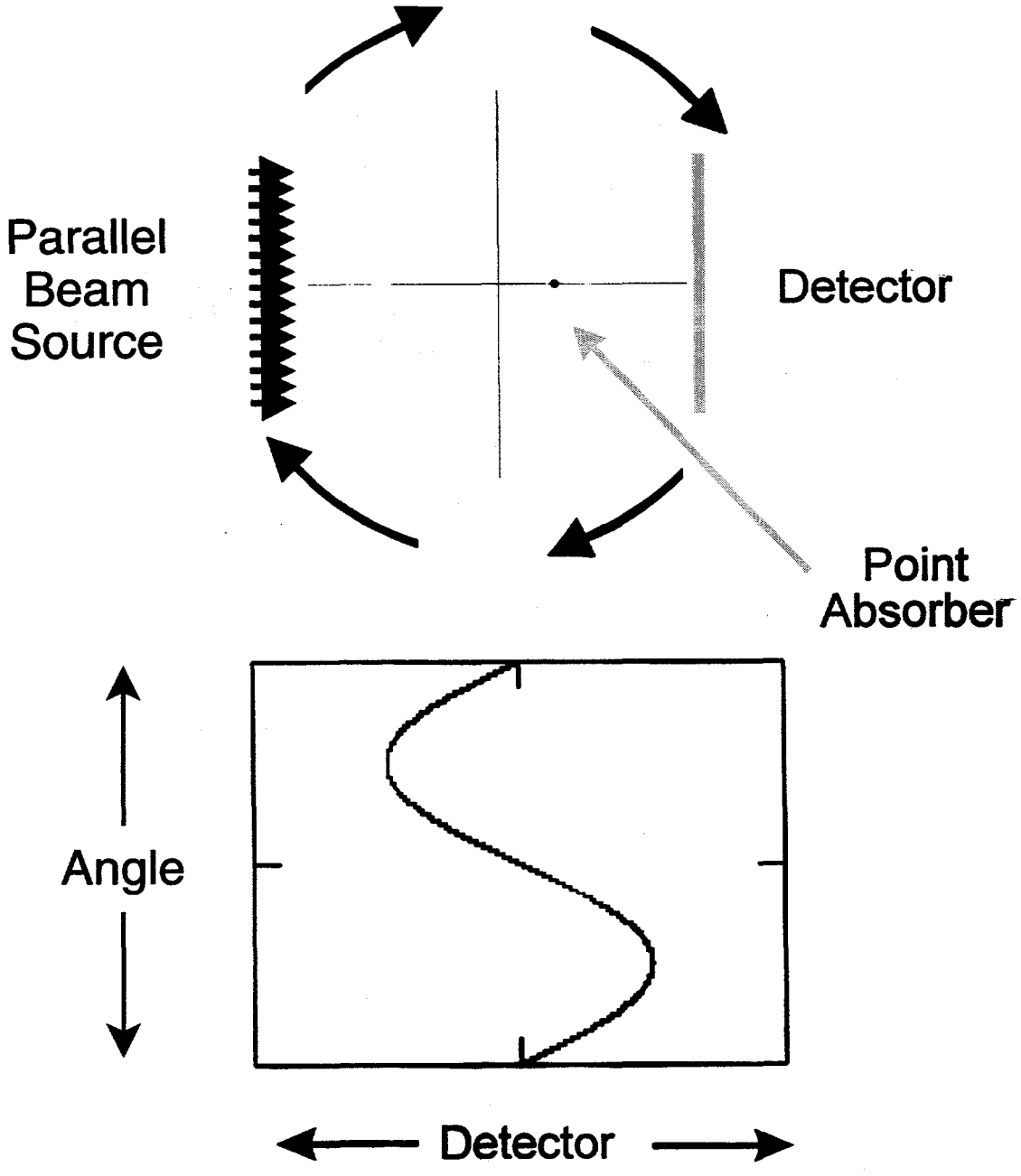

Transmission Computed Tomography

Parallel Beam Geometry

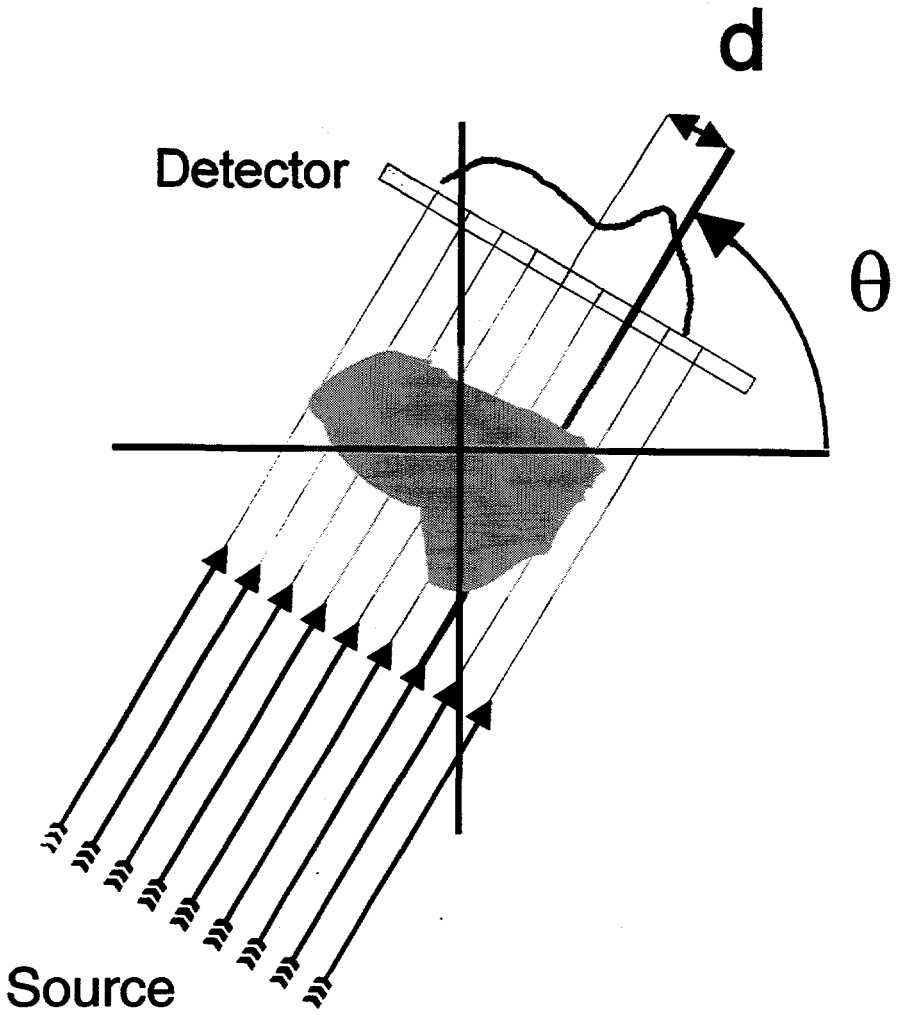

Transmission Computed Tomography

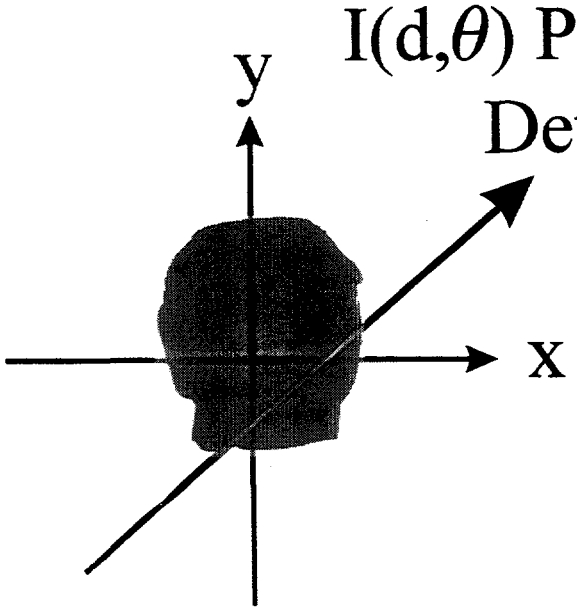

$I(d,\theta)$ Photons are Detected

$I_0(d,\theta)$Photons Enter the Object

Total attenuation, $p(d,\theta)$, along the line specified by (d,θ) is

$$p(d,\theta) = \ln[I_0(d,\theta)/I(d,\theta)]$$

Transmission CT Example

Original to Image

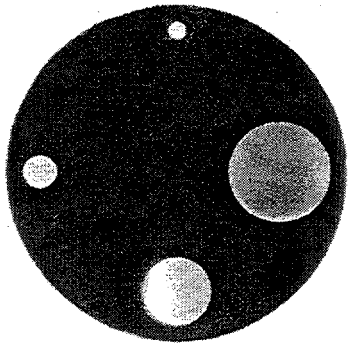

Red regions correspond to lower attenuation.

"Raw" Projection Data

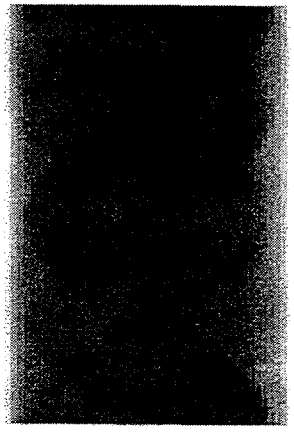

Projection Data (Sinogram)

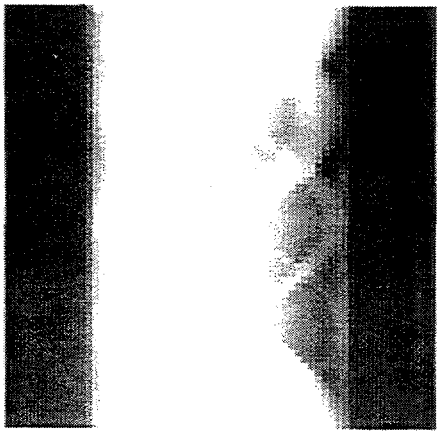

The raw projection data must be processed according to:

$$\log\left(\frac{I_0}{I}\right)$$

Reconstruction Stategies

I. Analytic Reconstruction Methods

Start with a model equation that predicts projection measurements for a particular distribution of attenuators. Invert this model to give an explicit expression for the distribution of attenuators in terms of the projections.

II. Iterative Reconstruction Methods

Start with a model equation that predicts projection measurements for a particular distribution of attenuators. Use this model to predict projections for an estimate of the attenuators. Iteratively refine the attenuator estimate based on comparisons between predicted and measured projections.

Transmission/Emission CT Reconstruction Methods

Analytic Methods

Advantages

1. Computationally efficient
2. Insight from analytic model

Disadvantages

1. Available for limited geometries
2. Difficult to Incorporate other physical aspects of imaging problem

Interative Methods

Advantages

1. Adaptable to broad range of geometries
2. Can incorporate other physical aspects of imaging problem

Disadvantages

1. Computationally inefficient
2. Limited insight from model problem

Backprojection of a Point Source

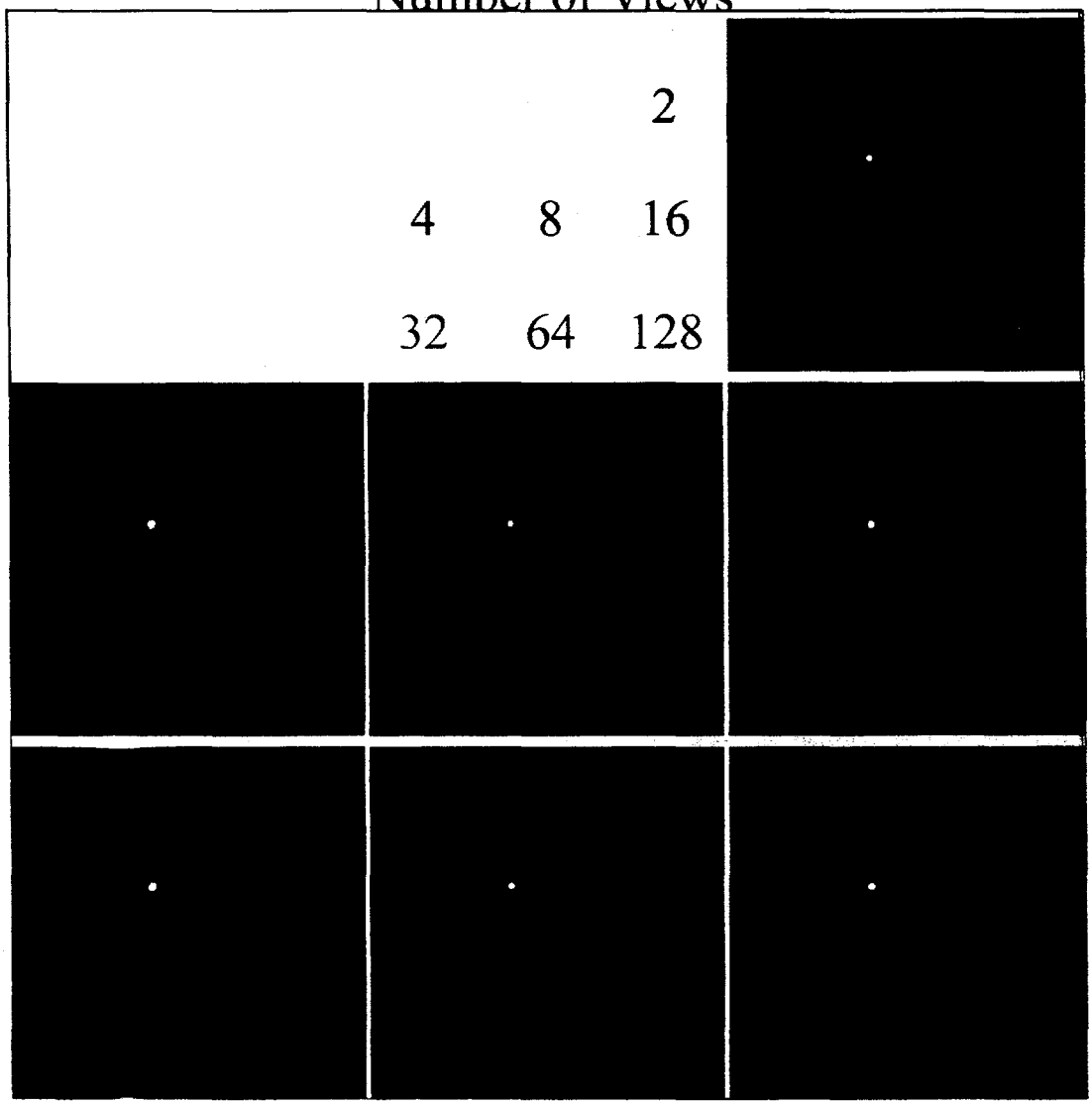

Backprojection from a Point Source

A single ray is "backprojected" from each "angular view."

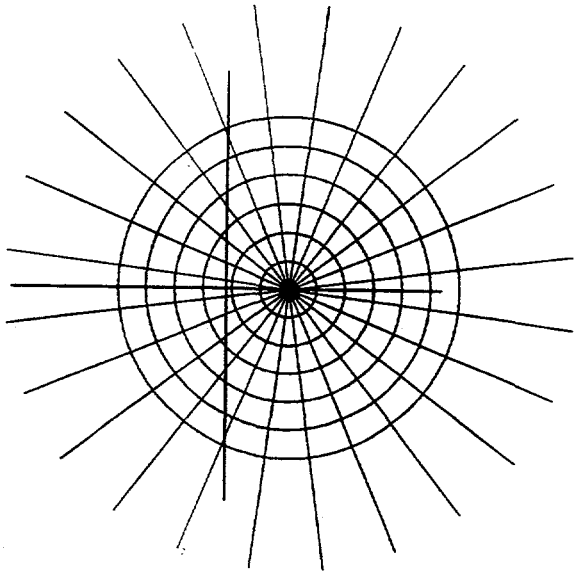

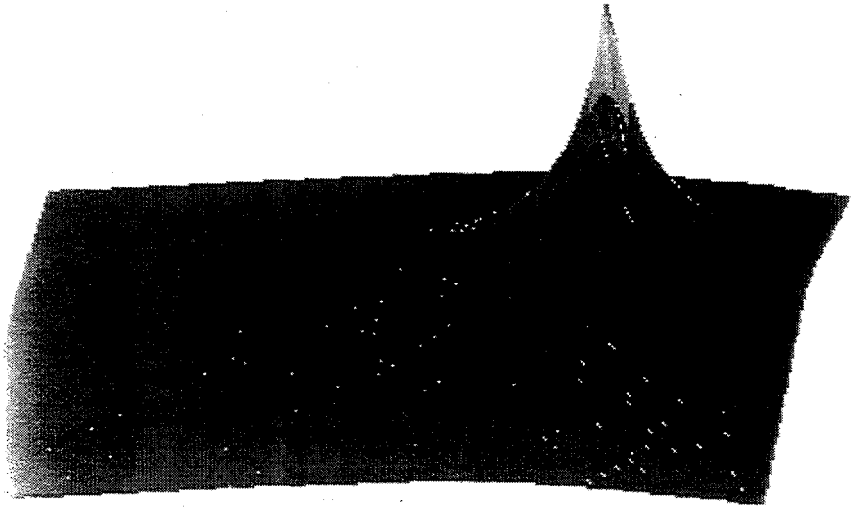

Log Scaled Surface Plot of Backprojected Image

The |ξ| High Pass Filter

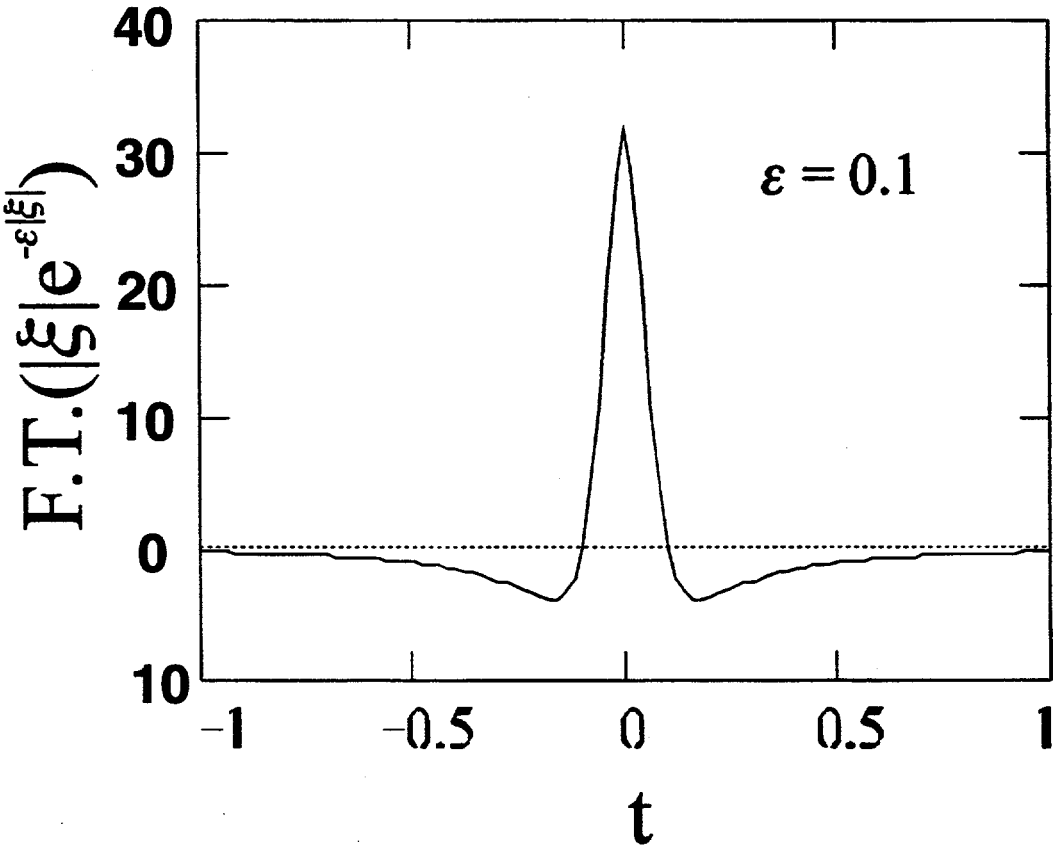

Applying the high pass filter |ξ| approximately corresponds to correlation with the function shown above (Fourier Convolution Theorem).

Filtered Backprojection of a Point Source

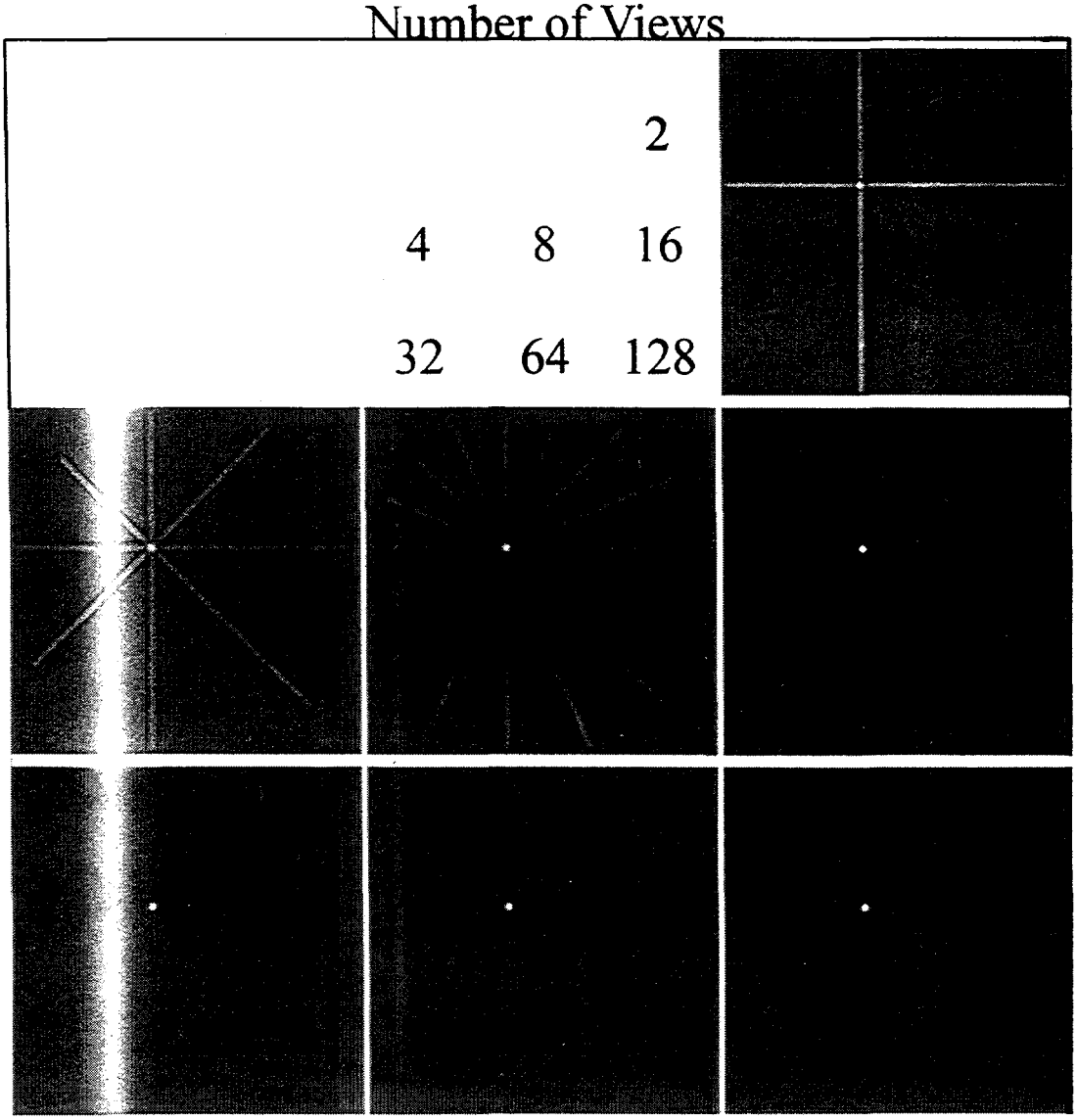

Reconstruction with Filtered Backprojection

Object to Image

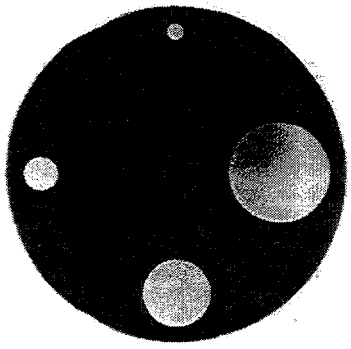

Projection Data
(Sinogram)

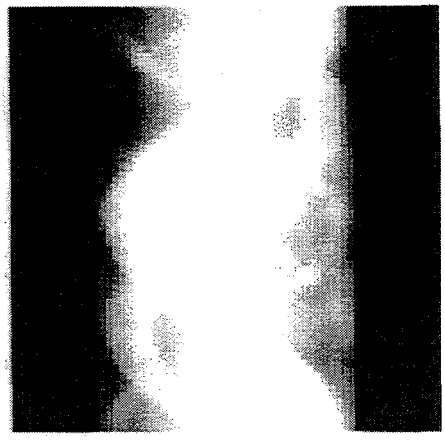

Filtered
Projections

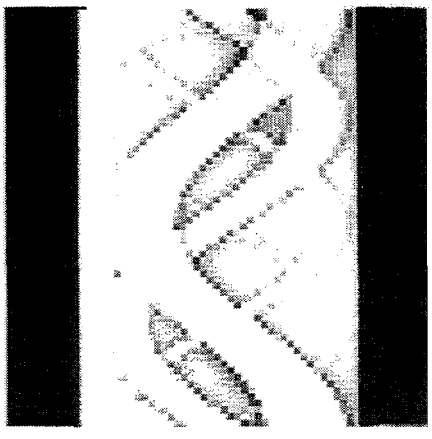

Reconstructed
Image

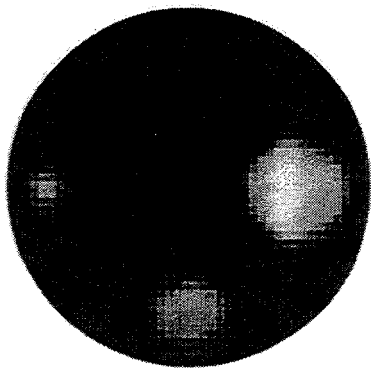

Design Considerations

I. Geometry

The filtered backprojection algorithm can be used for a limited number of geometries. These include:

Parallel Beam

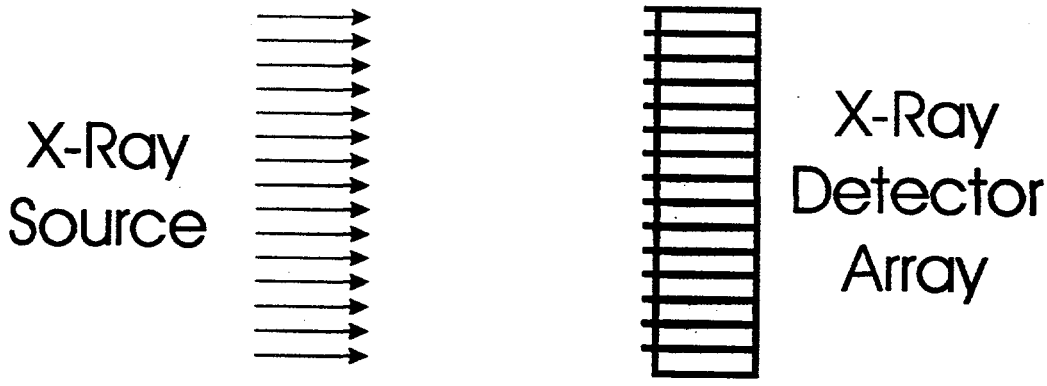

Fan Beam

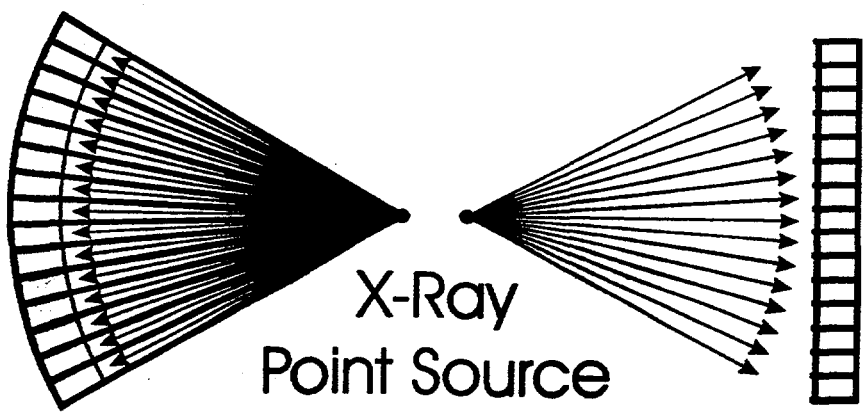

Design Considerations

II. Sampling Requirements Number of Detectors per View:

Simple considerations indicate that there should be two samples per detector width per view to achieve a reconstructed spatial resolution of approximatley one detector width.

View 1
+1/4 Detector Width

View 2
-1/4 Detector Width

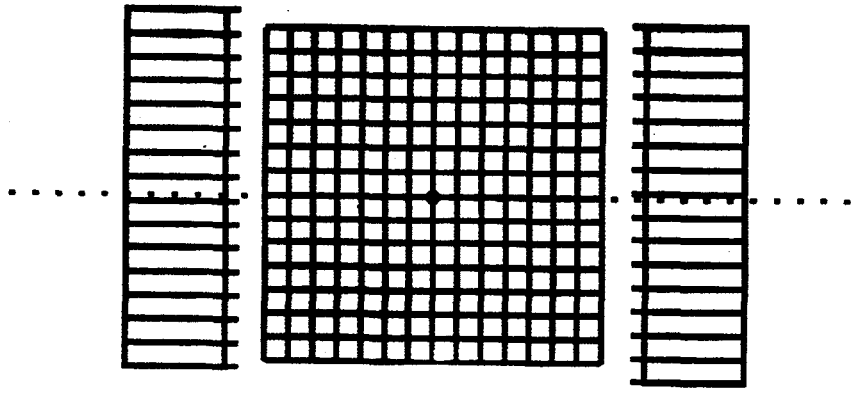

For Opposing Views, the Detector Arrays are shifted by 1/2 of a detector width

Design Considerations

II. Sampling Requirements
Number of Views:

Simplistic considerations indicate that the number of angular views of an object should be $\pi/2$ times the number of detectors.

Positioning Requirements:

Typical Commercial Medical CT scanners have a positioning accuracy of approximately 1/10 of a Detector Width.

Detector Dynamic Range:

Typical Commercial Medical CT Scanners use 20 to 22 bit A/D converters for projection measurements, and achieve a dynamic range of 10 to 12 bits in the reconstructed images.

Limitations of Analytic Reconstruction Methods

I. Restricted Scan Geometries

II. Truncation Errors

III. Focal Spot & Detector Size

IV. Sensitivity to Noise

V. Beam Hardening

VI. Motion

VII. Scatter

Reconstruction with Noisy Data

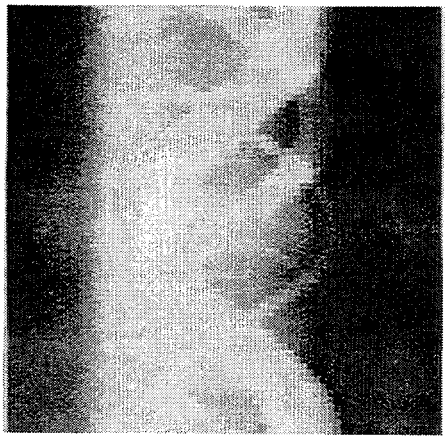

infinity

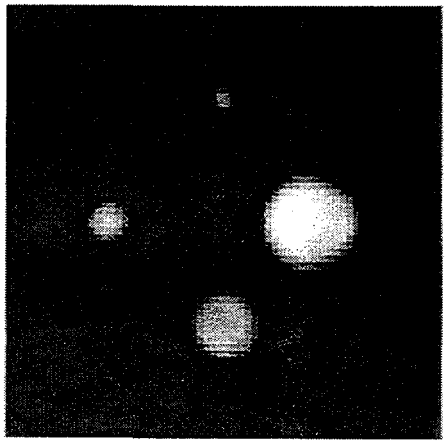

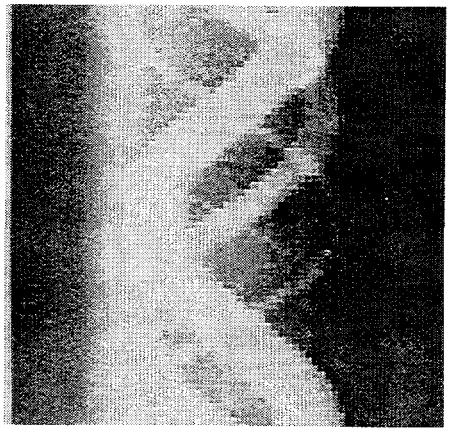

80000

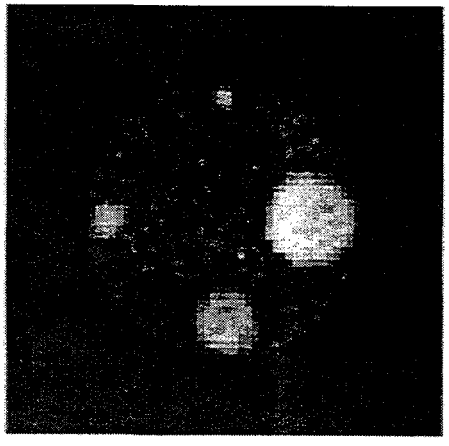

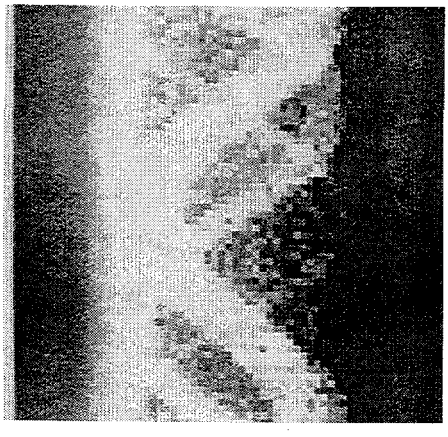

8000

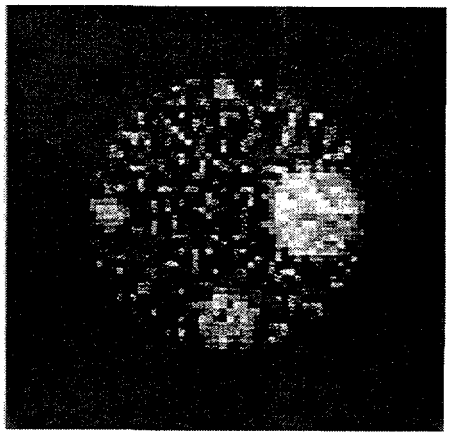

Incomplete Sampling due to Truncation

Object to Image

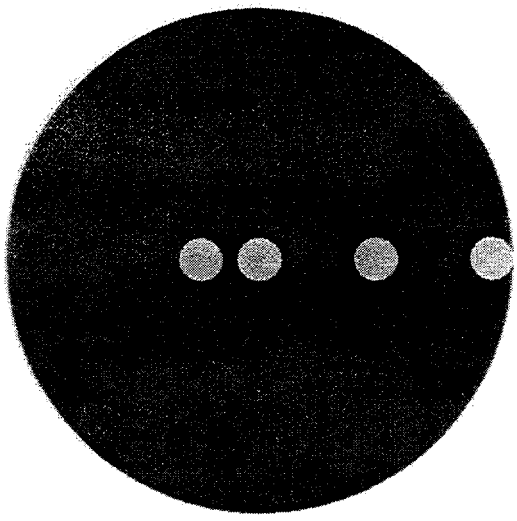

Projection Data

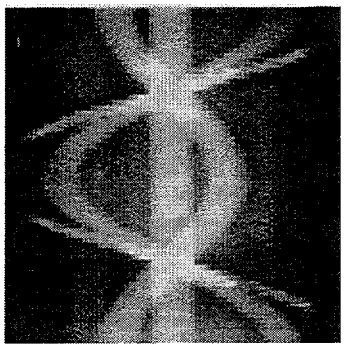

Reconstructed Image

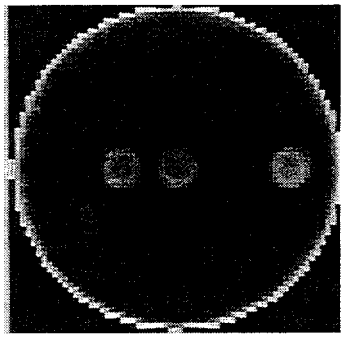

Incomplete Data due to strong absorber

Image reconstructed from noiseless data.

Attenuation in the upright region is approximatley 4x greater than in the darker region.

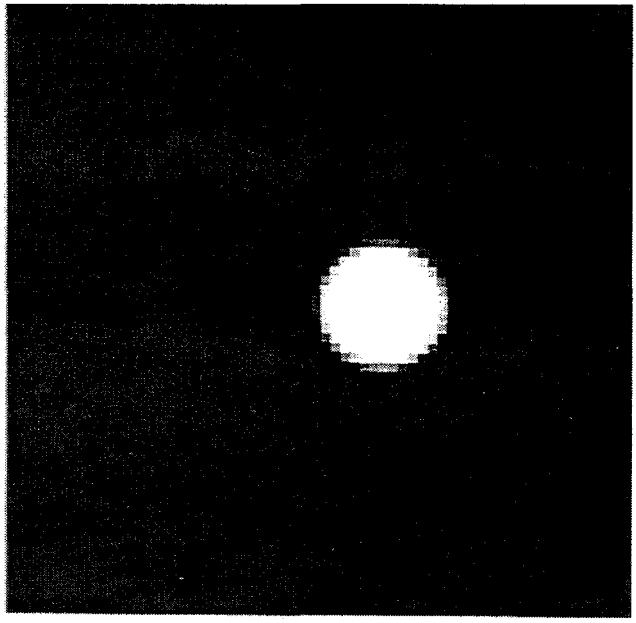

Image reconstructed from projection data including noise.

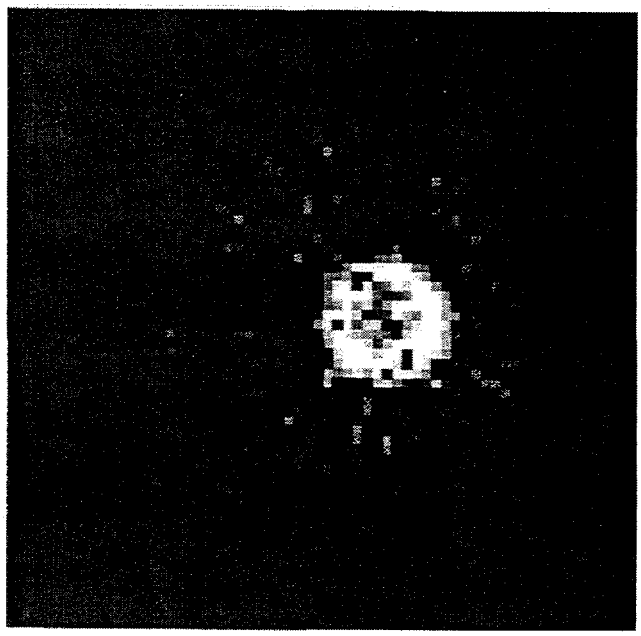

Beam Hardening Example

"High" Energy Image

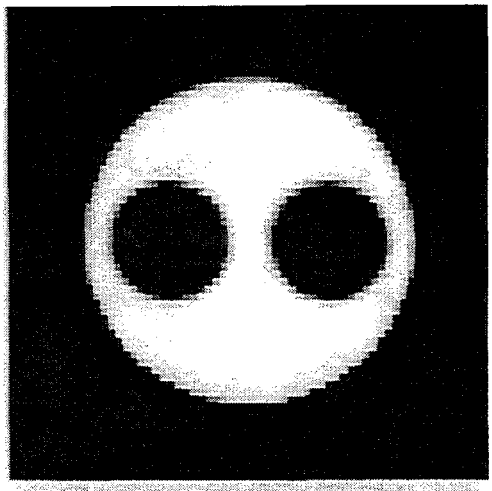

"Low" Energy Image

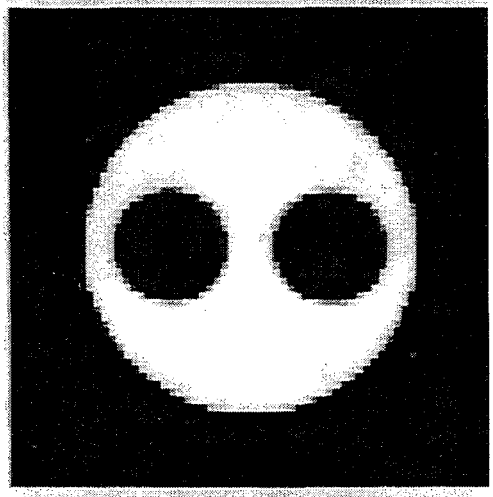

Beam Hardened Image

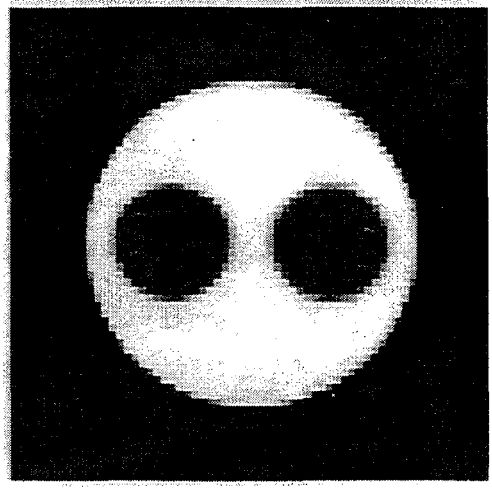

Iterative Reconstruction Methods

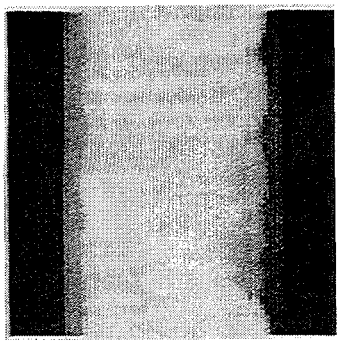

Sinogram

Comparator

Corrector

Stopping Rules

Projector

Initial Image Estimate

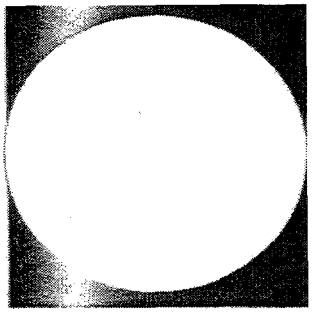

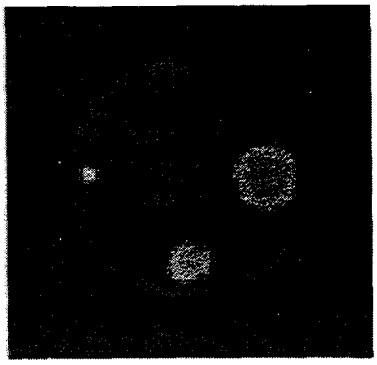

Reconstructed Image

The Alphabet Soup of Iterative Reconstruction Methods

(Abreviated Edition)

ART	Algebraic Reconstruction Technique
MART	Multiplicative Algebraic Reconstruction Technique
SIRT	Simultaneous Iterative Reconstruction Technique
MENT	Maximum Entropy
ML-EM	Maximum Likelihood - Expectation Maximization
CG/WLS	Conjugate Gradient / Weight Least Squares
SOR	Successive Simultaneous Over-relaxation Sequential

Jacobi, Gauss-Seidel, Kaczmarz

"Spokey" Phantom

Mean Image

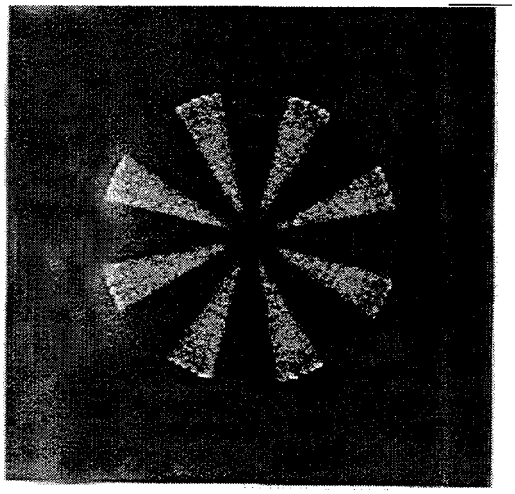

"Standard Deviation" Image

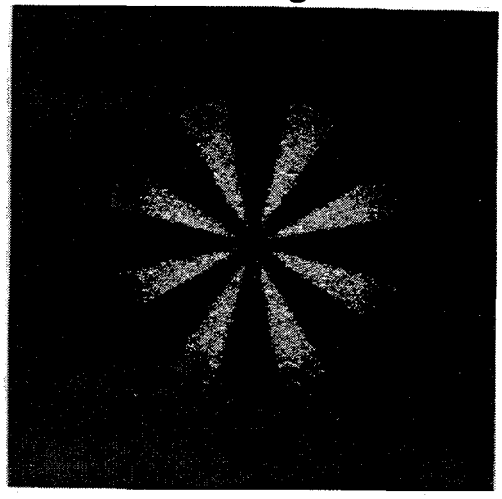

Simulated Projection Data (400 Realizations)
Reconstructed Using 30 ML-EM Iterations

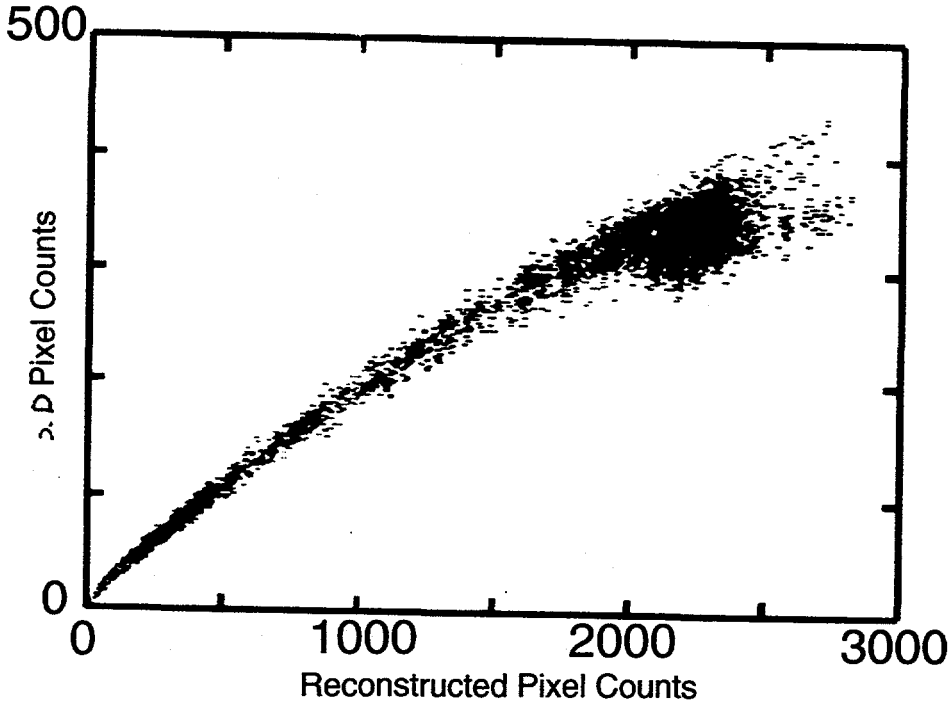

Summary

Analytic and Iterative Reconstruction Methods are Complimentary

Analytic methods provide computational efficiency at the expense of image accuracy,

while,

Iterative methods provide higher accuracy but carry a much greater computational burden.

Requirements on High Resolution Detectors

by
Andreas Koch
European Synchrotron Radiation Facility
BP 220, F-38043 Grenoble

For a number of microtomography applications X-ray detectors with a spatial resolution of 1 μm are required. This high spatial resolution will influence and degrade other parameters of secondary importance like detective quantum efficiency (DQE), dynamic range, linearity and frame rate. This note summarizes the most important arguments, for and against those detector systems which could be considered. This note discusses the mutual dependencies between the various figures which characterize a detector, and tries to give some ideas how to proceed in order to improve present technology.

Until now **X-ray film** has been the main choice if imaging resolution of 1 μm was required. The main disadvantage is that it takes much time to develop the film, scan it into the computer and eventually see the image. It is not considered to be an 'on-line' detector. Other drawbacks are the limited dynamic range and the poor linearity (see viewgraphs). The absorption of X-rays is poor for energies above 10 keV but this will be not much different for a few other detectors including luminescent screen based detectors.

Luminescent screen based detectors 'instantaneously' convert the X-ray image into a visible light image which can be registered by usual electronic detectors. This detector type therefore is 'on-line'. Even images with high dynamic range of 16 bits can be recorded and visualized within seconds. Systems with the required spatial resolution, however, are not commercially available. The main challenge is to fabricate the luminescent screen. There are mainly three types of screens: powder deposited screens, crystalline screens and structured screens.

Powder screens are most widely used. Luminescent powders are available in a huge variety of different chemical compositions. They are composed out of small grains with minimum grain size of, unfortunately, around 1 μm (commercially). So uniform layers of 1 μm cannot be produced, 2 μm is about the limit. The layer thickness is approximately proportional to the spatial resolution, in terms of fwhm of the pointspread function (PSF). Therefore, high resolution results often in a low DQE [1]. Even if the production of smaller grains would be feasible, the deposition of the phosphor gets more difficult. The deposition is usually done in a suspension of these grains in a liquid. The smaller the grain size, the more the suspension becomes a colloid and settling becomes more and more difficult. To optimize the detector, a fine grain powder out of high Z material, high density and high conversion efficiency of X-rays into light has to chosen. A resolution of 4 μm at 20% rms uniformity has been achieved (see viewgraphs) which is probably close to the achievable limit.

The resolution of crystalline screens does not only depend on their thickness but also on the optics used. High aperture optics will have a short depth of focus but good light collection efficiency. Additionally, parallax may cause a degradation in resolution. The optimum configuration will depend on the X-ray energy and the crystal used. Polishing methods probably do not provide crystals which are thin enough. Evaporation or epitaxial growth methods have to be used which restrict the choice of materials further. 3 μm with a YAG:Ce crystal grown on pure YAG has been obtained (viewgraphs). 1 μm resolution should be possible to achieve.

Structured screens provide some sort of light guiding perpendicular to the screen in order to avoid light spreading in the screen and to obtain a higher ratio of thickness over spatial resolution (again in fwhm of PSF). They can be produced from materials

growing in 'needle' like manner (e.g. CsI) [2] or be using masks filled with the luminescent material. A resolution of 1 μm has been reported by a group from Exxon (viewgraphs) [3].

Electron tube detectors employing **photoconductive targets** have a potential advantage w.r.t. the ratio of thickness to spatial resolution. The creation of electron hole pairs takes place along the path of the X-rays and in principal no lateral signal spreading occurs. Furthermore photoconductors like PbO, CdTe or Se provide good X-ray absorption which will be important at energies higher than 10 keV. This makes it interesting to study the potential properties of this system further. A resolution of 500 lp/mm has been reported (viewgraphs) [4].

More exotic approaches using physical or chemical processes to store a latent image. **Photoresist** can be used. When exposed with X-rays, followed by etching will leave a relief which can be read with an electron microscope. A resolution even of 0.06 μm has been achieved, 0.02 μm is estimated to be possible (viewgraphs) [5].

Another method could perhaps exploited for X-ray detection which is used for holographic recording at visible light. The sensitive target is a sandwich of a **thermoplastic and a semiconductor layer**. The thermoplastic layer is electrical isolating. It is charged to several kilovolts. The incident radiation creates charges which attract the ions on the thermoplastic layer. The layer deforms when heated up under the electrical forces. A relief is formed which again may be read out with an electron microscope [6]. Also for this system, submicron resolution should be possible. These last two systems of course are not 'on-line'. Their dynamic range and linearity have to be carefully looked at.

In conclusion, it seems to be most promising to improve luminescent screen detectors in terms of effort. Rather straightforward is the improvement of crystalline screens. More effort is required for structured screens. If high DQE and work at high energies is necessary, electron tubes with photoconductive target may be a very interesting choice. Their feasibility, however, have yet to be proven. Utmost resolution is obtained from photoresists.

References

[1] A.Koch and C. Riekel, Rev. Sci. Instrum. 67 (1996) 1737
[2] K. Oba, M. Ito, M. Yamaguchi and M. Tanaka, Adv. Electron. Electron Phys. 74 (1988) 247
[3] H.W. Deckman, J.H. Dunsmuir and S. Gruner, J. Vac. Sci. Technol. B7 (1989) 1832
[4] Y. Okamoto, T. Oguro, I. Kashima, D. Kanishi, T. Sakurai and T. Matsuki, Development of the Computed Electroradiography: Trial Manufacture of Digital Imaging System, Proceedings of RSNA 1992
[5] I. McNulty, Nucl. Instr. and Meth. in Phys. Res. A 347 (1994) 170
[6] Ultra-Res Corporation, Instant Holography System, Technical Documentation, 1996

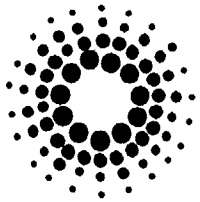

ESRF

REQUIREMENTS ON HIGH RESOLUTION DETECTORS

- Detector Requirements
- High Resolution X-Ray Imaging
- Test Results of: Thin Powder Screens and Thin Crystalls
- Thin Films of Luminescent Screens by Pulsed Laser Deposition
- Comparison Between Possible Detectors

Andreas Koch
Detector Group
European Synchrotron Radiation Facility
Grenoble, France

ESRF

DETECTOR REQUIREMENTS

only 2-dimensional detectors (alternatives: 0-dim or 1-dim detectors, scanning of detector or X-ray beam)

spatial resolution pixel size	... 5 µm ... 1 µm ... 0.01 µm (+ X-ray magnification) X-ray ← → X-ray F.T. Holography, Interferometry — Gabor Holography
detector area no. of pixels	> 500 x 500 pixels
energy range	5 - 50 keV
DQE = SNR^2_{out}/SNR^2_{in}	close to 1 for organic samples less critical for anorganic samples
readout noise	< 1 X-ph/pixel
absorption	high, for high DQE
dynamic range	> 1000
frame rate	≈ seconds
comments	high spatial resolution has priority

e.g. dose limit for skin: 10...100 Mrad
for 1 µm³ resolution element
10^3 ph @ 20 keV
∴ ≈ 3 Mrad

ESRF

DETECTOR CHARACTERISTICS

(area detectors for X-rays)

PRICE
DEVELOPING TIME

DETECTOR

SIGNAL IN

DETECTIVE QUANTUM EFFICIENCY (DQE)

SIGNAL OUT

Signal to Noise Ratio
Dynamic Range
Photon Energy
Intensity
Temporal Resolution
Spatial Resolution
Energy Resolution

non-stochastic degradation of signal:
non-uniformity of response,
non-linearity of response,
image distortion

More 'useful' Signal
but 'reduced Quality'

$$\text{Detective Quantum Efficiency (DQE)} = \frac{(\text{Signal to Noise Ratio}_{out})^2}{(\text{Signal to Noise Ratio}_{in})^2}$$

- expresses the noise added by the detector
- corresponds to the fraction of effectively detected photons
  (by an ideal detector, if shot noise limited)

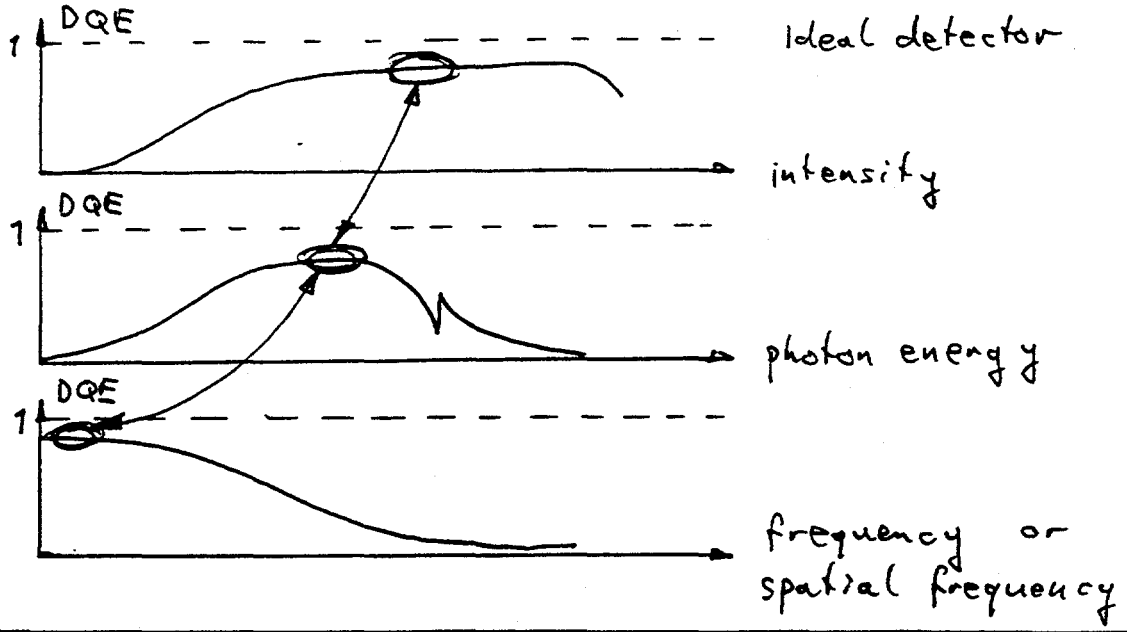

ESRF

DETECTOR CHARACTERISTICS
critical requirements

Resolution

vs.

DQE (absorption, readout noise)
exposure time
dose to sample

high resolution requires thin detection layers
therefore
low absorption of X-rays
low DQE
long exposure times
high dose to sample

X-ray energy

vs.

thickness of active detection area
spatial resolution
contrast of interference pattern

high X-ray energy requires thick absorbing detection material,
and/or high Z material
therefore
lower spatial resolution or lower DQE
lower contrast in interference pattern

e.g.: depths of interference pattern $\approx \frac{4\lambda \cdot (\text{sample - det. dist.})^2}{(\text{sample } \phi)^2} \approx 1\,\mu m$

λ: 50 keV; (sample - det. dist.): 100 mm; (sample ϕ): 1 mm

ESRF

HIGH RESOLUTION X-RAY IMAGING - PRINCIPLES

1. Conversion of X-rays ---> visible light ---> magnifying optics ---> electrons ---> 'bits'
   (Luminescent screen - CCD detectors)

(a) powder phosphors

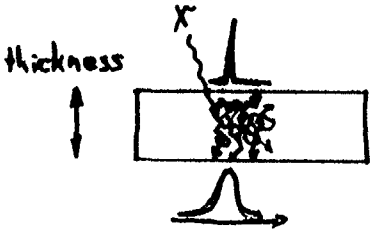

- wide range of phosphor materials available
- spatial resolution (FWHM of pointspread function) ~ thickness
- high light output
- realized: 3-4µm resolution (at ESRF)

(b) structured phosphors

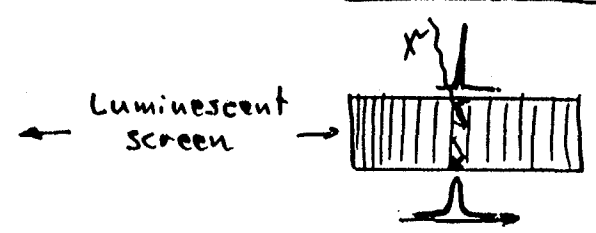

- e.g. CsI on structured substrate
- spatial resolution ~ 1/2 thickness
- e.g. phosphors filled into masks
- spatial resolution ~ 1/10 thickness
- realized: 1 µm resolution (Exxon Microtomography BL @ NSLS)

(c) thin film phosphor

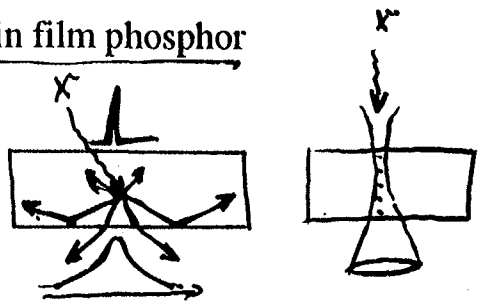

- limited range of phosphor, particular problems corr. to material and deposition process
- spatial resolution ~ thickness
  depth of focus of optics
  parallax
- possible: > 0.3 µm resolution (diffraction limit)
- realized: 3 µm resolution (ESRF)

DETECTOR DEVELOPMENTS

STRUCTURED SCREENS

Structured Growth of phosphors and substrate production with small structures, H.W. Deckman et al., Exxon, USA

CsI-grown on etched fibre-optic plate, aspect ratio 20:1

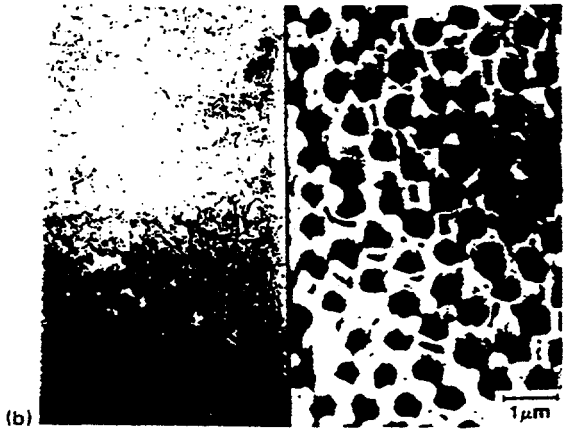

cell structure which used lithographic mask of polymer colloidal particles, CsI was evaporated into cells afterwards, aspect ratio 10:1

ESRF

HIGH RESOLUTION X-RAY IMAGING - PRINCIPLES

2. Conversion of X-rays ---> electron hole pairs ---> 'bits'
   (X-ray electron tube detectors)

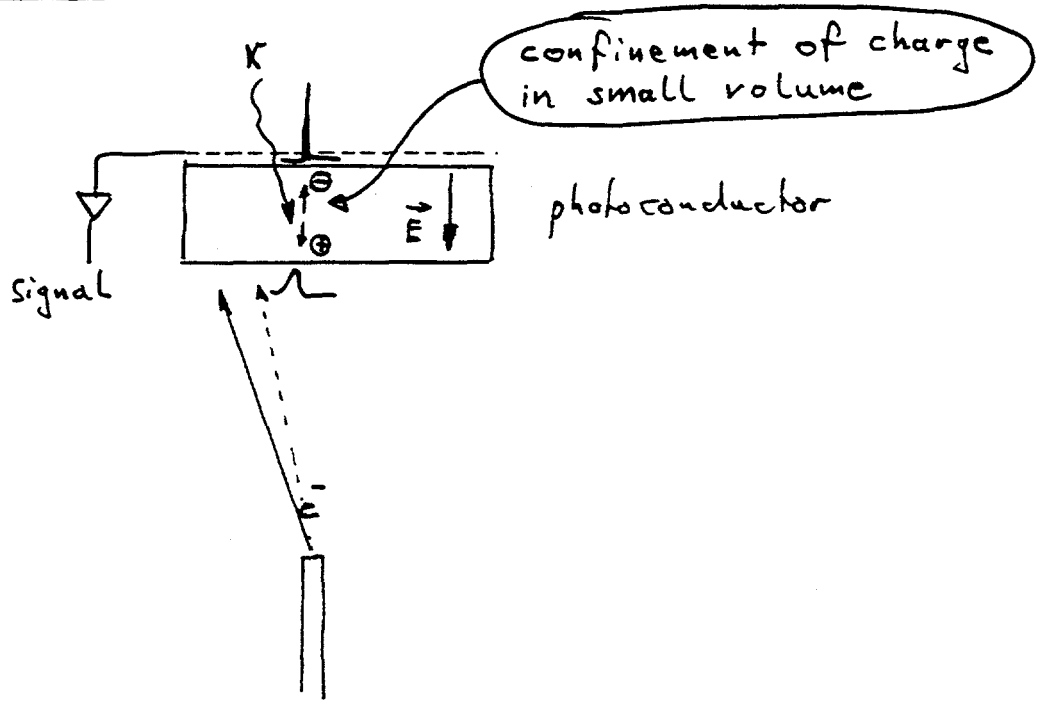

- spatial resolution: no direct relation to thickness , but parallax
- realized: 20 µm resolution (2 µm (?): Oguro and Okamoto, Kanagawa Dental College)
- possible: maybe < 1 µm? (combine photoconducting target with electron microscope)
- advantages:
  no 'signal spreading' like in luminescent screens
  well absorbing photoconductors like PbO, CdTe

ESRF

HIGH RESOLUTION X-RAY IMAGING - PRINCIPLES

3. Conversion of X-rays ---> chemical reaction ---> 'bits'

(a) film

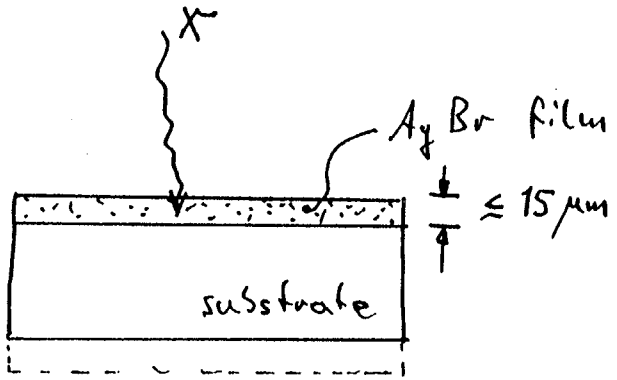

- AgBr film
- spatial resolution ~ grain size
- grain size increases with silver concentration (e.g. 1.7 µm grain size @ 8.5 % weight, 14 g/m^2)

- realized: > 0.3 µm resolution (holografic films)
  e.g. 1.7 µm resolution (X-ray film)

(b) photoresist

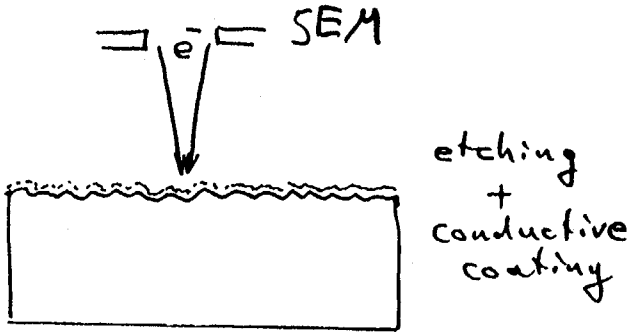

- PMMA resist, coated and read out by SEM
- spatial resolution: no specific relation to thickness

- realized: 60 nm resolution
- possible: > 20 nm resolution

ESRF

HIGH RESOLUTION X-RAY IMAGING - PRINCIPLES

4. Conversion of X-rays ---> thermoplastic deformation ---> 'bits'

Photosensitive semiconductor + thermoplastic film

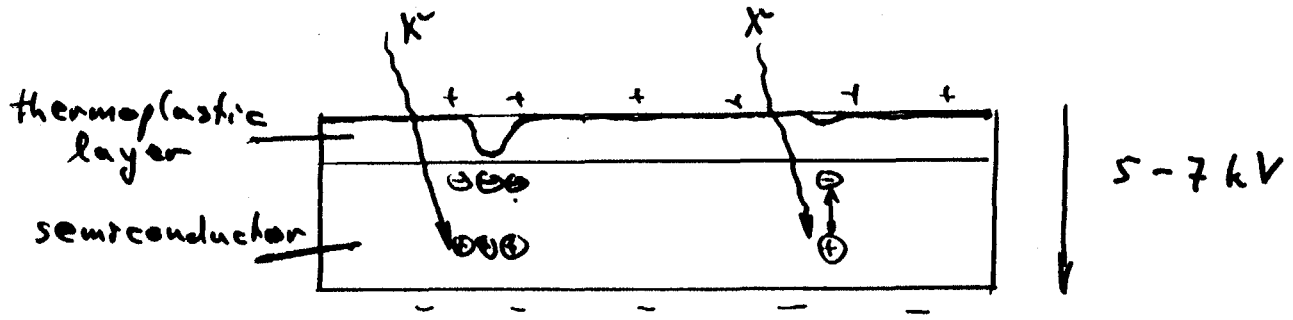

- principle:
  film is charged to typically 5-7 kV
  photons are absorbed in semiconductor layer and create electron / hole pairs
  electron/hole pairs charge film locally
  film is heated and charge pattern is transformed into relief

- spatial resolution:
  realized: 0.5 µm resolution (for holografic applications, Ultra-Res Co.)
  possible: maybe 0.2 µm

ESRF

X-RAY ABSORPTION FOR DIFFERENT DETECTION TARGETS

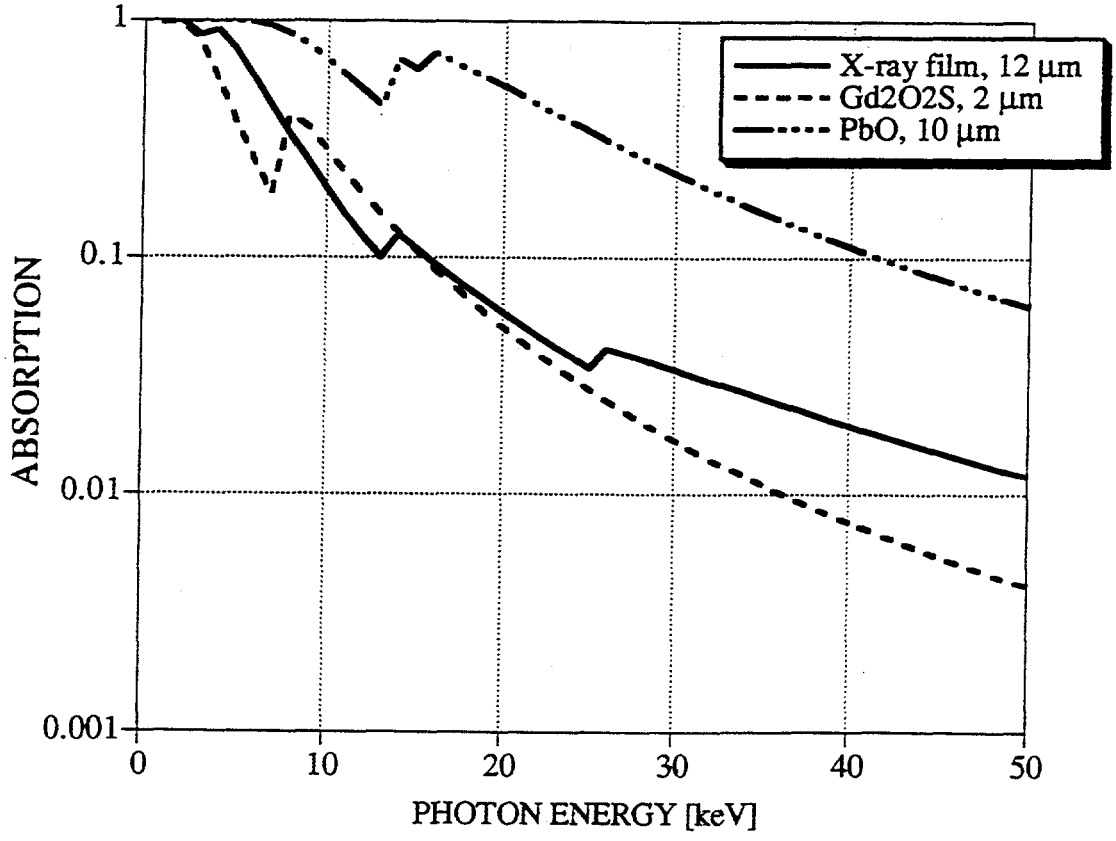

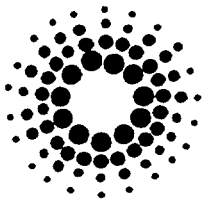

ESRF

CONSEQUENCES FOR DETECTOR CHOICE

1. Available (at least components)

• photoresist:	> 60 nm resolution
• X-ray film:	> 0.5 μm resolution
• X-ray electron tubes:	> 20 μm resolution (maybe < 10 μm)
• luminescent screen/CCD's:	> 3 μm resolution maybe 'Exxon detector'
• direct detection with CCD's:	> 7 μm (<10 keV)

2. Development - 'small' effort

- deposition of thin films of luminescent materials for luminescent screen/optics/CCD system
- **objective:** 1 μm resolution

3. Development - 'medium' effort

- structured screens for luminescent screen/optics/CCD system
- like Exxon group (mask out of shrinked polymeric particles)
- or masks with LIGA process
- **objective:** 1 μm resolution but higher absorption/resolution ratio than thin film screens

- adapting sytem with thermoplastic/semiconductor layer for X-rays?

4. Development - 'high' effort

- high resolution scanning of photconducters for X-ray electron tube
- highest absorption/resolution ratio expected
- **objective:** 1 μm resolution

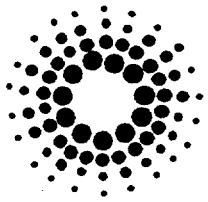

ESRF

ACTIVITIES IN THE DETECTOR GROUP

Test of luminescent screens

(a) powder deposited
(b) thin crystalls

	thickness	LSF (fwhm)	PSF (fwhm)	rel.sensitivity @ 18 keV	uniformity
YAG:Ce	5 µm	4.3 µm	2.8 µm	7.7	CCD limited
YVO4:Eu	2 µm	4.7 µm	4.0 µm	2.2	19% rms
BGO	20 µm	4.2 µm	3.6 µm	8.4	CCD limited
ZnS:Cu,Al	2 µm	4.0 µm	3.2 µm	6.7	42% rms
Gd2O2S:Tb	5 µm	5.7 µm	4.2 µm	100.0	8% rms

ESRF

EXPECTED PERFORMANCE

Detective Quantum Effficiency for
whole detector
with 1 µm thick Gd_2O_2S:Tb screen

corr. to ≈ 2µm powder deposition

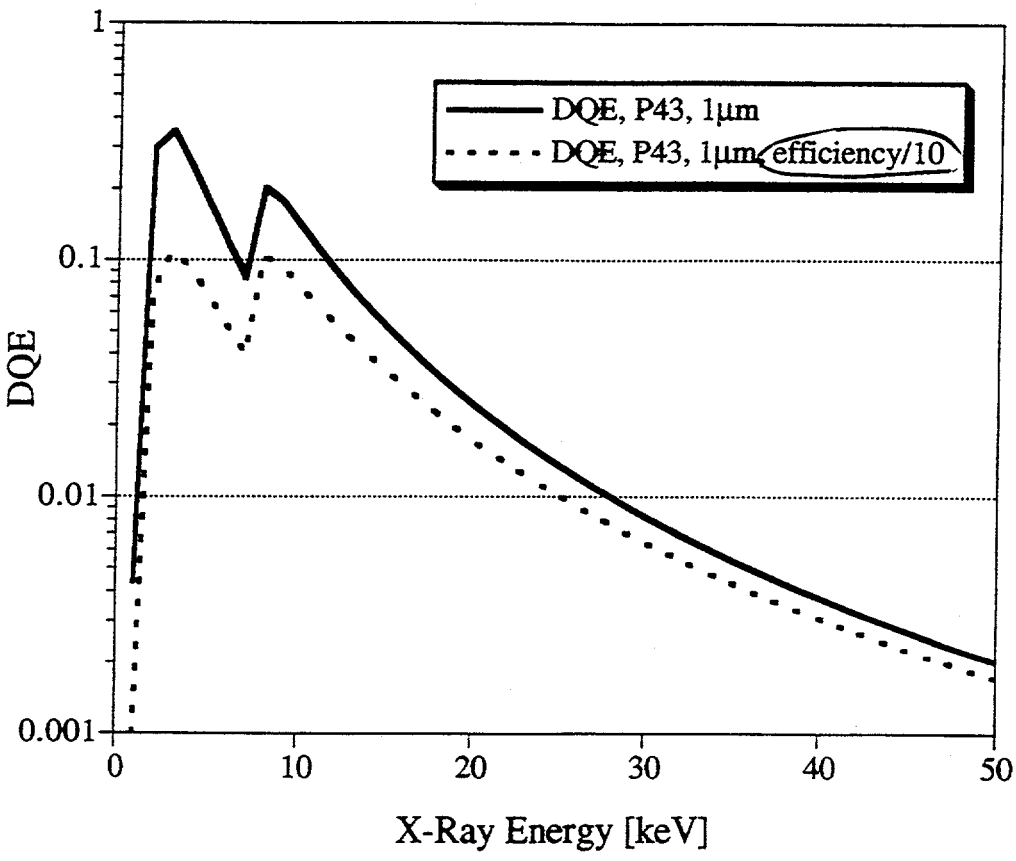

ZuS: Cu:AL

Volume %

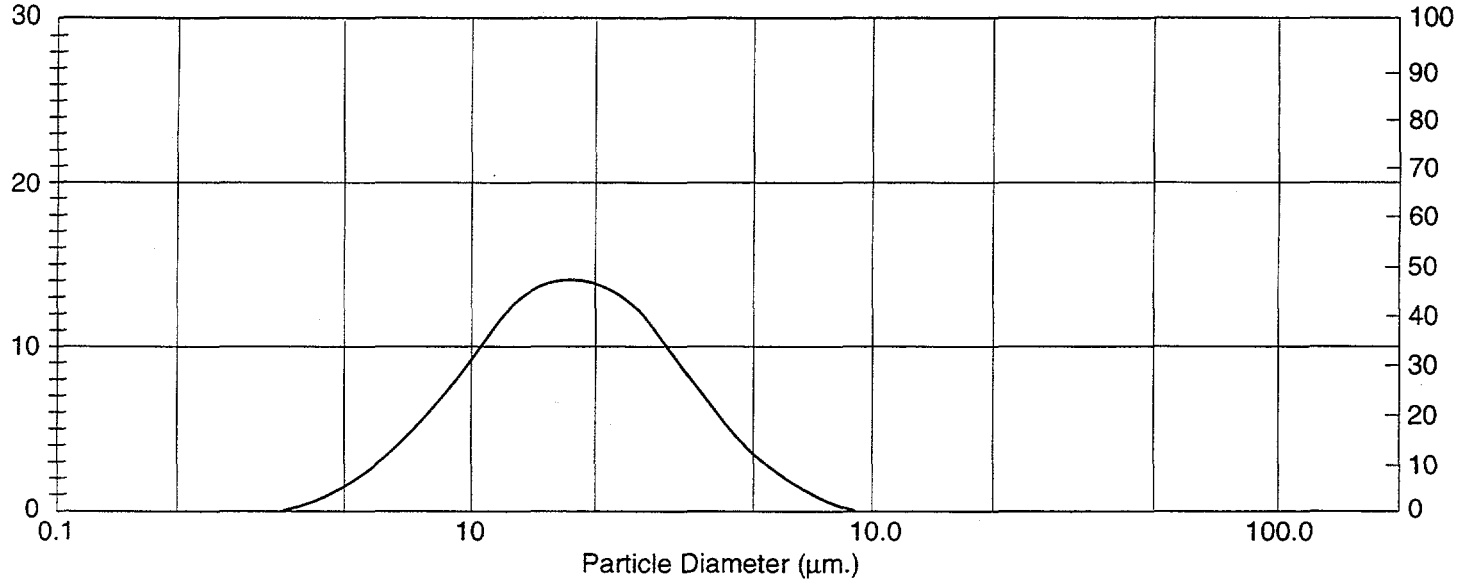

Malvern Instruments Ltd.
Malvern, U.K.

MasterSizer X Ver. 1.1a
Serial No. 6220

p. 1
05 Mar 96 11:10

yvo_4: Eu

Volume %

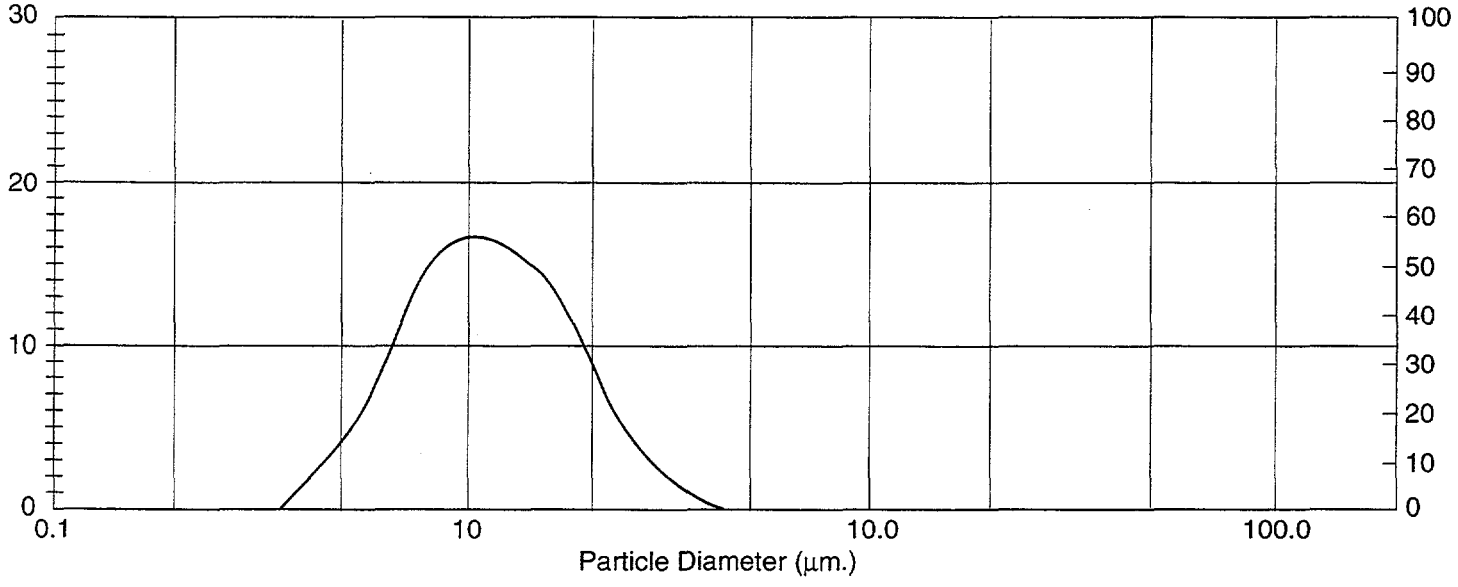

Malvern Instruments Ltd.
Malvern, U.K.

MasterSizer X Ver. 1.1a
Serial No. 6220

p. 2
05 Mar 96 11:22

Linespread Function (measured)

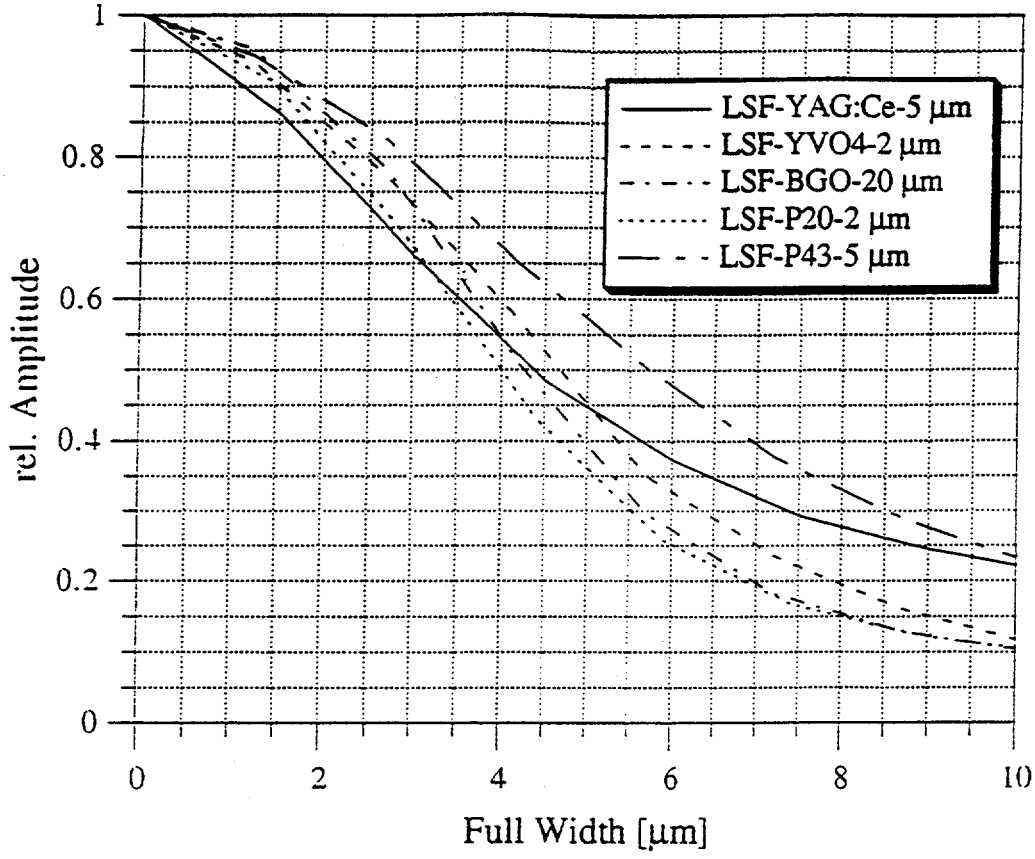

Pointspread Function (calculated)

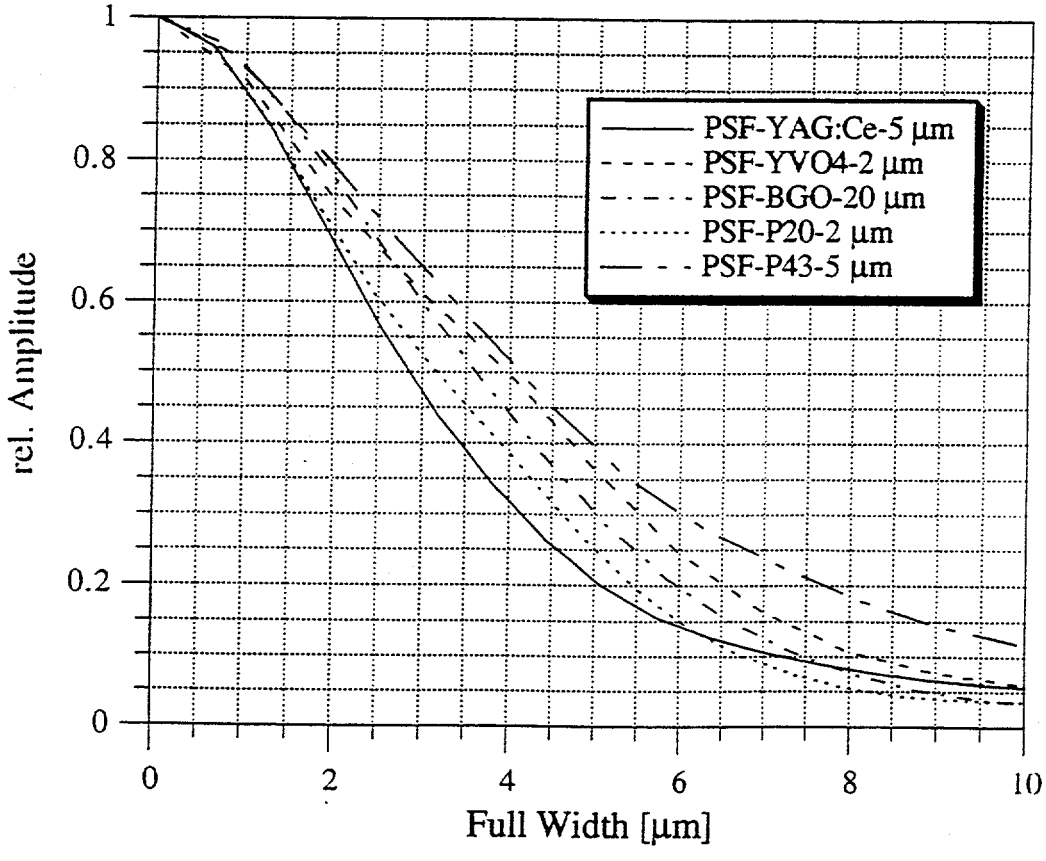

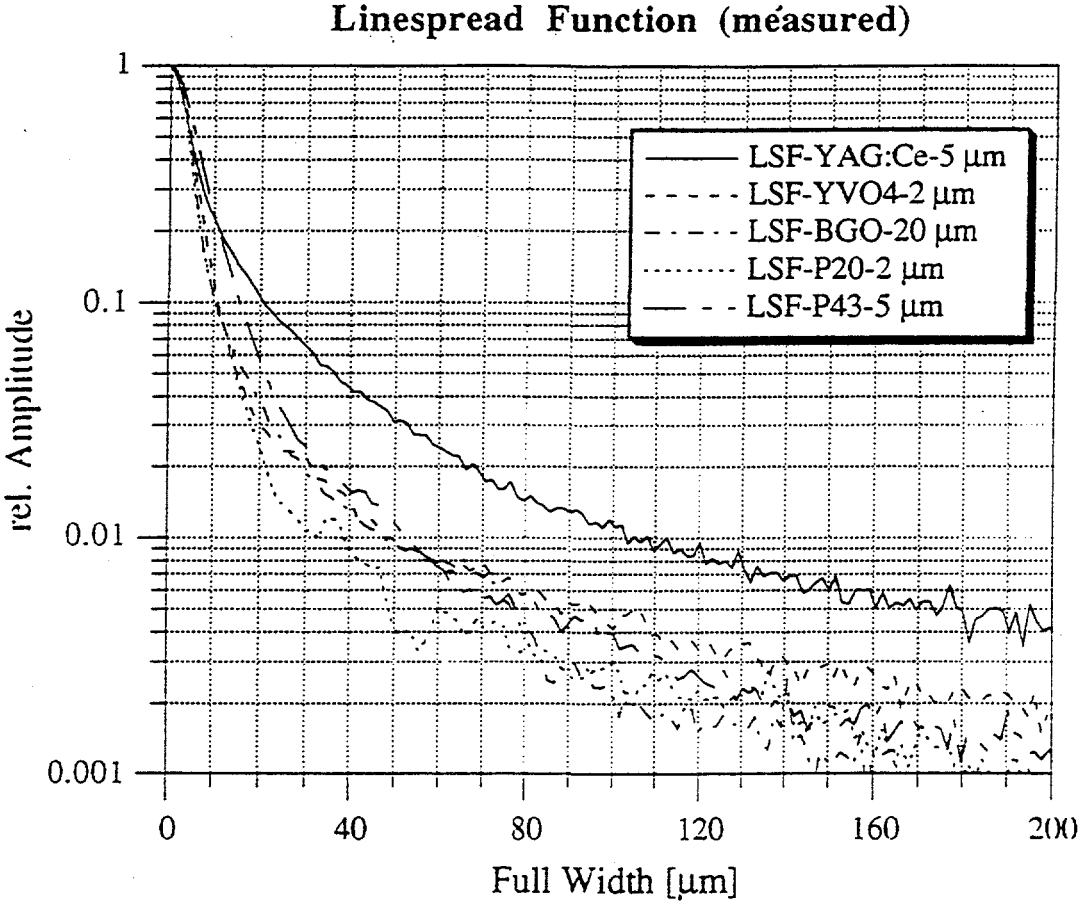
Linespread Function (measured)
1
0.1
0.01
0.001
rel. Amplitude
0
40
80
120
160
200
Full Width [µm]
LSF-YAG:Ce-5 µm
LSF-YVO4-2 µm
LSF-BGO-20 µm
LSF-P20-2 µm
LSF-P43-5 µm

ESRF

ACTIVITIES IN THE DETECTOR GROUP

Luminescent films by pulsed laser deposition

- objective: luminescent screen/optics/CCD detectors with < 5 μm ... 1 μm resolution
- request from: Microtomography, P. Spanne
  Topography BL, J. Baruchel
  Microfocus BL, Ch. Riekel
  ~~Sexafs BL, F. Comin~~
- process:

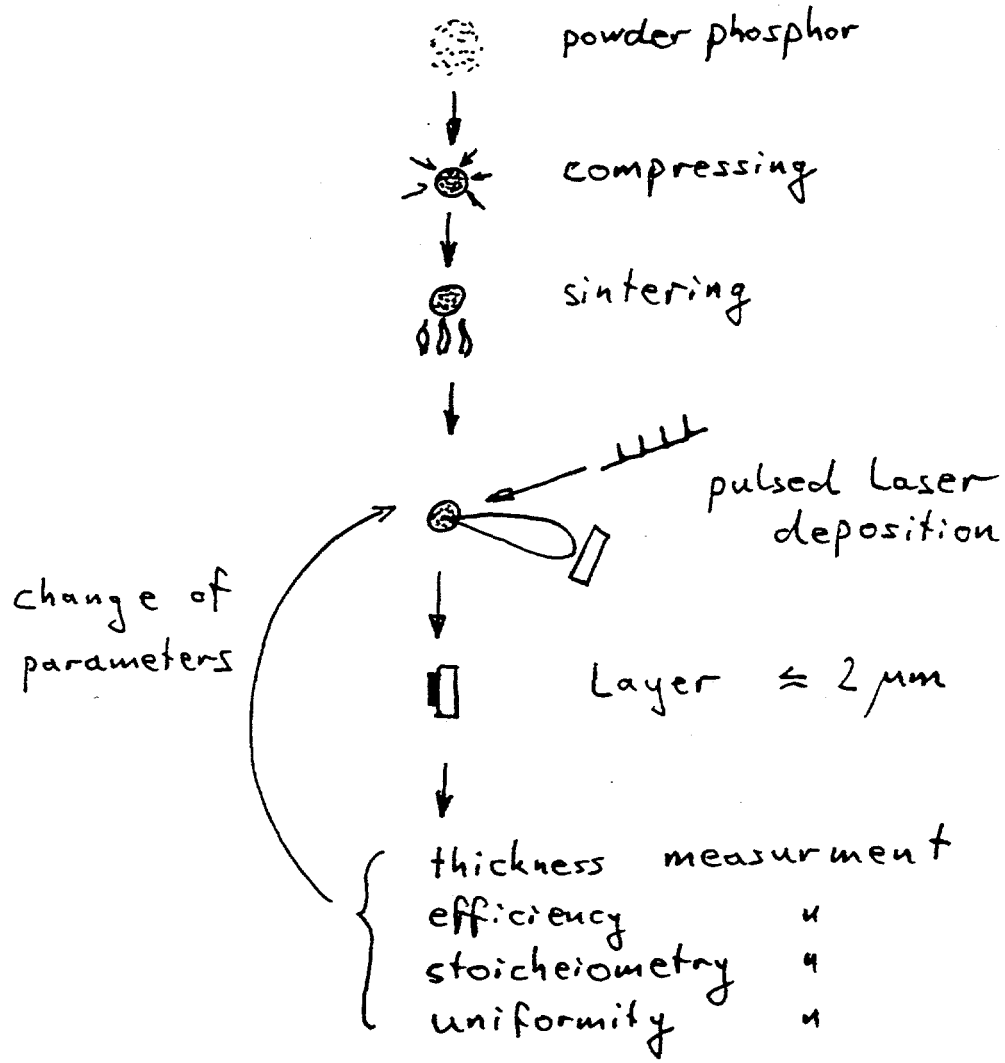

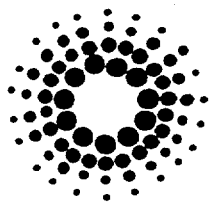

ESRF

LUMINESCENT FILMS BY PULSED LASER DEPOSITION

status of project:

- first layers produced and analysed
- stoicheiometry o.k.
- problems with homogenity
- optical system + CCD camera assembled

advantage of this deposition method:

- powder phosphors can be used, wide range available, different phosphors to adapt to:
  - absorption edges
  - emission wavelength
  - time response
- complicated stoicheiometric compositions are generally well preserved
- easy to handle c.f. other vacuum deposition techniques

ESRF

PERFORMANCE OF DIFFERENT DETECTORS

	Requirements	Luminescent Screen + CCD (available)	Luminescent Screen + CCD (expected, with thin film phosphors)	Structured Screens + CCD (Exxon)
spatial resolution pixel size	... 5 µm ... 1 µm ... 0.01 µm	3-4 µm	0.5 µm ... 2 µm	1 µm
detector area no. of pixels	> 500 x 500 pixels	o.k.	o.k.	o.k.
energy range	5 - 50 keV	o.k.	o.k.	o.k.
DQE $= SNR^2_{out}/SNR^2_{in}$	close to 1 for organic samples	≈ 0.02-0.2 @ 5-10 keV < 0.002-0.02 @ 30 keV	< 0.1 @ 5-10 keV < 0.004 @ 30 keV	close to 1 @ 5-10 keV < 0.05 @ 30 keV
readout noise	< 1 X-ph/pixel	o.k.	o.k.	o.k.
absorption	high, for high DQE	> 50% @ < 10 keV	> 20 %@ < 10 keV	> 50 %@ < 10 keV
dynamic range	> 1000	o.k.	o.k.	o.k.
frame rate	≈ seconds	o.k.	o.k.	o.k.
comments	high spatial resolution has priority		strong decrease in DQE @ high energies	segmented active area

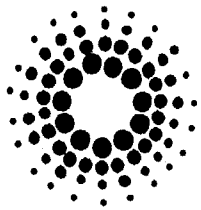

ESRF

PERFORMANCE OF DIFFERENT DETECTORS

	Directly Excited CCD's	X-Ray Electron Tubes	X-Ray Film	Photoresist
spatial resolution pixel size	> 7 µm decrease >10 keV	20 µm (< 10 µm?)	> 0.3 µm	60 nm
detector area no. of pixels	o.k.	o.k.	>> 500 x 500	>> 500 x 500
energy range	o.k.	o.k.	o.k.	o.k.
DQE $= SNR^2_{out}/SNR^2_{in}$	close to 1 @ < 10 keV < 0.001 @ 30 keV	> 0.5 @ 5-20 keV < 0.2 @ 30 keV	< 0.2 @ 10 keV < 0.03 @ 30 keV	?
readout noise	o.k.	o.k.	o.k.	?
absorption	low > 10 keV	> 50% @ < 20 keV	> 0.2 @ < 10 keV	?
dynamic range	< 1000	o.k.	≈ 100	?
frame rate	o.k.	o.k.	"off-line"	"off-line"
comments	dyn. range mismatch, rad. damage >10 krad	high ratio of abs./resol. possible	non-linear	electron microscope scanning

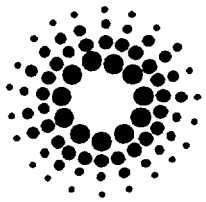

ESRF

CONCLUSIONS

- 1 μm resolution - luminescent film - CCD detector should be feasable.
- 3 μm fwhm of pointspread function has been realized.
- This detector will give comparable 'image quality' than film but will be an 'on-line' detector.

- Detectors with simultaneously better spatial resolution and DQE require a high development effort.
- Such detectors could be:
  - detectors with structured luminescent screens
  - detectors using photoconductive targets and electron beam readout

Dose Fractionation Theorem in 3-D Reconstruction (Tomography)

Robert M. Glaeser, Life Sciences Department, Donner Lab, LBNL.

Abstract*

It is commonly assumed that the large number of projections required for single-axis tomography precludes its application to most beam-labile specimens. However, Hegerl and Hoppe have pointed out that the total dose required to achieve statistical significance for each voxel of a computed 3-D reconstruction is the same as that required to obtain a single 2-D image of that isolated voxel, at the same level of statistical significance (2). Thus a statistically significant 3-D image can be computed from statistically insignificant projections, as along as the total dosage that is distributed among these projections is high enough that it would have resulted in a statistically significant projection, if applied to only one image. We have tested this critical theorem by simulating the tomographic reconstruction of a realistic 3-D model created from an electron micrograph. The simulations verify the basic conclusions of the theorem and extend its validity to the experimentally more realistic conditions of high absorption, signal-dependent noise, varying specimen contrast and missing angular range. Furthermore, the simulations demonstrate that individual projections in the series of fractionated-dose images can be aligned by cross-correlation because they contain significant information derived from the summation of features from different depths in the structure. This latter information is generally not useful for structural interpretation prior to 3-D reconstruction, owing to the complexity of most specimens investigated by single-axis tomography. These results, in combination with dose estimates for imaging single voxels (3) and measurements of radiation damage in the electron microscope (4), demonstrate that it is feasible to use single-axis tomography with soft X-ray microscopy of frozen-hydrated specimens.

1. Mc Ewen, B.F., Downing, K.H. and Glaeser, R.M. (1995) *Ultramicroscopy* 60: 357.

2. Hegerl, R. and Hoppe, W. (1976) *Z. Naturforsch.* 31a : 1717.

3. Sayre, D., Kirz, J., Feder, R., Kim, D.M. and Spiller, E. (1977) *Ultramicroscopy* 2: 337.

4. Glaeser, R.M. and Taylor, K.A. (1978) *J. Microscopy* 112: 127.

* This abstract describes work reported previously in (1). It is used here with only minor modification from the abstract published in (1).

ELSEVIER

Ultramicroscopy 60 (1995) 357–373

ultramicroscopy

The relevance of dose-fractionation in tomography of radiation-sensitive specimens

Bruce F. McEwen [a,*], Kenneth H. Downing [b], Robert M. Glaeser [b,c]

[a] *Laboratory of Cell Regulation, Division of Molecular Medicine, Wadsworth Center, New York State Department of Health, Empire State Plaza, P.O. Box 509, Albany, NY 12201-0509, USA*

[b] *Life Sciences Division, Lawrence Berkeley Laboratories, Berkeley, CA 94720, USA*

[c] *Department of Molecular and Cell Biology, University of California, Berkeley, CA 94720, USA*

Received 21 February 1995; accepted 21 June 1995

Abstract

It is commonly assumed that the number of projections required for single-axis tomography precludes its application to most beam-labile specimens. However, Hegerl and Hoppe have pointed out that the total dose required to achieve statistical significance for each voxel of a computed 3D reconstruction is the same as that required to obtain a single 2D image of that isolated voxel, at the same level of statistical significance. Thus a statistically significant 3D image can be computed from statistically insignificant projections, as long as the total dose that is distributed among these projections is high enough that it would have resulted in a statistically significant projection, if applied to only one image. We have tested this critical theorem by simulating the tomographic reconstruction of a realistic 3D model created from an electron micrograph. The simulations verify the basic conclusions of the theorem and extend its validity to the experimentally more realistic conditions of high absorption, signal-dependent noise, varying specimen contrast and missing angular range. Individual projections in the series of fractionated-dose images could be aligned by cross-correlation because they contained significant information derived from the summation of features from different depths in the structure. This latter information is generally not useful for structural interpretation prior to 3D reconstruction, owing to the complexity of most specimens investigated by single-axis tomography. These results demonstrate that it is feasible to use single-axis tomography with soft X-ray and electron microscopy of frozen-hydrated specimens.

1. Introduction

Tomography has become a valuable tool for obtaining three-dimensional (3D) images of subcellular structures (e.g. Refs. [1–4]). The majority of these structures are macromolecular assemblies, representing individual units that cannot be treated as identical copies of one another. In such applications the entire data set for the 3D reconstruction must be collected from the same unit structure, usually by tilting the sample about a single axis. Typically 60–150 projections are recorded, over as wide an angular range as possible (120°–140°).

Until recently the large number of projection im-

* Corresponding author.

SSDI 0304-3991(95)00082-8

ages required has been thought to preclude application of tomography to beam-labile preparations such as frozen-hydrated biological specimens. Instead, tomography has been primarily limited to embedded preparations stained with heavy metals, for which the total electron dose that can be tolerated has not been a major consideration. On the contrary, embedded specimens may even be pre-irradiated (i.e., given an added electron dose not used for imaging) to ensure stability of the plastic sections before commencing data collection [5]. Shot noise is not a concern for specimens that are stable in the electron beam because each projection is collected with enough illumination to form an image with high signal-to-noise ratio (S/N). Beam-sensitive samples present a dilemma, however, in which the structure of the specimen itself can change from one projection image to the next if the accumulated dose is too high, while the individual images will have a very high level of shot noise (i.e., a low S/N) if the accumulated dose is kept low.

Two recent experimental developments justify a reexamination of the role of shot noise in single-axis tomography. In electron microscopy, advances in automated tomography have improved the overall efficiency of data collection to the point where it is now feasible to apply the technique to thin, frozen-hydrated preparations [6,7]. In X-ray microscopy, advances in zone-plate optics have made it technically possible to use soft X-rays to visualize hydrated specimens that are several micrometers thick, with a resolution of 30–50 nm [8,9].

The complexity of the specimens used in soft X-ray imaging and in electron microscopy are roughly comparable in the sense that the sought-after resolution of individual features within the sample in both cases will tend to be about 20–200 times smaller than the thickness of the sample. Because of this complexity, it will generally be necessary to use tomographic 3D reconstruction for effective interpretation. Frozen-hydrated specimens, whether illuminated with electrons or X-rays, can only sustain a total dose of 10^{10} rad before extensive morphological damage becomes apparent [10,11]. Under conditions of such limited illumination, the trade off between radiation damage and shot noise becomes an important consideration in determining whether a statistically significant reconstruction will be possible because data must be recorded from a large number of different tilt angles.

Hegerl and Hoppe [12] introduced a critical theorem stating that "A three-dimensional reconstruction requires the same integral dose as a conventional two-dimensional micrograph provided that the level of significance and the resolution are identical". A very important point in understanding this theorem, and applying it in practice, has to do with recognizing that the proof requires (a) that the image – being a projection – is a linear function of the density of every voxel of the 3D object, and (b) the shot noise can be correctly represented as additive noise. Thus, while the proof developed by Hegerl and Hoppe dealt with only a single voxel that had non-zero density, linearity (i.e., additivity) renders trivial its generalization to an arbitrary collection of voxels with non-zero density.

In the context of the Hegerl–Hoppe theorem, a projection image is considered to be statistically significant only if the contribution made by the density in a single voxel is statistically significant. This is different from the usual understanding in which only the density of a projection (i.e. a 2D pixel) is required to be statistically significant. The linear superposition of voxels in a projection ensures that a projection-image will be significant if the contribution from each voxel is significant, but the reverse is not always true. The practical relevance of the Hegerl–Hoppe theorem is that it tells us that it is permissible to fractionate the dose that would be needed in order to record a single significant image, dividing it instead among an arbitrarily large number of images in a tilt series, each of which can no longer be statistically significant. The implication, then, of the theorem is that a statistically significant 3D reconstruction can be obtained from projections which are not statistically significant at the limiting resolution.

Although the Hegerl–Hoppe theorem has been controversial, there is no criticism of the fundamental mathematical analysis [13,14]. Instead criticism appears to have been made in reaction to the statement that "two-dimensional microscopy was in fact a waste of information" [15]. A helpful rebuttal of these criticisms has been published subsequently by Hegerl and Hoppe [16] (see Section 4). The unwillingness to accept the conclusions of the dose-frac-

tionation theorem, which some have expressed in the past, is clearly due to the wrong impression that the theorem was claimed to require that the total dose only produces statistical significance in the projections, but not necessarily in the images of single voxels. As stated above, however, the total dose must be sufficient to guarantee that the image of a single voxel will be statistically significant (which, in turn, guarantees that the projection will also be statistically significant) provided that the total dose is used for a single image rather than being fractionated into a 3D data set.

While the fundamental conclusion of the Hegerl–Hoppe theorem is mathematically sound, it also remains largely untested in experimental situations. There appears even to have been very little done to put the theorem to the test by the use of straightforward numerical simulations. Apart from demonstrating unambiguously the validity of the theorem, within the conditions stated for its derivation, numerical simulations are able to explore related questions that may be less amenable to analytic derivation. In X-ray microscopy, for example, it is important to know whether dose fractionation will still work in strongly absorbing (i.e., high-contrast) specimens, where the shot noise will become highly signal-dependent and the additive shot-noise assumption will no longer hold. Another important concern is to determine whether noisy projection images can still be adequately aligned to a common origin, an essential prerequisite if the theorem is to be put into practical application, and an issue that is not addressed as part of the derivation [16].

To test this important theorem and address the accompanying questions, we have implemented an extensive set of simulations of the 3D reconstruction process using a realistic model created from an actual electron micrograph. In addition to verifying the basic conclusion of the Hegerl–Hoppe theorem, we have extended its validity to the non-ideal, but experimentally more realistic, cases of high absorption, signal-dependent noise, varying specimen contrast and missing angular range. Finally, we show that, when the integral dose is partitioned among 180 projections, each projection of our "realistic model structure" still contains enough information to permit accurate alignment using the cross-correlation function. We also show that reconstruction is successful when the exposure is partitioned into 1800, or even 18 000, projections but at the latter level individual projections contain little or no information and cannot be aligned.

2. Methods

We have constructed models from an electron micrograph of a centriole scanned at 512×512 pixels (kindly provided by Dr. Conly L. Rieder). The centriole image was used to ensure that our model contained realistic levels of gray scale and spatial complexity. Although this image is actually a 2D projection from an epon section 0.25 μm thick, we have used it as if it were a 2D slice (i.e., only one voxel thick) from a 3D object. This is possible because many of the triplet microtubules in this particular image are aligned in the depth dimension and can thus be clearly recognized as the cross-sections of tubes.

The ability to detect a feature at a given noise level was defined as the ability to see that feature in difference images between two separate models where the feature was either present or absent. Hence each test required making a comparison between a model generated from the full centriole image and one generated from a centriole image with selected features removed.

2.1. Model A: full structure

The centriole image was first windowed to 384×384 pixels and then interpolated to 128×128 pixels, and a circular mask was applied with a diameter of 120 pixels (see row 1 of Fig. 1). Ninety new versions of the image were created by successive 1° rotations. The entire set of 91 images was then stacked to give a 3D model in which the centriole structure twists to form 1/4 of a turn of a helix. The circular mask ensured a uniform helical structure without truncation artifacts.

2.2. Model B: selected features removed

Three different-sized features were removed from the image: a full triplet centriole blade; a single

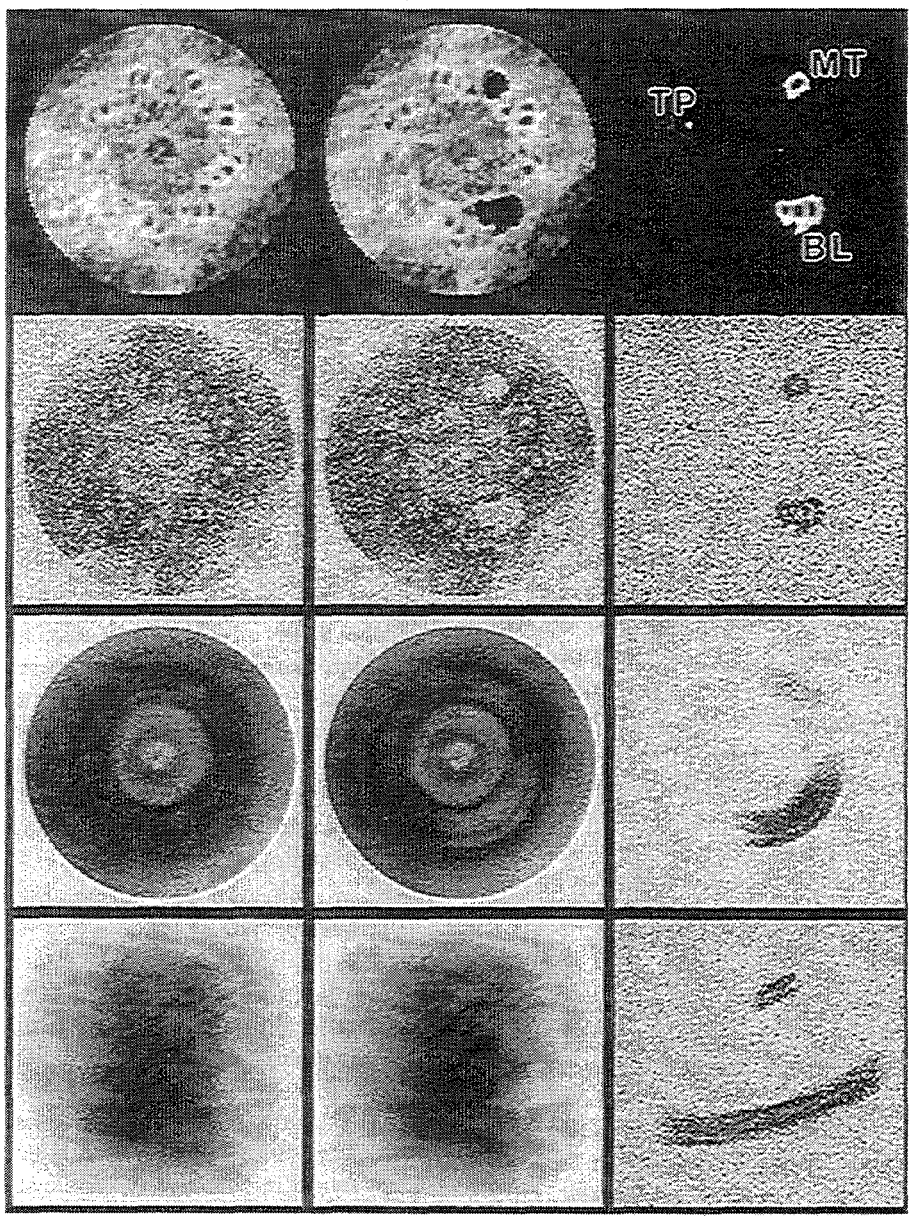

Fig. 1. Models used for the simulations. Columns 1–3 are: the full model (model A), the model with features removed (model B); and the difference between models A and B, respectively. Row 1 illustrates the central slice from each model. Model A was created by stacking 91 such slices successively rotated by 1° (see Section 2.1). The three features removed from model B are indicated as BL, blade, MT microtubule and TP microtubule tip. The tip is only removed from the central three slices, while the microtubule is removed from 31 slices and the blade from all 91 slices (see Section 2.2). Row 2 shows slices from row 1 imaged at 3.6×10^8 quanta per pixel. At this dose even the tip is evident in the difference image. Row 3 shows the 0° projections of the models imaged at 2×10^6 quanta per pixel (column 3 is the difference between the projections shown in columns 1 and 2). This is the fractionated dose, or the illumination level per projection when the dose used in row 2 is partitioned among a data set with 180 different views. The tip is no longer visible in the difference image, but densities derived from the blade and microtube are. Row 4 shows the $-60°$ projection of the models imaged at 2×10^6 quanta per pixel.

microtubule from a different blade; and the tip of an open microtubule in a third blade (see row 1 of Fig. 1). The features were arbitrarily chosen on the bottom, side and top of the image so that they would not overlap in any of the projections from the tilt series (tilt axis lies in the vertical direction in Fig. 1). The features were masked from the full-sized image (before windowing, interpolation and masking) and replaced by the background density, which was estimated as the average density of a small window from an area of minimum mass outside the centriole. The blade and microtubule were masked using an interactive procedure (see Ref. [17]), while the open microtubule tip was removed with a small circular mask 10 pixels in diameter. In the final binned down version of the image, this feature had a diameter of approximately 3 pixels.

The above masking procedure was used to create three different versions of the image: one in which the blade only was removed; one in which the blade and the microtubule were both removed; and one in which all three features were removed. The individual images were windowed, binned down and circularly masked exactly as for model A. The 3D model was constructed by stacking rotated versions of the images in such a way that all three features were missing from the middle three slices of the model (slices 45–47), the blade and microtubule were missing from 14 slices on either side of these (slices 31–44 and 48–61), and only the blade was missing from the remainder of the slices (slices 1–30 and 62–91). Thus the blade is absent from all of the slices of model B, the microtubule from 31 slices and the microtubule tip from 3 slices. The tip, therefore, represents a feature approximately at the resolution limit of the image and was used to visually track the recovery of desired resolution in the 3D reconstruction. The microtubule and the blade were used to monitor lower-resolution features.

2.3. Models L and H: modifications of model A to simulate low and high contrast

Variations of contrast between models A and B were simulated by changing the intensity of the blade, microtubule and tip in model A. In model L, their contrast was lowered by adding four times the density in each voxel of model B to each voxel in model A (i.e., the addition of two 3D image files). Each new voxel was then divided by five with the result that, in a comparison between model L and model B, the blade, microtubule and tip have only 1/5 of their contrast relative to a comparison between models A and B. Areas outside of these features retained their original density values. In a similar approach, model H was constructed by subtracting 0.8 times the density in each voxel in model B from each voxel in model A, followed by multiplying each voxel by five (see Fig. 6).

2.4. Computing projections and 2D slices with shot noise

The noisy data sets used for simulations of the 3D reconstructions were constructed from each of the four models in two steps. First the mass-density distribution was computed for 180 different projections over an 180° angular range with a 1° interval. The tilt axis was orthogonal to the cylindrical axis of the helical models (vertical direction in Fig. 1). In the second step, shot noise in the illumination was simulated by assigning to each pixel a number of incident quanta, X_n, drawn from a Poisson distribution [18] with mean X_m. The output density for each pixel was set equal to X_t, the number of quanta transmitted through the specimen:

$$X_t = \exp(-EP(I))\,X_n, \tag{1}$$

where $P(I)$ is the input density value of the pixel. $P(I)$ is the sum of voxel densities along a ray through the 3D model, in the direction of a particular projection. E is the extinction coefficient.

The value of E was selected as an input parameter to give the desired value for the maximum or average beam-absorption of the data set during each series of simulations. Similarly, the mean number of quanta per pixel, X_m, was selected to specify the illumination level. The same procedure was also used to generate simulated images of individual slices of the model as shown in row 2 of Fig. 1. Projections of models A, B and their difference are shown at 0° tilt angle in row 3 of Fig. 1 and at −60° in row 4 of Fig. 1. The latter emphasize how projections frequently provide a very confused picture of the actual 3D structure.

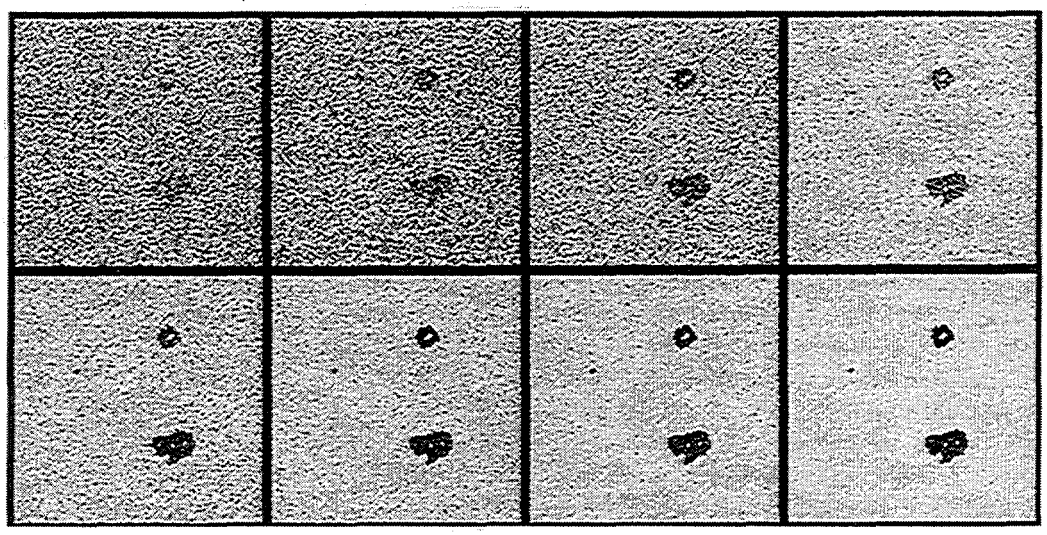

Fig. 2. Detection as a function of S/N. Difference images were computed from binary versions of the central slices from models A and B with S/N values between 1 and 9. The S/N values were specified by setting the absorption level to 1% and the mean dose values from 10^4 through 81×10^4 quanta/pixel (see Section 3.1 for details). The results of one such determination, for S/N values between 1 and 8, are shown. When this trial was repeated ten times, the microtubule tip was never detected when S/N = 1; it was detected 2 of the 10 trials when S/N = 2; 5 of the 10 trials when S/N = 3; 9 of the 10 trials when S/N = 4 or 5; and all 10 trials when S/N > 5. This result agrees with the Rose criterion, which states that a S/N of 5 or greater is required for reliable detection of features at the resolution limit.

2.5. *Signal-dependent noise*

The stochastic nature of absorption becomes a significant source of noise in strongly absorbing specimens. In this situation the number of quanta transmitted through the sample, X_t, was drawn from a binomial distribution [18] with the number of incident quanta, X_n, and the probability of transmission, $P = \exp(-EP(I))$, as input parameters. Thus, in the high absorption case, X_t is determined by two statistical distributions: the binomial distribution and a Poisson distribution with the latter being used to compute X_n.

2.6. *3D reconstruction from noisy projections*

The weighted back-projection method (see Ref. [19]) was used to compute reconstructions, and no non-linear restoration methods were applied. The reconstruction volumes were $128 \times 128 \times 128$ voxels. The middle slices (63–65) from reconstruction volumes derived from model B were subtracted from those derived from models A, L, or H to determine

Fig. 3. Difference images of single slices of either the model or the 3D reconstructions obtained with varying amounts of illumination. The extinction coefficient in Eq. (1) was set so that the average absorption in the projections was 1% (absorption in single slices is much less). The total dose in columns 1–4 is 0.2, 0.8, 3.2 and 8.9×10^8 quanta per pixel. Row 1 shows difference images from the central three slices of the models computed with the fractionated dose (1/180 of the total). No features are evident above the shot noise. Row 2 shows the same difference images computed with the full total dose. The microtubule tip becomes consistently evident at dose levels around 1×10^8 quanta per pixel. Row 3 shows slices from the 3D reconstructions computed from data sets where each projection is imaged with the fractionated dose. Again the tip becomes evident at a total dose of 10^8 quanta per pixel. Rows 4 and 5 show the slices from models A and B, respectively, that were used to compute the difference images in row 3.

the detectability of a feature in the 3D reconstructions. The difference maps could then be directly compared with difference maps taken from 0° projections or the middle slices (number 46) of the original models.

2.7. Software

All computations and visualizations of the results were carried out using the UNIX version of the SPIDER software package [20]. The formulation

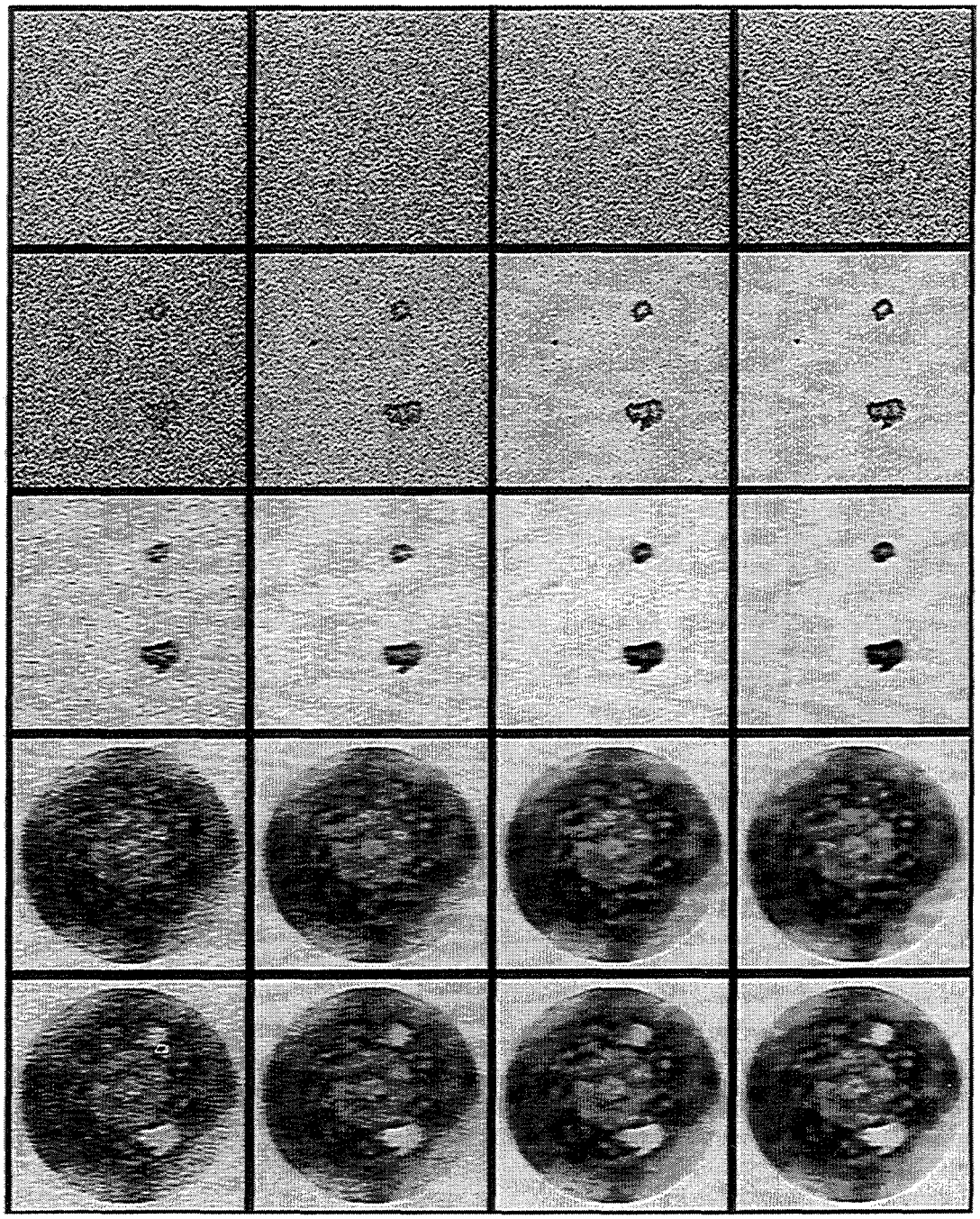

given in Sections 2.4 and 2.5 for simulation of imaging with limited illumination was written in FORTRAN and incorporated into our version of SPIDER. This new subroutine queries the user for the mean number of quanta per pixel, X_m, and the extinction coefficient, E.

3. Simulations of the 3D reconstructions

3.1. Tests of the imaging simulation

The capacity of the program to generate Poisson statistics over a large range of incident quanta was tested by computing a 2D image with the extinction coefficient set to zero. Since there is no absorption, the density of each pixel in the output image is equal to X_n, the number of incident quanta selected for that pixel by the program, and the standard deviation of the image is equal to the noise. Using this approach we determined that the signal-to-noise ratio, S/N, was equal to the square root of X_m, the mean number of quanta per pixel chosen, over a range of X_m from 4×10^9 to 2×10^9 (data not shown). This result demonstrated that the program generates a Poisson distribution of incident quanta over a larger range than used in these studies.

In an absorption model of image formation, the signal of interest is the difference between the number of quanta absorbed by neighboring voxels. If the maximum absorption is set to 1%, the maximum signal will be equal to $0.01\ X_m$. Since the noise is still $\sqrt{X_m}$, the maximum S/N becomes $0.01\sqrt{X_m}$ and, therefore, 25×10^4 quanta/pixel are required for S/N = 5. To test how well our ability to visually detect the signal conforms to the expectation that S/N must be 5 or higher, we created binary versions of the central slices of models A and B in which the background was set to zero and the specimen mass to an arbitrary but uniform value. Binary models were used for this test to ensure a uniform absorption level throughout the image. Images of these modified slices were computed with the extinction coefficient set for 1% absorption, and X_m values ranging from 10^4 to 81×10^4 quanta/pixel in increments that yield integer S/N values from one through nine. Representative examples of the results for S/N values of 1 through 8 are presented in Fig. 2. When this trial was repeated ten times, it was found that the microtubule tip (smallest feature in the difference images) could not be detected at all when S/N = 1; it could be detected in 2 of the 10 trials when S/N = 2; in 5 of the 10 trials when S/N = 3; in 9 of the 10 trials when S/N = 4 or 5, and in all 10 trials when S/N = 6, 7, 8, or 9. Thus, in agreement with the Rose criterion, we find that a S/N of 5 or greater is required for reliable detection of features at the resolution limit.

3.2. Verification of the Hegerl–Hoppe theorem with ideal data

Simulations that confirm the basic tenet of the Hegerl–Hoppe theorem are illustrated in Fig. 3. In this figure the columns delineate four different amounts of total illumination ranging from 0.2×10^8 to 8.9×10^8 quanta per pixel. The extinction coefficient was set so that the average density in projection corresponded to 1% absorption, and the maximum density corresponded to less than 3% absorption.

The first and second rows in Fig. 3 show the difference image for the sum of the middle three slices of models A and B (see Sections 2.1 and 2.2 above). The sum of the three middle slices of each model was used in these simulations because the microtubule tip is removed from these three slices in model B (see Section 2.2). Recall that the "limiting resolution feature" was represented by a three voxel cube rather than a single voxel for reasons related to Shannon sampling [21].

In the first row of Fig. 3 the difference images were computed from image pairs simulated to have 1/180 of the total dose (i.e., the amount of illumination that would be partitioned to each projection in the tilt series). None of the three features (blade, microtubule, or microtubule tip) can be detected above the noise level, demonstrating that the dose per projection is far less than that required to image features in a "single" slice of the models in a statistically significant fashion.

For comparison, the second row of Fig. 3 presents difference images for the middle slices of models A and B when the slices are imaged with the total reconstruction dose (i.e., 180 times the dose used in the first row). The features, particularly the micro-

tubule tip, become consistently recognizable above the noise at 10^8 quanta per pixel.

The third row of Fig. 3 illustrates the difference obtained for middle slices of the 3D reconstructions computed from the tomographically reconstructed data sets in which the dose used for each projection was as shown in the first row. The microtubule tip again becomes detectable at a total dose of 10^8 quanta per pixel, the same level as is required for detectability in single images of the 2D slices.

The fourth and fifth rows in Fig. 3 show the slices themselves, from 3D reconstructions of models A and B, that were used to compute the difference images in the third row of Fig. 3. Although the missing tip is difficult to see in the reconstructions, a sufficiently careful examination, such as by difference imaging, reveals its absence (i.e. row 3 of Fig. 3). Thus, while surrounding structural complexity alters the ease of detection, it does not alter detectability at a given level of statistical significance.

In 0° projections the blade and microtubule become apparent at much lower dose levels than in single slices (row 3 of Fig. 1 and data not shown). This fact is expected in advance, and it is due to summation effects from densities located at different levels. The microtubule tip, however, does not become apparent until the dose level reaches 10^8 quanta per pixel (data not shown). Taken together with the data illustrated in Fig. 3, these observations demonstrate that the same total dose is required to obtain statistical significance in a 3D reconstruction, in a 2D projection, or in an image of a single slice of the model. The latter result is equivalent to Hoppe and Hegerl's "Gedankenversuch" [16]. Inspection of the images in rows 4 and 5 of Fig. 3 confirmed that high resolution features are the first to be lost as the dose level is decreased.

3.3. Strongly absorbing samples

In their analytical derivation, Hegerl and Hoppe [12] assumed low contrast, as is typical of the electron microscope "weak phase objects" that motivated the investigation of dose fractionation at that time. To satisfy the criterion of low contrast, we set the extinction coefficient in the simulations shown in Fig. 3 so that the maximum absorption corresponding to any pixel in the projections was less than 3% of the incoming radiation. Absorption by a single voxel is very small under these conditions, of course, and this fact is responsible for the large number of quanta that must be used per pixel to ensure that the contribution from each voxel will be significant (as required by the theorem). In the case of electron

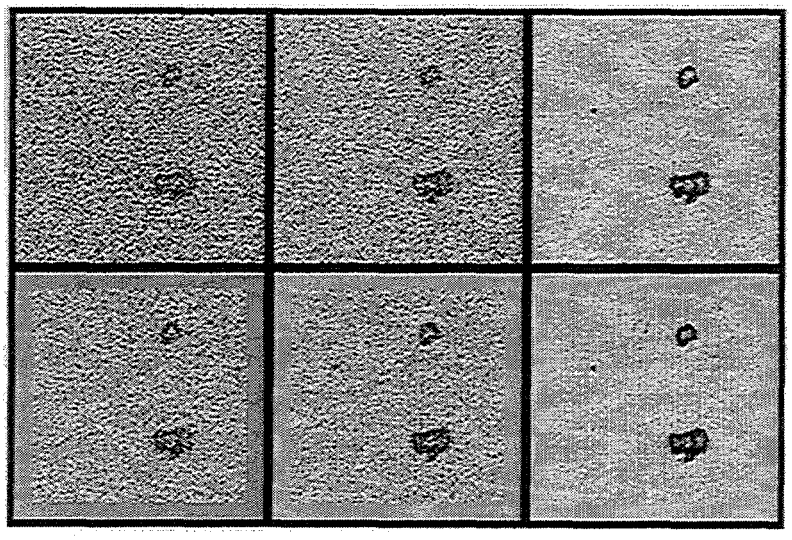

Fig. 4. High-absorption case. Non-linear imaging was simulated by setting the extinction coefficient so that the maximum and average adsorption were 84% and 50%, respectively (see Section 2.4). The dose levels in columns 1–3 are 0.9, 1.8 and 3.6×10^5 quanta per pixel, respectively. Difference images of the central slice from the model are shown in row 1 and from the 3D reconstructions in row 2.

microscopy, phase contrast gives a much stronger signal than would be expected if the signal were derived solely from such low levels of absorption. Thus far fewer quanta per unit area than used for our simulations are required for frozen-hydrated specimens imaged by cryo-electron microscopy (see Section 4 for strategies to determine total dose levels required). Our simulations, however, give a realistic estimate of the illumination levels required for soft X-ray microscopy. Furthermore, since shot noise at low absorption levels is generated almost exclusively from fluctuations of the incident illumination, our conclusions concerning the Hegerl–Hoppe theorem are independent of the mode of contrast formation.

Most soft X-ray microscopic applications, and several potential electron-microscopic applications, of single-axis tomography will involve specimens that absorb more strongly than the levels used in Fig. 3. To simulate these applications we have set the extinction coefficient so that the maximum absorption is 84% and the average is 50%. The results are seen in Fig. 4 where, as in Fig. 3, the columns delineate total dose levels. In this case the levels range from 9×10^4 to 36×10^4 quanta/pixel. Fewer quanta were required than for the low-absorption simulations because the higher absorption gives a much stronger, albeit non-linear, signal. The first row of Fig. 4 shows the difference images of slices

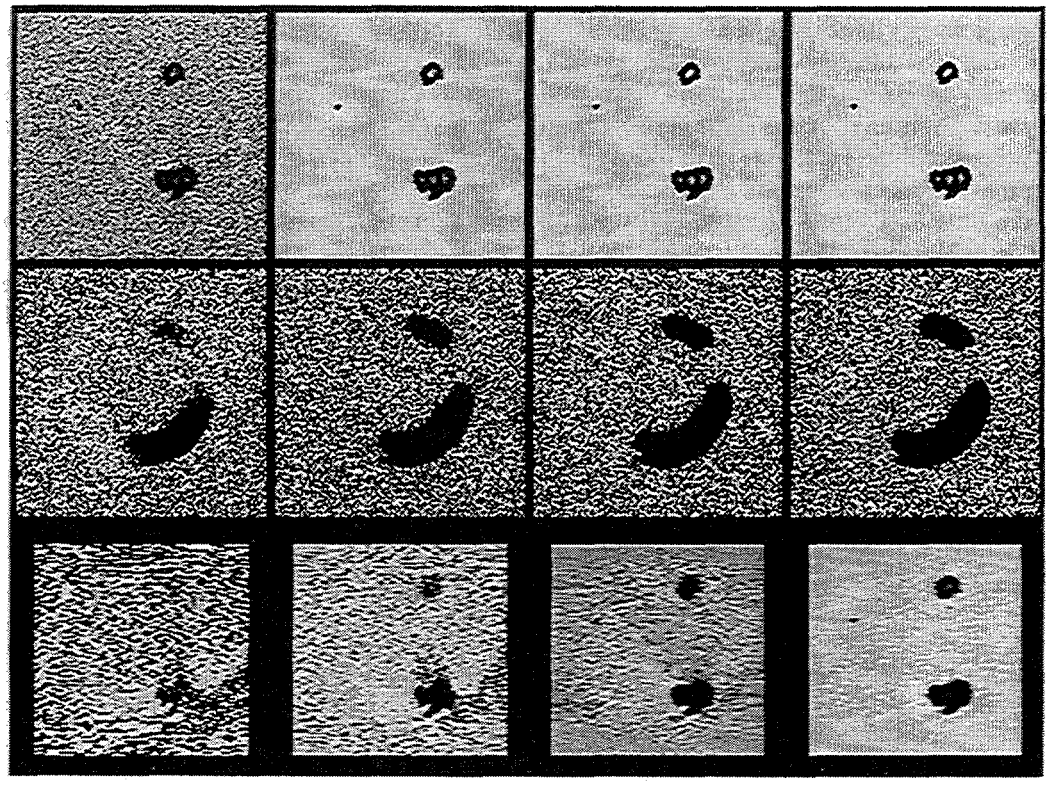

Fig. 5. Signal-dependent noise at extremely high absorption. The extinction coefficient was adjusted to yield a mean absorption of 99% in the projections (again absorption in single slices from the models is much less). Stochastic fluctuations in the number of incident quanta were simulated by random selection from a Poisson distribution with a specified mean value, and stochastic fluctuations in the fraction of those quanta that are actually absorbed in the column above each pixel were simulated by random selection of each pixel's absorption from a binomial distribution (see Section 2.5). The total exposure in columns 1–4 is 10^4, 10^5, 10^6 and 10^7 quanta/pixel. Row 1 shows difference images of central slices computed with the total dose. Difference density arising from the microtubule tip is clearly evident in all four images. Row 2 presents difference images of the zero-degree projections, also computed at the same total dose. The microtubule tip is barely detectable at 10^6 quanta/pixel. Results from the 3D reconstruction are shown in row 3. Again, the microtubule tip is detected when the dose levels are higher than 10^6 quanta/pixel.

from models A and B computed with the total dose (analogous to row 2 in Fig. 3). The second row shows the difference images of slices from the tomographic reconstructions (analogous to row 3 of Fig. 3). As in the case of a low-contrast specimen, the microtubule tip becomes distinct at approximately the same total dose in a 3D reconstruction, in a 2D projection and in a single slice from the model (i.e. 18×10^4 quanta per pixel).

At high absorption levels the stochastic nature of the absorption process also adds to the noise of the image (i.e., the noise becomes signal-dependent). We modeled the statistics of this process using the binomial distribution (Section 2.5). The effect of stochastic absorption was measured by applying the program to a blank image (image with uniform density). The "signal" in this test case still corresponds to the amount of absorption, even though the amount of absorption does not vary from one pixel to the next. When the absorption was set at values of 25%, 50%, 75%, 90% and 99%, the S/N was 50%, 37%, 20%, 12% and 3% of the S/N observed at 0% absorption. Thus the S/N depends upon the amount of absorption and will vary from pixel to pixel in the projection images: i.e., the noise is no longer "additive", as required in the analytical derivation of the dose fractionation theorem.

When the effect of stochastic absorption was included in the image simulations, again with 50% absorption by the average pixel in the projections, the results were indistinguishable from those presented in Fig. 4. This result demonstrates that dose

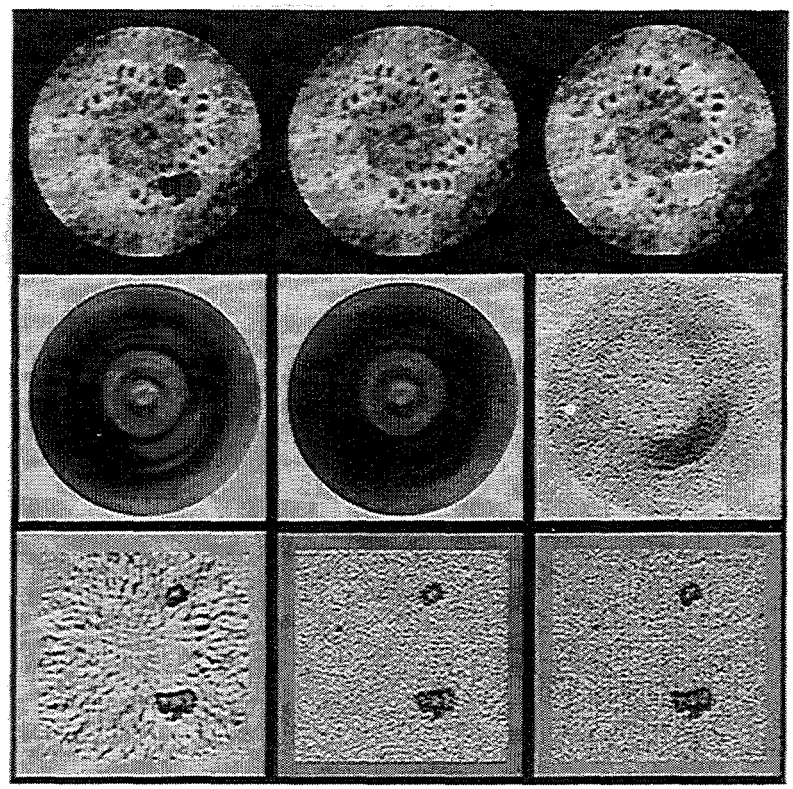

Fig. 6. The effect of varying contrast. The relative contrast of the blade, microtubule and tip were varied by making new versions of model A (see Section 2.3). The low- and high-contrast versions are shown in columns 1 and 3 while model A is shown in column 2 for comparison. These images have been individually scaled. Row 1 shows a single slice from each model. Row 2 shows 0° projections imaged at the fractionated dose. Row 3 presents difference images of the central slice from different 3D reconstructions. The total dose used for the low-, medium- (model A) and high-contrast versions was 1.8×10^8, 9.0×10^6 and 2.7×10^5 quanta per pixel, with the adsorption set to have a maximum value of 30%. Reconstruction artifacts are more visible in the 3D reconstruction of the low-contrast model, presumably because of the lower signal, relative to the rest of the structure, that is present in the difference image.

fractionation is still valid under conditions of moderate signal-dependent noise. We further tested this in the extreme case by setting the absorption level of the average pixel in the projections to 99%. As can be seen from rows 1 and 2 of Fig. 5, when the absorption is this high, projections require 10^3 times more quanta per pixel for significance than do single slices. This is because absorption levels and therefore, signal-dependent noise, are much greater in projections than in single slices. The 3D reconstruction requires the same total dose as the projections (row 3 of Fig. 5). This demonstrates that dose fractionation is still valid at this extremely high level of absorption, if the total dose required for significance is measured from projections and not single slices.

3.4. The effect of contrast

Next we tested the effect of variation in specimen contrast on the reconstruction. This was accomplished by changing the contrast of the blade, microtubule and tip relative to the rest of the structure (see Section 2.3).

Row 1 of Fig. 6 shows one central slice from the low- and high-contrast versions of the model (models L and H) on the left and right, with same slice from the original model (model A) in the middle. The 0° projections from these models are shown in row 2, while row 3 presents the difference images between central slices from 3D reconstructions of models L and B, A and B, and H and B at the

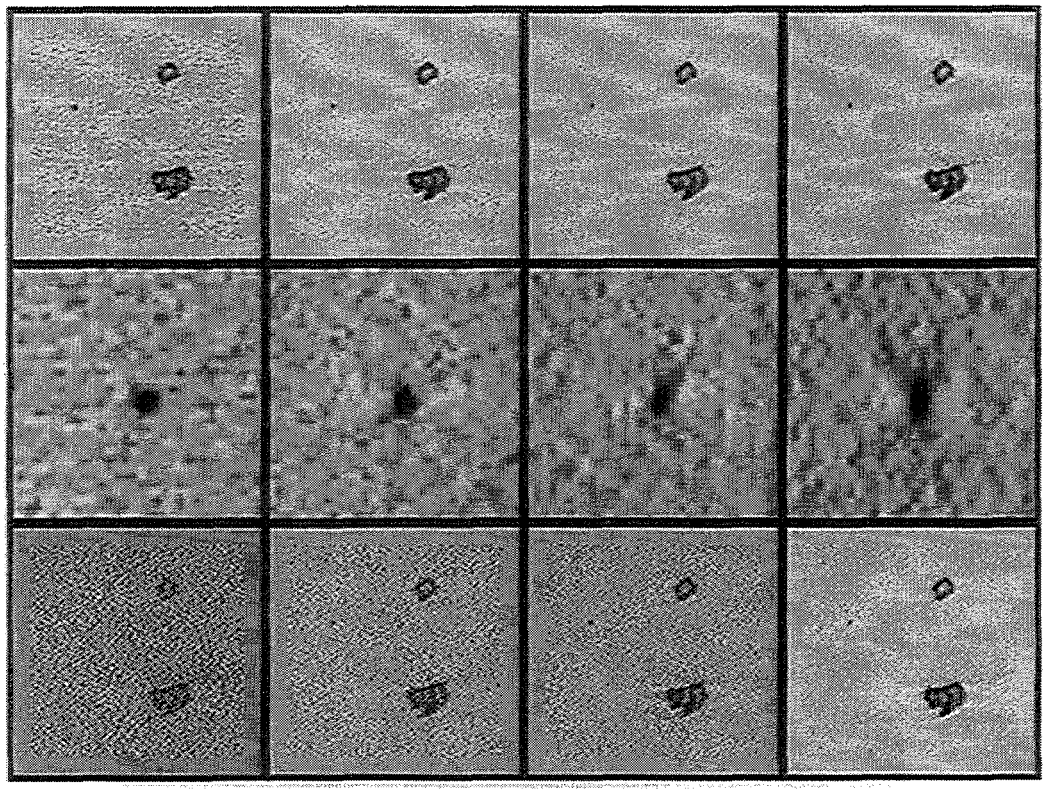

Fig. 7. The effect of an incomplete angular range. For rows 1 and 2 only, the angular range in columns 1–4 is the full 180°, 140°, 120° and 100°, respectively. The total dose was 3.2×10^8 for each of these reconstructions. Row 1 illustrates slices taken from each reconstruction. The light shadows on each side of the various features in columns 2–4 are a well known reconstruction artifact arising from the limited angular range [21]. Row 2 shows slices cut orthogonal to those in row 1. Here the tilt axis goes into the page (i.e., is orthogonal to the plane of the slice) instead of lying vertically in the plane of the slices. These slices show the tip magnified by a factor of 4, so that the elongation due to the limited angular range is evident. Row 3 presents slices from the 3D reconstruction computed with a 120° angular range and dose levels of 0.2, 0.8, 3.2 and 8.9×10^8 quanta per pixel. As with the full angular range, the tip becomes evident at 10^8 quanta per pixel, the same exposure that is required to image it in 2D slices (compare with row 2 and 3 of Fig. 3).

minimal total dose levels required for detection of the microtubule tip. In all three cases this was the same total dose as required to image the tip in a single slice or 2D projection of the model (data not shown).

In the low-contrast case, reconstruction artifacts contribute extraneous mass that is comparable in size and intensity to the microtubule tip. Normally these artifacts are not visible but the difference signal between models L and B, relative to the mass of the 3D structure, is only 1/5 of the difference signal between models A and B. This result indicates that if the relative contrast is too low there will be difficulties in interpretation due to the weakness of the signal. It is possible that the reconstruction artifacts would be less evident if the tilt series were sampled more finely, i.e., the dose fractionated into 900 or 1800 projections.

3.5. The effect of a missing wedge

In most applications of electron tomography only 120–140° of the full 180° angular tilt range can be recorded owing to technical limitations involved in mounting the specimen (see Ref. [22]). It is anticipated that applications involving soft X-ray microscopy will suffer a similar limitation. We have therefore simulated 3D reconstructions from data covering an incomplete tilt range by removing projections from both ends of the tilt range and adjusting the dose per projection so that the totals were the same as used in the experiments described in Section 3.2 (i.e., the doses used in Fig. 3). The top row in Fig. 7 demonstrates that the microtubule tip is recovered almost equally well in 3D reconstructions, computed from a total dose of 3.2×10^8 quanta per pixel, when the angular range is reduced from $\pm 90°$ (column 1) to $\pm 70°$ (column 2) or $\pm 60°$ (column 3), but some loss in recovery is evident for an angular range of only $\pm 50°$ (column 4). The light shadows seen on either side of the feature, when less than the full tilt range is used, are a well known artifact caused by the missing angular range [21]. The second row illustrates the expected, increasing elongation of specimen features (i.e., elongation of the point spread function) with increasing amount of missing angular range. The increased spreading of the signal and concomitant decrease in peak intensity with limited range of tilt is presumed to be the reason why dose fractionation is less effective for too much of a limitation in the range of tilt. These difference images of the microtubule tip were created by viewing the reconstruction in a direction parallel to the tilt axis, with a fourfold magnification (in all other views the tilt axis is vertical in the image plane). The bottom row shows the difference from 3D reconstructions computed with a $\pm 60°$ angular range and total doses varying from 0.20×10^8 to 8.9×10^8 quanta/pixel (i.e., analogous to columns 1–4 in row 3 of Fig. 3). As with the full angular range, the microtubule tip becomes distinct at about 10^8 quanta/pixel (compare with rows 2 and 3 of Fig. 3). These results demonstrate that the Hegerl–Hoppe theorem still holds for data with a substantial missing angular range.

Table 1
Alignment error versus imaging dose

Total dose [quanta/pixel $\times 10^6$]	Fractionated dose [quanta/pixel $\times 10^4$]	Average error [pixels]	Maximum error [pixels]
900	744	0.13	0.92
360	298	0.14	0.92
180 [a]	149 [a]	0.17	0.91
72	59.5	0.25	1.46
36	29.8	0.30	2.21
18	14.9	0.68	3.60
9.0	7.4	0.32	2.17
3.6 [b]	3.0 [b]	1.67	8.04

[a] Cut-off for obtaining full resolution in the 3D reconstruction.
[b] Alignment failed (picked the wrong cross-correlation peaks) for fractionated doses lower than 3×10^4 quanta/pixel.

3.6. Alignment

The above simulations demonstrate that features at the limiting resolution can be recovered in a 3D reconstruction computed from projections imaged with radiation levels grossly insufficient for detecting the contributions made by such features in individual 2D images. There would be no practical advantage to this effect, however, if each projection did not contain enough significant information to enable its alignment relative to the rest of the data set. We have applied a translational alignment scheme, based on the center of mass of the maximum peak in the cross-correlation function [23,24], to test our ability to align data sets with an angular range of 120° and 140°, and the results from the 120° data are presented in Table 1. The alignment is excellent (maximum error less than 1 pixel, average error less than 0.2 pixels) when approximately the minimum total dose required for recovery of the microtubule tip (1.8×10^8 quanta/pixel) is fractionated over the 120 projections of the data set (line 3, Table 1). The alignment is still reasonable at 1/5 to 1/20 of this total dose (lines 5–7 of Table 1). With the minimum total dose required to recover the microtubule tip, the alignment errors were so small that 3D reconstructions computed from aligned data were indistinguishable from those computed from unaltered (i.e., perfectly aligned) data sets (results not shown).

These results imply that projections contain significant information even when imaged at doses well below (in our example here, less by a factor of 10^3) those required to record the limiting-resolution features of the specimen. This is illustrated in rows 3 and 4 of Fig. 1, which show projections at the fractionated dose levels. In these projections, density derived from the microtubule and the blade is evident but the tip cannot be detected.

It might be argued that the circular mask used to make the models (see Section 2.1) gives the cross correlation an extra piece of information not found in biological specimens, and that this advantage may make the simulations in Table 1 more accurate than can be expected for real specimens. The mask, however, is only visible at tilt angles between $\pm 15°$ and, when results from this part of the range, and even from the range $\pm 20°$, are left out, the average

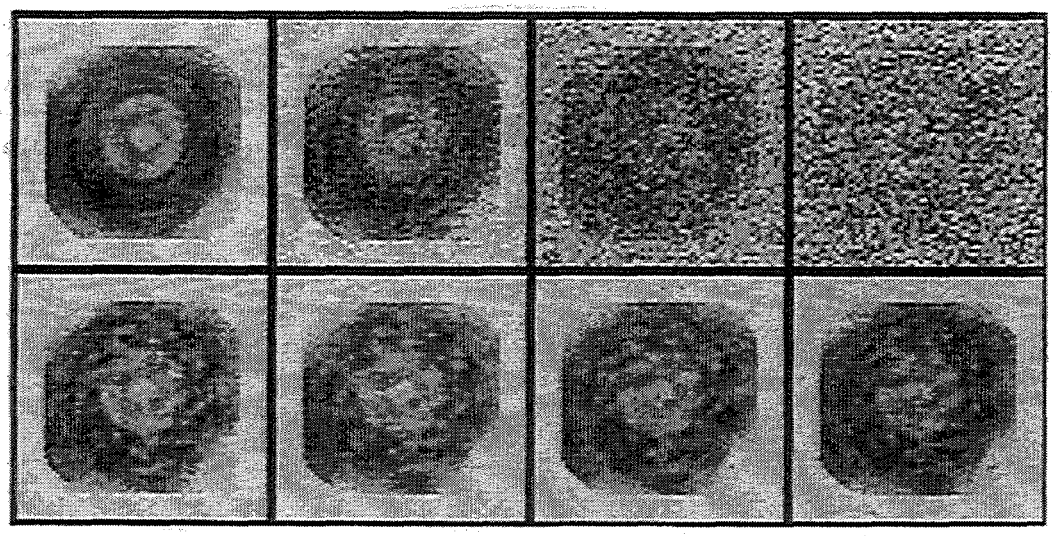

Fig. 8. Extreme fractionation of the dose. In columns 1–4 a total dose of 9×10^6 quanta/pixel has been fractionated among 36, 180, 1800 and 18 000 projections. All projections were computed from a modified version of model A (see Section 3.7) with an average absorption of 1%. Row 1 shows the zero degree projections, imaged at the fractionated dose, and row 2 central slices from the 3D reconstructions. The image quality of the 3D reconstructions remains roughly constant, despite the extreme degradation of individual projections with increased dose-fractionation.

alignment error actually decreases slightly. This demonstrates that the circular mask is not strongly affecting the accuracy of the alignment.

3.7. Extreme fractionation of the incident dose

The results of the previous section emphasize that, even though projections imaged at the fractionated doses do not record statistically significant information at the resolution limit, they do record significant information that is related to, but qualitatively different from, the 3D object density (see Section 4). The question then arises whether significant detail will be recovered in practice, in the 3D reconstruction, if the dose is fractionated until there is no (or very slight) density detectable on the individual projections. To answer this question we fractionated a total dose of 9×10^6 quanta per pixel between 36, 180, 1800 and 18 000 projections of a modified version of model A (thinner in z-dimension and binned down to $64 \times 64 \times 32$). The results of these trials are presented in Fig. 8 and they demonstrate that the 3D reconstruction is essentially independent of the number of views into which the total dose is fractionated, even in the extreme case of 18 000 views with little or no detectable density on each view. However, in the extreme case the projections of the data set lack sufficient density for alignment (see Table 1).

4. Discussion

The results of this study verify the Hegerl–Hoppe theorem and demonstrate its applicability to realistic experimental conditions. The importance of these findings lies in the fact that the total dose required to recover a specified resolution level in the 3D reconstruction can be determined prior to the experiment and fractionated over the whole tilt series, irregardless of the number of projections collected. In this way sensitive specimens can be spared the damaging effects of unnecessary radiation.

The prior controversy concerning dose-fractionation stems from different definitions of what is meant by "statistical significance", as it is applied to an image, rather than from disagreements about the mathematical formulation of the theorem [13–16]. Since a 2D projection is formed by the accumulation of signal from successive layers of the volume, projections generally contain considerably more contrast than would be obtained from a single 2D slice of the specimen if such a slice could be imaged [13,14,16]. For this reason a 2D projection can be recorded with statistical significance in the individual pixels of the projection at much lower dose levels than is required for the 3D volume, or, equivalently, for a 2D slice of the 3D volume. However, the goal of 3D reconstruction is to obtain structural information about a 3D object. In this regard it is important to remember that, although the higher contrast contained in projections is useful for alignment, the information contained in the projections is qualitatively different from the 3D object density [16], and the resulting 2D projection alone can be notoriously misleading when attempting to decipher the 3D structure (e.g., row 4 of Fig. 1). As the dose fractionation theorem shows, greater insight regarding the possibility of 3D reconstruction is gained if we define statistical significance in terms of the dose require to record a single volume element of a 3D object, as was done by Hegerl and Hoppe [12,16].

It is also important to note that the features which we have considered in our simulations are embedded in a larger object. We have even shown, as an example, that the Hegerl–Hoppe theorem is still valid when the contrast of our selected features is lowered fivefold relative to the rest of the object (Fig. 6). This result demonstrates that the theorem will hold for most, if not all biological specimens, rather than being restricted to a special class of sparse objects as argued in Ref. [14].

Nevertheless, there are other important and desirable scientific objectives that one might *like* to accomplish through the application of dose fractionation, but which can be calculated to lie outside the realm of physical possibility. Specifically, it would be impossible to use dose fractionation to do a tomographic reconstruction of a (single) biological macromolecule at a resolution of 0.35 nm. The reason is that the dose needed to obtain a statistically significant image of such a voxel requires an electron exposure ("dose") that is more than 10^4 times larger than the maximum exposure that can be tolerated, due to radiation damage [13,25].

Since signal accumulated from successive layers

of a 3D object can be recorded with statistical significance at much lower dose levels than signal from a single volume element, determining the total dose required for a 3D reconstruction from 2D projections is normally inappropriate. Rather, the only reliable method to compute the radiation dose required to recover a specified resolution level is to calculate it from known extinction coefficients and agreed criteria for statistical significance (i.e., the Rose criterion, for X-rays see Ref. [26]; for electrons, see Ref. [27]). For soft X-ray microscopy at ~ 50 nm resolution, which is the anticipated limit of present-generation instruments, statistically significant images (in the sense of Hegerl and Hoppe) can be obtained with 10^8 rad [26]. Since this dose can be fractionated over the whole tilt series, we expect it to be eminently feasible to compute a limiting-resolution 3D reconstruction without exceeding the 10^{10} rad limit at which extensive specimen damage occurs in frozen-hydrated specimens. This important conclusion means that it is worthwhile to build a soft X-ray microscope capable of 3D imaging of thick, frozen-hydrated specimens, using single-axis tomography.

In electron microscopy, the Hegerl–Hoppe theorem complements the recent development of automated data collection methods [6,7]. The latter has improved efficiency of data collection to the point where almost all of the electron exposure is used for image acquisition. Current evidence indicates that cryo-specimens can tolerate about 30 electrons per $Å^2$ before large scale structural damage occurs [10,11]. According to the table presented by Saxberg and Saxton [13], this level of exposure would permit the discrimination of protein (density about 1.5 times that of water) from water at resolutions of 5 nm or larger. By combining dose-fractionation with automated tomography, it is feasible to collect a reasonably large number of projections (e.g. at least 70 to 140) on cryo-specimens without exceeding a total dose of 30 $Å^2$. This number of projections would ensure resolution levels comparable to those achieved in present applications of tomography to beam-stable preparations. The use of low-noise CCD cameras for direct image acquisition also makes it feasible to record images at lower exposure than on film. This permits greater fractionation of the total dose.

The cross-correlation alignment scheme employed in our simulations is used less frequently than fiducial marker schemes [28] because the latter give a greater accuracy for rotational alignment (some schemes use both methods, see Ref. [24]). Although we did not attempt to simulate a fiducial marker scheme it is reasonable to expect that it will work at the same dose levels as the cross-correlation scheme because the colloidal gold beads used are much stronger scatters (or absorbers) of electrons and X-rays than the carbon, nitrogen and oxygen atoms that predominate in biological structures. In fact, to be an effective marker the gold bead must have more contrast in 2D projections than the rest of the specimen.

At present, the extreme fractionation demonstrated in Fig. 8 has no practical value for either electron microscopy or soft X-ray microscopy owing to technical limitations on data collection. However, current advances in image acquisition (i.e., CCD cameras), and in the speed, memory and disk capacity of computers, will soon make it feasible to routinely collect and process 500–1000 views/specimen. Thus, it is likely that the principle of dose-fractionation will, in the future, enable investigators to obtain the desired resolution by sampling 3D structures at angular intervals as small as 0.1°, without increasing the total dose.

5. Conclusions

Our simulations demonstrate that the Hegerl–Hoppe dose-fractionation theorem [12] is valid for a wide range of biological and similar specimens and for the experimental limitations that typify single-axis tomography. This means that the dose required to record a specified level of resolution from a 3D specimen can be fractionated among any number of different projections, and the specified resolution can still be recovered in a 3D reconstruction computed from these projections. Thus, a significant 3D reconstruction can be computed from "insignificant" projections. In most, if not all, cases the "insignificant projections" will contain adequate information, derived from the summation of features at different levels in the specimen, to enable alignment of the tilt series. From these results we conclude that it is possible to compute in advance the dose required for a 3D reconstruction, and that it is feasible to use

tomography with soft X-ray microscopy to obtain 50 nm resolution of frozen-hydrated specimens without causing extensive structural alterations. It is also feasible to use single-axis tomography with cryo-specimens in electron microscopy, where the limit of resolution is anticipated to be approximately 5 nm.

Acknowledgements

We wish to thank Dr. Conly L. Rieder and Mike Marko for providing the scanned image of the centriole that we used to construct our models, and Dr. Pawel Penczek for help in implementing the simulation program in SPIDER. We also wish to thank Dr. Penczek and Drs. David Agard, Joachim Frank, Reiner Hegerl, Bram Koster, Weiping Liu and Dieter Typke for helpful comments concerning the manuscript. This work was supported by the Office of Health and Environmental Research, US Department of Energy, under contract DE-AC03-76SF00098. In addition B.F.M. was supported, in part, by MCB-9420772 awarded by National Science Foundation, and by RR01219 awarded by the National Institutes of Health Biomedical Research Technology Program, National Center for Research Resources, Department of Health and Human Resources/Public Health Service, to support the Wadsworth Center's Biological Microscopy and Image Reconstruction facility as a National Biotechnological Resource.

References

[1] B.F. McEwen, J.T. Arena, J. Frank and C.L. Rieder, J. Cell. Biol. 120 (1993) 301.
[2] W.J. Landis, M.J. Song, A. Leith, L. McEwen and B.F. McEwen, J. Struct. Biol. 110 (1993) 39.
[3] R.A. Horowitz, D.A. Agard, J.W. Sedat and C.L. Woodcock, J. Cell. Biol. 125 (1994) 1.
[4] M.S. Ladinsky, J.R. Kremer, P.S. Furcinitti, J.R. McIntosh and K.E. Howell, J. Cell. Biol. 127 (1994) 29.
[5] P.K. Luther, Sample shrinkage and radiation damage, in: Electron Tomography, Ed. J. Frank (Plenum, New York, 1992) p. 39.
[6] K. Dierksen, D. Typke, R. Hegerl and W. Baumeister, Ultramicroscopy 49 (1993) 109.
[7] M.B. Braunfeld, A.J. Koster, J.W. Sedat and D.A. Agard, J. Microscopy 174 (1994) 75.
[8] C. Jacobsen, S. Williams, E. Anderson, M.T. Browne, C.J. Buckley, D. Kern, J. Kirz, M. Rivers and X. Zhang, Opt. Commun. 86 (1991) 351.
[9] H. Ade, X. Zhang, S. Cameron, C. Costello, J. Kirz and S. Williams, Science 258 (1992) 972.
[10] R.M. Glaeser and K.A. Taylor, J. Microscopy 112 (1978) 127.
[11] J.F. Conway, B.L. Trus, F.P. Booy, W.W. Newcomb, J.C. Brown and A.C. Steven, J. Struct. Biol. 111 (1993) 222.
[12] R. Hegerl and W. Hoppe, Z. Naturforsch. 31a (1976) 1717.
[13] B.E.H. Saxberg and W.O. Saxton, Ultramicroscopy 6 (1981) 85.
[14] M. van Heel, Optik 73 (1986) 83.
[15] W. Hoppe and R. Hegerl, in: Computer Processing of Electron Microscope Images, Ed. P.W. Hawkes (Springer, Berlin, 1980) p. 127.
[16] W. Hoppe and R. Hegerl, Ultramicroscopy 6 (1981) 205.
[17] B.F. McEwen, M.J. Song and W.J. Landis, J. Comput. Assist. Microsc. 3 (1991) 201.
[18] W.H. Press, B.P. Flannery, S.A. Teukolsky and W.T. Vetterling, Numerical Recipes (Cambridge University Press, Cambridge, 1988).
[19] M. Radermacher, Weighted back-projection methods, in: Electron Tomography, Ed. J. Frank (Plenum, New York, 1992) p. 91.
[20] J. Frank, B. Shimkin and H. Dowse, Ultramicroscopy 6 (1981) 343.
[21] J. Frank and M. Radermacher, Three-dimensional reconstruction of non-periodic macromolecular assemblies from electron micrographs, in: Advanced Techniques in Biological Electron Microscopy, Ed. J. Koehler (Springer, Berlin, 1986) p. 1.
[22] D.P. Barnard, J.N. Turner, J. Frank and B. McEwen, J. Microscopy 167 (1992) 39.
[23] J. Frank, B.F. McEwen, M. Radermacher, J.N. Turner and C.L. Rieder, J. Electron Microsc. Tech. 6 (1987) 193.
[24] J. Frank and B.F. McEwen, Alignment by cross-correlation, in: Electron Tomography, Ed. J. Frank (Plenum, New York, 1992) p. 205.
[25] R. Henderson, Q. Rev. Biophys. 28 (1995) 171.
[26] D. Sayre, J. Kirz, R. Feder, D.M. Kim and E. Spiller, Ultramicroscopy 2 (1977) 337.
[27] J. Frank and L. Al-Ali, Nature 256 (1975) 376.
[28] M.C. Lawrence, Least-squares method of alignment using markers, in: Electron Tomography, Ed. J. Frank (Plenum, New York, 1992) p. 197.

Dose Fractionation Theorem For 3-D Reconstruction

1. If *E* is the lowest exposure that will still give a statistically well-defined projection of an isolated voxel

2. then <u>all</u> voxels are statistically well defined in a 3-D reconstruction that is recorded with an exposure of *E*/m.

3. Proof of the theorem requires linearity of image formation. R. Hegerl & W. Hoppe, Naturforsch. 31a, 1717 (1976).

Reconstructions like this

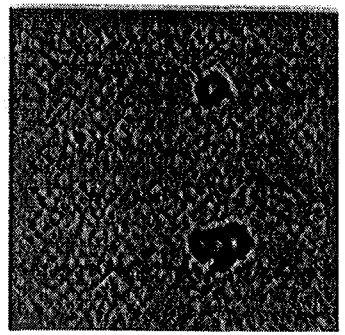

Can be obtained from images like this

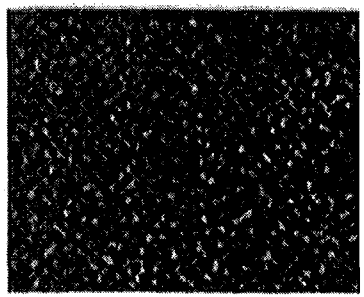

Feature-detection Depends Upon The Singal-to-noise Ratio

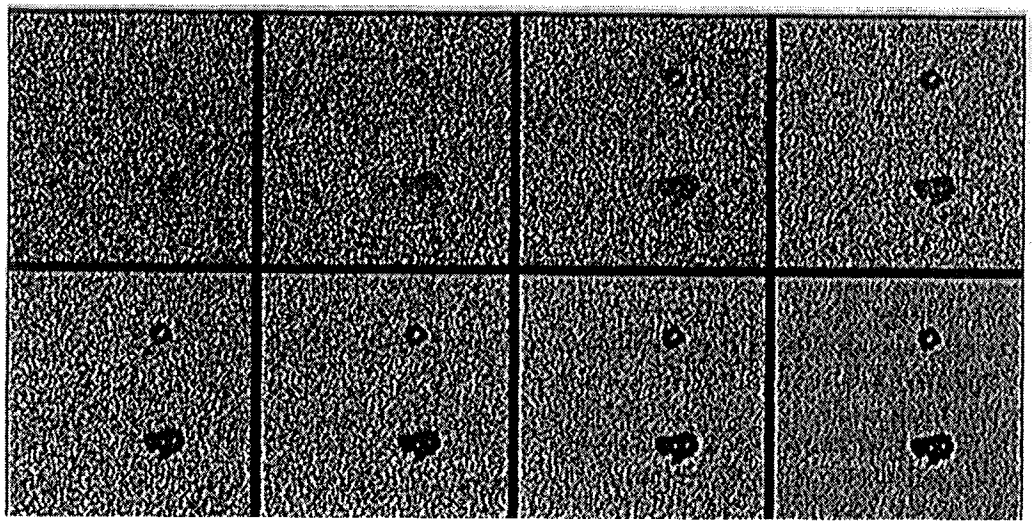

Why Is Dose-Fractionation Necessary (Prudent) In Biological X-ray Microtomography?

- Minimum-exposure requirement at 50nm resolution corresponds to ~10^8 rad: Sayre et al. Ultramicroscopy 60: 337 (1977).
- Typical reconstructions require ~ 100* evenly spaced projections over $\pm 60^\circ$ tilt, or better.
- The total dose of ~ 10^{10} rad is known to cause severe "bubbling" in frozen hydrated sample s (Cryo EM literature).

* Rule-of-thumb: π x thickness/resolution.

Intuitive Proof of the Projection Theorem

Data Collection

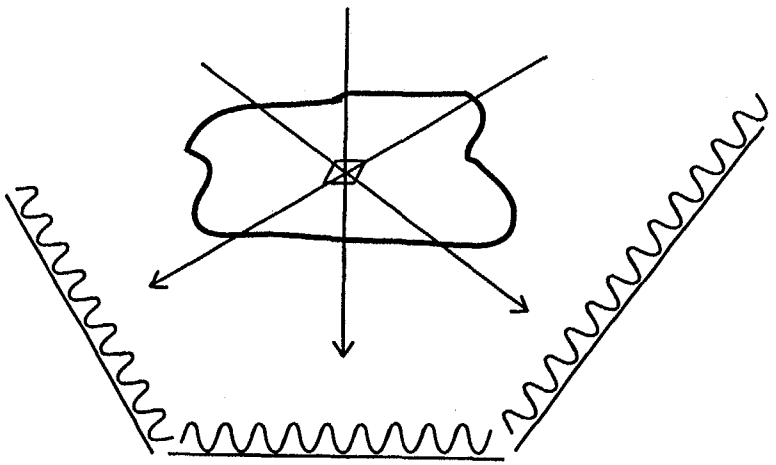

- "m" noisy images.
- The projection of a single voxel is not statistically well defined.

3-D Reconstruction by Back Projection

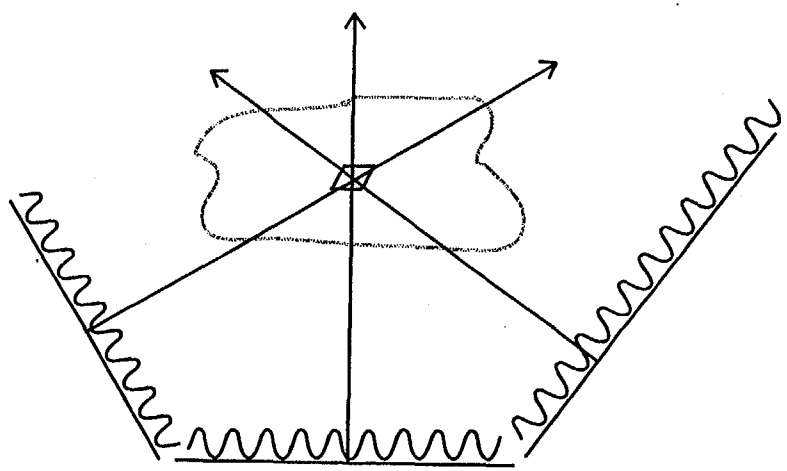

- The signal adds linearly, i.e. $\propto$ m.
- The noise adds in quadrature.
- The 3-D density becomes statistically well defined.

Model Structure Used To Demonstrate Dose Fractionation

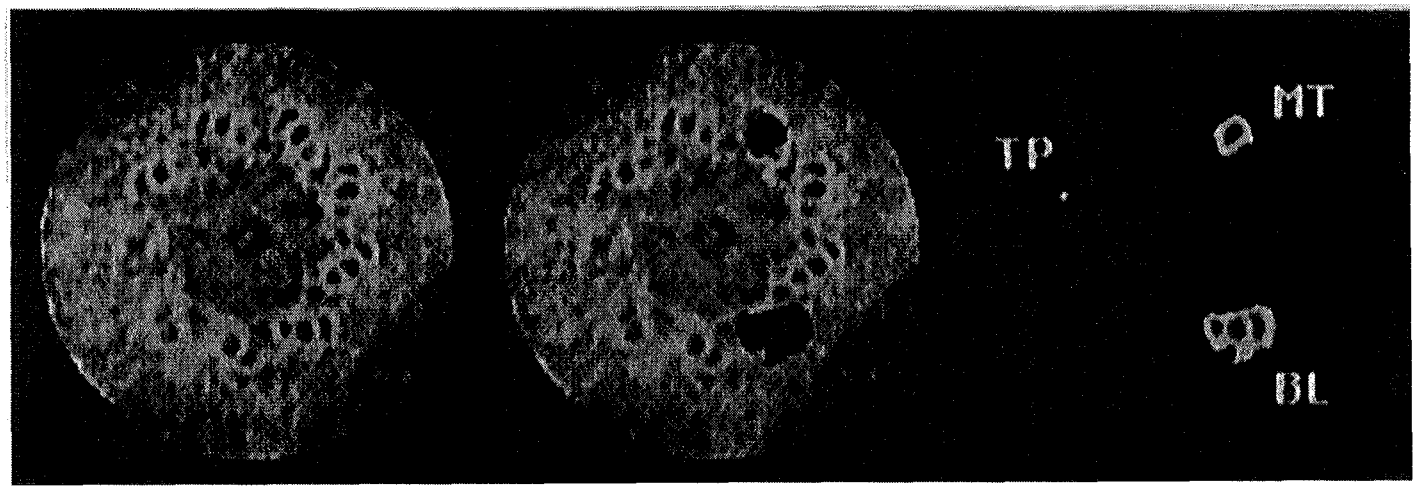

Simulation of Linear Imaging Feature Detection Is the Same in Projections And in 3-D Reconstructions

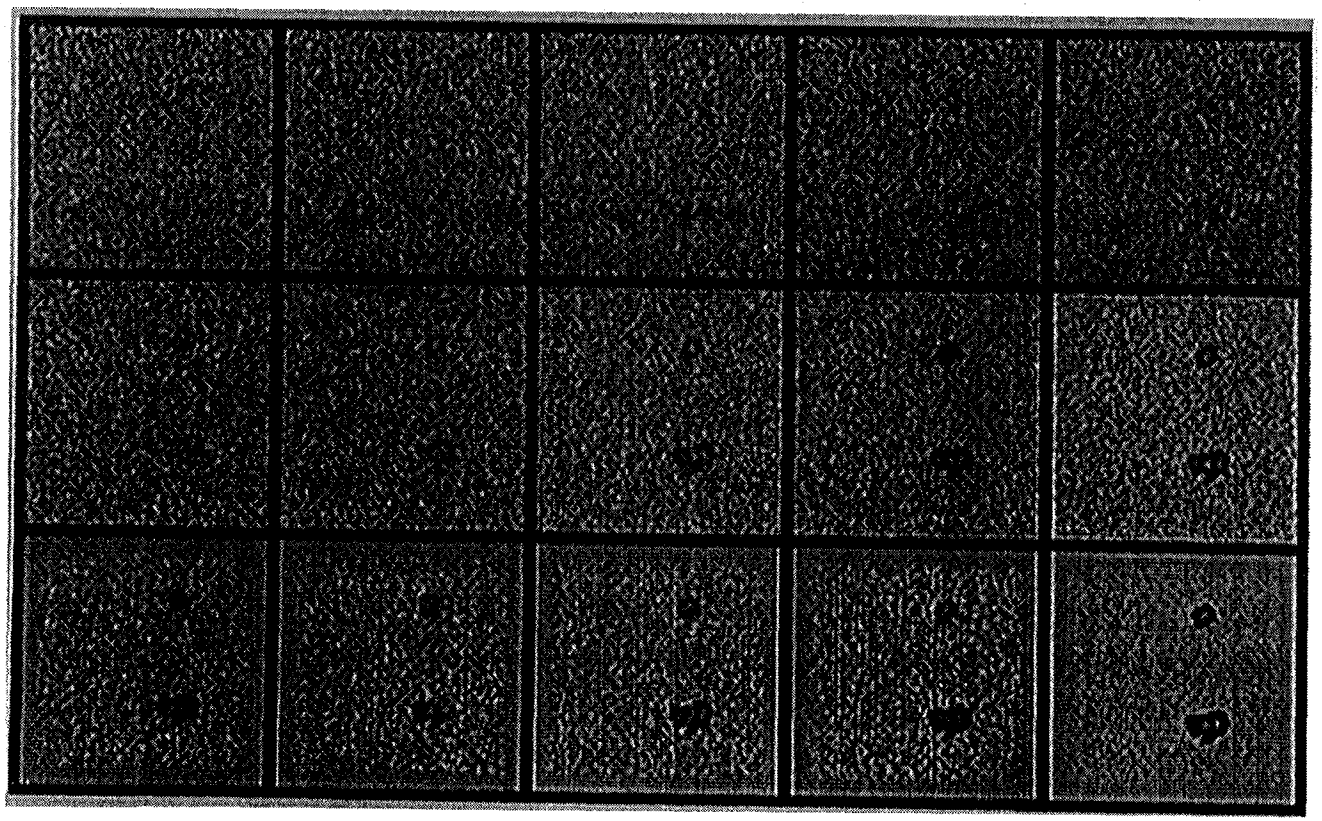

Error in Alignment By Cross Correlation Remains Small After Dose-fractionation

Total dose [quanta/pixel X 10^6]	Fractionated dose [quanta/pixel X 10^4]	Average error [pixels]	Maximum error [pixels]
900	744	0.13	0.92
360	298	0.14	0.92
180 [a]	149 [a]	0.17	0.91
72	59.5	0.25	1.46
36	29.8	0.30	2.21
18	14.9	0.68	3.60
9.0	7.4	0.32	2.17
3.6 [b]	3.0 [b]	1.67	8.04

[a] Cut-Off for obtaining full resolution in the 3-D reconstruction.

[b] Alignment failed (picked the wrong cross-correlation peaks) for fractionated doses lower than 3 X 10^4 quanta/pixel.

Simulation Demonstrates That Dose-factionation Still Applies for Non linear Imaging Conditions

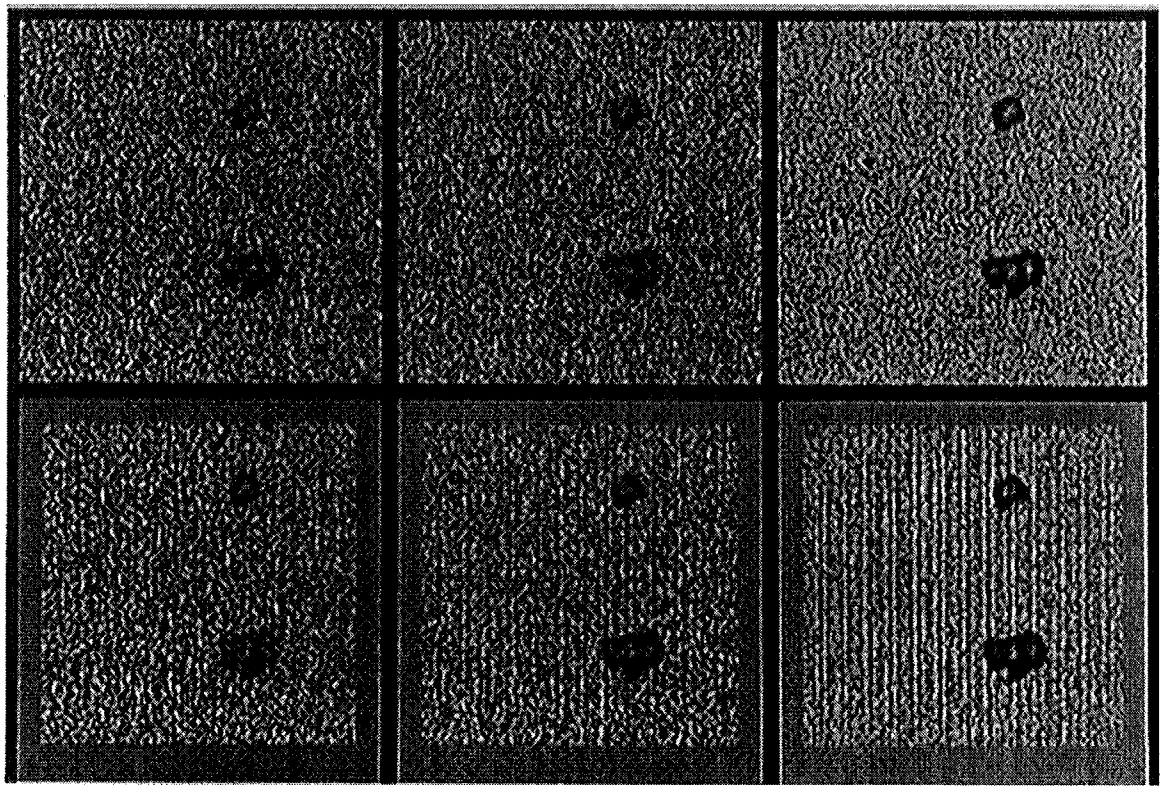

Tomography Is Essential For Complex Biological Structures

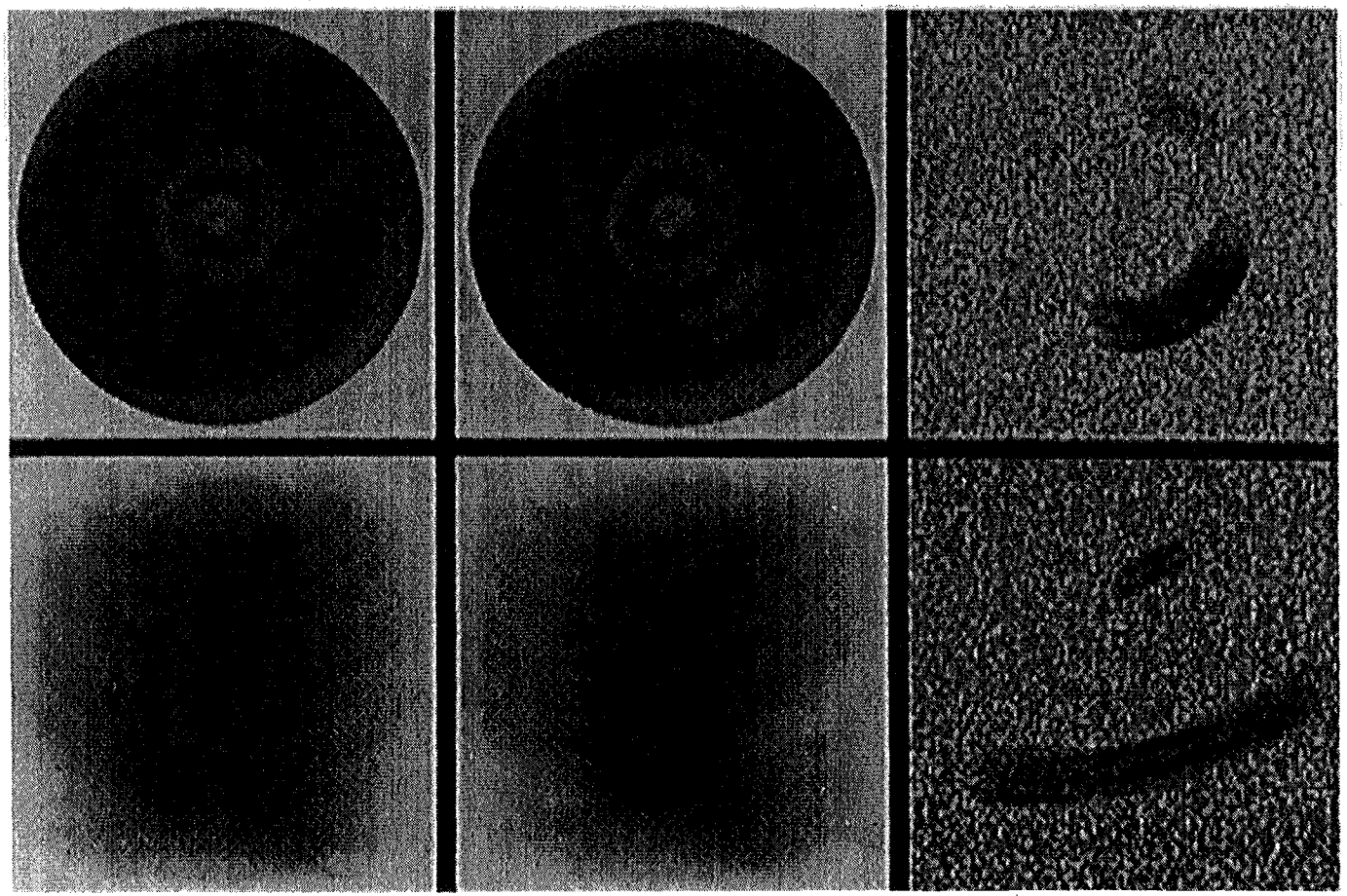

Summary and Conclusion;

1. Unacceptable x-ray doses would be required for "typical" applications of biological microtomography, if every voxel was recorded as a statistically defined projection, in every image.

2. The dose fractionation theorem (Hegerl and Hoppe) tells us that the total dose for a 3-D data set need not be any higher than that which is required for a well-defined image (projection) of an isolated voxel.

3. Simulations show that the theorem continues to be true even when strong absorption renders the images very non-linear.

4. Simulations also establish that images can be aligned under dose-fragmented conditions, an essential requirement for practical applications.

5. X-ray microtomography at 50nm resolution is expected to be readily feasible with frozen-hydrated biological samples.

Post-processing methods of rendering and visualizing 3-D reconstructed tomographic images

Stephen T.C. Wong
Radiology, Neurology, and Bioengineering
UCSF

SUMMARY

The purpose of this presentation is to discuss the computer processing techniques of tomographic images, after they have been generated by imaging scanners, for volume visualization. Volume visualization is concerned with the representation, manipulation, and rendering of volumetric data.[1] Since the first digital images were produced from computed tomography (CT) scanners in the mid 1970s, applications of visualization in medicine have expanded dramatically. Today, three-dimensional (3D) medical visualization has expanded from using CT data, the first inherently digital source of 3D medical data, to using data from various medical imaging modalities, including magnetic resonance scanners, positron emission scanners, digital ultrasound, electronic and confocal microscopy, and other medical imaging modalities. We have advanced from rendering anatomy to aid diagnosis and visualize complex anatomic structures to planning and assisting surgery and radiation treatment.[2] New, more accurate and cost-effective procedures for clinical services and biomedical research have become possible by integrating computer graphics technology with medical images. This trend is particularly noticeable in current market-driven health care environment. For example, interventional imaging, image-guided surgery, and stereotactic and visualization techniques are now steaming into surgical practice.

In this presentation, we discuss only computer-display-based approaches of volumetric medical visualization. That is, we assume that the display device available is two-dimensional (2D) in nature and all analysis of multidimensional image data is to be carried out via the 2D screen of the device. There are technologies such as holography and virtual reality that do provide a "true 3D screen". To confine the scope, this presentation will not discuss such approaches.

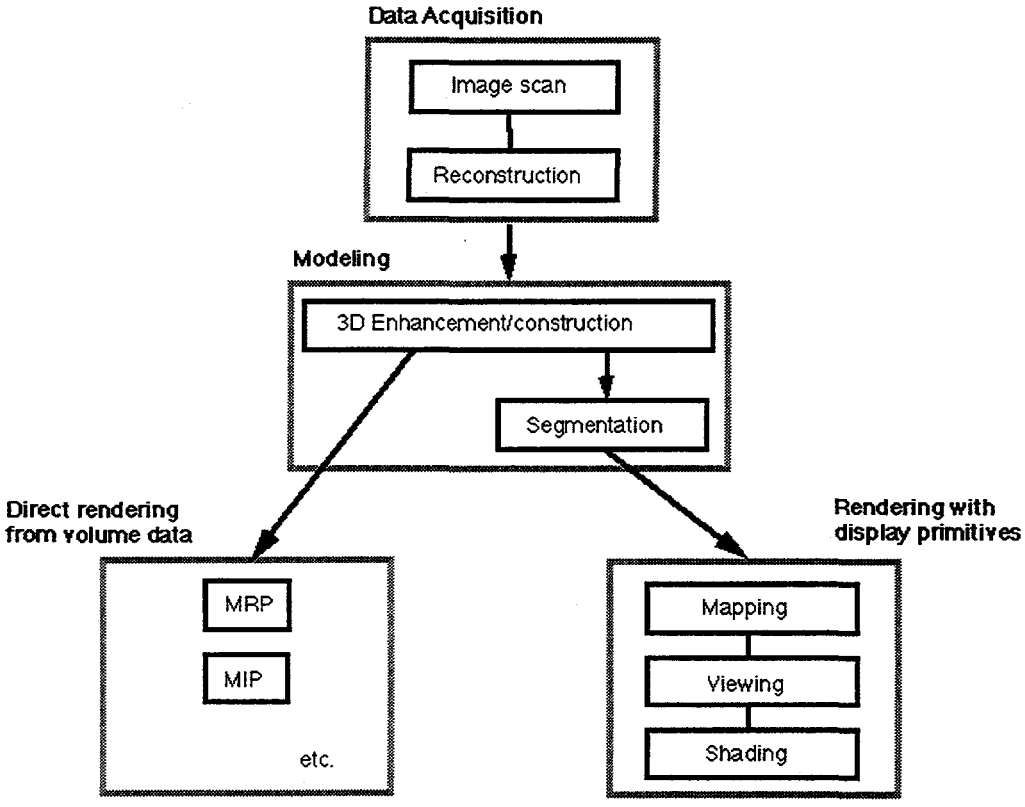

Figure 1. Volume visualization pipeline of tomographic images.

The flow of processing of 3-D tomographic images is shown in Figure 1.[3] The steps include data acquisition, modeling, and rendering. Data acquisition and image reconstruction are covered by other presentations in this workshop. In this presentation, mainly modeling and rendering are explained.

Modeling consists of two processes. The first is the construction of 3-D data from the original 2D tomographic images. The second step is the segmentation of target objects from the constructed 3-D data. The process of 3-D data construction can be considered as a kind of data estimation from a set of acquired tomographic axial images. In this process, the data that have been rendered as 2-D pixels are translated into the 3-D voxels. 3-D data construction is indispensable for the following 3-D processes in the pipeline. The spatial data-sampling pitch of the original tomographic images in the direction along the body (the Z-axis) is larger than that in the tomographic plane (the X- and Y-axis). This spatial data sampling also causes data to be distorted in the original images, a phenomenon known as the partial volume effect. Segmentation identifies and classifies interesting voxels and is necessary for the rendering algorithms that do not

directly deal with the 3-D constructed data. These algorithms require an intermediate data representation (display primitive). By choosing an appropriate display primitive, rendering can put special emphasis on such things as blood flow, aneurysm anatomy, or other functionality, depending on the intended medical application.

Volume rendering is a direct technique for visualizing volume primitives without any intermediate conversion of the volumetric dataset to surface representation. For example, maximum-intensity projection (MIP), which is routinely used in viewing CT angiogram, and multiplaner reconstruction (MPR). The availability of commercial graphics workstations nowadays also allow fast, direct manipulation of the entire three-dimensionally constructed data into 3D space.

Surface rendering, on the other hand, is an indirect technique for visualizing volume primitives by first converting them into an intermediate surface representation and then applying computer graphics techniques to render them. It can be further subdivided into three sequential processes, namely, mapping, viewing, and shading. Mapping involves the division of the objects, which are extracted by segmentation, into other more basic elements and expresses them mathematically. As a result, they can be efficiently handled in the following processes. Viewing deals with the hidden surface removal process according to viewing angle. In shading, the number and positions of light sources are considered and shadow effects are imparted to provide photorealistic effects in visualization.

It is worth noting that the post-processing techniques used in these steps are generic in nature; they can be applied to macroscopic or microscopic tomographic images. In this presentation, we will describe advanced methods available and demonstrated them with application examples.

References

1. A. Kaufman (ed.). *Volume visualization.* SIGGRAPH 93 Tutorial, ACM Press, 1993.

2. Special issue in Applications in Surgery and Therapy. M. Rhodes and D. Robertson, (eds.), *IEEE Computer Graphics and Applications*, vol. 16, no. 1, Jan. 1996 (See also the joint issue of *IEEE Computer* in the same topic, Jan. 1996).

3. T. Kihara. Three-dimensional medical image display and processing. in H. Adachi and J. Nagai (eds.), *Three-dimensional CT angiography*, Little, Brown and Company, Boston, 1995:35-62.

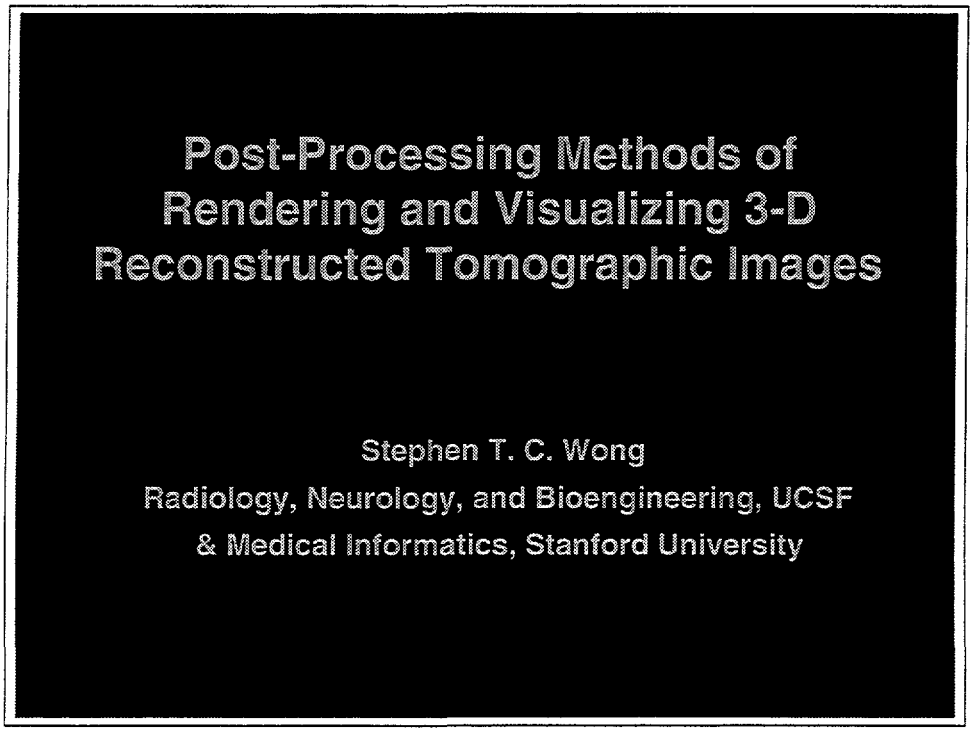

Post-Processing Methods of Rendering and Visualizing 3-D Reconstructed Tomographic Images


Contents
• Objective
• Background
• Applications
• Taxonomy
• Methodology
• Conclusion

Contents

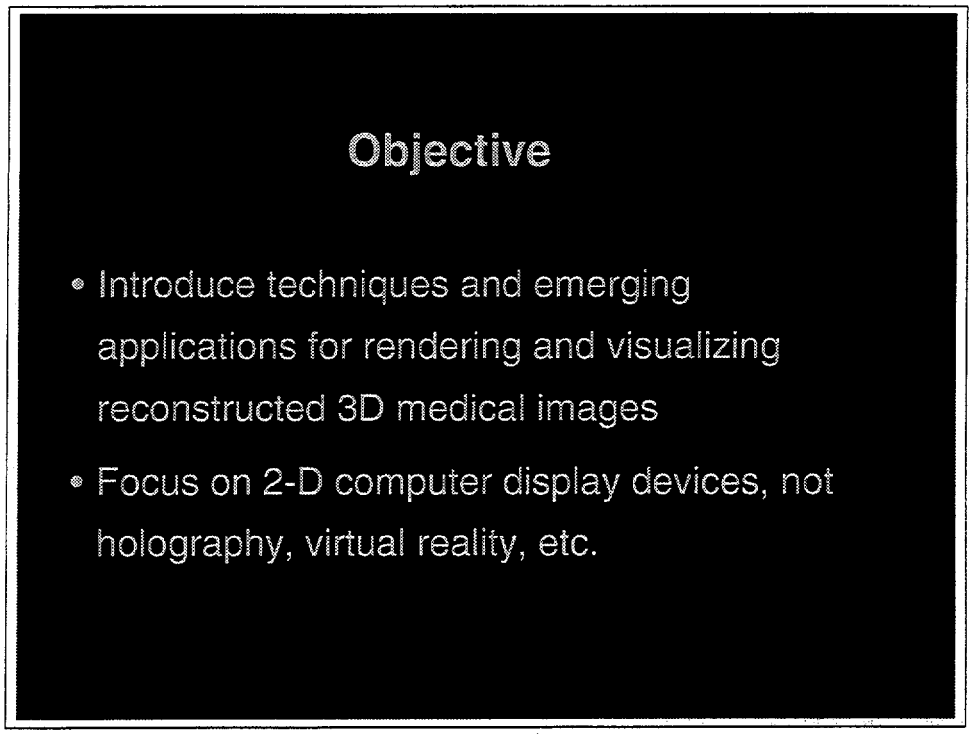
Objective
• Introduce techniques and emerging applications for rendering and visualizing reconstructed 3D medical images
• Focus on 2-D computer display devices, not holography, virtual reality, etc.

Objective

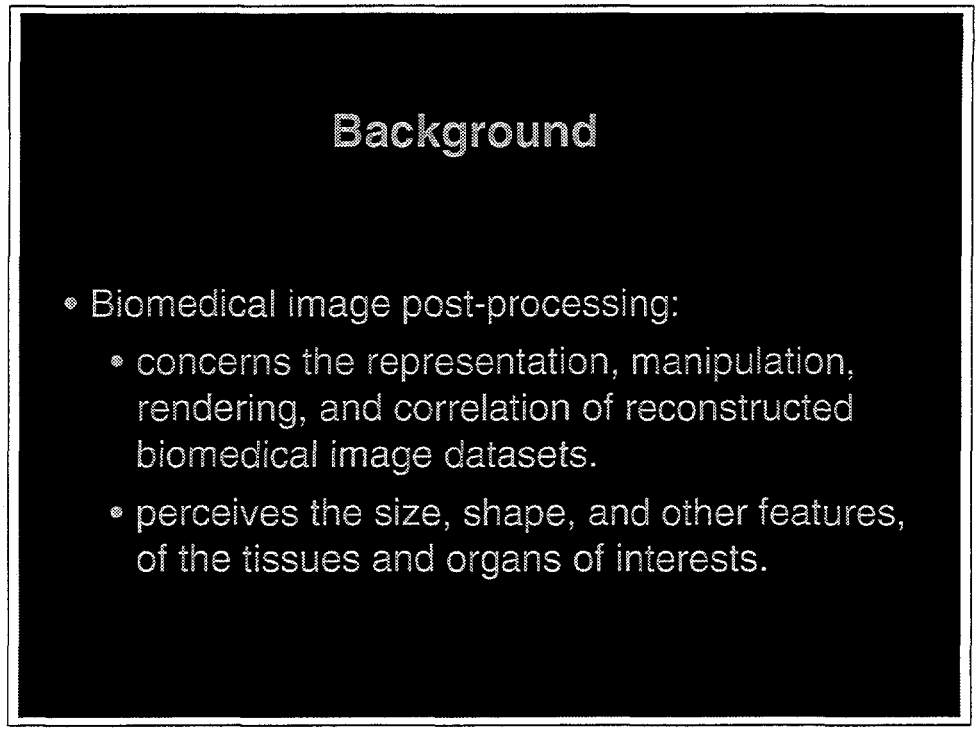
Background
• Biomedical image post-processing:
• concerns the representation, manipulation, rendering, and correlation of reconstructed biomedical image datasets.
• perceives the size, shape, and other features, of the tissues and organs of interests.

Background

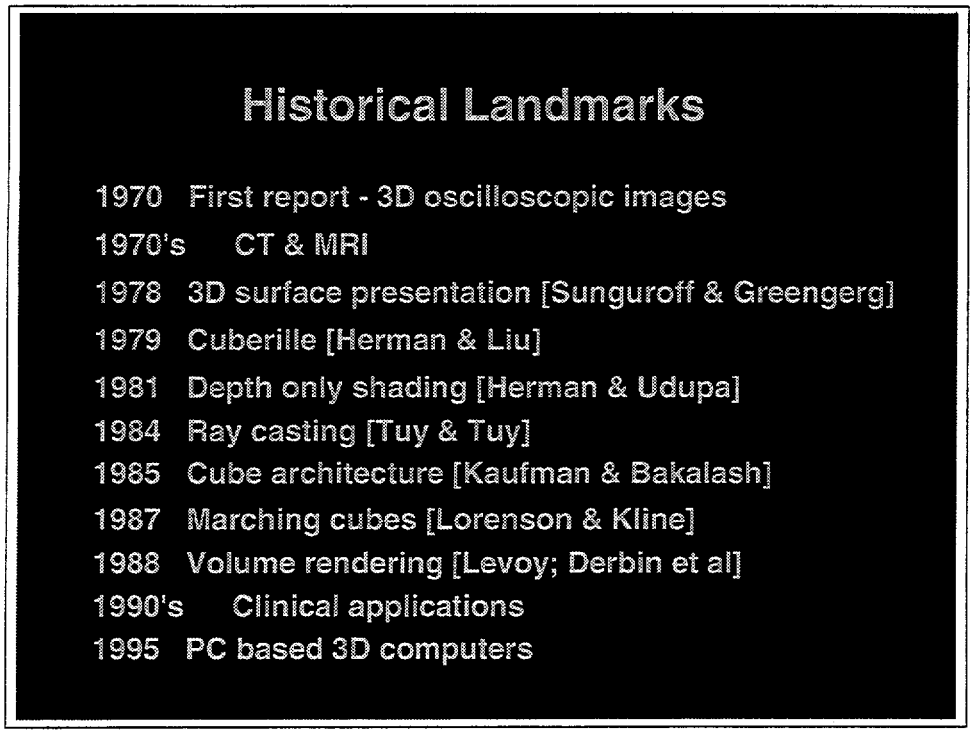

Historical Landmarks

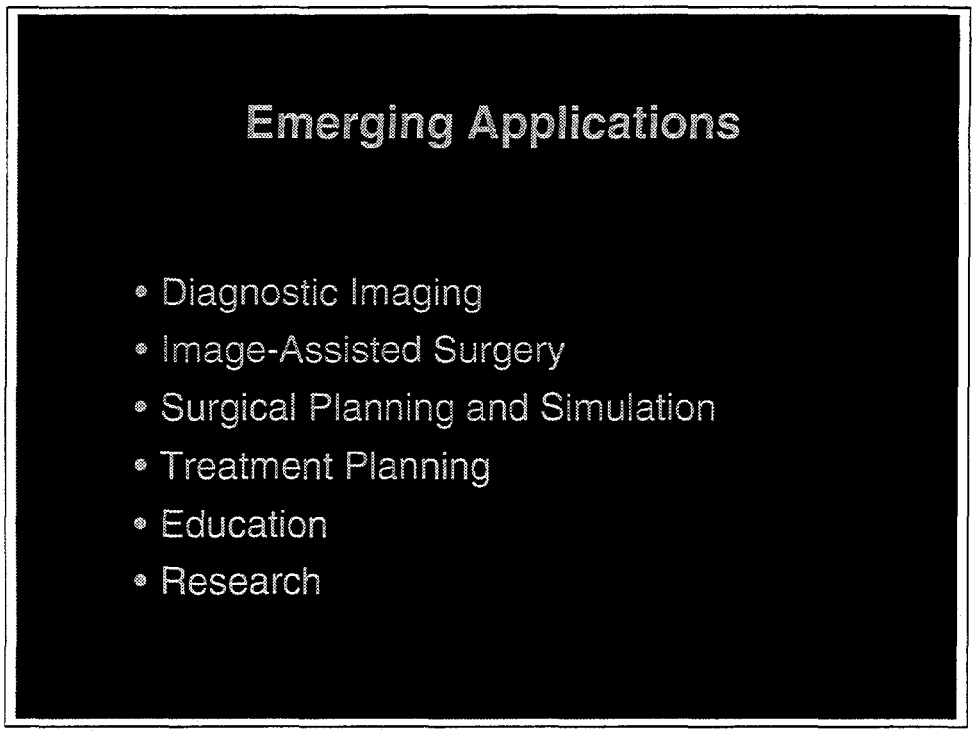

Emerging Applications

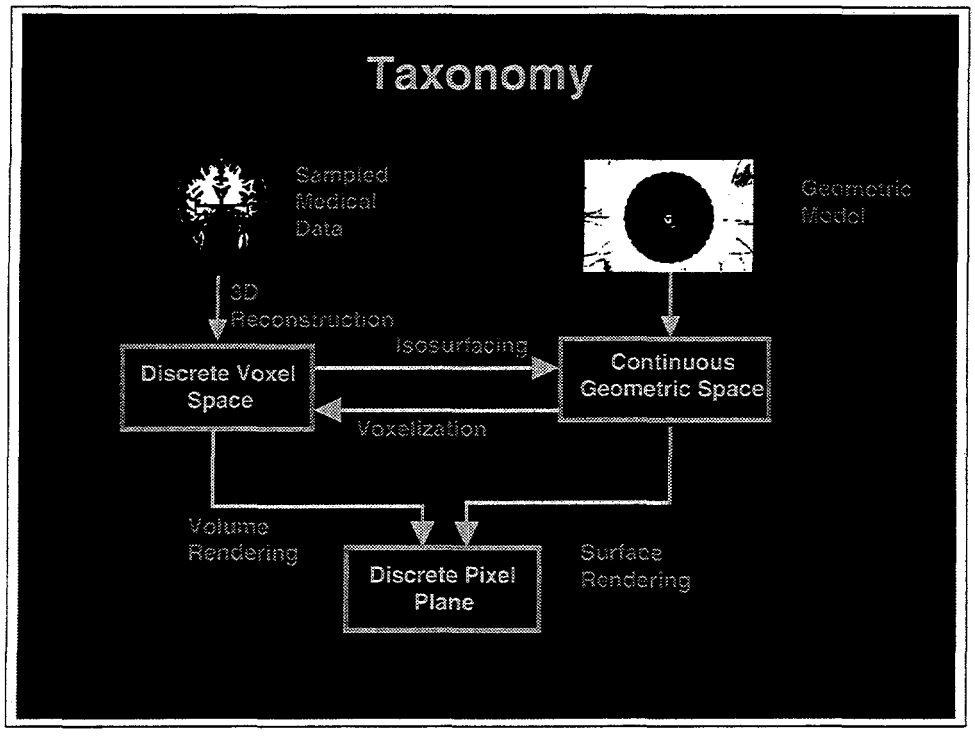
Taxonomy
Sampled Medical Data
Geometric Model
3D Reconstruction
Isosurfacing
Discrete Voxel Space
Continuous Geometric Space
Voxelization
Volume Rendering
Discrete Pixel Plane
Surface Rendering

Taxonomy

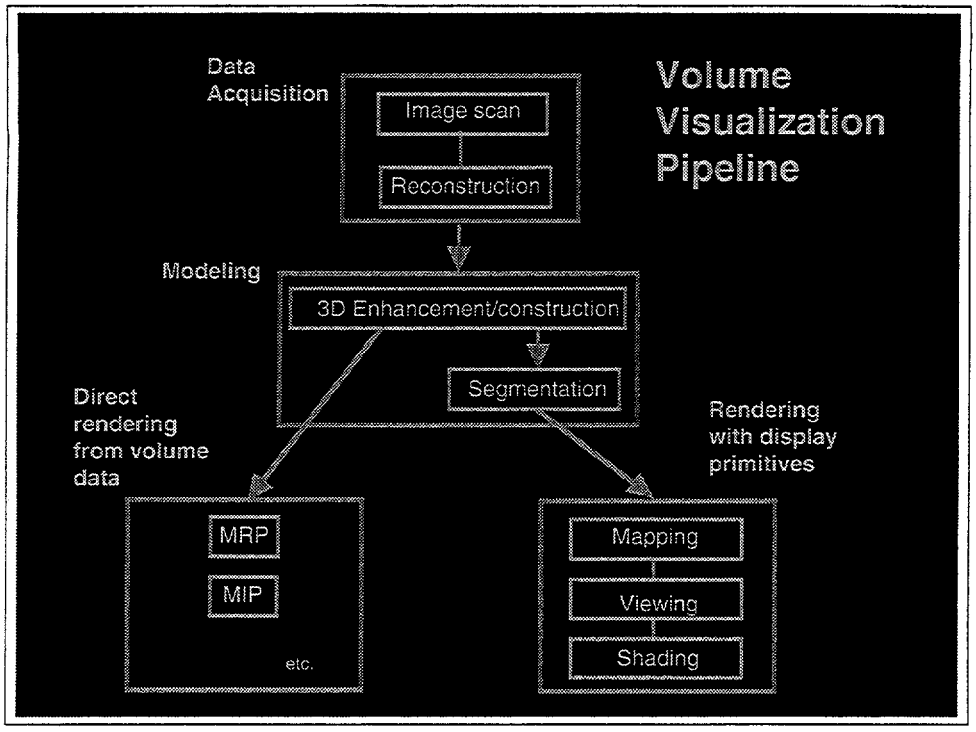
Volume Visualization Pipeline
Data Acquisition
Image scan
Reconstruction
Modeling
3D Enhancement/construction
Segmentation
Direct rendering from volume data
Rendering with display primitives
MRP
MIP
etc.
Mapping
Viewing
Shading

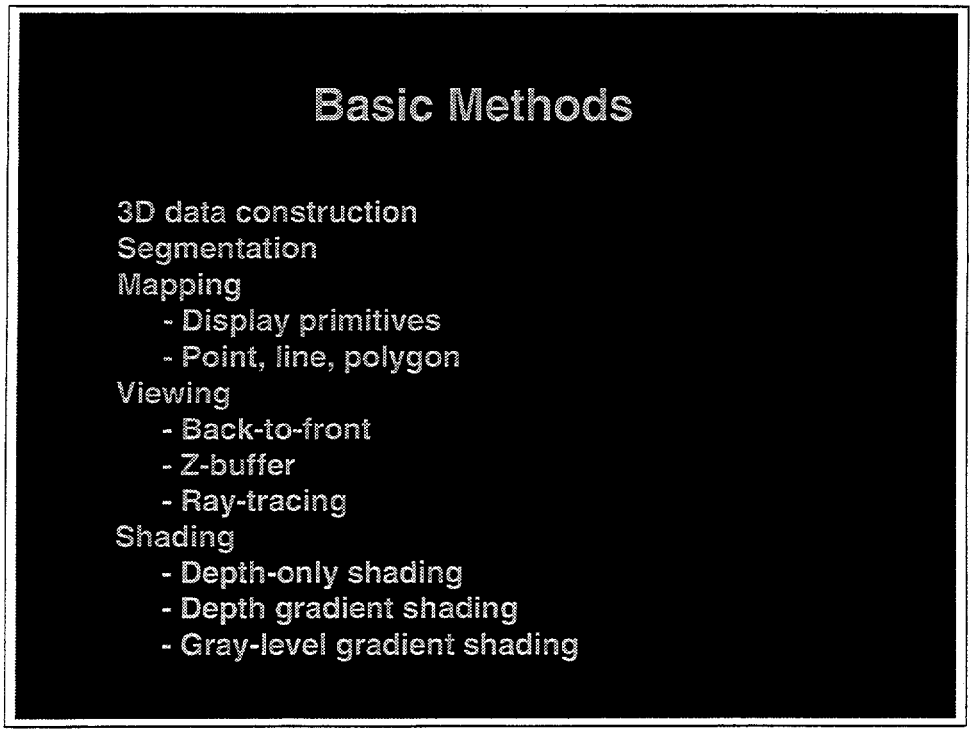

Basic Methods

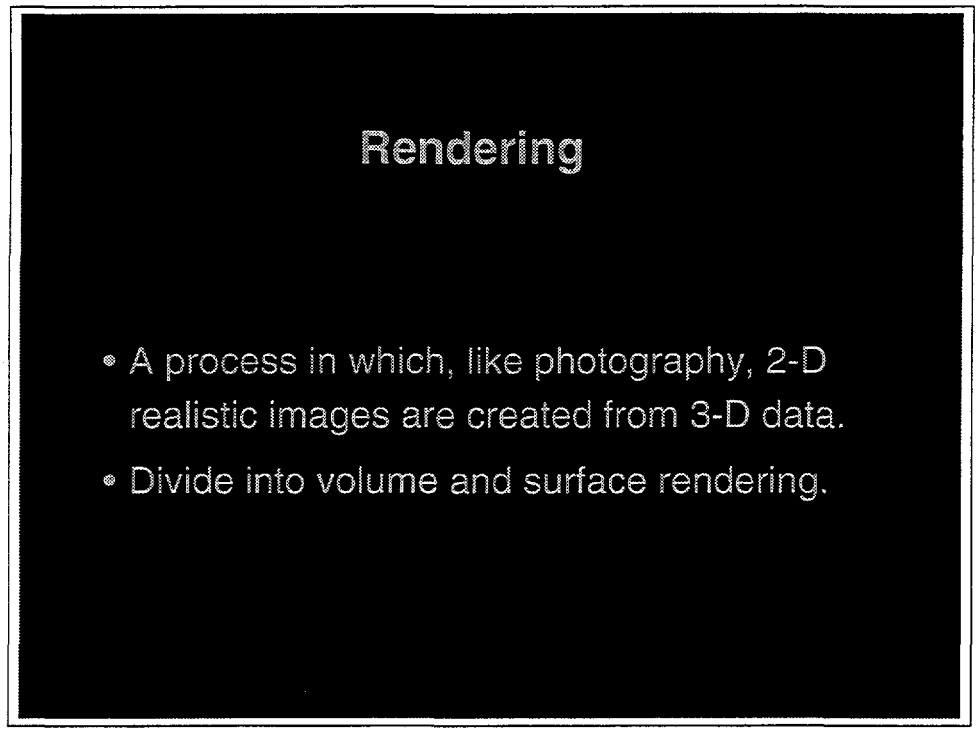
Rendering
• A process in which, like photography, 2-D realistic images are created from 3-D data.
• Divide into volume and surface rendering.

Rendering

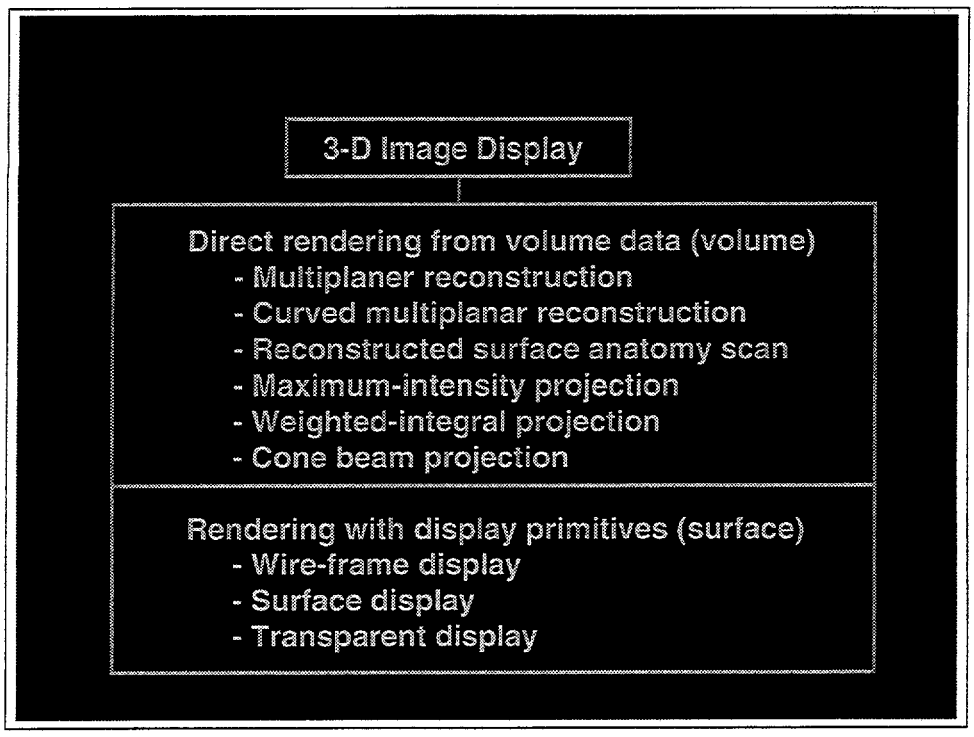
3-D Image Display
Direct rendering from volume data (volume)
- Multiplaner reconstruction
- Curved multiplanar reconstruction
- Reconstructed surface anatomy scan
- Maximum-intensity projection
- Weighted-integral projection
- Cone beam projection
Rendering with display primitives (surface)
- Wire-frame display
- Surface display
- Transparent display

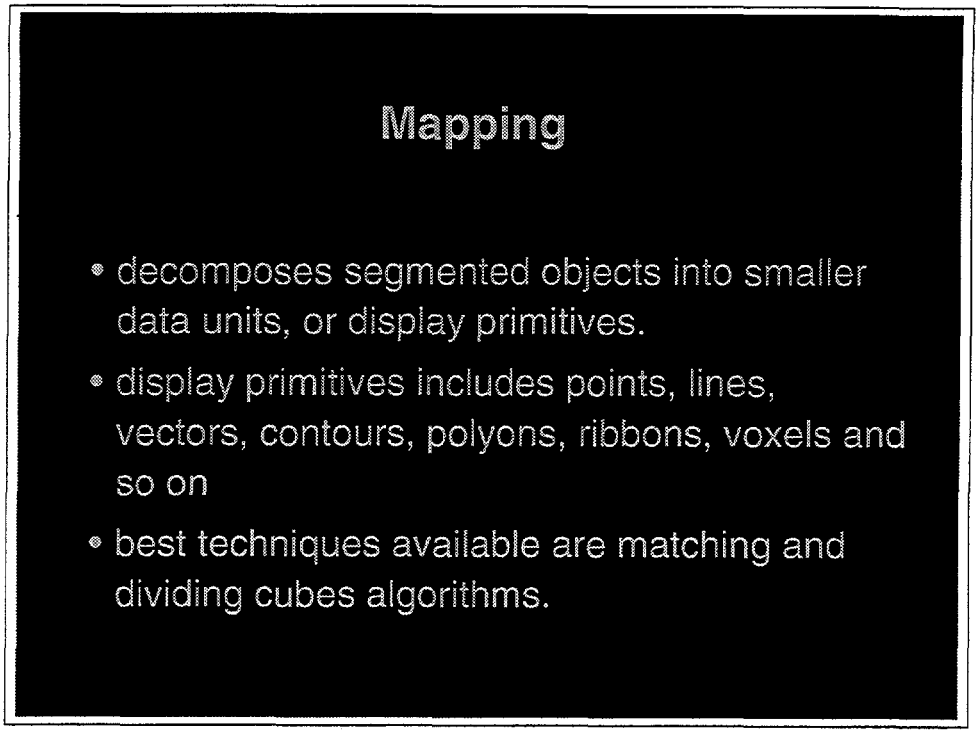
Mapping
• decomposes segmented objects into smaller data units, or display primitives.
• display primitives includes points, lines, vectors, contours, polyons, ribbons, voxels and so on
• best techniques available are matching and dividing cubes algorithms.

Mapping

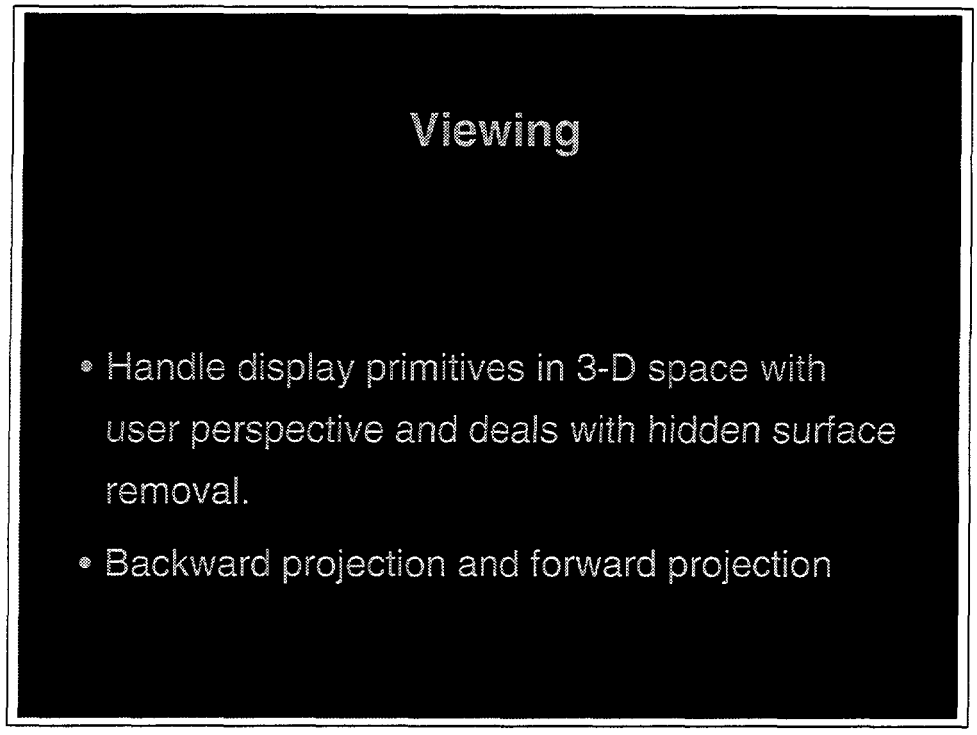
Viewing
• Handle display primitives in 3-D space with user perspective and deals with hidden surface removal.
• Backward projection and forward projection

Viewing

Transfer Function

Maps raw voxel value into presentable entities: color, intensity, opacity...

1. Raw data -> material (R, G, B, α, K_a, K_d, K_s)
2. Material -> shaded material

Transfer Function

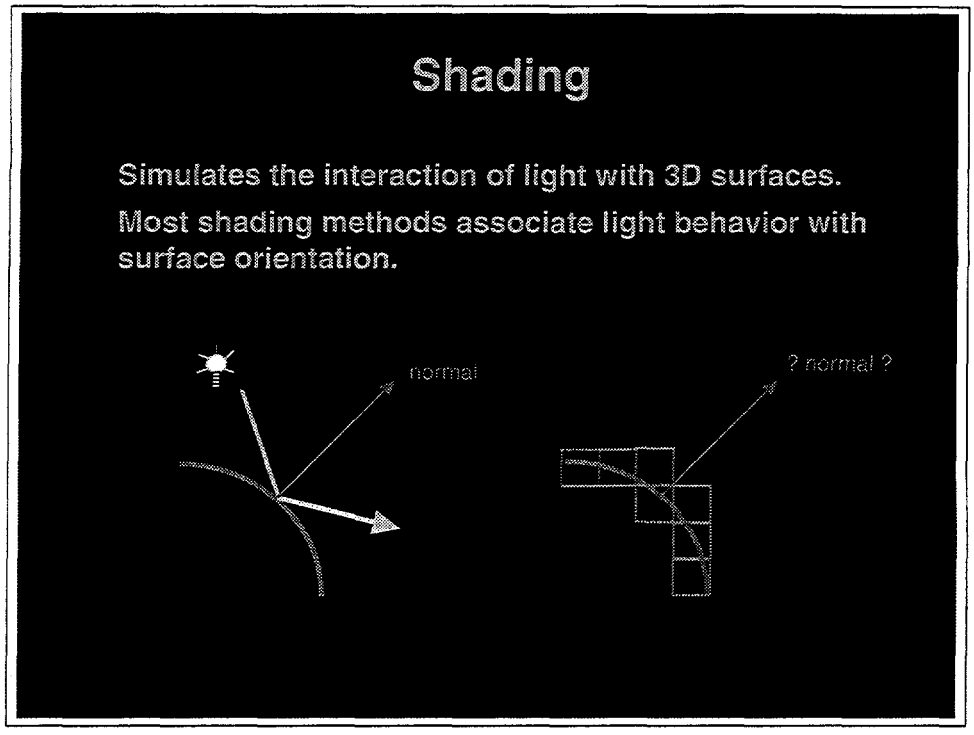
Shading
Simulates the interaction of light with 3D surfaces.
Most shading methods associate light behavior with surface orientation.
normal
? normal ?

Shading

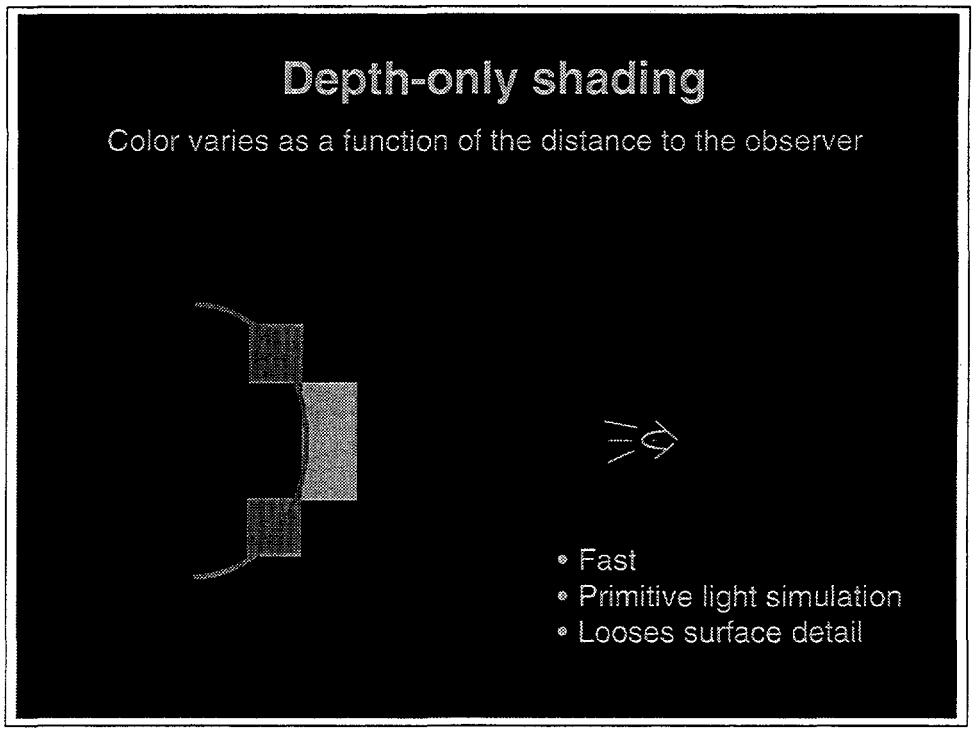

Depth-only shading

Depth gradient shading

the normal is approximated from the gradient of the depth (distance) values of the visible voxels

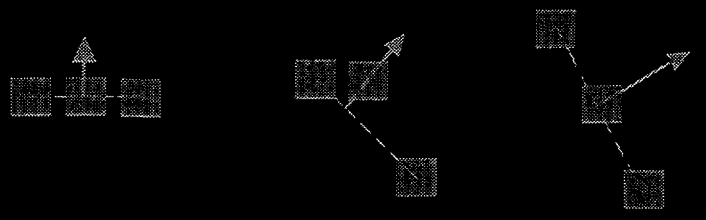

Central Difference: $N_x = D_{i-1,j} - D_{i+1,j}$ $N_y = D_{i,j-1} - D_{i,j+1}$

Forward Difference: $N_x = D_{i,j} - D_{i+1,j}$ $N_y = D_{i,j} - D_{i,j+1}$

Backward Difference: $N_x = D_{i,j} - D_{i-1,j}$ $N_y = D_{i,j} - D_{i,j-1}$

Depth gradient shading

Gray-level gradient shading

uses the gradient of voxel values as a measure of surface orientation

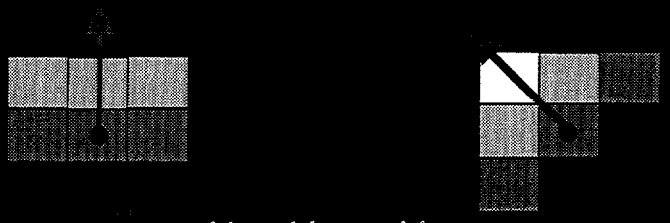

$$N_x = V_{i-1,j,k} - V_{i+1,j,k}$$
$$N_y = V_{i,j-1,k} - V_{i,j+1,k}$$
$$N_z = V_{i,j,k-1} - V_{i,j,k+1}$$
$$N = [N_x, N_y, N_z]$$

Gray-level gradient shading

Conclusions

- Merging computer graphics and medical imaging.
- Numerous research opportunities and emerging applications in biomedical image post processing.
- Techniques are generic and rendering hardware is becoming affordable.
- Pretty pictures are not the endpoint of scientific and clinical problems.
- Close collaboration between imaging devices and imaging informatics researchers -- there is no substitute of good data.

Conclusions

Neural Network and Its Application to CT Imaging

M. Nikravesh[2], A. Garg[1], A.R. Kovscek[2], L.M. Castanier[3], and T. W. Patzek[1,2]
[1]Department of Materials Science and Mineral Engineering
[2]Earth Sciences Division, Lawrence Berkeley National Laboratory
University of California at Berkeley
[3]Department of Petroleum Engineering, Stanford University

Abstract

We present an integrated approach to imaging the progress of air displacement by spontaneous imbibition of oil into sandstone. We combine Computerized Tomography (CT) scanning and neural network image processing. The main aspects of our approach are I) visualization of the distribution of oil and air saturation by CT, II) interpretation of CT scans using neural networks, and III) reconstruction of 3-D images of oil saturation from the CT scans with a neural network model. Excellent agreement between the actual images and the neural network predictions is found.

Introduction

During the past several years, various visualization methods have been used for fluid saturation determination during laboratory core flood experiments [1]. Some of the more common ones in use are transparent models [2], resistivity [3], microwave attenuation [4], NMR, MRI, X-ray, and gamma ray attenuation [5]. While most of these methods provide only average saturation and impose restrictions on experimental techniques, CT is a very fast and accurate technique with few restrictions on experimental conditions and offers fine spatial resolution [6]. Earlier investigators [7-10] have illustrated the importance of computerized X-ray tomography as a powerful tool for petroleum industry researchers.

In this paper, we use high resolution X-ray computerized tomography to obtain images of the cross-sectional distribution of kerosene and air in Berea sandstone cores as a function of time. Scans perpendicular to the axis of the core were made using a high resolution EMI 5005 (second generation) CT scanner. Each CT slice consists of a series of volume elements (voxels). Every voxel has its own characteristic attenuation, and can be mapped into a 2-D image matrix of picture elements (pixels). Using standard computer software, the 2-D fluid distributions at specific times and locations are visualized for each CT slice. CT is a fast, non-destructive imaging technique for determining in-situ fluid saturation with excellent 3-D resolution. Using this technique, attenuation differences as small as 0.1% with a cross sectional resolution of less than 1 mm^3 can be realized.

Imaging the process of spontaneous imbibition in a Berea core using CT scanning methods has many limitations. One such limitation is the number of slices that can be obtained in space and time. In order to obtain fluid saturation distribution in space and time throughout the core, a neural network model will be developed to interpolate between the CT images for a given position versus time and to extrapolate beyond the interval of time during which the images were collected.

Principles of CT Imaging

To obtain a CT slice of an object, an X-ray source is collimated to provide a thin beam which is received by an array of crystal detectors. X-ray photons which strike these crystals cause them to fluoresce with an intensity proportional to the number of photons received. When a body is placed in the beam between the source and detector array, only those photons that are not absorbed by the body reach the detectors. **Fig. 1a** illustrates the principles of X-ray tomography. The values attained when the detectors are read represent the beam attenuation by an object placed in the path of the X-rays. After all readings for a slice have been acquired and stored in a computer, a cross-sectional image or matrix of attenuation coefficients $\mu(x, y)$ is created. Radon [11] established the mathematical foundation for image reconstruction from projection data.

CT measures linear attenuation coefficients μ, which are defined by Beer's law:

$$I / I_o = e^{-(\mu/\rho)\rho x} \qquad \text{.....(1)}$$

where I_o is the source X-ray intensity, I is the intensity measured by the detectors, μ is the linear attenuation

coefficient, ρ is the density of the medium, μ/ρ is the linear mass attenuation coefficient, and x is the thickness of the material. If several materials are placed in the path of the X-ray beams, Beer's law can be generalized as:

$$I/I_O = e^{-\Sigma(\mu_i / \rho_i)\rho x_i} \quad \text{.....(2)}$$

where i is the material considered. If the object contains a mixture of components, the overall mass attenuation coefficient of the mixture is given by:

$$\mu_{mix} = \sum_i \mu_i S_i \quad \text{.....(3)}$$

where S_i is the saturation of the phase i, i.e., S_i is the volume fraction of component i such as water, oil or gas.

Different mechanisms are involved in the adsorption of X-rays. The relative importance of these mechanisms depends on the energy level of the incident X-rays. In general, μ depends on both electron density, ρ, and atomic number, Z. If the energy is above 100 keV, μ depends mostly on the electron density (Compton scattering). For energy below 100 keV, photo-electric adsorption is the main mechanism, depending mostly on the atomic number Z of the material studied. Thus,

$$\mu = \rho\left(a + bZ^{3.8} / E^{3.2}\right) \quad \text{.....(4)}$$

where a is the Klein-Nishira coefficient, ρ is the electron density, E is the energy level in keV, Z is the atomic number, and b is a constant with a value of 9.8×10^{-24} $keV^{3.2}$. Some conclusions that can be drawn from Eq. (4) are, I) heavier elements will attenuate more than the lighter ones, II) the coefficient of adsorption, μ, for a given material changes with the energy level of the source and this change depends mostly on the atomic number of the element considered, and III) by measuring adsorption at two or more energy levels, one can obtain two independent measurements. This will help in solution of three phase problems.

Since it is impractical to deal with the X-ray attenuation coefficient, μ, a new scale is defined based on the international standard unit of Hounsfield (H or CT number). On this scale, water has a value of zero and air has a value of -1000. Hence, each CT unit represents about a 0.1% change in the attenuation coefficient. Equation (5) defines the CT number

$$CT = \frac{\mu_x - \mu_{water}}{\mu_{water}} \times 1000 \quad \text{.....(5)}$$

where μ_x is the calculated X-ray attenuation coefficient. In most CT scanners, the range of CT unit varies from -1000, representing air, to 4000, representing very dense materials. Reservoir rocks typically fall in the range of 1000 to 2000 on this scale.

Saturation Determination

In order to obtain fluid saturations, Eq. (1) can be written as:

$$\log I = \log I_o\left[\mu_R \rho_R (1-\phi)x + \rho_f \mu_f \phi\right] \quad \text{.....(6)}$$

where μ_R is the adsorption of the rock, ρ_R is the density of the rock, μ_f is the adsorption of the fluids, ρ_f is the density of the fluids, and ϕ is the porosity. For two phases (kerosene-air system), the governing equation is given by

$$\rho_B \mu = \mu_R \rho_R (1-\phi) + \phi\left(\mu_k \rho_k + \mu_a \rho_a\right) \quad \text{.....(7)}$$

where ρ_B is the bulk density of the system, μ_k is adsorption coefficient of kerosene, ρ_k is the density of kerosene, μ_a is the adsorption coefficient of air, and ρ_a is the density of air. From the measurement of an evacuated core, $\mu_R \rho_R (1-\phi)$ is obtained. With μ_k and μ_a known, there are two equations with two unknowns:

$$\mu = \mu_k S_k + \mu_a S_a \quad \text{.....(8)}$$

where S_k and S_a are the saturation of kerosene and air respectively. Also,

$$S_k + S_a = 1 \quad \text{.....(9)}$$

By scanning a fully kerosene saturated core and a fully air saturated core, μ_k, and μ_a can be obtained.

Neural Networks

During the past several years, successful applications of neural networks to solve complex problems have increased exponentially. Considerable attention has been devoted to the use of neural networks as an alternative approach to interpolation and extrapolation, pattern recognition, statistical, and mathematical modeling. For example, back-propagation neural networks [12] were used to develop process models as substitutes for complicated empirical and mathematical models [13]. These models can be used as an alternative to statistical and time series analysis. Neural network analysis, unlike regression, does not require specification of structural relationships between the input and output data. However, identification using neural networks is more useful when large amounts of data are available. Once the networks are trained using sufficient information, they achieve excellent predictive capability and show excellent generalization performance. Neural networks may be trained to analyze, predict, and optimize waste management, electrochemical, reservoir, and chemical processes [14].

Multi-layer perceptron networks with a back-propagation learning algorithm are perhaps the most widely used for process modeling, identification, pattern recognition, and pattern classification. The typical network has an input layer, where data are presented to the network, an output layer, which holds the response of the network to a given input, and at least one hidden layer, which connects the input layer to the output layer. There is no theoretical

limit on the number of hidden layers, but typically there will be one. Each layer is fully connected to the succeeding layer with corresponding weights. The values of the weights represent the current state of knowledge of the network. These weights are adjusted to improve the network performance. They are either determined via an off-line algorithm such as the back-propagation algorithm [12], or adjusted on-line via a learning process [15]. In this paper, only multi-layer perceptron networks with a back-propagation learning algorithm were used.

Experimental Studies

An EMI 5005 (second generation) CT scanner at Stanford University was used in this study. **Fig. 1b** displays the scanner components. The scanner consists of a mainframe, rotational elements, and scanner electronics.

The cores were scanned at an energy level of 140 keV and a field size of 13 cm. A small field of scan was used to obtain better spatial resolution, as the number of pixels available remain constant. Slice thickness was made as small as possible, i.e., 3 mm (it varies from 1-10 mm), in order to minimize errors and maximize resolution. Greater slice thickness results in greater measurement error. Also a scan angle of 398° was used as it produces the highest resolution due to an overscan of 38°.

The core holder/experimental cell was constructed from acrylic which is relatively X-ray transparent. A schematic of the experimental setup is shown in **Fig. 2a**. The core holder, 6.4 cm in diameter and 21 cm long, is provided with two end caps for fluids to flow in and out of the core holder. The inlet endcap is connected to a fluid tank through a rubber tube. A control valve attached to the tank controls the flow of fluid from tank to coreholder. The outlet endcap is connected to a measuring vessel. The axis of the cylindrical Berea sandstone core was aligned with the axis of the core holder so that the core was exposed to uniform fluid saturation on all the sides. The sandstone used for this study has a porosity of 22% and a permeability of 300 md. Kerosene used as the hydrocarbon for this study has a specific gravity of 0.80 and viscosity of 1.152 cp at 21°C. Kerosene-air surface tension is 23-32 dynes/cm at 21°C.

Core preparation prior to the start of the experiment involved firing the cores for 24 hours at 750° C. This was done to remove effects of clay swelling and migration from the imbibition process. The cores were initially at 1 atm pressure and saturated with air. At the onset of the experiment, the first images were scanned at four different axial locations within the air-filled core holder in a single run to obtain dry core CT values (CT_{dry}). Four 3 mm thick axial scans were taken at 20 mm spacing. Location of the four faces with reference to the two end faces are shown in **Fig. 2b**. Later, the valve attached to the fluid tank was opened and kerosene filled the core holder until the whole core was uniformly submerged in kerosene. X-ray scanning was done along the core at the same locations to obtain CT values (CT_{exp}) at times of 1, 5, 10, 15, 25, 35, 50 minutes, and at every 60 minutes for next 240 minutes after the core was exposed to kerosene to obtain temporal distribution of kerosene within the core. The scanning procedure determined the average saturation of the core sample at each location. Scanning was also conducted at 24 hours and 48 hours after the start of kerosene imbibition. Weight of the core was measured at the beginning and end of the experiment for mass-balance calculations. Scanning was performed at the same axial locations in all the runs to obtain the spatial distribution of kerosene.

Results

For brevity, we only report images obtained at 5, 10, 15, and 25 minutes after the start of kerosene imbibition. This is because most of the observable dynamics of kerosene imbibition were found to have occurred in first 15 minutes of the experiment. An analysis of images obtained at later periods showed only very small changes in the overall kerosene saturation of the core.

For calculating kerosene saturation in any slice of the core, Eq. (13) is applied to each pixel of the slice:

$$S_{\text{kerosene}} = \frac{CT_{\text{kerosene}} - CT_{\text{exp}}}{CT_{\text{kerosene}} - CT_{\text{dry}}} \quad \text{.....(13)}$$

and

$$S_{\text{air}} = 1 - S_{\text{kerosene}} \quad \text{.....(14)}$$

$CT_{kerosene}$ is the CT value for a fully kerosene saturated core. In this study, slices obtained from X-ray scanning after 48 hours of kerosene imbibition were used to determine the fully kerosene saturated core CT values. From mass-balance calculations, the final kerosene saturation in the core is 80%. Thus to obtain accurate saturation values, values obtained from Eq. (13) were multiplied by a factor of 0.8. We are currently developing a better method of rescaling the images *directly from the raw X-ray attenuation data.*

For obtaining the CT_{dry} values to be used in Eq. (13), inner dry portions of the slices obtained after 1 minute of kerosene imbibition were used. To obtain kerosene saturation profiles, average kerosene saturation was calculated in annular rings of each slice, within circles at increasing radii, and finally in sectors. This averaging procedure is illustrated in **Fig. 2c.**

Fig. 3 shows a series of images obtained after the kerosene has imbibed into the core for 5, 10, 15, and 25 minutes at the four axial sections of the core. The images represent the distribution of kerosene saturation inside the core. In all these images, white represents zero kerosene saturation, and black represents the maximum kerosene

saturation or 100%. Figs. a-1 through d-1 are the images of Berea core after 5, 10, 15 and 25 minutes of kerosene imbibition at section 1, located 2 mm from the core face. In these images, there is a clear lack of an oil front, because axial flow dominates over radial flow in this section. Thus at all times, the whole slice appears uniformly saturated. There is the possibility of a kerosene front at very early times. However, nothing conclusive can be said from the information available. Also, kerosene saturation increases uniformly but consistently with time from image a-1 to d-1. Image d-1 appears to 80 % oil saturated.

Berea slices obtained at section 2, 22 mm away from the left core face, are shown in images a-2 through d-2. Due to location of the slices far away from the core faces, radial flow dominates in this section. This is seen as a clear front observed at early times and represented by a dark annulus at the edge of the slice. Image a-2 obtained after 5 minutes of kerosene imbibition shows a very sharp front, that gradually changes to a more diffuse front in image b-2, and finally disperses after 15 minutes as seen in images c-2 and d-2. In image a-2, kerosene is imbibing uniformly into the core from all the sides and imbibes radially into the sample as a sharp front. Analysis of the saturation-matrix shows that the front is dispersed over 3-4 mm range. In image b-2, the kerosene saturation annulus appears to be moving radially inside the core and has thickened as compared to image a-2. There is also a gradual increase in the kerosene saturation towards the core edges as would be expected. Image c-2 shows the kerosene saturation in Berea core after 15 minutes of imbibition. The kerosene front has dispersed by this time. High kerosene saturation values in the center of the section show that the kerosene has reached the center of the core. The kerosene saturation distribution after 25 minutes of imbibition is shown in image d-2. The image d-2 shows that approximately 80% kerosene saturation is obtained uniformly throughout the core and stays constant.

Again in section 3, 25 mm from the right face of the core, an imbibition pattern in time similar to that of section 2 is observed. Radial flow dominates and hence changes in kerosene concentration are observed radially with time. A sharp kerosene front in image a-3 changes to a slightly less sharp front in image b-3 and finally disperses in images c-3 and d-3.

A similar kerosene imbibition history is seen in images obtained at section 4, 5 mm from the right face of the core. Section 4, however, is quite different from section 1, especially at the early stages of the imbibition process. This is also due to a predominance of radial flow. A clear pattern can be seen from a-2 to a-4, and b-2 to b-4. A sharp front exists in the early part of the imbibition, then it diffuses slightly and finally disappears after 15 minutes, as shown in Figs. 3c-4 and 3d-4. However, the distribution of kerosene saturation in section 4 differs from those in sections 2 and 3. Around 10 minutes of imbibition, axial effects combine with radial flow. This cannot be seen in images 3c-4 and 3d-4 as the core reaches uniform saturation distribution and the axial flow effect is masked. In summary, the behavior of section 4 in the early stages of the imbibition process is similar to the behavior seen in section 2 and 3. In the late stages of imbibition, it is a combination of the behaviors of sections 1, 2 and 3.

History of average kerosene saturation in a circular annulus of the core at different radii is shown in **Fig. 4**. Here, average annular kerosene saturation is plotted as a function of radial distance and time. It shows the movement of a kerosene front, the knowledge of which is extremely important for interpolation between the images. In Fig. 4a through 4d, white shading represents zero kerosene saturation and black shading represents 100% kerosene saturation. Shades of gray represent intermediate saturations. Trends found in Figs. 4a through 4d are similar to those shown earlier in Fig. 3. At section 1 in Fig. 4a, 2 mm from the left face, at times 5-15 minutes, no change in kerosene saturation occurs radially due to predominant axial flow. Uniform increases in kerosene saturation between 5 and 15 minutes is observed. After 15 minutes, no further change in kerosene saturation occurs either radially or with time. Figs. 5b, 4c, and 4d at sections 2, 3, and 4, respectively, exhibit a similar trend in kerosene imbibition and a trend similar to that seen in Fig. 3 in sections 2, 3, and 4. Kerosene imbibition at 5 minutes occurs only at a radial distance of 20 mm, i.e., near the edge of the core. Kerosene first reaches the center of the core at 12 minutes. Also, a sharp kerosene front is seen during the first 15 minutes, after which the front disappears.

In order to smooth the kerosene saturation distribution, average kerosene saturation within a circle is presented as a function of time and radial distance in **Fig. 5**. The purpose of these plots is to show minute changes in the kerosene saturation fronts. Kerosene imbibition patterns observed earlier in Figs. 3 and 5 are exactly similar to those shown in Fig. 6 at all the four sections. A lack of front is seen in Fig. 5a at section 1, and sharp fronts in Figures 5b, 5c, and 5d at sections 2, 3, and 4 until 12 minutes. Beyond 15 minutes, the kerosene front becomes non-existent.

Fig. 6 is a plot of percent kerosene saturation versus axial distance from the closest core face at different times. In Fig. 6 at section 1, the core is saturated. Kerosene saturations range from 45 % to 82 % after 5 to 25 minutes of kerosene imbibition.

Plots of average kerosene saturation in a specific annular ring versus time is shown in **Fig. 7a through 7d**. A nearly uniform kerosene saturation is observed in Fig. 7a, representing section 1, at all times. Kerosene saturations increase from the edge to the center of the core at 5, 10,

and 15 minutes. The change in saturation with radial distance at 25 minutes is very small indicating that the core has reached a steady state. Figures 7b through 7d show a very sharp front at 5 minutes that changes to more diffuse front at 10 minutes and no front at times 15 minutes and 25 minutes. Similar trends can be observed in Figs. 7c and 7d, i.e., sections 2 and 3, respectively, and similar to that in Fig. 7d, i.e., section 4 at earlier times. However, the trend is different from Fig. 7d at later times and is a combination of sections 1, 2, and 3 at times 15 and 25 minutes.

Design of Neural Network Models

The network model for axial mapping has two nodes in the input layer representing the axial coordinate and elapsed time, both scaled uniformly between 0 and 1. It has 3 nodes in the hidden layer with nonlinear transfer function, and one node in the output layer predicting the total average saturation in each circular cross section, and also with nonlinear transfer function. The data in **Fig. 6** were used to train the network. Due to the limited volume of data available, all the data were used in the training. The model was trained until the prediction suffered upon continued learning. Figs. 6a and 6b show the performance of the network model for predicting the average oil saturation as a function of time and axial position. The results show perfect mapping and excellent prediction of the saturation for the training data set. Even though only 4 images were available in the axial direction, the model had excellent performance. Therefore, better performance with higher accuracy and confidence level will be expected if more axial information is introduced into the network model.

To model the radial behavior presented in Figs. 7a to 7d, a different neural network was designed. This network has three nodes in the input layer representing the axial coordinate, radial coordinate, and elapsed time, all scaled uniformly between 0 and 1. It has 15 nodes in the hidden layer with nonlinear transfer function, and one node in the output layer representing the average saturation in a circular ring. Data presented in Figs. 7a through 7d were used for training and testing the network model. The available data were divided into two groups, a testing and a training data set. The test data set was presented to the network, and the model was trained until the prediction suffered upon continued training. Figs. 7e through 7h show the performance of the network prediction for both the test and training data set. The mean error in the training data set is equal to 0.000249 with standard deviation equal to 0.000343. The mean error in test data set is equal to 0.000520 with standard deviation equal to 0.001257. Comparing Figs. 7a to 7d with Figs. 7e to 8h, one can see that the network for radial mapping has excellent prediction for both the test and training data set. We conclude that the radial network is trained with sufficient information and with data that span a wide range of system behavior; therefore, it is an excellent predictive tool.

3-D Reconstruction of Images

The network model developed earlier can be used for 3-D reconstruction of CT images and prediction of kerosene saturation. Our neural network methodology was used to reconstruct image d-4 in Fig. 3. This particular neural network model can predict the saturation of kerosene at each pixel as a function of axial and radial coordinate at a fixed time. The error predicted for reconstructing the 3-D images of the saturation distribution is less than 5 percent.

To show the usefulness of the model to predict the oil saturation at any point (axial and radial location and time) image b-2 in Fig. 3 is used. **Fig. 8a** shows the actual data. Fig. 8b shows the reconstruction of Fig. 9a based on linear interpolation in time. Figs. 3a-2 and 3c-2 were used for this interpolation. Comparing Fig. 8a with 8b, one can see that the two images are not similar, and the linear interpolation failed to reconstruct the actual data. As a remedy, the results from the linear interpolation were used in conjunction with the neural network prediction of the average saturation in each concentric ring with a thickness of 4 pixels. The result is shown in Fig. 8c. Comparison of Fig. 8a with 9c demonstrates that the model accurately reconstructed the actual image. The mean error in this case study is less than 10% with a standard deviation of 2.5%. To reduce the error further, a neural network model was developed to calculate the average saturation in a sector of 2 pixels in the radial direction and 10 degrees in the azimuthal direction. In addition, the axial images were also included into the interpolation model. In this study, images 3a-2, 3c-2, 3b-3, and 3b-4 in conjunction with the network model were used to reconstruct the image 9d. Comparing image 8a and 8d, one can see that the model reconstructed the actual image almost perfectly. The maximum expected error based on this technique is less than 5%.

Conclusions

Kerosene imbibition in a dry Berea core was successfully imaged using CT scans and correct fluid saturations were computed. Images scanned in the interior of the core show a sharp front propagating radially at short times. The front gradually diffuses and disperses totally after 15 minutes, as the entire cross-section fills with kerosene. Spontaneous imbibition of kerosene in an air-saturated Berea core with diameter 5.46 cm and length 6.7 cm is a comparatively fast process with most of the observable dynamics ending in 15 minutes. A relatively fast and accurate technique for imaging fluid flow in a porous medium, such as CT scanning, is quite adequate for tracking kerosene imbibition and for measuring the distribution of in-situ fluid saturations. However, CT experiments must be carefully designed to avoid excessive experimental error in a limited number of images that can be obtained in time

and space. As most of the observable dynamics of kerosene imbibition were over in 15 minutes, it was imperative to obtain images at several short time intervals. Also, it is important to scan all the images with a similar medium surrounding the core. A core imaged in surrounding media of different densities has different absolute values of attenuation coefficient, μ. CT values of such images lead to improper determination of saturations.

To train the neural networks for proper prediction of spatial and temporal distribution of fluids, a large number of data points are needed. Due to scanner limitations (heating up of cathode-ray tube), images could only be obtained at 4 time intervals during the first 15 minutes. Thus, data obtained from this experiment was in general quite insufficient for proper neural network modeling. Axial information was sparse and even though our network interpolated properly between the existing images we are uncertain as to its extrapolative quality at core ends. Fortunately, the homogeneous Berea sandstone core behaved predictably, and we obtained sufficient radial information to train the network.

Nomenclature

a = Klein-Nishira coefficient, (-)
b = constant in Eq. (4), 9.8×10^{-24},mL^2/t^2, $keV^{3.2}$
E = energy level, mL^2/t^2, keV
I = detected X-ray intensity, 1/t, counts/min
I_o = incident X-ray intensity, 1/t, counts/min
ϕ = porosity, percentage
ρ = density, m/L^3, gm/cc
S_i = saturation of the phase i, % PV
μ = linear attenuation coefficient, L^{-1}, cm^{-1}
x = thickness of material, L, mm
Z = atomic number

Acknowledgments

This work was supported by the Assistant Secretary for Fossil Energy, Office of Gas and Petroleum Technology, under contract No. DE-ACO3-76FS00098 to the Lawrence Berkeley National Laboratory of the University of California and is funded through the Natural Gas and Oil Technology Partnership. Support for the CT scan experiments was provided by the SUPRI-A Heavy Oil Industrial Affiliates Program and by U.S. Department of Energy under contract No. DE-FG19-87BC14126 to Stanford University.

References

1. Saraf, D. N., Petroleum Recovery Institute, Report No. 1981-6 (1987).
2. Van Meurs, P.: "The Use of Transparent Three-Dimensional Models for Studying the Mechanism of Flow Process in Oil reservoirs," *Trans. AIME*, 295 (1957).
3. Leverett, M.C.: "Flow of Oil-Water Mixtures Through Uncon-solidated Sands," *Trans. AIME*, 149 (1939).
4. Parson, R.W.: "Microwave Attenuation-A New Tool for Monitoring Saturation in Laboratory Flooding Experiments," *SPEJ*, 302 (1975).
5. Castellana, F. S., J. L. Spencer, and A. Cartolano : "Application of the Gamma Camera to studies of Flow and Mixing in Reactor Vessels," *Ind. Eng. Chem. Fund.*, **19**, 222 (1980).
6. Wellington, S. L and H. J Vinegar: "CT Studies of Surfactant-Induced CO2 Mobility Control," Paper SPE 14393 presented at the 1985 SPE Annual Meeting, Las Vegas, Sept. 22-25.
7. Vinegar, H. G and S. L. Wellington: "Tomographic Imaging of Three-Phase Flow Experiments," *Rev. Scientific Instruments* (Jan. 1987) 96-107.
8. Wang, S. Y., S. Aryal, and C. C. Gryte: "Computer Assisted Tomography for the Observation of Oil Displacement in Porous Media," *SPEJ* (February 1984) 53-55.
9. Garg, A, A.R. Kovscek, M. Nikravesh, L.M. Castainer, and T.W. Patzek : "CT Scan and Neural Network Technology for Construction of Detailed Distribution of Residual Oil Saturation During Waterflooding," Paper SPE 35737, SPE Western Regional Meeting, May 1996.
10. Hicks Jr., P. J., Narayan, K. R., and Deans, H.A.: "An Experimental Study of Miscible Displacement in Heterogeneous Carbonate Cores Using X-Ray CT," Paper SPE 20492, SPE Formation Evaluation, March 1994.
11. Radon, J.: " Uber die Bestimmung von Funktionen durch ihre Integralwerte langs gewisser Mannigfaltigkeiten," *Ber. Verb. Saechs. Akad. Wiss., Math. Phys. Kl.*, **69**, 262-277 (1917).
12. Rumelhart D.E., G.E. Hinton, R.J. Williams: "Learning Internal Representations By Error Propagation," Rumelhart and J. McClelland, editors. *Parallel Data Processing*, Vol 1, Chapter 8, Cambridge, MA: the M.I.T. Press, 318-362 (1986).
13. Nikravesh, M., A. R. Kovscek, T. W. Patzek, and R. M. Johnston: "Prediction of Formation Damage During Fluid Injection into Fractured, Low Permeability Reservoirs via Neural Networks,". Paper SPE 31103, SPE Formation Damage Symposium, Lafayette, LA, 1996.
14. Nikravesh, M., M. Soroush A. R. Kovscek, and T. W. Patzek: "Identification and Control of Industrial-Scale Processes via Neural Networks," Presented at Chemical Process Control V, Tahoe City, CA, Jan. 5-12, 1996.
15. Nikravesh. M., A.E. Farell, and T.G. Stanford: "Model Identification of Nonlinear Time Variant Processes via Artificial Neural Network," *Computers and Engineering*, to appear (1996).

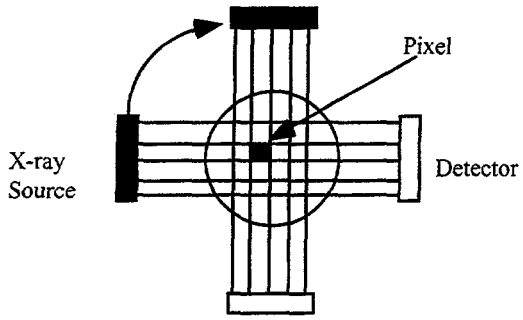

Fig. 1a-CT scanning process

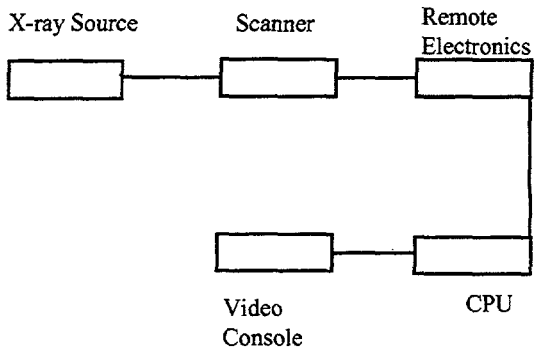

Fig. 1b-The scanner system

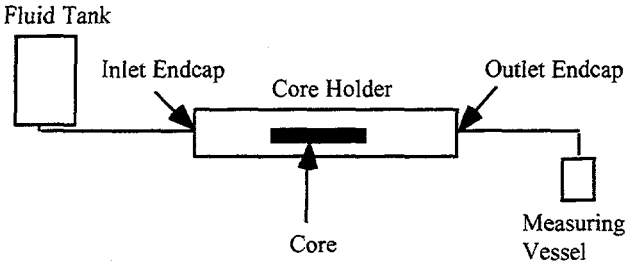

Fig. 2a-Schematic of experimental setup

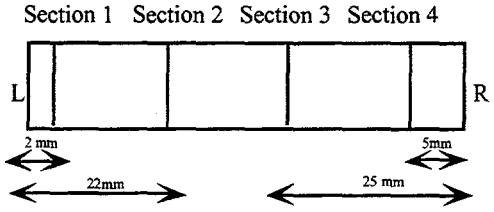

Fig. 2b- Schematic of sections scanned in the Berea core

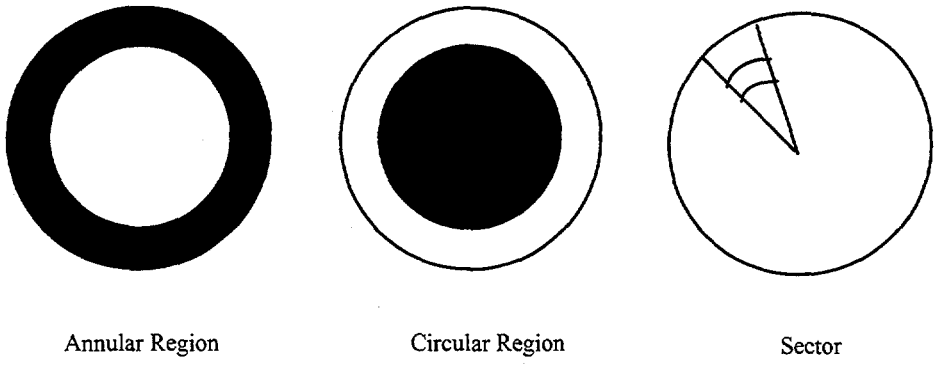

Fig. 2c-Schematic of configurations considered for kerosene average saturation calculation

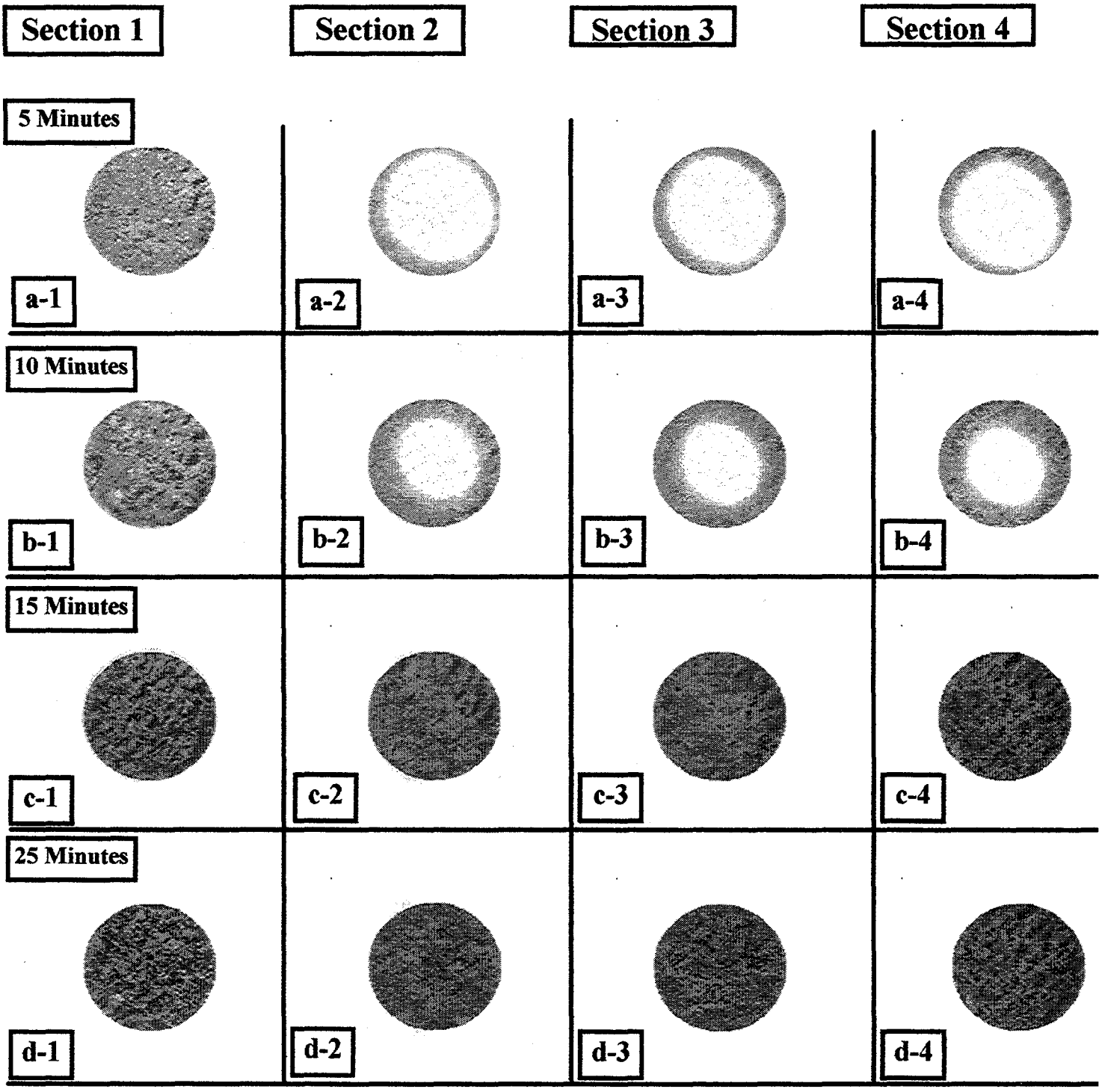

Fig. 3-CT images of kerosene imbibition into Berea Sandstone core.

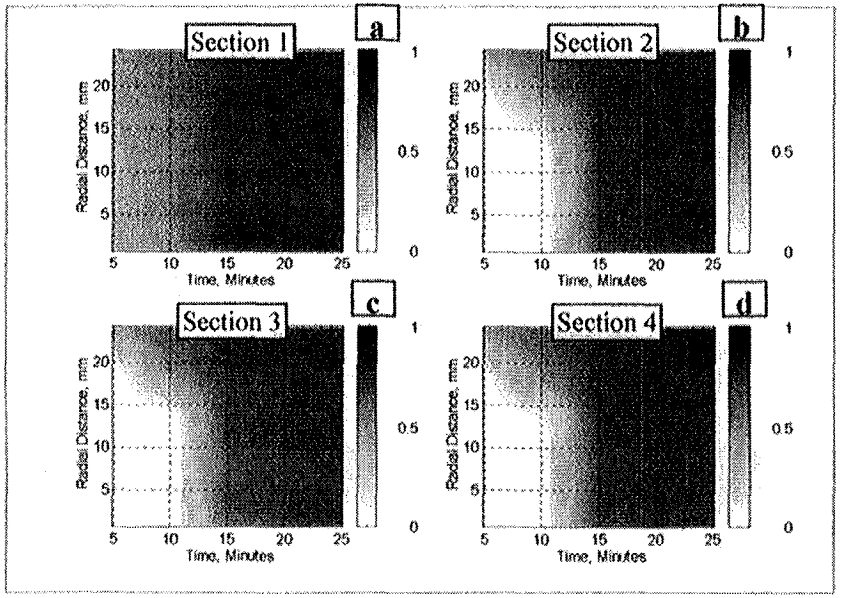

Fig. 4-Average oil saturation within a specific circular ring with a specific radius at different time.

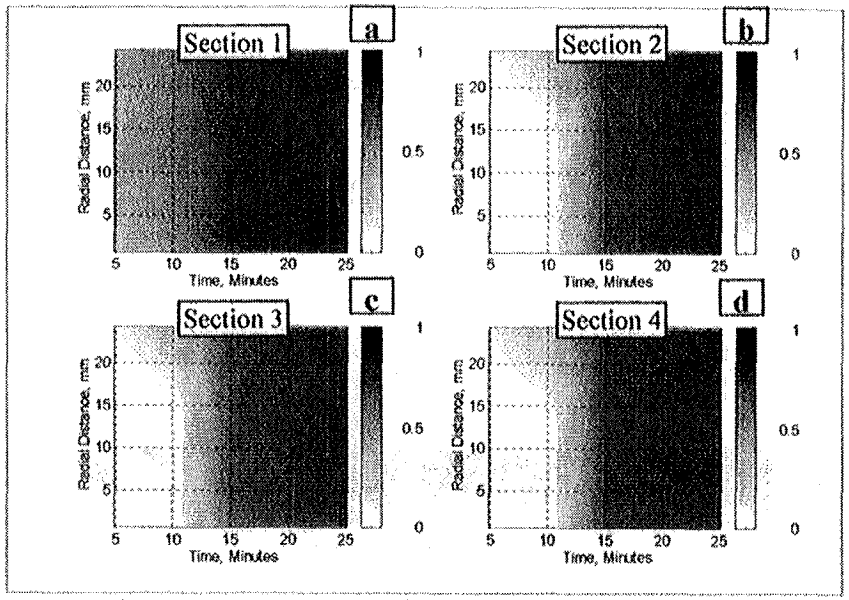

Fig. 5-Average oil saturation within a specific circle with a specific radius at different time.

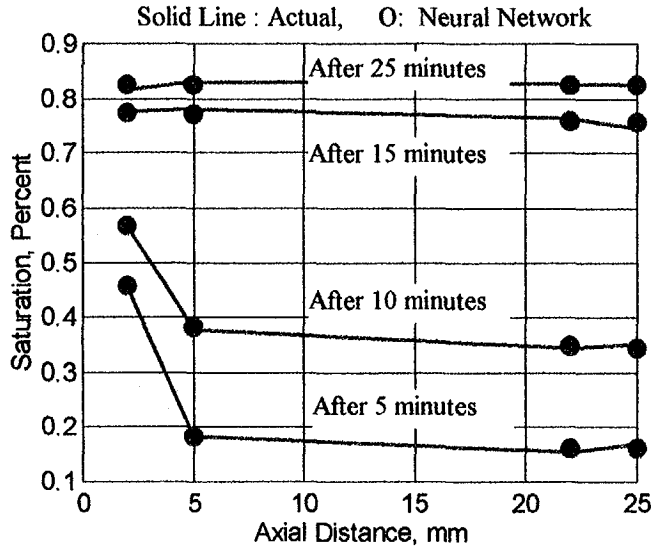

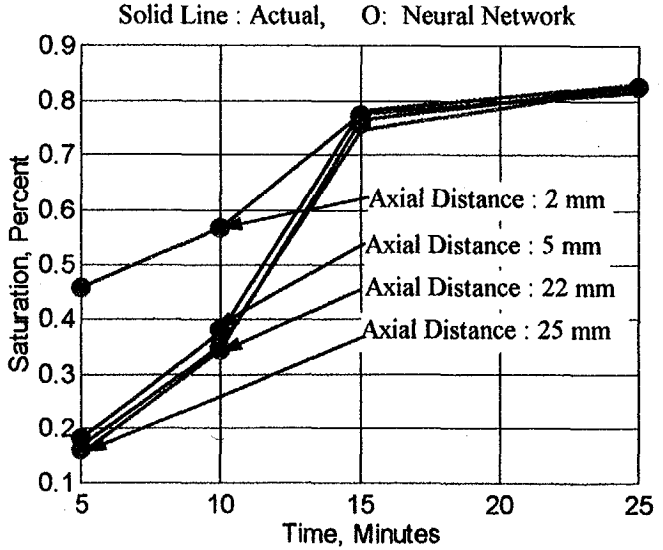

Fig. 6- Comparison between actual data and neural network prediction for average saturation in each section.

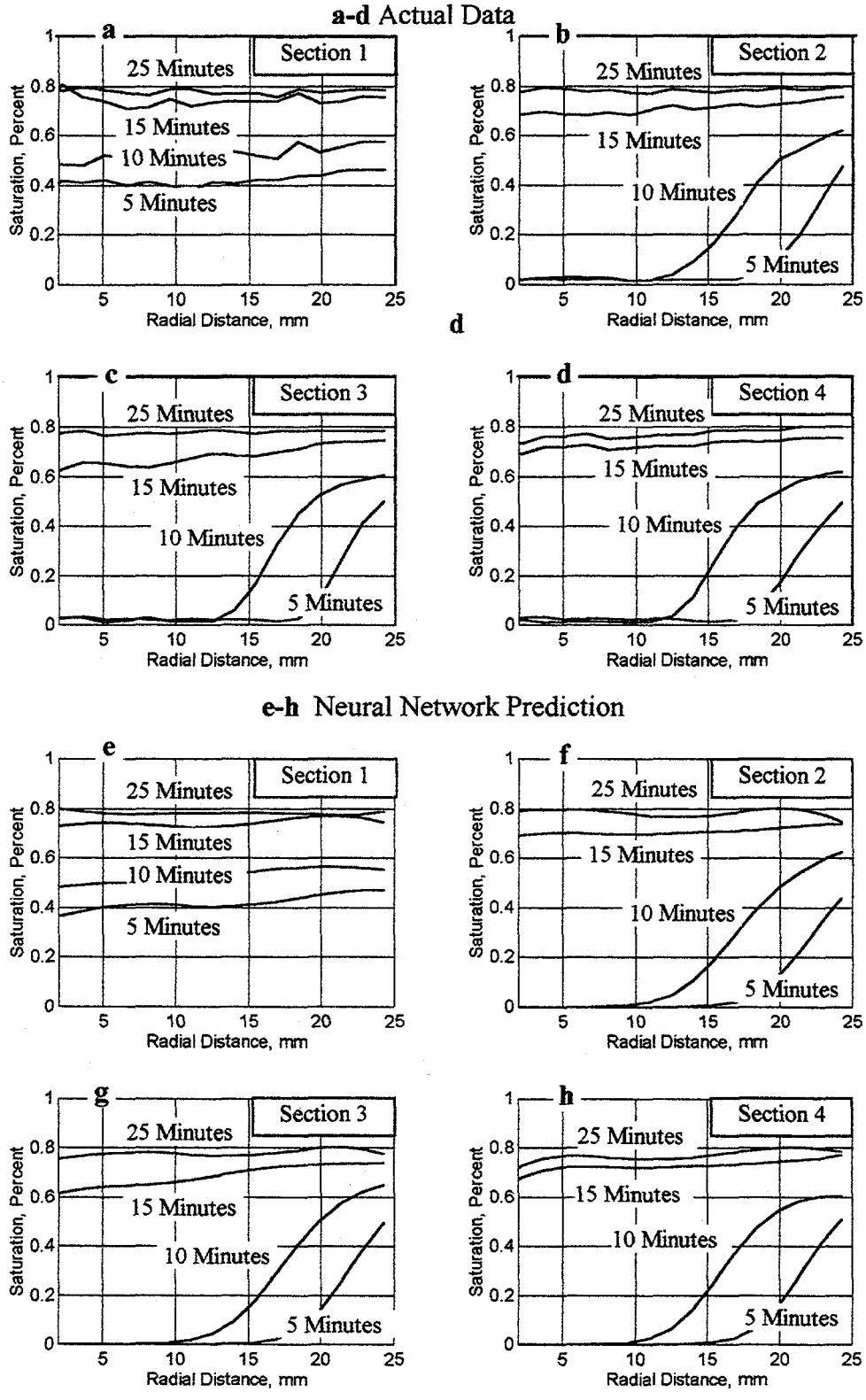

Fig. 7 Comparison between actual and neural network prediction for average oil saturation within a specific circular ring with a specific radius at different time.

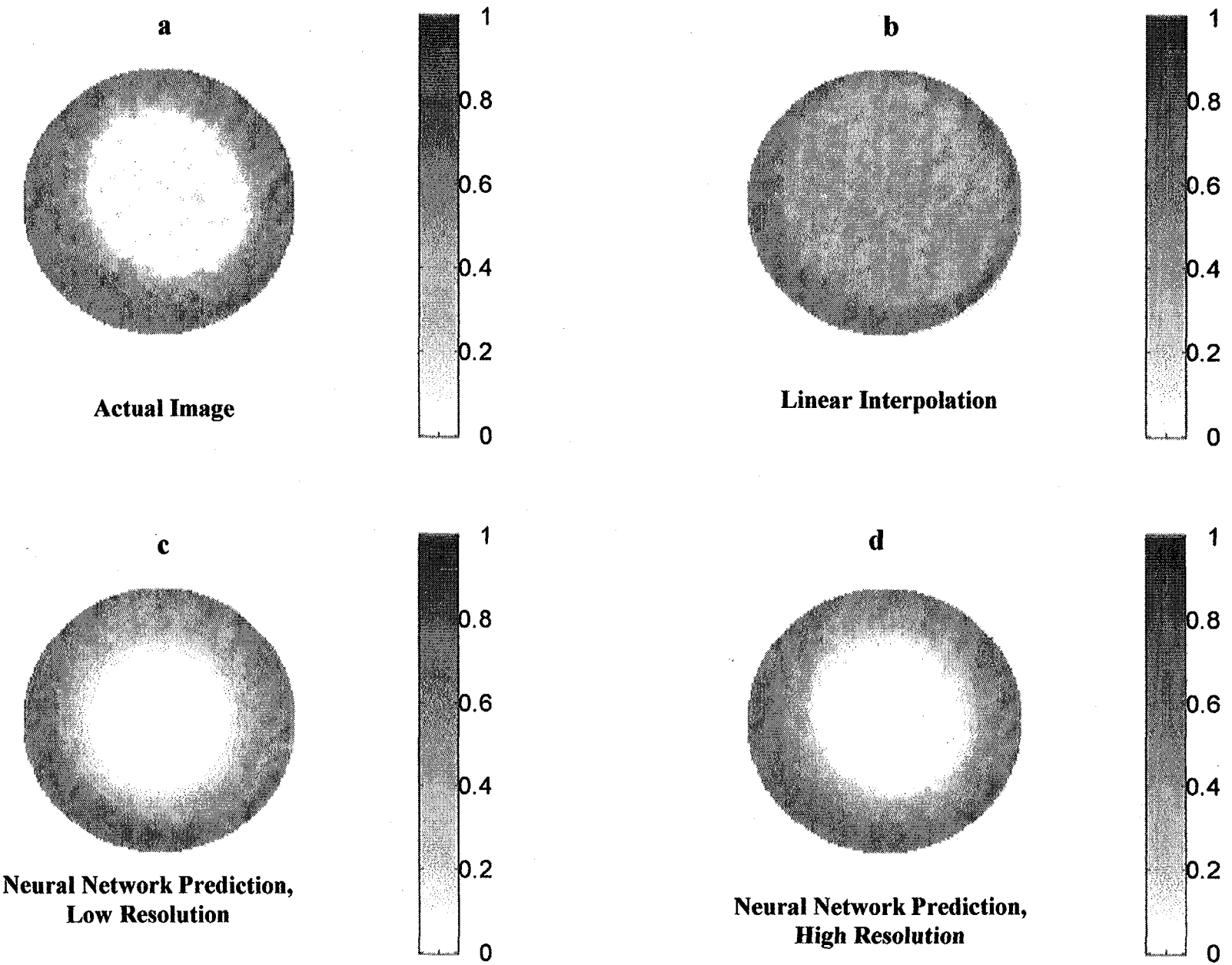

Fig. 8-Comparison between actual CT image with neural network prediction and linear interpolation.

X-RAY MICROTOMOGRAPHY OF POROUS MEDIA AT BROOKHAVEN

SUMMARY

- **Brief History of X-Ray Computed Microtomography at BNL**
- **Current Status & Progress of CMT at Beamline X27C**
- **Technical Achievements**
- **Future Plans**

Betsy A. Dowd, NSLS

HISTORY

- **Mid-1980's: The first CMT measurements were performed at BNL by Per Spanne (presently at ESRF) and Mark Rivers (Univ. of Chicago)**
  - **First generation scanning technique with single detector**
  - **Achieved resolution on the order of a few microns**
  - **Various sandstones and catalysts analyzed**
- **1994: A third generation CMT measurement was taken by Mark Rivers and Peter Eng of Univ. of Chicago**
  - **A cooled Charge-Coupled Device (CCD) provided a two dimensional detector for faster acquisition: multiple slices imaged simultaneously**
  - **Various scintillators for converting X-Ray to visible photons were tried: best results obtained with a YAG type scintillator**

CURRENT STATUS

- **A third-generation CMT scheme has been developed and tested at Beamline X27C at the Light Source during the past year under an Advanced Computational Technology Initiative (ACTI). Participants of the ACTI are:**

  BNL : D.P. Siddons, B. Dowd, B. Andrews, A. Peskin, K. Jones
  Mobil Corporation: W. Bell, M. Coles, R. Hazlett
  GTE Corporation

- **To date, over 50 reservoir sandstone, seal rock and catalyst samples have been analyzed for Mobil Corp. using the CMT apparatus at BNL. In addition, we have produced tomographic volumes of synthetic rock, meteorite fragments, basalts, wood cells, electrode material, and various insects.**

- **Samples ranged in size from less than 1 mm to 15 mm**

- **Resolution on the order of 3 microns achieved for smaller samples**

Brookhaven X-Ray CMT Apparatus

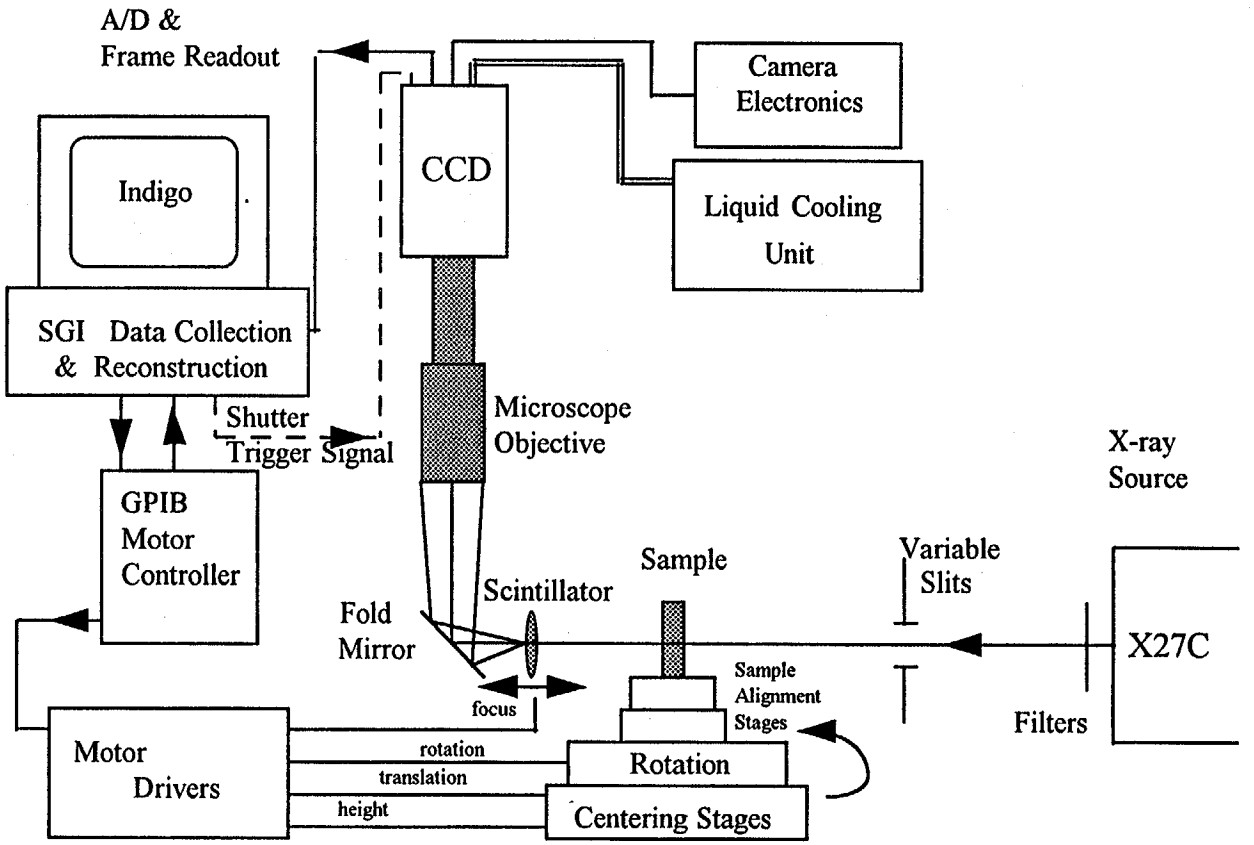

& PROGRESS: DATA COLLECTION APPARATUS

- **Source**
  Collimated, filtered X-Ray (Al, Cu, Zr, e.g.)

- **Image Collection**
  - **YAG scintillator converts X-Ray absorption map to visible**
  - **Commercial optics magnify and reimage phosphor onto CCD detector array**
    - **.75 to 3x zoom lens; 1x, 5x, 10x mag. lens for variable FOV, resolution**
  - **Inexpensive fold mirror allows positioning of CCD & optics at 90 degrees to X-Ray beam & minimizes scatter onto CCD array**
  - **Photometrics cooled CCD camera with Kodak KAF-1400 or KAF-6300 chip**

KAF-1400	KAF-6300
1317 x 1035 pixels, 6.8 μm pixel	3072 x 2048 pixels, 9.0 μm pixel
(8.98 mm x 7.04 mm)	(27.65 mm x 18.48 mm)

12 bits dynamic range
2 x 10^6 pixels/second readout time
Features binning & subarray readout

CURRENT STATUS & PROGRESS cont.

- **Image Storage & Slice Reconstruction**
  - **IBM 486, running Windows; Visual Basic program automates rotation of sample on stepping motor stage, and accesses PMIS Image Processing program for image exposure and storage**
    - **In progress: SGI Indigo with Innovision's Isee software will replace 486 for data collection and can process slices in "real-time" as views are collected**
  - **Images stored on remotely mounted 9 Gig drive on SGI Indigo for later or immediate reconstruction. A Convex 8-processor parallel computer is also available for fast reconstructions.**
  - **Pre-process raw data, feed into RecLBL program for reconstruction of up to 3072 slices simultaneously (KAF-6300 chip)**

CURRENT STATUS & PROGRESS cont.

- **Volume Rendering & 3-D Viewing**
  - **Volume rendering with IRIS or IBM Data Explorer on the Indigo**
  - **Fiber optic link from X27C beamline to onsite 3-D visualization facility for fast data transfer of large volumes**
  - **Onsite stereographic viewing facility available to users: features display system driven by Silicon Graphics Reality Station with a Reality Engine, two Raster Managers and a Multi-Channel Option to create dual viewports. Stereo effect acheived with 2 polarized projected images; audience views image through polarized glasses.**

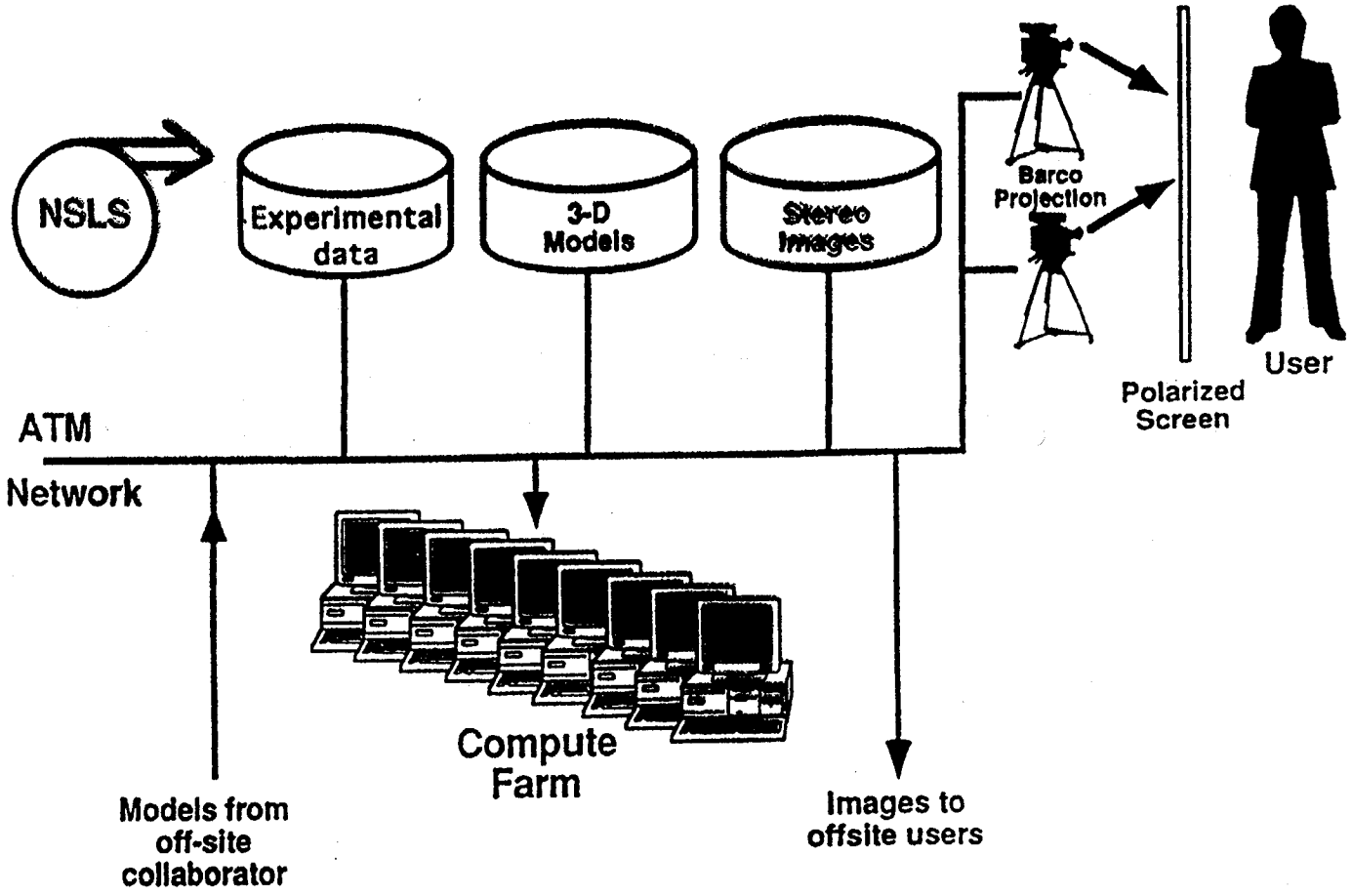

Visualization Facility: Systemic View

TECHNICAL ACHIEVEMENTS

- **3 microns resolution with porous samples**

- **Flexibility in Data Collection**
  - **Zoom capability--variable field of view; image samples over 1 inch**
  - **Subvolume correction for cylindrical porous samples written into software**
  - **Can redefine readout subarray of CCD for fast collection of time-dependent phenomena in a small area of interest (real-time flow, e.g.)**
  - **Can bin pixels; increases S/N, decreases readout-time for sample area**
  - **Variable energy of exposure offered by synchrotron X-Ray: reduces beam-hardening effects as well as enhances contrast**

- **User-friendly automated data collection & reconstruction (PRT starting up)**

- **Improved data collection & reconstruction time: total of 20 minutes for 4x4 binned set, i.e., 329 slices each with over 50,000 resolution cells (over 10 million voxels)**

Novel Technique for Subvolume Reconstruction

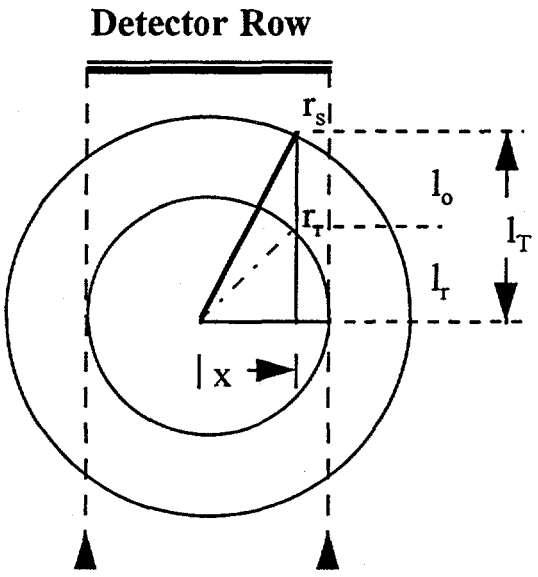

— r_r = radius of reconstructed area

- - - r_s = radius of sample

$2l_o$ = length of beam path outside reconstructed area

$2l_r$ = length of beam path through reconstructed area

Path lengths are a function of x, distance from the center of circle, which coincides with the center of the pixel row. From the geometry:

$$2l_o(x) = 2\left(\sqrt{r_s^2 - x^2} - \sqrt{r_r^2 - x^2}\right)$$

An average value of mu per pixel for the entire sample is calculated from the data. Each detector signal is then scaled by the factor $\exp[\mu l_o(x)]$ to effectively subtract out the effect of beam attenuation through the unreconstructed area. This scaled data is then used to reconstruct the subvolume of interest.

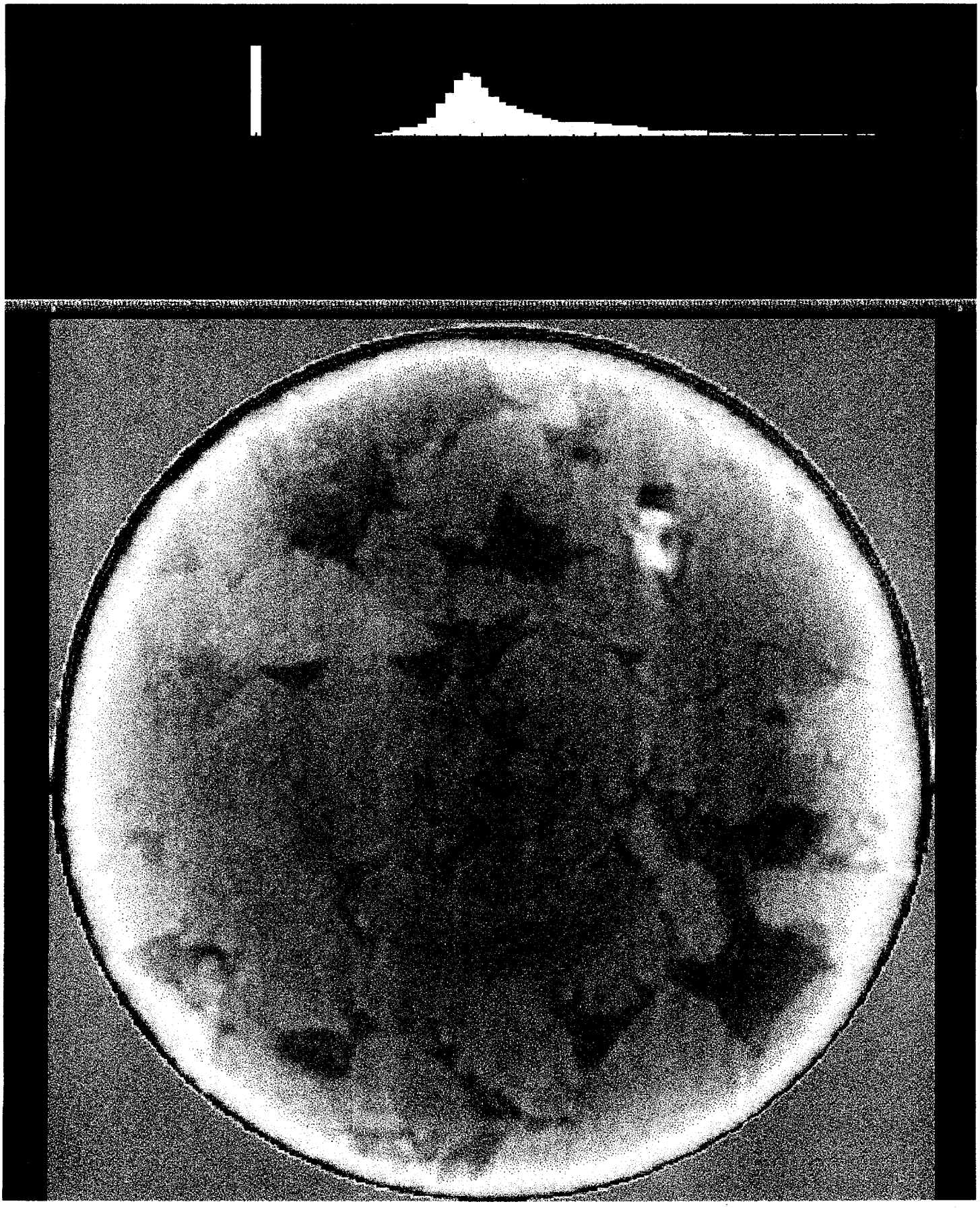

Slice from a reconstructed subvolume of reservoir sandstone:Uncorrected
The histogram shown above plots #pixels as a function of mu (values shown are relative)

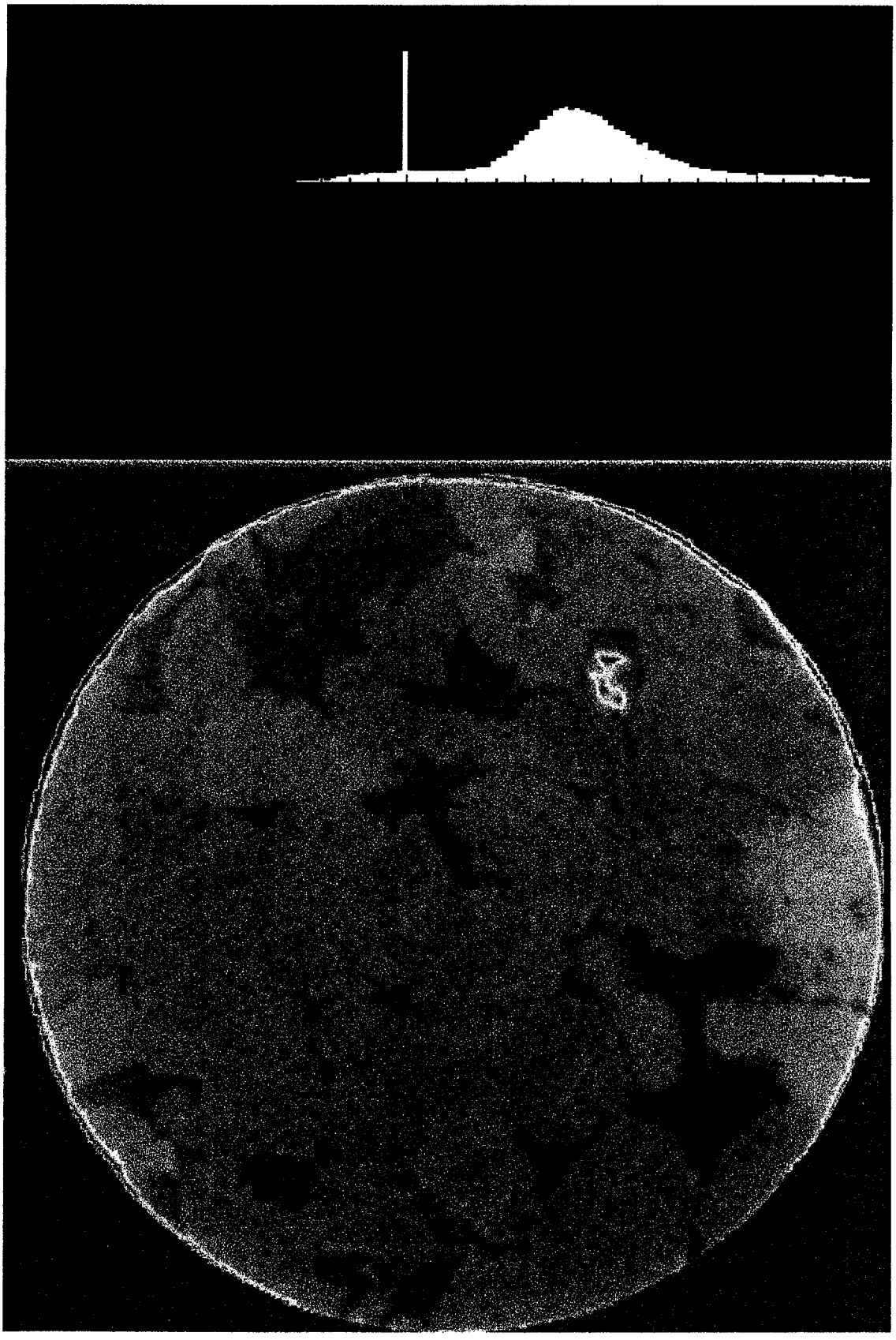

Slice from the corrected subvolume of reservoir sandstone with histogram

Basalt: 1mm D subvolume (slice) imaged from 6mm D full volume-No correction

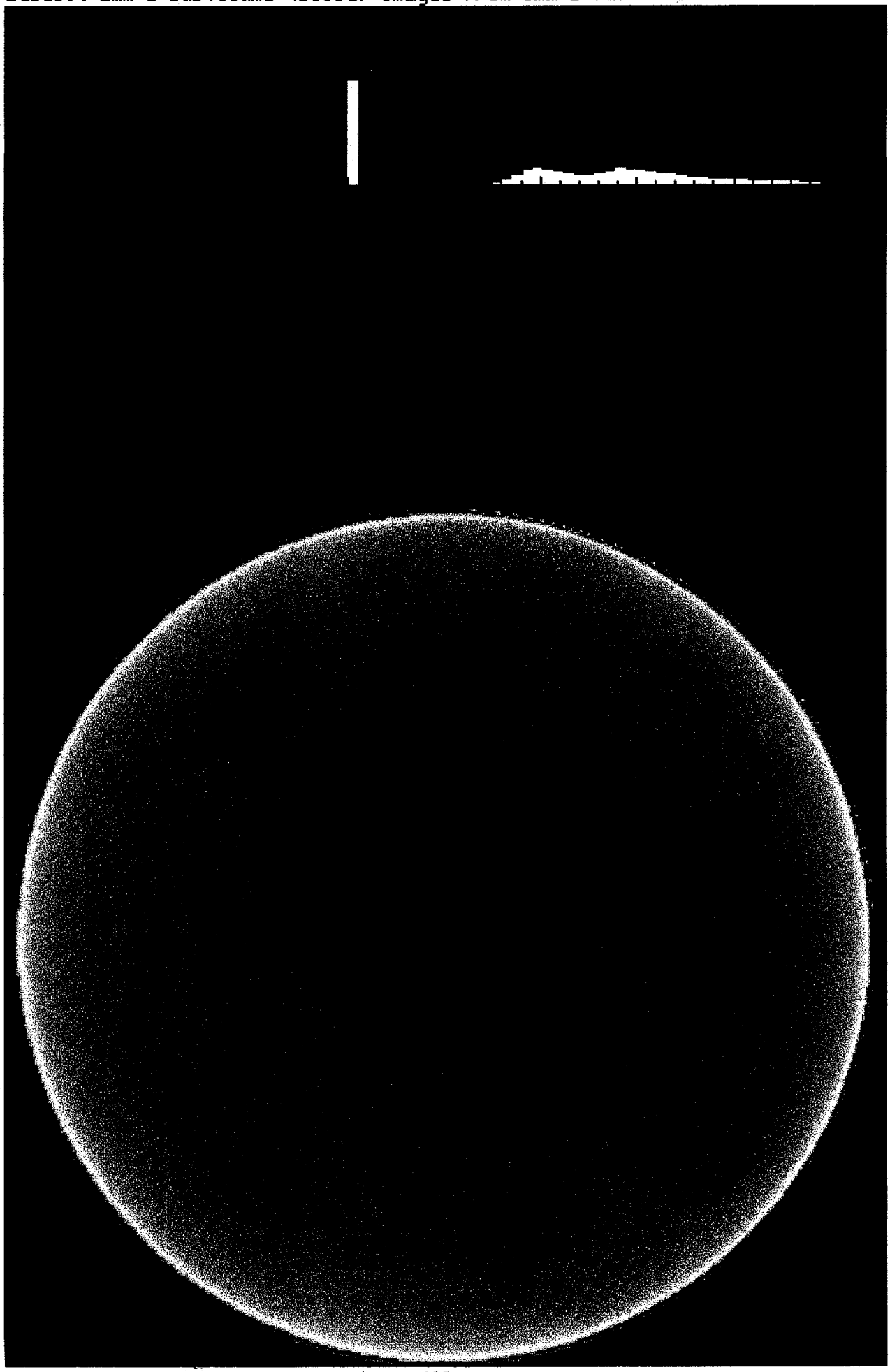

Basalt Corrected Subvolume

Note: Pore Size is on the order of FOV (1 mm)

SAMPLE VOLUMES

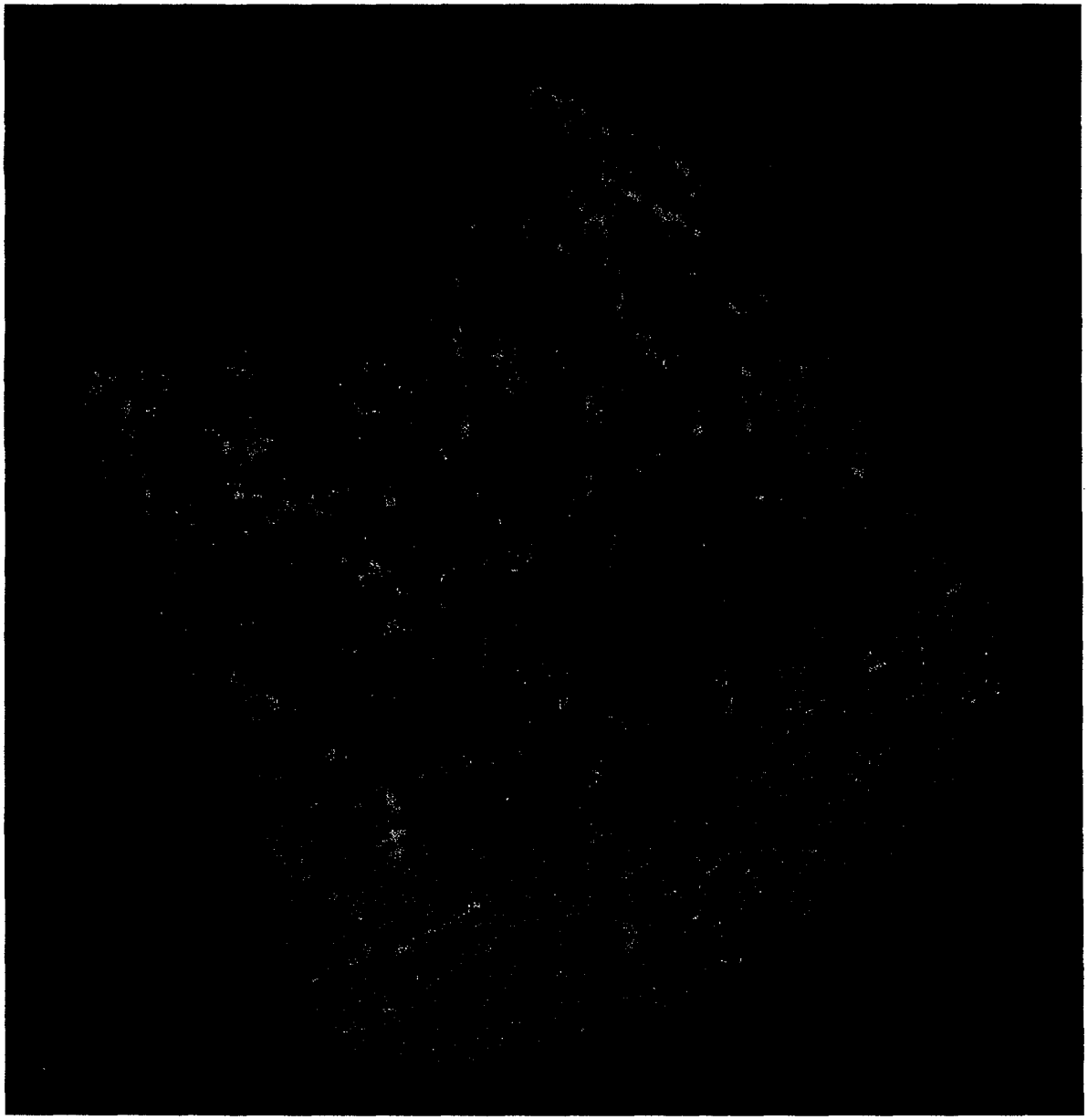

Volume Rendering of a reservoir sandstone from X-Ray CMT , D= 2mm
Pores (blue) are on the order of 15 to 20 microns

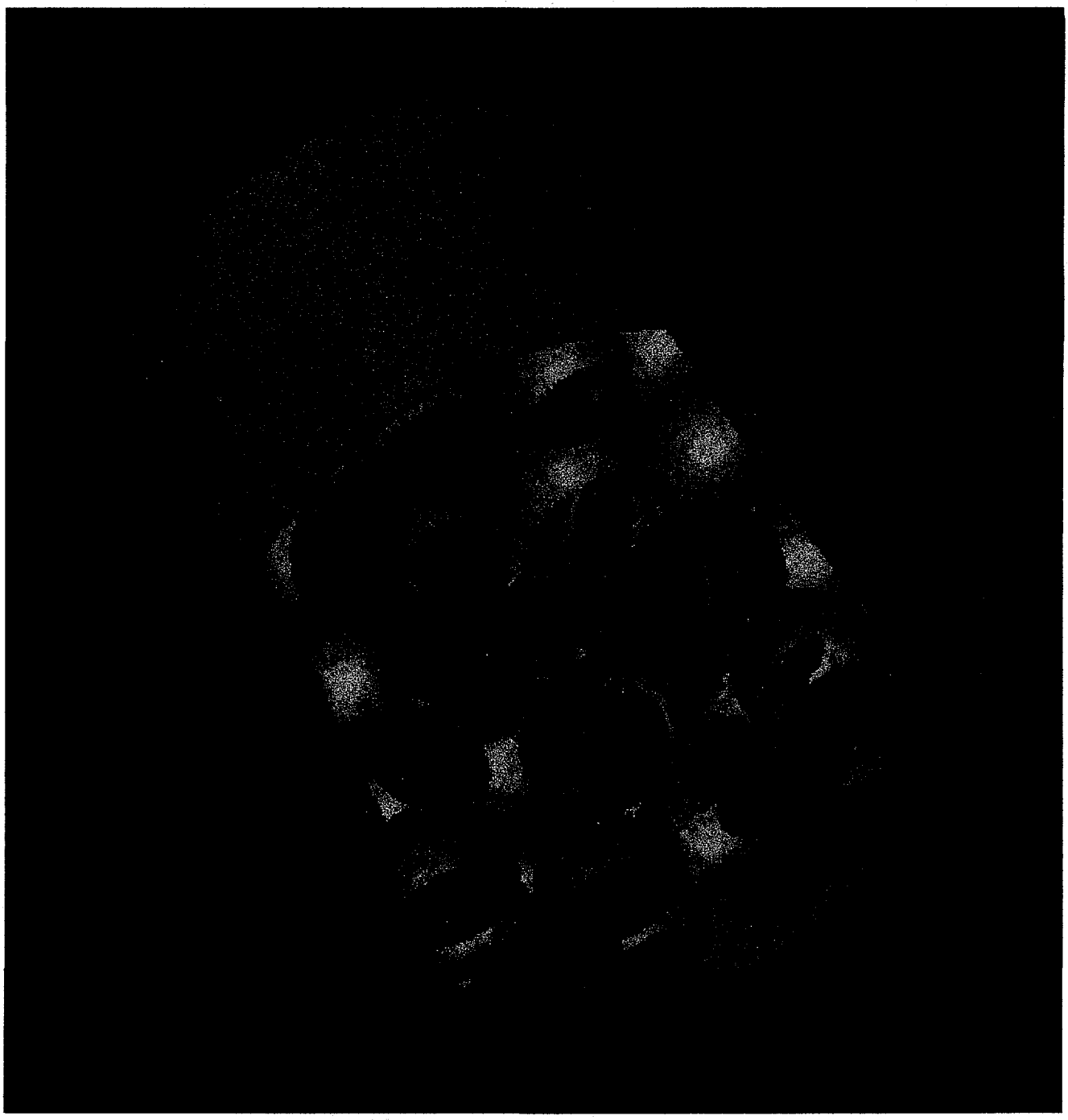

3-D Image rendered from X-Ray CMT data: .5mm D glass capillary, with 5 micron thick wall
Filled with 100 micron glass spheres

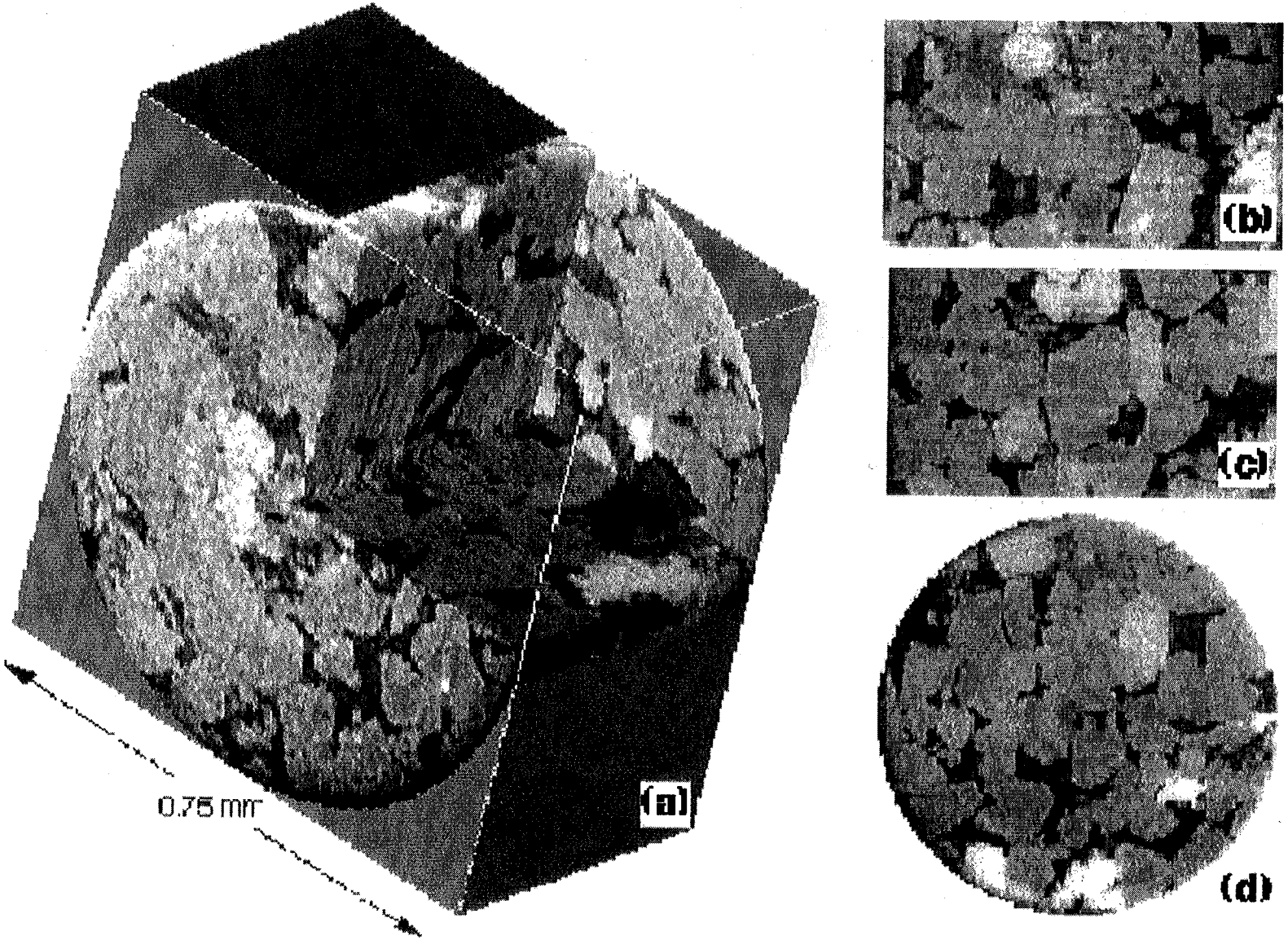

High resolution (2.7 micrometer) CMT subvolume of a North Sea Brent sandstone, k = 470 md:
a) 3-D perspective with cutaway, b) X-directional slice, c) Y-directional slice, d) Cross section.

Courtesy of Mary Coles & Randy Hazlett, Mobil Corporation

FUTURE PLANS

- **Addition of Monochromator for Source Energy Optimization for Contrast Enhancement & Reduction of beam hardening artifacts**

- **Characterize system resolution limits; optimize resolution of small samples**

- **Combine 3rd generation scheme with scanning (1st generation) technique to cover large samples without loss of resolution from zooming out**

- **Two dedicated X-Ray Microtomography Stations**
  - **PRT, User-dedicated facility**
  - **R&D facility for various tomographic techniques, such as phase contrast, fluorescence, edge-enhancement techniques, k-edge subtraction**